Paleozoic geodynamic evolution of Yili Blockin West Chinese Tianshan

Bo Wang

THÈSE PRÉSENTÉE À L'UNIVERSITÉ DE NANJING

POUR OBTENIR LE GRADE DE

DOCTEUR DE L'UNIVERSITÉ D'ORLÉANS

EN COTUTELLE

Discipline : Sciences de la Terre et de l'Univers

Spécialité : Géologie Structurale et Géodynamique

Par

WANG BO

Evolution géodynamique du Bloc de Yili (nord-ouest Chine) au Paléozoïque

Soutenue publiquement le 29 septembre 2006 devant le jury composé de :

M. **Zuyi ZHOU**	Professeur, Université de Tongji	Président
M. **Michel FAURE**	Professeur, Université d'Orléans	Directeur de thèse
M. **Liangshu SHU**	Professeur, Université de Nanjing	Directeur de thèse
M. **Dominique CLUZEL**	Professeur, Université d'Orléans	Rapporteur
M. **Yan CHEN**	Professeur, Université d'Orléans	Rapporteur
M. **Jacques CHARVET**	Professeur, Université d'Orléans	Rapporteur
M. **Jun GAO**	Chercheur, IGG-CAS	Examinateur
M. **Wenbin ZHU**	Professeur, Université de Nanjing	Examinateur

Evolution géodynamique du Bloc de Yili (nord-ouest Chine) au Paléozoïque

Résumé

Le Bloc de Yili est un domaine triangulaire limité par les branches nord et sud du Tianshan Chinois occidental. Il est considéré comme un micro-continent avec un substratum précambrien qui se prolonge vers l'Ouest au Kazakhstan, mais ses limites ne sont pas claires. Le Bloc de Yili est important pour comprendre l'évolution géodynamique du Tianshan Paléozoïque qui résulte de processus de subduction et collision polyphasés. Classiquement, la chaîne du Tianshan est divisée en trois domaines: le Tianshan Nord, le Tianshan Central et le Tianshan Sud. Mais nos travaux structuraux, géochimiques et paléomagnétiques suggèrent que ces domaines et leurs limites doivent être redéfinis.

Le bloc de Yili était auparavant considéré comme l'extension vers l'Ouest du Tianshan Central. En fait, il s'agit d'un arc magmatique Dévonien-Carbonifère situé sur un socle continental protérozoïque et une plate-forme sédimentaire du Paléozoïque inférieur. Des roches volcaniques d'âge Carbonifère sont très répandues sur les bordures du bloc de Yili. Leurs caractéristiques pétrologiques et géochimiques montrent 1) qu'il s'agit surtout d'andésites, de rhyolites et plus rarement de basaltes appartenant à la série calco-alcaline, 2) que les importantes anomalies en Nb et Ta s'accordent avec des magmas liés à une subduction, 3) que les dicriminations fondées sur les HFSE placent ces roches dans le champ des arcs continentaux. Les études isotopiques Rb-Sr et Sm-Nd indiquent que ces roches magmatiques sont issues d'un réservoir magmatique situé dans le manteau appauvri. En considérant les formations sédimentaires de faible profondeur associées au magmatisme, on suggère que les roches magmatiques carbonifères se sont formées sur une marge continentale active. Des datations, par ICP-MS ablation laser, de zircons issus de roches volcaniques et granitiques de l'ensemble du bloc de Yili, indiquent des âges compris entre 389 et 310 Ma, c'est à dire fini Dévonien moyen à Carbonifère supérieur.

La limite Nord du Bloc de Yili est représentée par les turbidites du Carbonifère supérieur et le mélange ophiolitique de Bayingou-Motuogou qui constituent le Tianshan Nord. Les données pétrologiques et géochimiques suggèrent que les turbidites et le mélange ophiolitique représentent un complexe de subduction. Le mélange ophiolitique résulterait d'une tectonique intraocéanique suivie de resédimentation et de déformation pendant la subduction du bassin océanique du Nord-Tianshan qui existait au moins depuis le Dévonien supérieur-Carbonifère inférieur d'après les faunes de radiolaires des cherts ophiolitiques. Les données structurales, pétrologiques, géochimiques et géochronologiques sur le mélange ophiolitique et les turbidites sont en faveur d'une subduction du bassin océanique de Nord-Tianshan vers le Sud, est responsable de la formation de l'arc magmatique de Yili. Comme ce complexe de subduction a été redéformé et charrié vers le Nord sur le bassin Cénozoïque du Junggar, la véritable suture du Nord Tianshan est cachée par les chevauchements cénozoïques. La prolongation orientale du Nord Tianshan se trouve dans l'arc de Bogda qui est composé de sédiments carbonifères, de volcanites et de granitoides. De nouvelles données géochimiques dans la région de Houxia indiquent que les dolérites, andésites et dacites rhyolitiques sont des volcanites d'arc d'affinité calco-alcaline. La cohérence temporelle et la corrélation spatiale entre le complexe de subduction du Tianshan Nord

et l'arc de Bogda suggèrent que la suture du Tianshan Nord se prolonge vers l'est, où elle serait cachée sous l'arc de Bogda par le chevauchement tertiaire.

La limite sud du bloc de Yili est une zone complexe polydéformée qui contient des roches métamorphiques de haute-pression (HP), des mélanges ophiolitiques, un socle fait de roches métamorphiques crustales et de roches sédimentaires de plate-forme, le tout affecté par des décrochements. L'étude géologique détaillée le long de la rivière Kekesu révèle l'existence d'une déformation ductile à faible pendage et dirigée vers le nord qui affecte des roches océaniques métamorphisées dans des faciès de HP (schistes bleus et éclogite) et des roches continentales interprétées comme la bordure méridionale du bloc de Yili. Des preuves d'une déformation ductile extensive dans le faciès schiste vert sont également rencontrées le long de la Rivière Kekesu. Des datations Ar/Ar par sonde laser de micas blancs dans des métapélites issues de schistes bleus rétromorphosés et de quartzites dans le faciès schiste verts donnent des âges compris entre 330 et 315 Ma qui sont interprétés comme l'âge de la fin de l'exhumation des roches de HP. La formation des roches de HP a été interprétée comme associée à une subduction vers le nord de l'océan du Tianshan, également responsable du magmatisme d'arc de la partie sud de Yili. Cependant, comme le magmatisme d'arc du bloc de Yili est significativement plus jeune que le pic du métamorphisme prograde (antérieur à 350 Ma) et même que la rétromorphose, et que l'analyse cinématique indique un mouvement vers le Nord, cette interprétation n'est pas étayée par nos données. Par ailleurs, la structure de la rivière Kekesu est en accord avec les données cinématiques vers le nord observées dans la région de Mishigou et Gangou, plus à l'Est. Cette dernière correspond à la suture entre le Tianshan Nord et Central. Dans le Tianshan Central, au sud du complexe métamorphique de HP, il n'existe pas d'arc magmatique Carbonifère, mais un arc Ordovicien -Silurien et des turbidites du même âge. Des calcaires et des grès du Carbonifère inférieur recouvrent en discordance l'arc d'âge Paléozoïque inférieur. Des roches métamorphiques protérozoïques représentent le substratum de cet arc.

Dans les régions de Aheqi, Wushi, Heiyingshan, sur le versant sud du Tianshan, on rencontre un mélange ophiolitique contenant des blocs de gabbros datés à 390 Ma avec une signature géochimique de bassin d'arrière arc. Par ailleurs, l'évolution de la plate-forme carbonatée du Tianshan Central vers des roches siliceuses (cherts rubanés et pélites siliceuses) suggère un approfondissement de cette marge continentale pendant le Dévonien. Ces données s'accordent avec l'existence d'un bassin marginal entre le Tianshan Central et le Tarim. Les observations de terrain suggèrent que le mélange est charrié du Sud vers le Nord sur les séries carbonatées dévoniennes du Tianshan Central. Cette déformation ductile s'est produite avant le dépôt des séries terrigènes et carbonatées du Carbonifère inférieur-moyen qui recouvrent en discordance le mélange ophiolitique et son substratum tectonique. Il faut cependant remarquer que les séries carbonifères sont déformées par des plis, parfois synschisteux, à vergence Sud. Mais l'âge de cette déformation n'est pas établi avec certitude. Il est peut-être Cénozoïque, mais des âges compris entre le Permien et le Paléocène ne peuvent pas être définitivement écartés. Ces observations sont en bon accord avec celles de la région de Kulehu et de Kumux-Yushugou. Ce mélange ophiolitique correspond au Tianshan sud, il a été souvent interprété comme des klippes déplacées du Nord vers le Sud. Dans notre interprétation, il est au contraire issu d'une suture méridionale qui sépare le Tianshan du Tarim.

Les deux limites nord et sud du bloc de Yili ont été redéformées par les décrochements permiens. Les turbidites du Tianshan Nord sont affectées par une foliation verticale et une

linéation horizontale associée à une cinématique dextre. Nos datations Ar/Ar sur roche totale indiquent un âge de 270 Ma qui correspond au mouvement de la faille du Tianshan Nord. Ceci s'accorde avec les données disponibles sur la Faille Principale du Tianshan (MTSF) où les datations se distribuent entre 280 et 250Ma. Les failles de Nalati et de Qinbulak recoupent la limite entre les blocs de Yili et du Tianshan Central. Nos observations en plusieurs points entre Kekesu, Laerdun, Sanghuyanzi confirment la cinématique dextre. Ces mouvements coulissants sont associés à un magmatisme intraplaque, représenté par des granites alcalins, des basaltes tholéiitiques continentaux, et des roches volcaniques acides. Les décrochements permiens apparaissent comme complètement indépendants de la tectonique de convergence N-S du Paléozoïque pré-permien. Ces coulissements jouent un grand rôle dans l'architecture finale du Tianshan.

Afin de mieux contraindre les mouvements coulissants d'âge Permien, des données paléomagnétiques ont été acquises sur des roches d'âge Ordovicien, Carbonifère et Permien dans le bloc de Yili et les régions voisines. Plus de 500 échantillons de roches volcaniques et sédimentaires ont été prélevés sur 61 sites. Les études magnétiques (minéralogie, démagnétisation, etc…) montrent que les porteurs de l'aimantation sont la magnétite et l'hématite. Après une étude soignée des caractéristiques de l'aimantation rémanente dans la région de Zhaosu, Xinyuan et Gongliu, deux pôles pour le Carbonifère supérieur (C2) et Permien supérieur (P2) sont calculés pour le bloc de Yili. La comparaison de ces pôles C2 et P2 avec ceux du même âge disponibles pour le Tarim, le Junggar et la Sibérie indique 1) qu'il n'y a pas de mouvement différentiel significatif entre le Bloc de Yili et le Junggar depuis le Carbonifère terminal ; 2) qu'il n'y a pas de mouvement latitudinal significatif entre ces blocs depuis le Carbonifère supérieur ; 3) qu'il existe des rotations anti-horaires d'environ 46± 15° et 32±15° entre l'ensemble Yili-Junggar par rapport au Tarim et à la Sibérie entre C2 et P2. Ces rotations sont accommodées par les décrochements dextres le long des failles bordières nord et sud du bloc de Yili et par le décrochement senestre de l'Irtish dans l'Altaï. Il en résulte un mouvement relatif d'environ 1000 et 600 km sur ces deux failles.

Finalement, en tenant compte des déformations Cénozoïques liées à la collision Inde-Asie, un modèle simple de l'évolution du bloc de Yili et de l'ouest du Tianshan chinois est proposé. Pendant l'Ordovicien et le Silurien inférieur, un bassin océanique appelé l'Océan Tianshan existait entre le Tianshan Central et le Bloc de Yili. Cet océan a commencé à se fermer par subduction vers le Sud pendant l'Ordovicien supérieur et le Silurien inférieur en produisant l'arc du Tianshan Central. Entre le Silurien moyen et le Dévonien moyen, l'Océan Tianshan continue de se fermer. La subduction océanique est suivie par la subduction continentale du Bloc de Yili sous le Tianshan Central qui est responsable de la formation des roches métamorphiques de HP. Simultanément à la fermeture de l'Océan Tianshan, une mer marginale s'ouvre au sud du Tianshan Central pendant le Dévonien inférieur à moyen. Pendant le Paléozoïque inférieur, les dépôts de grès et de calcaires suggèrent que la marge nord du bloc de Yili était une marge passive. Entre le Dévonien moyen et le Carbonifère inférieur, à cause de la fermeture de l'Océan Tianshan, les blocs de Yili et du Tianshan Central sont soudés pour former une seule masse continentale. A ce moment là, les roches de HP sont exhumées. La fermeture du bassin d'arrière arc est associée au charriage du mélange ophiolitique du Tianshan Sud. Simultanément, la subduction vers le sud d'un bassin océanique, appelé océan Nord Tianshan est responsable de la formation de l'arc magmatique de Yili et du complexe de subduction du Tianshan Nord. La subduction de l'Océan Nord Tianshan

s’achève au Carbonifère supérieur quand se produit la collision entre le Bloc de Yili et le Junggar. A la fin du Carbonifère, la convergence sub-méridienne (par rapport aux coordonnées actuelles) est achevée. Tous les blocs continentaux sont alors soudés. Au Permien, les décrochements dextres d’ampleur plurikilométrique perturbent la géométrie initiale. Par exemple, la continuité de l’arc du Tianshan Nord-Bogda est détruite.

Mots clés : Bloc de Yili, Chaîne du Tianshan, Xinjiang, Carbonifère, Paléozoïque, subduction, décrochement, suture, géochimie, paléomagnétisme, tectonique, géochronologie Ar/Ar, géochronologie U-Pb (ICP-MS).

Paleozoic geodynamic evolution of Yili Block in West Chinese Tianshan

Abstract

The Yili Block is a triangular area bordered by the northern and southern fault zones of the Western Chinese Tianshan Belt, it is considered as a micro-continental block with Proterozoic basement extending westward into Kazakhstan with unclear boundaries. The Yili Block is important for understanding the Paleozoic geodynamic evolution of the Tianshan Belt, which resulted from polyphase subduction-collision orogenies. The Tianshan Belt is classically divided into three subunits: North Tianshan, Central Tianshan and South Tianshan. But our structural, geochemical and paleomagnetic studies suggest that these subunits and their boundaries should be redefined.

The Yili Block, previously considered as a part of the Central Tianshan, is in fact a Late Paleozoic magmatic arc situated upon a Precambrian basement and an Early Paleozoic platform. Carboniferous volcanic rocks are widespread along the margins of Yili Basin. Petrological and geochemical features of Carboniferous volcanic rocks and granitoids show that: (1) volcanic rocks are mainly composed of andesite, rhyolite and minor basaltic rocks, granitoids consist of gabbro, diorite, granodiorite and granite, both volcanic and granitic rocks are belong to the calc-alkaline series, (2) magmatic rocks display prominent Nb-Ta negative anomalies consistent with subduction - related magmas, and (3) HFSE-based discriminations place volcanic rocks in the field of continental arcs, and granitoids in the field of syn-collisional granites or arc-type granites. Rb-Sr and Sm-Nd isotopic studies indicate that these magmatic rocks derived from a depleted magma reservoir of mantle source, and suffered an important contamination of upper crust or terrigenous sediments. Taking into account the shallow water sedimentation associated with the magmatism, the Carboniferous magmatic rocks are suggested to form in an active continental margin setting. Systematic zircon U-Pb ICPMS dating on the volcanic and granitic rocks from the whole Yili Block indicates that their ages range from 389~301 Ma, i.e. Late Middle Devonian to Carboniferous time, but the peak magmatism took place during 360~301 Ma.

The northern boundary of the Yili Block is represented by the North Tianshan Late Carboniferous turbidite and Bayingou-Motuogou ophiolitic mélange. Stratigraphical and petrological studies suggest that the turbidite and ophiolitic mélange form a subduction complex. The ophiolitic mélange was a result of intra-oceanic tectonism and seafloor redeposition and subsequent deformation during the subduction of the North Tianshan oceanic basin, which existed at least during Late Devonian to Early Carboniferous on the basis of the microfossils found in chert of ophiolite. Structural, kinematic, chronological and geochemical evidences from ophiolitic mélange and turbidite argue that a southward subduction of the North Tianshan oceanic basin is responsible for the formation of the Late Paleozoic Yili magmatic arc. Since this subduction complex was redeformed and thrust northward upon the Junggar Cenozoic basin, the real North Tianshan Suture is probably hidden by the Cenozoic thrust. New geochemical studies from Houxia area indicate that the dolerite, andesite and dacitic rhyolite show similar features with those of Yili arc, and therefore correspond to the North Tianshan arc. Temporal consistency and spatial correlation between the North Tianshan subduction complex and the North Tianshan Arc

suggest that the North Tianshan Suture extends probably eastwards until to the north of Bogdashan. More detailed studies are needed to test this conclusion.

The southern boundary of the Yili Block is a complicated deformation zone including high-pressure (HP) metamorphic complex, ophiolitic mélange, Proterozoic basement and platform sedimentary rocks, affected by strike-slip faulting. Detail geological survey along the Kekesu River revealed a top-to-the-North ductile shearing that is developed both in ocean-derived HP rocks and in the southern margin of the Yili Block. Evidences for an extensional event, formed in retrograde greenschist facies conditions, are recognized in the HP metapelites. Ar-Ar laser probe dating of white mica in retrogressed blueschist facies metapelites and in greenschist facies quartzite provides 330-315 Ma ages that are interpreted as the date of the exhumation of the HP rocks. Taking into account the previous results, HP/UHP metamorphism should have taken place earlier than 350Ma. Since the final magmatism of the Yili Arc is significantly younger than both peak metamorphism and retrograde metamorphism, and the top-to-the-North kinematics of the HP rocks, our results do not support the previous interpretation of the north directed subduction of the "South Tianshan Ocean" producing the Yili magmatic arc. Near to the HP metamorphic belt, Ophiolitic mélange of Changawuzi-Qiongkushitai areas extends eastward joining with Gangou - Mishigou ophiolitic mélange, mafic rocks yield ages from Ordovician to Silurian, and the kinematics of Gangou ophiolitic mélange is consistent with that of Kekesu HP metamorphic rocks. To the south of Kekesu HP metamorphic complex, Qiongkushitai and Gangou mélange zone, Ordovician-Silurian arc-type volcano-sedimentary rocks were recognized to be unconformably covered by Carboniferous sandstone and carbonate. Proterozoic amphibolite facies metamorphic rocks are distinguished as the basement of this volcanic arc, which is defined as the Central Tianshan block. Therefore, the metamorphic and mélange zone is interpreted as a southward subduction of Tianshan Ocean beneath the Central Tianshan block generating the Ordovician-Silurian volcanic arc.

In Aheqi, Wushi and Heiyingshan areas, along the southern slope of the Central Tianshan, a Late Devonian-Early Carboniferous ophiolitic mélange includes ca 390 Ma gabbro blocks with a back-arc-basin geochemical affinity. Moreover, the evolution from platform carbonate sedimentation to banded cherts deposition argues for a progressive deepening of the southern margin of the Central Tianshan Block that is responsible for the opening of a marginal oceanic basin between the Central Tianshan and Tarim during the Early to Middle Devonian. Field observation and kinematics suggest that the mélange has been thrust to the North above the deformed Silurian-Devonian volcaniclastic rocks and marble series. This ductile shearing occurred before the deposition of the Lower Carboniferous sandstone and limestone that unconformably cover the mélange and its tectonic substratum. These observations are quite consistent with those from Kulehu and Kumux-Yushugou areas. Therefore, this ophiolitic mélange zone that stretches from Aheqi to Kumux is defined as the South Tianshan Mélange Belt. This mélange has previously often been considered as south-directed tectonic klippes, but our study indicates that they are actually thrust from South to North, and rooted in the southernmost suture of the Chinese Tianshan Belt.

The two boundaries of the Yili Block have been reworked by the Permian strike-slip faulting. North Tianshan Fault redeformed the southern part of North Tianshan Carboniferous turbidite (the northern boundary of the Yili Block). First-hand kinematic results suggest that the North Tianshan Fault is a dextral ductile strike-slip fault, new Ar-Ar whole rock dating constraint this deformation

from 285 to 245 Ma that is consistent with the age of Main Tianshan Shear Zone (280~250Ma). The Nalati Fault that extends eastwards joining with the Qingbulak Fault cut the southern boundary of the Yili Block, kinematic observations from Kekesu, Laerdun Pass and Sangshuyuanzi coherently indicate a dextral shearing, previous chronological study also provide ~280 Ma age. The Permian right-lateral faulting is associated with alkaline magmatic rocks, such as continental tholeiite, felsic volcanic rocks and alkaline granite. Late Permian redbeds and conglomerate are widespread in whole Tianshan Belt and unconformably cover the pre-Permian rocks. Therefore, Permian tectonics appears to be geodynamically distinct from the convergent orogeny of the Tianshan Belt, and plays an important role on the final formation of its present architecture.

In order to better constrain Permian transcurrent tectonics, primary paleomagnetic results on Ordovician, Carboniferous and Permian rocks are obtained from the Yili Block and its adjacent areas. More than 500 sedimentary and volcanic samples were collected from 61 sites. Laboratory measurements on rock magnetism and magnetic remanence indicate that the magnetite and hematite are principal remanent carriers for characteristic remanent magnetization. After careful analysis of reliable characteristic remanences from Zhaosu, Xinyuan and Gongliu areas and detailed discussion on remanence ages, two primary poles of Late Carboniferous and Late Permian are calculated for the Yili Block. Comparison of these paleomagnetic poles of the Yili Block with coeval poles of Junggar, Tarim and Siberia indicates (1) no significant relative motion between the Yili and Junggar blocks since Late Carboniferous, (2) no significant or weak latitudinal relative motion occurred since Late Carboniferous among these blocks, but (3) the 46.2°±15.1° and the 31.6°±15.1° counterclockwise rotations of the Yili-Junggar blocks with respect to Tarim and Siberia took place during Late Carboniferous to Permian. These rotations are accommodated by the Permian dextral strike-slip faults along the northern and southern sides of the Tianshan Belt and sinistral strike-slip faulting along the Erqishi Fault of the Altay Belt, resulting in about 1000 km and 600 km lateral displacements in the Tianshan and Altay belts, respectively.

Finally, on the basis of the removal of Permian lateral displacement and Cenozoic reactivation during the Indo-Asian collision, a simplified evolutionary model involving the Yili Block and its adjacent areas is proposed. During the Ordovician-Early Silurian, an oceanic basin called the Tianshan Ocean existed between the Yili Block and the Central Tianshan Block. This ocean began to close by southward subduction beneath the Central Tianshan during Late Ordovician and Silurian generating the Central Tianshan volcanic arc. From Middle Silurian to Middle Devonian time, the Tianshan Ocean was progressively closing. The oceanic subduction was followed by the continental subduction of the southern part of the Yili Block and resulted in the development of the HP metamorphic complex. Coevally with the closure of the Tianshan Ocean, a marginal sea opened to the South of the Central Tianshan Block, as suggested by the ophiolitic mélange and the progressive deepening of the southern margin of the Central Tianshan Block during the Early to Middle Devonian. During the Early Paleozoic, the limestone and sandstone deposits suggest that the northern margin of the Yili Block was a passive margin. From the Late Devonian to Early Carboniferous, due to the closure of the Tianshan Ocean, the Yili and Central Tianshan Blocks were welded together to form a single continental mass. At that time, the HP metamorphic rocks were exhumed. The closure of the back arc basin was accommodated by a south-directed subduction below the Tarim Block as suggested by the northward thrusting of the

South Tianshan ophiolitic mélange. During Late Mid-Devonian to Early Carboniferous, southward subduction of an oceanic basin, called the North Tianshan Ocean was responsible for the Yili magmatic arc and the North Tianshan accretionary prism. The oceanic subduction ended in Late Carboniferous when the continental collision occurred between Junggar Block and the Yili Block. At the end of the Carboniferous, the N-S convergence finished when all the continental blocks were amalgamated. Permian lateral large-scale displacement dragged the main blocks of Central Asia close to their present position, and probably also disturbed original continuity (e.g. Yili and Bogda magmatic arcs).

Keywords: subductionary suture, strike-slip faulting, kinematics, geochemistry, paleomagnetism, Ar-Ar geochronology, Zircon U-Pb, Yili Block, Tianshan Belt, Paleozoic.

Sommaire

Available online at www.sciencedirect.com
SCIENCE DIRECT®
Journal of Asian Earth Sciences xxx (2006) xxx–xxx
Journal of Asian Earth Sciences
www.elsevier.com/locate/jaes

Geochemical constraints on Carboniferous volcanic rocks of the Yili Block (Xinjiang, NW China): Implication for the tectonic evolution of Western Tianshan

B. Wang [a,b,*], L.S. Shu [a], D. Cluzel [b], M. Faure [b], J. Charvet [b]

[a] Department of Earth Sciences, Nanjing University, Nanjing 210093, China
[b] ISTO UMR 6113, University of Orléans, F45067 Orléans, Cedex 2, France

Received 26 May 2005; received in revised form 20 January 2006; accepted 7 February 2006

Abstract

The Yili Block is important for understanding the Late Paleozoic geodynamic evolution of Central Asia. It is bounded to the north by the Northern Tianshan Carboniferous flysch and ophiolitic mélange. The center of the Block is dominated by Carboniferous sedimentary rocks with intercalation of volcanic rocks. Petrological and geochemical features of these Carboniferous volcanic rocks show that: (1) they belong to the calc-alkaline series, (2) they display prominent Nb–Ta negative anomalies consistent with subduction-related magmas, and (3) HFSE-based discriminations place these volcanic rocks in the field of continental arcs. The depositional evolution of the sedimentary series shows evidence for Carboniferous sedimentation in a basin instead of rifting as previously proposed. All these evidences, together with the occurrence of contemporaneous turbidites and ophiolitic mélange along the northern boundary of the Yili Block, allow us to infer that the northern border of the Yili Block was a continental active margin during the Carboniferous. The Late Carboniferous southward subduction that finally closed the Late Devonian to Early Carboniferous North Tianshan oceanic basin was followed by Permian–Mesozoic polyphase transcurrent faulting.

Keywords: Geochemistry; Volcanic rocks; Continental arc; Carboniferous; Yili Block; Chinese Tianshan Belt

1. Introduction

The "Yili Block" represents the easternmost part of a large continental block, which mainly occurs in Kazakhstan where it is known as the "Ili" block (Sengör and Natal'in, 1996). This large continental unit is bounded by suture zones and large scale strike-slip faults (Fig. 1). It is composed of several tectonic units and their history of amalgamation remains controversial. A first model suggests a progressive growth of the Asian continent in the Paleozoic by colliding fragments in a continuously converging setting (Natal'in and Sengör, 1994; Sengör et al., 1993; Shi et al., 1994; Shu et al., 2000). Alternatively, it has been suggested that the Tarim plate formed during the Late Proterozoic, and thereafter, the Yili Block was rifted from Tarim during the Ordovician. The final suturing event occurred between the Tarim, the Junggar, and the Kazakhstan blocks during the Late Paleozoic (Chen et al., 1999; Gao et al., 1995, 1997, 1998; Ma et al., 1993; Xiao et al., 1992). The final stages of suturing are still poorly understood as well. Models of continuous convergence (Gao et al., 1998; Xiao et al., 1992), or alternatively, marginal rifting and subsequent re-amalgamation (Che et al., 1996; Xia et al., 2003) have been proposed. In this paper, we intend to clarify the Carboniferous evolution of the northern part of the Yili Block by studying the Carboniferous volcanic rocks.

In Western China, the Yili Block geographically lies west of the Xinjiang Uygur Autonomous Region and is geologically one of the main parts of the Chinese Tianshan

* Corresponding author. Tel.: +33 0 2 3849 4660; fax: +33 0 2 3841 7309.
E-mail addresses: bo.wang@univ-orleans.fr, wangbo1996@nju.org.cn (B. Wang).

1367-9120/$ - see front matter © 2006 Published by Elsevier Ltd.
doi:10.1016/j.jseaes.2006.02.008

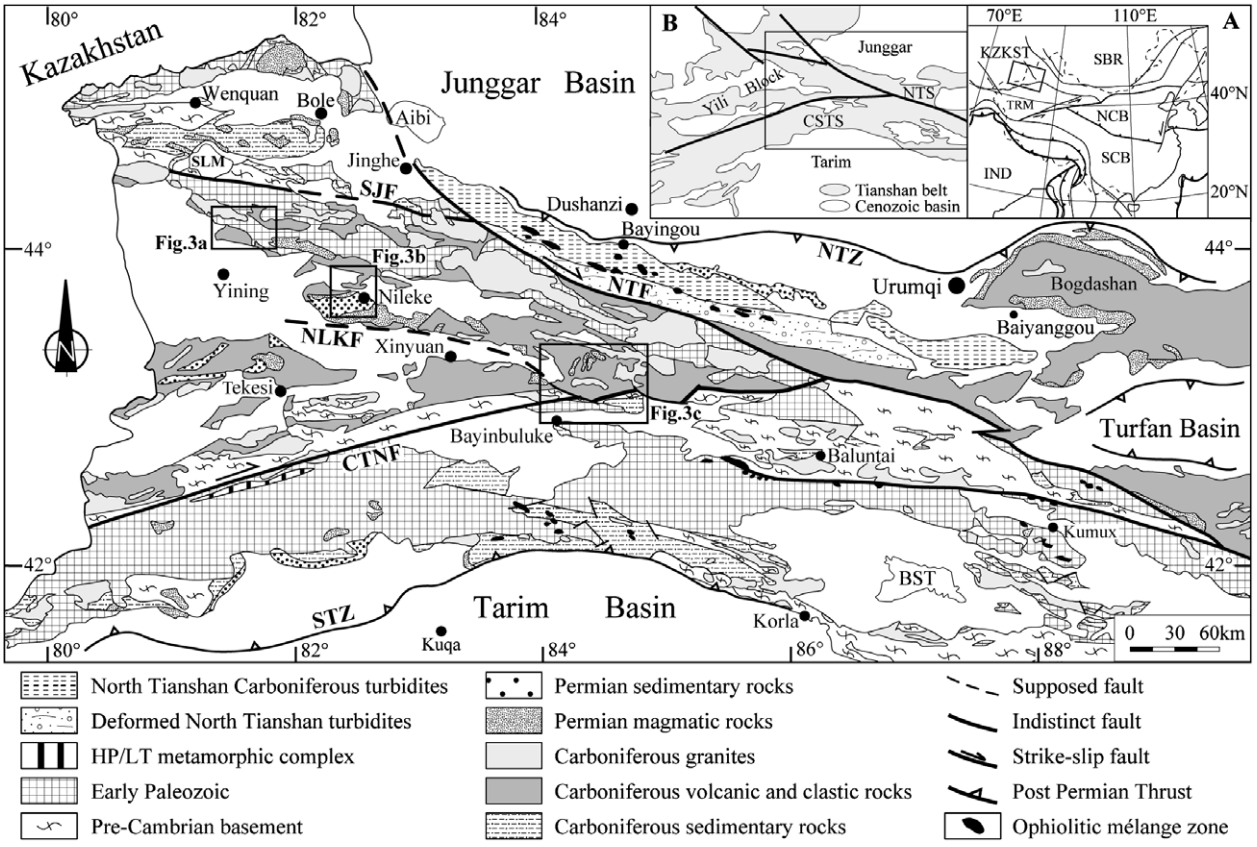

Fig. 1. Simplified geological map of the Western Tianshan Belt showing the localities of the main tectonic boundaries (modified from XBGMR, 1992). Inset A shows the location of inset B, which defines the Yili Block, the North Tianshan (NTS), the Central-South Tianshan (CSTS), Junggar and Tarim. Abbreviations: NTZ, the Northern Thrust Zone; STZ, the Southern Thrust Zone; NTF, the Northern Tianshan Fault; CTNF, the Central Tianshan Northern Margin Fault; SJF, the Sailimu (SLM)-Jinghe Fault; NLKF, the Nileke Fault; SLM, Sailimu Lake; BST, Bositeng Lake. KZKST, Kazakhstan; SBR, Siberia; TRM, Tarim; NCB, North China Block; SCB, South China Block; IND, India.

Belt. It separates the Northern Tianshan (NTS) to the north and the Central-Southern Tianshan (CSTS) to the south, respectively (inset B of Fig. 1). The Yili Block is in contact with the NTS along the North Tianshan Fault (NTF in Fig. 1; Zhou et al., 2001) and with the CSTS along the Central Tianshan Northern Margin Fault (Xiao et al., 1992; CTNF in Fig. 1). The Sailimu (SLM)-Jinghe Fault (SJF in Fig. 1) separates the Yili Block to the south from the "Bole Block" to the north. These boundaries were also defined and discussed by Sengör and Natal'in (1996). Late Paleozoic volcanic and volcano-sedimentary rocks are widely developed in the northern, southern and eastern margins of the Yili Block, while Mesozoic and Cenozoic terrestrial sedimentary rocks cover the interior of the Yili Block, which is called the Yili Basin. The volcanic and volcano-sedimentary rocks were dated as Carboniferous by paleontologic and radiochronologic methods (Li et al., 1998; XBGMR, 1993). Since the 1990's, the tectonic setting of Carboniferous volcanism in the Yili Block has been a matter of debate. It has been interpreted either as an active margin (Gao et al., 1997, 1998; Jiang et al., 1995; Xiao et al., 1992) or as a continental rift (Che et al., 1996; Chen et al., 2001; Xia et al., 2002, 2003). Until now, only a few detailed geochemical data were available and thus the tectonic setting of these rocks was poorly constrained. In this paper, we describe the geochemical features of Yili Carboniferous volcanic rocks, and discuss their tectonic setting in relation to the published data. Geochemical evidence, combined with the occurrence of a Late Carboniferous ophiolitic mélange that crops out to the north of the Yili Block, allows us to propose a simplified model of the geological evolution and final amalgamation of Central Asia during the Late Paleozoic.

2. Geological background

The Yili Block is a triangular area that extends more than 1000 km across the borderlines of China, Kazakhstan and Kyrgyzstan, and its geodynamic evolution since the Late Paleozoic is closely related to the Tianshan Belt (Fig. 1). The eastern part of the Yili Block is one of the main parts of the Western Chinese Tianshan (WTS) Belt, which is bounded by two major active thrusts, the southern thrust zone (STZ) and the northern thrust zone (NTZ) that separate the WTS Belt from the Tarim Basin and the Junggar Basin (Fig. 1), respectively. The Chinese Tianshan Belt is generally divided into three units: the Northern, the Central and the Southern Tianshan belts, which are separated

from one other by regional-scale strike-slip faults (Allen et al., 1993, 1999; Coleman, 1989; Ma et al., 1993; Windley et al., 1990). The geological evolution of the Tianshan Belt has been discussed during the last two decades. Generally, it is considered a result of multiphase amalgamation and accretion of various micro-continents that include the Yili Block, magmatic arcs and terranes throughout the Paleozoic (Coleman, 1989; Shi et al., 1994; Shu et al., 2000, 2002). It was deformed again by Cenozoic intra-continental tectonics and subsequently uplifted in response to the India-Asia collision (Avouac et al., 1993; Burchfiel et al., 1999; Cunningham et al., 1996; Shu et al., 2003; Tapponnier and Molnar, 1979).

The Proterozoic basement of the Yili Block crops out along its boundaries (Fig. 1). The Meso- to Neoproterozoic carbonates and clastic rocks of the Jixian and Qingbaikou formations are developed in the Sailimu Lake (SLM)-Wenquan area and southeast of Tekesi. The Sinian red sandstone and minor "tillite" (Gao et al., 1998; XBGMR, 1993; Xia et al., 2002) are exposed to the south of SLM. Precambrian amphibolite facies metamorphic rocks mainly crop out in the Bingdaban–Baluntai area, south of Urumqi. They were also recognized at Nalati Pass, north of Bayinbuluke, and in the Haerke Mountains, south of Tekesi (Fig. 1), and respectively dated by U–Pb method on zircon at 882 ± 33 Ma (Chen et al., 2000a) and 709 ± 13 Ma (Chen et al., 2000b). Lower and Middle Paleozoic strata are mainly developed along the northern margin of the Yili Block. Cambrian and Ordovician rocks consist of chert, and carbonates and predominantly crop out in the Sailimu Lake and Guozigou area (Fig. 1). Silurian flysch and intercalated calc-alkaline volcanic and volcano-sedimentary rocks are distributed along the southern side of NTF and along the eastern margin of the Yili Block (XBGMR, 1993; Zhou et al., 2001). The Devonian is only represented by granitoids in the Yili Block.

Carboniferous rocks are widespread in the study area and are divided into two parts ranging from Early Carboniferous (C1) to Late Carboniferous (C2). Each part consists of several formations as shown in Fig. 2 that correlate with the international stratigraphic chart (ICS, 2004). The lower part (C1), ca. 3500 m thick, is predominantly composed of limestone, sandstone and shale with subordinate volcanic rocks. The upper part (C2), which unconformably overlies C1, consists of limestone intercalated with volcaniclastic sandstone and massive volcanic rocks (Fig. 2). The base-

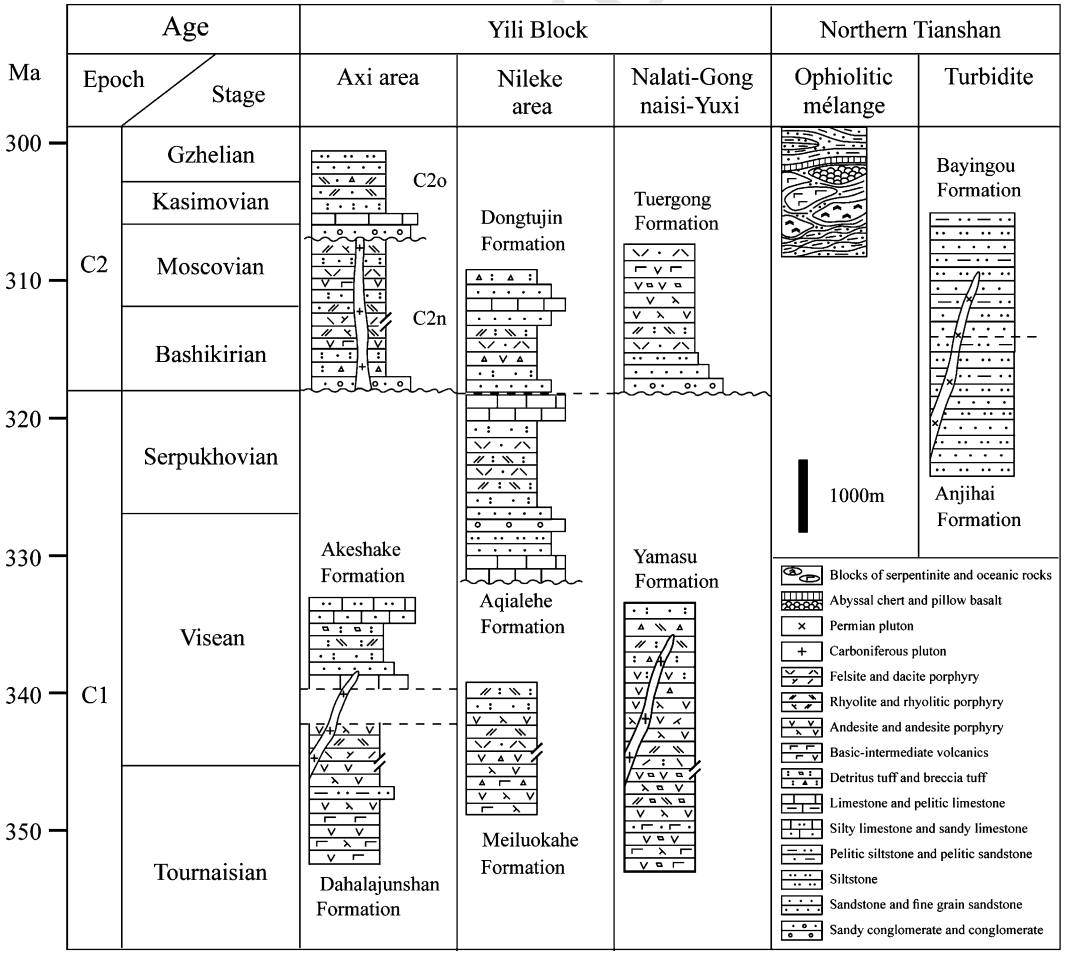

Fig. 2. Schematic Carboniferous chronostratigraphic columns of the Yili Block and the Northern Tianshan Belt compared to the international stratigraphic chart (ICS, 2004). Time scale and stratigraphy modified from XBGMR (1992, 1993). C2o, the Oyiman Formation; C2n, the Naogaitu Formation.

ment and pre-Carboniferous rocks are croscut by voluminous granitoids of Carboniferous age (XBGMR, 1993; Figs. 1 and 2). This lithotectonic unit is quite different from that of the North Tianshan Belt, where Carboniferous rocks consist of turbidite flysch and ophiolitic mélange (Fig. 2). Due to possible tectonic duplication, the thickness of the North Tianshan flysch is difficult to establish. However it is estimated to be between 5000 and 10,000 m thick. On paleontological grounds (ammonoids and plant fossils), the flysch has been correlated to the upper half of C1 to C2 (XBGMR, 1993; Fig. 2). The mélange zone contains metre- to kilometer-scale blocks of Late Devonian to Early Carboniferous oceanic lithosphere such as radiolarian-bearing cherts (Xiao et al., 1992) along with reworked Carboniferous flysch boulders (Fig. 2), and therefore formed during Late the C2 interval.

Permian terrestrial sandstone and conglomerate unconformably overlie all the older rocks. A prominent bimodal volcanic association developed in the Nileke area (Figs. 1 and 3b; Wang et al., 1997; XBGMR, 1992, 1993). Felsic and/or mafic magmatism is also recognized and discussed for the Bayingou area of Bogdashan (Allen et al., 1995; Shu et al., 2005). Permian plutonic rocks are also widespread in the study area. Lateral shear zones deformed the boundaries of the Yili Block during the Late Carboniferous–Early Permian and underwent polyphase reactivation during the early Mesozoic (Bazhenov et al., 1999; Laurent-Charvet et al., 2002, 2003; Shu et al., 1999, 2003).

3. Representative geological sections of Carboniferous volcanic rocks

About 200 samples of Carboniferous volcanic rocks were collected for this study from the Axi section of the northern Yining, the northern Nileke section and the Nalati–Gongnaisi–Yuxi section as shown in Fig. 1. Samples are listed in Table 1 and the sample locations are shown in Fig. 3. The rocks mainly belong to the basic-inter-

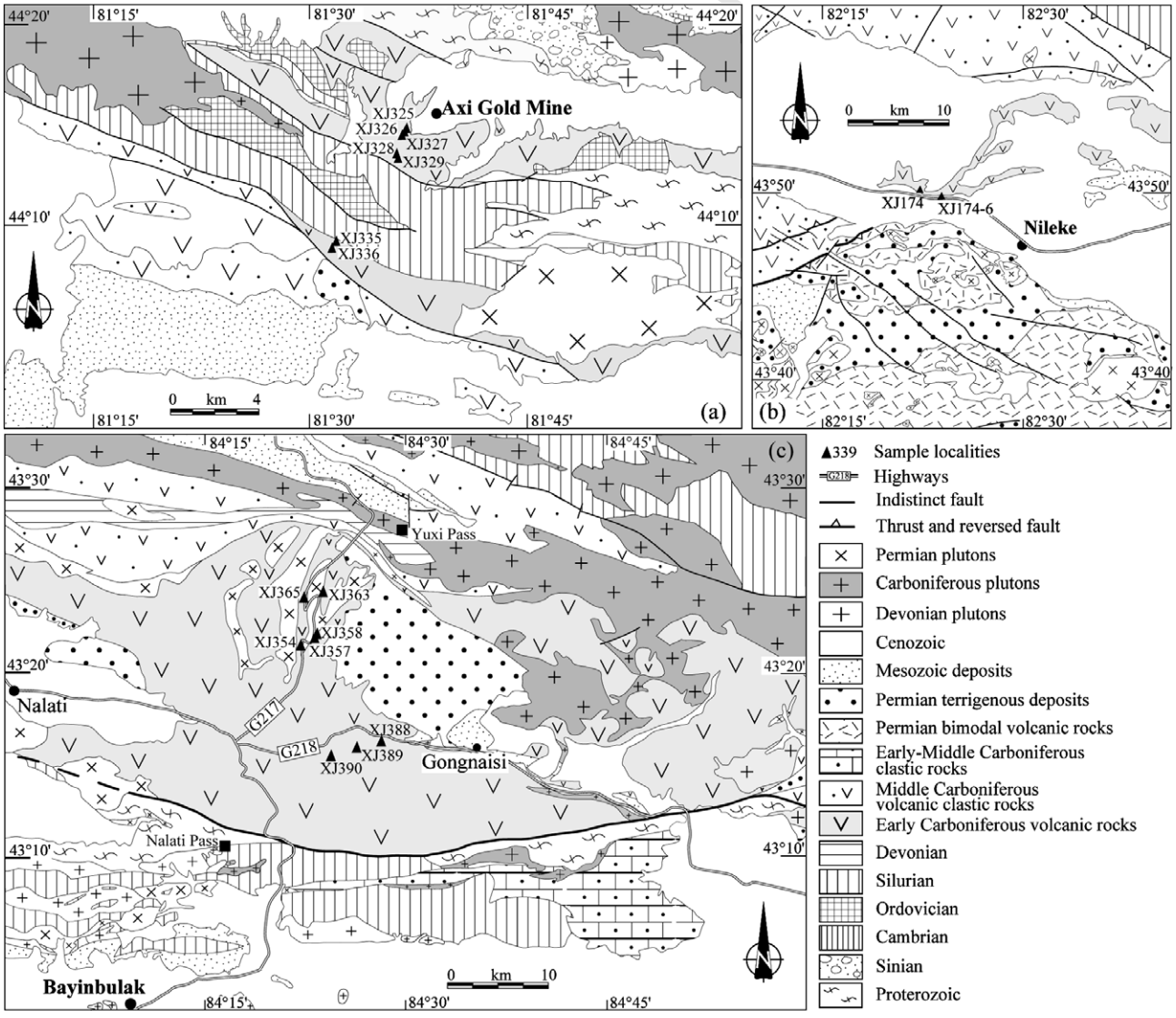

Fig. 3. Geological maps of (a) the Axi section, (b) the Northern Nileke section and (c) the Nalati–Gongnaisi–Yuxi section.

Table 1
ICP-MS whole rock analyzed results of representative samples from the Yili Block

Samples	The Axi section								The Northern Nileke section			The Nalati–Gongnaisi–Yuxi section							
	XJ-325	XJ-326	XJ-327	XJ-328	XJ-329	XJ-335	XJ-335-1	XJ-336	XJ-174	XJ-174-1	XJ-174-6	XJ-363	XJ-365	XJ-388	XJ-389	XJ-390	XJ-354	XJ-357	XJ-358
SiO_2 (wt%)	53.42	54.04	53.18	55.19	59.21	68.81	67.42	68.83	49.70	50.61	66.54	57.43	68.71	46.63	46.56	50.05	56.15	55.93	36.55
TiO_2	0.84	0.85	0.94	1.21	0.90	0.44	0.38	0.43	0.99	0.93	0.71	0.98	0.89	0.94	0.90	1.11	0.85	2.22	1.80
Al_2O_3	16.54	16.78	17.20	16.55	16.32	15.71	14.15	15.62	19.60	19.02	15.86	17.51	13.00	18.44	17.28	18.60	17.63	13.86	26.61
Fe_2O_3	8.21	7.21	7.94	7.52	5.58	3.12	1.91	2.52	10.26	9.74	4.30	7.33	4.18	8.32	8.96	9.65	8.49	10.48	24.62
MnO	0.12	0.13	0.13	0.12	0.10	0.13	0.19	0.11	0.40	0.22	0.14	0.19	0.13	0.70	1.18	0.30	0.20	0.36	0.15
MgO	3.13	3.40	5.98	4.43	3.30	0.36	0.41	0.36	4.33	3.94	1.29	1.56	0.69	3.57	2.67	2.94	1.95	2.82	0.02
CaO	6.83	7.99	3.32	6.97	3.51	1.46	5.06	1.75	4.92	7.19	1.16	2.63	1.12	8.83	6.55	4.52	1.81	3.97	0.26
Na_2O	3.05	2.80	5.21	3.21	3.32	3.88	1.55	4.24	4.80	4.12	5.36	3.68	2.82	2.81	2.66	6.13	3.11	4.43	0.10
K_2O	0.60	0.52	0.22	2.24	2.97	4.12	3.49	3.16	0.99	1.22	4.01	6.53	6.58	3.77	6.27	1.59	7.05	3.40	0.22
P_2O_5	0.16	0.16	0.18	0.25	0.18	0.12	0.11	0.10	0.25	0.24	0.16	0.60	0.19	0.28	0.23	0.22	0.54	0.92	0.58
LOI	8.39	7.79	5.96	2.23	4.42	2.09	5.98	2.51	4.52	2.72	1.21	1.45	0.89	5.88	6.45	5.36	1.73	1.41	9.44
Total	101.29	101.67	100.26	99.91	99.79	100.23	100.64	99.63	100.75	99.95	100.72	99.88	99.20	100.18	99.69	100.46	99.50	99.80	100.36
Sc (ppm)	23.49	24.05	27.27	22.58	16.74	3.552	2.978	3.022	31.2	30.46	12.84	13.86	26.52	24.7	16.64	11.25	27.81	28.36	22.29
Ti	4746.1	5096.7	5484.9	8417	5237.1	2756.1	2351.7	2557.1	5655.1	5459.4	4134.3	4924.2	15014	10797	5405.7	4987.2	5444.6	4921.4	5844.7
V	130.4	180.3	229.6	197.3	129.8	18.59	21.31	15.8	253.5	243.2	45.46	102.4	169.6	572.9	105.4	12.17	278.6	241.8	231.4
Cr	62	65.07	95.27	62.18	74.07	3.014	2.759	5.727	33.8	30.53	5.416	10.58	2.697	50.92	5.476	10.77	85.73	16.89	10.82
Mn	866.8	937.8	975.8	920.9	738	939.9	1410.8	801.3	2865.6	1704.8	989.7	1502.7	2534	1029.5	1366.7	870.5	5174.8	6698.6	2034.2
Co	18.69	20.47	26.23	21.56	16.95	4.174	2.22	3.538	28.47	26.94	5.944	12.66	17.33	13.02	23.52	2.124	28.56	14.45	32.86
Ni	21.45	22.84	33.06	41.01	32.13	2.519	4.616	4.754	18.44	18.97	3.471	7.678	2.95	16.96	13.73	6.644	59.24	11.36	21.67
Cu	20.78	71.54	174.2	60.34	70.41	5.416	16.06	5.83	22.58	84.56	11.31	156.8	9.101	22.39	295.8	5.357	21.95	50	34.76
Zn	64.45	56.89	69.08	71.22	57.55	70.74	74.71	110	254.5	90.27	153.6	135.4	172.6	46.38	101.7	147.6	667.1	398	158.7
Ga	17.07	18.26	23	19.09	19.01	18.83	17.4	18.75	17.36	18.36	15.63	17.72	18.46	32.86	17.75	13.75	18.68	16	17.71
Ge	0.879	0.957	1.271	1.245	0.966	1.09	1.471	1.258	0.983	1.25	1.155	1.434	1.677	2.2	1.174	1.251	1.311	1.394	0.855
Rb	24.08	22.9	5.84	86.8	126	142.2	141.2	111.4	21.87	27.52	118.2	262.6	162.9	9.573	252.5	196.3	144.7	295.4	84.55
Sr	194.8	201.9	124.4	463.3	194.2	145.5	86.66	128.5	457.2	613.1	105.4	221.6	338.4	4382	344.2	19.96	486.8	509.3	306.7
Y	19.29	21.09	23.3	30.77	26.19	26.9	25.31	29.24	18.78	19.55	34.7	28.36	54.52	22.94	30.9	59.77	22.13	19.8	27.84
Zr	124.7	134.5	165.2	220.2	209	208.8	189.8	210.8	62.81	78.11	261.8	222.2	237.5	212.2	198.4	352.8	79.16	61.46	113.4
Nb	5.976	6.396	8.115	10.35	11.11	34.39	31.53	32.51	3.158	3.16	13.33	10.3	9.415	9.828	10.97	13.49	3.524	2.445	4.302
Ba	575.6	180.4	26.37	353.8	538.4	638.4	99.68	441.5	197	339.7	933.2	928.3	772.3	141.7	682.5	183.4	883.5	2234.9	108.2
La	14.73	15.17	18.67	23.11	27.55	49.49	41.37	50.25	10.23	10.18	36.72	29.06	26.29	38.68	37.54	25.54	19.29	12.6	10.73
Ce	32.35	34.03	41.36	50.95	58.06	93.61	81.05	95.04	22.99	22.28	73.64	68.6	62.48	164.6	79.44	62.73	37.59	26.94	25.06
Pr	3.938	4.202	5.078	6.22	6.757	10.19	8.941	10.63	3.109	2.979	8.309	8.586	8.559	39.01	10.51	8.941	4.793	3.529	3.541
Nd	15.99	17.42	20.14	25.38	26.29	35.51	31.35	36.66	13.96	13.48	32.66	34.45	39.06	213.2	42.66	39.34	20.68	16.06	15.63
Sm	3.7	3.878	4.389	5.507	5.571	6.021	5.839	6.225	3.237	3.257	6.592	7.41	9.726	36.19	8.467	9.875	4.86	3.835	4.046
Eu	0.99	1.053	1.232	1.307	1.169	1.181	1.422	1.164	1.189	1.13	1.52	1.462	2.719	5.207	1.72	2.317	1.297	0.953	1.335
Gd	3.874	3.998	4.641	5.682	5.267	4.922	5.164	5.132	3.757	3.653	6.897	6.581	11.17	7.621	7.151	11.03	4.89	4.202	4.921
Tb	0.62	0.642	0.707	0.904	0.839	0.807	0.817	0.834	0.573	0.559	1.051	0.961	1.664	0.782	1.025	1.729	0.72	0.614	0.776
Dy	3.551	3.769	4.176	5.268	4.875	4.623	4.31	4.694	3.441	3.346	6.177	5.204	9.904	3.867	5.476	10.37	4.113	3.555	4.787
Ho	0.709	0.746	0.858	1.06	0.988	0.916	0.816	0.952	0.695	0.674	1.27	1.025	1.974	0.842	1.091	2.115	0.815	0.728	0.995
Er	2.04	2.086	2.339	2.922	2.685	2.609	2.336	2.685	1.904	1.863	3.62	2.843	5.419	2.631	3.073	6.183	2.175	2.013	2.801
Tm	0.316	0.322	0.364	0.437	0.417	0.4	0.353	0.426	0.277	0.294	0.573	0.447	0.802	0.458	0.454	0.946	0.336	0.303	0.447
Yb	2.108	2.212	2.403	2.951	2.639	2.813	2.393	2.941	1.869	1.9	3.879	2.892	5.309	3.422	3.07	6.316	2.22	2	2.898
Lu	0.335	0.366	0.394	0.481	0.426	0.475	0.388	0.493	0.308	0.311	0.663	0.486	0.857	0.569	0.498	1.035	0.362	0.325	0.477
Hf	3.437	3.521	4.16	5.405	5.744	5.825	5.012	5.577	1.673	1.951	7.012	4.807	5.962	4.996	4.989	9.168	2.066	1.692	2.804
Ta	0.437	0.446	0.567	0.701	0.874	2.34	2.087	2.193	0.183	0.194	0.866	0.666	0.611	0.558	0.686	0.845	0.204	0.146	0.261
Th	4.016	4.128	5.895	7.989	10.87	23.85	20.69	22.23	1.272	1.217	11.12	16.07	6.425	10.78	17.55	10.06	4.351	2.883	1.97
U	1.043	1.139	1.558	1.994	3.119	4.147	4.922	4.513	0.39	0.337	2.846	2.996	1.979	3.061	4.297	2.811	1.124	1.059	0.551

mediate volcanic series, but also include a few acidic volcanic rocks, tuff, and greywackes.

3.1. The Axi section

This section is located 30 km to the north of Yining City. It is composed of sandstone and basic to intermediate volcanic rocks (Fig. 3a). In the northern part of the section, the Early Carboniferous volcanic rocks are correlated to the Dahalajunshan Formation (C1d) (XBGMR, 1993). Pyroxene-bearing andesites yield a Rb–Sr whole rock–mineral isochron age of 345.9 ± 9 Ma and a ^{40}Ar–^{39}Ar plateau age of 325.1 ± 0.6 Ma (Li et al., 1998). The Dahalajunshan Formation is mainly composed of basalt, andesite and minor rhyolite and dacite. The Dahalajunshan Formation is overlain unconformably by the Akeshake Formation (C1ak), which is mainly composed of sandstone and limestone (XBGMR, 1993). To the south, the intermediate to acidic volcanic and volcano-sedimentary rocks in the lower part of the Late Carboniferous Naogaitu Formation (C2n) are overlain by limestone, mudstone, siltstone and sandstone of the Oyiman Formation (C2o) (Fig. 2).

3.2. The northern Nileke section

Along the highway to the northeast of Nileke County (Fig. 3b), the Aqialehe Formation (C1a) (Fig. 2; XBGMR, 1993) consist of intermediate to acidic volcaniclastic rocks.

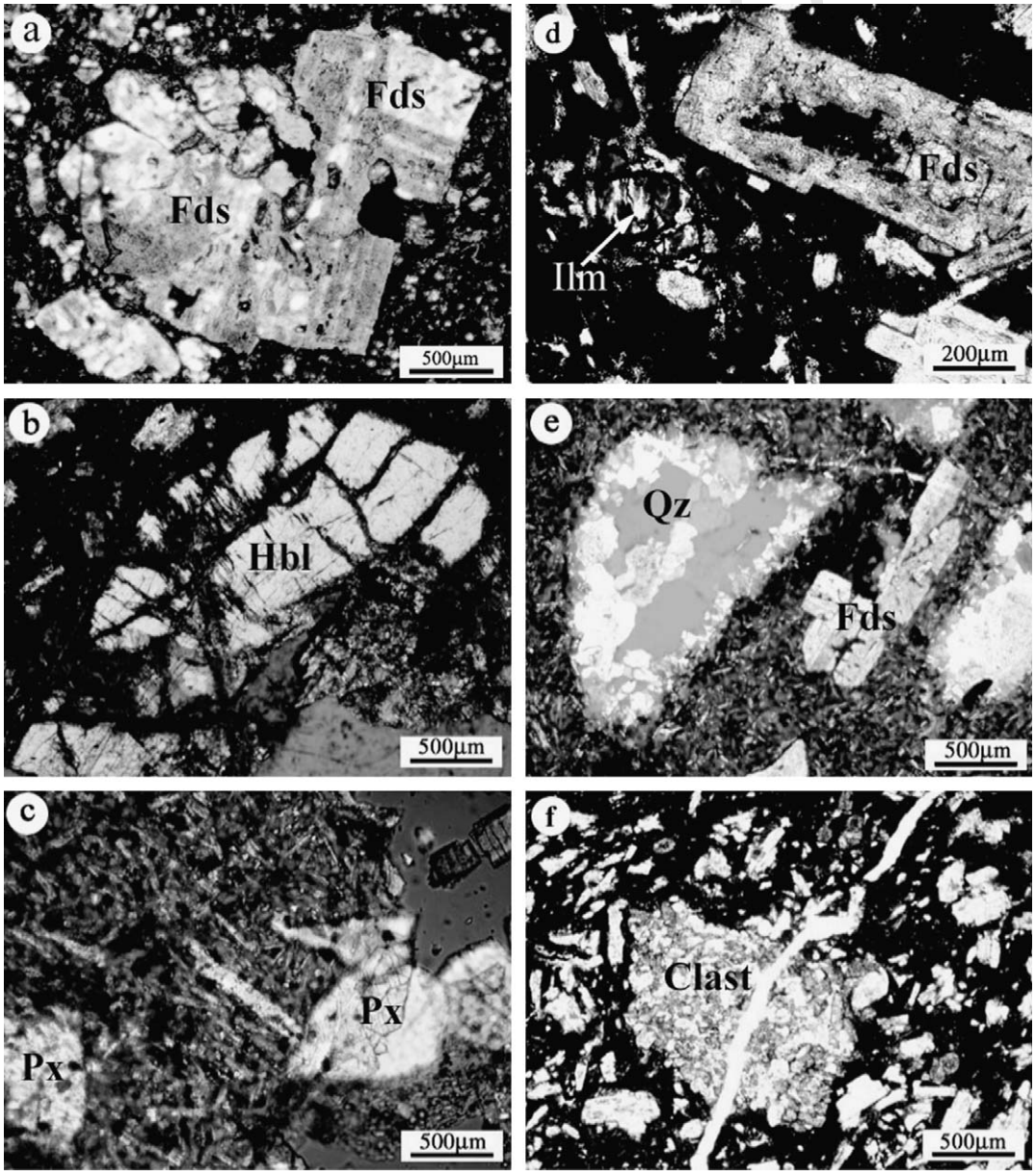

Fig. 4. Photomicrographs of volcanic rocks of the Yili Block. (a) Sample XJ174-6 showing volcanic micro-texture and feldspar phenocrysts with multiple twins, (b) hornblende phenocrysts in sample XJ388, (c) sample XJ328 showing pyroxene phenocrysts and plagioclase needles in the matrix, (d) strongly altered feldspar and ilmenite mineralization in sample XJ325, (e) sample XJ365 showing feldspar and quartz-infilled vesicle, (f) andesite clast in sample XJ325. Abbreviation of minerals: Fds: feldspar; Hbl: hornblende; Px: pyroxene; Ilm: ilmenite; Qtz: quartz.

Although no age was documented for these volcanic rocks, they are correlated with the Early Carboniferous rocks that laterally crop out in the Borohoro Mountains, south of NTF (XBGMR, 1993; Fig. 1). In this area, Early Carboniferous rocks consist of sandstone, conglomerate and limestone in the lower part, while volcanic and volcaniclastic rocks are predominate in the upper part (XBGMR, 1993; Che et al., 1996). In this section, basalt, andesite, tuffaceous andesite, dacite, rhyolite, volcanic breccia and greywacke are widespread with intercalation of tuffaceous-sandy rhythmites. Fragments of feldspar and quartz phenocrysts, clasts of andesite, pyroclastic rock and clastic rock may be observed both in hand-samples and in thin sections (Fig. 4).

3.3. The Nalati–Gongnaisi–Yuxi section

This section includes two segments from Nalati County to Gongnaisi along the G218 National highway, and from Nalati to Yuxi along the G217 national highway, respectively (Fig. 3c). Both segments are mainly composed of Carboniferous andesitic rocks, unconformably overlain by Early Permian conglomerate, sandstone and siltstone (XBGMR, 1993). Both the volcanic rocks and the sedimentary strata are intruded by undated basic-intermediate dykes (XBGMR, 1992). The Nalati–Yuxi segment is composed of a large volume of porphyritic andesite referred to as the Yamansu Formation (C1y) (Fig. 2) and characterized by 2–5 cm andesine phenocrysts. The Yamansu Formation is overlain by the C2 terrigenous deposits yielding plant fossils (XBGMR, 1993) that suggest an Early Carboniferous age. In the Gongnaisi area, the unconformable Late Carboniferous siltstone, sandstone and conglomerate also display prominent volcanic rocks matched by a more diverse series of volcanic rocks: porphyritic andesite and dacite, felsitic porphyry, albitophyre and intermediate-acidic tuff.

4. Petrography and mineral composition of volcanic rocks

In most of the volcanic rocks, the plagioclase phenocrysts are altered to calcite and/or albite. Phenocryst and glass matrix can be commonly identified (Figs. 4a–e). The volcanic rocks are dominated by euhedral to subhedral plagioclase occurring both as phenocrysts and as fine needles in the groundmass (Figs. 4c and e), some of which show multiple twins and compositional zonation (Figs. 4a and d–e). Hornblende is frequently observed as phenocrysts (Figs. 4b and c) and in the groundmass, some parts of the hornblende having been altered to epidote and chlorite. Vesicles in some samples were filled with calcite and microcrystalline quartz (Fig. 4e). Clasts of andesite are observed in some samples (Fig. 4f).

Four polished thin sections of andesite from the northern Nileke section and the Nalati–Gongnaisi–Yuxi section were analyzed for mineral composition. Analysis was made on a JEOL JXA-8800 M electron microprobe located at the State Key Laboratory of Mineral Deposits, Nanjing University. Analysis was at 20 kV with a 2×10^{-8} Å electron beam width. Synthetic and natural minerals were used as standards. The analytical results (Table 2) show that most of the plagioclase grains are albite and some grains have been replaced by calcite. This is evidence of low temperature recrystallisation. Therefore the "mobile element" compositions are to be considered carefully for geodynamic interpretation.

5. Geochemistry and geological implications

5.1. Analytical methods

Nineteen representative samples of the three sections were analyzed for geochemical study. Major elements were determined by X-ray fluorescence (XRF) following the procedure described by Janney and Castillo (1997). Trace elements, including rare earth elements (REE), were determined by a PE-Elan 6000 ICP-MS. Both analyses were performed at the Guangzhou Institute of Geochemistry, Chinese Academy of Sciences. The analytical technique for ICP-MS analysis is similar to that described by Li (1997). Analytical errors are 1–3% for major elements and generally less than 0.7–10% for most trace elements. Major and trace elements data are shown in Table 1.

Table 2
Electron microprobe analyzed data of mineral compositions of andesite in the Yili Block

Samples	XJ325			XJ354			XJ388			XJ390		
Analyses	1	2	3	4	5	6	7	8	9	10	11	12
Minerals	Ab(C)	Ab(C)	Si(R)	Ab(C)	Ab(C)	Ab(C)	Hbl(C)	Cal(C)	Hbl(C)	Cal(R)	Ab(C)	Ab(C)
Na_2O	11.673	0.076	0.007	10.112	11.669	10.235	0.407	0.078	0.314	0.036	10.349	9.368
K_2O	0.115	0.016	0.025	0.237	0.069	0.273	0.023	0.004	–	0.018	0.58	0.688
MnO	0.004	0.301	–	0.015	–	0.007	0.093	2.18	0.148	1.447	0.089	–
MgO	0.906	1.757	0.146	1.528	0.004	0.058	13.388	0.393	14.693	0.412	0.064	0.081
TiO_2	0.038	0.139	0.08	0.037	0.005	–	0.777	0.008	0.477	–	0.093	0.016
FeO	0.457	0.799	3.65	0.628	0.059	0.309	7.884	0.45	7.199	0.329	0.633	0.711
Al_2O_3	22.086	0.62	0.441	20.91	20.553	21.542	5.99	0.155	4.141	0.151	21.831	22.216
CaO	0.443	52.54	–	3.477	2.195	0.342	22.007	56.584	21.744	56.743	0.586	0.617
SiO_2	65.48	3.236	93.364	62.838	66.628	67.133	48.7	1.321	49.718	0.382	66.695	65.999
Total	101.2	59.484	97.713	99.782	101.18	99.899	99.269	61.173	98.434	59.518	100.92	99.696

Abbreviations: Ab = albite. Si = silica. Cal = calcite. Hbl = hornblende. C = center. R = rim.

5.2. Results

Some samples exhibit relative high loss of ignition (LOI), especially samples XJ325, XJ326 and XJ358 that have LOI > 7% (Table 1). The compositions of mobile elements are likely to have changed and geochemical discriminations based on these elements cannot be used. Therefore in the following section, we only use geochemical diagrams based upon "immobile" elements such as REE, Zr, Ti, Yb, etc.

On the Nb/Y versus Zr/Ti diagram (Fig. 5; Winchester and Floyd, 1976), volcanic rocks from each section are divided into three sub-groups: andesite (including one basaltic andesite), rhyodacite and trachyandesite. This diagram shows a linear differentiation trend within the calc-alkaline series field. Three samples (XJ335, XJ335-1 and XJ336) from the Axi section plot in the trachyandesite field due to their distinctive lower Ti contents that likely resulted from ilmenite fractionation.

All the analyzed volcanic rocks have relatively high total REE concentrations ranging from 66 to 219 ppm (Table 1).

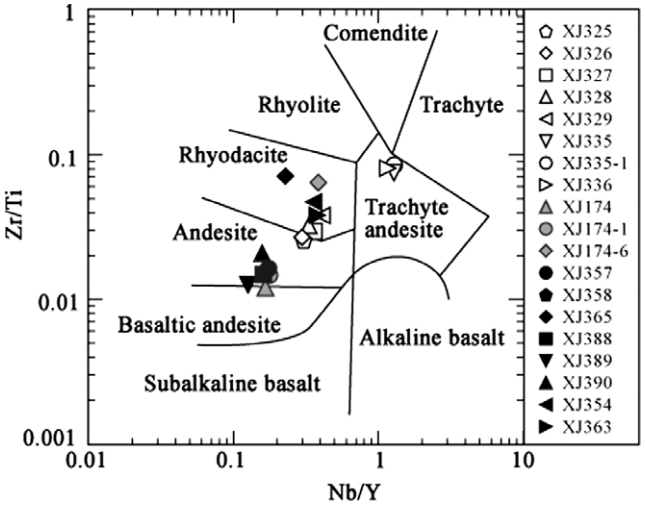

Fig. 5. Nb/Y versus Zr/Ti diagram (Winchester and Floyd, 1976) plotting the volcanic rocks of the Yili Block. Open symbols: volcanic rocks of the Axi section; grey symbols: volcanic rocks of the northern Nileke section; black symbols: volcanic rocks of the Nalati–Gongnaisi–Yuxi section.

Negative Eu anomalies (δEu = 0.6113–0.9135) occur in most of volcanic rocks of the Axi and Nalati–Gongnaisi–Yuxi sections except sample XJ390. indicating crystal fractionation of plagioclase (Rollinson, 1993). Volcanic rocks of the northern Nileke section have no obvious Eu anomalies (δEu = 0.9975–1.0417) except XJ174-6 (δEu = 0.6838). The Chondrite-normalized REE distribution patterns (Fig. 6; using the normalizing values of Sun and McDonough, 1989) are characterized by a negative slope with $(La/Yb)_N > 2.66$, indicating the fractionation of LREE relative to HREE. This feature is consistent with the calc-alkaline character of these rocks.

On the REE and trace element expanded spider diagrams (Fig. 7; Pearce, 1982, 1983), LILE such as K, Rb, Th and Ba are prominently enriched relative to MORB, while HFSE (Zr, Hf, Ta and Sm) have MORB-like concentrations. Nb and Ta display moderate negative anomalies relative to Th and Ce. All samples have Nb contents of more than 3 ppm, similar to those of continental arc basalts (3.3 ± 1.6 ppm) and considerably higher than those of oceanic arc basalts (1.5 ± 1.0 ppm; McCulloch and Gamble, 1991). The Nb–Ta depletion is a common feature of calc-alkaline magmas generated from sources that contain a Nb receptor (metasomatized mantle wedge) or from already Nb-depleted sources (most crustal sources) (Hawkesworth et al., 1995; Rollinson, 1993; Pearce and Peate, 1995).

5.3. Tectonic setting of the volcanic rocks

The N-MORB normalized spider diagram (Pearce, 1982, 1983) shows a pronounced enrichment of LILE and a characteristic depletion of Ta and Nb (Fig. 7). Replotting already published data (Che et al., 1996) indicates that the volcanic rocks of Guozigou, immediately to the west of Yining, and those of Tekesi, south of Yining (Fig. 1), display similar geochemical features (Fig. 7a) that are typical of: (1) subduction-related magmas; (2) magmas generated by the partial melting of lower continental crust; or (3) mantle-derived magmas significantly contaminated by continental crust. Sr, Nd and Pb isotopic studies are needed in

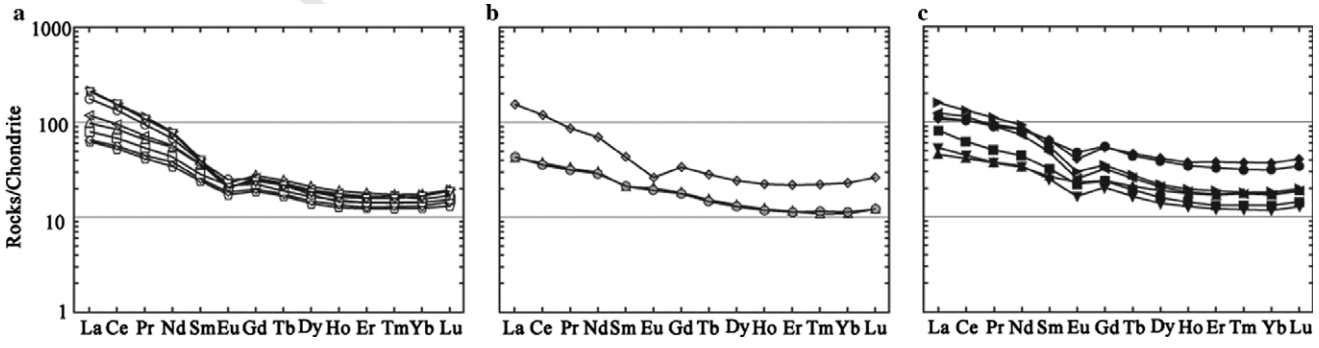

Fig. 6. Chondrite normalized REE patterns of volcanic rocks from the Yili Block. Normalizing values are from Sun and McDonough (1989). (a) Volcanic rocks of the Axi section; (b) volcanic rocks of the northern Nileke section; (c) volcanic rocks of the Nalati–Gongnaisi–Yuxi section. Symbols same as Fig. 5.

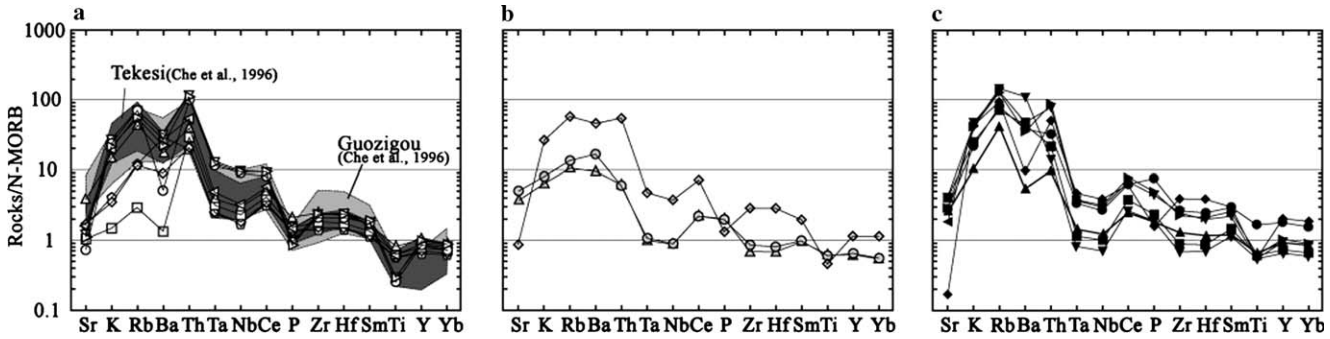

Fig. 7. N-MORB normalized spider diagrams of the volcanic rocks from the (a) Axi section, (b) northern Nileke section and (c) Nalati–Gongnaisi–Yuxi section, showing subduction related enrichment of LIL elements relative to HFS elements. Normalizing values are from Pearce (1983). Data of volcanic rocks from Tekesi and Guozigou are after Che et al. (1996). Symbols same as Fig. 5.

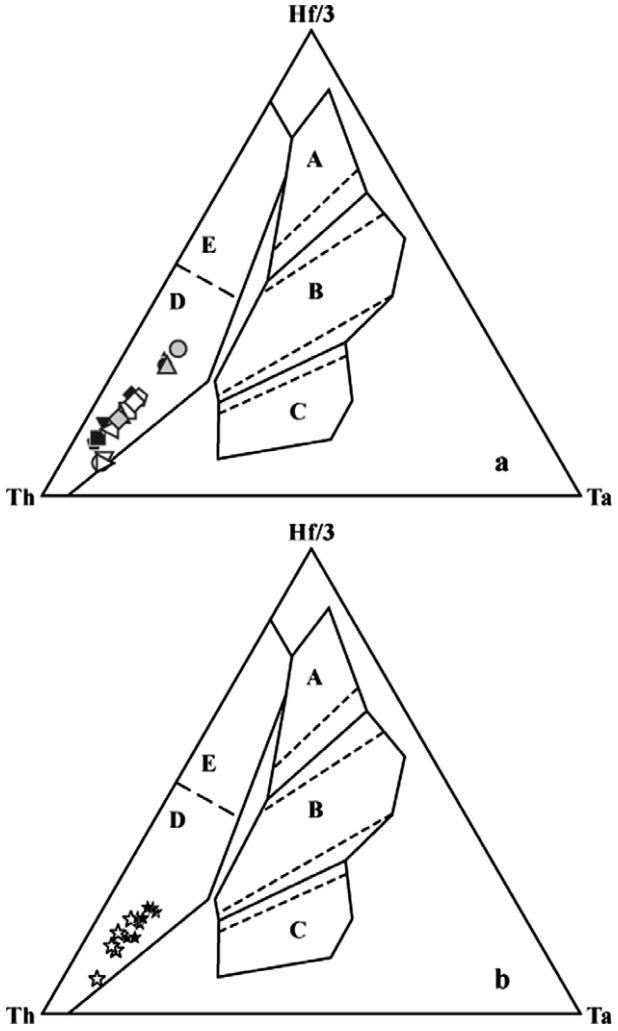

Fig. 8. Th–Hf–Ta discrimination diagrams (after Wood et al., 1979) of volcanic rocks from the Yili Block showing subduction-related calc-alkaline compositions. (a) This study, symbols same as Fig. 5; (b) Black stars: volcanic rocks of Guozigou; open stars: volcanic rocks of Tekesi, all data are from Che et al., 1996. Fields: A, N-MORB; B, E-MORB and within-plate tholeiites; C, alkaline within-plate basalts; D, calc-alkaline basalts; E, Island-arc tholeiites.

order to provide compelling evidence concerning the origin of these volcanic rocks. However, "immobile element" ratios may eliminate some unlikely possibilities. In the case of magmas generated in a rifting environment as proposed by Perry et al. (1987) and Davis (1991), partial melting of the lower crust is generally triggered by high heat flow related to uplift of the asthenosphere. In addition, the early stages of uplift generate intraplate magmas (continental tholeiites or alkaline basalts). This is obviously not the case of the Yili Carboniferous volcanic rocks that display calc-alkaline features only. Moreover, in rift environments, the hybridation of asthenosphere (OIB-like) and lithosphere (MORB-like) sources generally occurs and results in variable Ta/Hf ratios on the Hf–Th–Ta diagram (Wood et al., 1979). On the Hf/3–Th–Ta triangular diagram (Fig. 8), all our samples (Fig. 8a), as well as those of Che et al. (1996) (Fig. 8b), plot along linear trends between typical calc-alkaline and IAT end-members without evidence for any occurrence of an intraplate (high Ta/Th) component. Therefore, the rifting hypothesis relative to partial melting of lower continental crust and contamination by the crust is considered unlikely.

The Th/Yb vs Nb/Yb diagram (Fig. 9) distinguishes continental arc from oceanic-arc magmas (Pearce and Peate, 1995). All the samples plot within the continental-arc field and in the overlapping field of oceanic and continental arcs. The volcanic rocks in each section display a single linear trend depending upon slightly variable but high Th/Yb ratios, due to higher Th and/or lower Yb contents (Table 2). Since Yb is essentially "immobile", these high Th/Yb ratios presumably reflect the influence of subduction-derived fluids, resulting in Th enrichment. Although further isotopic evidence is needed to strengthen this interpretation, it may be concluded that Carboniferous calc-alkaline volcanic rocks of the Northern Yili Block are likely to have erupted in a continental active margin setting.

6. Ophiolitic mélange of the Northern Tianshan Belt

Ophiolitic mélanges are widely accepted as indicators of paleo-subduction and generally occur in association with island-arc volcanic rocks (Coleman, 1984, 1989; Zhang and Zhou, 2001; Zhang et al., 1984). In the study area, ophiolitic mélange was found in the Bayingou (Gao et al., 1998; Li, 1993; Xiao et al., 1992)–Motuoshalagou–

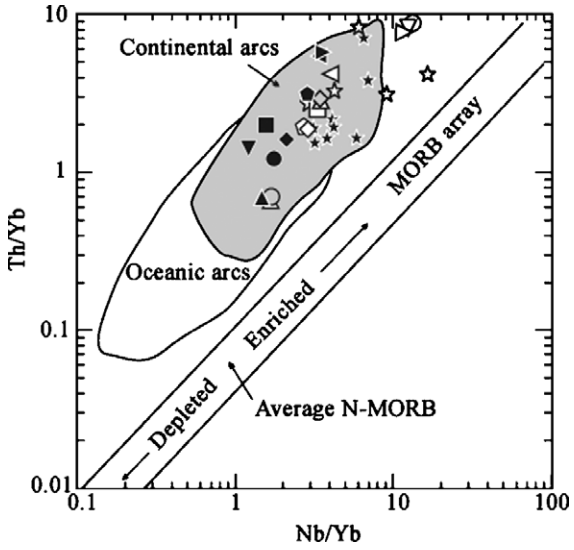

Fig. 9. Th/Yb versus Nb/Yb diagram after Pearce and Peate (1995) showing the subduction related continental arc affinities of the Carboniferous volcanic rocks of the Yili Block. Symbols same as in Figs. 5 and 8.

Gurt (Li and Du, 1994) zone located north of the Yili Block (Fig. 1). The mélange is composed of oceanic crust rocks, serpentinized peridotite, and flysch. The published geochemical results on the Bayingou and Gurt mafic rocks allow three magma types to be distinguished: N-MORB, OIB and IAT (Li and Du, 1994; Xiao et al., 1992; Zhang and Zhou, 2001), suggesting genesis within an oceanic basin. The petrological and geochemical similarities of Bayingou, Motuoshalagou and Gurt ophiolitic rocks, along with the occurrence of Late Devonian to Early Carboniferous radiolarian and conodont fossils in cherts of the Bayingou mélange (Xiao et al., 1992) and C1-2 radiolarians in cherts of the Gurt mélange (Li and Du, 1994), allow us to infer that they were probably derived within a single Late Devonian to Early Carboniferous oceanic basin. Closure of this basin during subduction generated the active continental margin calc-alkaline magmatism in the Yili Block.

Although detailed petrological and structural studies of this unit are beyond the scope of this paper, the ophiolitic mélange and the North Tianshan turbidite can be interpreted as a subduction–accretion complex, and the northward thrusting observed in these units corresponds to south-dipping subduction of the oceanic basin. On the basis of age constraints provided by the active margin magmatic activity, this basin probably closed due to southward subduction during Tournaisian and Visean times. Since the mélange includes the C1 to C2 turbidite blocks (Fig. 2), it probably formed in the Late Carboniferous due to collision between the Yili Block and the North Tianshan and the Junggar Plate (Gao et al., 1998).

7. Discussion

In all studied sections, the calc-alkaline volcanic rocks are closely associated with either carbonate sedimentary rocks or shallow water clastic deposits. In general, the Carboniferous sequence of the Yili Block displays a regressive character with a progressive evolution from a gently subsiding platform during the Early Carboniferous (C1) towards a Late Carboniferous sedimentation environment. No evidence for deepening or accelerating subsidence is found. Therefore, the calc-alkaline volcanic rocks erupted at the C1–C2 boundary cannot be related to a rifting event as proposed earlier by Che et al. (1996) and Xia et al. (2002, 2003) on the basis of "Within-plate basalt" discrimination diagram (i.e., Zr–Zr/Y). In contrast, an active margin setting is consistent with: (1) the overall geochemical features of the erupted rocks, (2) evolution from a platform to a shallow water or terrestrial environment due to a C1–C2 tectonic event, (3) accumulation of turbidite to the north of the Yili Block, and (4) the formation of a Late Carboniferous ophiolitic mélange. This tectonic setting is also consistent with that of the Bogda Arc in northern Eastern Tianshan, which is considered to be a Carboniferous continental volcanic arc formed by subduction of the Junggar Paleo-ocean (Charvet et al., 2001) or Turkestan Ocean (Heubeck, 2001; Sengör and Natal'in, 1996).

Carboniferous volcanic arc rocks are widespread in the Yili Block. From north to south, they crop out nearly 200 km wide, which is uncommon for a volcanic arc. Such a width might not be a primary feature of this arc but probably was the result of later multiphase transcurrent displacements. On the basis of paleomagnetic data in the West Tianshan Belt in Kyrgyz (Bazhenov et al., 1999), earlier sinistral shearing along the southern boundary (CTNF) and later dextral shearing along the northern boundary (NTF) have been distinguished. The earlier event is proposed to have taken place during the "Early–Late Permian", but is still poorly constrained by structural and geochronological data. The later one, which is considered to have occurred during Late Permian to Early Jurassic times, is corroborated by kinematic and radiochronological studies. The Ar–Ar dating on biotite and muscovite from ductilely sheared slates or mylonites in the East Tianshan Belt constrains the age of this dextral wrenching at 280–250 Ma (Laurent-Charvet et al., 2002, 2003; Shu et al., 1999). Further evidence of Permian transcurrent faulting within the interior of the Yili Block, such as the "Nilak fault" (Zhao et al., 2003; NLKF in Fig. 1), needs to be documented.

It is worth noting that Early Permian deposits unconformably overlie the Carboniferous strata. In most places, terrestrial Permian sediments are associated with intraplate volcanic rocks, such as alkaline basalt or continental tholeiites and associated felsic rocks (Allen et al., 1995; XBGMR, 1993). Moreover in the Baiyanggou area (Fig. 1), Permian alkaline pillow basalts are associated with chert and turbidite deposited in a narrow and deep basin that likely formed in a transtensional setting (Shu et al., 2005). Therefore we suggest that southward subduction closed the northern Tianshan oceanic basin and generated the active continental margin magmatism and ophiolitic mélange. This event was followed by Permian to Mesozoic

regional intra-continental extension and transtensional faulting that was responsible for opening of the pull-apart basin, such as Turfan Basin (Fig. 1; Allen et al., 1995; Natal'in and Sengör, 2005) associated with intraplate magmatism and the formation of the present shape of the Yili magmatic arc.

8. Conclusions

Carboniferous volcanic rocks in the Yili Block erupted along a continental active margin as evidenced by (1) their calc-alkaline geochemistry, (2) prominent Nb–Ta negative anomalies, (3) high Th/Ta and Hf/Ta ratios, and (4) marginal sedimentary series intercalated with volcanic rocks. The occurrence of a Late Carboniferous ophiolitic mélange and turbiditic rocks exhibiting a north-directed thrusting is attributed to a southward subduction of the North Tianshan oceanic basin, which was responsible for Yili calc-alkaline magmatism. This subduction was followed by Permian–Mesozoic intra-continental extension and transtensional faulting.

Acknowledgements

We would like to give our special appreciation to Prof. Ma Y.J., Wang J.L., Xu X., Wang B.L., Wang Y., Zhu B.Y., Guo H. (Bureau of National project 305, Xinjiang Uygur autonomous Region, China) and Li Y.A. (Xinjiang Bureau of Geology and Mineralogy Institute) for giving us their great help and support for field work. The constructive reviews by Dr. Natal'in and another anonymous reviewer significantly improved the earlier version of this study, Dr. J. Lytwyn, the editorial assistant and Dr. Romain Augier improved the English. This research was supported by the State Key Project for Basic Research of China (No. 2001CB409804).

References

Allen, M.B., Sengör, A.M.C., Natal'in, B.A., 1995. Junggar and Alakol basins as Late Permian to? Early Triassic extensional structures in a sinistral shearing zone in the Altaid orogenic collage, Central Asia. Journal of the Geological Society of London 152, 327–338.

Allen, M.B., Vincent, S.J., Wheeler, P.J., 1999. Late Cenozoic tectonics of the Kepingtage thrust zone: interactions of the Tien Shan and Tarim basin, northwest China. Tectonics 1 (4), 639–654.

Allen, M.B., Windley, B.F., Zhang, C., 1993. Paleozoic collisional tectonics and magmatism of the Chinese Tien Shan, Central Asia. Tectonophysics 220, 89–115.

Avouac, J.P., Tapponnier, P., Bai, M., You, H., Wang, G., 1993. Active thrusting and folding along the northern Tien Shan and Late Cenozoic rotation of the Tarim relative to Dzungaria and Kazakhstan. Journal of Geophysical Research 9 (B4), 6755–6804.

Bazhenov, M.L., Burtman, V.S., Dvorova, A.V., 1999. Permian paleomagnetism of the Tien Shan fold belt, Central Asia: post-collisional rotations and deformation. Tectonophysics 31 (2-4), 303–329.

Burchfiel, B.C., Brown, E.T., Deng, Q.D., Feng, X.Y., Li, J., Molnar, P., Shi, J.B., Wu, Z.M., You, H.C., 1999. Crustal shortening on the Margins of the Tien Shan, Xinjiang, China. International Geology Review 41, 665–700.

Charvet, J., Laurent-Charvet, S., Shu, L.S., Ma, R.S., 2001. Paleozoic continental accretions in Central Asia around Junngar Block: new structural and geochronological data. Gondwana Research 4 (4), 590–592.

Che, Z.C., Liu, L., Liu, H.F., Luo, J.H., 1996. Review on the ancient Yili rift, Xinjiang, China. Acta Petrologica Sinica 1 (3), 478–490, in Chinese with English abstract.

Chen, D.L., Liu, L., Che, Z.C., Luo, J.H., 2001. Geochemical characteristics and tectonic implication of Carboniferous volcanites in the Luotuogou area of Middle Tianshan. Acta Petrologica Sinica 1 (3), 378–384, in Chinese with English abstract.

Chen, C.M., Lu, H.F., Jia, D., Cai, D.S., Wu, S.M., 1999. Closing history of the southern Tianshan oceanic basin, western China: an oblique collisional orogeny. Tectonophysics 302, 23–40.

Chen, Y.B., Hu, A.Q., Zhang, G.X., Zhang, Q.F., 2000a. Zircon U–Pb age of granitic gneiss on Duku highway in western Tianshan of China and its geological implications. Chinese Science Bulletin 4 (7), 649–653.

Chen, Y.B., Hu, A.Q., Zhang, G.X., Zhang, Q.F., 2000b. Precambrian basement age and characteristics of Southwestern Tianshan: Zircon U–Pb geochronology and Nd–Sr istopic composition. Acta Petrologica Sinica 1 (1), 91–98, in Chinese with English abstract.

Coleman, R.G., 1984. The diversity of ophiolites. Geology Mijnbouw 63, 141–150.

Coleman, R.G., 1989. Continental growth of Northwest China. Tectonics 8, 621–635.

Cunningham, W.D., Windley, B.F., Dorjnamjaa, D., Badamgarov, J., Saandar, M., 1996. A structural transect across the Mongolian Western Altai: active transpressionnal mountain building in central Asia. Tectonics 1 (1), 142–156.

Davis, P.M., 1991. Continental rift structures and dynamics with reference to teleseismic studies of the Rio Grande and East African rifts. Tectonophysics 19 (2–4), 309–325.

Gao, J., He, G.Q., Li, M.S., 1997. Paleozoic orogenic processes of Western Tianshan Orogen. Earth Science-Journal of China University of Geosciences 22 (1), 28–32, in Chinese with English abstract.

Gao, J., He, G.Q., Li, M.S., Xiao, X.C., Tang, Y.Q., Wang, J., Zhao, M., 1995. The mineralogy, petrology, metamorphic PTDt trajectory and exhumation mechanism of blueschist, south Tianshan, northwestern China. Tectonophysics 250, 151–168.

Gao, J., Li, M.S., Xiao, X.C., Tang, Y.Q., He, G.Q., 1998. Paleozoic tectonic evolution of the Tianshan Orogen, northern China. Tectonophysics 287, 213–231.

Hawkesworth, C., Turner, S., Gallagher, K., Hunter, A., Bradshaw, T., Rogers, N., 1995. Calc-alkaline magmatism, lithospheric thinning and extension in the Basin and Range. Journal of geophysical research 100 (B7), 10271–10286.

Heubeck, C., 2001. Assembly of Central Asia during the middle and late Paleozoic. In: Hendrix, M.S., Davis, G.A. (Eds.), Paleozoic and Mesozoic Tectonic Evolution of Central Asia: From Continental Assembly to Intracontinental Deformation, 194. Memoir-Geological Society of America, Boulder, Colorado, pp. 1–22.

ICS (International Commission on Stratigraphy), 2004. International Stratigraphic Chart.

Janney, P.E., Castillo, P.R., 1997. Geochemistry of Mesozoic Pacific MORB: constraints on melt generation and the evolution of the pacific upper mantle. Journal of Geophysical Research 102, 5207–5229.

Jiang, C.Y., Wu, W.K., Zhang, X.R., Cui, S.S., 1995. The change from island arc to rift valley: evidence from volcanic rocks of Awulale area. Acta Petrologica et Mineralogica 1 (4), 289–300, in Chinese with English abstract.

Laurent-Charvet, S., Charvet, J., Monie, P., Shu, L.S., 2003. Late Paleozoic strike-slip shear zones in eastern Central Asia (NW China): new structural and geochronological data. Tectonics 2 (2), 1099–1101.

Laurent-Charvet, S., Charvet, J., Shu, L.S., Ma, R.S., Lu, H.F., 2002. Palaeozoic late collisional strike-slip deformations in Tianshan and Altay, eastern Xinjiang, NW China. Terra Nova 1 (4), 249–256.

Li, H.Q., Xie, C.F., Chang, H.L., Cai, H., Zhu, J.P., Zhou, S., 1998. Study on Metallogenetic Chronology of Nonferrous and Precious Metallic

Ore Deposits in North Xinjiang. Geology Publishing house, China, Beijing, pp. 100–127 (in Chinese with English abstract).

Li, S.H., Du, Q., 1994. The ophiolites in Motogou-Gurt of Wusu County. Xinjiang Geology 1 (3), 265–271, in Chinese with English abstract.

Li, X.D., 1993. Late Paleozoic evolution of oceanic basin and thrust structure in northern Tianshan, Xinjiang. Xinjiang Geology 1 (3), 207–214, in Chinese with English abstract.

Li, X.H., 1997. Geochemistry of the Longsheng ophiolite from the southern margin of Yangtze carton, SE China. Geochemistry 31, 323–337.

Ma, R.S., Wang, C.Y., Ye, S.F., 1993. Tectonic Framework and Crustal Evolution of Eastern Tianshan Mountains. Publishing House of Nanjing University, Nanjing, p. 225 (in Chinese with English abstract).

McCulloch, M.T., Gamble, J.A., 1991. Geochemical and geodynamical constraints on subduction zone magmatism. Earth and Planetary Science Letters 102, 358–374.

Natal'in, B.A., Sengör, A.M.C., 1994. The tectonic setting of the Tien Shan within the Altaid orogenic belt. In: Geological Society of America Abstracts with program, Annual meeting, Seattle, pp. A464.

Natal'in, B.A., Sengör, A.M.C., 2005. Late Paleozoic to Triassic evolution of the Turan and Scythian platforms: the pre-history of the Paloe-Tethyan closure. Tectonophysics 40 (3–4), 175–202.

Pearce, J.A., 1982. Trace element characteristics of lavas from destructive plate boundaries. In: Thorpe, R.S. (Ed.), Andesites: Orogenic Andesites and Related Rocks. Wiley, Chichester, UK, pp. 525–548.

Pearce, J.A., 1983. Role of the sub-continental lithosphere in magma genesis at active continental margins. In: Hawkesworth, C.J., Norry, M.J. (Eds.), Continental Basalts and Mantle Xenoliths. Shiva Press, Nantwich, UK, pp. 230–249.

Pearce, J.A., Peate, D.W., 1995. Tectonic implications of the composition of volcanic arc magmas. Annual Review of Earth and Planetary Sciences 23, 251–285.

Perry, F.V., Baldridge, W.S., DePaolo, D.S., 1987. Role of asthenosphere and lithosphere in the genesis of Late Cenozoic basaltic rocks from the Rio Grande Rift and adjacent regions of the southwestern United States. Journal of Geophysical Research 92, 9193–9213.

Rollinson, H.R., 1993. Using Geochemical Data: Evaluation, Presentation, Interpretation. Longman scientific technical, New York, pp. 48–213.

Sengör, A.M.C., Natal'in, B.A., 1996. Paleotectonics of Asia: fragments of a synthesis. In: Yin, A., Harrison, M. (Eds.), The Tectonic Evolution of Asia. Rubey Colloquium. Cambridge University Press, Cambridge, pp. 486–640.

Sengör, A.M.C., Natal'in, B.A., Burtman, V.S., 1993. Evolution of the Altaid tectonic collage and Paleozoic crust growth in Eurasia. Nature 364, 299–307.

Shi, Y.S., Lu, H.F., Jia, D., Howell, D.G., 1994. Paleozoic plate tectonic evolution of the Tarim and western Tianshan Regions, Western China. International Geological Review 36, 1058–1066.

Shu, L.S., Charvet, J., Guo, L.Z., Lu, H.F., Laurent-Charvet, S., 1999. A Large scale Paleozoic dextral strike-slip shear zone: the Aqikkudug-Weiya zone along the Northern margin of Central Tianshan belt, Xinjiang, NW China. Acta Geologica Sinica 7 (4), 148–162.

Shu, L.S., Charvet, J., Lu, H.F., Laurent-Charvet, S., 2002. Paleozoic accretion-collision events and kinematics of ductile deformation in the central-southern Tianshan Belt, China. Acta Geologica Sinica 76 (3), 308–323.

Shu, L.S., Chen, Y.T., Lu, H.F., Charvet, J., Laurent-Charvet, S., Yin, D.H., 2000. Paleozoic accretionary terranes in Northern Tianshan, NW China. Chinese Geochemistry 1 (3), 193–202.

Shu, L.S., Wang, B., Yang, F., Lu, H.F., Charvet, J., Laurent-Charvet, S., 2003. Polyphase tectonic events and Mesozoic–Cenozoic basin-range coupling in the Chinese Tianshan belt. Acta Geologica Sinica 7 (4), 457–467.

Shu, L.S., Zhu, W.B., Wang, B., Faure, M., Charvet, J., Cluzel, D., 2005. The post-collision intracontinental rifting and olistostrome on the southern slope of Bogda Mountains, Xinjiang. Acta Petrologica Sinica 2 (1), 25–36, in Chinese with English abstract.

Sun, S.S., McDonough, W.F., 1989. Chemical and isotopic systematics of ocean island basalts: implications for mantle composition and processes. In: Saunders, A.D., Norry, M.J. (Eds). Magmatism in the Ocean Basins. Geological Society, London, Special Publications, pp. 313–345.

Tapponnier, P., Molnar, P., 1979. Active faulting and Cenozoic tectonics of the Tienshan, Mongolia and Baykal regions. Journal of Geophysical Research 84, 3425–3459.

Wang, B.Y., Li, Q., Liu, J.B., 1997. Geological structures of the Middle Tianshan Mountains along the Dushanzi-Kuqa highway. Xinjiang Geology 1 (2), 135–154, in Chinese with English abstract.

Winchester, J.A., Floyd, P.A., 1976. Geochemical magma type discrimination: application to altered and metamorphosed basic igneous rocks. Earth and Planetary Science Letters 28, 459–469.

Windley, B.F., Allen, M.B., Zhang, C., Zhao, Z.Y., Wang, G.R., 1990. Paleozoic accretion and Cenozoic redeformation of the Chinese Tien Shan range, Central Asia. Geology 18, 128–131.

Wood, D.A., Joron, J.L., Treuil, M., 1979. A re-appraisal of the use of trace elements to classify and discriminate between magma series erupted in different tectonic setting. Earth and Planetary Science Letters 45, 326–336.

XBGMR (Xinjiang Bureau of Geology and Mineral Resources), 1992. Geological map of Xinjiang Uygur Autonomy Region, Geological Publishing House, Beijing, four sheets, scale 1:1,500.000.

XBGMR (Xinjiang Bureau of Geology and Mineral Resources), 1993. Regional geology of Xinjiang Uygur Autonomy Region. Geology Publishing House, Beijing, pp. 1–841 (in Chinese with English abstract).

Xia, L.Q., Xu, X.Y., Xia, Z.C., Li, X.M., Ma, Z.P., Wang, L.S., 2003. Carboniferous post-collisional rift volcanism of the Tianshan Mountains, Northwestern China. Acta Geologica Sinica 7 (3), 338–360.

Xia, L.Q., Zhang, G.W., Xia, Z.C., Xu, X.Y., Dong, Y.P., Li, X.M., 2002. Constraints on the timing of opening and closing of the Tianshan Paleozoic oceanic basin: evidence from Sinian and Carboniferous volcanic rocks. Geological Bulletin of China 2 (2), 55–62, in Chinese with English abstract.

Xiao, X.C., Tang, Y.Q., Feng, Y.M., Zhu, B.Q., Li, J.Y., Zhao, M., 1992. Tectonic Evolution of the Northern Xinjiang and its Adjacent Regions. Geology Publishing House, Beijing, pp. 12–47 (in Chinese with English abstract).

Zhang, Q., Zhou, G.Q., 2001. Ophiolites in China. Science Press, Beijing, pp. 1–182 (in Chinese with English abstract).

Zhang, Z.M., Liu, J.G., Coleman, R.G., 1984. An outline of the plate tectonics of China. Bulletin of Geological Association of America 95, 295–312.

Zhao, J.M., Liu, G.D., Lu, Z.X., Zhang, X.K., Zhao, G.Z., 2003. Lithospheric structure and dynamic processes of the Tianshan orogenic belt and the Junggar basin. Tectonophysics 376, 199–239.

Zhou, D., Graham, S.A., Chang, E.Z., Wang, B.Y., Hacker, B., 2001. Paleozoic tectonic amalgamation of the Chinese Tianshan: Evidence from a transect along the Dushanzi-Kuqa highway. In: Hendrix, M.S., Davis, G.A. (Eds.), Paleozoic and Mesozoic Tectonic Evolution of Central Asia: From Continental Assembly to Intracontinental Deformation, 194. Boulder, Colorado, Geological Society of America Memoir, pp. 23–46.

Geodinamica Acta 19/3-4 (2006) XX-XX

Geodinamica Acta

Late Paleozoic tectonic evolution of the northern West Chinese Tianshan Belt

Bo Wang [a,b,*], Michel Faure [b], Dominique Cluzel [b], Liangshu Shu [a], Jacques Charvet [b], Sebastien Meffre [c], Qian Ma [a]

[a] *Department of Earth Sciences, Nanjing University, Nanjing, 210093, China*
[b] *ISTO UMR 6113, University of Orléans, F45067, Orléans, Cedex 2, France*
[c] *School of Earth Sciences, University of Tasmania, Hobart, Australia*

Received: 13/02/06, accepted 03/05/06

Abstract

The northern West Chinese Tianshan is divided into three subunits: Carboniferous turbidite, ophiolitic mélange and Yili magmatic arc. Stratigraphical and petrological studies suggest that the turbidite and ophiolitic mélange form a subduction complex. The ophiolitic mélange that forms the North Tianshan suture was a result of intra-oceanic tectonism and subsequent redeposition and deformation during the subduction of the North Tianshan oceanic basin. The Yili arc-type granitoids are constained by single zircon U-Pb radiochronology between 361 and 309 Ma. The first-hand kinematic results on the deformed turbidite suggest that this suture zone was reworked by a Permian ductile dextral strike-slip fault. An evolutionary model of the study area allows three events to be distinguished: 1) Late Devonian to Carboniferous subduction of the oceanic basin below the Yili Block producing Yili magmatic rocks and subduction complex, 2) Late Carboniferous complete closure of this basin, 3) Permian right-lateral strike-slip faulting generating pull-apart basins and alkaline magmatism. A prominent reactivation during the Indo-Eurasia collision provoked the northward thrusting of the Paleozoic units upon the Cenozoic sediments of the Junggar Basin, consequently, hiding the bulk of this Late Paleozoic suture.

Keywords: Paleozoic subduction; strike-slip shearing; mélange; zircon U-Pb dating; Tianshan

1. Introduction

The Tianshan range, extending E-W over 3000 km from NW China to Kazakhstan and Kyrgyzstan, separates the Tarim Basin to the South from the Junggar Basin to the North. It is a key region for understanding the Late Paleozoic geodynamic evolution of Central Asia. The Paleozoic Tianshan orogenic belt is considered to result from the accretion and/or collision of continental blocks, magmatic arcs and subduction complexes [1-6]. The Tianshan orogenic belt can be subdivided in several ways. Geographically, the West Chinese Tianshan (WTS) develops from Urumqi to the Chinese border (Fig. 1). Topographically, it consists of two E-W elongated ranges surrounding the Yining basin, which is also called "Yili Block". From a tectonic point of view, the Chinese Tianshan orogen is generally divided into North, Central and South domains. The Yili Block, located between the North and Central Tianshan domains, played an important role on the

* Corresponding author.
Tel: +33.2.38.49.46.60 - *Fax:* 33.2.38.41.73.09
E-mail address: bo.wang@univ-orleans.fr

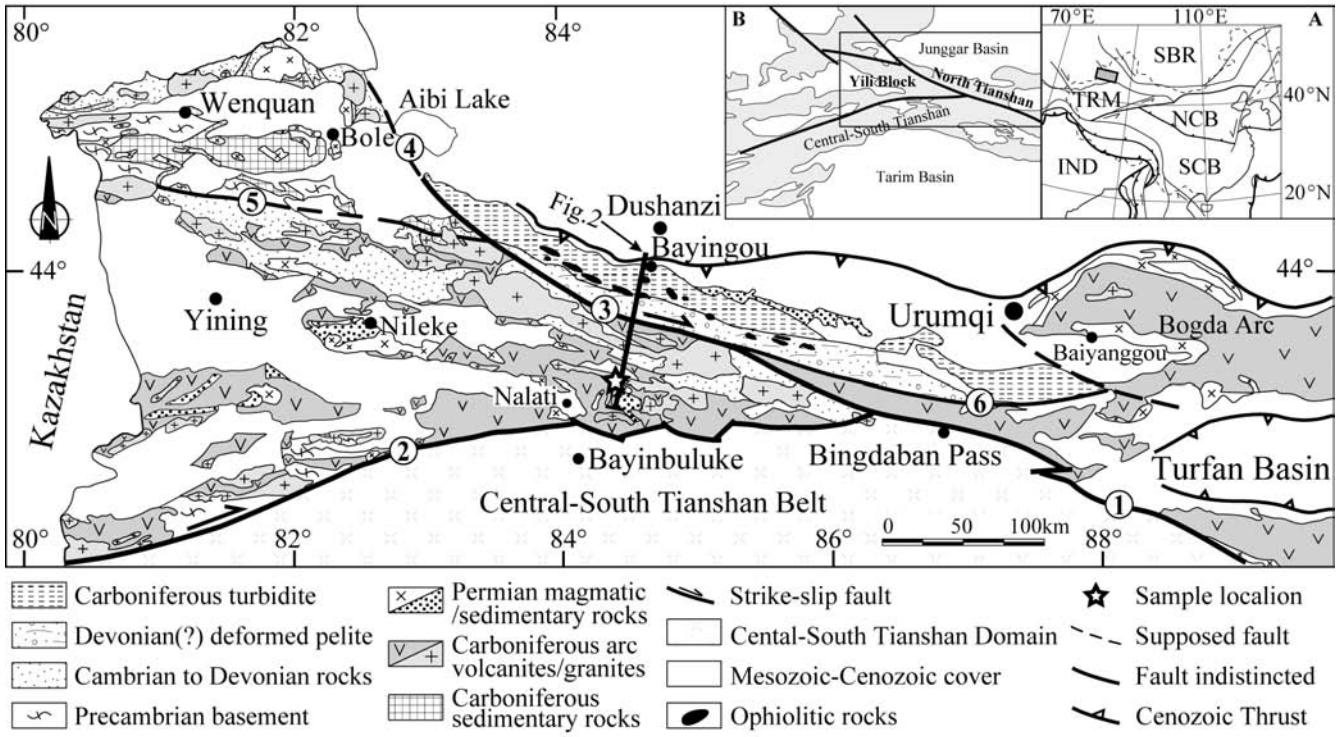

Fig. 1 Structural map of northern West Chinese Tianshan belt (modified from XBGMR [11]). Insert A shows the location of the study area in Central Asia, inset B defines the North Tianshan and the Yili Block. 1, Main Tianshan Shear Zone (MTSZ); 2, the Northern Central Tianshan Fault after Gao et al. [18]; 3, North Tianshan Fault; 4, Aibi Lake Fault; 5, Sailimu- Jinghe Fault; 6, Houxia Fault.

Paleozoic evolution of WTS, but its tectonic feature and the relationship with the North Tianshan are still poorly constrained. This study aims at clarifying the Late Paleozoic tectonic evolution of the northern WTS Belt, and we focused on the ophiolitic mélange, turbidite, the Yili magmatic arc as well as shear zone crossing the highway from Dushanzi to Nalati (Fig. 1 and 2). The tectonic significance of ophiolitic rocks is discussed and a geodynamic evolutionary model of the North Chinese Tianshan is proposed.

2. Structure of the northern WTS

The WTS consists of several units bounded by strike-slip faults (Fig. 1). The north side of the Central-South Tianshan Belt is bordered by the Main Tianshan Shear Zone (MTSZ, fault 1 in Fig. 1) [4, 5, 7], which separates the Central-South Tianshan Belt from the "Bogda Arc" [4]. To the West it merges with fault 2 separating the Yili Block to the Northwest from the Central-South Tianshan Belt to the south. To the North, the North Tianshan Fault (NTF, fault 3 in Fig. 1) [8], which is also named Junggar Fault [9] or Borohoro Fault [10], divides longitudinally the northern range of WTS along the Borohoro Range into the Yili Block and the North Tianshan Domain. Aibi Lake Fault (fault 4 in Fig. 1) is the northwest extension of the NTF. Sailimu-Jinghe Fault (fault 5 in Fig. 1) separates the Yili Block from the "Bole Block". Although a detailed discussion of the Bole Block is beyond the scope of this paper, it is worth noting that it strongly differs from the Yili Block and therefore is a very peculiar domain in the tectonic framework of WTS. Lastly, the "Houxia Fault" (fault 6 in Fig. 1) separates Carboniferous arc-related rocks that are exposed around the Turfan Basin from the North Tianshan terrigenous rocks (Fig. 1). In the following sections, we present northern WTS located to the east of the Sailimu-Jinghe Fault, and up to Urumqi. This area can be subdivided into three lithotectonic units: 1) Carboniferous turbidite, 2) ophiolitic mélange and 3) Yili magmatic arc (I, II and III, respectively in Fig. 2). The units I and II constitute one single subduction complex, i.e. the North Tianshan subduction complex, but the contrasted lithology allows the distinction of two different units.

2.1. Carboniferous turbidite

The northern slope of the Borohoro Range consists of a turbiditic formation developing WNW-ESE for 300 km long and about 20 km wide. On the basis of plant fossils, these terrigenous rocks are assigned to the Bayingou Formation of Late Carboniferous age [11]. This unit is estimated to be between 5,000 and 10,000 m thick although it is difficult to establish because of possible tectonic duplication. Sandstone beds present variable thickness ranging from a few centimeters to 1 m (Fig. 3a, b). Typical Bouma sequences can be observed. Some deep-water ichnofossils (*Chondrites sp.* and *Helminthoidda Labyrinthica*) were found in sandstone [11] indicating deep sea fan deposition. Sandstone grains and conglomerates pebbles consist of terrigenous, volcanic, plutonic and siliceous clasts with only minor carbonate

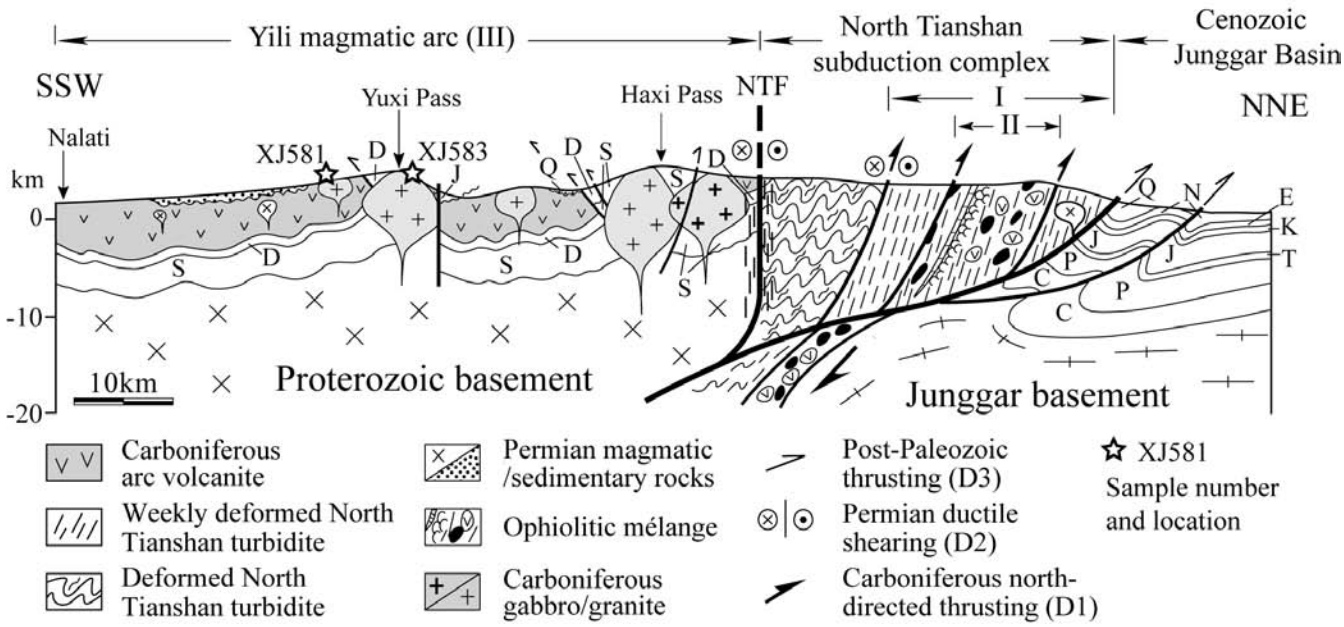

Fig. 2 Crustal scale cross section from Dushanzi to Nalati showing the polyphase deformation: Carboniferous D1 thrusting, Permian D2 shearing, and Cenozoic D3 thrusting. The dextral strike-slip fault partly reworks the Carboniferous suture (thickness of strata are after Liu and Li [24]). S, D, C, P, T, J, K, E, N and Q represent Silurian, Devonian, Carboniferous, Permian, Triassic, Jurassic, Cretaceous, Paleogene, Neogene and Quaternary, respectively.

clasts. Petrographic study indicates that the plutonic clasts are dominantly composed of granodiorite, diorite and gabbro. The volcanic clasts have calc-alkaline geochemical features [12]. Although detailed mapping is not available, load casts, graded bedding and cross laminations allow us to recognize both normal and upside down sequences that infer isoclinal folding or thrust stacking. Up-to-the-North thrust faults are also observed. Therefore, the turbidite series was likely involved in north verging recumbent fold and thrust sheets.

2.2. Ophiolitic mélange

Ophiolitic rocks are present within the turbiditic formation. According to the available geological maps [11, 13], these rocks crop out discontinuously for about 250 km long and 5~15 km wide (Fig. 1). In the regional geology, they are referred to as the Shadawang Formation [11]. Several areas are already well acknowledged to investigate the ophiolites [14-19]. In the Bayingou section, 30 km to the south of Dushanzi (Fig. 1), the dominant rocks are serpentinized peridotite (Fig. 3c), gabbro, diabase, basalt, chert, plagiogranite and rare limestone. Black or red scaly mudstone and light yellow-green greywacke often surround the other rock types. Mafic greywacke that might be easily confused with gabbro corresponds actually to gabbroic sandstone.

In the field, the ophiolitic rocks crop out in two ways: either as continuous sequences of massive basalt, pillow lava and overlying red chert (Fig. 3d) that develop for a few tens meters, or as centimetre to kilometre size isolated bodies of mafic-ultramafic or sedimentary rocks included in a schistose mudstone matrix. In the latter occurrence, the blocks exhibit without any regular organization but distribute rather randomly in the matrix. Sandstone phacoids are included in the scaly mudstone (Fig. 3e). Mafic and ultramafic blocks occur as olistoliths within the turbidite. Pebbly mudstone bearing angular blocks of gabbro, basalt, sandstone, chert and limestone are described in Gurt and Motoshalagou sections [8, 17], northwest of Bayingou.

On the basis of geochemistry, three types of mafic rocks are distinguished: N-MORB, OIB and IAT [14, 15, 17], indicating the genesis of oceanic basin. These lithological and geochemical features are compliant with the interpretation of the rocks as an ophiolitic suite. However, the absence of coherent ophiolitic bodies larger than one kilometre or so, the widespread blocky habitus of the rocks and the importance of sedimentary facies opposite to the magmatic ones suggest that this whole suite represent a mélange unit formed during the closure of an oceanic basin. The cherts associated with the mafic rocks yield Late Devonian to Early Carboniferous radiolarians and conodonts [15, 17], and one plagiogranite block yields a zircon U-Pb SHRIMP age of 325±7 Ma [20]. Both suggest a Late Paleozoic age for ophiolite formation. The tectonic significance of the ophiolitic mélange and its geodynamic setting will be discussed in the forthcoming sections.

2.3. Yili magmatic arc

The Yili Block contains voluminous volcanic rocks of Carboniferous age [11, 21] (Fig. 1). The volcanic rocks consist of basaltic andesite, andesite, rhyodacite, dacitic andesite, tuff and volcano-sedimentary rocks. They are closely associated with limestone and shallow water clastic deposits. The evolution of sedimentary facies of the Yili Block infers a progressive change from a gently subsiding platform during

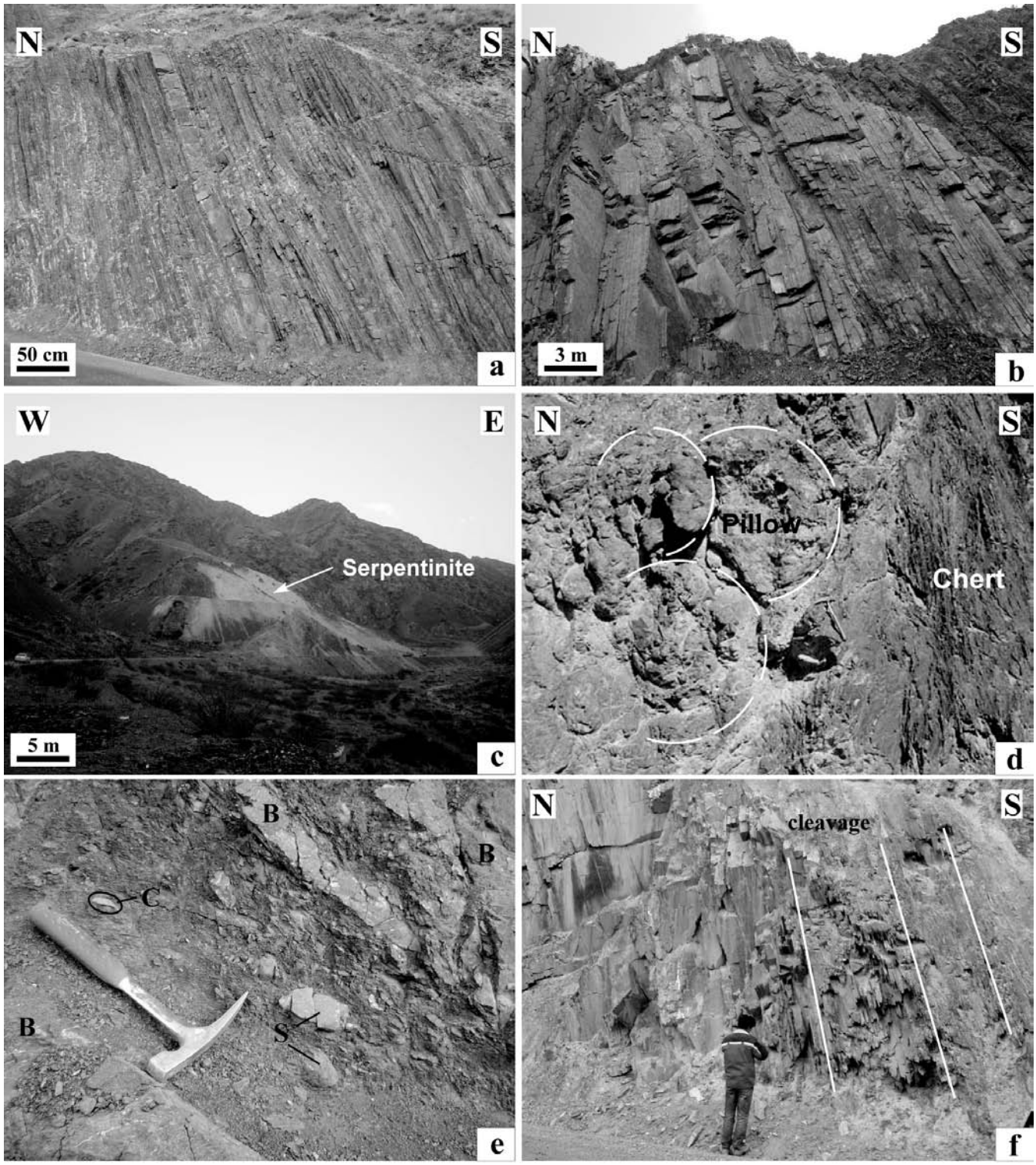

Fig. 3 Field photographies of the North Chinese Tianshan subduction complex. (a, b) Carboniferous turbidite dipping at high angle to the south; (c) decameter-size serpentinite block in Bayingou ophiolitic mélange; (d) pillow lavas and overlying red chert and pelite in mélange; (e) green sandstone (S), Late Devonian-Early Carboniferous red chert (C), tholeiitic basalt (B) included in red pelitic matrix of the mélange; (f) Slate at the south of the mélange, the subvertical cleavage contains a sub-horizontal mineral-stretching lineation.

the Early Carboniferous towards a Late Carboniferous filling up environment [22]. Geochemical analyses of the volcanic rocks show that they belong to calc-alkaline series and formed in a continental active margin setting [22, 23].

Arc-type granodiorite, diorite and tonalite are widespread within the Yili Block (Fig. 4a). The granodiorite is mainly composed of plagioclase, hornblende and minor

Table 1: Zircon U-Pb data of granitoids from the Yili Block

Plots	Ratios						Ages						Disc.(%)
	$^{207}Pb/^{235}U$	1σ	$^{206}Pb/^{238}U$	1σ	$^{207}Pb/^{206}Pb$	1σ	$^{206}Pb/^{238}U$	1σ	$^{207}Pb/^{206}Pb$	1σ	$^{207}Pb/^{235}U$	1σ	
XJ581													
MA23C2	0.1044	0.0108	0.0167	0.0003	0.0480	0.0054	107	2.1	99	264	101	10	2.1
MA23C5	0.1541	0.0098	0.0245	0.0003	0.0449	0.0029	156	1.9	-61	159	145	9	1.9
MA23C11	0.1794	0.0094	0.0247	0.0004	0.0520	0.0029	157	2.4	284	126	168	8	2.4
MA23C7	0.3593	0.0103	0.0482	0.0004	0.0531	0.0016	303	2.4	332	69	312	8	2.4
MA23C8	0.3708	0.0182	0.0482	0.0009	0.0533	0.0027	303	5.4	342	115	320	14	5.4
MA23C12	0.3861	0.0109	0.0489	0.0005	0.0565	0.0016	306	3.4	471	61	332	8	3.4
MA23C9	0.3592	0.0123	0.0490	0.0004	0.0526	0.0019	309	2.6	311	83	312	9	2.6
MA23C3	0.3647	0.0085	0.0494	0.0003	0.0523	0.0013	311	2.1	300	57	316	6	2.1
MA23C6	0.3685	0.0101	0.0502	0.0004	0.0528	0.0014	316	2.4	320	62	319	8	2.4
MA23C10	0.3646	0.0095	0.0510	0.0004	0.0515	0.0014	321	2.4	263	61	316	7	2.4
MA23C4	0.3707	0.0153	0.0515	0.0005	0.0514	0.0021	324	3.2	261	93	320	11	3.2
MA23C1	0.3907	0.0150	0.0532	0.0006	0.0520	0.0021	334	3.5	285	93	335	11	3.5
XJ583													
MA23M11	0.3494	0.0216	0.0483	0.0008	0.0537	0.0033	304	5.3	357	138	304	16	5.3
MA23M9	0.3560	0.0214	0.0486	0.0007	0.0540	0.0033	306	4.7	373	138	309	16	4.7
MA23M7	0.3673	0.0261	0.0488	0.0008	0.0558	0.0040	306	5.4	445	157	318	20	5.4
MA23M8	0.3342	0.0239	0.0487	0.0010	0.0530	0.0039	306	6.6	329	168	293	18	6.6
MA23M12	0.3612	0.0289	0.0490	0.0010	0.0551	0.0044	307	6.2	417	179	313	22	6.2
MA23M3	0.3588	0.0226	0.0492	0.0009	0.0565	0.0035	308	5.5	473	136	311	17	5.5
MA23M4	0.3832	0.0247	0.0495	0.0008	0.0578	0.0038	309	5.0	521	144	329	18	5.0
MA23M10	0.3306	0.0245	0.0491	0.0008	0.0513	0.0039	310	5.4	256	174	290	19	5.4
MA23M6	0.3662	0.0256	0.0495	0.0008	0.0560	0.0040	310	5.3	453	160	317	19	5.3
MA23M2	0.3953	0.0227	0.0500	0.0009	0.0594	0.0034	312	5.7	583	123	338	17	5.7
MA23M5	0.3250	0.0246	0.0504	0.0010	0.0502	0.0040	318	6.2	202	187	286	19	6.2
MA23M1	0.3705	0.0280	0.0511	0.0010	0.0574	0.0045	319	6.6	508	173	320	21	6.6

Disc. (%) denotes percentage of discordance

quartz as well as biotite (Fig. 4b). Single zircon grains of one granodiorite and one microdiorite samples collected along the highway from Dushanzi to Nalati (Fig. 1 and 2) are dated using a Hewlett Packard HP 4500 ICP-MS fitted with a Nd-YAG Laser operating at 213 nm at the University of Tasmania (Australia). The U-Pb isotopic results are presented in Table 1 and in Fig. 5. The granodiorite XJ583 yields an age of 309±3Ma (MSWD=0.63) with an isolated peak in the histogram. The microdiorite XJ581 presents a main peak age of 315±3Ma (MSWD=4.6) with 4 out of 120 analyses scattering from the main peak in histogram, their relatively high U/Pb ratio is interpreted as due to a Pb loss. Geochronology of the calc-alkaline granites from other places in the Yili Block (Work in progress) indicates that the oldest age for arc-related magmatism is 361 Ma. This plutonic event that lasted for about 50 millions years was contemporaneous with congenetic volcanic activity, i.e. basalt and dacitic andesite from the same area yielding SHRIMP U-Pb zircon ages ranging from 354 Ma to 313 Ma [23].

The tectonic setting and age of the Yili magmatic rocks are consistent with those of the Middle Devonian to Carboniferous Bogda calc-alkaline volcanic rocks [4, 24], and sharply contrast with those of the Permian intra-plate granites, alkaline basalts or continental tholeiites and associated felsic rocks that crop out in Nileke and Baiyanggou areas (Fig. 1) [11, 25].

3. Polyphase deformation in the northern WTS

Three principal phases of deformation, called D1 to D3, are recognized in the northern WTS Belt. They are presented here in the retro-tectonic order (from younger to older) in order to remove the effects of younger deformations on the older ones.

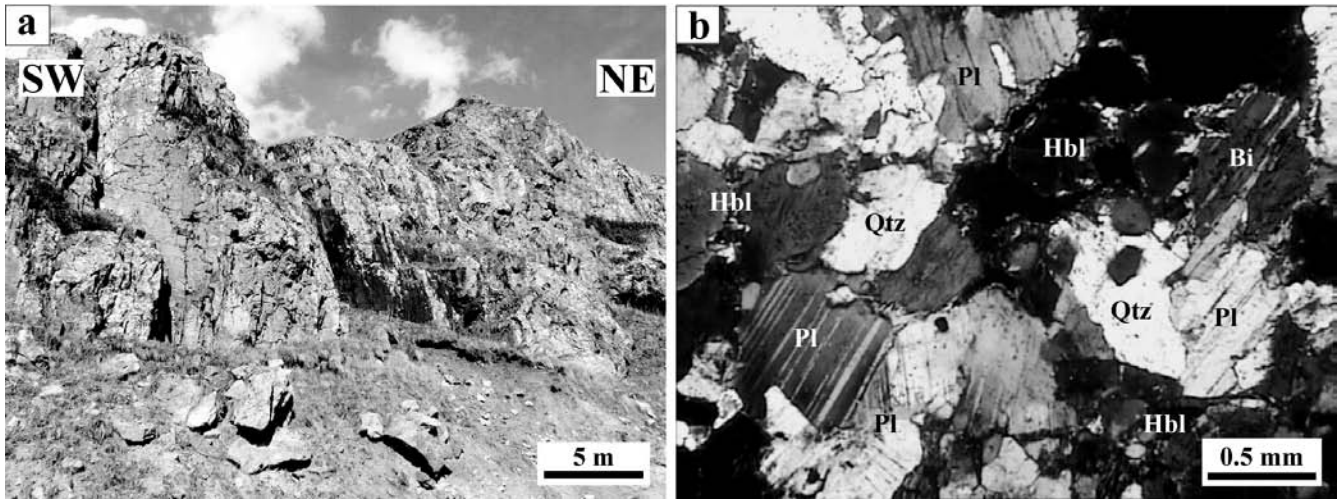

Fig. 4 (a) Field photography of arc-type granitoids in the Yili Block; (b) Micro-photography of a granodiorite showing the plagioclase (Pl), hornblende (Hbl), quartz (Qtz) and biotite (Bi).

3.1. Cenozoic intracontinental thrusting (D3)

The northern piedmont of the Tianshan Belt, at the contact with the Junggar Basin, consists of a thick succession (nearly 10 km) of Triassic-Neogene terrigenous deposits formed by fluvial erosion of the range (Fig. 2) [26]. Kilometre scale north verging folds and high to intermediate angle brittle thrusts accommodate a N-S shortening of the south margin of the Junggar Basin. According to detailed structural, geomorphological and magneto-stratigraphic results, the Paleozoic rocks (either turbidites or volcanic rocks) are thrusted over the Mesozoic to Neogene continental sediments with a throw of several tens kilometres [27-30]. As a consequence, prominent tectonic features, such as the Late Paleozoic suture between the Yili and Junggar blocks, have been concealed and cannot be recognized in the field (Fig. 2).

3.2. Permian dextral strike-slip faulting (D2)

As observed along the Dushanzi-Nalati highway and other parallel routes, the southern part of the turbidite unit is lithologically dominated by black mudstone, sandstone, minor chert and volcani-clastic rocks. Although attributed to the Devonian [11], these rocks remain undated since they are mainly clastic. They underwent a ductile deformation characterized by a steeply dipping slaty cleavage (Fig. 3f) with a subhorizontal mineral-stretching lineation. In the field, kinematic criteria are rare, but sigmoidal cleavage, lensoids and asymmetrically sheared clasts suggest a dextral sense of shear, which is confirmed by microscopic observations (Fig. 6). Quartz and feldspar clasts exhibiting asymmetric pressure shadows (Fig. 6a), shear bands (Fig. 6b), sigmoidal biotite (Fig. 5c), sheared andalusite or elongated quartz ribbons with oblique sub-grain fabrics (Fig. 5d) are common microstructures. Therefore, the present boundary between the turbidite, ophiolitic mélange and the Yili Block is a ductile right-lateral strike-slip fault, i.e. the NTF (fault 3 in Fig. 1, Fig. 2) [8]. The age of the shearing is not settled yet, on the basis of paleomagnetic data in the West Tianshan Belt in Kyrgyzstan, Bazhenov et al. [31] proposed that a dextral strike-slip event occurred during the Late Permian to Early Jurassic. However, in the study area, Jurassic coal bearing sandstone that covers the volcanic rocks are not deformed by the ductile shearing, that should therefore be older than Jurassic. Moreover, in East Chinese Tianshan, the MTSZ (fault 1 in Fig. 1) is dated at 280-250 Ma from syn-kinematic biotites by Ar-Ar method [4, 7]. Since the NTF and MTSZ appear to be cartographically continuous, a Permian age can be tentatively inferred for the NTF.

3.3. Carboniferous north-directed thrusting (D1)

In the turbidite unit, a series of tight isoclinal folds marked by siliceous layers are locally well developed. Due to the intense D2 dextral shearing, it is difficult to state whether these folds were formed during the D2 event or ealier. If the latter is the case, the fold asymmetry indicates a northward vergence. Bedding-parallel shear zones, sometimes marked by chlorite or illite coatings and N-S trending slicken-lines indicate a north-directed shearing. Similar low temperature shear zones can be observed around the ophiolite blocks in the mélange. These thrust faults are difficult to date, indeed, some of them might have been formed during the Cenozoic D3 event. However, on some surfaces, shearing related horizontal slicken-lines overprint steeply dipping striaes. This structural succession allows us to infer that the Carboniferous turbidite and ophiolitic mélange units experienced a top-to-the-north shearing before the D2 right-lateral shearing. Thus a Late Carboniferous age appears likely for this D1 event.

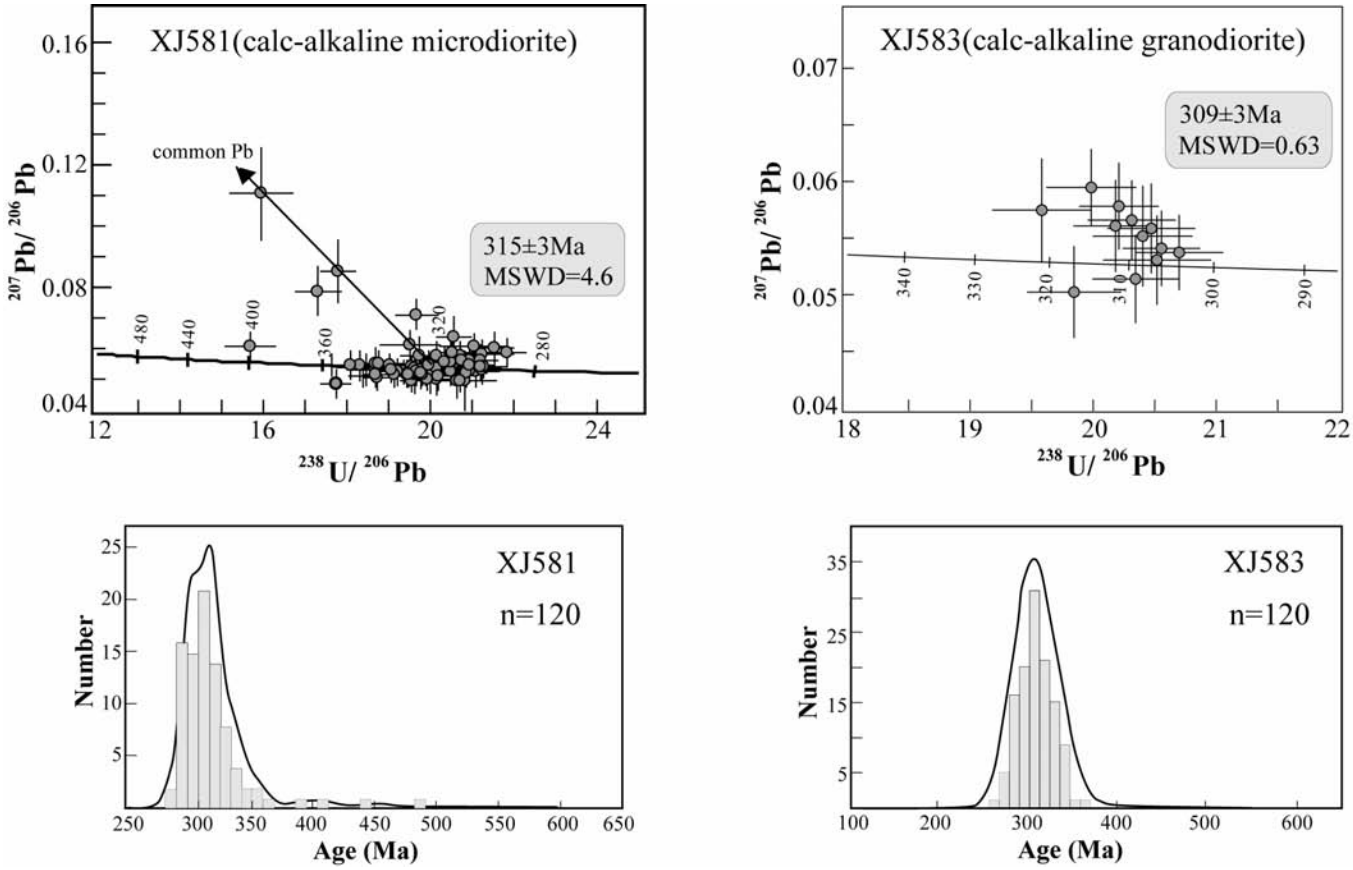

Fig. 5 Concordia diagrams of ICP-MS U-Pb zircon analytical results and histograms showing the age distribution for the arc-related calc-alkaline granitoids from the Yili Block (see Fig. 1 and 2 for samples localities).

4. Discussion

4.1. Implication of the ophiolitic rocks

The formation of the North Tianshan ophiolitic mélange is still controversial, and it was interpreted either as in situ disrupted ophiolites [15] or as klippes [18]. Since all the typical lithologies are represented in the field, previous researchers regarded these rocks as an ophiolitic nappe that was thrusted upon the turbidite [15-17]. However, a complete continuous ophiolitic sequence is lacking, and the oceanic rocks are always disrupted and mixed with sediments. In addition, the ophiolitic blocks and the surrounding sedimentary rocks often display sheared boundaries.

Sedimentary as well as tectonic processes may form a mélange [32]. In most outcrops, mafic and ultramafic rocks are mixed together with gabbroic sandstone, greywacke and pelite. This suggests that the oceanic rocks underwent an intra-oceanic tectonic event that was responsible for unroofing of peridotite and gabbro, shearing and subsequent re-deposition on the ocean floor. Finally, the already mixed magmatic and sedimentary rocks are included in the turbidite, as trench fill deposits during subduction. The sheared block-in-matrix structure supports a tectonic process active during accretion. According to the mélange classification proposed by Raymond [32] we interpret this ophiolitic mélange as a sheared olistostrome with exotic blocks.

4.2. Geodynamic evolution of the northern West Tianshan

The bulk architecture of the northern WTS Belt is due to a poly-orogenic evolution. As recognized by many authors on the basis of geological and geophysical studies [27-30], the Paleozoic rocks are thrusted to the north upon the Junggar Basin. Consequently, the primary Paleozoic structures are partly erased or concealed by the Cenozoic ones. Moreover, the D2 shearing might also hide initial relationships between the tectonic elements that formed the North Tianshan domain.

On the basis of high pressure metamorphic rocks with Sm-Nd and Ar-Ar ages around 350-315 Ma, some previous researchers proposed that the Yili magmatic arc resulted from the closure of a "South Tianshan Ocean" situated to the south of the Yili Block [18, 33-35]. However, older K-Ar ages ranging from 482 Ma to 415 Ma on these metamorphic rocks both in NW China and in Kyrgyzstan [31, 36] suggest that the high pressure event might be older than Yili arc magmatism. Moreover, there is no detailed structural analysis nor kinematic evidence supporting a northward subduction of "South Tianshan Ocean" below the Yili Block. Thus, on the basis of the previous studies and our own results, we propose a geodynamic model accounting for the evolution of the North Tianshan domain and the Yili Block (Fig. 7). In

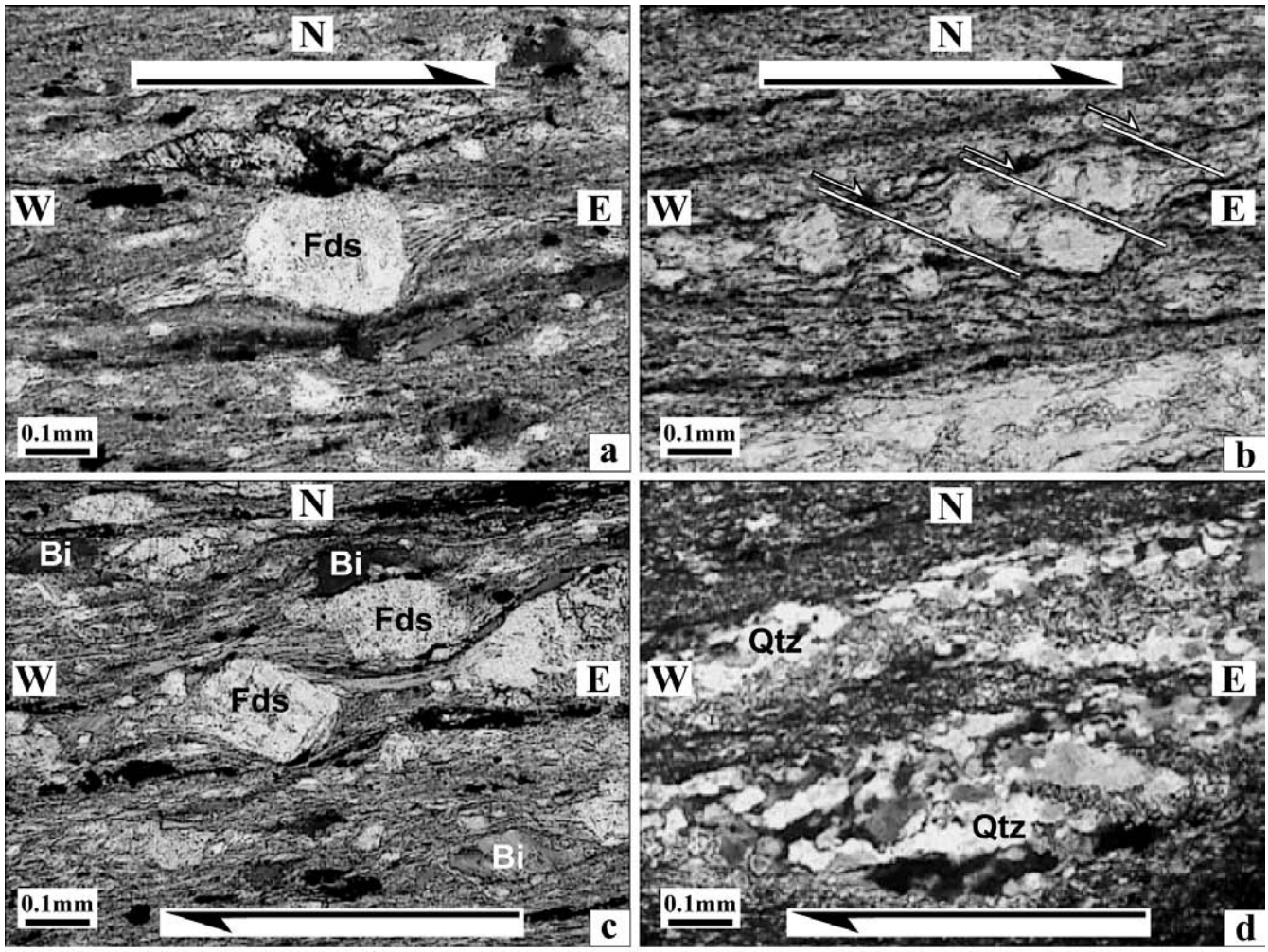

Fig. 6 Microscopic-scale shear criteria in slate along the North Tianshan Fault showing dextral ductile deformation. (a) feldspar clasts with asymmetric quartz and biotite pressure shadows; (b) shear-bands; (c) sigmoidal biotites and asymmetrically sheared feldspar clasts; (d) elongated quartz ribbons with an oblique shape fabric of recrystallized grains. In the field, the subvertical foliation contains a subhorizontal E-W trending mineral-stretching lineation (Fig. 3f). Mineral abbreviations: Fds, feldspar; Bio, biotite; Qtz, quartz.

our geodynamic model, the Yili magmatic arc is considered as the result of the south-directed subduction of an oceanic lithosphere located to the north of the Yili Block, remnants of this oceanic lithosphere are found in the ophiolitic mélange. Thus we assume that in Late Devonian to Carboniferous times, the subduction of an oceanic basin (i.e. "North Tianshan oceanic" [15]) below the Yili Block produced the magmatic arc and accretionary complex composed of turbidite and ophiolitic mélange.

The closure of the North Tianshan oceanic basin in Late Carboniferous resulted in the northward obduction and re-deformation of the ophiolitic mélange. Then a prominent change led to the end of N-S convergence and the beginning of intra-continental transcurrent tectonics. This event was due to either: 1) collision between the continental blocks with Precambrian basements (the Yili Block and the Junggar block, which is alternatively considered as a trapped Paleozoic ocean [37]), or 2) the progressive change from N-S convergence during the earlier stages to NE-SW convergence in the final stages.

The intra-continental transcurrent tectonism is represented by the Permian dextral strike-slip faulting. By comparison with eastern Chinese Tianshan, this event is assumed to take place between 280 and 250 Ma [5, 7]. This lateral transcurrent faulting was likely responsible for local crustal thinning and opening of pull-apart basins (e.g. the Turfan Basin in Fig. 1) [38, 39] in which marine deep-water sediments and alkaline pillow lavas accumulated, e.g. in Baiyanggou area [25]. The pull-apart basins are also associated with intra-plate magmatic rocks, such as alkaline granite, basalt, continental tholeiite and felsic volcanic rocks [11, 38].

On the basis of magmatic, sedimentologic and tectonic evidence, the Permian intra-continental large-scale strike-slip tectonics appears to be geodynamically distinct from the Late Devonian to Carboniferous oceanic convergence that built up the West Chinese Tianshan Belt. Therefore, any reconstruction of the Late Paleozoic Central Asia should take into account these lateral displacements. For instance, the Permian transcurrent faulting was geometrically likely to trigger the

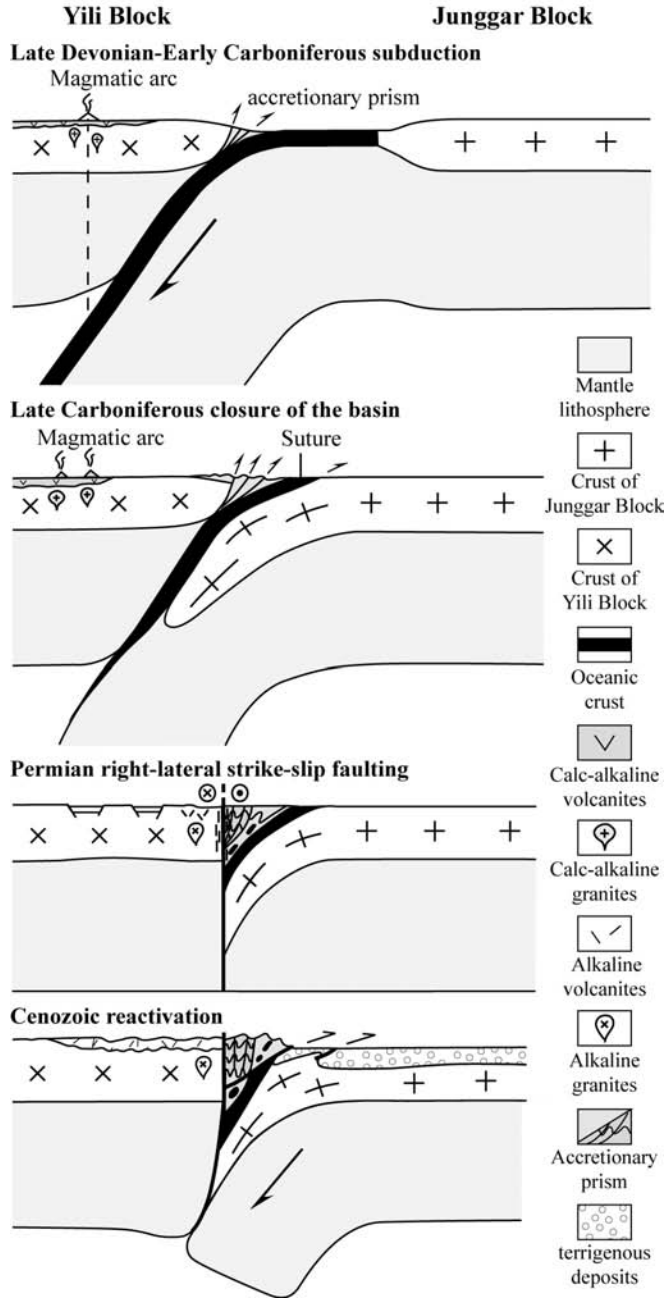

Fig. 7 Simplified geodynamic evolution of the northern West Chinese Tianshan Belt. In Late Devonian-Early Carboniferous, south directed subduction of an oceanic basin below the Yili Block led to the formation of a magmatic arc and an accretionary complex. In Late Carboniferous, the oceanic basin was closed, and the ophiolitic mélange was re-deformed. In Permian, the suture zone was reworked by dextral strike-slip fault. During Cenozoic, the intracontinental reactivation induced the thrusting of the North Tianshan Domain upon the Junggar sedimentary basin, the Paleozoic suture became "cryptic", i.e. hidden below the Paleozoic rocks.

lateral displacement of the Bogda Arc from its original place. Such displacement that was suggested to provoke strike-slip imbrication at the scale of the whole Central Asia Orogen [40] is still need to be documented quantitatively. A Paleomagnetic study that might provide such a constraint on the amount of E-W displacement is presently in progress.

5. Conclusion

Poly-orogenic events and multiple tectonic overprints arise some difficulties for reconstructing the geodynamic evolution of the Tianshan Belt. Taking into account the Cenozoic events, our study provides some new evidence to better understand the Paleozoic evolution of the northern WTS Belt. The polyphase evolutionary model proposed in this paper is comparable with the tectonic framework of the adjacent areas, and might be used to interpret the geodynamics of Central Asia Orogen. Regionally, Late Paleozoic subduction, accretion and collision of the Junggar Block play an important role on the building of the Central Asia, and the Permian post-collisional transcurrent event is widely recorded, but remains to be fully understood.

Acknowledgements

We thank the Bureau of National project 305 (Xinjiang Uygur autonomous Region, China) for field assistance. This is a contribution to the State Key Project for Basic Research of China (2001CB409804). Dr. J. Gao and S. Dominguez are thanked for valuable advices to improve this paper.

References

[1] Coleman R.G., Continental growth of Northwest China, Tectonics 8 (1989) 621-635.

[2] Windley B.F., Allen M.B., Zhang C., Zhao Z.Y., Wang G.R., Paleozoic accretion and Cenozoic redeformation of the Chinese Tien Shan range, Central Asia, Geology 18 (1990) 128-131.

[3] Allen M.B., Windley B.F., Zhang C., Paleozoic collisional tectonics and magmatism of the Chinese Tien Shan, Central Asia, Tectonophysics 220 (1993) 89-115.

[4] Shu L.S., Charvet J., Guo L.Z., Lu H.F., Laurent-Charvet S., A Large scale Paleozoic dextral strike-slip shear zone: the Aqikkudug-Weiya zone along the Northern margin of Central Tianshan belt, Xinjiang, NW China, Acta Geologica Sinica 73(4) (1999) 148-162.

[5] Laurent-Charvet S., Charvet J., Shu L.S., Ma R.S., Lu H.F., Palaeozoic late collisional strike-slip deformations in Tianshan and Altay, eastern Xinjiang, NW China, Terra Nova 14(4) (2002) 249-256.

[6] Shu L.S., Charvet J., Lu H.F., Laurent-Charvet S., Paleozoic accretion-collision events and kinematics of ductile deformation in the central-southern Tianshan Belt, China, Acta Geologica Sinica 76(3) (2002) 308-323.

[7] Laurent-Charvet S., Charvet J., Monie P., Shu L.S., Late Paleozoic strike-slip shear zones in eastern Central Asia (NW China): new structural and geochronological data, Tectonics 22(2) (2003) 1099-1101.

[8] Zhou D., Graham S.A., Chang E.Z., Wang B.Y., Hacker B., Paleozoic tectonic amalgamation of the Chinese Tianshan: Evidence from a transect along the Dushanzi-Kuqa highway, In: Hendrix M.S., Davis G.A. (Eds.), Paleozoic and Mesozoic tectonic evolution of central Asia: from continental assembly to intracontinental deformation, Geological Society of America Memoir, Boulder, Colorado, 194 (2001) pp. 23-46.

[9] Sengör A.M.C., Natal'in B.A., Paleotectonics of Asia: Fragments of a synthesis, In: Yin A., Harrison M. (Eds.), The Tectonic Evolution of Asia. Rubey Colloquium, Cambridge University Press, Cambridge, (1996) pp. 486-640.

[10] Zhao J.M., Liu G.D., Lu Z.X., Zhang X.K., Zhao G.Z., Lithospheric structure and dynamic processes of the Tianshan orogenic belt and the Junggar basin, Tectonophysics 376 (2003) 199-239.

[11] XBGMR (Xinjiang Bureau of Geology and Mineral Resources), Regional geology of Xinjiang Uygur Autonomy Region, Geology Publishing House, Beijing, 1993, pp.1-841 (in Chinese with English abstract).

[12] Jin H.J., Li Y.C., The flysch facies of Middle Carboniferous in the northern tianshan, Xinjiang, Acta Sedimentologica Sinica 7(1) (1989) 49-57(in Chinese with English abstract).

[13] BGSX (Bureau of geological survey of Xinjiang Uygur Autonomous Region), Geological map of People's Republic of China, 1:200000 Wusu sheet (L-45-XXXI) and geological survey report, (1977) (in Chinese).

[14] Wu J.Y., Liu C.D., Geological features of Bayingol ophiolite complexes in North Tien Shan, Xinjiang, Acta Petrologica Sinica 2 (1989) 76-87 (in Chinese).

[15] Xiao X.C., Tang Y.Q., Feng Y.M., Zhu B.Q., Li J.Y., Zhao M., Tectonic evolution of the northern Xinjiang and its adjacent regions, Geology Publishing House, Beijing, 1992, 169 p. (in Chinese with English abstract).

[16] Li X.D., Late Paleozoic evolution of oceanic basin and thrust structure in northern Tianshan, Xinjiang, Xinjiang Geology 11(3) (1993) 207-214 (in Chinese with English abstract).

[17] Li S.H., Du Q., The ophiolites in Motogou-Gurt of Wusu County, Xinjiang Geology 12(3) (1994) 265-271 (in Chinese with English abstract).

[18] Gao J., Li M.S., Xiao X.C., Tang Y.Q., He G.Q., Paleozoic tectonic evolution of the Tianshan Orogen, northern China, Tectonophysics 287 (1998) 213-231.

[19] Wang Z.H., Sun S., Li J.L., Hou Q.L., Qin K.Z., Xiao W.J., Paleozoic tectonic evolution of the northern Xinjiang, China: Geochemical and geochronological constraints from the ophiolites, Tectonics 22(2) (2003) 1014 doi: 10.1029/2002TC001396.

[20] Xia L.Q., Xia Z.C., Xu X.Y., Li X.F., Ma Z.P., Wang L.S., Carboniferous Tianshan igneous megaprovince and mantle plume, Geological Bulletin of China 23(9-10) (2004) 903-910 (in Chinese with English abstract).

[21] Li H.Q., Xie C.F., Chang H.L., Cai H., Zhu J.P., Zhou S., Study on metallogenetic chronology of nonferrous and precious metallic ore deposts in north Xinjiang, China, Geology Publishing house, Beijing, 1998, pp. 100-127 (in Chinese with English abstract).

[22] Wang B., Shu L.S., Faure M., Cluzel D., Charvet J., Geochemical Constraints on Carboniferous Volcanic rocks of Yili Block (Xinjiang, NW China); implication on tectonic evolution of Western Tianshan, Journal of Asian Earth Sciences, 2006, in press.

[23] Zhu Y.F., Zhang L.F., Gu L.B., Guo X., Zhou J., The zircon SHRIMP chronology and trace element geochemistry of the Carboniferous volcanic rocks in western Tianshan Mountains, Chinese Science Bulletin 50(19) (2005) 2201-2212.

[24] Charvet J., Laurent-Charvet S., Shu L.S., Ma R.S., Paleozoic continental accretions in Central Asia around Junngar Block: new structural and geochronological data, Gondwana Research 4(4) (2001) 590-592.

[25] Shu L.S., Zhu W.B., Wang B., Faure M., Charvet J., Cluzel D., The post-collision intracontinental rifting and olistostrome on the southern slope of Bogda Mountains, Xinjiang, Acta Petrologica Sinica 21(1) (2005) 25-36 (in Chinese with English abstract).

[26] Liu C.Y., Li T.H., Formation of sedimentary basins and terrane movement in northwestern China, In: Wiley T.J., Howell D.G., Wong F.L. (Eds.), Terrane analysis of China and the Pacific rim, Circum-Pacific Council for Energy and Mineral Resources Earth Science Series, Houston, Texa, 13 (1990) 227-229.

[27] Avouac J.P., Tapponnier P., Bai M., You H., Wang G., Active thrusting and folding along the northern Tien Shan and Late Cenozoic rotation of the Tarim relative to Dzungaria and Kazakhstan, J. Geophys. Res. 98(B4) (1993) 6755-6804.

[28] Hendrix M.S., Dumitru T.A., Graham S.A., Late Oligocene-Early Miocene unroofing in the Chinese Tian Shan: An early effect of the India-Asia collision, Geology 22 (1994) 487-490.

[29] Poupinet G., Avouac J.P., Jiang M., Wei S., Kissling E., Herquel G., Guilbert J., Paul A., Wittlinger G., Su H., Thomas J.C., Intracontinental subduction and Palaeozoic inheritance of the lithosphere suggested by a teleseismic experiment across the Chinese Tien Shan, Terre Nova 14 (2002) 18-24.

[30] Charreau J., Chen Y., Gilder S., Dominguez S., Avouac J.P., Sen S., Sun D.J., Li Y.A., Wang W.M., Magnetostratigraphy and rock magnetism of the Neogene Kuitun He section (northwest China): implications for Late Cenozoic uplift of the Tianshan mountains, Earth Planet. Sci. Lett. 230(1-2) (2005) 177-192.

[31] Bazhenov M.L., Burtman V.S., Dvorova A.V., Permian paleomagnetism of the Tien Shan fold belt, Central Asia: post-collisional rotations and deformation, Tectonophysics 312(2-4) (1999) 303-329.

[32] Raymond L.A., Classification of mélange, Geol. Soc. Am. Spec. Pap. 198 (1984) 7-19.

[33] Tang Y.Q., Gao J., Zhao M., Li J.Y., Wang J., The ophiolites and blueschists in the southwestern Tianshan orogenic belt, Xinjiang, Northwest China, Geological Publishing House, Beijing, 1995, pp. 30-59.

[34] Gao J., Klemd R., Eclogite occurrences in the western Tianshan high-pressure belt, Xinjiang, western China, Gondwana Res. 3 (2000) 33–38.

[35] Gao J., Klemd R., Formation of HP-LT rocks and their tectonic implications in the western Tianshan Orogen, NW China: geochemical and age constraints, Lithos 66(2003) 1–22.

[36] Tagiri M., Yano T., Bakirov A., Nakajima T., Uchiumi S., Mineral parageneses and metamorphic P-T paths of ultrahigh-pressure eclogites from Kyrghyzstan Tien-Shan, Island Arc 4(1995) 280–292.

[37] Carroll A.R., Liang Y.H., Graham S.A., Xiao X.C., Hendrix M.S., Chu J.C., Mcknight C.L., Junggar basin, northwest China: trapped late Paleozoic ocean, Tectonophysics 181 (1990) 1~14.

[38] Allen M.B., Sengör A.M.C., Natal'in B.A., Junggar and Alakol basins as Late Permian to? Early Triassic extensional structures in a sinistral shearing zone in the Altaid orogenic collage, Central Asia, J. Geol. Soc. Lon. 152 (1995) 327-338.

[39] Natal'in B.A., Sengör A.M.C., Late Paleozoic to Triassic evolution of the Turan and Scythian platforms: The pre-history of the Paloe-Tethyan closure, Tectonophysics 404(3-4) (2005) 175-202.

[40] Sengör A.M.C., Natal'in B.A., Burtman V.S., Evolution of the Altaid tectonic collage and Paleozoic crust growth in Eurasia, Nature 364 (1993) 299-307.

Artile Soumise à ***Tectonics***

Tectonics of the Yili Block in the southern part of the Western Chinese Tianshan, and its Paleozoic geodynamic evolution

Bo Wang[1, 2,*], Michel Faure[1], Liangshu Shu[2], Koen de Jong[1], Dominique Cluzel[1], Jacques Charvet[1], Sébastien Meffre[3], Gilles Ruffet[4], Qian Ma[2]

1: Institut des Sciences de la Terre d'Orléans, UMR CNRS 6113, Université d'Orléans, Bâtiment Géosciences, 45067 Orléans cedex 2, France
2: Department of Earth Sciences, Nanjing University, 210093, Nanjing, China
3: School of Earth Sciences, University of Tasmania, Hobart Tasmania 7001, Australia
4: Géosciences Rennes, UMR CNRS 6118, Université de Rennes 1, 35042, Rennes, France
* Corresponding author, Email: bo.wang@univ-orleans.fr or wangbo1996@nju.org.cn (B. Wang), Tel: +33.2.38.49.46.60; Fax: +33.2.38.41.73.09

Abstract

Field survey along the Kekesu River (South of Yili Block) documents a top-to-the North ductile shearing older than the Permian dextral wrenching. This event is responsible for the thrusting of the Tianshan Ocean rocks, metamorphosed under blueschist-eclogite facies, upon the Yili continental basement. 330-315 Ma $^{40}Ar/^{39}Ar$ laser probe plateau datings on white mica from retrogressed blueschist-facies metasediments constrain the age of the greenschist-facies retrogression that occurred during the exhumation of the high-pressure metamorphic rocks. The South Tianshan ophiolitic mélange overthrusts to the North above Silurian-Devonian marbles of Central Tianshan in Devonian-Carboniferous times. Therefore, the Yili Block cannot be the extension of Central Tianshan. Three ophiolitic sutures formed by southward subduction are recognized. The closure of the Tianshan Ocean led to the collision between the Yili Block and Central Tianshan, the Southern suture separates Central Tianshan from Tarim, the northern one lies between the Yili Block and Junggar.

Keywords: Yili Block, Tianshan, Ar-Ar daing, U-Pb ICPMS, high-pressure metamorphism, ophiolitic mélange.

1. Introduction

The Tianshan Belt is one of the main parts of the Central Asia Orogenic Belt (CAOB) [*Burtman*, 1975; *Coleman*, 1989; *Zonenshain et al.*, 1990; *Sengör et al.*, 1993; *Jahn et al.*, 2000; *Brookfield*, 2000; *Dobretsov and Buslov*, 2001; *Buckman and Aitchison*, 2004] and plays an important role on the assembly of the Eurasian continent. The present-day Tianshan range results from recent N-S crustal shortening accross the Tarim and Junggar Blocks during the Cenozoic Indo-Asia collision [*Molnar and Tapponnier*, 1975; *Tapponnier and Molnar*, 1979; *Nelson et al.*, 1987; *Avouac et al.*, 1993; *Hendrix et al.*, 1994; *Allen et al.*, 1999; *Burchfiel, et al.*, 1999;

Poupinet et al., 2002; *Shu et al.*, 2003; *Charreau et al.*, 2005]. The crustal shortening is accommodated by North and South directed thrusting of Paleozoic units over the Mesozoic and Cenozoic Junggar and Tarim basins on the northern and southern sides of the Tianshan range, respectively. Moreover, several crustal scale transcurrent faults are identified as responsible for large displacements along the belt [*Allen et al.*, 1995; *Bazhenov et al.*, 1999; *Shu et al.*, 1999; *Laurent-Charvet et al.*, 2002; 2003; *Zhao et al.*, 2003; *Wang et al.*, 2004a]. The latest Paleozoic to Early Mesozoic strike-slip faulting and the Cenozoic thrust reactivation both severely modified the pre-Late Carboniferous regional structure of the mountain belt [*Wang et al.*, 2006a, 2006b]. Despite the long history of reactivation, it is widely accepted that the Tianshan Belt is a Paleozoic orogen due to multiphase accretion and amalgamation of various micro-continents and magmatic arcs between the Kazakh, Junggar and Tarim continents [*Coleman*, 1989; *Shi et al.*, 1994; *Shu et al.*, 2000, 2002]. Three ophiolitic belts or ophiolitic mélange zones are recognized within the Tianshan Belt [*Windley et al.*, 1990; *Xiao et al.*, 1990, 1992, 2004; *Allen et al.*, 1992; *Ma et al.*, 1993; *Gao et al.*, 1998; *Chen et al.*, 1999].

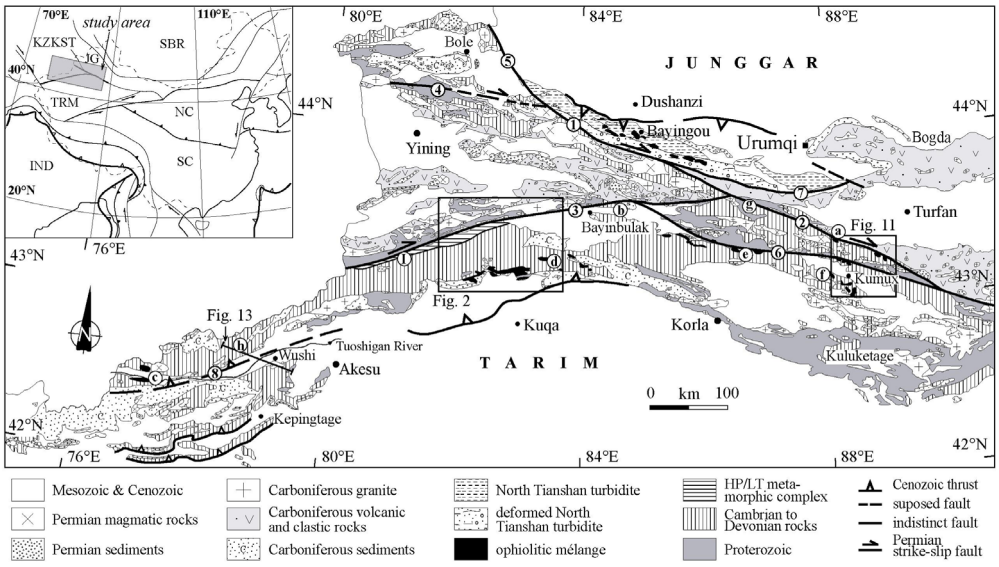

Figure 1. Geological map of the Chinese Western Tianshan Belt (modified from XBGMR [1993]). Numbers 1 to 8 correspond to the main faults, 1=North Tianshan Fault (NTF), 2=Main Tianshan Shear Zone (MTSZ), 3=Nalati Fault, 4=Jinghe Fault, 5=Aibi Fault, 6=Qingbulak Fault, 7=Houxia Fault, 8=South Tianshan Fault (STF). Letters refer to the localities cited in the text, a=Mishigou, b=Qiaohuote copper mine NE of Bayinbulak, c=Aheqi, d=Kule, e=Wuwamen, f=Yushugou, g=Shenglidaban. Inset shows the location of the study area in Central Asia. SBR=Siberia, NC=North China Block, SC=South China Block, KZKST=Kazakhstan Plate, JG=Junggar Block, TRM=Tarim Block, IND=India Plate.

In China, the Tianshan Belt is divided into three subunits, namely, the North Tianshan, Central Tianshan and South Tianshan [*Ma et al.*, 1993]. However, the detailed definition of each domain and their boundaries are still controversial.

The Yinning area is a triangular Mesozoic-Cenozoic sedimentary basin within the western Chinese Tianshan Belt. It widens westward to Kazakhstan and is bounded on its northern and southern limits by two Paleozoic ranges (Figure 1). It is considered as a micro-continent (or Yili Block) with a Precambrian crystalline basement [*Allen et al.*, 1992; *Coleman*, 1994; *Chen et al.*, 1999; *Wang et al.*, 2006a, 2006b]. This crustal block is also regarded as the westward extension of the "Central Tianshan Terrane" [*Zhou et al.*, 2001] or the main part of the "Yili-Central Tianshan Plate" [*Gao et al.*, 1998]. The Yili Block is also considered as a Late Paleozoic magmatic arc overlying

an Early Paleozoic platform underlain by a Proterozoic basement [*Allen et al.*, 1992; *Gao et al.*, 1998; *Chen et al.*, 1999; *Zhou et al.*, 2001; *Wang et al.*, 2006a]. Alternatively, the Central Tianshan is defined as an Early Paleozoic volcanic arc overlain by Late Paleozoic platform-type sedimentary rocks, both arc and cover are installed upon a Proterozoic basement [*Windley et al.*, 1990; *Ma et al.*, 1993; *Chen et al.*, 1999; *Laurent-Charvet et al.*, 2002]. This later definition is consistent with that given for the Eastern Tianshan [*Ma et al.*, 1997; *Xiao et al.*, 1992].

Moreover, three ophiolitic belts are generally assigned by most of previous researchers to two sutures zones, namely the North Tianshan Suture and South Tianshan Suture [e.g. *Windley et al.*, 1990; *Allen et al.*, 1992; *Gao et al.*, 1998; *Chen et al.*, 1999; *Zhou et al.*, 2001] (Figure 1). The South Tianshan Suture is defined by the ophiolites and metamorphic rocks that crop out discontinuously along the Qingbulak and Nalati faults (faults 6 and 3 in Figure 1). Ophiolitic mélanges, such as those at Kumux, Yushugou, Wuwamen and Kule (Figure 1), are interpreted as thrust sheets transported from this suture to the south [*Windley et al.*, 1990; *Gao et al.*, 1998; *Allen et al.*, 1992; *Zhou et al.*, 2001]. In the southern part of the Yili Block, two zones of ophiolitic mélange and high-pressure (HP) metamorphic complex are interpreted as the result of the closure of the South Tianshan Ocean during Silurian to Early Carboniferous [*Chen et al.*, 1999; *Zhou et al.*, 2001]. However, these ophiolites are poorly dated, and most of the available geochronological data were obtained by Ar-Ar or Rb-Sr methods (Table 1).

In order to shed light on the Paleozoic regional structure of the Tianshan Belt, we performed field observations and detailed structural analyses in three well targeted key areas across the southern part of the Yili Block and the Chinese Tianshan Belt (Figure 1) during a four-years period. Newly obtained U-Pb, ^{40}Ar-^{39}Ar and paleontological results, and our previous results from the northern part of the Yili Block [*Wang et al.*, 2006a, 2006b], enable us to present a new model for the Paleozoic geodynamic evolution of the Western Chinese Tianshan Belt emphasizing several south directed subductions and arc collisions.

2. Geological overview of the western part of the Chinese Tianshan Belt

More and more studies on the Chinese Tianshan Belt allow the constitution of an overall geological framework. In this section, we synthesize the previous research published in both Chinese and international literatures and our own field observation. In the following, we subdivide the western part of the Paleozoic Chinese Tianshan Belt into North Tianshan, Bole Block, Yili Block, Central Tianshan and South Tianshan (Figure 1).

2.1. The North Tianshan.

This domain is located to the north of the North Tianshan Fault (NTF, fault 1 in Figure 1) [*Allen et al.*, 1992; *Zhou et al.*, 2001] and the Main Tianshan Shear Zone (MTSZ, fault 2 in Figure 1) [*Shu et al.*, 1999, 2002; *Laurent-Charvet et al.*, 2002]. The North Tianshan consists of Late Carboniferous volcaniclastic turbidites incorporating dismembered ophiolite that includes Late Devonian-Early

Carboniferous cherts dated by radiolarians and conodonts, pillow basalts, gabbro and serpentinized peridotite [*Xiao et al.*, 1992; *Carrol*, 1995; *Gao et al.*, 1998; *Chen et al.*, 1999; *Zhou et al.*, 2001; *Wang et al.*, 2006a, 2006b]. This turbidite is interpreted as a trench fill deposit that formed in an accretionary complex [*Chen et al.*, 1999; *Zhou et al.*, 2001] produced by the southward subduction of an oceanic basin located between the Junggar and Yili blocks [*Xiao et al.*, 1992; *Wang et al.*, 2006a, 2006b]. The Southern part of the turbidite was deformed by a dextral ductile shearing zone, which took place in Late Permian [*Shu et al.*, 1999; *Laurent-Charvet et al.*, 2002; *Wang et al.*, 2006b]. To the east of Urumqi, the North Tianshan includes the Bogda volcanic arc that is composed of the Late Devonian to Carboniferous calc-alkaline volcanic rocks and granites widely distributing around the Turfan Basin [*Shu et al.*, 1999; *Laurent-Charvet*, 2001] Figure 1). Permian continental red beds unconformably overlying Carboniferous rocks and felsic granite intrusion can be observed in the whole North Tianshan area [*XBGMR*, 1993; *Allen et al.*, 1995].

2.2. The Yili Block.

The Yili Block is a triangular area that widens to the west spreading into Kazakhstan and Kirgyzstan, and it is located between the NTF and Nalati Fault (faults 1 and 3 in Figure 1) [*Zhao et al.*, 2003]. The Nalati Fault is considered as the eastern extension of the Nikolaev Tectonic Line that stretches westward into Kyrgyzstan [e.g. *Wang et al.*, 1990; *Tagiri et al.*, 1995; *Zhou et al.*, 2001]. The Yili Block is considered as a microcontinent [*Allen et al.*, 1992; *Coleman*, 1994] with a Proterozoic basement croping out along its northern and southern boundaries (Figure 1) [*Gao et al.*, 1998; *Zhou et al.*, 2001; *Wang et al.*, 2006a]. Early Paleozoic rocks are composed of shelf-continental slope sedimentary sequences [*XBGMR*, 1993; *Chen et al.*, 1999; *Wang et al.*, 2006a] and distribute mainly at the northern margin of the Yili Block (Figure 1). Carboniferous sedimentary rocks are closely associated with large volume of calc-alkaline volcanic and plutonic rocks [*Wang et al.*, 2006a] (Figure 1) yielding zircon U-Pb ages ranging between 360 and 310 Ma [*Zhu et al.*, 2005; *Wang et al.*, 2006b]. Trace element and isotopic analyses indicate that these magmatic rocks formed in an active margin setting [*Wang et al.*, 2006a, and in preparation].

2. 3. The Bole Block.

This area is geologically different from both the North Tianshan and the Yili Block. There, Devonian to Carboniferous sedimentary rocks were deposited directly over the Precambrian basement [*XBGMR*, 1993]. Carboniferous rocks consist of conglomerate, sandstone, and platform limestone, but arc volcanites are absent. The widespread Permian alkaline magmatic rocks are similar to those found in the whole Tianshan area [*Chen et al.*, 2000]. The Bole Block is separated from the North Tianshan and the Yili Block by two strike-slip faults (faults 4 and 5 in Figure 1). Our structural survey in this region suggests that the Bole Block was not put in contact with the other domains before Late Permian [Wang et al., in preparation]. In the following, the Bole Block will not be considered.

Table 1. Compilation of published radiometric ages of the main tectonic and magmatic events in Chinese Western Tianshan Belt.

Tectonic events	Locations	minerals	rocks	methods	ages	references
NTF	Borohoro	biotite	pluton	Ar-Ar	260.1±3.4	Yin et al., 1996
NTF	Haxilegen	biotite	pluton	Ar-Ar Plateau	267.7±1.8	Zhou et al., 2001
NTF	Haxilegen	biotite	pluton	Ar-Ar Plateau	275.3±1.9	Zhou et al., 2001
MTSZ	Bingdaban	biotite	orthogneiss	Ar-Ar	290-245Ma	Laurent-Charvet et al., 2003
Yili	Guozigou	zircon	granite	U-Pb ICPMS	389±6	Wang et al., in preparation
magmatic	Haxilegen	zircon	granite	U-Pb ICPMS	301±7	Wang et al., in preparation
arc	Yuxi	zircon	granite	U-Pb ICPMS	315±3	Wang et al., 2006b
	Yuxi	zircon	granite	U-Pb ICPMS	309±3	Wang et al., 2006b
	Laerdun	whole rock	pluton	Rb-Sr isochron	334.9±28	Zhu and Sun, 1986
	Nalati	biotite	pluton	Ar-Ar Plateau	355.1±10.7	Hao and Liu, 1993
	Nalati	biotite	pluton	K-Ar	327	Gao, 1993
	Nalati	whole rock	pluton	Rb-Sr isochron	339	Wang et al., 1990
	Nalati	biotite	granite	K-Ar	327	**XGS, 1987**
	Zhaosu	biotite	pluton	K-Ar	334.4	Gao, 1993
	Zhaosu	biotite	pluton	K-Ar	345.6	Gao, 1993
	Zhaosu	zircon	granite	U-Pb ICPMS	358±11	Wang et al., in preparation
	Zhaosu	zircon	granite	U-Pb ICPMS	361±6	Wang et al., in preparation
	Qiongkushitai	zircon	granite	U-Pb ICPMS	313±4	Wang et al., in preparation
	Kekesu	zircon	granite	U-Pb ICPMS	338±8	Wang et al., in preparation
	Kekesu	zircon	granite	U-Pb ICPMS	341±6	Wang et al., in preparation
Bogda arc	Tianchi	biotite	pluton	K-Ar	313	Hu et al., 1986
	Juluotage		granite?	K-Ar	300	Wang et al., 1990
	Juluotage		granite?	K-Ar	307	XBGMR, 1993
Nalati	Bayinbulak	K-feldspar	pluton	Ar-Ar Plateau	265.3±2.4	Zhou et al., 2001
Fault	Nalati	biotite	mylonite	Ar-Ar	250±7.9	Cai et al., 1996
High	Changawuzi		pluton	K-Ar	534	XBGMR, 1993
pressure	Changawuzi		pluton	U-Pb	400	XBGMR, 1993
metamorphic	Changawuzi		pluton	K-Ar	405	XBGMR, 1993
complex	Changawuzi	pyroxene	gabbro	Ar-Ar	439.4±26.7	Hao and Liu, 1993
	Changawuzi	phengite	blueschist	Ar-Ar	315	Jia, 1996
	Changawuzi	glaucophane	blueschist	Ar-Ar	350.9±2	Xiao et al., 1990
	Kyrgyzstan		blueschist		410±15	Dobretsov et al., 1987
	Qiongkushitai	phengite	blueschist	Ar-Ar	415.4±2.3	Gao, 1993
	Qiongkushitai	phengite	blueschist	Ar-Ar	419.6±3.9	Gao, 1993
	Kekesu	phengite	blueschist	Ar-Ar	345.4±6.5	Gao et al., 1995
	Kekesu	Garnet,glaucophane	eclogite	Sm-Nd whole rock	346±3	Gao and Klemd, 2003
	Kekesu	phengite	blueschist	Ar-Ar Plateau	344±1~331±2	Gao and Klemd, 2003
	Kekesu	sodic amphibole	eclogite	Ar-Ar Plateau	401±1	Gao et al., 2000
	Kekesu	muscovite	eclogite	Ar-Ar Plateau	381±1	Gao et al., 2000
	Kekesu	sodic amphibole	blueschist	Ar-Ar Plateau	370+1	Gao et al., 2000
	Kekesu	muscovite	blueschist	Ar-Ar Plateau	364+1	Gao et al., 2000
	Kekesu	white mica	blueschist	K-Ar	327±9~309±9	Klemd et al., 2005
	Kekesu	white mica	blueschist	Ar-Ar	328±0.5~311±5	Klemd et al., 2005
	Kekesu	white mica	blueschist	Rb-Sr isochron	313±4~302±3	Klemd et al., 2005
	Kekesu	white mica	blueschist	Ar-Ar Plateau	316.3±2.2	This study
	Kekesu	white mica	blueschist	Ar-Ar Plateau	330.7±0.3	This study
	Kekesu	white mica	greenschist	Ar-Ar	322.8±0.4	This study
Central	Bayinbulak	zircon	pluton	U-Pb	378	Hu et al., 1986
Tianshan	Bayinbulak	zircon	granite	U-Pb	421±11	Han et al., 2004
plutons	Yeyungou	zircon	granite	U-Pb	475.2±2.6	Han et al., 2004
	Kumux	zircon	granite	U-Pb	457.4±1.8	Han et al., 2004
southern	Kule	biotite	quartz schist	Ar-Ar	370±4.8	Cai et al., 1996
Tianshan	Yushugou	zircon	gabbro	U-Pb	378.2±6.3	Jiang et al., 2000
mélange	Heiyingshan	zircon	gabbro	U-Pb ICPMC	392±5	This study
South Tianshan	Bosten Lake	biotite	diorite	Ar-Ar	347	Yin et al., 1996
plutons	Bosten Lake	K-feldspar	diorite	Ar-Ar	333	Yin et al., 1996
Permian	Borohoro	whole rock	pluton	Rb-Sr	292±15	Wang et al., 1990
magmatism	Borohoro	biotite	pluton	Ar-Ar	254.5±4.8	Yin et al., 1996
	North of Nileke	zircon	granite	U-Pb ICPMC	272±6	Wang et al., in preparation
	North of Nileke	zircon	granite	U-Pb ICPMC	266±6	Wang et al., in preparation
	Haxilegen	zircon	granite	U-Pb ICPMC	280±5	Wang et al., in preparation
	Haxilegen	zircon	granite	U-Pb ICPMC	294±7	Wang et al., in preparation
	North Bayingbulak	K-feldspar	granite	Ar-Ar Plateau	274.8±0.4	Wang et al., 2004
	Manas		pluton	K-Ar	285	XBGMR, 1993
	Tianchi	biotite	pluton	K-Ar	265.5	Hu et al., 1986
	Tianchi	biotite	pluton	K-Ar	256.3	Hu et al., 1986
	Juluotage		granite	K-Ar	292	Wang et al., 1990
	Juluotage		granite	K-Ar	293	XBGMR, 1993
	Bosten Lake	biotite	gneiss	Ar-Ar	286	Yin et al., 1996
	Bosten Lake	horblende	diorite	Ar-Ar	262	Yin et al., 1996
	Kumux	zircon	granite	U-Pb ICPMC	252±4	Wang et al., in preparation
	Kekesu	zircon	granite	U-Pb ICPMC	277±3	Wang et al., in preparation

2.4. The Central Tianshan.

This domain is sometimes defined by previous researchers as a wedge-like

region bounded by faults 2, 3 and 6 (Figure 1). Fault 6, called the Qingbulak Fault, has been considered as a suture zone between the Central Tianshan and South Tianshan [*Windley et al.*, 1990; *Allen et al.*, 1992]. As stated in section 1, the central Tianshan is often correlated with the Yili Block [e. g. *Gao et al.*, 1998; *Zhou et al.*, 2001]. According to our own field observations and the reassessment of the available 1:200 000 geological maps, the Late Devonian-Carboniferous arc-type magmatic rocks are only distributed to the north of the Faults 2 and 3, namely MTSZ and Nalati Faults. The contemporaneous strata to the south of these faults, are exclusively sedimentary rocks with minor plutons (Figure 1). All these rocks are neither metamorphic nor highly deformed. On the basis of our new data presented in the following sections, we argue that the Yili Block is a microcontinent distinct from the Central Tianshan. Moreover, in the eastern part of the Chinese Tianshan, the Central Tianshan is considered as an Early Paleozoic magmatic arc represented by deformed calc-alkaline metavolcanic rocks yielding a Rb-Sr isochron age of ca. 470 Ma [*Ma et al.*, 1993, 1997; *Shu et al.*, 1999; *Laurent-Charvet et al.*, 2002]. Similar arc rocks are observed in Western Tianshan in Bayinbulak and north of Kumux (localities a and b in Figure 1, respectively) [*Laurent-Charvet et al.*, 2001; *Wang et al.*, 2004b].

2.5. The South Tianshan.

It corresponds to the wide domain south of the Nalati and Qingbulake Faults (faults 3 and 6 in Figure 1), and is defined as a Paleozoic passive continental margin of the Tarim continent [*Windley et al.*, 1990; *Allen et al.*, 1992; *Gao et al.*, 1998; *Chen et al.*, 1999; *Zhou et al.*, 2001]. In fact, two different rock assemblages of Middle Paleozoic age are recognized in this area. North of the ophiolitic mélanges of Kumux, Heiyingshan and Aheqi (Figure 1), Silurian-Devonian strata are ductilely deformed marbles and clastic rocks [*Wang et al.*, 1997], whereas Cambrian through Devonian strata south of this mélange zone are gently folded shallow marine carbonate and continental sandstone with minor volcanic clasts attributed to the sedimentary cover of the Tarim continent [*Windley et al.*, 1990; *Allen et al., 1992*; *Gao et al.*, 1998].

Middle Devonian-Early Carboniferous ophiolitic mélanges are already recognized east of the Kuqa meridian [e.g. *Windley et al.*, 1990; *Gao et al.*, 1998; *Allen et al.*, 1992; *Liu*, 2001; *Zhou et al.*, 2001] (Figure 1). During our field survey this unit has been recognized in several places west of Kuqa. These ophiolitic mélanges are generally considered as south-directed nappes rooted in the Qingbulak Fault (fault 6 in Figure 1). However, our kinematic studies indicate a top-to-the-North sense of shear (cf. Sections 6 and 7), therefore, the ophiolitic mélanges of the South Tianshan Suture can hardly come from the north, and a new geodynamic framework must be considered.

As shown above, some problems arise to define the Yili Block, Central Tianshan, South Tianshan and the intervening suture zones. In the following, we present several key sections through the Yili Block, high-pressure metamorphic complex, ophiolitic mélange zones in the southern Tianshan area and the northern margin of Tarim Block. Then, our understanding on the tectonic division and geodynamic evolution of the Tianshan Belt is discussed.

3. The Kekesu-Heiyingshan transect

Southwest of Bayinbulak (Figure 1), the Haerkeshan range forms the highest peaks of the Chinese Tianshan range, and is therefore rather difficult to reach. The Kekesu-Heiyingshan transect (Figures 2 and 3), parallel to the southern segment of the Dushanzi-Kuqa (Duku) highway [*Wang et al.*, 1997; *Zhou et al.*, 2001], covers the southern branch of the Yili Block and the Southern Tianshan. We surveyed the northern segment of this transect along the Kekesu River upstream of Tekesi and the southern segment from Heiyingshan up to 40 km northwestward. In this section, the lithology and bulk geometry of each tectonic unit are described from North to South and synthesized in an interpretative general cross section in Figure 3.

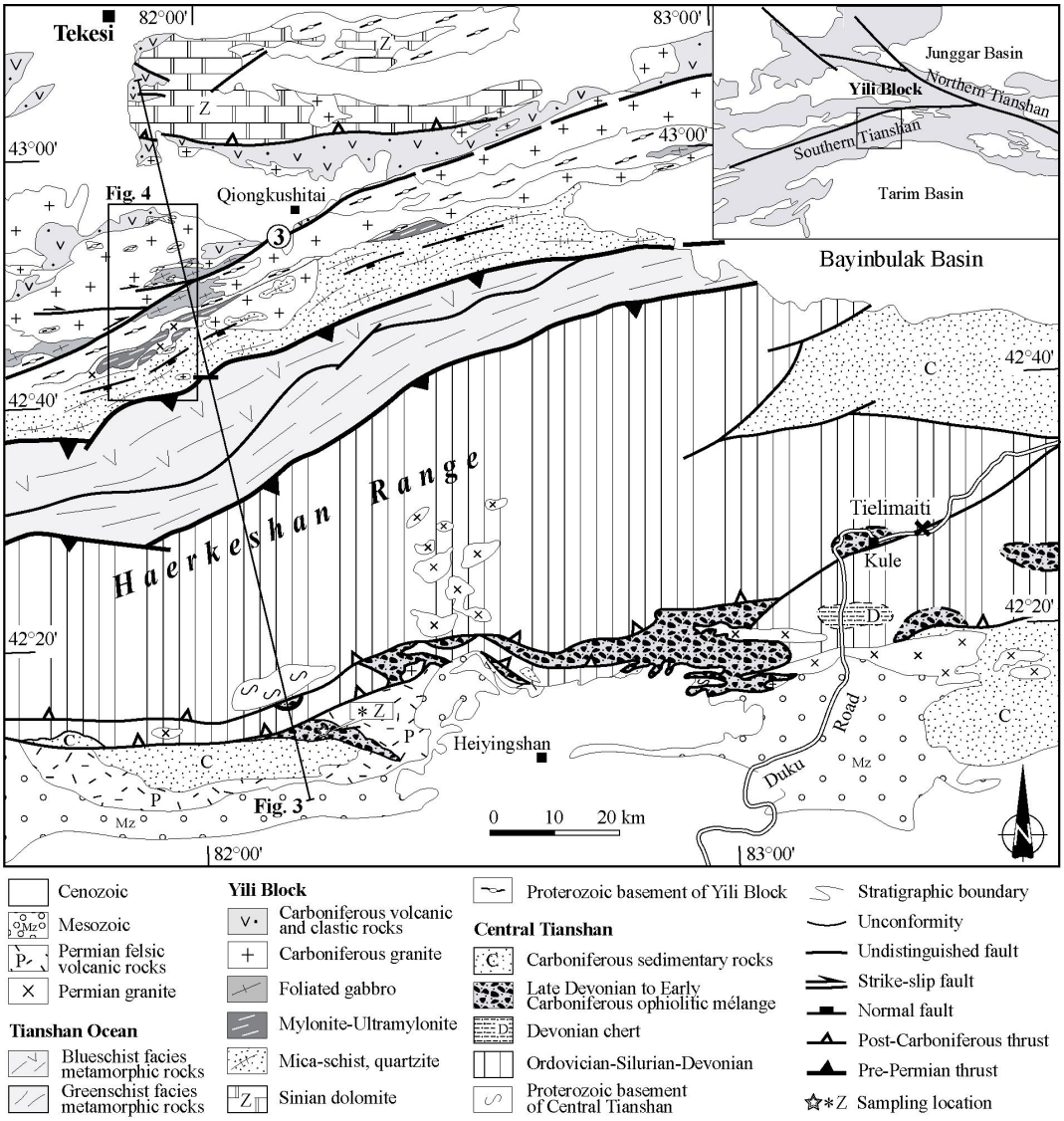

Figure 2. Geological map of Kekesu-Heiyingshan transect (modified from XBGMR [1979, 1993] and Gao et al. [1995, 2000, 2003]). Inset shows the location of transection in Chinese Western Tianshan Belt. * and Z indicate the sampling localities of radiolarian chert and zircon U-Pb dated gabbro, respectively.

3.1. The Yili magmatic arc

The northernmost part of the Kekesu section is dominated by Carboniferous limestone and sandstone associated with magmatic rocks. Volcanites are andesite, rhyolite, trachyte and tuff; basalt occurs rarely. Plutons of coarse grained granodiorite,

tonalite and granite with K-feldspar megacrysts, pegmatite and aplite dykes are well developed. Trace elements geochemistry and isotopic data of porphyritic volcanites and granites with centimeter-sized megacrysts indicate that these rocks are calc-alkaline in composition and was generated in an active continental marginal setting [*Wang et al.*, 2006a, and in preparation]. The age of a calc-alkaline granite is constrained by zircon U-Pb ICPMS dating at 341±6 Ma (Figure 4). The REE, isotopic and geochronological data of the Yili Block magmatic rocks have been studied in several places [*Li et al.*, 1998; *Zhu et al.*, 2005; *Wang et al.*, 2006a, 2006b, in preparation]. Radiometric ages, ranging between 360 and 310 Ma, and REE geochemistry support the accepted interpretation that during the Carboniferous, the Yili Block was a continental based magmatic arc.

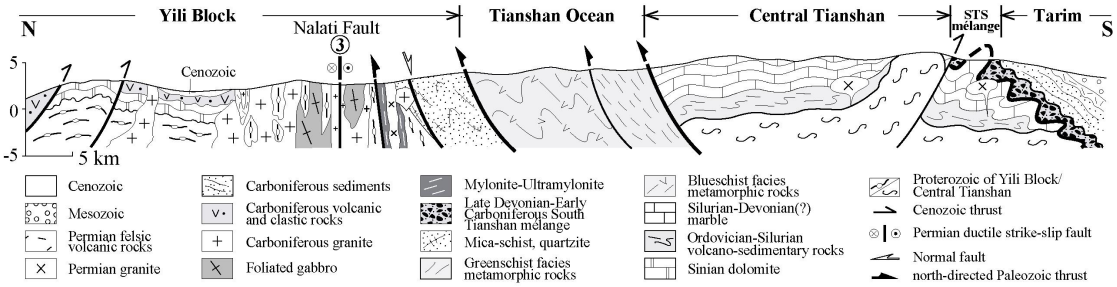

Figure 3. Interpretative cross section from Tekesi to Heiyingshan located in Figure 2. Three continental masses, from North to South, Yili Block, Central Tianshan and Tarim, respectively are separated by two zones of oceanic rocks

3.2. The Proterozoic basement

The continental basement of the Carboniferous Yili arc is characterized by stromatolite bearing Neoproterozoic (Sinian) dolomite and Meso to Paleoproterozoic metamorphic rocks. Ortho and paragneiss are well exposed along the Kekesu River, and East of Qiongkushitai (Figures 2 and 4). In the study area, Early Paleozoic strata do not occur but they are observed in the northern part of the Yili Block [*Gao et al.*, 1998; *Wang et al.*, 2006a] (Figure 1).

From Wenquan to the south (Figure 4), a 20-km-wide zone of ductilely deformed granitoids, gabbros and gneiss is developed. The mafic magmatic rocks might correspond to the root of the Yili arc, but geochemical and geochronological data are lacking. Near the Nalati Fault (number 3 in Figure 1), the rocks are ductilely deformed (see section 4). Along the Kekesu River, biotite-muscovite micaschist, micaceous quartzite, and biotite gneiss are well exposed south of 42°45’ (Figure 4). Some gneiss contain K-feldspar augen and ellipsoidal enclaves of biotite, thus they are likely derived from granitoids intrusive into a micaschist and quartzite series. We interpret this sequence of metamorphosed magmatic and sedimentary rocks as the southernmost, highly deformed, margin of the Yili Block. To the south, this zone is in thrust contact with the HP metamorphic complex. The polyphase deformation experienced by these rocks is described in section 4.

3.3. The blueschists and eclogite complex

The blueschists and eclogites that crop to the south of the Proterozoic basement of the Yili Block along the Kekesu River (Figure 2 and 4) form part of a 200 km long belt that develops in the northern slope of Haekeshan Range. The belt of

eclogite-facies metamorphic rocks continues westward to the south Tianshan areas of Kyrgyzstan (Atbashy eclogite belt yielding garnet with inclusions of coesite pseudomorphs) [*Dobretsov et al.*, 1987; *Tagiri et al.*, 1995] and of Tajikistan (Fan-Karategin blueschist belt) [*Volkova and Budanov*, 1999]. To the East, this belt disappears west of the Bayinbulak basin. In agreement with the previous authors [e. g.

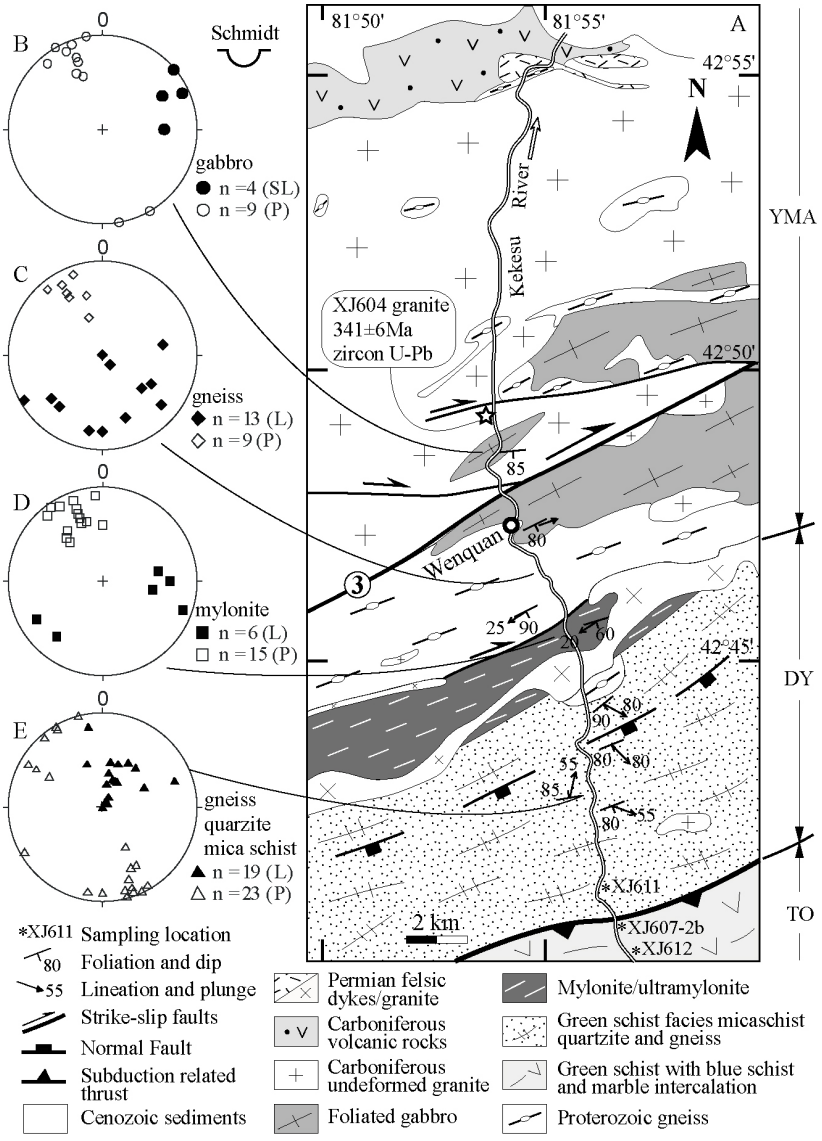

Figure 4. Structural data along the Kekesu River, located in Figure 2 (modified from XBGMR [1979] and Gao [2000]). A: Structural map, YMA corresponds to the Yili Magmatic Arc and its deformed gneissic basement, DY is the southern part of the Yili Block that was deformed and metamorphosed during the northward thrusting of the HP rocks, TO corresponds to the Tianshan Ocean presently characterized by HP oceanic rocks. Number 3 is the Nalati fault (the same as fault 3 in Figure 1). B to E: Schmid plots (lower hemisphere) of the planar and linear elements along the section, faults and foliations are represented by their pole. B: plot of the vertical brittle faults (P) and subhorizontal slickenlines (SL) related to brittle dextral shearing. C: plot of the subvertical to SE dipping foliation (P) showing the scattering of the stretching lineation (L). The average NW-SE trend is associated with top-to-the-NW shearing. D: subvertical foliation and subhorizontal lineation well developed in mylonites and ultramylonites, this fabric is associated with a dextral wrenching coeval with the deformation along fault 3. E: subvertical foliation and lineation observed in gneiss, micaschist and quartzite, most of the lineations are developed during a top-to-the-N shearing, however some shear criteria indicate also a normal fault geometry. For detail of the structural analysis, see section 4.

Gao et al., 1995; *Gao and Klemd*, 2003], We divide the metamorphic rocks along the Kekesu River into: 1) a northern subunit dominated by micaschists and muscovite-quartzites and mafic rocks metamorphosed under HP conditions; and 2) a

southern subunit composed of greenschists, quartzschists and minor marbles, without HP rocks (Figure 2). In the northern subunit, blueschists are present as meter sized blocks, lenses, boudins and thin layers preserved within metapelites retrogressed under greenschist facies conditions [*Gao et al.*, 1995, 2000; *Gao and Klemd*, 2003]. The petrology, mineralogy, geochemistry and geochronology of blueschists and eclogites in this complex are fairly well known [e. g. *Gao et al.*, 1995, 1999; *Tagiri et al.*, 1995; *Volkova and Budanov*, 1999; *Gao and Klemd*, 2000, 2003; *Klemd et al.*, 2002, 2005]. *Wei et al.* [2003] underlined that the blueschists and eclogites did not experience identical peak-metamorphic conditions. However, the Ultra High pressure metamorphic character of these rocks is hotly debated. According to some authors, the HP metamorphic complex experienced P and T peak conditions of 2.0±0.1 GPa and 550±50°C, respectively [*Klemd 2003*; *Klemd et al.*, 2002; *Gao and Klemd*, 2003], but others argue in favor of Ultra High pressure metamorphic conditions of 2.5 GPa or even 5.0 GPa [*Wei et al., 2003*; *Zhang et al.*, 2003a, 2003b].

In the Kekesu River, the blueschist facies metamorphism is overprinted by a greenschist facies event developed during the nearly isothermal retrogression [*Gao et al.*, 2003; *Klemd et al.*, 2005]. In both subunits, the protoliths of the sedimentary rocks are quite similar. They are interpreted as pelagic argillites, siliceous shales and chert [*Gao et al.*, 1995]. On the basis of mineralogical and geochemical studies, the magmatic rocks are considered to derive from basalt and volcaniclastic rocks with MORB and OIB signature. Therefore, the protoliths of the HP metamorphic rocks including both oceanic crust and sedimentary rocks are likely formed in an oceanic basin [*Gao et al.*, 2003], which is usually named “South Tianshan Ocean”, and in this paper we simply define it as Tianshan Ocean for avoiding to arise spatial confusion. Nevertheless, the OIB geochemical affinity of some mafic rocks suggests that a seamount-like setting may account for a part of these oceanic rocks. The HP metamorphic complex is interpreted as an accretionary wedge due to a north-directed subduction [*Gao et al.*, 1995, 1998; *Gao and Klemd*, 2003]. Although we acknowledge the subduction tectonic setting, our structural analysis suggests that the subduction is south-directed (see section 4).

3.4. The Central Tianshan Block

The upper stream of the Kekesu River exposes a rock succession quite different from the previous ones. There, Silurian limestone overthrusts the blueschis and eclogite complex northward. Due to practical difficulties, this domain is poorly investigated. However, similar rocks crop out along the Duku road, 80 km eastward (Figure 2). South of Bayinbulak, Early to Middle Carboniferous weakly deformed and unmetamorphozed conglomerate, sandstone and carbonates unconformably overlie Devonian granite dated at 378 Ma by zircon U-Pb method [*Hu et al.*, 1986] (Table 1). Similar unconformable relationship between the Carboniferous deposits and the older rocks is described by previous authors [e. g. *Zhou et al.*, 2001] on the northern slope of the Tielimaiti Pass (Figure 2), where, Silurian turbidite with volcaniclastic rocks and minor limestone are well developed. On the southern side of Tielimaiti pass, the Silurian rocks consist of recrystallized platform limestones with intraformational

breccia, they are overlain by Early Devonian carbonate, conglomerate, sandstone and chert [*XBGMR*, 1993; *Zhou et al.*, 2001]. This Paleozoic series is weakly or unmetamorphozed but deformed by south vergent folds. Moreover, near Kule (Figure 2), an ophiolitic mélange crops out. As shown below in section 3.5, this formation is similar to that observed in Heiyingshan (Figure 2). These ophiolitic mélanges from allochthonous thrust sheets displaced from South to North upon marbles of the Central Tianshan. Lastly, west of Heiyingshan (Figure 2), the Early Paleozoic series is underlain by Proterozoic gneiss corresponding to the metamorphic basement of the Central Tianshan.

We suggest that the whole Paleozoic sedimentary succession forming the highest part of the Haerkeshan range represent passive margin rocks deposited upon a Proterozoic continental basement. In the following, we assign this domain, south of the HP metamorphic complex and north of the ophiolitic mélange, to the Central Tianshan Block. However, it is worth to note that there is some divergence in the terminology and geodynamic interpretation, since some authors call this area South Tianshan or assign it to the northern margin of Tarim Block [*Allen et al.*, 1992; *Gao et al.*, 1998; *Zhou et al.*, 2001, and references therein]. In our view, the Central Tianshan is separated from Tarim by the ophiolitic mélange zones that is better fitted for "South Tianshan" and will be discussed in next sections.

3.5. The Heiyingshan ophiolitic mélange

3.5.1. Field setting

The southernmost part of the Kekesu-Heiyingshan transect is dominated by an ophiolitic mélange zone (Figure 2). Good exposures are located about 30km NW of Heiyingshan. The ophiolitic blocks include basalt, sometimes with a pillow lava structure (Figure 5a), gabbro and peridotite. Peridotite is strongly sheared, serpentinized and cut by calcite veins (Figure 5b). Blocks of chert, limestone and sandstone are also common elements of the mélange. They display variable sizes ranging from tens of centimeters to several hundreds of meters. Bedding is well preserved in sandstone and limestone blocks that might be confused with the sedimentary matrix. However, the lensoid geometry and changing attitude of the bedding comply with a blocky nature of these rocks. All blocks occur in a sedimentary matrix composed of laminated calcareous turbidite or siliceous cherty mudstone (Figure 5c). The sandstone beds are often disrupted, and pebbly mudstones are locally well developed. In most cases, the matrix is strongly sheared so that a scaly fabric develops in the pelitic facies. Sometimes, quartz or calcite fibers crystallize in pressure shadows around clasts (Figure 5d), rendering the distinction between synsedimentary and postsedimentary deformation difficult. The planar structures such as bedding or cleavage have an average N40°E strike but due to later folding, the dip is either northward or southward. The Heiyingshan ophiolitic mélange is separated from the ductilely deformed Silurian-Devonian marbles, slates and volcaniclastic rocks by a high angle, South-directed, brittle reverse fault of Cenozoic age [*XBGMR*, 1983] (Figures 2 and 3). The marble and clastic rocks are well recrystallized but unmetamorphozed (Figure 5e). The megascopic planar fabric is a composite

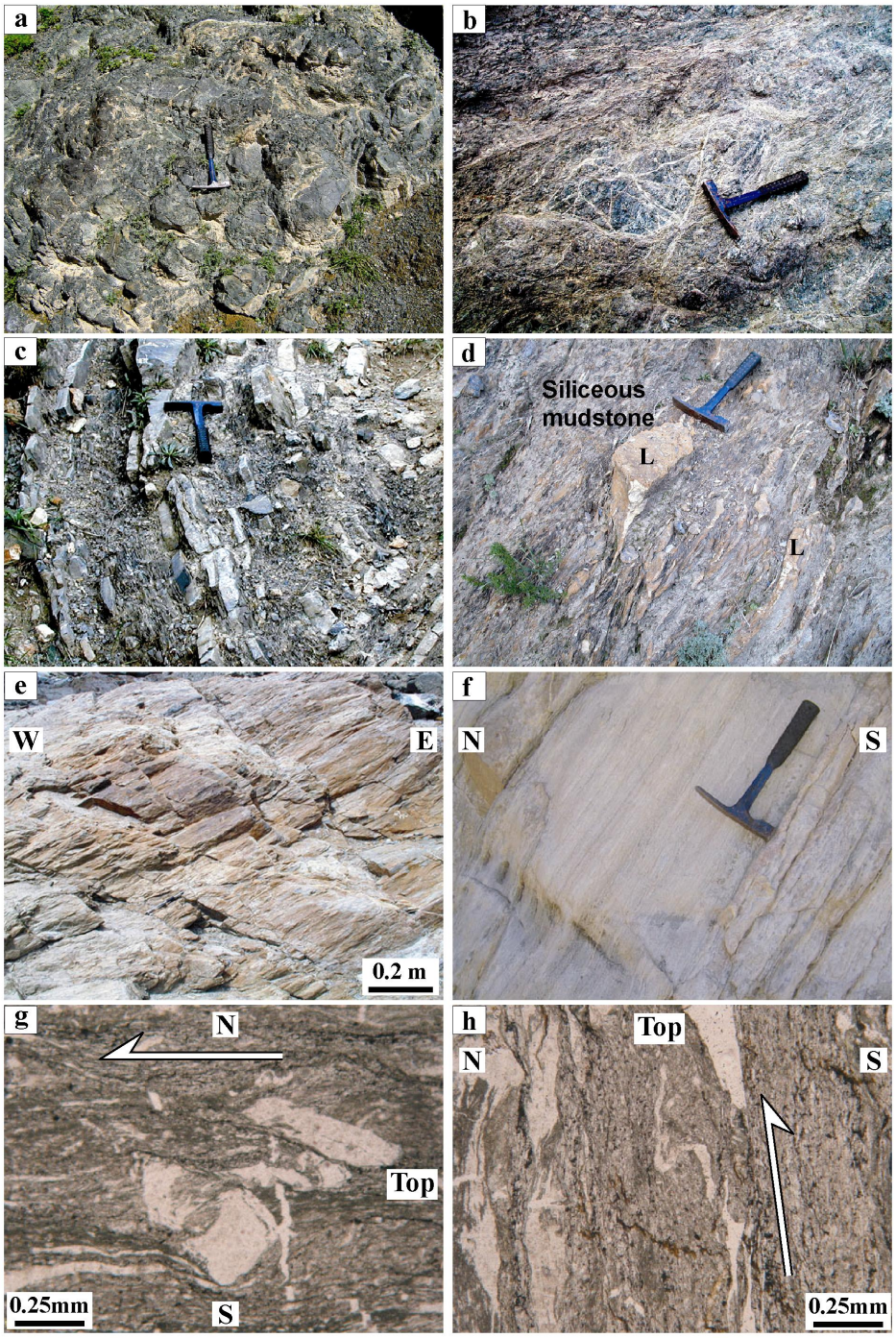

Figure 5. Field photographs of the South Tianshan ophiolitic mélange, (a) pillow lava in Heiyingshan ophiolitic mélange, (b) sheared serpentinized peridotite with calcite veins, (c) calcareous turbidite with disrupted beds corresponding to the matrix of the Heiyingshan mélange, (d) chert and limestone blocks included in the sheared matrix of the Heyingshan mélange, (e) foliated Devonian marble corresponding to the tectonic substratum (i.e. autochthonous basement) exposed north of Heiyingshan mélange, the cleavage is dipping to the northwest, (f) mylonitic and recrystallized Devonian marble of Biediele valley, northwest of Wushi, corresponding to the tectonic substratum (i.e. autochthonous basement) of the ophiolitic mélange, (g) and (h) microscopic photoes of foliated volcaniclastic rocks, located below the marble series of the Biediele valley; along the N-S trending lineation asymmetric clasts (g) and drag folds (h) show a top-to-the-North shearing.

bedding-foliation surface that occasionally contains a N-S trending mineral lineation. Due to the intense recrystallization, the kinematic indicators related to the submeridian lineation are difficult to observe, nevertheless some top-to-the-N shear criteria can be recognized. The ophiolitic mélange observed in Kule area south of the Tielimaiti pass, along the Duku road (Figure 2) [*Gao et al.*, 1998], is similar to that

described here in Heiyingshan.

3.5.2. New stratigraphic constraints.

On the basis of coral, brachiopoda, gastropoda and crinoid fossils found in limestone and sandstone blocks, the ophiolitic mélange is referred to as the Aertengkesi Formation of Late Silurian-Early Devonian [*XBGMR*, 1983; 1993]. However, the age of the matrix of the mélange is certainly younger. Four siliceous mudstone samples from the matrix (see Figure 2 for sampling locality) yield abundant radiolarian, such as *Archocyrtium cf. procerum Cheng, Archocyrtium venustum Cheng, Archocyrtium cf. ludicrum Deflandre, Archocyrtium cf. mirousi Gourmelon, Trilonche almae (Won), Stigmosphaerostylus Pantotolma Braun, Stigmosphaerostylus vulgaris Won, Stigmosphaerostylus wuppertalensis Won), Stigmosphaerostylus cf. Tortispina Ormiston et Lane, Holoeciscus foremanae sp., Albaillella paradoxa sp*. These fossils, determined by Y. Wang at Nanjing Institute of Geology and Paleontology, Chinese Academy of Sciences, China, are common in the *Holoeciscus foremanae* and *Albaillella paradoxa* assemblages of Late Devonian and Early Carboniferous ages, respectively. Thus, a Late Devonian-Early Carboniferous (Famennian-Tournaisian) age likely represents the time of formation of the mélange. This age is consistent with that derived from a block of radiolarian chert in the mélange of northeastern Heiyingshan (Figure 2) [*Liu*, 2001].

Table 2. Zircon U-Pb data of gabbro from the Heiyingshan ophiolitic mélange.

Plots	Abundance				Atomic ratios						Apparent age （Ma）						Disc.
	U	1	Pb	1	$^{206}Pb/^{238}U$	1	$^{207}Pb/^{235}U$	1	$^{207}Pb/^{206}Pb$	1	$^{206}Pb/^{238}U$	1	$^{207}Pb/^{235}U$	1	$^{207}Pb/^{206}Pb$	1	(%)
	ppm		ppm														
JA19D2	170	10	16	1	0.061	0.001	0.45	0.03	0.056	0.004	381	6	374	21	451	146	6
JA19D12	348	16	32	2	0.062	0.001	0.44	0.02	0.056	0.002	386	4	373	14	460	98	4
JA19D1	306	15	28	1	0.062	0.001	0.47	0.02	0.059	0.003	389	4	390	17	564	113	4
JA19D5	210	10	22	1	0.063	0.001	0.47	0.03	0.059	0.003	394	5	393	19	559	122	5
JA19D11	320	17	28	2	0.063	0.001	0.45	0.03	0.056	0.004	395	5	380	20	451	140	5
JA19D8	459	34	41	3	0.064	0.001	0.51	0.04	0.062	0.004	399	5	420	24	657	152	6
JA19D9	417	18	37	2	0.064	0.001	0.51	0.03	0.062	0.003	402	5	420	18	665	114	5
JA19D10	358	18	33	2	0.064	0.002	0.46	0.04	0.054	0.005	398	10	386	26	386	201	10
JA19D7	601	27	65	3	0.064	0.001	0.46	0.02	0.056	0.002	401	4	381	12	446	84	4
JA19D3	441	20	43	2	0.067	0.001	0.48	0.02	0.056	0.002	419	4	398	14	446	87	4
JA19D6	269	12	21	1	0.070	0.001	0.52	0.03	0.057	0.003	434	6	422	18	482	108	6

Disc. (%) denotes percentage of discordance.

3.5.3. New LA-ICP-MS U-Pb radiometric dating.

A 5 kg gabbro sample has been collected from the Heiyingshan ophiolitic mélange (see Figure 2 for sampling locality). The rock is well crystallized with 1-1.5 cm sized pyroxene and plagioclase. Zircon grains were obtained by crushing, sieving through water elutriation, heavy liquids and magnetic separations, and finally by handpicking under binocular microscope. These grains are euhedral, colorless and without zonation or fracture. The euhedral shape of zircon grains indicates a magmatic origin. Laser ablation U-Pb dating of selected zircons was carried out at the

University of Tasmania, Australia, using a Hewlett Packard HP 4500 quadrupole Inductively Coupled Plasma Mass Spectrometer (ICP-MS) coupled with a 213nm NewWave Merchantek UP213 Nd-YAG Laser.

The U-Pb isotopic results are presented in Table 2 and plotted in the Concordia diagram (Figure 6). Nine of 11 plots allow us to calculate a Concordia age of 392 ± 5 Ma (MSWD = 1.8) that is interpreted as the crystallization age of the gabbro, suggesting the age of ophiolite. Two other plots give older ages at 420 and 433 Ma that should represent old inherited cores, probably corresponding to the earlier stage of oceanic crust formation.

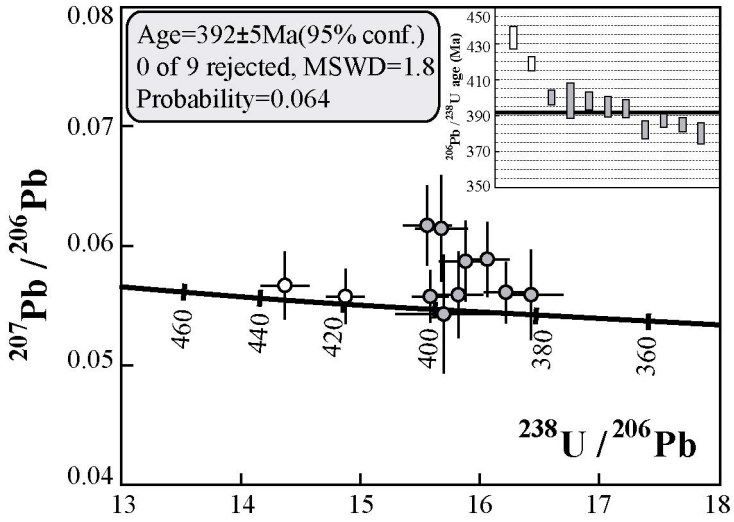

Figure 6. Concordia diagram of ICPMS-LA U-Pb dating of zircons from a gabbro block in the Heiyingshan ophiolitic mélange.

3.6. The Carboniferous deposits

To the south of the Heiyingshan mélange, Early Carboniferous sandstone and limestone crop out. As in many places of southern Tianshan, (cf. the Kumux, Wushi and Aheqi areas in sections 6 and 7), the Carboniferous and Permian rocks are folded or cut by South-directed reverse faults that probably developed during the Cenozoic tectonics. However, as suggested by the lack of ductile deformation, and in agreement with available maps [*XBGMR*, 1983], it is likely that the Carboniferous rocks cover unconformably the ophiolitic mélange and underlying strata (Figures 2 and 3).

3.7. A general cross section

The above-defined tectonic units are placed in a general interpretative cross section (Figure 3). The northern part of the section corresponds to the Yili Block with a Proterozoic basement overlain by a Paleozoic sedimentary cover, upon which a Carboniferous magmatic arc develops. The southern part of the arc is ductilely deformed by a dextral strike-slip fault, called the Nalati Fault or Nikolaiev Tectonic Line (fault 3 in Figure 1). However, as presented in section 4, this ductile event overprinted an older one. More to the south, metamorphic rocks, interpreted as the southernmost part of the Yili Block, are highly deformed by a top-to-the-North ductile shearing. The Yili continental rocks are overthrust by mafic magmatic and marine

sedimentary rocks metamorphosed under HP conditions. These rocks, belonging to the Tianshan Ocean form a thrust nappe emplaced from South to North above the Yili Block. Therefore, conversely to most of previous interpretations [e. g. *Gao et al.*, 2003; *Zhou et al.*, 2001], the Nalati fault does not correspond to a suture zone but is simply a late wrench fault cutting through the Yili Block. The true ophiolitic suture lies more to the South. The HP metamorphic complex is overthrust by Silurian-Devonian marble that represents the sedimentary cover of the Proterozoic basement of the Central Tianshan Block. The southernmost part of the Central Tianshan Block is tectonically overlain by the South Tianshan ophiolitic mélange, which is unconformably covered by weakly deformed Carboniferous rocks. The structural constraints acquired along the Kekesu River supporting our geodynamic interpretation are presented in the next section.

4. The polyphase deformation along the Kekesu River

Along the Kekesu River, three ductile deformation phases are recognized. Namely, from younger to older, normal faulting, dextral wrenching, and top-to-the-north thrusting. Since the second event is the most conspicuous, it will be presented first.

4.1.Strike-slip shearing

Our observation was performed in a wide zone around Wenquan (from 42°55'N to 42°45'N; Figure 4A). Gabbro and granite belonging to the Yili magmatic arc form undeformed lenses surrounded by subvertical brittle shear planes with subhorizontal N80E trending slickenlines (Figures 4B and 7A). Due to the increse in deformation, the same gabbro is mylonitized farther South. Steeply SE-dipping shear planes with a subhorizontal ENE-WSW trending stretching and mineral lineation, marked by boudinaged pyroxenes or feldspar ribbons, characterize the mylonites and ultramylonites (Figure 4D). Dykes of red K-feldspar granite intrude in the deformed rocks. Some of these dykes are folded with axial planes parallel to the foliation, and other dykes are boudinaged within the foliation (Figure 7g and 7h). On the XZ plane of the strain ellipsoid, i.e. in sections parallel to the foliation and parallel to the lineation, drag folds and asymmetric boudins indicate a dextral sense of shear (Figure 7b and 7c). The same kinematics is shown by structures observed at the microscope scale. The most representative are sigma-type porphyclast of feldspar or pyroxene clasts, sigmoidal mica-fish, biotite pressure shadows around clasts, and elongated quartz ribbons with an oblique shape fabric of recrystallized grains (Figures 7d and 5e).

This ductile deformation corresponds to a dextral wrenching that occurs all along the Nalati Fault (fault 3 in Figure 1) [*Yin and Nie*, 1996; *Gao et al.*, 1997, 1998]. North of Bayinbulak, at the Laerdun Pass (Figure 1), granitic rocks are intensely deformed in a 50m-wide, E-W to NE-SW trending, vertical ultramylonite zone that contains a subhorizontal stretching lineation. In thin sections, sigma and delta-type fabrics (Figure 7f) confirm the dextral sense of shear. Biotite from this ultramylonite yields an $^{40}Ar/^{39}Ar$ age of 250±7.9 Ma [*Cai et al.*, 1996]. In the same area, biotite and

K-feldspar from foliated granite are dated by the $^{40}Ar/^{39}Ar$ method at 285 Ma and 270 Ma, respectively [*Zhou et al.*, 2001] (Table 1).

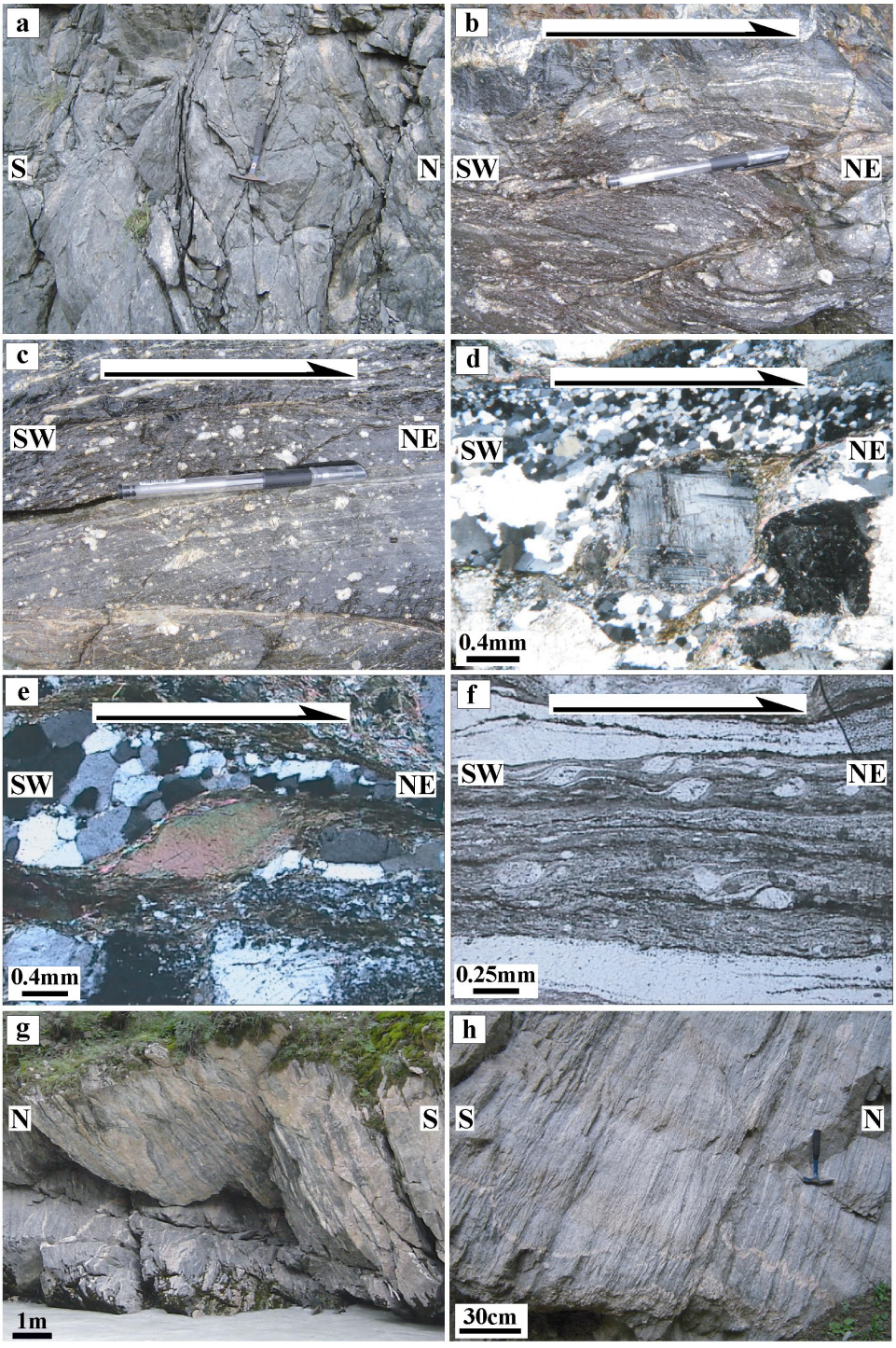

Figure 7. Photographs and photomicrographs of structures associated to the dextral shearing along the Nalati fault. (a) cataclastic gabbro north of Wenquan village showing the lensoid fabric due to vertical brittle fractures. These surfaces exhibit subhorizontal slickenlines induced by dextral strike-slip fault (diagram B in figure 4), (b) mylonite with drag folds and asymmetric feldspar clasts showing dextral shearing, (c) ultramylonite with s-type asymmetric feldspar clasts, (d) thin section cut perpendicular to the foliation and parallel to the lineation of a mylonitic granite (sample XJ674); the s-type feldspar clasts and recrystallized quartz grains with an oblique shape fabric, (e) foliated gabbro showing mica-fish and quartz recystallization fabrics, (f) ultra-mylonite of Laerdun Pass showing dextral sigma and delta-type clasts, (g) boudinaged and sheared gabbro intruded by pink granitic dykes, both are foliated and protomylonitized by the dextral wrenching, (h) folded granite dyke in well foliated, accounting for shortening perpendicular to the foliation.

4.2.Top-to-the North thrusting

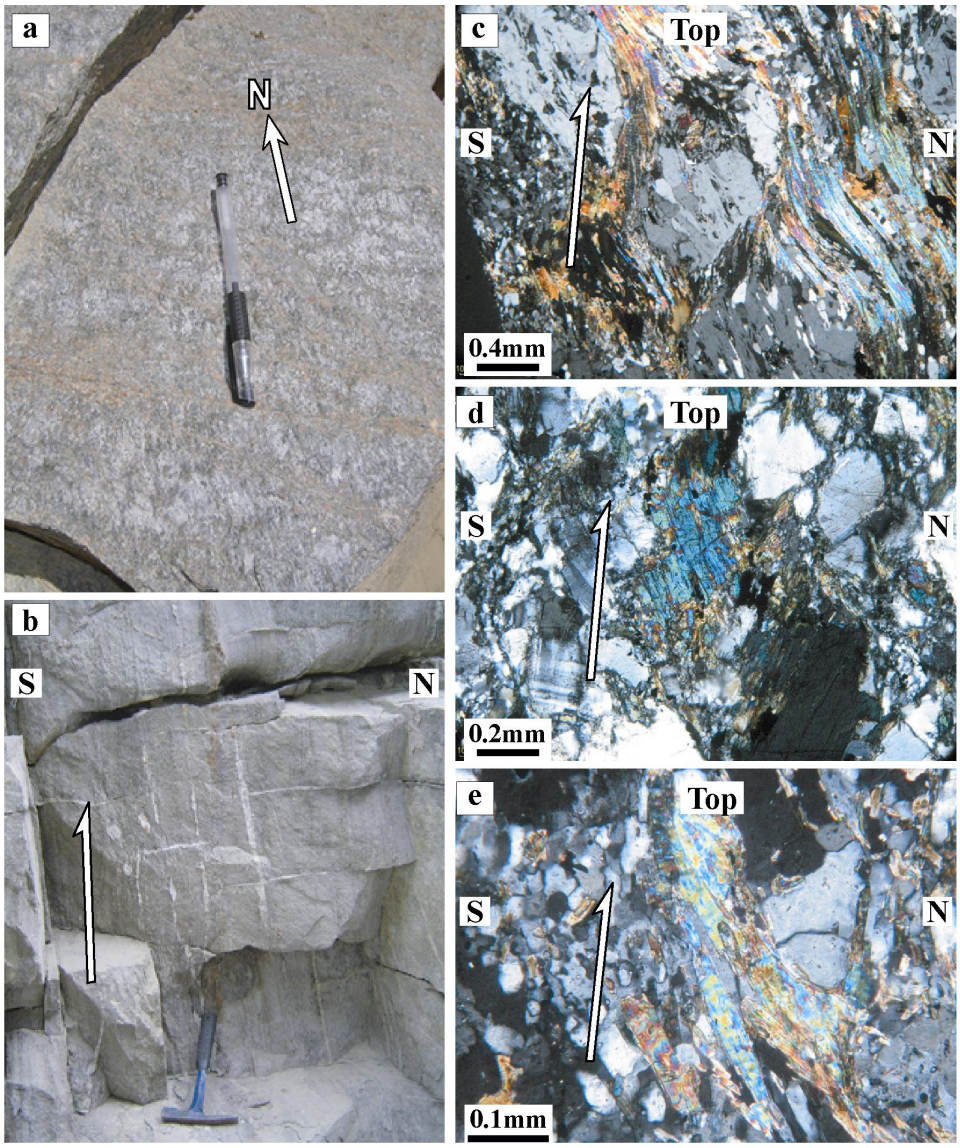

Figure 8. Field photographs and photomicrographs of deformation features associated to the northward shearing. (a) orthogneiss with submeridian lineation steeply dipping to the south, (b) greenschist facies siliceous sandstone with quartz veins parallel to the foliation, the asymmetric shape of the boudins indicate top-to-the-North movement, the tension gashes perpendicular to the foliation are post-folial structures but the geometry agrees with a subvertical stretching, (c) muscovite-albite micaschist with top-to-the-North shear bands, (d) sheared orthogneiss, (e) sigmoidal muscovite indicating top-to-the North shearing.

South of the strike-slip shear zone of the Kekesu River, the foliation in gneiss and micaschists is steeply dipping to the SE (Figures 2 and 4). In addition to the conspicuous dextral wrenching deformation, an older structural element is distinguished in the metamorphic rocks. A N-S to NW-SE trending mineral lineation can be observed on the foliation surface (Figures 4C, 4E and 8a). In orthogneiss, K-feldspar clasts and biotite clots form a submeridian linear structure (Figure 8a). The lineation dip varies from 20 to 65° and locally up to 80°, with a scattering from SE to SW. Similar planar and linear structures are also observed in ultramylonitic shear zones. Asymmetric plagioclase porphyroclasts show a top-to-the-North movement, which is also observed in thin section (Figures 8d and 8e). In the muscovite-bearing quartzite and biotite gneiss corresponding to the deformed part of the Proterozoic basement, the subvertical foliation also contains a down-dip stretching lineation with

a top-to-the NW shearing. In agreement with previous structural studies [*Gao et al.*, 1995], the top-to-the-North shearing is also observed in the HP rocks. At the macroscopic scale, sigmoidal quartz veins parallel to the foliation indicate also a top-to-the-North movement (Figure 8b). Albite-biotite micaschist and quartzite are characterized by a NE-SW trending, steeply dipping foliation, and a subvertical stretching lineation (Figure 4E). Intrafolial a-type folds with axes parallel to the lineation are also observed [*Gao et al.*, 1995]. In thin section, the micaschists contain asymmetric albite porphyroblasts with biotite pressure shadows that show a-top-to-the-NW shearing (Figure 8c). We interpret the top-to-the-North shearing event as the result of the emplacement of the HP metamorphic complex situated to the south of the highly deformed part of the Yili Block (Figures 2, 3 and 4). It is worth to note that this kinematics has been previously interpreted as a later thrusting event that took place at the end of the Early Carboniferous [*Gao et al.*, 1995; 2003]. The radiometric age of this northward is not established yet, but it is older than the strike-slip shearing because a K-granite that is petrologically similar to the one we dated at 341± 6 Ma is not affected by the flat-lying ductile shearing.

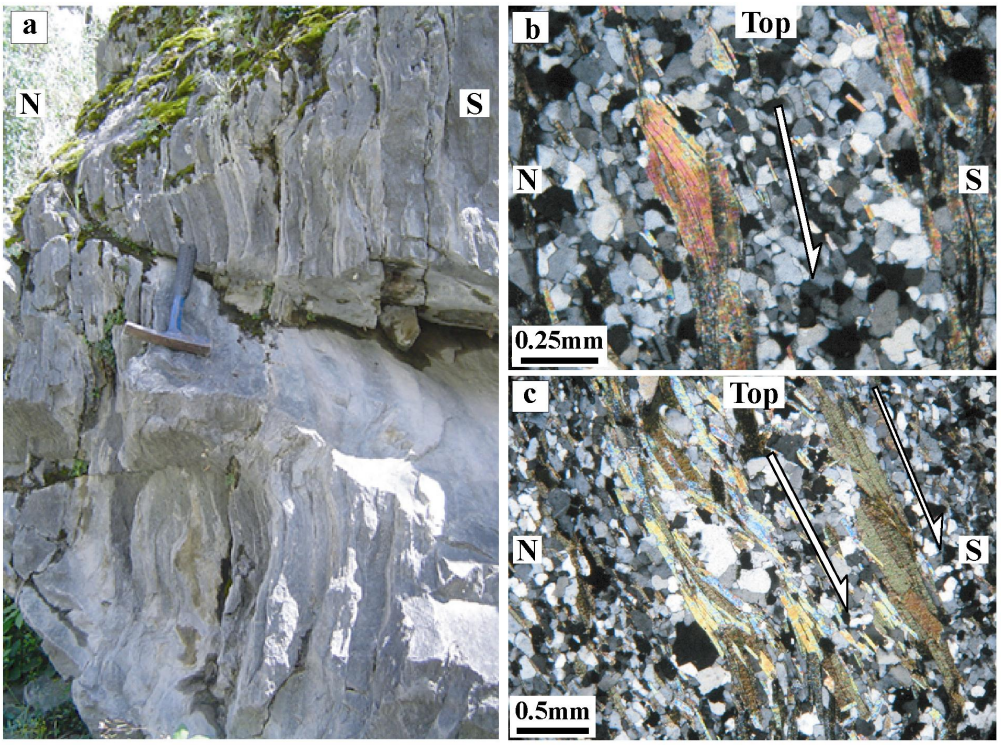

Figure 9. Field and photomicrographs of structures related to normal shearing. (a) quartz riched micaschist with a folded vertical foliation, the subhorizontal axial planes argue for a vertical shortening, (b) and (c) sigmoidal muscovite and recrystallized quartz ribons showing a top-to-the-South ductile shearing interpreted here as normal faulting.

4.3.Normal faulting

In the northern and central parts of the highly deformed basement rocks, immediately north of the HP metamorphic complex (Figure 4), the subvertical foliation is deformed by folds with flat-lying axial planes sometimes associated with a subhorizontal crenulation cleavage. This feature complies with a vertical shortening (Figure 9). Moreover, in some mica rich zones in metapelites, another kinematics can be observed at the microscope scale. In sections cut perpendicular to the foliation and

parallel to the vertical lineation (XZ planes), sigmoidal muscovite and recrystallized quartz ribbons with an oblique grain shape fabric indicate a downward movement of the southern side (Figures 9c and 9d). This kinematics that develops in greenschist facies conditions can be interpreted in two ways. Firstly, it might represent a tilted south-directed thrust. Secondly, this ductile shearing might indicate a normal faulting. Since this top-to-the-South event appears as restricted to mica rich domains that localized shearing, and formed during a greenschist facies metamorphic, the extensional shearing interpretation is preferred here in Figures 3 and 4. However, additional work is necessary in order to assess the local or regional character of this event.

5. Ar-Ar Geochronological constraints

5. 1. Previous isotopic age constraints on HP metamorphics.

A number of researchers have given much effort to constrain the age of the high-pressure metamorphism in southern Tianshan. A glaucophane from the Changawuzi high-pressure metamorphic belt yielded an $^{40}Ar/^{39}Ar$ age of 350.9 ± 2.0 Ma [*Xiao et al.*, 1992]. *Gao et al.* [1995] obtained an $^{40}Ar/^{39}Ar$ plateau age of 345.5 ± 7 Ma on phengite, and an eclogite from the same area yielded a Sm-Nd (omphacite, garnet, glaucophane, whole rock) errorchron age of 343 ± 44 Ma [*Gao and Klemd*, 2003]. The Sm-Nd garnet-glaucophane age of 346 ± 3 Ma is concordant with the $^{40}Ar/^{39}Ar$ age of 343.7 ± 1.3 Ma on crossite from the same exposure [*Gao and Klemd*, 2003]. Consequently, the latter authors regarded an age of about 345 Ma as the best approximation for the age of the eclogite-facies metamorphism.

High-pressure metamorphic rocks of the southern Tienshan zone have also yielded older isotopic ages. Phengites from blueschists at Qiongkushitai (Figure 2) yielded a dome-shaped age spectrum, the top of which yielded an $^{40}Ar/^{39}Ar$ plateau age of 415.4 ± 2.3 Ma [*Gao*, 1993]. In Akeyazi, SW of Kekesu River (Figures 1 and 2), *Gao et al.* [2000] obtained $^{40}Ar/^{39}Ar$ plateau ages of 401.4 ± 1.4 Ma (sodic amphibole) and 380.7 ± 1.2 Ma (phengite) from the rim of an eclogite body and of 370.4 ± 1.2 Ma (sodic amphibole) and 363.9 ± 0.5 Ma (phengite) from its blueschist-facies matrix. *Dobretsov et al.* [1987] obtained K-Ar ages of about 410 and 350 Ma on whole rock samples from the Atbashy belt (Kyrgyzstan).

Although it cannot be excluded that older ages constrain an earlier phase of subduction-accretion metamorphism, as seems to be the case in many of the Paleozoic belts in China [*de Jong et al.*, 2006], we regard these ages, however, at least in part, as less reliable. The dome-shaped phengite age spectrum of *Gao* [1993] is probably due to the degassing of mixed phases according to a classic interpretation of such kind age spectra [*Wijbrans and McDougall*, 1986; *de Jong*, 2003]. Thus the $^{40}Ar/^{39}Ar$ plateau age of 415.4 ± 2.3 Ma is probably not geologically meaningful. *Klemd et al.* [2005] suggested that the $^{40}Ar/^{39}Ar$ ages ranging from 401 to 364 Ma obtained by *Gao et al.* [2000] from the same area were due to excess Ar incorporation. Inspection of $^{37}Ar/^{39}Ar$ and $^{38}Ar/^{39}Ar$ ratios by *Gao et al.* [2000], however, reveals that the sodic amphibole is too rich in K and the white mica too rich in Ca, implying that material of insufficient purity was dated. Consequently, the somewhat elevated ages of ca. 380 to

364 Ma obtained by *Gao et al.* [2000] on phengite concentrates are probably due to the presence of an older Ca-rich contaminant phase. The K-Ar age of 410 ± 15 Ma from the Atbashy belt [*Dobretsov et al.*, 1987] is probably due to the multi-mineral character inherent to whole rock samples. The high-pressure metamorphism related to subduction and accretion in the southern Tianshan thus appears to have occurred in Early Carboniferous time, at around 350 Ma. Yet, it must be borne in mind that the meaning of the epidote blueschist-facies metamorphism in the western Tianshan is regarded as a retrograde stage (500-530°C, 1.0-1.2 Gpa) by *Zhang et al.* [2002] with respect to an earlier UHP eclogite-facies event (500-600°C, 2.6-2.7 Gpa). Although this view is contested by *Klemd* [2003], obviously it cannot be excluded that the eclogites have been formed earlier than 350 Ma. The more so, *Wei et al.* [2003] underscored that the eclogites experienced a range of metamorphic peak conditions, which differ at least in part from those experienced by the blueschists.

Gao and Klemd [2003] obtained an $^{40}Ar/^{39}Ar$ plateau age of 331.0 ± 2.0 Ma on phengite, from the same sample as the dated crossite, which they interpreted as constraining the age of tectonic transport of the HP-LT rocks to higher crustal levels. *Klemd et al.* [2005] have obtained ages between 313.0 and 301.6 Ma (Rb-Sr) and 310.9 and 311.6 Ma ($^{40}Ar/^{39}Ar$) on phengite and/or paragonite from blueschist-facies rocks that formed during or after the transition from the eclogite-facies to the epidote-blueschist-facies and subsequently experienced an incipient greenschist-facies overprint. These white mica ages, which average at around 310 Ma, are thus are up to 50-35 Ma younger than the eclogite-facies metamorphism. It is not clear in how far significantly younger ages obtained from eclogite-facies metamorphic rocks in this area (referred as "preliminary" SHRIMP U-Pb zircon age of <310 ± 5 Ma by *Zhang et al.*, 2003a) and in the southern Tianshan of Kyrgyzstan (267 ± 5 Ma; Omp-Grt-Ph-WR, Rb-Sr isochron) [*Tagiri et al.*, 1995] are influenced by effects of retrograde fluid-assisted recrystallization following the high-pressure event.

5.2. Sample description

Three samples for $^{40}Ar/^{39}Ar$ dating were taken from the Kekesu River. This area belongs to the belt of mainly blueschist and greenschis-facies metabasites and metagraywackes, which contain numerous lenses and blocks of eclogites, ultramafics and marbles.

Sample XJ607-2b (GPS: 42°40.6'N, 81°56.9'E) is a foliated and lineated garnet-bearing blueschist that contains substantial amounts of chlorite and white mica. Variations in modal amounts of preferentially orientated blue amphibole and epidote define a layering at the scale of several millimeters. Amphibole occurs as ~1 mm-long crystals with a distinctive deep blue to pale violet pleochroism and forms sheave-like aggregates. Crystals are strongly zoned, usually with deep bluish cores and lighter shades in rims; when included in garnet they have a uniform dark blue to purple colour. The lighter coloured rims may be intergrown with green chlorite or be replaced by this mineral. Chlorite occurs between pulled apart albite crystals. White mica generally occurs in chlorite-rich layers (that may contain relics of blue amphibole) as individual crystals, or as aggregates with a decussate structure. White

mica and chlorite may be intergrown along their basal cleavages. Tabular strain-free crystals are 500-1500 μm in length. Undeformed white mica has overgrown amphibole-rich layers locally.

Table 3. $^{40}Ar/^{39}Ar$ analytical data of laser step-heating of white mica single grains from the valley of the Kekesu river, SW Tianshan

Step	$^{40}Ar_{Atm}$(%)	$^{39}Ar_K$(%)	$^{37}Ar_{Ca}/^{39}Ar_K$	$^{40}Ar^*/^{39}Ar_K$	Age (Ma)
XJ607-2b, muscovite of Retrograde garnet-bearing blueschist (J=0.00539485)					
1	57.0	0.9	0.000	39.79	350.8 ± 33.3
2	26.6	0.5	0.265	44.96	391.8 ± 75.8
3	24.8	4.5	0.131	36.27	322.4 ± 8.4
4	20.3	7.8	0.155	35.32	314.6 ± 4.2
5	12.6	26.7	0.109	35.38	315.1 ± 1.6
6	11.8	20.2	0.120	35.12	313.0 ± 1.6
7	13.9	15.4	0.176	35.24	313.9 ± 2.3
8	11.7	11.6	0.643	36.57	324.8 ± 3.2
9	6.8	4.6	1.847	36.31	322.7 ± 7.7
10	5.6	3.1	0.916	35.03	312.2 ± 10.3
fusion	1.6	4.7	0.515	35.62	317.1 ± 9.6
XJ611, muscovite of Greenschist-facies garnet-chlorite-mica quartzite (J=0.00539318)					
1	11.4	0.9	0.128	24.49	223.8 ± 3.4
2	0.6	0.6	0.000	32.86	294.4 ± 3.7
3	0.6	1.3	0.000	34.50	307.8 ± 1.6
4	0.5	1.9	0.013	35.80	318.5 ± 1.4
5	1.3	1.7	0.061	35.81	318.5 ± 1.5
6	1.0	6.9	0.031	36.08	320.7 ± 0.6
7	0.7	8.7	0.031	36.30	322.5 ± 0.6
8	0.9	3.3	0.060	36.04	320.4 ± 0.8
9	0.7	9.0	0.018	36.44	323.6 ± 0.6
10	0.5	40.2	0.023	36.35	322.9 ± 0.7
11	0.8	8.0	0.039	35.81	318.5 ± 0.8
fusion	1.1	17.5	0.061	36.42	323.5 ± 0.9
XJ612, muscovite of Retrograde blueschist (J=0.00539568)					
1	13.3	0.5	0.415	38.51	340.6 ± 5.7
2	4.3	0.5	0.080	39.22	346.3 ± 5.1
3	5.1	1.5	0.001	38.54	340.9 ± 1.8
4	5.0	2.4	0.072	37.62	333.4 ± 1.3
5	1.9	16.6	0.014	37.32	331.0 ± 0.6
6	1.0	14.2	0.018	37.29	330.8 ± 0.6
7	1.0	12.8	0.016	37.34	331.2 ± 0.6
8	0.8	22.2	0.019	37.23	330.2 ± 0.6
9	0.8	8.5	0.039	36.82	326.9 ± 0.6
10	2.3	1.3	0.025	37.96	336.2 ± 1.8
11	3.0	1.4	0.056	37.83	335.1 ± 2.2
fusion	1.5	18.1	0.022	36.81	326.9 ± 2.5

Data obtained with a defocussed laser; fusion for the final step is achieved by beam focusing.

Sample XJ612 (GPS: 42°40.2'N, 81°57.4'E) is a lineated rock with a principal foliation that is defined by differences in modal amounts of preferentially orientated blue amphibole and epidote, along which green chlorite and white mica have grown. This layering at the scale of several millimeters curves around porphyroclasts of metamorphic clinopyroxene that contains inclusions of glaucophane displaying an orientation parallel to the external foliation. The principal foliation is cut by slightly deformed tension gashes filled with carbonate. Blue amphibole crystals (~1 mm-long) are moderately zoned with darker cores and lighter rims. The amphibole is overgrown and replaced by both chlorite and albite. White mica (150-1500 μm long) generally occurs parallel to the main foliation, and is in part intergrown with chlorite along their basal cleavages. Undeformed crystals and aggregates of intergrown chlorite and white

mica cross-cut the amphibole-rich layers occasionally.

Sample XJ611 (GPS: 42°41.1'N, 81°56.3'E) is an inequigranular garnet-bearing chlorite-mica quartzite with an ill-defined foliation. Equidimensional quartz crystals reveal a moderate dynamic recrystallization, mainly by sutured boundaries and development of sub grains. White mica is present as 100-1000 µm long and strain free crystals in the quartz matrix. These white micas have occasionally grown along the basal cleavages of chlorite that forms large porphyroblasts. Abundantly present garnet, which is devoid of glaucophane inclusions, is not chloritized nor retrogressed. Minor carbonate occurs as large crystals that overgrow the matrix.

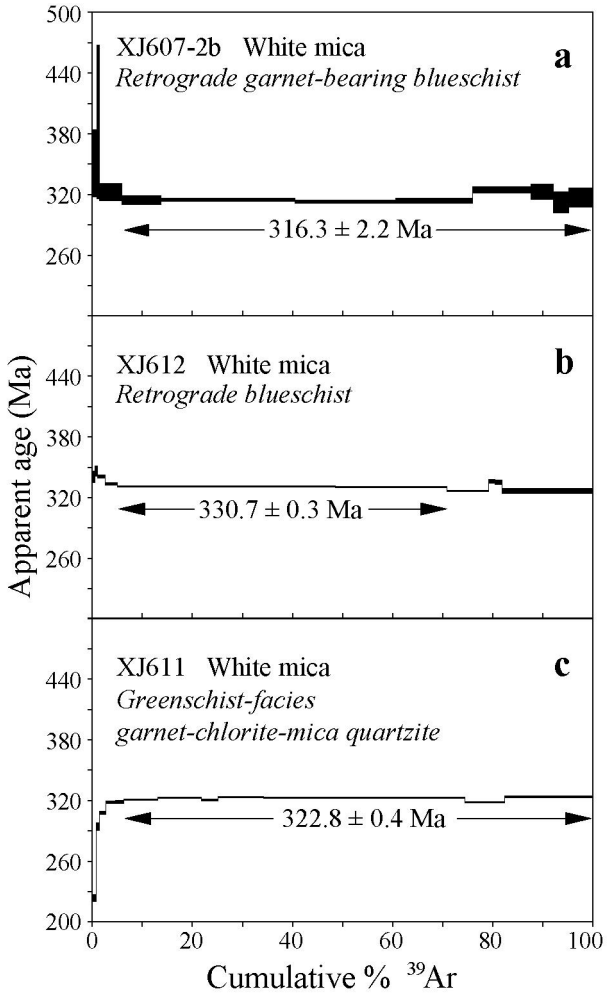

Figure 10. 40Ar/39Ar age spectra acquired by laser step-heating of phengite single grains from retrogressed blueschists (a) and (b) and a greenschist-facies quartzite (c) from the valley of the Kekesu river.

5.3. $^{40}Ar/^{39}Ar$ dating results

Single grains of K white mica were analyzed by incremental heating with an $^{40}Ar/^{39}Ar$ laser probe (CO_2 Synrad®). Minerals were carefully handpicked under a binocular zoom microscope from the 0.3-2 mm size fraction of the crushed rocks. The samples were wrapped in Al foil envelopes (11 mm × 11 mm × 0.5 mm), which were stacked in an irradiation can, with flux monitors inserted after every 8 to 10 samples. Standard Sanidine TCR-2 (with an age of 28.34 Ma according to *Renne et al.* [1998])

was used as flux monitor. Samples and standards were irradiated for 13.33 hours at the McMaster reactor (Hamilton, Canada) with a total flux of 1.7×10^{18} n×cm^{-2}. The sample arrangement allowed us to monitor the flux gradient with a precision of ±0.2%. The step-heating experimental procedure has been described in detail by *Ruffet et al.* [1991, 1995]. Blanks are performed routinely at the start of an experiment and repeated typically after each third run, and are subtracted from the subsequent sample gas fractions. Analyses are performed on a Map215® mass spectrometer.

Plateau ages (PA) were calculated if 70% or more of the $^{39}Ar_K$ was released in at least three or more contiguous steps, and the individual step ages of the plateau segment agree to within 1σ or 2σ of the integrated age. Pseudo-plateau ages, with less than 70% of $^{39}Ar_K$ released, can also be defined. The $^{40}Ar/^{39}Ar$ analytical data are listed in Table 3, and portrayed as age spectra in Figure 10. All errors are quoted at the 1σ level. Step-heating resulted in flat age spectra for all samples for substantial parts of the gas release with comparable ages that are, however, discordant at the 1σ confidence level. White mica from strongly retrogressed blueschist (XJ607-2b) yielded a plateau age of 316.3 ± 2.2 Ma, whereas the mineral from a moderately retrogressed blueschist (XJ612) yielded a pseudo-plateau age of 330.7 ± 0.3 Ma (Figures 10a and 10b). White mica in greenschist-facies metamorphic quartzite XJ611 gave a plateau age of 322.8 ± 0.4 Ma (Figure 10c).

5.4. Interpretation of the ages

The 330-315 Ma $^{40}Ar/^{39}Ar$ K-white mica ages that we obtained are up to about 50 Ma younger than the radiometric ages obtained by *Xiao et al.* [1992], *Gao et al.* [1995] and *Gao and Klemd* [2003] on high-pressure metamorphic rocks in the southern Tianshan. The retrograde mineralogy characterized by abundant late-stage chlorite and albite growth and textural relationships (intergrown mica-chlorite that has overgrown the main foliation) imply that white mica in samples XJ607-2b and XJ612 was formed during retrogression of the blueschist-facies metamorphic assemblage. The strongest retrogressed blueschist (XJ607-2b) has the lowest plateau age of 316.3 ± 2.2 Ma, whereas XJ612 that shows a lesser degree of retrogression yielded a plateau age of 330.7 ± 0.3 Ma. We, thus, interpret these latest Early to Late Carboniferous (Mississippean) dates as age constraints on the retrograde recrystallization of the blueschist-facies mineral assemblage during exhumation. The pseudo-plateau age of 330.7 ± 0.3 Ma for white mica from greenschist-facies quartzite XJ611 agrees with such a timing. This explanation corroborates the interpretation by *Klemd et al.* [2005] of a comparable spread in a data set of Rb-Sr and $^{40}Ar/^{39}Ar$ ages of K-white micas from retrogressed blueschists about 85 km westward along strike.

6. Gangou-Kumux transect

In southern Tianshan, an ophiolitic mélange trends from Aheqi to Kumux, through Heiyingshan, Kule, Wuwamen, and Yushugou (Figure 1). Other ophiolitic mélanges are described in the Gangou and Mishigou areas. But as shown in this section, the Gangou-Kumux transect (Figure 11) exposes two distinct zones of ophiolitic rocks, it is therefore a key region for understanding the tectonics of the

Tianshan Belt. This area has been already described by *Windley et al.* [1990], *Allen et al.* [1992], *Laurent-Charvet* [2001], *Shu et al.* [2004] and *Xiao et al.* [2004], but our additional investigation allows us to propose a different interpretation from that of previous authors.

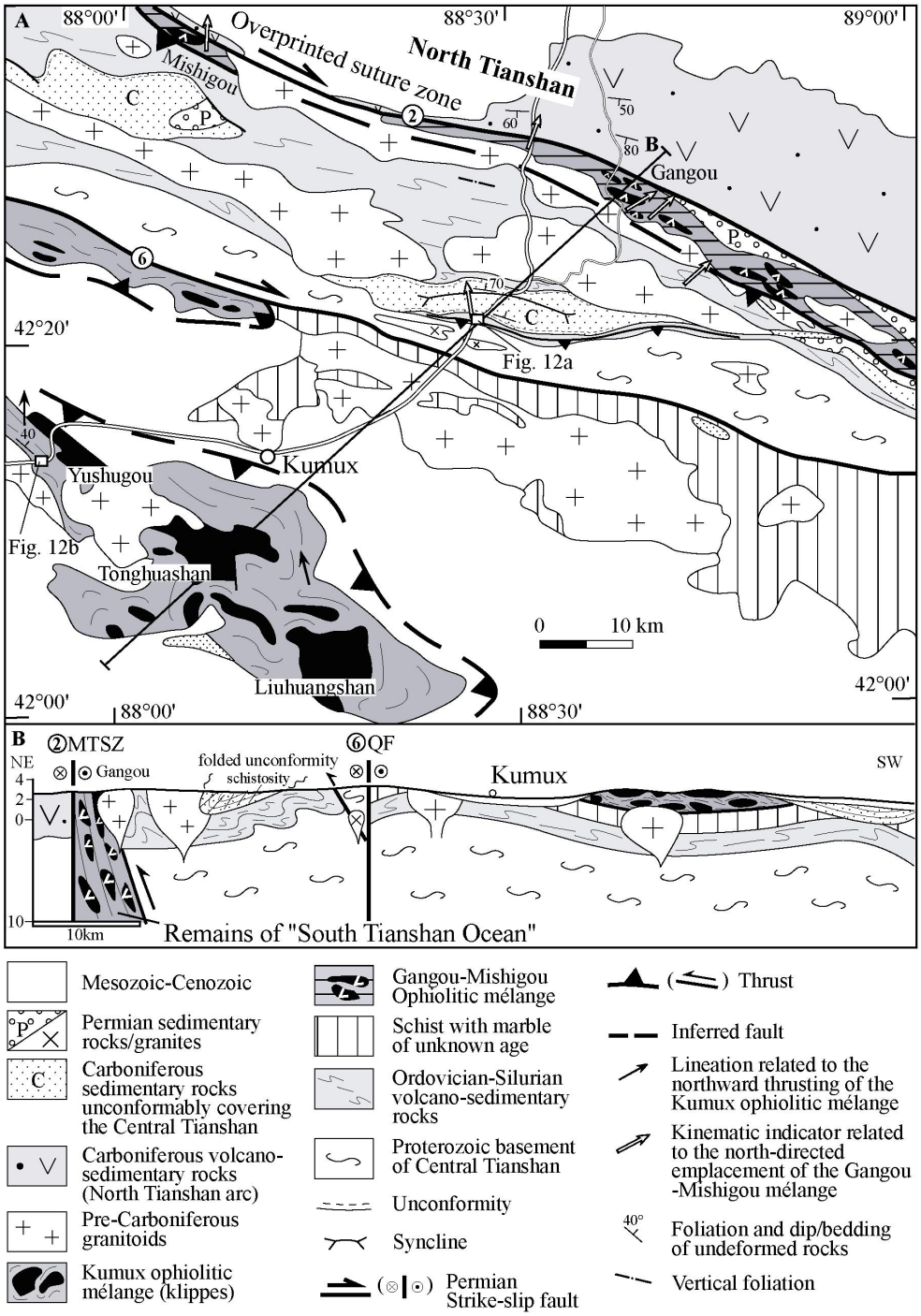

Figure 11. (A) Schematic geological map of Kumux-Gangou transect (Modified from XBGMR [1959], Allen et al. [1992] and Laurent-Charvet [2001]). (B) Cross section, located in A. In spite of conspicuous dextral strike-slip faulting along the MTZ and Qinnbulak faults (faults 2 and 6, respectively), older flat-lying ductile shear events can be recognized. The MTZ overprints the ophiolitic mélanges observed in Gangou and Mishigou that corresponds to the South Tianshan Ocean. In Mishigou, kinematic indicators argue for a top-to-the-North shearing. North vergent folds, also observed in the Silurian turbidite (Figure 12a), are unconformably overlain by Early Carboniferous shallow water deposits. The Qingbulak fault is not a suture zone. South of Kumux, the ophiolitic mélange is a klippe transported from South to North as shown by shear criteria (cf. Figure 12b) and rooted south of Kumux.

6.1. The Gangou-Mishigou mélange

In Gangou and Mishigou areas (Figure 11A), along the southern side of the MTSZ (fault 2 in Figure1), blocks of serpentinite, gabbro, marble and chert are included in a coloured schistose matrix forming an ophiolitic mélange [*Allen et al.*, 1992; *Laurent-Charvet*, 2001]. In the mélange, both blocks and matrix are ductilely deformed by a conspicuous vertical foliation and subhorizontal stretching lineation. Kinematic indicators are consistent with a dextral shearing. However, more to the South, reverse faults and bedding-cleavage relationships in folds developed in the matrix show a northward vergence (Figures 11A and 11B) [*Allen et al.*, 1992; *Laurent-Charvet*, 2001]. This ophiolitic mélange zone is considered as the North Tianshan Suture [*Windley et al.*, 1990; *Allen et al.*, 1992; *Gao et al.*, 1995, 1998; *Zhou et al.*, 2001] that extends to Shenglidaban (locality g in Figure 1) and Bayingou, south of Dushanzi. However, according to our field investigation, a different correlation can be proposed. The mélange is overthrust to the north by an Ordovician volcanic and sedimentary series, composed of andesite, dacite, basalt, tuff, pyroclastic rocks and greywacke, which in turn is overlain by north verging folded and sheared Silurian turbidite [*Laurent-Charvet*, 2001] (Figure 11). A gabbro from the mélange yields a Rb-Sr whole rock age at 468 Ma, and a deformed basalt gives an age at 422 Ma [*Che et al.*, 1994]. Undeformed granitic plutons intrude the mélange and Ordovician to Silurian strata (Figure 11), but these plutons remain undated. It is worth to note that Carboniferous volcanic arc rocks are exclusively distributed to the north of the MTSZ. Conversely, to the south of the MTSZ, Early Carboniferous conglomerate, sandstone and shallow water limestone unconformably overly Early Paleozoic volcano-sedimentary rocks and granitoids. The Silurian turbidite is deformed by N-verging folds and flat-lying shear zones (Figure 12a). The occurrence of granitoids older than Carboniferous, presence of a Proterozoic basement, and lack of a Carboniferous arc suggests that this region is different form the North Tianshan as well as the Yili Block (Figures 1 and 10) [*Wang et al.*, 2006b]. Another possibility is to correlate the pre-Carboniferous Gangou-Mishigou ophiolitic mélanges to the HP metamorphic complex described above in sections 3 and 4.

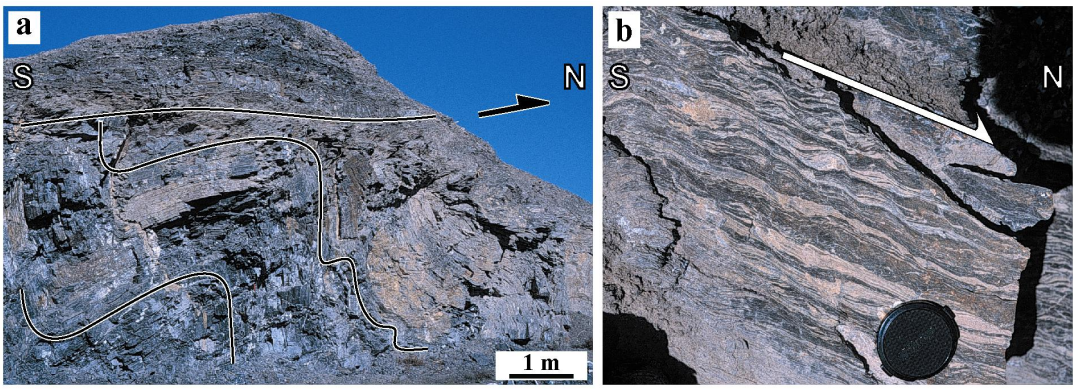

Figure 12. Examples of top-to-the-North shearing along the Gangou-Kumux transect (located in figure 11). (a) North vergent folds and flat-lying shear zone in the Silurian turbidite, (b) asymmetrically sheared layers in the metapelitic matrix of the ophiolitic mélange near Yushugou.

6.2. The Kumux ophiolitic mélange

The Qingbulak Fault (fault 6 in Figure 1) has been regarded as the South Tianshan Suture reworked by a dextral ductile strike-slip fault [*Windley et al.*, 1990;

Allen et al., 1992]. This fault separates Proterozoic orthogneiss to the north from marbles and micaschists to the south [*Laurent-Charvet*, 2001]. South of Kumux, a 50-km-long and 30-km-wide mélange develops in the Liuhuangshan, Tonghuashan and Yushougou massifs (Figure 11). In Liuhuangshan and Tonghuashan, abundant blocks of marble, crinoid bearing limestone, radiolarian bearing red chert, gabbro, basalt and serpentinite are surrounded by schistose metapelite, metasandstone and deformed conglomerate [*Laurent-Charvet*, 2001]. The limestone blocks contain abundant brachiopoda and coral fossils of Late Ordovician to Late Silurian [*XBGMR*, 1959]. Although, the age of the mélange matrix is poorly constrained, a Middle Devonian, or younger, age can be inferred since Early-Middle Devonian radiolarian fossils are found in a chert block in Liuhuangshan mélange [*Gao et al.*, 1998].

In Yushugou, slices of serpentinite, deformed cumulate gabbro, amphibolite and granulite are enclosed in highly sheared metapelites and metasandstones corresponding to the matrix of the ophiolitic mélange (Figure 12b). A ductile deformation produced a flat-lying foliation and a submeridian stretching lineation in the mélange matrix and to a lesser extent in some of the blocks. Numerous asymmetric criteria such as pressure shadows, sigmoidal quartz veins or shear bands indicate a top-to-the-North ductile shearing related to the emplacement of the Kumux ophiolitic mélange (Figure 11) [*Laurent-Charvet*, 2001]. Thus, since the Kumux ophiolitic mélange was displaced to the North, it is unlikely that the Qingbulak Fault represents the root zone of the mélange. Available geochronological studies from the Kumux mélange are rare. A pyroxene amphibolite and a basalt from Liuhuangshan are dated at 452±19 Ma and 340±4Ma, respectively by the Rb-Sr method on whole rock [*Ma et al.*, 1990; *Wu et al.*, 1992]. Amphibole from a gabbro of Tonghuashan yields a K-Ar age of 420±14 Ma, and a cumulate gabbro of Yushugou give a K-Ar age of 437 Ma [*Zhang*, 1985]. Zircons from a granulite block in Yushugou are dated by U-Pb SHRIMP method at 390±11Ma and 392±7 Ma [*Zhou et al.*, 2004], and single zircon grains from a gabbro block in Yushugou yield a U-Pb age of 378±6 Ma [*Jiang et al.*, 2000].

7. Wushi-Aheqi deformation-mélange zone

Along the southern part of the Tianshan Belt, ophiolitic mélanges similar to those described in Kumux and Heiyingshan are exposed in Wushi and Aheqi areas (Figure 1).

7.1. The Biediele section

The Biediele River, located 60 km northwest of Wushi County, provides an excellent section to study the deformation of the Paleozoic rocks. The southern part of the section corresponds to a 3 km thick series of steeply (ca 50-70°) north dipping Permian sandstone, calcareous sandstone and conglomerate. Load casts and graded beddings indicate that this series is frequently upside down and deformed by south-verging folds. The contact with the underlying limestone and sandstone series of Early-Middle Carboniferous age is not observed, an unconformity is reported [*XBGMR*, 1993] but a high angle thrust is also possible. A South-directed high angle

thrust separates the Carboniferous and Devonian rocks in the footwall and hangingwall, respectively (Figure 13). The pre-Carboniferous rocks exhibit structural features quite distinct from the Carboniferous-Permian series. The Devonian and Silurian rocks consist of mylonitic marble (Figure 5f) and schistose clastic and volcaniclastic rocks, respectively. The foliation, deformed by South-verging folds, contains a N-S to NW-SE trending stretching lineation and intrafolial folds attesting for intense ductile shearing. In spite of extensive recrystallization in the marbles, several kinematic criteria such as asymmetric quartz fibers around pyrite grains, sigmoidal clasts and drag folds indicate a top-to-the-North shearing (Figures 5g and 5h). These pre-Carboniferous rocks and those developing to the north of the Heiyingshan ophiolitic mélange are probably belonging to the same formation. In the Biediele valley, ophiolitic mélange does not crop out. We interpret this absence as the result of the post-Permian (Cenozoic?) deformation. In the cross-section of Figure 13, we assume that the ophiolitic mélange has overthrust the Silurian-Devonian sedimentary rocks before the deposition of the Carboniferous rocks. Subsequently, the stack of nappes and its discordant Carboniferous cover were deformed together by south-vergent folds.

Southwestward of Wushi, the Lower Carboniferous mudstone, sandstone and fluvial conglomerate unconformably cover the Cambrian to Devonian sedimentary rocks (Figures 1 and 13) that belong to the northern margin of Tarim Block underlain by Sinian sandstone and Proterozoic metamorphic basement exposed near Akesu area (Figure 1). In agreement with previous studies, the Sinian to Neogene sedimentary series is deformed by south directed imbricate thrusts related to the Late Cenozoic tectonics [*Allen et al.*, 1999, and references therein]. According to available seismic data, an active fault, called the South Tianshan Fault (STF, fault 8 in Figures 1 and 13), passing along the Tuoshigan River separates the Tianshan Belt from the Tarim Block (Figure 1) [*Allen et al.*, 1999; *Zhao et al.*, 2003]. Although we did not study them in detail, we underline that the Devonian rocks of the northern part of the Tarim Block, predominantly composed of red sandstone and pelite, are significantly different from the Devonian rocks of the Biediele River. Since the ophiolitic mélange has been thrust northward upon Devonian marbles, and to the farther south, the Devonian rocks exhibit a quite distinct facies, the ophiolitic mélange must be rooted in the South Tianshan Fault. The geodynamic interpretation will be discussed in section 8.

7.2. The Aheqi section

We investigated the relationship between the southern flank of Tianshan and the Tarim Block in Aheqi (locality c in Figure 1), located 150 km southwestward of the Wushi County. In the north, an ophiolitic mélange consists of meter to kilometer-sized limestone or bedded chert blocks included in schistose grey-green pelite and siliceous turbidite. Along a 5-km-long section, only one block of mafic volcanite has been observed, but according to the available geological maps [*XBGMR*, 1961], mafic and ultramafic rocks are exposed close to the state border with Kirghizstan, further to the northwest of the section. Bedding in the sandstone and cleavage in the pelite display an average NE-SW trend (ca N50E to N70E), which is consistent with that of

Heiyingshan ophiolitic mélange. More to the NW, kilometer- thick massive limestone might be the equivalent of the autochthonous series of the Beideile River. However, due to the intense recrystallization, the ductile planar and linear structures have been erased.

To the South of the Aheqi ophiolitic mélange, Late Carboniferous limestones containing coral fossils overlie conformably Early Carboniferous red mudstone, coarse grain sandstone and conglomerate intercalations. These rocks do not display any ductile shearing or metamorphism, but both Early and Late Carboniferous beds are locally overturned and deformed by South-vergent recumbent folds.

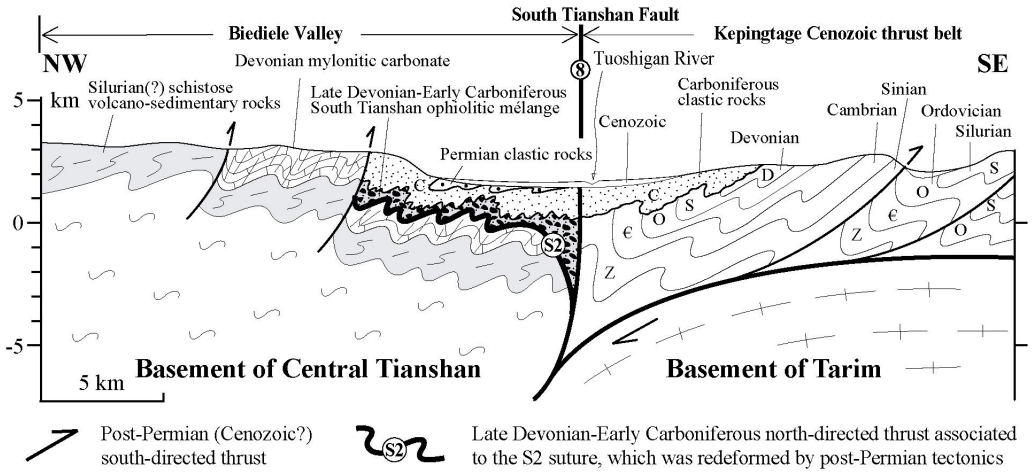

Figure 13. Schematic cross section of the Wushi area (located in figure1) showing the bulk geometry of the South Tianshan. In agreement with Allen et al. [1999], in the Kepintage area, the Sinian to Carboniferous series belongs to a thrust-and-folds belt related to the Cenozoic underthrusting of the Tarim below the Tianshan. In the Biediele valley, the South directed high angle thrusts events are attributed to the same Cenozoic event since Permian sandstone is folded. The ophiolitic mélange overthrusts northward a ductilely deformed series of Devonian marble and volcano-clastic rocks. Although folded by the Cenozoic event, the Carboniferous rocks unconformably cover the ophiolitic mélange. The South Tianshan Fault (number 8 same to that in Figure 1) appears as a reworked pre-Carboniferous suture zone between Tarim and Central Tianshan.

8. Discussion

8.1. Present-day structure

The present-day structure of the Tianshan Belt is the direct consequence of the Cenozoic Eurasia-India collision [e. g. *Molnar and Tapponnier*, 1975; *Tapponnier and Molnar*, 1979; *Nelson et al.*, 1987; *Avouac et al.*, 1993; *Hendrix et al.*, 1994; *Burchfiel, et al.*, 1999; *Poupinet et al.*, 2002; *Shu et al.*, 2003]. The earthquake focal mechanisms and seismological tomography document active intracontinental subduction [*Allen et al.*, 1999; *Vinnik et al.*, 2004] (Figure 14). To the south, the Tarim lithosphere is subducting northward. As a consequence, the Paleozoic to Cenozoic sedimentary cover of the Tarim Proterozoic basement is folded, and imbricated southward [e. g. *Allen et al.*, 1999]. Along the Tuoshigan River, the active South Tianshan Fault represents the present-day boundary between the Tarim and the Tianshan Belt. It is likely that this fault extends at depth and joins with the subducting Tarim basement. As stated above, the lithological differences of the Paleozoic sedimentary series on both sides of the fault, suggests that the South Tianshan Fault corresponds to a reactivated Paleozoic suture (cf. below). Similarly, the present-day northern boundary of the Tianshan belt is a North-directed Cenozoic thrust. The footwall of the thrust is formed by ca 10-12 km thick post-Carboniferous sedimentary rocks of the Junggar

basin, folded and sheared towards the North. The hangingwall of the fault consists of Carboniferous turbidites and ophiolitic mélanges corresponding to an accretionary prism formed during the closure of the oceanic basin that separated the North part of the Tianshan from the Junggar Block [*Wang et al.*, 2006b].

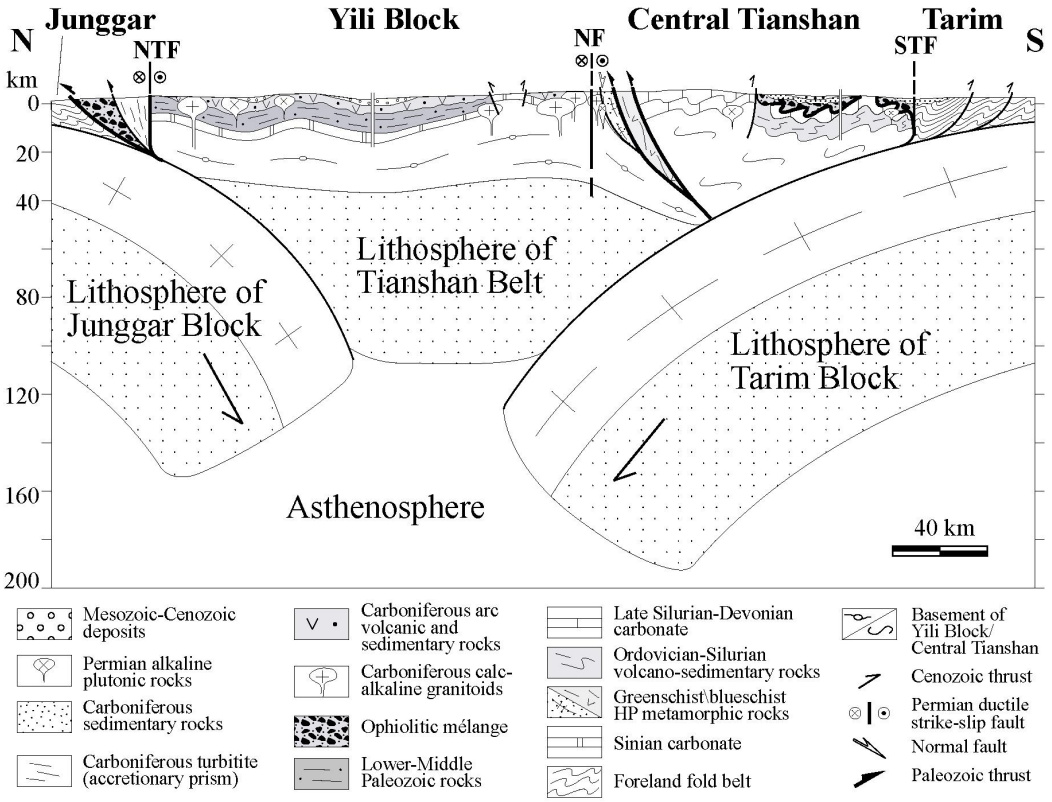

Figure 14. Present-day lithosphere-scale cross section from Junggar to Tarim. The Cenozoic continental subduction, responsible for the double vergent structure of the Tianshan Belt disturbed the Paleozoic structure. The boundaries between Junggar Basin, Yili Block, Central Tianshan Tarim correspond to Paleozoic sutures reworked during the Permian dextral wrenching and the Cenozoic shortening. NTF: North Tianshan Fault, NF: Nalati Fault (Nikolaiev Tectonic Line), STF: South Tianshan Fault. The deep structure is after Zhao et al. [2003] and Wang et al. [2004a].

8.2.Permian tectonics and magmatism

Permian transcurrent displacements that affected entire Central Asia, also played an important role in the evolution of the Chinese Tianshan Belt [e. g. *Sengor et al.*, 1993, *Allen et al.*, 1995]. In the Tianshan region, Late Permian red beds composed of fine to coarse sandstone, conglomerate with multicomponent pebbles are widespread (Figure 1) [*Caroll et al.*, 1995; *Allen et al.*, 1995; *Cui et al.*, 1996]. A well-documented regional unconformity of Late Permian over pre-existing rocks argues for a major break in the orogenic processes in the Tianshan Belt during the Permian.

Several E-W trending, anastomosing, large-scale strike-slip faults, such as the North Tianshan Fault, Main Tianshan Shear Zone, Nalati Fault, Jinghe Fault, Qingbulak Fault, and Houxia Fault are responsible for the domainal structure of the Chinese Western Tianshan (Figure 1). Kinematic and paleomagnetic studies show that they are dextral ductile shear zone active between 280 to 250 Ma [*Cai et al.*, 1996; *Bazhenov et al.*, 1999; *Shu et al.*, 1999; *Zhou et al.*, 2001; *Laurent-Charvet et al.*, 2002, 2003]. This Permian transcurrent faulting is also coeval with the development

of pull-apart basins characterized by a chaotic sedimentation in which Carboniferous limestone, sandstone and volcanic rocks are reworked as olistoliths enclosed in a terrigeneous matrix [*Allen et al.*, 1995; *Shu et al.*, 2005]. The faults are also the feeder zones for interstratified lava flows.

Early to Late Permian magmatic rocks distribute ubiquitously in the Tianshan Belt, but most of them are located along the strike-slip faults (Figure 1). Along the northern margin of the Yili Block, large elongated plutons of K-feldspar granite yield zircon U-Pb ages of 280±5Ma, 266±6 Ma and 294±7Ma, a K-granite from north of Yining yields zircon U-Pb age of 272±6 Ma (Table 1) [*Wang et al.*, in preparation]. In north of Kumux, undeformed granite intruding in the Proterozoic orthogneiss yields a zircon U-Pb age of 252±4 Ma. An undeformed red granite from the Kekesu area is dated at 277±3 Ma [*Wang et al.*, in preparation]. In Bole area, igneous rocks yield ages of 280~270 Ma by K-Ar and $^{40}Ar/^{39}Ar$ methods [*Chen et al.*, 1994; 2000]. A tholeiite from Baiyanggou, southeast of Urumqi yield a zircon SHRIMP age of 245 Ma [*Shu et al.*, 2005].

As a whole, the Permian magmatic rocks belong to bimodal suites. Numerous geochemical studies indicate alkaline signatures [*Allen et al.*, 1992; *Chen et al.*, 1994, 1999, 2000; *Shu et al.*, 2005; *Wang et al.*, in preparation]. This alkaline magmatism points to an important thermal input from the mantle at the end of the Paleozoic in the Tianshan Belt that might be also responsible for partial or total resetting of the older tectono-metamorphic events. For instance, it may account for the "young" Ar/Ar biotite ages of 259±3.3 Ma and 245±0.3 Ma yielded by the quartz micaschists from Kule and Changawuzi ophiolitic mélanges, respectively [*Cai et al.*, 1995; *Hao and Liu*, 1993].

Therefore, the available tectonic and magmatic data suggest that during the Permian, the Tianshan Belt experienced a continental scale wrenching. In agreement with previous studies [e. g. *Bazhenov et al.*, 1999], our new paleomagnetic results from the Yili Block comply with an anti-clockwise rotation of the Yili Block respect to the Tarim Block that took place between Late Carboniferous and Late Permian. Such a rotation is likely accommodated by the dextral strike-slip faults distributed within the whole Tianshan orogen [*Wang et al.*, submitted].

8.3. Sutures and their ages

As outlined above, several ophiolitic mélange zones distribute from west to east along the Tianshan range. These mélanges occur mainly in the Bayingou, Gangou-Mishigou, Kekesu-Changawuzi, Aheqi, Heiyingshan, Kule, Wuwamen and Kumux areas (Figure 1). Since the Bayingou and Gangou-Mishigou mélanges are close to the NTF and MTSZ, respectively, and appear nearly aligned in a NW-SE trend, they are often considered as belonging to the same North Tianshan Suture formed by a southward subduction [e.g. *Windley et al.*, 1990; *Allen et al.*, 1992; *Gao et al., 1998*; *Zhou et al.*, 2001]. However, as shown in section 6, taking into account a] the age difference between the Late Devonian-Early Carboniferous of Bayingou mélange and the Late Ordovician-Silurian of Gangou-Mishigou mélange and, b) the spatial relationships between the two mélange zones with respect to the adjacent

volcanic arcs, namely Yili arc to the south of Bayingou mélange, and Ordovician-Silurian Central Tianshan arc to the south of Gangou-Mishigou mélange, we propose that these two mélange zones belong to two different sutures. The Bayingou mélange and related subduction complex represent the North Tianshan Suture. It is worth to note that due to the Cenozoic tectonics, the true ophiolitic suture is not exposed. The mélange was formed during a southward subduction that was also responsible for the genesis of the Yili magmatic arc as well as the Bogda volcanic arc. To the East, the Bogda magmatic arc overthrusted the Meso-Cenozoic sedimentary rocks of the Junggar basin, and consequently hides the Paleozoic suture zone. The westward extension of the North Tianshan suture is offset by the Aibi Fault (fault 5 in Figure 1), but it is likely that this suture zone extends in Kazakhstan. The final suturing along the North Tianshan Suture occurred at the end of Carboniferous [e. g. *Zhou et al.*, 2001; *Wang et al.*, 2006b]. In Figures 15-17, this cryptic suture is labelled S3.

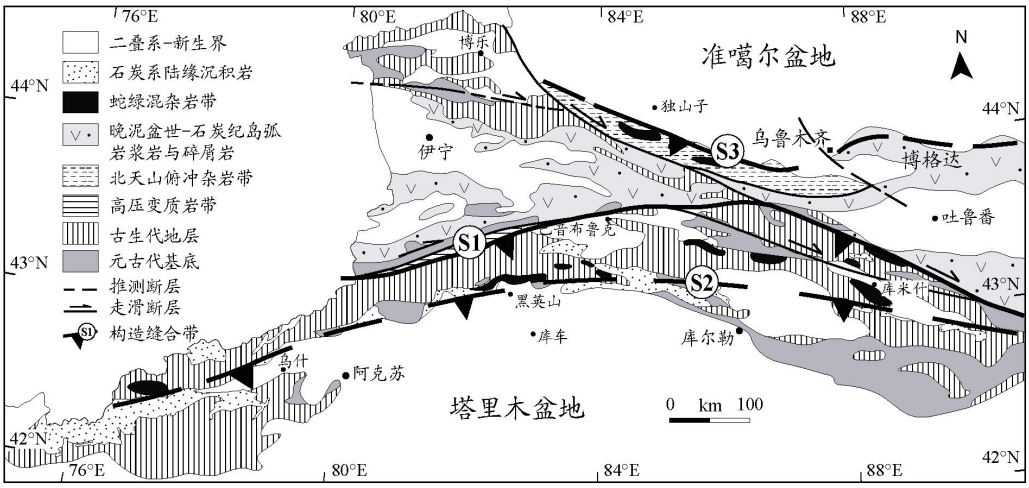

Figure 15. Simplified tectonic map of the Chinese West Tianshan Belt showing the three sutures recognized in this study. S1: Early Paleozoic Tianshan Suture along the Kekesu-Mishigou-Gangou lineament separates Central Tianshan to the south from the Yili Block and North Tianshan to the north; S2: Late Devonian-Early Carboniferous Suture along the South Tianshan Faults separates Central Tianshan from the Tarim; S3: Late Paleozoic North Tianshan Suture separates the Yili Block and North Tianshan from Junggar.

Except the North Tianshan mélange, all other ophiolitic mélanges that develop in the Tianshan belt are regarded by most of previous researchers as formed in one single ophiolitic suture, i.e. the South Tianshan Suture or the Qingbulak Fault, and most of mélange areas are tectonic slices thrust to the south from this suture. In fact, the Kekesu HP metamorphic oceanic rocks, Changawuzi ophiolite and Gangou-Mishigou ophiolitic mélange are suggested to form around 410-440 Ma, and the HP metamorphism is proposed to take place around 350-330 Ma [e.g. *Gao et al.*, 1998; *Klemd et al.*, 2005], thus the South Tianshan Suture previously defined as a northward subduction producing the Carboniferous Yili magmatic arc is unlikely since the age of the magmatic rocks in the Yili Block ranging from 360 Ma to 310 Ma [*Li et al.*, 1998; *Zhu et al.*, 2005; *Wang et al.*, 2006b] is younger than that of the HP metamorphism. In addition, the top-to-the-North kinematics inferred from the HP metamorphic complex [*Gao et al.*, 1995; this study, section 4] and Gangou-Mishigou area (section 6) indicates that these metamorphic oceanic rocks should be related to a southward subduction. Ordovician to Silurian calc-alkaline volcanic and volcaniclastic rocks that

develop to the south of the Kekesu - Nalati - Mishigou - Gangou ophiolites also agree with a South-directed subduction. Thus, the Changawuzi, Kekesu, Mishigou, Gangou ophiolites correspond to the Early Paleozoic Tianshan Ocean that closed before Late Devonian by south-directed subduction. These ophiolites form the oldest suture in the Chinese Tianshan Belt and are referred to as S1 suture (Figures 15-17).

Finally, the ophiolitic mélanges that crop out in Aheqi, Heiyingshan, Kule, Wuwamen and Kumux areas consist of a Late Devonian to Early Carboniferous matrix and enclosed various oceanic derived blocks including ca 400-380 Ma gabbros. Conversely to previous studies, our kinematic analyses in both the mélange and its underlying tectonic substratum, agree with the interpretation of thrusted slices diplaced from South to North. The geochemistry of the Wuwamen ophiolite suggests that it formed in a back arc basin setting [*Dong et al.*, 2005], which is different from the Kekesu-Mishigou-Gangou oceanic crust. Therefore, we propose that this mélange zone may originate in a third suture, of Late Devonian-Early Carboniferous age. In Figures 15-17, this suture is defined as S2. To the West, it partly corresponds to the South Tianshan Fault, from Akesu to Korla, S2 is hidden below the Meso-Cenozoic sedimentary deposits of the North Tarim basin. Presumably, S2 continues eastward to north of the Proterozoic basement of the Tarim Block, and then to the South of Kumux, but the exact pattern could not be verified as these places are impossible to reach.

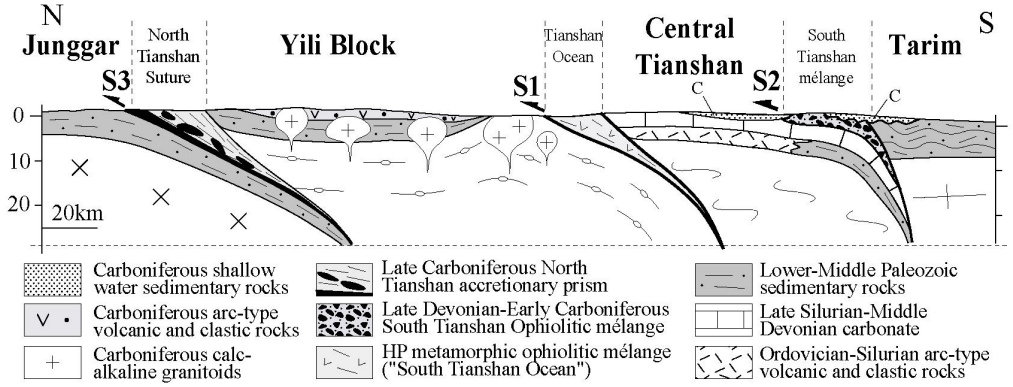

Figure 16. Pre-Permian reconstruction of the Chinese West Tianshan Belt. In order to emphasize the primary structure of the Tianshan Belt, the sedimentary and magmatic rocks yonger than Carboniferous have been omitted. The three sutures identified in figure 15 separate four continental blocks, namely from South to North, Tarim, Central Tianshan, Yili and Junggar.

8.4. Pre-Permian Tectonic divisions of the Chinese Tianshan Belt

In the Western Chinese Tianshan, the Permian and Cenozoic overprints severely complicate the tectonic reconstruction of the Paleozoic Tianshan. The present-day intracontinental subductions (Figure 14) do not represent the pre-Permian relationships between the Tianshan Belt and adjacent Junggar and Tarim basins. For instance, the true North Tianshan suture is a cryptic one, hidden below the Cenozoic trust of the northern part of the Tianshan belt above the Mesozoic-Cenozoic sedimentary series. In order to better understand the pre-Permian tectonics, it is also necessary to compensate for the effect of Permian intracontinental wrenching. However, the amount of belt-parallel displacement is presently unknown. Figure 15 is a simple reconstruction of the pre-Permian structure of the Chinese Tianshan Belt

showing the above defined three oceanic sutures and intervening continental blocks, namely from North to South, Junggar, North Tianshan, Yili Block, Central Tianshan and Tarim.

The North Tianshan represents the Middle to Late Carboniferous accretionay complex located to the south of the true S3 ophiolitic suture formed by the southward subduction of the Junggar basin below the Yili Block. The continental or oceanic nature of the basement of the Junggar Block is controversial. On the basis of gravity and seismic data, some authors [e.g. *Yang et al.*, 1986; *Sengör et al.*, 1993; *Gao et al.*, 1998] propose a continental craton, alternatively a remnant back-arc basin with an oceanic crust is suggested [e.g. *Caroll et al.*,1990; *Chen and Jahn*, 2004; *Jahn*, 2004]. Although a general discussion on this problem is beyond the scope of this paper, the large area (ca 130. 000 km^2), and the 10-12 km of sediment thickness in the Junggar basin argue for a continental crust.

The Yili Block is a Late Devonian-Carboniferous magmatic arc sitting on an Early Paleozoic platform and a Proterozoic basement. The North Tianshan Fault (NTF, Fault 1 in Figures 1 and 15) separates the Yili Block from the North Tianshan. However, there is no evidence that the NTF existed before the Permian, and thus the North Tianshan could have formed the northern margin of the Yili Block (Figure 16).

The Central Tianshan represents the domain located between the S1 and S2 sutures, with Ordovician to Silurian arc volcanites and sedimentary rocks deposited on a Proterozoic basement. In the northern and central parts of the Central Tianshan, the unmetamorphozed Silurian turbidites are sheared and folded with a northward vergence. The deformed Early Paleozoic series are unconformably overlain by Carboniferous terrigeneous rocks and carbonates. In the southern part of the Central Tianshan, Silurian and Devonian marbles are ductilely deformed and are tectonically overlain by a Late Devonian-Early Carboniferous ophiolitic mélange. The interpretation proposed here for the Central Tianshan is different from previous reconstructions, in which the Yili and Central Tianshan were considered as a single microcontinent [*Windley et al.*, 1990; *Allen et al.*, 1992; *Gao et al.*, 1998; *Zhou et al.*, 2001].

The southernmost part of the Tianshan range is dominanted by ophiolitic mélanges, which are defined here as South Tianshan mélange zone rooted in the S2 suture. To the south of the S2 suture, a continuous series of weakly deformed Paleozoic strata overlies a Proterozoic basement. These rocks, well exposed in the Kepingtage and Kuluketage mountains, belong to the northern passive margin of the Tarim Block (Figures 1, 16). The significant difference between the Devonian rocks on both sides of the S2 suture agrees with this interpretation. To the North of the S2 suture, the Devonian rocks consist dominantly of platform carbonates and chert, whereas to the South of S2 suture, red sandstone is widespread. Conversely, the Carboniferous sandstone and limestone, that crop out from Aheqi to South of Kumux and unconformably cover the Devonian and older rocks, are similar on both sides of S2 suture.

8.5. Tectonic evolution of the Chinese West Tianshan

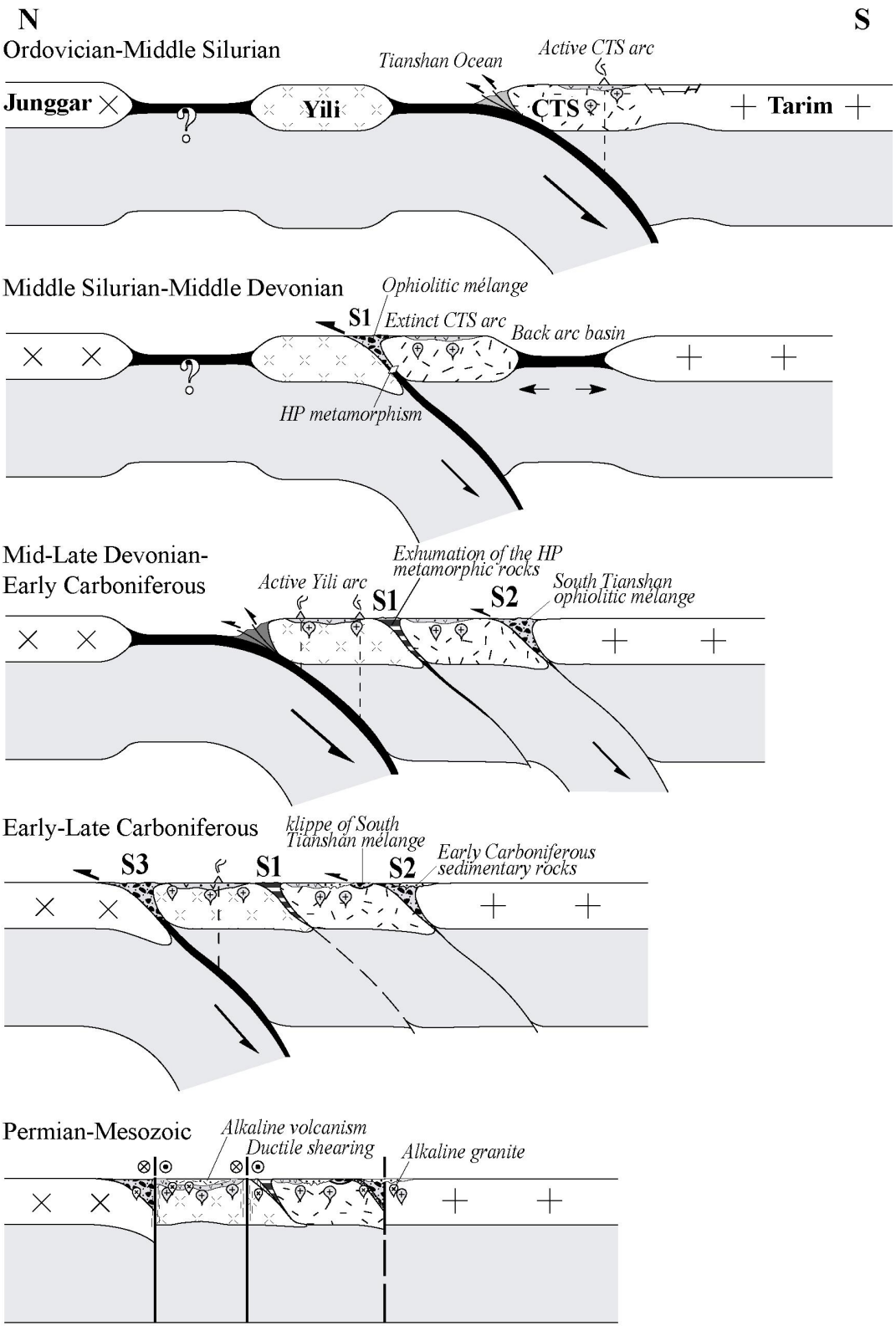

Figure 17. Simplified geodynamic evolution of the Chinese West Chinese Tianshan Belt (modified from Laurent-Charvet [2001]). In this model, the continental convergence between Junggar and Tarim is accommodated by three diachronous and south-directed subduction zones. The Early Paleozoic closure of the Tianshan Ocean is responsible for the collision of the Yili Block with Central Tianshan. This microcontinent is the drifted northern part of the Tarim continent and rewelded again to Tarim at the end of Devonian. Lastly, the Junggar continent collided with northern part of the Yili Block at the end of Carboniferous.

On the basis of the above presented data, a simple scenario is proposed as evolutionary cross-sections in Figure 17. This model emphasizes the displacements at high angle to the belt, orogen-parallel wrenching is not taken into account since evidence for the pre-Permian strike-slip is not documented. During the Ordovician-Early Silurian, an oceanic basin called the Tianshan Ocean existed between the Yili Block and the Central Tianshan Block (Figure 17). This ocean began to close by southward subduction beneath the Central Tianshan during Late Ordovician and Silurian generating the Central Tianshan volcanic arc. At that time, the Central Tianshan was a part of the Tarim Continent. From Middle Silurian to Middle Devonian time, the Tianshan Ocean was progressively closing. The oceanic subduction, followed by the continental subduction of the southern part of the Yili Block was responsible for the development of the HP metamorphic complex. Coevally with the closure of the Tianshan Ocean, a marginal sea opened to the South of the Central Tianshan Block, as suggested by the ca 400-380 Ma gabbro blocks with a back-arc-basin geochemical affinity found in the ophiolitic mélange. Moreover, the evolution from a carbonate platform to banded cherts argue for a progressive deepening of the southern margin of the Central Tianshan Block during the Early to Middle Devonian. During the Early Paleozoic, the limestone and sandstone deposits suggest that the northern margin of the Yili Block was a passive margin. A possible ocean separating the south Junggar from the Yili Block is assumed in Figure 17.

From the Late Devonian to Early Carboniferous, due to the closure of the Tianshan Ocean, the Yili and Central Tianshan Blocks are welded together to form a single continental mass. At that time, the HP metamorphic rocks were exhumed. The closure of the back arc basin was accommodated by a south-directed subduction below the Tarim Block as suggested by the northward thrusting of the South Tianshan ophiolitic mélange. At the same time, the existence of an oceanic basin, called the North Tianshan Ocean [e.g. *Xiao et al.*, 1992] can be documented. The Yili magmatic arc and the North Tianshan accretionary prisme comply with a southward subduction of the North Tianshan Ocean. The oceanic subduction ended in Late Carboniferous when the continental collision occurred between Junggar Block and the Yili Block. At the end of the Carboniferous, the submeridian convergence (with respect to the present geographic coordinates) finished when all the continental blocks were amalgamated.

The Permian intracontinental tectonics is characterized by dextral ductile strike-slip associated with alkaline magmatism. The regional unconformity of the Permian red beds deposits shows that the Paleozoic Tianshan orogeny definitely ended. As discussed above, this mountain belt was reactivated by Cenozoic intracontinental subductions due to the Indo-Asia collision.

9. Conclusions

The study of the Western part of the Chinese Tianshan, and particularly of the South branch of the Yili Block in several key areas, has allowed us to offer new structural and geochronological insights on the Paleozoic evolution of the belt. A detailed survey along the Kekesu River documents three deformation events. The most conspicuous one corresponds to a ductile dextral shearing along the Nalati Fault

(or Nikolaiev Tectonic Zone) that agrees well with the Permian wrenching that was previously described throughout the Tianshan Belt. An older event produced structures such as low angle foliation and submeridian stretching lineation associated to a top-to-the-North ductile shearing. This event is coeval with a blueschist-eclogite facies metamorphism that is developed in mafic and sedimentary rocks formed in an oceanic basin. The flat-lying ductile deformation is interpreted as the result of the northward emplacement of an ophiolitic nappe upon the Yili Block. Lastly, evidence for an extensional event, coeval with a greenschist facies metamorphism is recognized in the high-pressure rocks.

$^{40}Ar/^{39}Ar$ laser probe dating of white mica in retrogressed blueschist facies metapelites and in a greenschist facies quartzite provides 330-315 Ma ages that are interpreted as the age of the final exhumation of the HP rocks. In agreement with previous studies, the age of the HP metamorphic event cannot be younger than Early Carboniferous. Moreover, the evidence of the Late Ordovician-Silurian volcanic arc above the continental Central Tianshan Block, recognized to south of the HP rocks, argues for the closure of the Tianshan Ocean as soon as Silurian.

Along the southern slope of the Tianshan range, a Late Devonian-Early Carboniferous ophiolitic mélange including ca 400 Ma gabbro and Late Devonian-Early Carboniferous (Fammenian-Tournaisian) chert blocks has been thrust to the North over a Silurian-Devonian marble series. This ductile shearing occurred before the deposition of the Early-Middle Carboniferous sandstone and limestone series that unconformably covers the mélange and its tectonic substratum. The geochemistry of the mafic rocks blocks included in the mélange suggests that these rocks were formed in a marginal sea rather than in a wide oceanic basin.

In the Chinese Western Tianshan Belt, we distinguish three ophiolitic sutures. The oldest one, of Early-Middle (?) Devonian age corresponds to the closure of the Tianshan Ocean through a southward subduction and subsequent collision between the Yili Block and Central Tianshan. The southern one, of Late Devonian-Early Carboniferous age, is the root zone of the South Tianshan ophiolitic mélange. The northern suture that separates the Yili Block with its Carboniferous magmatic arc from the Junggar Block is actuallly represented only by the subduction complex and ophiolitic mélange of the North Tianshan. This Late Carboniferous suture is widely hidden by north-directed Cenozoic thrusts.

Acknowledgements

Colleagues of the Bureau of National project 305, Xinjiang Uygur autonomous Region are thanked for their help for facility during fieldwork. This work has been supported by the State Key Project for Basic Research of China (No. 2001CB409804). Funding of a part of research of the first author in France by the French Embassy in Beijing is greatfully acknowledged.

References

Allen, M.B., B.F. Windley, and C. Zhang (1992), Paleozoic collisional tectonics and magmatism of the Chinese Tien Shan, Central Asia, *Tectonophysics*, *220*, 89-115.

Allen, M.B., A.M.C. Sengör, and B.A. Natal'in (1995), Junggar, Turfan and Alakol basins as Late Permian to?

Early Triassic extensional structures in a sinistral shear zone in the Altaid orogenic collage, Central Asia, *J. Geol. Soc. London, 152*, 327-338.

Allen, M.B., S.J. Vincent, and P.J. Wheeler (1999), Late Cenozoic tectonics of the Kepingtage thrust zone: Interation of the Tien Shan and Tarim Basin, northwest China, *Tectonics*, *18(4)*, 639-654.

Avouac, J.P., P. Tapponnier, M. Bai, H. You, and G. Wang (1993), Active thrusting and folding along the northern Tien Shan and Late Cenozoic rotation of the Tarim relative to Dzungaria and Kazakhstan, *J. Geophys. Res., 98(B4)*, 6755-6804.

Bazhenov, M.L., V.S. Burtman, and A.V. Dvorova (1999), Permian paleomagnetism of the Tien Shan fold belt, Central Asia: Post-collisional rotation and deformation, *Tectonophysics, 312(2-4)*, 303-329.

Brookfield, M.E. (2000), geological development and Phanerozoic crustal accretion in the western segment of the southern Tienshan (Kyrgyzstan, Uzbekistan and Tajikistan), *Tectonophysics, 328*, 1-14.

Buckman, S., and J.C. Aitchison (2004), Tectonic evolution of Paleozoic terranes in West Junggar, Xinjing, NW China, in *Aspects of the tectonic evolution of China,* edited by J. Malpas, C.J.N. Fletcher, J.R. Ali, and J.C. Aitchison, *Geol. Soc., London, Spec. Publ., 226,* pp. 101-129.

Burchfiel, B.C., E.T. Brown, Q.D. Deng, X.Y. Feng, J. Li, P. Molnar, J.B. Shi, Z.M. Wu, and H.C. You (1999), Crustal shortening on the Margins of the Tien Shan, Xinjiang, China, *Int. Geol. Rev., 41*, 665-700.

Burtman, V.S. (1975), Structural geology of variscan Tien Shan, USSR, *Am. J. Sci., 275(A)*, 157-186.

Cai, D.S., H.F. Lu, D. Jia, S.M. Wu, and C.M. Chen (1996), 40 Ar/ 39 Ar dating of the ophiolite mélange in the southern Tien Shan and the mylonite in the southern rim of central Tien Shan and their tectonic significance, *Sci. Geol. Sin., 31(4)*, 384-390 (in Chinese with English abstract).

Carroll, A.R., Y. Liang, S. Graham, X. Xiao, M.S. Hendrix, J. Chu, and C.L. McKnight (1990), Junggar basin, NW China: trapped late Paleozoic ocean, *Tectonophysics, 186*, 1-14.

Carroll, A.R., S.A. Graham, M.S. Hendrix, D. Ying, and D. Zhou (1995), Late Paleozoic tectonic amalgamation of NW China: sedimentary records of the northern Tarim, northwestern Turpan, and southern Junggar basins, *Geol. Soc. Am. Bull., 107*, 571-594.

Charreau, J., Y. Chen, S. Gilder, S. Dominguez, J.P. Avouac, S. Sen, D.J. Sun, Y.A. Li, and W.M. Wang (2005), Magnetostratigraphy and rock magnetism of the Neogene Kuitun He section (northwest China): implications for Late Cenozoic uplift of the Tianshan mountains, *Earth Planet. Sci. Lett., 230(1-2)*, 177-192.

Che, Z.C., H.F. Liu, and L. Liu (1994), *The Formation and Evolution of the central Tianshan orogenic belt,* 135 pp., Geological Publishing House, Beijing (in Chinese with English abstract).

Chen, B., and B.M. Jahn (2004), genesis of post-collisional granitoids and basement nature of the Junggar Terrane, NW China: Sm-Nd isotope and trace elements evidence, *J. Asian Earth Sci., 23,* 691-703.

Chen, C.M., H.F. Lu, D. Jia, D.S. Cai, and S.M. Wu (1999), Closing history of the southern Tianshan oceanic basin, western China: an oblique collisional orogeny, *Tectonophisics, 302*, 23-40.

Chen, J.F., D.G. Chen, X.M. Li, T.X. Zhou, and K.A. Foland (1994), K-Ar and 40Ar/39Ar geochronology of granites from the Alataw Mountains, northwest Xinjiang, China, *Acta Petrol. Sin., 10(2)*, 184-192 (in Chinese with English abstract).

Chen, J.F., T.X. Zhou, Z. Xie, X. Zhang, and X.S. Guo (2000), Formation of positive $e_{Nd}(T)$ granitoids from the Alataw Mountains, Xinjiang, China, by mixing and fractional crystallization: implication for Phanernozoic crustal growth, *Tectonophysics, 328,* 53-67.

Coleman, R.G. (1994), Terrains (units) in the Western half of the geodynamic map, *Stanford-China Geosciences industrial affiliates program annual review,* pp. 1-8, Stanford University, Palo Alto, USA.

Coleman, R.G. (1989), Continental growth of northwest China, *Tectonics, 8(3)*, 621-635.

Cui, Z.L., Z.C. Mei, H.J. Qu, S.Y. Chen, G.Q. Zheng, L. Yang, J.X. Liu, Y.H. Wu, and L.P. Xiong (1996), A study on the Upper Permian of the Yili Basin, Xinjiang, *Geol. J. China Univ., 2(3)*, 332-338 (in Chinese with English abstract).

Cunningham, W.D., B.F. Windley, D. Dorjnamjaa, J. Badamgarov, and M. Saandar (1996), A structural transect across the Mongolian Western Altai: Active transpressional mountain building in central Asia, *Tectonics, 15(1)*, 142-156.

De Jong, K. (2003), Very fast exhumation of high-pressure metamorphic rocks with excess ^{40}Ar and inherited ^{87}Sr, Betic Cordilleras, southern Spain, *Lithos, 70,* 91-110.

De Jong, K., W.J. Xiao, B.F. Windley, H. Masago, and C.H. Lo (2006), Ordovician $^{40}Ar/^{39}Ar$ phengite ages from the blueschist-facies Ondor Sum subduction-accretion complex (Inner Mongolia) and implications for the early Paleozoic history of continental blocks in China and adjacent areas, *Am. J. Sci.*, in Press.

Dobretsov, N.L., R.G. Coleman, J.G. Liou, and S. Maruyama (1987), Blueschist belt in Asia and possible periodicity of blueschist facies metamorphism, *Ofioliti, 12*, 445-456.

Dong, Y.P., D.W. Zhou, G.W. Zhang, C.L. Zhang, L.Q. Xia, X.Y. Xu, and X.M. Li (2005), Tectonic setting of the Wuwamen ophiolite at the southern margin of Middle Tianshan Belt, *Acta Petrol. Sin., 21(1),* 37-44 (in Chinese with English abstract).

Gao, J. (1993), Plate tectonics and geodynamics of the orogenesis of the southwest Tianshan, Ph.D. thesis, 90 pp., Chinese Academy of Geological Sciences, Beijing.

Gao, J. (2000), Geological map of high-pressure low-temperature metamorphic belt in the western Tianshan Mountains, northwest of China (1:200 000), Hebei Geological Survey (China).

Gao, J., and R. Klemd (2000), Eclogite Occurrences in the Southern Tianshan High-Pressure Belt, Xinjiang, Western China, *Gondwana Res., 3(1)*, 33-38.

Gao, J., and R. Klemd (2003), Formation of HP-LT rocks and their tectonic implications in the western Tianshan Orogen, NW China: geochemical and age constraints, *Lithos, 66*, 1-22.

Gao, J., G.Q. He, M.S. Li, X.C. Xiao, and Y.Q. Tang (1995), The mineralogy, petrology, metamorphic PTDt trajectory and exhumation mechanism of blueschists, south Tianshan, northwestern China, *Tectonophysics, 250*, 151-168.

Gao, J., G.Q. He, and M.S. Li (1997), Paleozoic orogenic processes of Western Tianshan Orogen, *Earth Sci. J. China Univ. Geosci., 22 (1)*, 28-32 (in Chinese with English abstract).

Gao, J., M.S. Li, X.C. Xiao, Y.Q. Tang, and G.Q. He (1998), Paleozoic tectonic evolution of the Tianshan Orogen, northern China, *Tectonophysics, 287*, 213-231.

Gao, J., L.F. Zhang, and S.W. Liu (2000), The 40Ar/39Ar age record of formation and uplift of the blueschists and eclogites in the western Tianshan Mountains. *Chin. Sci. Bull., 45*, 1047–1051.

Han, B.F., G.Q. He, T.R. Wu, and H.M. Li (2004), Zircon U-Pb dating and geochemical features of Early Paleozoic granites from Tianshan, Xinjiang: Implications for tectonic evolution, *Xinjiang Geology, 22(1)*, 4-11 (in Chinese with English abstract).

Hao, J., and X.H. Liu (1993), Ophiolite mélange time and tectonic evolutional model in South Tien Shan area, *Sci. Geol. Sin., 28(1)*, 93-95 (in Chinese with English abstract).

Hendrix, M.S., T.A. Dumitru, and S.A. Graham (1994), Late Oligocene-Early Miocene unroofing in the Chinese Tian Shan: An early effect of the India-Asia collision, *Geology, 22*, 487-490.

Hu, A.Q., Z.G. Zhang, J.Y. Liu, J.H. Peng, J.B. Zhang, D.J. Zhao, S.Z. Yang, and W. Zhou (1986), U-Pb age and evolution of Precambrian metamorphic rocks of the middle Tianshan uplift zone, eastern Tianshan, China, *Geochimica, 1,* 23-35 (in Chinese with English abstract).

Jahn, B.M. (2004), The Central Asia Orogenic Belt and growth of the continental crust in the Phanerozoic, in *Aspects of the tectonic evolution of China,* edited by J. Malpas, C.J.N. Fletcher, J.R. Ali, and J.C. Aitchison, *Geol. Soc., London, Spec. Publ., 226,* pp. 73-100.

Jahn, B.M., W.L. Griffin, and B.F. Windley (2000), Continental growth in the Phanerozoic: evidence from Central Asia, *Tectonophysics, 328*, 1-227.

Jia, M. (1996), Petrology, geochronology, and tectonic significance of the south Tianshan blueschist belt, NW China, M.S. thesis, 50 pp., Stanford University, Californian (USA).

Jiang, C.Y., Y.M. Mu, X.N. Zhao, and H.B. Zhang (2000), The geological features and tectonic significance of a mafic-ultramafic complex belt at the northern margin of the southern Tien Shan fold belt, China, *Journal of Xi'an Engineering University, 22(2)*, 1-6 (in Chinese with English abstract).

Klemd, R. (2003), Ultrahigh-pressure metamorphism in eclogites from the western Tianshan high-pressure belt (Xinjiang, western China)-Comment, *Am. Mineral.*, 88, 1153-1156.

Klemd, R., F. Schröter, T.M. Will, and J. Gao (2002), P-T evolution of glaucophane-clinozoisite bearing HP-LT rocks in the western Tianshan orogen, NW China, *J. Metamorph. Geol., 20,* 239-254.

Klemd, R., M. Bröcker, B. R. Hacker, J. Gao, P. Gans, and K. Wemmer (2005), New age constraints on the metamorphic evolution of the high-pressure/low-temperature belt in the western Tianshan mountains, NW China, *J. Geol., 113,* 157–168.

Laurent-Charvet, S.(2001), Accrétions continentales en Asie centro-orientale: évolution géodynamique et structurale du Tianshan et du Junggar oriental (nord-ouest Chine) au Paléozoïque, Ph.D. thesis, University of Orléans, Orléans (France).

Laurent-Charvet, S., J. Charvet, L.S. Shu, R.S. Ma, and H.F. Lu (2002), Palaeozoic late collisional strike-slip deformations in Tianshan and Altay, eastern Xinjiang, NW China, *Terra Nova, 14(4),* 249-256.

Laurent-Charvet, S., J. Charvet, P. Monie, and L.S. Shu (2003), Late Paleozoic strike-slip shear zones in eastern Central Asia (NW China): new structural and geochronological data, *Tectonics, 22(2),* 1099-1101.

Li, H.Q., C.F. Xie, H.L. Chang, H. Cai, J.P. Zhu, and S. Zhou (1998), *Study on metallogenetic chronology of nonferrous and precious metallic ore deposts in north Xinjiang, China,* pp. 100-127, Geology Publishing house, Beijing (in Chinese with English abstract).

Liu, Y. (2001), Early Carboniferous radiolarian fauna from Heiyingshan South of the Tianshan Mountains and its geotectonic significance, *Acta geol. Sin., 75(1)*, 101-108.

Ma, R.S., S.F. Ye, C.Y. Wang, and G.B. Liu (1990), Framework and evolution in the East Tianshan Orogenic belt, *Geosci. Xinjiang, 2,* 21-36 (in Chinese with English abstract).

Ma, R.S., C.Y. Wang, and S.F. Ye (1993), *Tectonic framework and crustal evolution of Eastern Tianshan Mountains*, 225 pp., Publishing House of Nanjing University, Nanjing (in Chinese with English abstract).

Ma, R.S., L.S. Shu, and J.Q. Sun (1997), *Tectonic evolution and metallization in the Eastern Tianshan belt, China*, 202 pp., Geological Publishing House, Beijing (in Chinese with English abstract).

Molnar, P., and P. Tapponnier (1975), Cenozoic tectonics of Asia: Effects of a continental collision, *Science, 189,* 419-426.

Nelson, M.R., R. McCaffrey, and P. Molnar (1987), Source parameters for eleven earthquakes in the Tien Shan, central Asia: Determined by P and SH waveform inversion, *J. Geophys. Res., 92,* 12, 629-12, 648.

Poupinet, G., J.P. Avouac, M. Jiang, S. Wei, E. Kissling, G. Herquel, J. Guilbert, A. Paul, G. Wittlinger, H. Su, and

J.C. Thomas (2002), Intracontinental subduction and Palaeozoic inheritance of the lithosphere suggested by a teleseismic experiment across the Chinese Tien Shan, *Terre Nova, 14,* 18-24.

Renne, P.R., C.C. Swisher, A.L. Deino, D.B. Karner, T.L. Owens, and D.J. DePaolo (1998), Intercalibration of standards, absolute ages and uncertainties in $^{40}Ar/^{39}Ar$ dating, *Chem. Geol. 145*, 117-152.

Ruffet, G., G. Féraud, and M. Amouric (1991), Comparison of ^{40}Ar-^{39}Ar conventional and laser dating of biotites from the North Trégor Batholith, *Geochim. Cosmochim. Acta 55*, 1675-1688.

Ruffet, G., G. Féraud, M. Ballèvre, and J.R. Kiénast (1995), Plateau ages and excess argon in phengites: an ^{40}Ar-^{39}Ar laser probe study of Alpine micas (Sesia zone, Western Alps, northern Italy), *Chem. Geol. (Isotope Geoscience Section), 121,* 327-343.

Sengör, A.M.C., B.A. Natal'in, and V.S. Burtman (1993), Evolution of the Altaid tectonic collage and Paleozoic crust growth in Eurasia, *Nature, 364,* 299-307.

Shi, Y.S., H.F. Lu, D. Jia, and D.G. Howell (1994), Paleozoic plate tectonic evolution of the Tarim and western Tianshan Regions, Western China, *Int. Geol. Rev., 36,* 1058-1066.

Shu, L.S., J. Charvet, L.Z. Guo, H.F. Lu, and S. Laurent-Charvet (1999), A large-scale Palaeozoic dextral ductile strike-slip zone: the Aqqikkudug-Weiya zone along the northern margin of the Central Tianshan belt, Xinjiang, NW China, *Acta Geol. Sin., 73(2),* 148-162.

Shu, L.S., H.F. Lu, J. Charvet, S. Laurent-Charvet, and D.H. Yin (2000), Paleozoic accretionary terranes in Northern Tianshan, NW China, *Chin. Geochem., 19(3),* 193-202.

Shu, L.S., J. Charvet, H.F. Lu, and S. Laurent-Charvet (2002), Paleozoic accretion-collision events and kinematics of ductile deformation in the central-southern Tianshan Belt, China, *Acta Geol. Sin., 76(3),* 308-323.

Shu, L.S., B. Wang, F. Yang, H.F. Lu, J. Charvet, and S. Laurent-Charvet (2003), Polyphase Tectonic Events and Mesozoic-Cenozoic Basin-Range Coupling in the Chinese Tianshan belt, *Acta Geol. Sin., 77(4),* 457-467.

Shu, L.S., W.B. Zhu, B. Wang, M. Faure, J. Charvet, and D. Cluzel (2005), The post-collision intracontinental rifting and olistostrome on the southern slope of Bogda Mountains, Xinjiang, *Acta Petrol. Sin., 21(1)*, 25-36 (in Chinese with English abstract).

Steiger, R.H. and E. Jäger (1977), Subcommission on geochronology: convention on the use of decay constants in geo- and cosmology, *Earth Planet. Sci. Lett., 36,* 359-362.

Tagiri, M., T. Yano, A. Bakirov, T. Nakajima, and S. Uchiumi (1995), Mineral parageneses and metamorphic P-T paths of ultrahigh-pressure eclogites from Kyrghyzstan Tien-Shan, *Island Arc, 4,* 280–292.

Tapponnier, P., and P. Molnar (1979), Active faulting and Cenozoic tectonics of the Tienshan, Mongolia and Baykal regions, *J. Geophys. Res., 84,* 3425-3459.

Vinnik, L.P., C. Reigber, I.M. Aleshin, G.L. Kosarev, M.K. Kaban, S.I. Oreshin, and S.W. Roecker (2004), Receiver function tomography of the central Tien Shan, *Earth Planet. Sci. Lett., 225,* 131-146.

Volkova, N.I., and V.I. Budanov (1999), Geochemical discrimination of metabasalt rocks of the Fan-Karategin transitional blueschist/greenschist belt, South Tianshan, Tajikistan: seamount volcanism and accretionary tectonics, *Lithos, 47(3-4),* 201-216.

Wang, B., L.S. Shu, D. Cluzel, M. Faure, and J. Charvet (2006a), Geochemical Constraints on Carboniferous Volcanic rocks of Yili Block (Xinjiang, NW China); implication on tectonic evolution of Western Tianshan, *J. Asian Earth Sci.,* available online.

Wang, B., M. Faure, D. Cluzel, L.S. Shu, J. Charvet, and S. Meffre (2006b), Late Paleozoic tectonic evolution of the northern West Tianshan, NW China, *Geodin. Acta*, in press.

Wang, B.Y., Q. Li, and J.B. Liu (1997), Geological structures of the Middle Tianshan Mountains along the Dushanzi-Kuqa highway, *Xinjiang Geology, 15(2),* 135-154 (in Chinese with English abstract).

Wang, C.Y., Z.E. Yang, H. Luo, and W.D. Mooney (2004a), Crustal structure of the northern margin of the eastern Tien Shan, China, and its tectonic implications for the 1906 M~7.7 Manas earthquake, *Earth Planet. Sci. Lett., 223,* 187-202.

Wang, Z.L., J.W. Mao, J.M. Yang, W. Chen, and Z.H. Zhang (2004b), 40Ar-39Ar age of K-feldspar from K-feldspar granite in the Qiaohuote Copper deposit, Bayinbulak, Xinjiang, and its geological significance, *Acta Geol. Sin., 78(2),* 428-434.

Wang, Z.X., J.Y. Wu, X.C. Lü, J.G. Zhang, and C.D. Liu (1990), Polycyclic tectonic evolution and metallogeny of the Tianshan mountains, 217 pp., Science Press, Beijing (in Chinese with English abstract).

Wei, C., J. R. Powell, and L.F. Zhang (2003), Eclogites from the south Tianshan, NW China: petrological characteristic and calculated mineral equilibria in the Na2O-CaO-FeO-MgO-Al2O3-SiO2-H2O system, *J. Metamorph. Geol., 21,* 169–179.

Wijbrans, J.R., and I. McDougall (1986), $^{40}Ar/^{39}Ar$ dating of white micas from an Alpine high-pressure metamorphic belt on Naxos (Greece): the result of resetting of the argon isotopic system, *Contrib. Min. Petrol., 93,* 187-194.

Windley, B.F., M.B. Allen, C. Zhang, Z.Y. Zhao, and G.R. Wang (1990), Paleozoic accretion and Cenozoic redeformation of the Chinese Tien Shan range, Central Asia, *Geology, 18,* 128-131.

Wu, W., C. Jiang, F. Yang, and L. Li (1992), The Yushugou-Tonghuashan structural mixtite in Xinjiang, *J. X'ian Coll. Geol., 14,* 8-13 (in Chinese with English abstract).

XBGMR (Xinjiang Bureau of Geology and Mineral Resources) (1959), *geological map 1:200 000, Kumux sheet (K-45-17)*.

XBGMR (Xinjiang Bureau of Geology and Mineral Resources) (1961), *geological map 1:20 0000, Aheqi-Kuogart sheet (K-43-29, K-43-30)*.

XBGMR (Xinjiang Bureau of Geology and Mineral Resources) (1979), *geological map 1:200 000, Zhaosu sheet (K-44-10)*.

XBGMR (Xinjiang Bureau of Geology and Mineral Resources) (1983), *geological map 1:20 0000, Heiyingshan sheet (K-44-10)*.

XBGMR (Xinjiang Bureau of Geology and Mineral Resources) (1993), *Regional geology of Xinjiang Uygur Autonomy Region*, Geological Publishing House, Beijing (in Chinese with English abstract).

Xiao, W.J., L.C. Zhang, K.Z. Qin, S. Sun, and J.L. Li (2004), Paleozoic accretionary and collisional tectonics of the eastern Tianshan (China): implications for the continental grouth of Central Asia, *Am. J. Sci., 304*, 370-395.

Xiao, X.C., Y.Q. Tang, J.Y. Li, M. Zhao, Y.M. Feng, and B.Q. Zhu (1990), Geotectonic evolution of northern Xinjiang, *Xinjiang Geol. Sci., 1,* 47-68.

Xiao, X.C., Y.Q. Tang, Y.M. Feng, B.Q. Zhu, J.Y. Li, and M. Zhao (1992), *Tectonic evolution of the northern Xinjiang and its adjacent regions*, pp. 12-47, Geology Publishing House, Beijing (in Chinese with English abstract).

Yang, Z.R., H.Z. Yin, and H.M. Gu (1986), On the basement of Junggar Basin, *Geotecton. Metallog., 10(3),* 263-271 (in Chinese with English abstract).

Yin, A., and S.Y. Nie (1996), A Phanerozoic palinspastic reconstruction of China and its neighboring regions, in *The Tectonic Evolution of Asia*, edited by A. Yin, and M. Harrison, pp. 442-485, Rubey Colloquium, Cambridge University Press, Cambridge.

Zhang, L., D.J. Ellis, and W. Jiang (2002), UHP metamorphism in western Tianshan, China, Part I: Evidences from coesite pseudomorphs in garnet and quartz exsolution in omphacite and in eclogites, *Am. Mineral.*, 87, 853–860.

Zhang, L.F., D.J. Ellis, R.J. Arculus, W. Jiang, and C. Wei (2003a), "Forbidden zone" subduction of sediments to 159 km depth: the reaction of dolomite to magnesite_aragonite in the UHPM metapelites from western Tianshan, China, *J. Metamorph. Geol., 21,* 523–529.

Zhang, L.F., D.J. Ellis, S. Williams, and W. Jiang (2003b), Ultrahigh-pressure metamorphism in eclogites from the western Tianshan, China—Reply. *Am. Mineral.*, 88, 1157–1160.

Zhang, L.C., and N.Y. Wu (1985), Tectonics and evolution of the Tianshan Mountains, *Xinjing Geology, 3(3),* 1-14 (in Chinese with English abstract).

Zhao, J.M., G.D. Liu, Z.X. Lu, X.K. Zhang, and G.Z. Zhao (2003), Lithospheric structure and dynamic processes of the Tianshan orogenic belt and the Junggar basin, *Tectonophysics, 376,* 199-239.

Zhou, D., S.A. Graham, E.Z. Chang, B.Y. Wang, and B. Hacker (2001), Paleozoic tectonic amalgamation of the Chinese Tianshan: Evidence from a transect along the Dushanzi-Kuqa highway, in *Paleozoic and Mesozoic tectonic evolution of central Asia: from continental assembly to intracontinental deformation, Geol. Soc. Am. Memoir, 194,* pp. 23-46, edited by M.S. Hendrix, and G.A. Davis, Boulder, Colorado, USA.

Zhou, D.W., L. Su, P. Jian, R.S. Wang, X.M. Liu, G.X. Lu, and J.L. Wang (2004), Zircon U-Pb SHRIMP ages of Yushugou ophiolitic terrane in Southern Tianshan and their tectonic implications, *Chin. Sci. Bull., 49(13),* 1415-1419.

Zhu, Y.F., L.F. Zhang, L.B. Gu, X. Guo, and J. Zhou (2005), The zircon SHRIMP chronology and trace element geochemistry of the Carboniferous volcanic rocks in western Tianshan Mountains, *Chin. Sci. Bull., 50(19),* 2201-2212.

Zonenshain, L.P., M.I. Kuzmin, and L.M. Natapov (1990), Geology of the USSR: A Plate Tectonic Synthesis, *AGU Geodynamics Series, 242.*

Article Soumise à ***EPSL***

Primary Carboniferous and Permian paleomagnetic results from the Yili Block (NW China) and their geodynamic implications on the evolution of Chinese Tianshan Belt

Bo Wang[a,b,*], Yan Chen[b], Sheng Zhan[b,c], Liangshu Shu[a], Michel Faure[b], Dominique Cluzel[b], Jacques Charvet[b], Sébastien Laurent-Charvet[d]

[a]*Department of Earth Sciences, Nanjing University, 210093, Nanjing, China*
[b]*Institut des Sciences de la Terre, UMR CNRS 6113, Université d'Orléans, 45067, Orléans, France*
[c]*Key Laboratory of Orogenic Belts and Crustal Evolution, Peking University, 100871, Beijing, China*
[d]*Institut Géologique Albert-de-Lapparent, 95092, Cergy-Pontoise, France*

* Corresponding author. Tel.: +86 25 8592 7531; fax: +86 25 8368 6061.
E-mail: wangbo1996@nju.org.cn or bo.wang@univ-orleans.fr (B. Wang).

Abstract

In order to better understand the tectonic role of the Yili Block on the Paleozoic evolution of the Chinese Tianshan Belt, we performed a primary paleomagnetic study on Carboniferous and Permian rocks from different areas in the Yili Block, NW of China. More than 320 sedimentary and volcanic samples were collected from 39 sites. Except for the Ordovician samples from the Axi area showing a weak and unstable magnetic remanence, the majority of this collection present characteristic remanent magnetization carried by magnetite and hematite. Though positive fold test has been observed on the part of Early Carboniferous rocks, a general remagnetisation of these rocks has been identified due to Late Carboniferous magmatism in this area. Moreover, all Early and Late Carboniferous samples of Zhaosu and Xinyuan areas located in the interior of the Yili Block yield stable and coherent magnetic directions with exhaustively reversed magnetic polarity. The Late Carboniferous is considered as the remanent age since these rocks are covered or intruded by synchronous magmatic rocks of the Yili arc, which lasted until to –310 Ma. The C_2 paleomagnetic pole is therefore calculated at 68.6°N, 290.6°E with A_{95}=6.4° and n=15. The Late Carboniferous rocks from Yuxi section located close to deformation zone present a coherent magnetic inclination but significant different declination with respect to other areas and are suspected to have probably experienced a local rotation. Although no fold test can be performed due to the monoclinal bedding, stable magnetic components are isolated from Late Permian (P_2) red beds of the Gongliu area with also a solo reversed magnetic polarity, and the P_2 paleomagnetic pole of the Yili Block has been, therefore, calculated from the characteristic remanent magnetization: 79.7°N, 172.0°E with A_{95}=11.3° and n=5. Comparison of the C_2 and P_2 paleomagnetic poles of the Yili Block with coeval poles of Junggar, Tarim and Siberia indicates (1) no significant relative motion between the Yili and Junggar blocks since the Late Carboniferous, (2) no significant or weak latitudinal relative motion occurred since the Late Carboniferous among these blocks, but (3) the 46.2°±15.1° and the 31.6°±15.1° counterclockwise rotations of the Yili-Junggar blocks with respect to Tarim and Siberia took place during C_2 to P_2. These rotations are accommodated by the Permian dextral strike-slip faults along the northern and southern sides of Tianshan Belt and sinistral

strike-slip faulting along the Erqishi Fault of Altay Belt, resulting in about 1000 km and 600 km lateral displacements in the Tianshan and Altay belts, respectively.
Keywords: Yili Block; Tianshan Belt; Paleozoic; paleomagnetism; rotation; lateral displacement.

1. Introduction

The "Yili Block" represents a triangular shape sandwiched within the Tianshan Belt and widening westwards into Kazakhstan and Kyrgyzstan (Fig. 1a modified after [1]). It is considered as a microcontinent with a Precambrian basement separating the Tianshan Belt into northern and southern branches [2-6]. The Yili Block, therefore, occupies an important position for the understanding of the tectonic evolution of the Tianshan Belt. It is widely accepted that the Tianshan Belt is a Paleozoic orogenic belt due to multiphase accretion and amalgamation of various micro-continents, and magmatic arcs [7-10]. However, there are still controversies on procedures of amalgamation and chronological constraints. Generally, the Tianshan Belt is considered to be formed by subdution-collisional orogeny [2, 4, 11-15], i.e. the Yili Block and the Central Tianshan microcontinent (Fig. 1b) were rifted from the Tarim Plate in the Cambrian, and were re-accreted to Tarim during Ordovician to Early Carboniferous due to the multiphase subduction of oceanic crust. A southward subduction of an oceanic crust beneath the Yili Block during the Late Devonian to the Late Carboniferous terminated the convergent phases of mountain building in the Tianshan Belt. Nevertheless, some authors considered the Tianshan Belt as a part of Altaid orogenic collage, which was produced mainly by strike-slip faulting [16, 17]. Recently, some researchers suggested that an oceanic crust existed in the southern Tianshan until the end of Permian on the basis of radiolarian microfossils found in South Tianshan ophiolitic mélange [18, 19]. Besides, a Late Carboniferous to Early Permian continental rifting is also proposed according to geochemical and isotopic studies on the volcanic rocks in the Tianshan Belt [20, 21]. These results suggest a divergent tectonics and a subsequent re-convergence in the Tianshan area during the Carboniferous and Permian, and therefore arise a controversy on the final evolution of the Tianshan Belt. In addition, Permian transcurrent faulting is widely observed, especially ductile strike-slip faults are geologically well documented in the whole northern Xinjiang area [6, 22-25]. Two main dextral strike-slip faults are recognised along the northern and the southern sides of the Tianshan Belt, and a sinistral strike-slip fault is distinguished in the Altay Belt. However, the southern fault of the Tianshan Belt was previously interpreted as a sinistral strike-slip fault [16, 26], which is also suggested on the basis of a significant westward deflection of magnetic declination [27, 28], but this is not consistent with the geological observation and kinematic results from Chinese Tianshan area [29, 30], where no paleomagnetic data are available up to now to constrain this event and consequent lateral displacement.

In order to test different evolutionary models for the Tianshan belt and to improve the understanding of the final orogenic procedures, this paleomagnetic study was carried out on Ordovician to Permian rocks in the Yili Block. The comparison of paleomagnetic data from this study with the previous results from Junggar, Tarim and Siberia blocks will better constrain the tectonic evolution of the Chinese Tianshan Belt during the Late Paleozoic time.

2. Geological setting and paleomagnetic sampling

The Western Chinese Tianshan Belt is divided into five subunits, namely North Tianshan domain, Bole Block, Yili Block, Central Tianshan domain and South Tianshan mélange zone (Fig. 1b). The Precambrian basement exposed in the Yili Block, Central Tianshan areas is composed of Meso- to Neoproterozoic carbonates, clastic rocks and amphibolite facies metamorphic rocks, which are quite similar to the basement of Tarim Plate [6, 14, 31, 32]. In the Yili block, Early Paleozoic rocks are of Cambrian to Ordovician carbonates and clastic rocks, and Silurian flysch (e.g. north of Yining area in Fig. 2a). The Devonian is mainly represented by granitoids. However, in Central Tianshan, Ordovician to Silurian volcano-sedimentary rocks and lava argue for an Early Paleozoic volcanic arc. Whereas, in the southern Central Tianshan, Silurian-Devonian shelf limestones are ductile deformed and tectonically overlain by an ophiolitic mélange [12, 15, 30, 31]

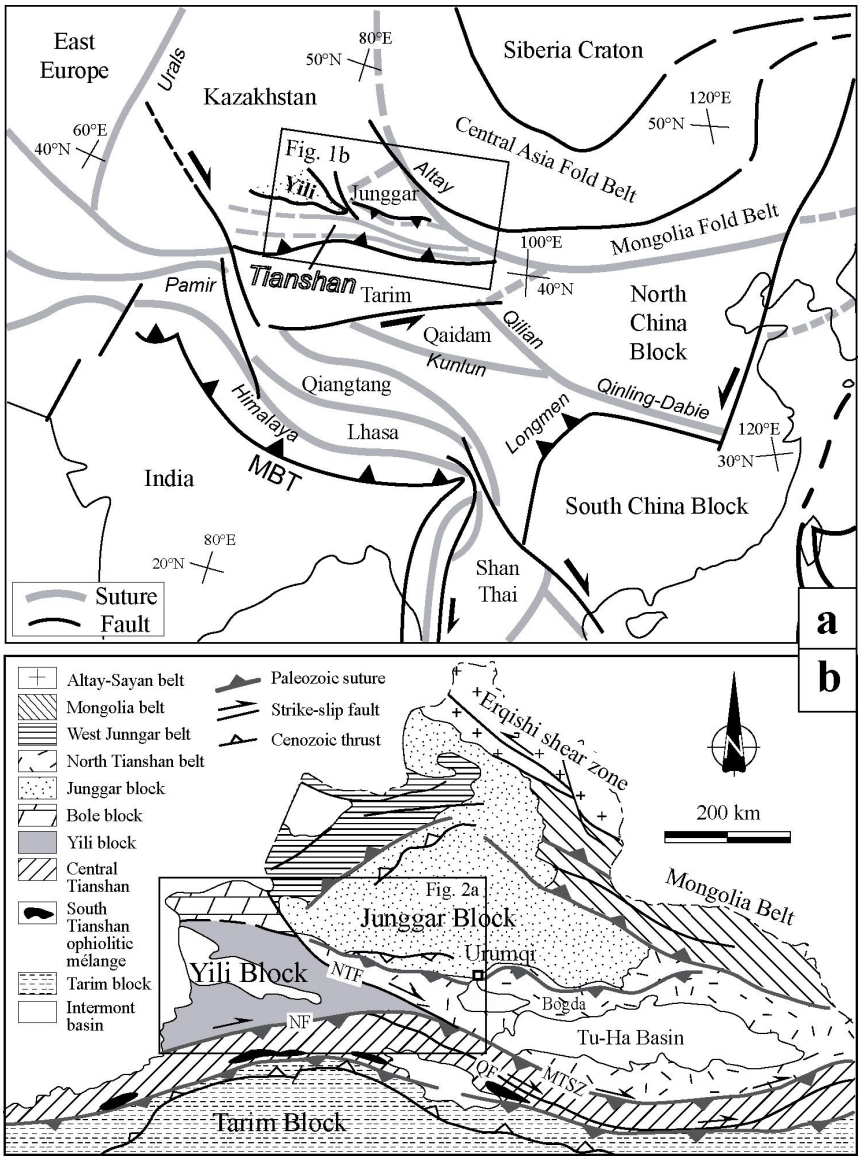

Figure 1. (a) Tectonic sketch map of Central Asia (modified after [1]) showing the main tectonic blocks including the Yili Block, (b) structural map of Chinese Tianshan Belt and its adjacent areas. Paleozoic sutures, Permian strike-slip faults and Cenozoic thrusts are shown.

Abbreviations: NTF, North Tianshan Fault; NF, Nalati Fault; MTSZ, Main Tianshan Shear Zone; QF, Qingbulake Fault.

The Carboniferous is a key period for distinguishing different tectonic units and understanding the evolution of the Western Chinese Tianshan. In this study, the Lower and Upper Carboniferous subdivision (C_1 and C_2) of the international stratigraphic chart system [33] is used rather than the Lower, Middle and Upper Carboniferous (C_1, C_2 and C_3) of the initial stratigraphic subdivisions defined by [31]. The formation and facies of Carboniferous rocks are highly variable depending on the different tectonic units and different sections. In the Yili Block, the Lower Carboniferous is, ca. 3,500 m thick, predominantly composed of limestone, sandstone and shale with subordinate volcanic rocks, and the Upper Carboniferous consists of limestone intercalated with volcanoclastic sandstone and massive volcanic rocks (Fig. 2). Both Lower and Upper Carboniferous rocks are associated with the contemporaneous granitoids. Several geochronological studies on the volcanic and granitic rocks from the Axi, Yuxi, Xinyuan and Zhaosu areas (Fig. 2a) provide Rb-Sr whole rock isochron, $^{40}Ar/^{39}Ar$ plateau and zircon U-Pb (SHRIMP and ICPMS) ages ranging from 360 Ma to 309 Ma [6, 34, 35]. Geochemical and isotopic studies suggest that the Yili Block was an active continental margin during the Late Devonian to Late Carboniferous [5, 14, 36].

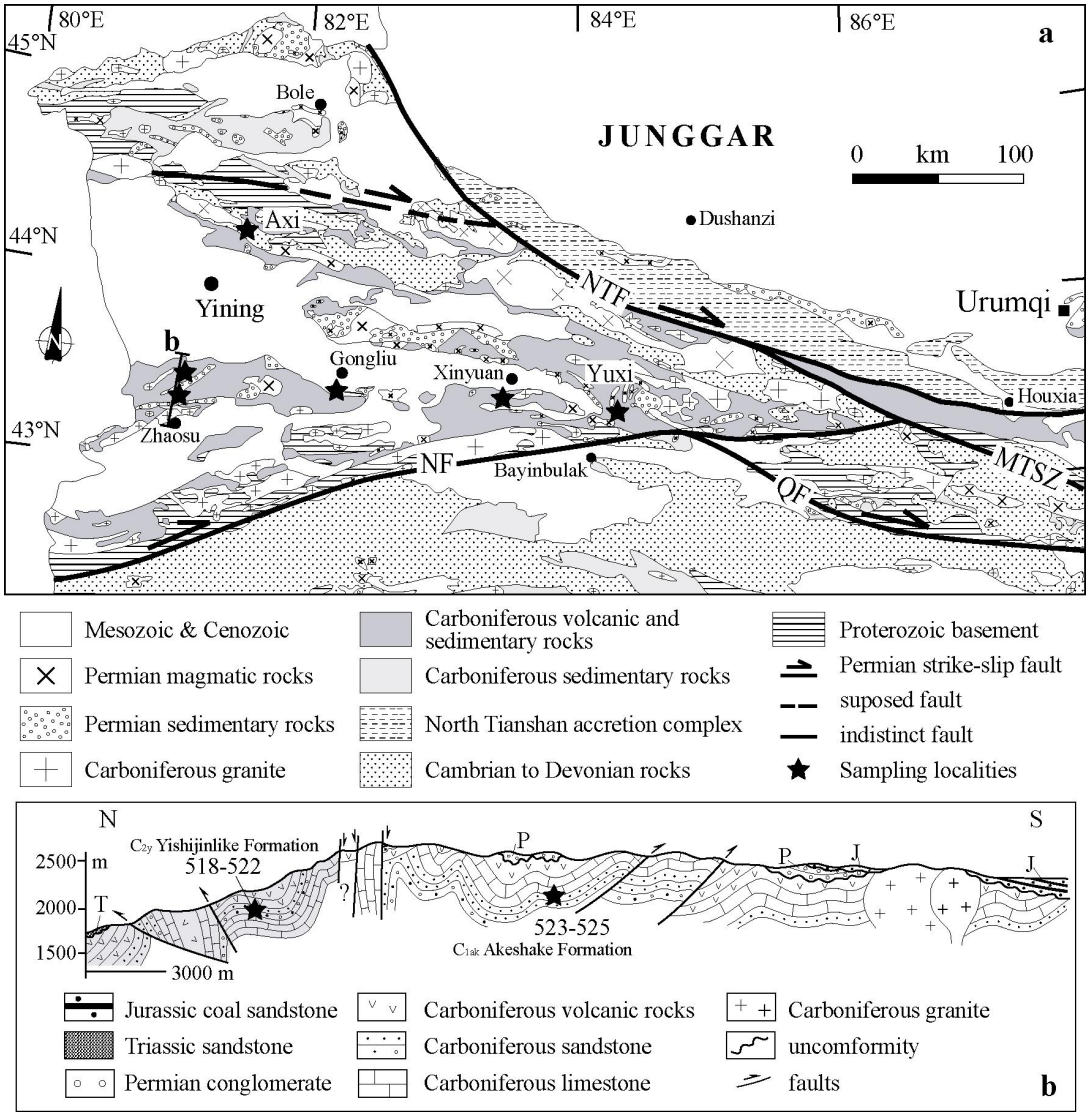

Figure 2. (a) Geological map of the Yili Block and adjacent areas indicating the sampling localities, (b) simplified cross section of Zhaosu area.

Contrarily, the Carboniferous rocks in southern Tianshan are exclusively composed of conglomerate, carbonate, sandstone and pelite [31]. Early Carboniferous strata cover unconformably pre-exiting lithotectonic units including Central Tianshan Silurian-Devonian deformed rocks, South Tianshan ophiolitic mélange, and Early Paleozoic platform sedimentary rocks of northern margin of Tarim [30]. In North Tianshan, the Carboniferous rocks are represented by Upper Carboniferous turbiditic flysch and ophiolitic mélange, forming an accretion complex due to the subduction of an oceanic basin [2, 6, 11, 13, 37].

In the whole Western Chinese Tianshan Belt, Permian terrestrial sandstone and conglomerate unconformably overlie the older rocks (Fig. 2). Lower to Upper Permian bimodal volcanic and plutonic rocks are widespread but sporadic (Fig. 2a; [22, 31, 37-40]). Lateral shear zones overprinted the Paleozoic sutures during Permian and underwent multiphase reactivation during the early Mesozoic [23-25, 28, 41]. The Tianshan Belt is reactivated again by the Cenozoic intra-continental deformation and subsequently uplifted in response to the India-Asia collision [41-46].

In the Yili Block, more than 320 cores of 39 sites are paleomagnetically sampled from 5 localities (Fig. 2a and Table 1). Ordovician sandstone and pelitic limestone are collected from Axi, north of Yining County. Early to Late Carboniferous red sandstone, volcanoclastic sandstone, basalt and andesite are collected from Zhaosu, Xinyuan and Yuxi areas. Basalt and andesite are presented as massif blocks, their beddings are estimated from the underlaying or overlaying sedimentary rocks. Late Permian red beds are collected from the Gongliu area. Detailed sampling information may be found in Table 1. Depending on strata thickness, 6 to 12 cores were drilled from each site with a portable gasoline drill. Each core was orientated by both magnetic and solar compasses, when it was possible. The average of differences between these two azimuths is about 4.0°±3.4°, and this value is used for the orientation corrections to those samples measured only by magnetic compass as well as for the trends of bedding.

3. Laboratory methods

All core samples were cut into one or two standard cylinders with 2.2cm in length and 2.5cm in diameter for laboratory measurements. Several methods were applied to magnetic mineralogical investigations: thermal magnetic (Curie point) experiment using an AGICO KLY-3S kappabridge susceptibility-meter coupled with a CS3 furnace, the acquisition of Isothermal Remanent Magnetization (IRM) using an IM30 pulse magnetizer and the measurements of Anisotropy of Magnetic Susceptibility (AMS) by KLY3 kappabridge susceptibility-meter were carried out in Laboratoire du Magnétisme des Roches d'Orléans (LMRO). Magnetic hysteretic curves were performed in Laboratoire du Paléomagnétisme of Institut de Physique du Globe de Paris (IPGP) at St Maur.

At least 6 cores were chosen from each site to carry out thermal and/or alternating magnetic field (AF) demagnetization in LMRO and IPGP, with a laboratory built furnace and LDA-3 demagnetizer, respectively. About 15 steps have been applied to progressive magnetic remanence cleaning with intervals varying from 20 to 150°C for thermal and 1 to 20 mT for AF demagnetization. The magnetic remanence of specimens with relative weak Natural Remanent Magnetization (NRM) was measured with 2G in-line three-axis AF demagnetizer (IPGP) and that of specimens with high NRM was measured with JR-5 spinner magnetometer (LMRO and IPGP).

The magnetic remanent directions were isolated by principal component analysis [47], the

mean directions are computed by Fisher [48] spherical statistics using paleomagnetic software packages offered by Cogné [49] and PMGSC (version 4.2), a PC windows based paleomagnetic data analysis program by R. Enkin (unpublished).

4. Measurement results

Parallel to magnetic mineralogical study, a plot of remanence measurement has been performed as well by thermal and AF demagnetization. The directions isolated from characteristic magnetic components (ChrM) of both techniques are consistent, however, the thermal one is more efficient due to magnetic remanent carriers (see following for the detail), so the latter has been principally used to clean the magnetic remanence.

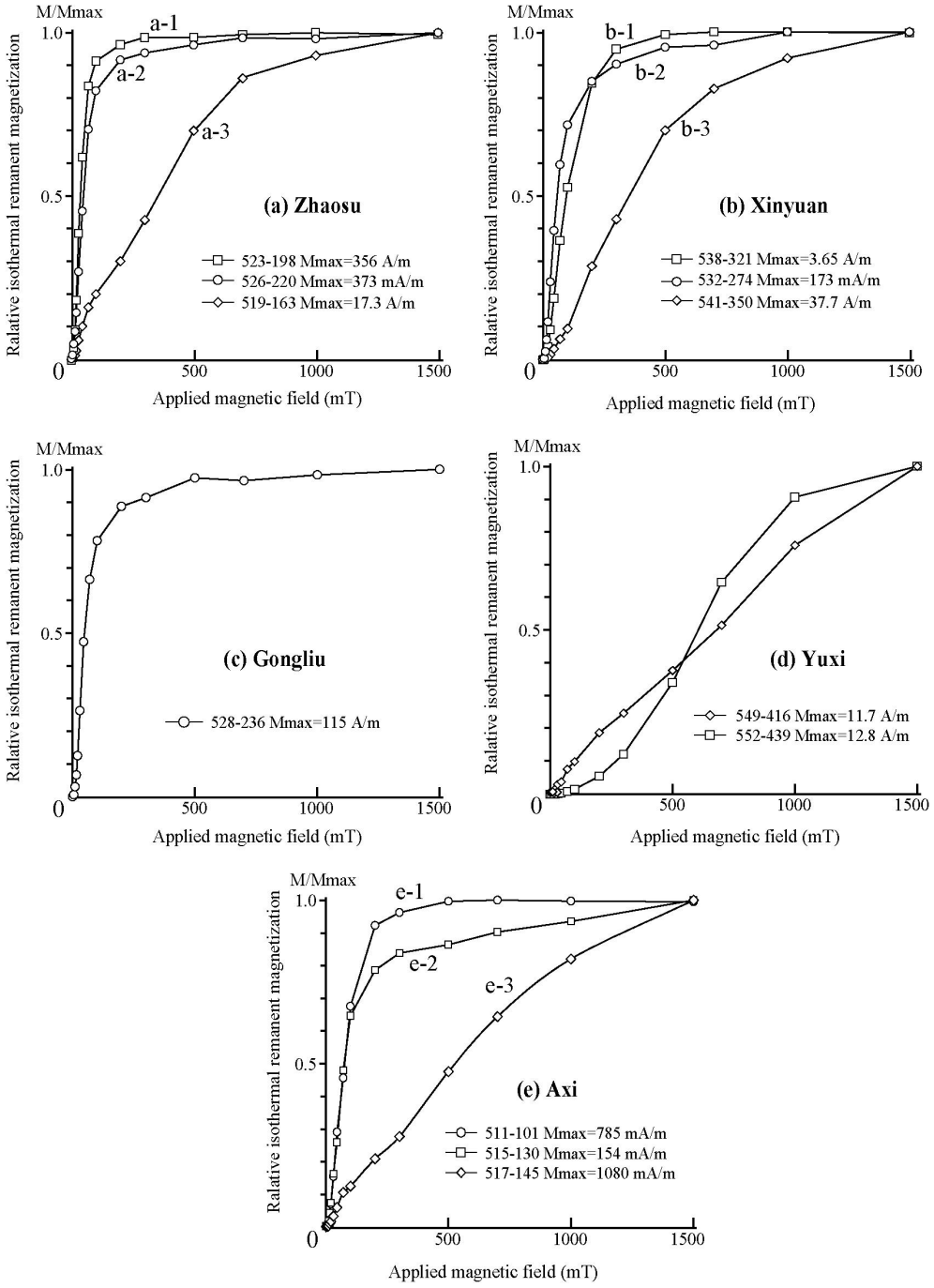

Figure 3. Isothermal magnetization results of representative cores from each sampled locality.

Table 1. Paleomagnetic sampling and measurement results from the Yili Block

Site	Coordinates	Rocks	Age	Strike/dip	n/N*	P	Dg	Ig	Ds	Is	k	α_{95}
Zhaosu area												
523	43.3°N, 81.0°E	Andesitic sandstone	$C_1ak(C_2)^{\#}$	110/12	6/8	R	185.1	-43.5	181.1	-55.0	140.7	6.5
524	43.3°N, 81.0°E	Red sandstone	$C_1ak(C_2)$	245/25	6/8	R	190.4	-63.0	174.0	-40.3	354.9	3.2
525	43.3°N, 81.0°E	Sandstone	$C_1ak(C_2)$	255/26	6/9	R	184.0	-63.7	176.1	-38.4	324.7	3.7
526	43.3°N, 81.6°E	Yellow sandstone	$C_1ak(C_2)$	230/78	7/10	R	258.6	-41.8	188.6	-29.2	220.0	4.1
Mean					4	R	207.3	-57.8			10.5	29.8
									180.2	-40.9	46.9	13.6
518	43.5°N, 81.1°E	Red sandstone	C_2y	270/18	6/8	R	153.1	-61.8	163.1	-45.3	197.6	4.8
519	43.5°N, 81.1°E	Red sandstone	C_2y	305/22	6/8	R	116.3	-57.5	149.0	-54.0	66.7	6.0
520	43.4°N, 81.1°E	Sandstone	C_2y	270/20	6/10	R	169.1	-57.2	179.0	-39.1	43.1	9.3
521	43.4°N, 81.1°E	Sandstone	C_2y	280/15	6/8	R	171.6	-57.9	176.4	-43.4	84.4	7.3
522	43.4°N, 81.1°E	Sandstone	C_2y	250/12	6/9	R	145.7	-63.5	149.7	-51.8	80.4	6.2
Mean					5	R	151.6	-61.2			48.0	11.2
									164.7	-47.4	50.7	10.9
Xinyuan area												
532	43.3°N, 83.3°E	Tuffaceous sandstone	C_1aw	287/48	9/9	-	-	-	-	-	-	-
533	43.3°N, 83.3°E	Tuffaceous sandstone	C_1aw	285/51	8/8	-	-	-	-	-	-	-
534	43.3°N, 83.3°E	Tuffaceous sandstone	C_1aw	292/52	8/9	-	-	-	-	-	-	-
535	43.3°N, 83.3°E	Tuffaceous sandstone	C_1aw	268/45	8/8	-	-	-	-	-	-	-
536	43.3°N, 83.3°E	Tuffaceous sandstone	C_1aw	272/48	9/9	-	-	-	-	-	-	-
537	43.3°N, 83.3°E	Basalt	$C_1aw(C_2)$	240/47	7/9	R	181.5	-24.0	179.9	16.9	6.1	21.2
538	43.3°N, 83.3°E	Basaltic tuff	$C_1aw(C_2)$	237/49	8/8	R	167.9	-27.4	166.6	18.9	35.9	7.7
539	43.3°N, 83.3°E	Basalt	$C_1aw(C_2)$	237/49	8/8	R	156.2	-30.5	155.4	18.0	11.2	14.3
540	43.3°N, 83.3°E	Basalt	$C_1aw(C_2)$	237/49	8/12	R	160.5	-36.6	216.7	-64.4	35.0	7.8
541	43.4°N, 83.3°E	Rhyolitic sandstone	$C_1aw(C_2)$	38/48	6/7	R	149.0	-5.2	160.8	-48.7	289.7	3.9
542	43.4°N, 83.3°E	Rhyolitic sandstone	$C_1aw(C_2)$	29/47	6/7	R	145.5	-9.5	161.5	-49.2	187.6	4.9
Mean**					6	R			165.3	-36.4	37.7	11.0
Gongliu area												
527	43.4°N, 82.5°E	Red sandstone	P_2x	93/40	6/8	R	186.5	-17.7	189.5	-59.3	11.0	14.1
528	43.4°N, 82.5°E	Red sandstone	P_2x	93/45	6/8	R	194.9	-6.2	201.6	-49.8	8.7	14.9
529	43.4°N, 82.5°E	Red sandstone	P_2x	95/48	6/7	R	187.5	-14.6	190.3	-62.5	38.7	10.9
530	43.4°N, 82.5°E	Red sandstone	P_2x	92/49	6/8	R	187.7	-25.6	200.9	-73.9	74.3	7.8
531	43.4°N, 82.5°E	Red sandstone	P_2x	100/41	6/9	R	189.4	-16.6	189.4	-57.6	123.4	5.8
Mean					5	R	189.3	-16.2			111.7	7.3
									194.1	-60.7	76.1	8.8
Yuxi area												
549	43.4°N, 84.4°E	Andesite	C_2t	54/15	6/7	R	214.4	-35.7	225.7	-39.3	380.6	3.4
550	43.4°N, 84.4°E	Andesite	C_2t	54/15	6/7	R	212.0	-35.3	223.1	-39.6	411.8	3.3
551	43.4°N, 84.4°E	Andesite	C_2t	54/15	6/7	R	213.0	-37.5	225.1	-41.4	64.7	8.4
552	43.4°N, 84.4°E	Colorful sandstone	C_2t	54/15	6/9	R	207.3	-39.1	220.0	-44.4	60.0	8.7
553	43.4°N, 84.4°E	Andesite	C_2t	54/15	6/7	R	216.9	-32.6	226.9	-35.7	179.2	5.0
554	43.4°N, 84.4°E	Andesite	C_2t	54/15	6/8	R	204.9	-38.0	217.0	-44.0	124.9	4.1
Mean					6	R	211.5	-36.4			354.3	3.6
									223.1	-40.8	350.1	3.6
Axi area												
510	44.2°N, 81.5°E	Grey pelite	O_2l	290/40	9/9	-	-	-	-	-	-	-
511	44.2°N, 81.5°E	Grey pelite	O_2l	260/77	10/10	-	-	-	-	-	-	-
512	44.2°N, 81.5°E	Grey pelite	O_2l	285/78	7/8	-	-	-	-	-	-	-
513	44.2°N, 81.5°E	Grey pelite	O_2l	80/72	7/8	-	-	-	-	-	-	-
514	44.2°N, 81.5°E	Grey pelite	O_2l	255/80	6/7	-	-	-	-	-	-	-
515	44.2°N, 81.5°E	Black limestone	O_2l	320/58	7/7	-	-	-	-	-	-	-
516	44.2°N, 81.5°E	Black limestone	O_2l	320/58	8/8	-	-	-	-	-	-	-
517	44.2°N, 81.5°E	Red pelite	O_2l	320/45	6/8	-	-	-	-	-	-	-

** n, measured sample number; N, collected sample number;*
#, Ages within the parentheses represent the age of remanence;
***, locality mean direction calculated with 4 in situ directions of sites 537-540 and 2 tilt-corrected directions of sites 541 and Abbreviations: P, polarity; R, reversed; O2l, Ordovician Lelengeledaban Formation(Fm); C1ak and C1aw are Early Carboniferous Akeshake Fm and Awulale Fm; C2y and C2t are Late Carboniferous Yishijilike Fm and Tuergong Fm; P2x, Late Permian Xiaoshansayi Fm; Dg, Ig, Ds, Is are declination (D) and inclination (I) in geographic (g) and stratigraphic (s) coordinates, k is the best estimate of the precision parameter, α95 is the radius that mean direction lies within 95% confidence.4.1. Zhaosu area*

4.1 Zhaosu section

Two Carboniferous formations are sampled: Early Carboniferous Akeshake Formation (C_{1ak}) exposed in the south and Late Carboniferous Yilishijilike Formation (C_{2y}) [50] exposed in the north of the Zhaosu area (Fig. 2b; Table 1).

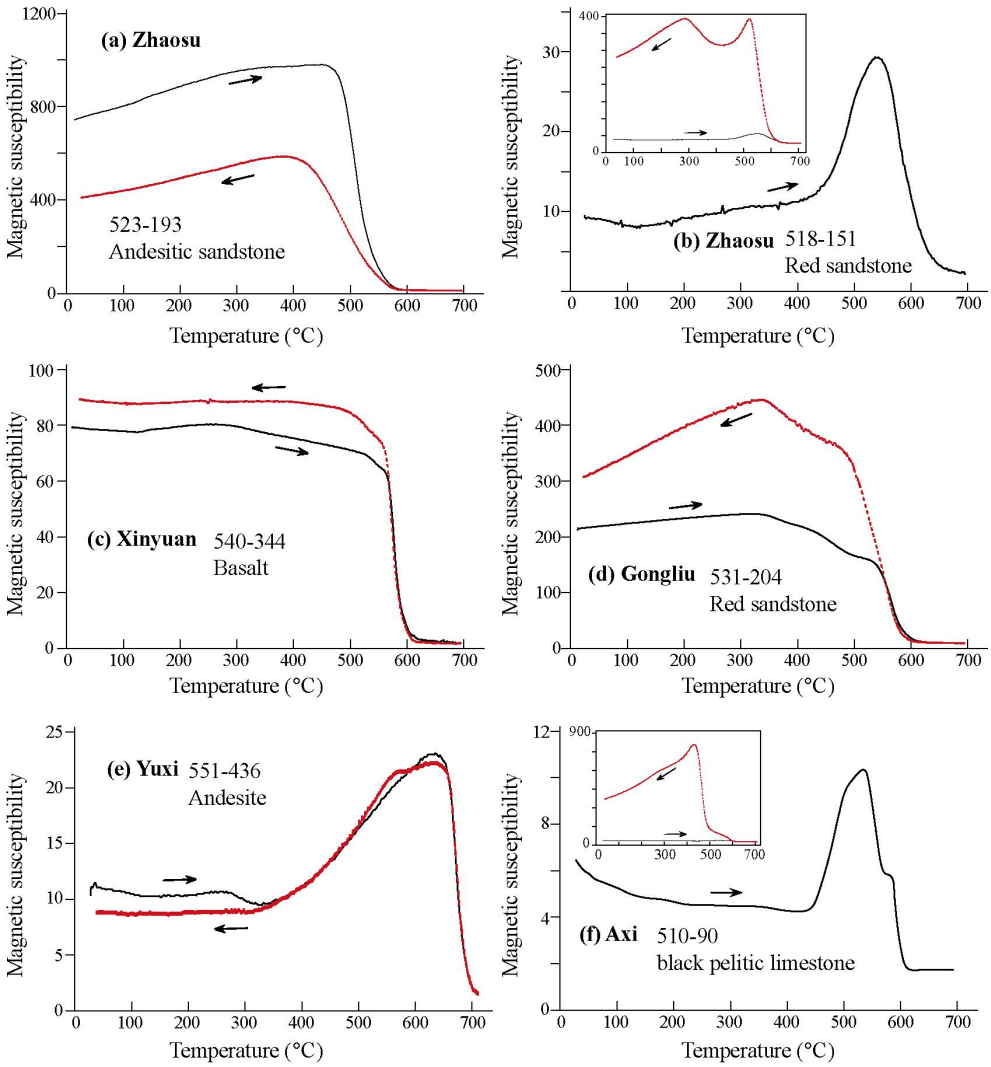

Figure 4. Results of thermomagnetic Curie temperature analyses on representative lithologies of the Yili Block.

4.1.1. C_{1ak} Akeshake Formation

Its lithology is composed of red sandstone occasionally bearing andesitic volcanic clasts, and yellow sandstone (Fig. 2b; Table 1). IRM measurement shows an abrupt increase with the total saturation at about 200 mT (Figs. 3a-1 and 3a-2), indicating predominantly low-coercivity magnetic minerals in rocks. Thermal magnetic measurements display a sharp drop of magnetic susceptibility of sandstone and andesite at around 580°C (Fig. 4a), showing the existence of titanium-poor magnetite. Two components are isolated from 22 out of 25 measured samples. The low temperature components up to about 150°C show dispersed direction carried by viscous minerals. High temperature component is usually isolated from 250-300 to 580°C in Zijderveld [51] projection (Fig. 5a), indicating that the magnetic remanence in these rocks is mainly carried by magnetite. In geographic coordinates (Fig. 5b), samples of sites 523 and 526 show a relative less steep inclination (<45°) with respect to the sites 524-525, and site 526 displays a westward deflection of declination due to the effect of asymmetric syncline. But all samples show coherent directions with reversed polarity in stratigraphic coordinates (Fig. 5c). Site-mean directions in geographic (g) and stratigraphic (s) coordinates are listed in Table 1 and

an age-mean direction is therefore calculated for this locality: Dg=207.3°, Ig =-57.8°, *k*=10.5, α_{95g}=29.8° and Ds=180.2°, Is=-40.9°, *k*=46.9, α_{95s}=13.6° with n=4 (Table 1). Enkin's [52] DC fold test gives a positive answer to this formation with the maximum k value at 74.4% ± 49.7%.

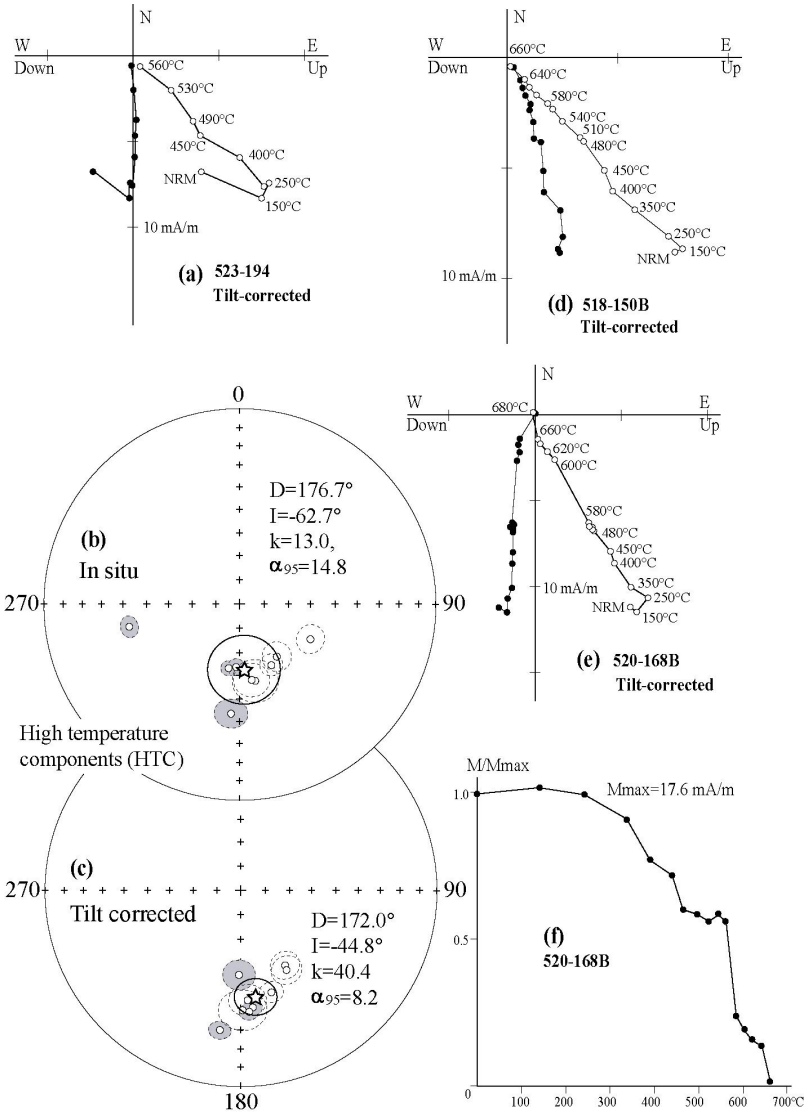

Figure 5. Measurement results from Zhaosu area. (a-c) Orthogonal projection of sample demagnetization (Zijderveld, 1967) in stratigraphic coordinates and (d) normalized intensity curves of progressive demagnetization. White (black) circles represent vertical (horizontal) plans. (e) and (f) equal-area stereoplots for site-mean directions isolated from high temperature components in geographic and stratigraphic coordinates, respectively. Grey shadowed confidential circles represent the sites of Early Carboniferous (C_{1ak}), and open confidential circles correspond to the sites of Late Carboniferous (C_{2y}). Stars represent the locality-mean directions.

4.1.2. C_{2y} Yilishijilike Formation

Five sites of red sandstones were sampled from a monoclinal section of about 200 m in stratigraphic thickness. IRM measurement of C_{2y} red sandstone (Fig. 3a-3) shows a rapid increase to about 150 mT with 20% of maximum magnetization, and a linear increase of IRM with 80% saturation at about 700 mT, then continue to increase gently without any saturation up

to about 1500 mT, suggesting the association of low and high coercive magnetic minerals in the rocks. This observation is confirmed by magnetic hysteresis measurements where "soft" and "hard" magnetic minerals are well defined (Fig. 6a). Moreover, these rocks show two blocking temperatures at around 580°C and 680°C (Figs. 5d-5f), implying the presence of both magnetite and hematite. Thermal magnetic experiment also shows an evident drop of magnetic susceptibility from 550–620°C during the heating process (Fig. 4b), however, an important increase of the magnetic susceptibility has be observed during the cooling, indicating a mineral oxidation happened during the thermal experiments (Fig. 4b). It seems that this mineral transformation doesn't influence the remanent measurements since the directions isolated from both unblocking spectra are stable and consistent with only reversed polarity (Figs. 5d and 5e). The above observations suggest that magnetite and hematite are main paleomagnetic carriers in Late Carboniferous sandstone, and both recorded the same paleomagnetic field. An age-mean direction has been calculated for this locality: Dg=151.6°, Ig=-61.2°, *k*g=48.0, α_{95g}=11.2°, and Ds=164.7°, Is=-47.4°, *k*s=50.7, α_{95s}=10.9° with n=5 (Table 1). No fold test could be concluded because of similar bedding, though the precision parameters (*k*) are improved after tilt-corrections.

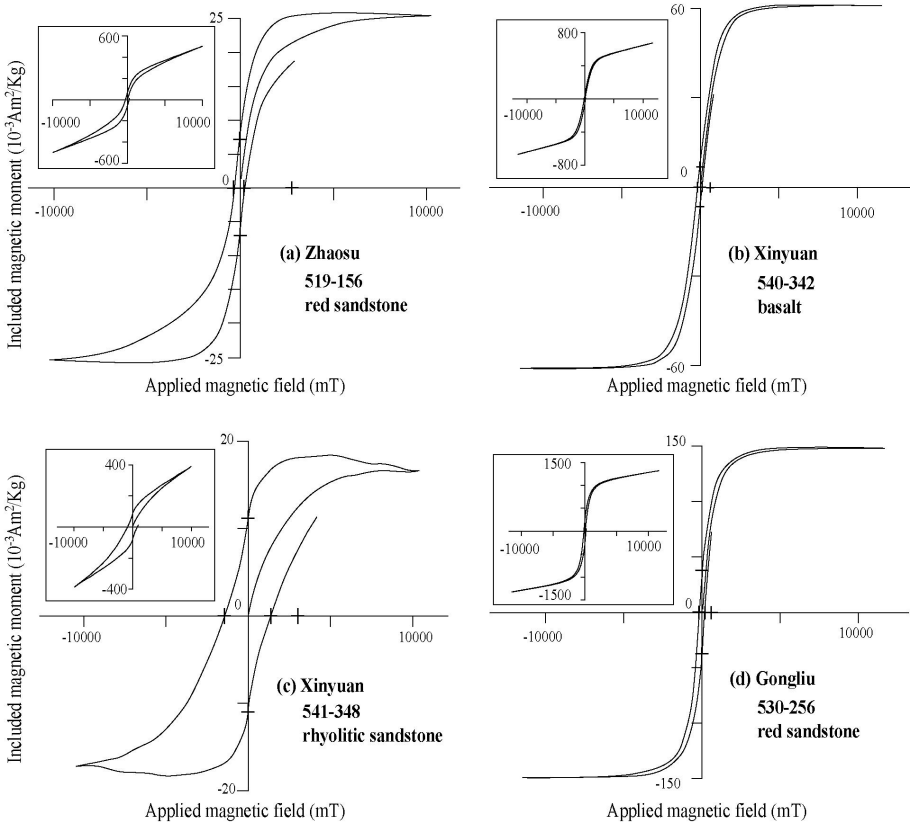

Figure 6. Representative hysteresis loops of samples from the Yili Block

4.2. Xinyuan area

Volcanoclastic sandstone and basalt of Early Carboniferous Awulale Formation (C_{1aw}) [53] were collected from 11 sites in the south of Xinyuan County (Fig. 2a). Low-coercivity magnetic minerals (predominantly titanium-poor magnetite) are identified as the principal remanent carrier for tuffaceous sandstone and basaltic rocks on the basis of (a) abrupt IRM increase with a total magnetic saturation at about 200 mT (Figs. 3b-1 and 3b-2), (b) Curie temperature point at around 580°C (Fig. 4c) and (c) narrow wasp-waisted hysteresis loops (Fig. 6b). But mixture

of low and high coercivity magnetic minerals in rhyolitic sandstone are meanwhile identified by gradually increasing IRM curve (Fig. 3b-3) and wasp-waisted hysteresis loops (Fig. 6c).

Five sites of tuffaceous sandstone (Sites 532-536, Table 1) show very week NRM (usually less than 1 mA/m). Demagnetisation on most of samples displays an important viscous component that may be cleaned up to 350°C and close to Present Earth Field (PEF; Fig. 7a). After the removal of the magnetic viscosity, most of specimens show random directions due to weak remanent intensity and few specimens show "stable" directions, which are also not far from PEF (Fig. 7b). So, no mean-site directions could be calculated.

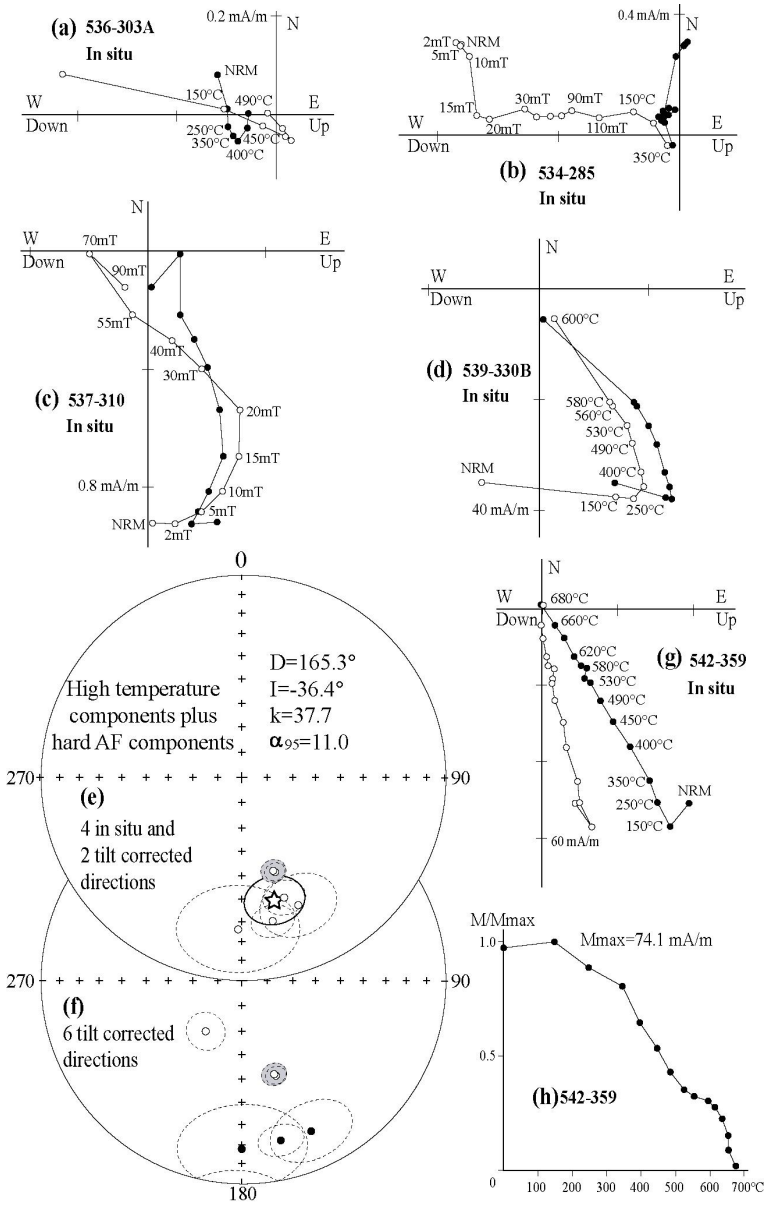

Figure 7. Measurement results from Xinyuan area. (a-d) and (g) Orthogonal projection (Zijderveld, 1967) in geographic coordinates and (h) normalized intensity curves of progressive demagnetization. White (black) circles represent vertical (horizontal) plans. (e) and (f) equal-area stereoplots for high temperature and hard AF components. Grey shadowed confidential circles represent the Sites 541 and 542, see text (4.2.2 and Discussion) for detailed explication. Stars represent the locality-mean direction. White (black) circles in (e) and (f) represent reversal (normal) polarities of site-mean direction.

Four sites of basalts (Sites 537 to 540, Table 1) show relatively stable and coherent magnetic behaviours. Magnetic remanence of these basalts is eliminated at about 90~110 mT or 580°C (Figs. 7c and 7d), both indicate that the poor-titanium magnetite is the main magnetic remanent carrier. High temperature and AF components are isolated from all measured specimens, showing more consistent paleomagnetic directions with reversed polarity in geographic coordinates than in stratigraphic ones (Table 1). The bedding of basalts seems well constrained by those of overlying sandstone and underlain limestone. Tilt corrected directions are, however, much less clustered than in situ directions with a ratio of 0.06 for ks/kg, indicating a negative fold test (Figs. 7e and 7f).

The remaining 2 sites of red rhyolitic sandstone (Sites 541 and 542) show two blocking temperatures at around 580°C and 680°C (Figs. 7g and 7h), implying the presence of the association of magnetite and hematite. A good consistency may be observed between high temperature components isolated from magnetite and hematite. No fold test may applied as their bedding is constant, however, the directions isolated from high temperature component are more coherent with those of basalt in stratigraphic coordinates than in geographic ones (Table 1), a locality-mean has been, therefore, calculated of these 2 sites in stratigraphic coordinates with 4 basalt sites in geographic ones (see Discussion for detail explication; Table 1, Fig. 7e).

4.3. Gongliu area

To the southeast of Gongliu County (Fig. 2a), an excellent exposure of Late Permian red beds E-W extending with huge thickness more than 2000 m is referred to as Xiaoshansayi Formation (P_{2x}) on the basis of plant fossils [54]. At the bottom of this formation, red conglomerate bearing pebbles of 1~100 cm in size are in unconformable contact with the underlain Early Permian alkaline volcanic rocks. Red sandstones were collected from a 300m-long section across the beddings. Titanium-poor magnetite seems to be the main remanent carrier with minor proportion of hematite according to rapid IRM saturation at about 200 mT (Fig. 3c), sharp drop of magnetic susceptibility at Curie point of about 580°C (Fig. 4d) and typical narrow wasp-waisted magnetite hysteresis (Fig. 6d). A significant oxidation can be observed during thermal magnetic experiment (Fig. 4d), however, this new formed and magnetic mineral seems to have not severely disturbed the demagnetisation (Figs. 8a-8d). The directions isolated from magnetite and hematite are well consistent (Figs. 8a, 8c and 8d). All cores display two different remanence components, where the HTC yield a site-mean direction: Dg=189.3°, Ig=-16.2°, kg=111.7, α_{95g}=7.3° and Ds=194.1°, Is=-60.7°, ks=76.1, α_{95s}=8.8° with n=5 (Table 1; Figs. 8e and 8f). The fold test is inconclusive as the variation of bedding is not important enough.

4.4. Yuxi area

Late Carboniferous Colourful sandstone developed as a 15-m-thick layer within the andesite near the Yuxi pass (Fig. 2a). Six sites of andesite and sandstone were collected from the Tuergong Formation (C_{2t} [55], Table 1). Linear or sub-linear IRM curves show characteristic high coercive minerals (Fig. 3d), thermal magnetic experiments identified hematite as the corresponding ones (Fig. 4e). Stable high temperature components isolated from magnetic demagnetisation yield a mean direction at: Dg=211.5°, Ig=-36.4°, kg=354.3, α_{95g}=3.6° and Ds=223.1°, Is=-40.8°, ks=350.1, α_{95s}=3.6° with n=6 (Table 1).

4.5. Axi area

Aiming at obtaining Pre-Carboniferous paleomagnetic data, Middle Ordovician pelitic rocks of the Lelengeledaban Formation (O_{2l}) [56] are sampled from Axi area (Fig. 2a). Magnetite and hematite are suggested to be main magnetic minerals by IRM curves with very weak remanent intensity (Fig. 3e). Thermal magnetic experiments show an obvious oxidation and an important proportion of magnetite may be formed during the heating (Fig. 4f). The NRM of pelitic rocks is very heterogeneous and varies from 0.096 to 6.98 mA/m with an average of 0.25 mA/m. No any stable component may be isolated after the removal of viscous magnetisation.

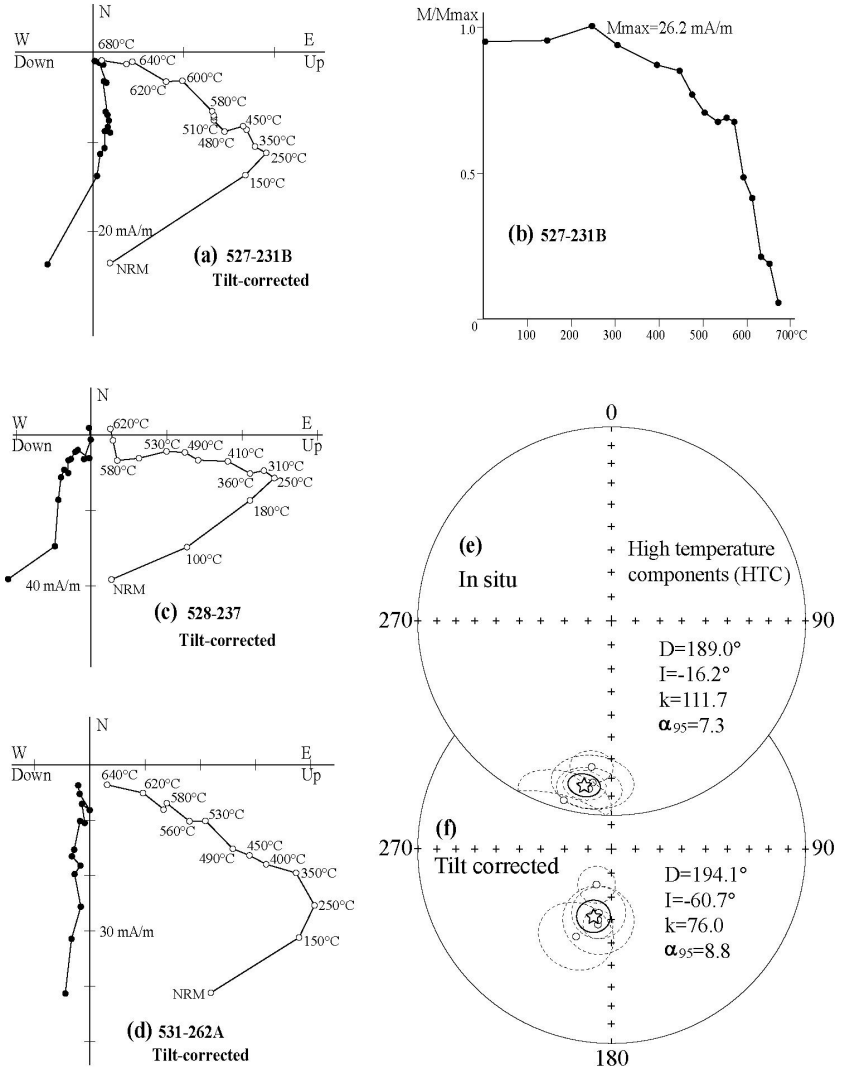

Figure 8. Measurement results from Gongliu area. (a) and (c-d) Orthogonal projection (Zijderveld, 1967) in stratigraphic coordinates and (b) normalized intensity curves of progressive demagnetization. White (black) circles represent vertical (horizontal) plans. (e) and (f) equal-area stereoplot for high temperature components in geographic and stratigraphic coordinates, respectively. Stars represent the locality mean of directions.

5. Discussion

Except for the samples from the Axi section that yield no reliable magnetic component, laboratory magnetic mineralogical analyses and thermal/AF demagnetisations have successfully isolated two magnetic components, namely viscous and characteristic remanent

magnetisations from 4 out of 5 Late Paleozoic sections. The former one clearly shows a record of the recent geomagnetic field with a negative fold test (Dg=348.4°, Ig=67.1°, *k*g=15.9, α_{95g}=3.1° and Ds=350.2°, Is=52.9°, *k*s=3.3, α_{95s}=7.9° with n=185). However, the stable titanium-poor magnetite and hematite have been identified as principal magnetic remanent carriers for the latter one. The following evidences may reinforce to argue that the ChrM may be used to tectonic implications: (1) the positive fold test has been observed from Zhaosu area; (2) the solo reversed polarity with significantly distinguishable mean directions from PEF and other Mesozoic and Cenozoic one. However, as mentioned above, this area has experienced multiphase tectonic and magmatic events. Before putting forward their tectonic implications of these new paleomagnetic data, their reliability and remanent age should be discussed.

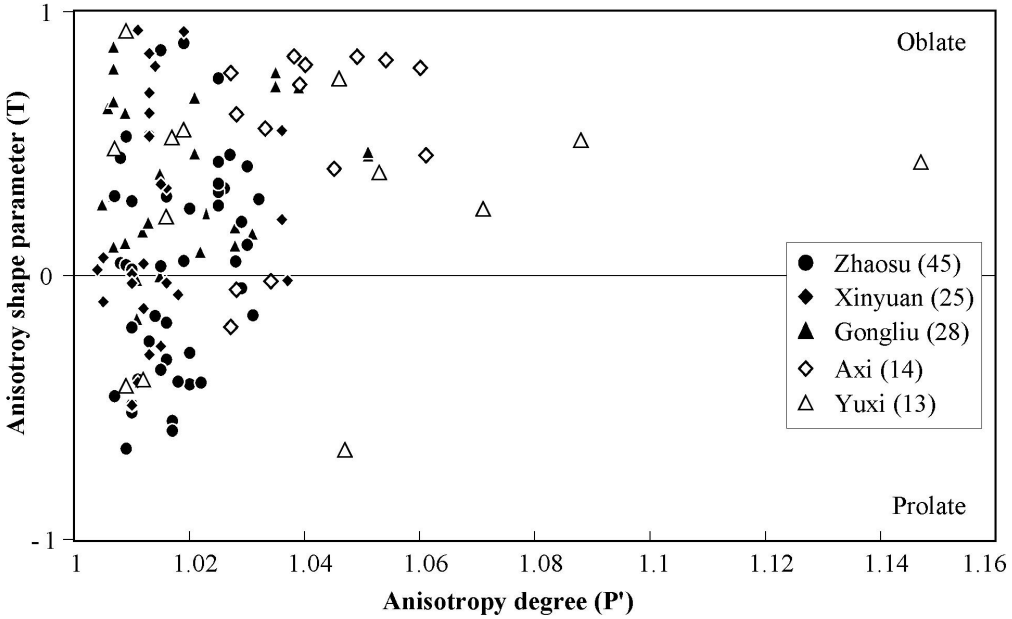

Figure 9. Plots of anisotropy degree (P') versus anisotropy shape (T) of magnetic susceptibility for volcanic and sedimentary rocks in the Yili Block and its adjacent areas. P' = exp{2[(lnK1-lnKm)^2+(lnK2-lnKm)^2+(lnK3-lnKm)^2]$^{1/2}$}, and T=2ln(K2/K3)/ln(K1/K3)-1, where K1, K2 and K3 are principal axes of the magnetic fabrics and Km is their average.

5.1. Reliability and remanent age of paleomagnetic data

It is well documented that the Tianshan belt has experienced multiphase tectonic events since the Late Paleozoic. In order to make acknowledge on the degree of deformation for our paleomagnetic collection, Anisotropy of Magnetic Susceptibility (AMS) measurements were performed. Figure 9 reveals a relatively weak anisotropy degree with P'< 1.05 for most samples though some from Yuxi and Axi seem to have higher and heterogeneous P' values. This observation may indicate that the sampling zones have not posterily suffered severe deformation at least at sample-seized scale.

Table 1 shows rock ages of our collection ranging from Early Carboniferous to Late Permian. The exclusive reversal polarity revealed from ChrM seems coherent with the Permo-Carboniferous Reversed Superchron (PCRS), e.g. by [57]. However, as described in Geological Setting, some volcanic rocks cover on Lower Carboniferous sediments, the folding sometimes is younger that these volcanic events, and younger magmatic plutons are often found near sampling sites, so we can't simply say the remanence isolated from ChrM is primary

or calculate age-mean directions and corresponding paleomagnetic poles.

For the Late Permian rocks of Gongliu area, their age is well constrained by abundant plant fossils and unconformity of underlain Early Permian volcanic rocks. Though the statistic precision parameter (*k*) slightly decreases, the fold test is not conclusive due to weak bedding variation. Thus, the solo reversed polarity from about 300m-thick section may indicate that the magnetic remanence has been acquired before –250 Ma (the upper limit of PCRS), i.e. similar to the Late Permian rock age. So, a paleomagnetic pole has been calculated for P_2 period: λ=79.7°N, ϕ=172.0°E, A_{95}=11.3° with n=5 (Table 2).

Four sites from Early Carboniferous Akeshake formation (C_{1ak}) show also only reversed polarity with a positive fold test. If the paleomagnetic collection is representative for this geologic period, the normal polarity should be identified by demagnetisation as the C_1 and C_2 limit is close to the lower limit of PCRS (~325 Ma). Geologically, Early Permian intra-continental volcaniclastic rocks [22, 31, 40] overlay unconformably on the folded Late Carboniferous volcano-sedimentary rocks in the Yili Block [31], indicating that folding occurred before Early Permian magmatism. Moreover, the site-mean directions of the Early Carboniferous are very close to those of the Late Carboniferous, and both of them are obviously different from the direction of Late Permian red-beds (Table 1). This unconformity and positive fold test exclude the possibility of Early Permian overprint. Additionally, since both C_1 and C_2 sandstones are covered by homochronous volcanic rocks and intruded by granites, which are dated by zircon U-Pb from 361±6 Ma to 309±3Ma [6, 35], suggesting that the thermal event corresponding to the Yili magmatic arc lasted until the end of Late Carboniferous. This prominent thermal event may make pre-existed rocks to be remagnetised. It is, therefore, reasonable to suggest that both Early and Late Carboniferous rocks of Zhaosu area recorded an identical paleomagnetic direction during Late Carboniferous magmatism in the Yili Block. An overall mean direction is, thus, calculated for both Early and Late Carboniferous sites: Dg=176.7°, Ig=-62.7°, kg=13.0, α_{95g}=14.7° and Ds=172.0°, Is=-44.8°, ks=40.4, α_{95s}=8.2° (Table 1; Figs. 5b-5c).

Similar situation occurs for Early Carboniferous rocks from Xinyuan area. All reliable directions of basalts from Sites 537-540 show a reversed polarity in geographic coordinate but with a negative fold test (Table 1; Figs. 7e and 7f), indicating latter overprint instead of primary magnetization for these Early Carboniferous samples. Due to the high occurrence of volcanic rocks dated at 313±4 Ma [35]and granite at 315±3 and 309±3 Ma in the sampling area [6] (Fig. 2a), it is reasonable to propose a Late Carboniferous (~310 Ma) age for the thermally remagnetization. Concerning the two rhyolitic sandstones sites (Sites 541-542), although the reversal polarity is identified in both coordinates, their directions in stratigraphic coordinates with respect to those in geographic ones seem more consistent with either the in-situ directions of 4 volcanic sites or the locality-mean direction of Zhaosu area. The age of the rhyolitic sandstone is, in fact, questionable. No any direct age constraint has been obtained or documented from this formation although referred to as Early Carboniferous [31, 53]. In the point of view of regional tectonics and stratigraphic correlation [31, 53], it is clear that the emplacement of the rhyolite is younger than the basalt dated at 354±5 Ma (zircon U-Pb SHRIMP by Zhu et al. [35]). Moreover, no any direct contact between these two lithostratigraphic units can be observed in the field, geological and stratigraphic knowledge allow to exclude a syncline and to suggest an unconformity contact. According to the above

arguments, it is not unreasonable to consider that the rhyolitic sandstone is of late of Early Carboniferous or Late Carboniferous. Thus, 4 in-situ paleomagnetic directions of basalts and 2 tilt-corrected directions of rhyolitic sandstones are used to calculate an average direction at: D=165.3°, I=-36.4°, k=37.7, α_{95}=11.0°for the Late Carboniferous magnetisation from Xinyuan area (Table 1; Fig. 7e).

As to paleomagnetic results from Yuxi area, 6 Late Carboniferous sites present well grouped reversal directions without fold test due to monoclinal bedding (Table 1). The magnetic inclinations from this locality are consistent with those from Zhaosu and Xinyuan areas, but this area shows a significant different declination with respect to other two. As this sampling locality is situated in an active tectonic zone (Fig. 2a), the difference in declination may be explained by a local rotation of the Yuxi sampling zone with respect to the Yili Block.

According to above direction analyses and geologic arguments, a C_2 paleomagnetic pole may be calculated for the Yili Block from Zhaosu and Xinyuan areas: λ=68.6°N, ϕ=290.6°E, A_{95}=6.1° with n=15 (Table 2).

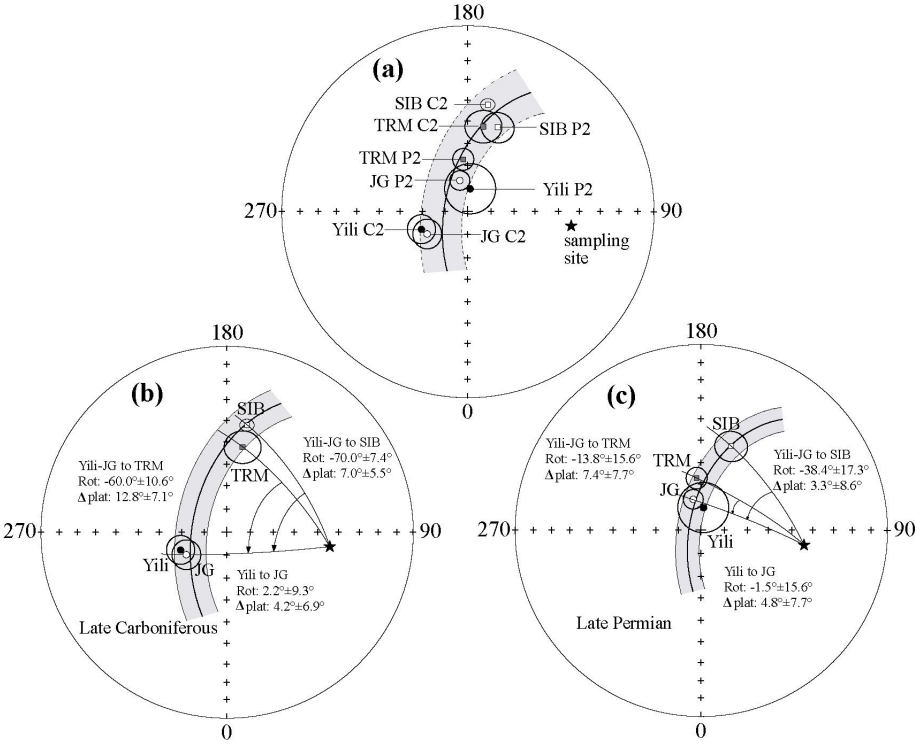

Figure 10. (a) Equal-area projections of Late Carboniferous and Late Permian poles of Yili Block, Tarim (TRM), Junggar (JG) and Siberia (SIB), showing that little or no relative latitudinal movement among these blocks, (b) small circle passing through Late Carboniferous poles and grand circles from sampling site to each pole showing significant longitudinal differences between different blocks, (c) no significant longitudinal differences between Yili, Junggar and Tarim shown by small circles passing through Late Permian pole, but a significant longitudinal difference exited between Siberia and the other blocks at Late Permian time. Rot and Δplat stand for relative rotation and convergence with corresponding uncertainties. The positive mean value stands for clockwise rotation and latitudinal shortening, respectively.

5.2. Comparisons of paleomagnetic data from Yili and other adjacent blocks

Up to now, no paleomagnetic data were documented from the Yili Block, except some data obtained from the western Tianshan of Kyrgyzstan [27, 28, 58]. Most of these data were derived from the deformation belt, e.g. "North Tianshan tectonic zone" located in the extremely northwestern part of the Tianshan Belt (Fig. 1a). These studied areas can't be considered as a part of a rigid block, some deflections of declination with respect to the reference blocks (e.g. Tarim and Siberia) may be, therefore, interpreted as the result of strike-slip faulting within the orogenic belt, rather than the representative rotation of a rigid body [28]. In fact, the Yili Block is accepted as a microcontinent with the Precambrian basement [2-6, 14], it extends westwards into Kazakhstan with an unclear boundary, and its eastern boundaries are the southern and northern branches of the Tianshan range (Fig. 1). These boundaries were highly deformed during the Tianshan orogeny, but the interior of the block is much less deformed. This may be recognized by the good consistency between the C_2 paleomagnetic results from Zhaosu and Xinyuan areas located near to the center of the Yili Block with about 200 km apart (Figs. 2a, 5f and 7e). Thus, the paleomagnetic poles derived from these areas are representative for the whole Yili block (Table 2).

In order to understand the kinematic relationships during the Late Paleozoic between the Yili Block and adjacent blocks, previous paleomagnetic results on the Tarim, Junggar and Siberia blocks are analysed and listed in Table 2. Late Carboniferous and Late Permian poles of Tarim Block have been well documented by numerous studies [59-68], these data are very consistent with each other within the relatively weak uncertainty (Table 2), the Late Carboniferous and Late Permian mean poles are recalculated at 51.5°N, 169.1°E, A_{95}=7.7° and 66.8°N, 184.1°E, A_{95}=4.9, respectively. Van der Voo [69] presented Late Carboniferous and Late Permian paleomagnetic poles of Siberia Block (Table 2). As for the Junggar Block, few results have been reported from the Urumqi area and northwestern region of the Junggar Basin (Fig. 1b; [70-73]), but the available data are quite dispersed, and the ages of magnetization are often undetermined (Table 2). For example, the paleomagnetic results from the south and northwest of the Junggar basin by Li et al. [71] are not consistent, an important second overprinting is proposed, the ages of primary or secondary magnetization are roughly restricted between Late Carboniferous and Permian, i.e. a long and variable interval from 20 to 75 Ma. Such uncertainty in age and variability in paleomagnetic pole make them unfeasible to compare with those from other blocks. Only one relatively reliable paleomagnetic pole derived from the northwest of the Junggar basin [71] may be taken for the Late Carboniferous period (Table 2). Concerning the Late Permian period, two paleomagnetic poles have been obtained from Urumqi [72] and Tianchi areas [73] (Table 2). However, the former study shows that only 26 (4 sites) out of 78 samples from Urumqi display directly observable directions, and the other samples are analysed by the grand circle technique with an important uncertainty. In addition, magnetic remanence of these Late Permian sediments is viscous, magnetic directions are relatively dispersed within and among sites, the paleomagnetic pole is calculated with single samples instead of by site-mean directions. Paleomagnetic directions derived from Tianchi section seem to be relatively stable, and passed a positive fold test, therefore, these latter results are accepted for the Late Permian paleomagnetic pole of the Junggar block (Table 2).

Figure 10a shows paleomagnetic poles of each block for each geologic epoch. Late Carboniferous pole of the Yili Block is very close to that of Junggar with an angular difference of 7.7°±6.6°, but far away from coeval poles of Tarim (120.5°±7.0°) and Siberia (119.0°±5.1°;

Fig. 10b). Small circles centred at the sampling site show no significant latitudinal differences of 4.2°±6.9° between Yili and Junggar, and relatively weak latitudinal differences of 12.8°±7.1° between Yili and Tarim, and of 7.0°±5.5° between Yili and Siberia (Fig. 10b). The case will be changed when looking at relative rotations. The Yili Block has no significantly rotation of 2.2°±9.3° with respect to Junggar, but significantly counterclockwise (CCW) rotations of 60.0°±10.6° and 70.0°±7.4° with respect to Tarim and Siberia, respectively (Fig. 10b). Late Permian poles of Yili Block, Junggar and Tarim become almost consistent within uncertainty (<12.1°±9.9°), but they are significantly different from the pole of Siberia (>24.1°±6.8°; Fig. 10c). All latitudinal differences of the Yili Block become no significant of 4.8°±7.7°, 7.4°±7.7° and 3.3°±8.6° with respect to Junggar, Tarim and Siberia, respectively (Fig. 10c). The counterclockwise rotation of Yili keeps the same of 1.5°±15.6° with Junggar, becomes no significant of 13.8°±15.6° with Tarim and remains still important of 38.4°±17.3° with Siberia (Fig. 10c).

Table 2. Synthesis of Late Carboniferous and Late Permian paleomagnetic poles from the Yili, Junggar, Tarim and Siberia blocks

Areas	Site	n/N	Polarity	Ages	Dg	Ig	Ds	Is	k	α95
Zhaosu	523	6/6	R	C2(C1)[#]	185.1	-43.5	181.1	-55.0	140.7	6.5
	524	6/6	R	C2(C1)	190.4	-63.0	174.0	-40.3	354.9	3.2
	525	6/6	R	C2(C1)	184.0	-63.7	176.1	-38.4	324.7	3.7
	526	6/6	R	C2(C1)	258.6	-41.8	188.6	-29.2	220.0	4.1
	Mean	4	R	C2(C1)	207.3	-57.8			10.5	29.8
							180.2	-40.9	46.9	13.6
	518	6/6	R	C2	153.1	-61.8	163.1	-45.3	197.6	4.8
	519	6/6	R	C2	116.3	-57.5	149.0	-54.0	66.7	6.0
	520	6/6	R	C2	169.1	-57.2	179.0	-39.1	43.1	9.3
	521	6/6	R	C2	171.6	-57.9	176.4	-43.4	84.4	7.3
	522	6/6	R	C2	145.7	-63.5	149.7	-51.8	80.4	6.2
	Mean	5	R	C2	151.6	-61.2			48.0	11.2
							164.7	-47.4	50.7	10.9
	Mean	9	R		176.7	-62.7			13.0	14.7
							172.0	-44.8	40.4	8.2
Xinyuan	537	7/8	R	C2(C1)	181.5	-24.0	179.9	16.9	6.1	21.2
	538	8/8	R	C2(C1)	167.9	-27.4	166.6	18.9	35.9	7.7
	539	8/8	R	C2(C1)	156.2	-30.5	155.4	18.0	11.2	14.3
	540	8/8	R	C2(C1)	160.5	-36.6	216.7	-64.4	35.0	7.8
	541	8/8	R	C2(C1)	149.0	-5.2	160.8	-48.7	289.7	3.9
	542	8/8	R	C2(C1)	145.5	-9.5	161.5	-49.2	187.6	4.9
	Mean*	6	R	C2(C1)			165.3	-36.4	37.7	11.0
	Mean**	15	R	C2			169.1	-41.5	36.6	6.4
Yuxi	549	6/6	R	C2	214.4	-35.7	225.7	-39.3	380.6	3.4
	550	6/6	R	C2	212.0	-35.3	223.1	-39.6	411.8	3.3
	551	6/6	R	C2	213.0	-37.5	225.1	-41.4	64.7	8.4
	552	6/6	R	C2	207.3	-39.1	220.0	-44.4	60.0	8.7
	553	6/6	R	C2	216.9	-32.6	226.9	-35.7	179.2	5.0
	554	6/6	R	C2	204.9	-38.0	217.0	-44.0	124.9	4.1
	Mean	6			211.5	-36.4			354.3	3.6
							223.1	-40.8	350.1	3.6
Gongliu	527	6/6	R	P2	186.5	-17.7	189.5	-59.3	11.0	14.1
	528	6/6	R	P2	194.9	-6.2	201.6	-49.8	8.7	14.9
	529	6/6	R	P2	187.5	-14.6	190.3	-62.5	38.7	10.9
	530	6/6	R	P2	187.7	-25.6	200.9	-73.9	74.3	7.8
	531	6/6	R	P2	189.4	-16.6	189.4	-57.6	123.4	5.8
	Mean	5	R	P2	189.3	-16.2			111.7	7.3
							194.1	-60.7	76.1	8.8

[#], Ages within the parentheses represent the age of rocks;
*, site mean direction calculated with 4 in situ directions of basalts (sites 537-540) and 2 tilt-corrected
**, locality mean direction from Zhaosu and Xinyuan Late Carboniferous directions.

5.3. Tectonic implications

According to the above paleomagnetic data analyses, relatively slight latitudinal differences (if any) of Yili with respect to Junggar, Tarim and Siberia have been obtained which are often less than uncertainty, indicating that no important relative latitudinal movement between the Yili Block and the other blocks took place since the Late Carboniferous. This observation is quite consistent with geological evidences, from which, the principal orogeny of the Tianshan Belt due to the convergences among Junggar, Yili and Tarim is considered to have been completed at the end of the Late Carboniferous [2, 6, 11, 14]. The remaining small convergent latitudinal differences of the Yili Block relative to the other blocks since Late Permian should correspond to the Cenozoic intra-continental subduction of Tarim and Junggar beneath the Tianshan Belt, and consequent N-S crustal shortening [40, 42-46, 74].

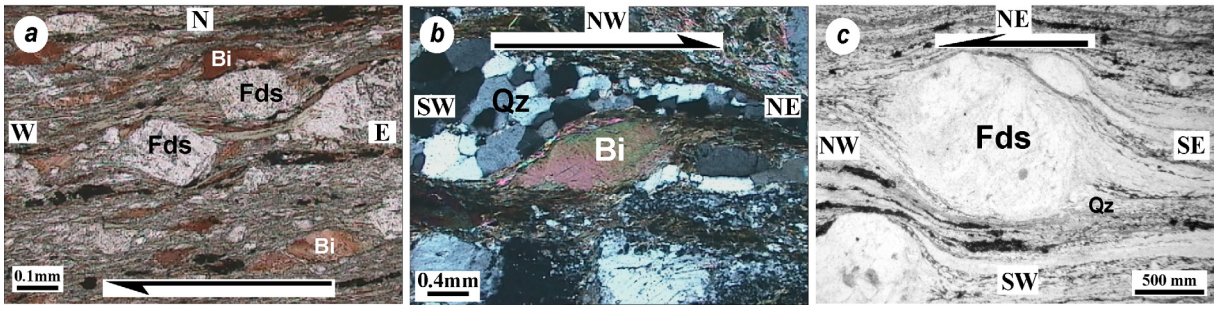

Figure 11. Microscopic kinematic indicators from ductile strike-slip shear zones, (a) feldspar clasts with biotite pressure shadow showing dextral signature of the North Tianshan shear zone; (b) mica-fish and oblique quartz sub-grain textures indicating dextral shearing along the Nalati Fault; (c) sigmoidal feldspar clast with pressure shadows of quartz and biotite showing sinistral movement of the Erqishi shear zone in the Altay Belt.

The good consistency between the poles from Yili and Junggar may indicate that these two blocks were welded since the Late Carboniferous and they might be paleomagnetically considered as a single block since that time. In another word, if there is any relative motion between them, it should be under the paleomagnetic uncertainty. As described above, the significant polar differences of the Yili Block with respect to Tarim and Siberia essentially reveal the CCW rotations of Yili-Junggar related to Tarim and Siberia. These CCW rotations are estimated of 60.0°±10.6° and 70.0°±7.4° since the C2 period, and of 13.8°±15.6° and 38.4°±17.3° since the P2 period (Fig. 10). These observations allow us to estimate the relative rotation from Late Carboniferous to Late Permian by subtracting the relative motion since P2 from that since C2. Consequently, during the C2-P2 interval, the CCW rotation of the Yili-Junggar Block attained about 46.2°±15.1° with respect to Tarim, and 31.6°±15.1° to Siberia. Since Late Permian, this CCW rotation of Yili-Junggar with respect to Tarim becomes not significant within uncertainty (13.8°±15.6°), but remains still significant of 38.4°±17.3° with respect to Siberia. Since all four blocks were amalgamated at the end of Late Carboniferous, the relative rotations between blocks were accommodated by strike-slip faulting along their boundaries and therefore resulted in lateral displacements. The northern and southern boundaries of the Yili Block correspond to two ductile shear zones (Fig. 1b). To the north, the North Tianshan Fault (NTF) [6, 17, 37, 75] extends eastward merging in the Main Tianshan Shear Zone (MTSZ) [23-25]. The kinematics of the ductile shearing along the MTSZ

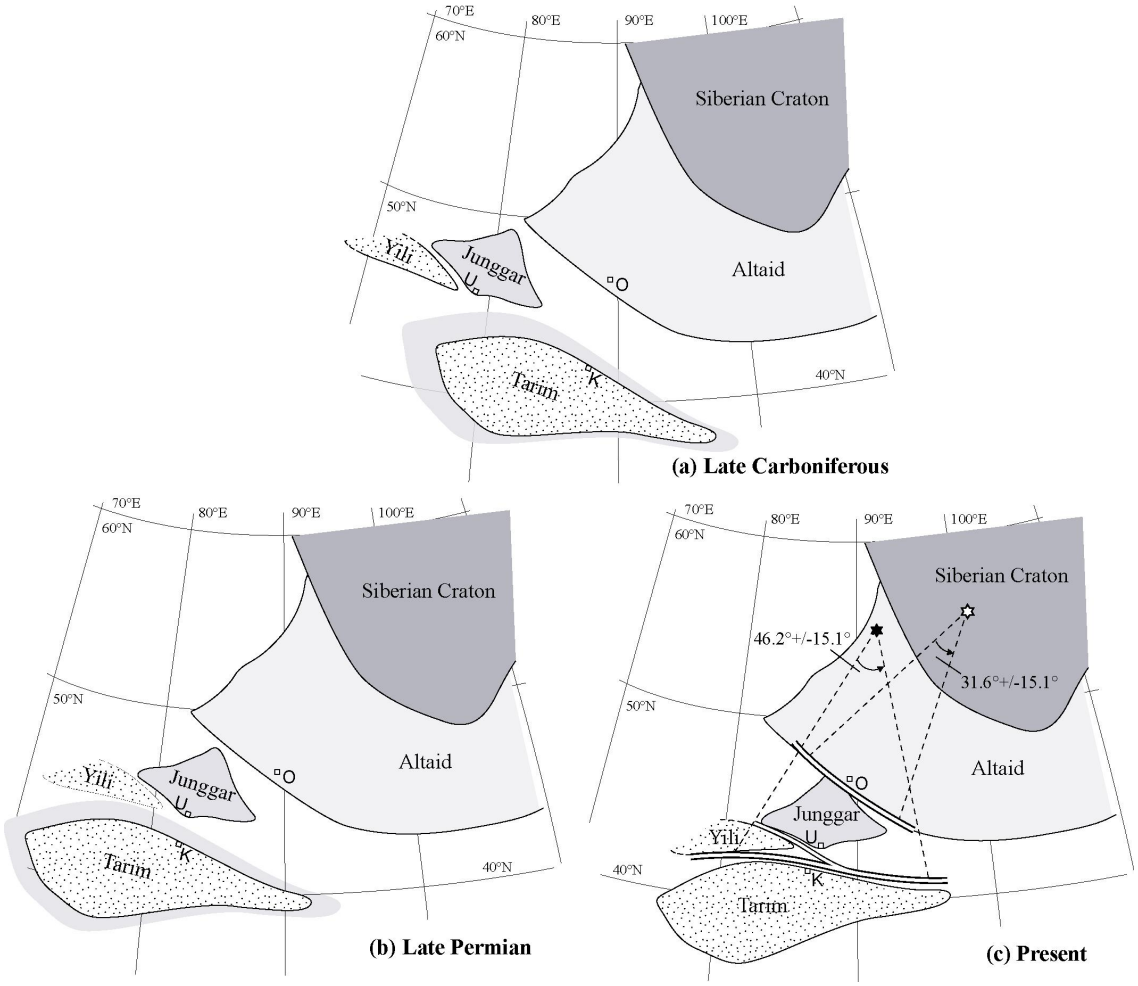

Figure 12. Simplified reconstruction maps showing the relative rotations of major blocks and consequent lateral displacements along their boundaries by fixing Siberia at its present position. Late Carboniferous (a), Late Permain (b) and Present (c) states are compared. Shadowed zones around the Tarim indicate the subducted margins of Tarim during Cenozoic intra-continental deformation. K, U and O stand for Korla, Urumqi and Ölgij (Mongolian).

and NTF is dextral [6, 24, 25] (Figs. 1b, 2a and 11a). To the south, the Nalati Fault (NF) [75] and Qingbulak Fault [2, 11, 15] (QF) extend sub-parallelly to the NTF and MTSZ. The Nalati Fault, also regarded as the Nikolaev Tectonic Line [26, 76], is the most significant structure. Previous studies proposed a left- lateral slip [14, 16, 22, 28], but field structural analyses based on kinematic indicators suggest a right-lateral strike-slip faulting [29, 30] (Fig. 11b). In order to account for the paleomagnetic and structural data, simplified paleogeographic reconstructions of these rotation patterns are proposed in Figure 12a, 12b and 12c at C2, P2 and Present periods, respectively. The quantitative estimation of the lateral displacements corresponding to the CCW rotation of Yili-Junggar with respect to Tarim, requires the definition of an Euler pole of relative motion, around which, one crustal block rotates with respect to another along a major fault. In the Tianshan Range, two strike-slip shear zones form an arcuate belt separating Junggar to the north from Tarim to the south (Fig. 12c). The best fitting small circle passing through this belt allows us to estimate the Euler pole position at about 55°N, 92°E with a radius of about 13° (distance between the pole and the belt; Fig. 12c). The 46.2°±15.1° CCW rotation

of Junggar-Yili with respect to Tarim, therefore, corresponds to a right-lateral displacement of 1160±380 km along these strike-slip faults (Figs. 12a and 12b). This sum of motion may be explained by two opposite displacements of Yili-Junggar and Tarim along the Tianshan shearing zones from C2 to P2. During this period, Yili-Junggar experienced an eastward movement of 670±320 km, and Tarim went westwards of 360±270 km, with respect to Siberia, respectively (Figs. 12a and 12b). It is worth to note that the Central Tianshan located between the Yili Block and Tarim is not involved in our simplified reconstruction.

Similarly, the CCW rotation of Yili-Junggar relative to Siberia is accommodated by a sinistral shearing along the Erqishi ductile shear zone in the Altay Belt (Figs. 1b, 12a, 12b and 12c). A sinistral kinematics has been widely recognized by structural analyses [22-25] (Fig. 11c). On the basis of the curved shape of the shear zone (Fig. 12), an Euler pole is estimated at 56°N, 101°E with a radius of about 11° (Fig. 12c). The 31.6°±15.1° anticlockwise rotation of Junggar-Yili with respect to Siberia observed in this study corresponds to a displacement of 670 ±320 km along the Erqishi Fault during Late Carboniferous to Late Permian (Fig. 12b), and the remaining 38.4°±17.3° anticlockwise rotation implies a continuous displacement of 820± 370 km occurred in post-Permian time (Fig. 12b). This may indicate that Yili-Junggar continued its eastward movement together with Tarim after the Permian (Figs. 12b and 12c). This motion essentially ended up before the Cretaceous because Cretaceous paleomagnetic data from Junggar, Mongolia as well as Siberia do not show significant differences among them [77, 78].

Ar-Ar geochronological studies on the ductile deformed rocks from shear zones indicate that Tianshan dextral strike-slip faultings took place during 290~240 Ma [24, 25, 29, 37, 79]. Erqishi sinistral strike-slip faulting is proposed to occur from 290 Ma to 240 Ma [25], and continued through Triassic to Early Jurassic [22]. Such large-scale and contemporaneous displacements along the southern right-lateral and northern left-lateral boundaries of Yili-Junggar blocks enable us to suggest a eastward wedging of Yili-Junggar between Tarim and Siberia. Meanwhile, further paleomagnetic and geological studies on Early Permian of the Yili and Junggar blocks is needed to better constrain the timing of relative motions as well as to better understand the mechanism of such tectonics.

6. Conclusions

This first paleomagnetic study is performed on sedimentary and volcanic rocks from the Yili Block. Magnetic mineralogical analyses show titanium-poor magnetite and hematite as the principal remanence carriers. Except the samples from the Axi area showing weak and unstable magnetic remanence, most samples demagnetised by thermal and AF techniques demonstrate both viscous and stable components, the former gives a magnetic direction close to PEF and the latter presents characteristic remanent magnetisation. The reversal polarity is exhaustively obtained from these Early and Late Carboniferous rocks and Late Permian red beds. A general remagnetisation of Early Carboniferous rocks has been observed due to the Late Carboniferous Yili arc magmatism. Two paleomagnetic poles of Late Carboniferous and Late Permian for the Yili Block are calculated from stable directions. Comparisons of both poles to the coeval poles of Tarim, Junggar and Siberia indicate that (1) The consistence of poles from Yili and Junggar implies no or weak relative motion between them since the Late Carboniferous; (2) no significant or weak relative latitudinal movement occurred between these 4 blocks since Late

Carboniferous; (3) 46.2°±15.1° and 31.6°±15.1° counterclockwise rotations of the Yili-Junggar blocks with respect to Tarim and Siberia, respectively, took place from Late Carboniferous to Late Permian. These rotations correspond to the eastward motions of Yili-Junggar with respect to Tarim (1160±380 km) along the dextral strike-slip faults in the Tianshan Belt and to Siberia (670±320 Km) along the left-lateral Erqishi Fault in the Altay belt. These conclusions are supported by both field structural and kinematic observations as well as geochronologic studies in these tectonic zones.

Acknowledgement

This study is supported by the State Key Project for Basic Research of China (No. 2001CB409804). French Embassy in Beijing is appreciated for financing part of research of the first author in France. Paleomagnetic data were analyzed using R. Enkin's and J. P. Cogne's computer program packages.

References

[1] R.J. Enkin, Y. Chen, V. Courtillot, J. Besse, L. Xing, Z. Zhang, Z. Zhuang, J. Zhang, A Lower Cretaceous pole from South China and the Mesozoic hairpin turn of the Eurasian apparent polar wander path, J. Geophys. Res. 96 (1991) 4007-4028.

[2] M.B. Allen, B.F. Windley, C. Zhang, Paleozoic collisional tectonics and magmatism of the Chinese Tien Shan, Central Asia, Tectonophysics 220 (1992) 89-115.

[3] R.G. Coleman, Terrains (units) in the Western half of the geodynamic map, In: Stanford-China Geosciences industrial affiliates program annual review, Stanford University, Palo Alto, USA, 1994, pp.1-8.

[4] C.M. Chen, H.F. Lu, D. Jia, D.S. Cai, S.M. Wu, Closing history of the southern Tianshan oceanic basin, western China: an oblique collisional orogeny, Tectonophisics 302 (1999) 23-40.

[5] B. Wang, L.S. Shu, D. Cluzel, M. Faure, J. Charvet, Geochemical Constraints on Carboniferous Volcanic rocks of Yili Block (Xinjiang, NW China); implication on tectonic evolution of Western Tianshan, J. Asian Earth Sci. (2006) online available.

[6] B. Wang, M. Faure, D. Cluzel, L.S. Shu, J. Charvet, S. Meffre, Late Paleozoic tectonic evolution of the northern West Tianshan, NW China, Geodin. Acta (2006) in press.

[7] R.G. Coleman, Continental growth of northwest China, Tectonics 8 (3) (1989) 621-635.

[8] Y.S. Shi, H.F. Lu, D. Jia, D.G. Howell, Paleozoic plate tectonic evolution of the Tarim and western Tianshan Regions, Western China, Int. Geol. Rev. 36 (1994) 1058-1066.

[9] L.S. Shu, H.F. Lu, J. Charvet, S. Laurent-Charvet, D.H. Yin, Paleozoic accretionary terranes in Northern Tianshan, NW China, Chin. Geochem. 19 (3) (2000) 193-202.

[10] L.S. Shu, J. Charvet, H.F. Lu, S. Laurent-Charvet, Paleozoic accretion-collision events and kinematics of ductile deformation in the central-southern Tianshan Belt, China, Acta Geol. Sin. 76 (3) (2002) 308-323.

[11] B.F. Windley, M.B. Allen, C. Zhang, Z.Y. Zhao, G.R. Wang, Paleozoic accretion and Cenozoic redeformation of the Chinese Tien Shan range, Central Asia, Geology 18 (1990) 128-131.

[12] R.S. Ma, C.Y. Wang, S.F. Ye, Tectonic framework and crustal evolution of Eastern Tianshan Mountains, Publishing House of Nanjing University, Nanjing, 1993 (in Chinese with English abstract).

[13] X.C. Xiao, Y.Q. Tang, Y.M. Feng, B.Q. Zhu, J.Y. Li, M. Zhao, Tectonic evolution of the northern Xinjiang and its adjacent regions, Geology Publishing House, Beijing, 1992 (in Chinese with English abstract).

[14] J. Gao, M.S. Li, X.C. Xiao, Y.Q. Tang, G.Q. He, Paleozoic tectonic evolution of the Tianshan orogen, northwestern China, Tectonophysics 287 (1998) 213-231.

[15] S. Laurent-Charvet, Accrétions continentales en Asie centro-orientale: évolution géodynamique et structurale du Tianshan et du Junggar oriental (nord-ouest Chine) au Paléozoïque, PhD thesis, University of Orleans, Orleans (France), 2001.

[16] A.M.C. Sengör, B.A. Natal'in, V.S. Burtman, Evolution of the Altaid tectonic collage and Paleozoic crust growth in Eurasia, Nature 364 (1993) 299-307.

[17] A.M.C. Sengör, B.A. Natal'in, Palaeotectonics of Asia: Fragments of a synthesis, In: A. Yin, M. Harrison (Eds.), The tectonic evolution of Asia, Rubey Colloquium, Cambridge University Press, Cambridge, 1996, pp. 486-640.

[18] Y.J. Li, Z.M. Wang, H.R. Wu, Z.B. Huang, Z.J. Tan, J.C. Luo, Discovery of radiolarian fossils from the Aiketik group at the western end of the South Tianshan Mountains of China and its implications, Acta Geol. Sin. 76 (2) (2002) 146-154.

[19] Y.J. Li, L.D. Sun, H.R. Wu, G.Y. Zhang, G.L. Wang, Z.B. Huang, Permo-Carboniferous radiolarians from the Wupata'erkan group, Western South Tianshan, Xinjiang, China, Acta Geol. Sin. 79 (1) (2005) 16-23.

[20] L.Q. Xia, X.Y. Xu, Z.C. Xia, X.M. Li, Z.P. Ma, L.S. Wang, Carboniferous post-collisional rift volcanism of the Tianshan Mountains, Northwestern China, Acta Geol. Sin. 77 (3) (2003) 338-360.
[21] L.Q. Xia, X.Y. Xu, Z.C. Xia, X.M. Li, Z.P. Ma, L.S. Wang, Petrogenesis of Carboniferous rift-related volcanic rocks in the Tianshan, northwestern China, Bull. Geol. Soc. Am. 116 (3-4) (2004) 419–433.
[22] M.B. Allen, A.M.C. Sengör, and Natal'in, B.A., Junggar, Turfan and Alakol basins as Late Permian to ?Early Triassic extensional structures in a sinistral shear zone in the Altaid orogenic collage, Central Asia, J. Geol. Soc. Lond. 152 (1995) 327-338.
[23] L.S. Shu, J. Charvet, L.Z. Guo, H.F. Lu, S. Laurent-Charvet, A large-scale Palaeozoic dextral ductile strike-slip zone: the Aqqikkudug-Weiya zone along the northern margin of the Central Tianshan belt, Xinjiang, NW China, Acta Geol. Sin. 73 (2) (1999) 148-162.
[24] S. Laurent-Charvet, J. Charvet, L.S. Shu, R.S. Ma, H.F. Lu, Palaeozoic late collisional strike-slip deformations in Tianshan and Altay, eastern Xinjiang, NW China, Terra Nova 14 (4) (2002) 249-256.
[25] S. Laurent-Charvet, J. Charvet, P. Monie, L.S. Shu, Late Paleozoic strike-slip shear zones in eastern Central Asia (NW China): new structural and geochronological data, Tectonics 22 (2) (2003) 1099-1101.
[26] V.S. Burtman, Structural geology of variscan Tien Shan, USSR, Am. J. Sci. 275(A) (1975) 157-186.
[27] L.M. Bazhenov, A. Chauvin, M. Audibert, N.M. Levashova, Permian and Triasic paleomagnetism of the southwestern Tien Shan: timing and mode of tectonic rotations, Earth Planet. Sci. Lett. 118 (1993) 195-212.
[28] M.L. Bazhenov, V.S. Burtman, A.V. Dvorova, Permian paleomagnetism of the Tien Shan fold belt, Central Asia: Post-collisional rotation and deformation, Tectonophysics 312 (2-4) (1999) 303-329.
[29] A.Yin, S.Y. Nie, A Phanerozoic palinspastic reconstruction of China and its neighboring regions, in: A. Yin, Harrison, M. (Eds.), The Tectonic Evolution of Asia, Rubey Colloquium, Cambridge University Press, Cambridge, 1996, pp. 442-485.
[30] B. Wang, M. Faure, L.S. Shu, K. de Jong, D. Cluzel, J. Charvet, S. Meffre, G. Ruffet, Tectonics of the Yili Block in the southern part of the Western Chinese Tianshan, and its Paleozoic geodynamic evolution, Tectonics, submitted.
[31] XBGMR(Xinjiang Bureau of Geology and Mineral Resources), Regional geology of Xinjiang Uygur Autonomy Region. Geology Publishing House, Beijing, 1993 (in Chinese with English abstract).
[32] Y.B. Chen, A.Q. Hu, G.X. Zhang, Q.F. Zhang, Zircon U-Pb age of granitic gneiss on Duku highway in western Tianshan of China and its geological implications, Chin. Sci. Bull. 45 (7) (2000) 649-653 (in Chinese with English abstract).
[33] ICS (International Commission on Stratigraphy), International Stratigraphic Chart, 2004.
[34] H.Q. Li, C.F. Xie, H.L. Chang, H. Cai, J.P. Zhu, S. Zhou, Study on metallogenetic chronology of nonferrous and precious metallic ore deposts in north Xinjiang, China, Geology Publishing House, Beijing, 1998, pp. 100-127 (in Chinese with English abstract).
[35] Y.F. Zhu, L.F. Zhang, L.B. Gu, X. Guo, J. Zhou, The zircon SHRIMP chronology and trace element geochemistry of the Carboniferous volcanic rocks in western Tianshan Mountains, Chin. Sci. Bull. 50 (19) (2005) 2201-2212 (in Chinese with English abstract).
[36] C.Y. Jiang, W.K. Wu, X.R. Zhang, S.S. Cui, The change from island arc to rift valley: evidence from volcanic rocks of Awulale area, Acta Petrol. Mineralog. 14 (4) (1995) 289-300 (in Chinese with English abstract).
[37] D. Zhou, S.A. Graham, E.Z. Chang, B.Y. Wang, B. Hacker, Paleozoic tectonic amalgamation of the Chinese Tianshan: Evidence from a transect along the Dushanzi-Kuqa highway, in: M.S. Hendrix, G.A. Davis (Eds.), Paleozoic and Mesozoic tectonic evolution of central Asia: from continental assembly to intracontinental deformation, Boulder, Colorado, Geol. Soc. Am. Mem. 194, 2001, pp. 23-46.
[38] XBGMR (Xinjiang Bureau of Geology and Mineral Resources), Geological map of Xinjiang Uygur Autonomy Region (scale 1:1500000), Geological Publishing House, Beijing, 1992.
[39] B.Y. Wang, Q. Li, J.B. Liu, Geological structures of the Middle Tianshan Mountains along the Dushanzi-Kuqa highway, Xinjiang Geol. 15 (2) (1997) 135-154 (in Chinese with English abstract).
[40] L.S. Shu, W.B. Zhu, B. Wang, M. Faure, J. Charvet, D. Cluzel, The post-collision intracontinental rifting and olistostrome on the southern slope of Bogda Mountains, Xinjiang, Acta Petrol. Sin. 21(1) (2005) 25-36 (in Chinese with English abstract).
[41] L.S. Shu, B. Wang, F. Yang, H.F. Lu, J. Charvet, S. Laurent-Charvet, Polyphase Tectonic Events and Mesozoic-Cenozoic Basin-Range Coupling in the Chinese Tianshan belt, Acta Geol. Sin. 77 (4) (2003) 457-467.
[42] P. Tapponnier, P. Molnar, Active faulting and Cenozoic tectonics of the Tienshan, Mongolia and Baykal regions, J. Geophys. Res. 84 (1979) 3425-3459.
[43] J.P. Avouac, P. Tapponnier, M. Bai, H. You, G. Wang, Active thrusting and folding along the northern Tien Shan and Late Cenozoic rotation of the Tarim relative to Dzungaria and Kazakhstan, J. Geophys. Res. 98 (B4) (1993) 6755-6804.
[44] W.D. Cunningham, B.F. Windley, D. Dorjnamjaa, J. Badamgarov, M. Saandar, A structural transect across the Mongolian Western Altai: Active transpressionnal mountain building in central Asia, Tectonics 15 (1) (1996) 142-156.
[45] B.C. Burchfiel, E.T. Brown, Q.D. Deng, X.Y. Feng, J. Li, P. Molnar, J.B. Shi, Z.M. Wu, H.C. You, Crustal shortening on the Margins of the Tien Shan, Xinjiang, China, Int. Geol. Rev. 41 (1999) 665-700.
[46] J. Charreau, Y. Chen, S. Gilder, S. Dominguez, J.P. Avouac, S. Sen, D.J. Sun, Y.A. Li, W.M. Wang, Magnetostratigraphy

and rock magnetism of the Neogene Kuitun He section (northwest China): implications for Late Cenozoic uplift of the Tianshan mountains, Earth Planet. Sci. Lett. 230 (1-2) (2005) 177-192.
[47] J.L. Kirschvink, The least squares line and the analysis of paleoamgnetic data, Geophys. J. R. Astron. Soc. 62 (1980) 699–718.
[48] R. Fisher, Dispersion on a sphere, Proc. R. Soc. London, Ser. A 217 (1953) 295–305.
[49] J.P. Cogné, A MacintoshTM application for treating paleomagnetic data and making plate reconstructions, Geochem. Geophys. Geosyst. 4 (1) (2003) 10.1029/2001GC000227.
[50] XBGMR (Xinjiang Bureau of Geology and Mineralogy Resources), Geological map (scale 1:200000), Zhaosu sheet (K-44-10), 1979.
[51] J.D.A. Zijderveld, A.C. demagnetization of rocks: Analysis of results, in: D.W. Collinson, K.M. Creer, S.K. Runcorn (Eds.), Methods on Paleomagnetism, Elsevier, New York, 1967, pp. 245–286.
[52] R.J. Enkin, The direction-correction tilt test: An all-purpose tilt/fold test for paleomagnetic studies, Earth Planet. Sci. Lett. 212 (2003) 151–166.
[53] XBGMR (Xinjiang Bureau of Geology and Mineralogy Resources), Geological map (scale 1:200000), Xinyuan sheet (K-44-10), 1975.
[54] XBGMR (Xinjiang Bureau of Geology and Mineralogy Resources), Geological map (scale 1:200000), Gongliu sheet (K-44-5), 1979.
[55] XBGMR (Xinjiang Bureau of Geology and Mineralogy Resources), Geological map (scale 1:200000), Tuokuzi, Kumalak sheet (K-45-1), 1973.
[56] XBGMR (Xinjiang Bureau of Geology and Mineralogy Resources), Geological map (scale 1:200000), Sailimuhu sheet (K-44-34), 1988.
[57] M.W. Hounslow, V.I. Davydov, C.T. Klootwijk, P. Turner, Magnetostratigraphy of the Carboniferous: a review and future prospects, Newsl. Carbonif. Stratigr. 22 (2004) 35-40.
[58] L.M. Bazhenov, A.Q. Collins, K.E. Degtyarev, N.M. Levashova, A.V. Mikolaichuk, V.E. Pavlov, R. Van der Voo, Paleozoic northward drift of the North Tianshan (Central Asia) as revealed by Ordovician and Carboniferous paleomagmatism, Tectonophysics 366 (2003) 113-141.
[59] G.L. Cheng, Y.H. Bai, Y.A. Li, Paleomagnetism of Lower Permian in the Wushi-Aksu area of Xinjiang, Seismology and Geology 5 (4) (1983) 12 (In Chinese).
[60] Y.H. Bai, G.L. Cheng, Q.G. Sun, Y.H. Sun, Y.G. Li, Y.J. Dong, D.J. Sun, Late Paleozoic polar wander path for the Tarim platform and its tectonic significance, Tectonophysics 139 (1987) 145-153.
[61] Y.P. Li, M. McWilliams, A. Cox, R. Sharps, Y.A. Li, Z.J. Gao, Z.K. Zhang, Y.J. Zhai, Late Permian paleomagnetic pole from dikes of the Tarim craton, China, Geology 16 (1988) 275-278.
[62] P.L. McFadden, X.H. Ma, M.W. McElhinny, Z.K. Zhang, Permo-Triassic magnetostratigraphy in China: northern Tarim, Earth Planet. Sci. Lett. 87 (1988) 152-160.
[63] Y.J. Zhai, Z.K. Zhang, Y.P. Li, Q. Li, Y. Li, M. McWilliams, A. Cox, R. Sharps, A study of Upper Carboniferous paleomagnetism for the Tarim block, Geoscience 2 (1988) 43-56.
[64] Z. Meng, J. Zheng, Palaeomagnetic investigations of the Apparent Polar Wander path of Tarim and relative motions between sub-tectonic units, in: Q. Zhou, J. Zheng (Eds.), Tectonic Synthetis of Tarim, Science Press, Beijing, 1990, pp. 50-87 (in Chinese with English abstract).
[65] D.J. Fang, H.L. Chen, G.H. Jin, Y.B. Guo, Z.L. Wang, X.D. Tan, S.H. Yin, Late Paleozoic and Mesozoic paleomagnetism and tectonic evolution of Tarim terrane, in: T.J. Wiley, D.G. Howell, F.L. Wong (Eds.), Terrane analysis of China and the Pacific rim, Houston (USA), Circum-Pacific Council for Energy and Mineral Resources, Earth Science Series 13, 1990, pp. 251-255.
[66] D.J. Fang, G.H. Jin, L.P. Jiang, P.Y. Wang, Z.L. Wang, Paleozoic paleomagnetic results from Tarim basin and their tectonic implication, Acta Geophys. Sin. 39 (4) (1996) 522-531 (in Chinese).
[67] Z. Meng, Palaeomagnetic study of Upper Palaeozoic erathem along the southwestern margin of Tarim block, China, Acta Sedimentol. Sin. 9 (1991) 105-109 (in Chinese with English abstract).
[68] S. Gilder, X.X. Zhao, R.S. Coe, Z. Meng, V. Courtillot, J. Besse, Paleomagnetism and tectonics of the southern Tarim basin, northwestern China, J. Geophys. Res. 101 (1996) 22 015-22 031.
[69] R. Van der Voo, Paleomagnetism of the Atlantic, Tethys and Iapetus Oceans, Cambridge University Press, Cambridge, 1993.
[70] Y.P. Li, R. Sharps, M. McWilliams, A. Nur, Y.G. Li, Q. Li, and W. Zhang, Paleomagnetic results from Late Paleozoic dikes from the northwestern Junggar block, Northwestern China, Earth Planet. Sci. Lett., 94 (1989) 123-130.
[71] Y.P. Li, R. Sharps, M. McWilliams, Y.G. Li, Q. Li, W. Zhang, Late Paleozoic Paleomagnetic results from the Junggar block, Northwestern China, J. Geophys. Res. 96 (1991) 16 047-16 060.
[72] R. Sharps, Y.P. Li, M. McWilliams, Y.G. Li, Paleomagnetic investigation of Upper Permian sediments in the South Junggar Basin, China, J. Geophys. Res. 97 (1992) 1753-1765.
[73] S.Y. Nie, D.B. Rowley, R. Van der Voo, M.S. Li, Paleomagnetism of Late Paleozoic rocks in the Tianshan, Northwestern

China, Tectonics 12 (1993) 568-579.
[74] Y. Chen, J.P. Cogné, V. Courtillot, New Cretaceous paleomagnetic poles from the Tarim Basin, Northwestern China, Earth Planet. Sci. Lett. 114 (1992) 17-38.
[75] J.M. Zhao, G.D. Liu, Z.X. Lu, X.K. Zhang, G.Z. Zhao, Lithospheric structure and dynamic processes of the Tianshan orogenic belt and the Junggar basin, Tectonophysics 376 (2003) 199-239.
[76] Z. Wang, J. Wu, X. Lei, J. Zhang, G. Liu, Polycyclic tectonic evolution and metallogeny of the Tianshan Mountains, Sciences Publishing House, Beijing, 1990 (in Chinese with English abstract).
[77] Y. Chen, V. Courtillot, J.P. Cogné, J. Besse, Z. Yang, R. Enkin, The configuration of Asia prior to the collision of India: Cretacecous paleomagnetic constraints, J. Geophys. Res. 98 (1993) 21 927-21 941.
[78] F. Harkand, J.P. Cogné, V. Kravchinsky, A new Late Cretaceous paleomagnetic pole for the west of Amuria block (Khurmen Uul, Mongolia), Earth Planet. Sci. Lett. 236 (2005) 359-373.
[79] D.S. Cai, H.F. Lu, D. Jia, S.M. Wu, C.M. Chen, 40Ar/39Ar dating of the ophiolite mélange in the southern Tien Shan and the mylonite in the southern rim of central Tianshan and their tectonic significance, Sci. Geol. Sin. 31(4) (1996) 384-390 (in Chinese with English abstract).

第一章　前言

第一节　研究现状及存在问题

1. 研究背景

造山作用是板块构造理论的重要组成部分。对不同形式的板块俯冲、碰撞作用以及不同方式的地壳增生过程的研究，极大地丰富了板块构造理论。板块构造理论诞生初期，环太平洋型洋陆俯冲造山作用，是国际地质学界讨论的热点。上世纪 70~80 年代，碰撞造山作用成为国际地质学研究的主要问题。上世纪末以来，造山带与大陆动力学已成为国际地质学界关注的焦点，大陆地壳的生长方式、生长位置、生长速率及成矿效应等都是极具挑战性的前沿问题。中亚造山带是显生宙陆壳增生最显著的地区之一（Coleman, 1989；Zonenshain et al., 1990；Sengör et al., 1993），因而受到国际地质学界的普遍关注。

截止目前，针对中亚造山带组织实施的国际地质对比计划 IGCP283、IGCP420 和数十项双边、多边国际合作项目，极大提高了中亚造山带的地质研究程度。美国国家科学基金会、德国科学研究会、法国科研中心以及英国、澳大利亚的科研机构先后投入资金支持天山大陆动力学的研究项目。国际地质对比计划 IGCP480 则于 2004 年提出了一个 5 年计划，其中一部分内容是在每年组织国际地质学家针对中亚造山带重要的研究进展举行现场研讨会。近十年来，从大陆动力学角度提出了中亚陆壳增生方式、演变过程等重要科学问题。通过跨国界重要构造带的对比研究，改善了中亚地区构造分区和连接方案，对阐明中亚地质演化的整体规律有重大意义。

迄今为止，国际公认的造山带类型主要有：环太平洋型造山带，以洋-陆俯冲作用为特征；阿尔卑斯-喜马拉雅型造山带，以陆-陆碰撞作用为特征。而中亚造山带应属另一个类型，以古生代多陆块拼合造山和中新生代盆山耦合为重要特征。古生代多块体-小洋盆格局演变包含了比环太平洋型造山更复杂的侧向增生过程，多块体拼合后的岩浆上涌、地壳垂向增生也比阿尔卑斯-喜马拉雅型造山作用更为显著，中新生代盆山耦合使古生代造山带经历了陆内造山的改造和叠加。因此，中亚造山带以古生代地壳双向增生造山和中新生代陆内造山明显有别于其它两种造山带类型，这种复杂的地质演变过程形成了中亚型造山带独特的地质构造格局。

经过数十年的研究，我国地质学家认为，位于中亚腹地的天山造山带具有多块体镶嵌、多缝合带连接、盆山耦合的大地构造格局，经历了古生代地壳双向增生和中新生代陆内造山等重要过程（Sun et al., 1991；肖序常等，1992；何国琦等，1994；任纪舜等，1999；邓启东等，2000）。多期次蛇绿岩、多类型高压变质岩和多成因花岗岩带的产出，指示地壳侧向增生过程复杂多样。另外，广泛发育的后碰撞基性岩带、富碱岩带和多处深源岩石包体的发现，表明碰撞后地壳垂向增生在天山岩石圈演化过程中具有重要意义。近年来，十数条地球物理综合剖面，初步勾勒出天山造山带与两侧盆地的岩石圈、软流圈结构特征与复杂耦合关系。总之，作为中亚造山带重要组成部分的天山造山带经历了古生代地壳双向增生过程和中新生代陆内造山作用的强烈叠加改造，造山和增生机制比环太平洋、阿尔卑斯等造山带更复杂，具有独特的地质发展历史。

2. 研究历史及现状

天山是中亚地区重要的造山带之一，引起了中外地质学家的广泛兴趣。上世纪初，前苏联地质学家穆什凯夫提出了天山由三个弧形山脉组成的认识。Suess 于 1904 提出天山属于阿尔卑斯褶皱带的想法（Suess, 1904）。上世纪 20 年代，纳利夫金将天山划分为时代不同的北、

中、南弧，并认为天山的构造和岩浆活动从北向南迁移。在此基础上，前苏联地质学家尼古拉耶夫于 1933 年提出中弧与南弧之间的界线是天山最重要的构造带，即所谓“尼古拉耶夫”线。

中国地质学家从上世纪 30 年代开始，逐渐在天山开展地质调查，早期的工作主要集中在古生物和地层学方面。黄汲清（1954）系统阐述了天山地质构造特征，并提出了天山华里西多旋回褶皱带的概念。迄今为止，关于天山的地质认识绝大部分基于新疆地矿局所完成的 1：20 万区域地质调查报告。而新疆地矿局在 1975 年 1：50 万地质填图时，将天山划分为北天山、中天山和南天山褶皱带，这也是天山构造区划中最常用的三分方案。另外，其他一些地质学家也提出了三分的思想，如前苏联学者西尼村等在上世纪 50 年代末提出，中天山为加里东褶皱带，而北天山和南天山则为华里西褶皱带；张文佑等（1959）也从构造形态上将天山分为北、中、南三部分；类似的分法还有胡冰等（1964）的北天山向斜褶皱带、中天山结晶基底和南天山向斜褶皱带。

板块构造理论产生以来，对天山板块构造的认识最早是基于对蛇绿岩的研究上。李春昱等（1982）认为中国天山属于哈萨克斯坦陆块的一部分，其中南天山分布有三条不同时代的蛇绿岩带及混杂堆积带，并大体上与山脉走向平行，从而推测古洋壳不断向北消减；而北天山石炭纪蛇绿岩与东准噶尔卡拉麦里蛇绿岩相连，为西伯利亚板块与哈萨克斯坦及中朝板块之间的最后缝合带。刘东生等（1981）将长阿吾孜-那拉提南缘断裂（即尼古拉耶夫构造带）当作一条古板块缝合带，将天山分为南、北两部分，其中南部的塔里木板块沿该缝合带向北俯冲。后来他们又提出在天山北部存在一条博罗科努山缝合带，从而天山地区被分为三个板块：南部塔里木、中部巩乃斯和北部准噶尔。与此同时，张志勇（1983）通过对天山石炭纪火山岩的研究，指出北天山艾比湖-头苏泉断裂为一俯冲缝合带，并将天山分为北部洋壳板块和南部大陆板块两部分。陈哲夫等（1985）也将天山一分为二，北天山为洋壳区，觉罗塔格为岛弧，南天山为弧后盆地。张良臣等（1985）则认为天山处于准噶尔-哈萨克斯坦、伊犁-依塞克湖和塔里木三大陆块的接合部位。一些古地磁学家，如 Bai YH et al.（1987）、Li YP et al.（1988）和翟永建等（1988）提出，石炭纪时哈萨克斯坦地块与塔里木地块沿南天山一带发生碰撞。

进入上世纪 80 年代以来，为了促进天山地质研究及开发其矿产资源，国家连续批准执行了 4 轮科技攻关重大项目，并专门成立了科技攻关 305 项目和西部 973 项目，对天山开展了系统的研究。王作勋等（1990）在对天山不同地区蛇绿岩及相关岩浆岩研究的基础上，认为天山的板块活动可以追溯到中晚元古代；震旦纪-二叠纪期间，天山地壳经历了多次开、合的手风琴式多旋回构造演化。肖序常等（1992）详尽阐述了天山大地构造划分，认为天山属于哈萨克斯坦板块，并分为北天山晚古生代活动大陆边缘、伊犁-中天山陆块和南天山早-中古生代活动大陆边缘三部分，各单元又可以再分为若干个地体。汤耀庆等（1995）通过对天山西南部蛇绿岩和高压变质岩的系统研究，提出哈尔克山南、北两缘存在 2 条蛇绿岩带，北缘蛇绿岩时代为早古生代晚期，南缘蛇绿岩时代为晚泥盆世-早石炭世，其中北缘西部为长阿吾孜-科克苏高压变质带。刘本培等（1996）认为天山西南部在早古生代和中古生代之间从塔里木北缘被动大陆边缘转换为伊犁-依塞克湖板块南缘的活动大陆边缘，并提出，两板块的陆-陆碰撞发生在二叠纪早期。马瑞士等（1993）提出，东天山阿齐库都克-尾亚一带的蛇绿岩为早古生代碰撞缝合的标志，其南侧依次为中天山火山岛弧和南天山边缘海盆地，而准噶尔盆地东缘的卡拉麦里蛇绿岩则代表晚古生代缝合带，其南侧为绵延千余公里的北天山博格达岛弧和哈尔里克岛弧。姜常义等（2001）提出，东天山地区古生代洋盆形成于奥陶纪-中泥盆世，在晚泥盆世-早石炭世已经关闭并在石炭世末形成残留海盆，并于晚石炭世末-早二叠世发生陆-陆碰撞。

近年来，随着投入的增加以及各种仪器设备精度的提高，一些高质量的研究成果发表在国内外刊物上，为认识天山造山带的构造演化积累了大量详尽而可靠的地质资料。如很多学者对天山不同时代岩浆岩进行了地球化学、同位素和年代学研究（周有勤等，1993；王居里等，1995；姜常义等，1995，1999；Chen JF et al., 1994, 2000；Gao et al., 1998；陈丹玲等，2001；熊小林等，2001；Xia LQ et al., 2003, 2004；Zhao ZH et al., 2003；赵振华等，2003；王强等，2003；Wang ZL et al., 2004；夏林圻等，2004；韩宝福等，2004；舒良树等，2005；朱永锋等，2005，2006；孙桂华等，2005；钱青等，2006），也有学者对不同地区蛇绿岩的地球化学、构造属性和地质年代进行了研究（高俊等，1995；王学潮等，1995；姜常义等，2000；董云鹏等，2001）；而其他一些学者则对天山造山带内高压变质和（或）变形岩石进行了精细的研究，为认识造山过程中构造变形作用及其年代提供了证据（高俊等，1993；郝杰等，1993；蔡东升等，1996；舒良树等，1997；Gao et al., 1995，2000，2003；Shu et al., 1999，2002，2004；Zhou et al., 2001；Klemd et al., 2002，2005；Laurent-Charvet et al., 2002, 2003；Zhang et al., 2002a, 2002b, 2003a, 2003b；赵明等，2002；Li et al., 2003；Wei et al., 2003）。另外，对天山构造基底（胡霭琴等，1998；陈义兵等，1999，2000；Hu et al., 2000）和地壳结构（Bump et al., 1998；卢德源等，2000；胥颐等，2000，2001；Poupinet et al.,2002；Zhao et al., 2003；Vinnik et al., 2004；Wang CY et al., 2004；朱英等，2004）的研究同样对理解天山构造演化具有十分重要的意义。

3. 存在问题

经过几十年的研究，目前人们多趋于认为天山是由多个地块或岛弧在古生代经过多期俯冲、碰撞作用形成的复杂造山带。然而，就具体的大地构造单元划分、板块俯冲方式和造山时代等问题，至今仍存在不同程度的争议。同时，随着研究的深入，一些新的科学问题也随之而来。这些科学问题很大程度上影响了人们对天山造山带大地构造和动力学演化的认识，给我们合理恢复其造山过程留下了诸多疑惑。总结起来，目前关于天山造山带古生代构造演化研究中存在的问题，主要有以下几个方面：

（1）目前被大多数学者所接受的天山造山带三分方案（北天山、伊犁-中天山和南天山）（王作勋等，1990；肖序常等，1992；马瑞士等，1993，1997）的基础是对天山地区不同蛇绿岩带、毗邻火山岛弧和天山地壳基底的认识。然而，在该方案中，关于伊犁-中天山和南天山的定义存在很多疑惑之处，如前者的构造基底非常复杂，包括了若干个次级前寒武纪地块，如巴伦台地块和那拉提地块等（王作勋等，1990）。另外，作为伊犁-中天山北界的巴音沟和米什沟蛇绿岩带，其构造属性和时代均不同，而其南界的蛇绿岩，即长阿吾孜-乌瓦门一带，也存在类似的问题。

（2）对天山古生代造山模式的认识分歧较大。有学者指出，天山古生代的造山过程主要以走滑拼贴为主（Sengör et al., 1993, 1996），而另外一些学者则认为天山造山作用主要以俯冲、碰撞模式为主，仅在碰撞后期发生区域走滑剪切作用（Windley et al., 1990；Allen et al., 1992；Shi YS et al., 1994； Gao et al., 1998；Chen et al., 1999；Shu et al., 1999；Laurent-Charvet, 2001； Xiao et al., 2004）。另外，在俯冲模式中，关于俯冲的极向也存在不同的认识，而且在东、西天山互不一致。大部分学者认为天山北部缝合带在西天山为一个极向向南的俯冲带（Windley et al., 1990；马瑞士等，1993，1997；舒良树等，1997；Gao et al., 1998；Laurent-Charvet et al., 2001； Shu et al., 2002），但也有学者认为它是一个向北的或者在东天山朝北的俯冲带（Allen et al., 1992；Xiao WJ et al., 2004）。类似的争议在天山南部缝合带也存在（Windley et al., 1990；Gao et al., 1998；Allen et al., 1992；马瑞士等，1993；Laurent-Charvet et al., 2001）。

（3）关于造山时代，一般认为天山具有早古生代和晚古生代两期造山作用，而最晚的俯冲碰撞作用也在晚石炭世末-早二叠世初结束。然而近来一些学者从南天山蛇绿岩中发现

了晚二叠世的放射虫硅质岩（李曰俊等，2001；Li YJ et al., 2002, 2005），而另外一些学者则从哈尔克山高压变质岩中获得 250 Ma 左右甚至更年轻的同位素年龄（Brookfield, 2000；Zhang et al., 2005；张立飞等，2005），从而认为天山碰撞造山事件最晚一直到三叠纪结束。

（4）一直以来，伊犁地区石炭纪火山岩被认为是晚古生代火山岛弧的产物（姜常义等，1995；Gao et al., 1998；李华琴等，1998；朱永峰等，2005）。然而，近来一些学者通过对该地区及邻区火山岩地球化学的研究，提出了伊犁石炭纪-二叠纪大陆裂谷的认识，甚至认为，广泛分布在伊犁地区的火山岩可能是地幔柱活动的标志，而原来被认为是缝合带的巴音沟蛇绿岩则被认为是与地幔柱有关的“红海型”洋盆的地质记录（Xia et al., 2003, 2004；夏林圻等，2004，2005；徐学义等，2005a, 2005b, 2006a, 2006b）。

（5）天山在碰撞造山之后经历了板内拉张和挤压再造山过程的改造（姜常义等，2001；马瑞士等，1993），特别是新生代以来由于印藏碰撞引起的陆内造山作用造成了天山快速隆升、地壳缩短增厚，对古生代造山带的改造作用非常明显（Tapponnier and Molnar, 1979; Avouac et al., 1993; Hendrix et al., 1994; Allen et al., 1999; Burchfiel, et al., 1999; Shu et al., 2003; Charreau et al., 2005；邓启东等，2001）。因此剔除后期构造叠加的影响，恢复古生代造山作用的原貌是认识天山构造演化中十分关键的步骤。然而在西天山，与古生代造山作用有关的韧性变形不太发育，且大多被新生代脆性构造所改造，所以区分古生代构造和后期改造是一件非常困难的工作，以致于很多新生代变形往往被误认为是与古生代造山作用有关的构造。

（6）发生在天山二叠纪期间的区域大型走滑剪切作用已被广泛认同，然而对各走滑剪切带运动方向的认识仍有争议，特别是中天山北缘那拉提断裂及东延青布拉克断裂，以往一直被认为是左旋走滑带（Sengör et al., 1993；Gao et al., 1998；Bazhenov et al., 1999, 2003），而 Yin et al.（1996）通过研究剪切带运动学特征，认为是右旋走滑。

第二节 论文选题及研究内容

1. 论文选题

伊犁地区是以往天山三分方案中伊犁-中天山地块的重要组成部分。然而，伊犁和中天山在古生代构造演化以及构造变形等方面存在很大差异，如伊犁奥陶纪-志留纪地层主要为浅水陆源沉积为特征，而中天山同时代的岩层都是火山岩和火山碎屑岩；伊犁地区普遍发育石炭系火山岩，而中天山石炭系为陆源碎屑沉积地层。这些差异表明伊犁和中天山在古生代期间经历了不同的构造演化，二者具不同构造属性。因此研究伊犁及中天山古生代构造演化，对于确认天山大地构造划分具有重要意义。

伊犁地区广泛分布的石炭系火山岩成因环境是当前地质界争论较多的问题。以往的研究通常注重对火山岩或侵入岩地球化学特征的研究，而较少涉及对岩浆喷发序列、岩浆岩与伴生沉积岩岩相学等基本地质特征的认识。为了判断这些岩浆岩的构造环境，需要综合运用地质地层学特征、岩石地球化学特征、同位素组成及地质时代，并结合区域构造背景，从而准确把握其物质来源和成因。正确认识该岩浆岩序列的构造意义，是合理恢复伊犁地块及天山构造演化的主要因素之一。

天山地区三条主要蛇绿混杂岩带是认识天山构造演化的关键。迄今为止，关于三条蛇绿混杂岩带的形成时代、构造属性和变形特征仍存在较多争议。在伊犁地块南、北两缘，分别发育巴音沟蛇绿混杂岩带、长阿吾孜-穹库什太蛇绿混杂岩带及科克苏高压变质岩带，它们与邻区其他蛇绿混杂岩带的相互联系是划分天山大地构造单元的重要边界，它们的岩石学、年代学和构造变形特征，则是确定洋壳俯冲方向和俯冲时代的基本证据。伊犁南缘蛇绿混杂岩带与天山南部黑英山-库米什一带蛇绿混杂岩带的相互关系目前尚有不同的认识，无论后

者是前者的构造推覆体还是单独的一条缝合带，都将对天山洋陆转换和变形期次的认识产生重要的影响。

此外，伊犁南、北两缘分别是那拉提断裂和北天山断裂，二者均为大型走滑剪切带。关于前者的运动动向一直有两种不同的认识，而后者也只是由天山主断裂进行推测，没有直接的运动学和年代学证据。对这两个走滑断裂带及其东延部分的研究，有助于认识天山造山带多期构造变形特征，也便于了解后造山变形作用对古生代造山带的改造程度。

由此可见，伊犁及其周缘边界带涵盖了目前西天山地区存在的主要地质问题，因此是研究伊犁以及天山造山带古生代构造演化的关键区域。贯穿天山南北的三条主要交通要道（乌鲁木齐-伊宁、独山子-库车和乌鲁木齐-库尔勒），分别经过我国境内伊犁地区的西部、东部和东、西天山分界线，为该地区地质工作提供了天然的地质剖面。

2. 研究内容

（1）通过研究新生代构造变形对古造山带的构造叠加，了解后期构造作用对古生代造山带的改造，从而避免将新生代变形误作为古生代的变形构造。在进行大地构造单元划分时，充分考虑碰撞后陆内拉张作用及大型走滑剪切作用可能对原始构造单元相对位置的改变。

（2）应用板块构造和大陆动力学理论，研究伊犁地块周缘蛇绿混杂岩的分布、变形特征、时代和大地构造背景，恢复古洋盆位置、洋陆格局与洋陆转换。

（3）对伊犁地区火山岩进行喷发序列、岩石学、地球化学、同位素地质学和地质年代学等方面的系统研究，并对与之伴生的花岗岩进行类似的系统研究，分析岩浆作用时代及其形成环境和构造意义。

（4）研究蛇绿混杂岩和高压变质岩的变形运动学和年代学，对比岩浆岛弧与毗邻缝合带之间的时、空匹配关系，进而分析板块俯冲的方式、俯冲-碰撞的时代。

（5）对韧性剪切带进行构造运动学和热年代学研究，确定变形性质、运动动向和变形时代。

（6）从伊犁地块及邻区古生代地层中获取古地磁数据，对比与天山造山作用有关的主要陆块同时代古地磁极，检验天山构造演化的不同模式，并定量估算后碰撞侧向走滑距离。

3. 技术方法

采用野外调查与室内研究相结合、宏观与微观相结合、常规测试和重点实验相结合，沉积学、构造地质学、矿物岩石学、地球化学、同位素地质学、地质年代学和古地磁学等多学科相配合的方法开展研究。

野外地质工作中，预先设计路线，对跨越不同构造单元、存在争议问题较多的典型剖面进行重点观察与系统采样。对这些剖面的岩石学、构造变形等方面进行对比研究，绘制详细的地质构造剖面图，系统测量地质产状要素和运动学要素，采集新鲜、代表性的样品。

室内研究中，通过对岩浆岩的薄片观察和鉴定，分析主元素、不相容元素、稀土元素（ICPMS）和同位素（Sm-Nd，Rb-Sr）等的组成，研究其物源和构造环境。应用电子探针、同位素测年（U-Pb ICPMS, $^{40}Ar/^{39}Ar$）等现代测试手段，为该论文研究提供必要的基础数据。鉴定定向样品薄片，分析运动学标志，结合野外观察与测量，恢复构造变形期次、性质和运动方向。应用超导磁力仪等高灵敏度仪器，对古地磁样品进行磁清洗和磁性矿物学研究，获得可靠的古地磁数据。

最后，进行多学科资料的综合对比，总结归纳，建立造山带演化的地球动力学模型。

第三节　工作量和主要研究成果

1. 工作量

本论文在中法联合培养博士生的模式下进行。论文工作自2002年夏野外工作始，于2003年9月正式进入博士学位论文的研究阶段。在4年期间，先后四次野外工作，历时7个月，累计行程近万公里，途径新疆中、北部4个地区（伊犁、阿克苏、吐鲁番和哈密）、4个自治州（昌吉、巴音郭楞、博尔塔拉和克孜勒苏）和2个市（乌鲁木齐和克拉玛依），工作区面积约200000 km^2。野外和室内工作量见表1-1。其中室内研究工作在法国奥尔良大学历时21个月，南京大学15个月。

表1-1　完成的野外和室内研究工作量一览表

序号	项　　目	工 作 量	备　注
1	野外综合地质调查	20000 km^2；210天	共4次
2	考察地质剖面	>800 km（23条）	一些剖面多次反复考察
3	地质点	730个	绝大部分有GPS坐标
4	岩石标本	520件	不含古地磁
5	古地磁岩芯	510个	8条剖面61个采点
6	运动学要素统计点	93个	7条剖面(包括断层擦线)
7	岩石学薄片鉴定	320片	南京大学和奥尔良大学
8	构造定向薄片鉴定	270片	奥尔良大学
9	地球化学ICPMS全分析	65件	法国南锡实验室(45)和广州地化所(20)
10	电子探针矿物学分析	11件	南京大学(5)、法国BRGM(3)、奥尔良(3)
11	花岗岩锆石U-Pb ICPMS测年	15件	澳大利亚Tasmania大学
12	蛇绿岩锆石U-Pb ICPMS测年	1件	澳大利亚Tasmania大学
13	变质岩白云母Ar-Ar测年	4件	法国Rennes大学
14	变形岩石黑云母Ar-Ar测年	3件	法国Rennes大学
15	变形岩石角闪石Ar-Ar测年	1件	法国Rennes大学
16	变形岩石全岩Ar-Ar测年	2件	法国Rennes大学
17	岩浆岩Sm-Nd同位素测试	8件	法国南锡实验室
18	古地磁剩磁清洗实验	432件	奥尔良古地磁实验室和巴黎全球物理所
19	AMS磁学实验	197件	奥尔良古地磁实验室
20	居里温度磁学实验	16件	奥尔良古地磁实验室
21	IRM磁学实验	18件	奥尔良古地磁实验室
22	磁滞回归曲线实验	8件	巴黎全球物理所St Maur磁学实验室
23	新疆1:20万、1:50图件分析	42幅	覆盖面积50000km^2

2. 主要认识和创新点

本研究在以下几方面取得了一些新的认识，其创新点表现在：

（1）强调了新生代陆内造山作用对古生代造山带的改造作用。恢复古造山带构造演化史，必须剔除后期构造变形。本论文认为，新生代造成的天山南、北两缘宽达数十公里的推覆体可能将原始缝合带掩盖，而现今所观察到的大型断裂带则是后期构造变形带。

（2）应用古地磁学方法首次定量地估算了二叠纪后碰撞期区域大型走滑作用的运动量和运动方向，重新评价了该走滑剪切作用对早期形成的造山带的改造作用，认为二叠纪期间沿天山剪切带发生的千余公里侧向走滑运动可能使各构造单元之间相对位置发生明显改变。

（3）应用古地磁数据检验晚石炭世以来天山造山带构造演化，认为晚石炭世时，伊犁及准噶尔、塔里木之间已基本完成碰撞造山作用，晚石炭世-晚二叠世期间天山地区未发生明显的大陆开、合事件。晚二叠世时，所有陆块已经聚合在一起，因此不支持三叠纪碰撞造山、不支持二叠纪与地幔柱有关的大陆裂谷作用的认识。

（4）注重从沉积学的角度研究伊犁地区石炭纪火山岩与伴生沉积岩的岩相特征、火山岩喷发序列等，结合火山岩和同期侵入岩的地球化学、同位素和年代学数据，判定其形成的

构造环境和时代，认为伊犁地区在中泥盆世末-石炭纪末期间为一活动大陆边缘，而不是裂谷。

（5）根据蛇绿混杂岩带变形运动学、与之毗邻火山岛弧的时间、空间分布，本文对构造缝合带的划分、俯冲方式以及碰撞时代进行了探讨，认为传统上作为北天山缝合带的巴音沟和干沟-米什沟蛇绿混杂岩带其实属于两个不同时代不同构造位置的俯冲带，前者为北天山缝合带，向东可能延伸到博格达山以北，形成于晚石炭世末，为天山最晚的缝合带，与伊犁、北天山晚古生代火山岛弧的形成有关。而传统上的南天山缝合带则分解为两个不同的缝合带，其中干沟-米什沟蛇绿混杂岩带和科克苏高压变质岩带属于天山洋缝合带，从奥陶纪开始俯冲，最后在晚泥盆世-早石炭世早期碰撞，其运动学和时代特征表明该带的俯冲极向朝南，与伊犁晚古生代活动陆缘无关。天山地区最南部的黑英山-乌瓦门-库米什蛇绿混杂岩带代表南天山早-中古生代弧后盆地，以快速拉张、快速关闭为特征。

（6）通过对缝合带构造位置的判断、前寒武纪基底分布和各构造单元古生代古地理环境的对比分析，对天山大地构造划分进行了讨论。本论文把作为伊犁-中天山板块的巴伦台地块与传统的南天山划归为一个具有前寒武纪基底的微大陆地块，称之为中天山地块，与伊犁地块、北天山和塔里木之间均以缝合带为界。中天山地块向东延伸，与东天山相应的构造单元可以对应。

第二章 伊犁地块及其邻区区域地质背景

第一节 天山及伊犁地块的地理与构造位置

天山位于中亚腹地，为亚洲主要山系之一。它东起中国甘肃-新疆交界，近东西向向西延伸进入哈萨克斯坦和吉尔吉斯斯坦境内，全程长约 3000 km，宽约 250~350 km（图 2-1）。在中国境内，长逾 1700 km 的天山山脉横亘于新疆维吾尔族自治区中北部，将其一分为二，以北为准噶尔盆地，以南为塔里木盆地（图 2-1，2-2，2-3）。总体而言，天山具有东低西高的地形特点，其中最高峰——托木尔峰高达 7435m，平均海拔近 3000 m（图 2-4），与两侧盆地高差超过 2000m，因此构成准噶尔盆地和塔里木盆地之间一道天然屏障。习惯上，中国天山以乌鲁木齐为界分为东天山和西天山，东窄西宽、呈喇叭形向西分为南北两支，分别为博罗科努山和哈尔克山，而伊宁盆地就位于西天山南北两支之间（图 2-2，2-3）。伊宁盆地在中国境内是一个三角形地带，然而它向哈萨克斯坦延伸，面积超过 50000 km^2（图 2-3，2-6），区域上称之为“伊犁（Ili）盆地”。

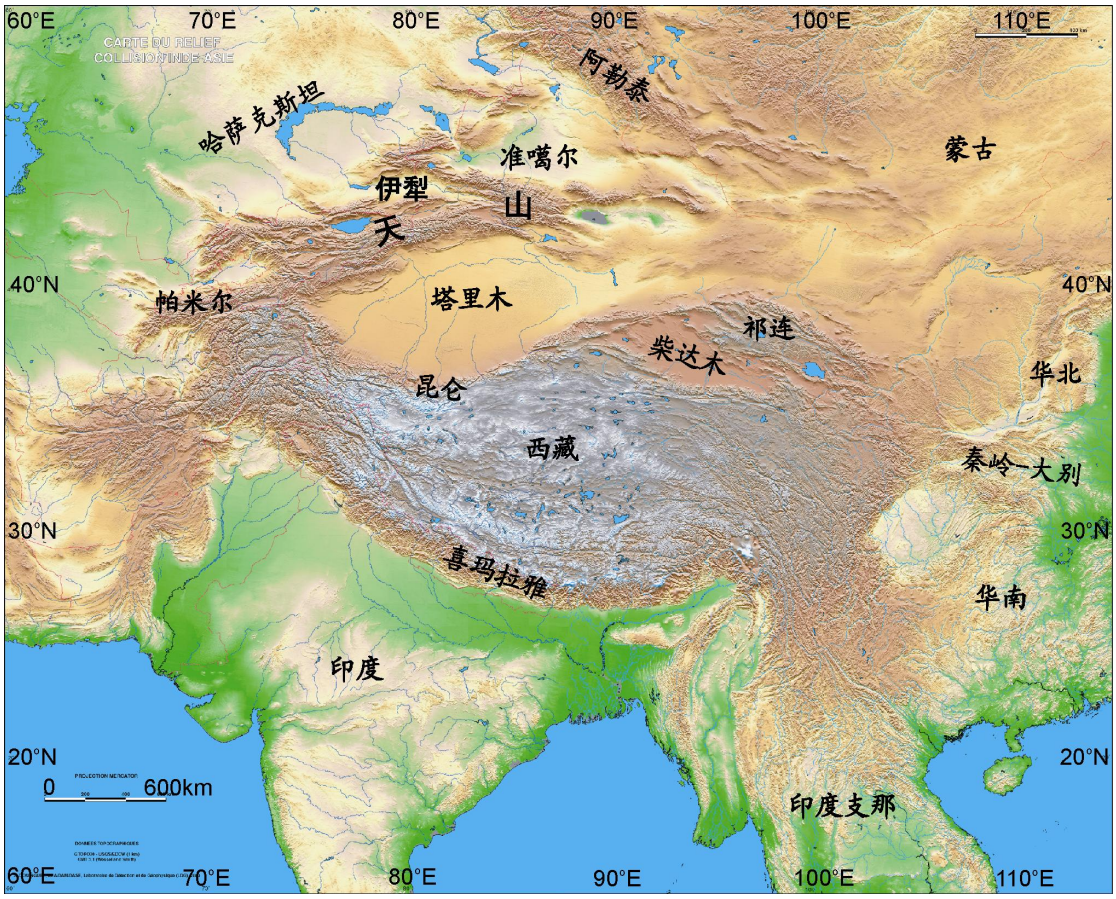

图 2-1 中亚地区数字地形地貌图（GTOPO30，NASA）

伊犁盆地是一个中、新生代沉积盆地，在其周缘发育有元古代-古生代完整的地层序列，这些地层通常被当作天山造山带的一部分。后者则被认为是中亚造山带（CAOB；Burtman, 1975; Coleman, 1989; Zonenshain et al., 1990; Sengör et al., 1993; Jahn et al., 2000，2004；Brookfield, 2000; Khain et al., 2003；Dobretsov and Buslov, 2004；Buslov et al., 2004；Buckman and Aitchison, 2004；Zhang et al., 2005）的重要组成部分（图 2-2），在欧亚大陆的形成过程中，发挥了重要作用。中亚造山带的形成与演化，是一系列大陆板块在古生代期间彼此相互作用的结果，这些大陆块体主要有西伯利亚、哈萨克斯坦、东欧大陆、准噶尔、塔里木、华

北、柴达木和西藏等（图 2-1，2-2）。各大陆板块之间均以造山带相隔，如东欧与西伯利亚-哈萨克斯坦之间的乌拉儿造山带、华北与西伯利亚之间的蒙古-鄂霍次克（Okhotsk）褶皱带、西伯利亚和准噶尔之间的阿勒泰-生延（Sayan）造山带、西藏与塔里木及柴达木之间的昆仑造山带，而天山造山带则位于准噶尔与塔里木及伊犁之间（图 2-2）。

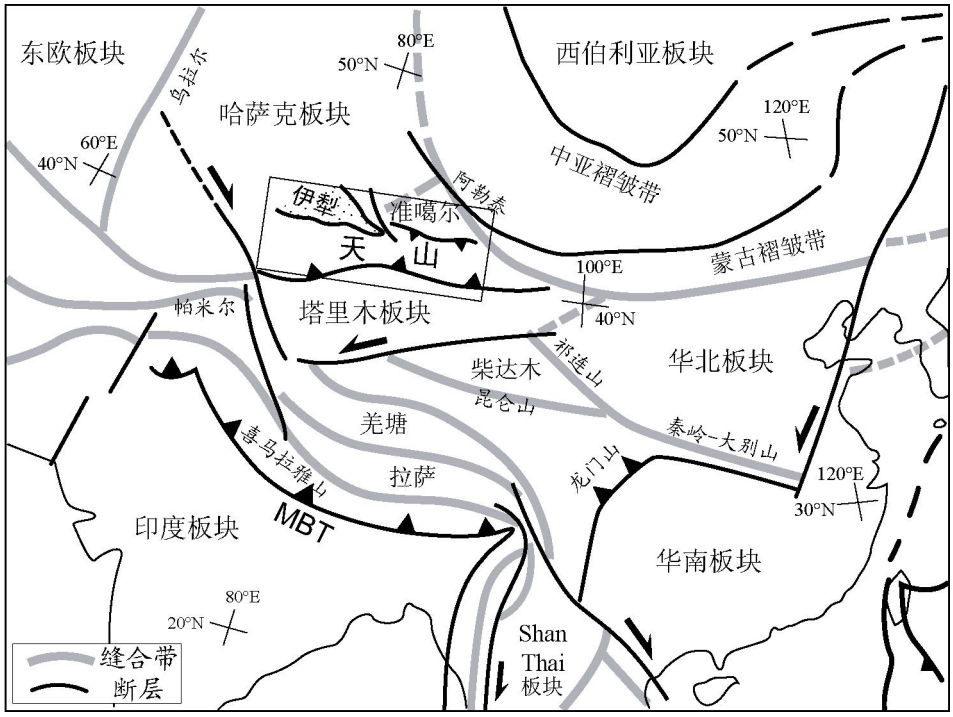

图 2-2 中亚地区地质构造简图（据 Enkin et al., 1991 并修改）

第二节 区域地质背景

现今的天山造山带主要是新生代以来，由于印-藏碰撞作用引起的塔里木、准噶尔和伊犁地块南北向地壳缩短的产物（Molnar and Tapponnier, 1975; Tapponnier and Molnar, 1979; Nelson et al., 1987; Avouac et al., 1993; Hendrix et al., 1994; Allen et al., 1999; Burchfiel, et al., 1999; Poupinet et al., 2002; Shu et al., 2003; Charreau et al., 2005）。现有的地震资料显示，准噶尔和塔里木地块岩石圈分别向天山之下俯冲（图2-4；Poupinet et al., 2002；Zhao et al., 2003），其中准噶尔地壳向天山俯冲到46~50-60 km深度（Bump et al., 1998；Wang et al., 2003），而塔里木地壳则向天山俯冲至70 km深度（Vinnik et al., 2004）。结果，在天山南北缘与盆地交接带，形成了双向逆冲褶皱、断裂系（图2-5；舒良树等，2004）。另外，从地貌图（图2-3）和地质图（图2-6，2-7）可以看出，天山造山带中发育有一系列东西向的断裂带，前人研究表明，它们是切过天山主脊的大型走滑剪切带（Allen et al., 1995; Bazhenov et al., 1999; Shu et al., 1999; Laurent-Charvet et al., 2002; 2003; Zhao et al., 2003）。后期的构造变形作用对天山古生代构造格局造成了强烈的叠加、改造（Shu et al., 2003；郭召杰等，2006）。

经过前人几十年的研究，人们已趋于认为天山是一个由不同的大陆板块、微地块和岩浆岛弧经过俯冲、碰撞、增生作用形成的古生代造山带（Coleman, 1989; Shi et al., 1994; Shu et al., 2000, 2002）。前人通常根据蛇绿混杂岩带将天山及其邻区分为若干个大地构造单元，从南向北分别为塔里木、南天山、中天山、伊犁、北天山和准噶尔。对这些构造单元基底及蛇绿混杂岩带构造属性的认识，是恢复天山造山带古生代构造演化的关键和前提。

1. 前寒武纪基底

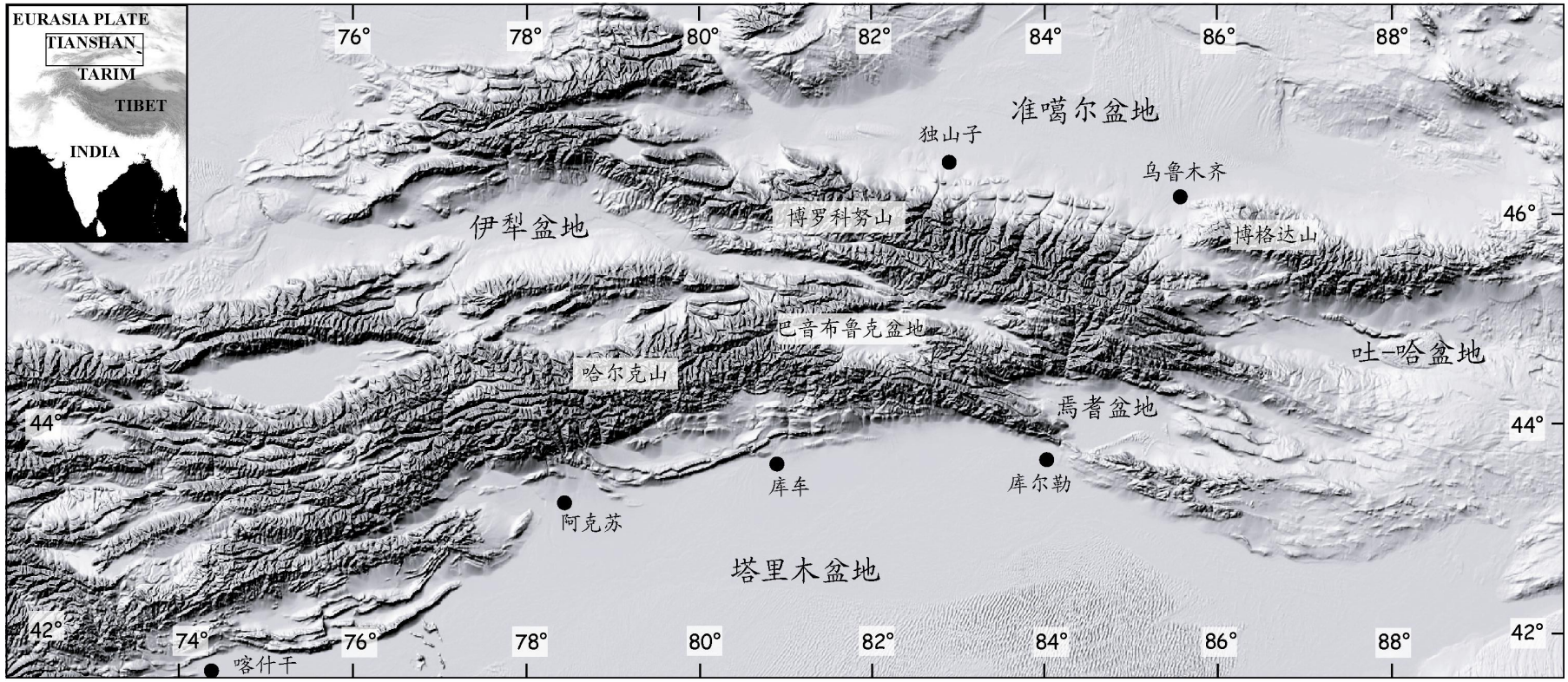

2-3 天山造山带数字地形地貌图（引自 J.Charreau（2005）改编 GTOPO30，NASA）

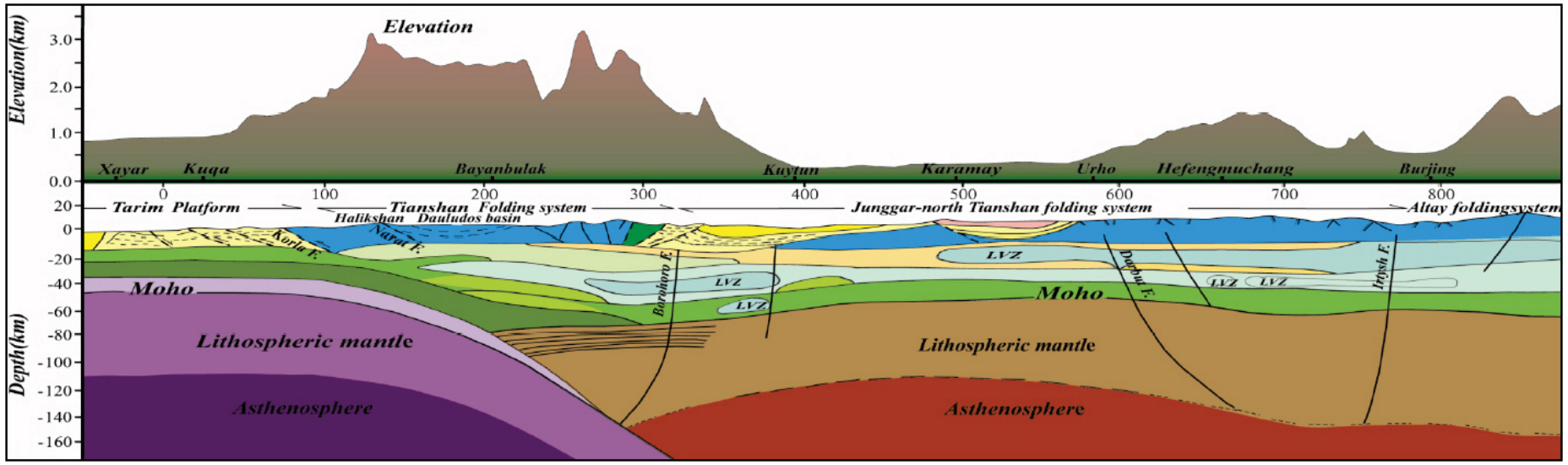

图 2-4 天山及其邻区岩石圈结构（据 Zhao et al., 2003；彩图引自"前陆盆地断层相关褶皱理论及应用国际研讨会（北京，2005）"野外指南）

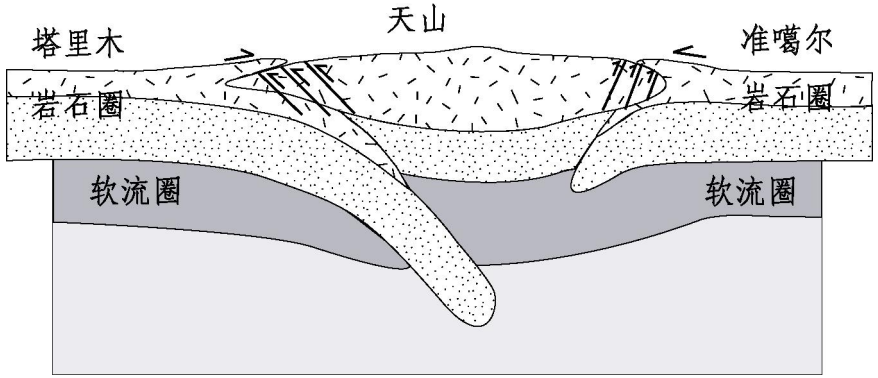

图 2-5 天山南、北缘盆山转换带双向逆冲成因机制（据舒良树，2004 内部地质报告）

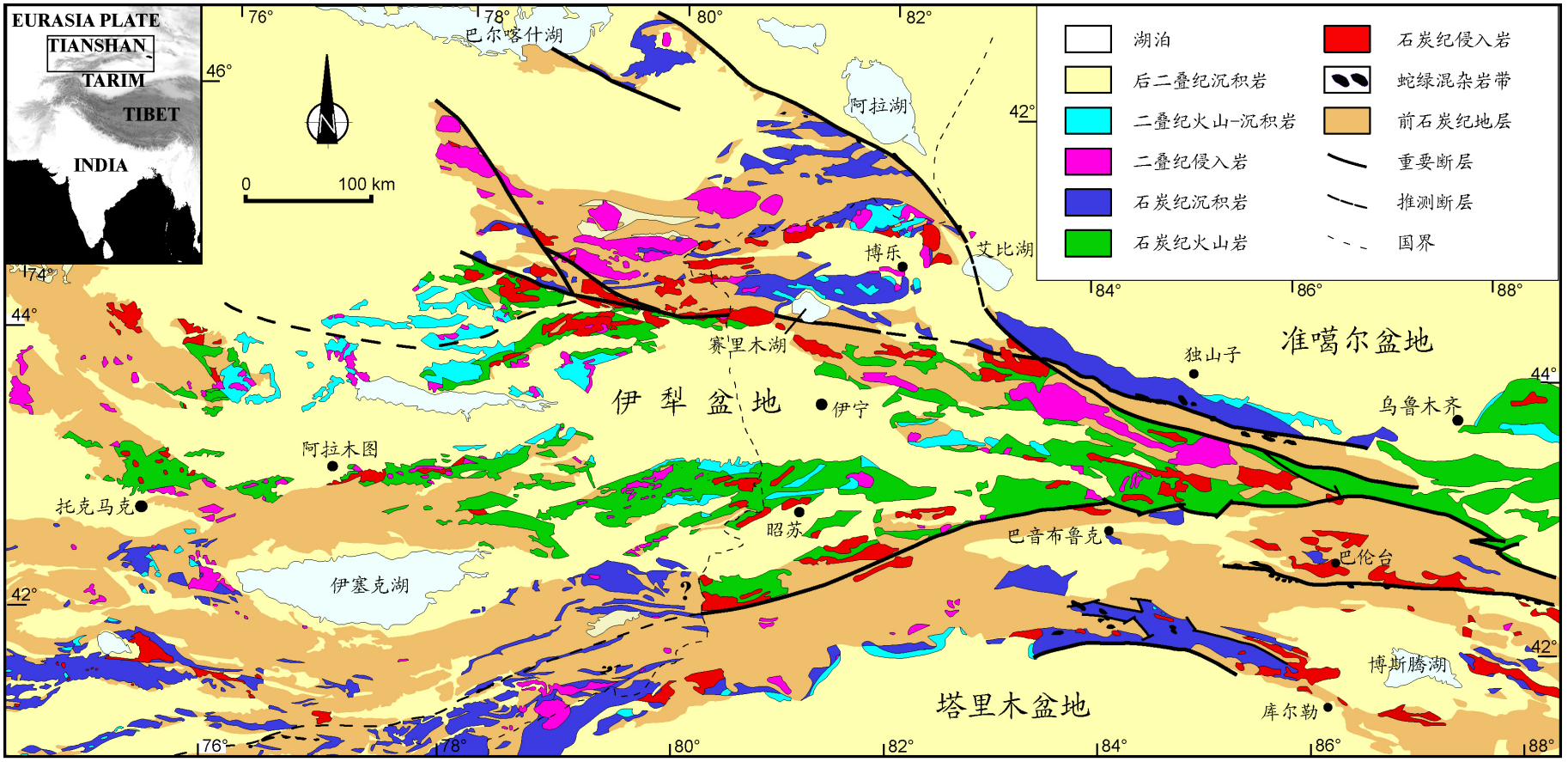

图 2-6 天山造山带石炭纪-二叠纪及其基底地质简图

1.1. 塔里木盆地基底性质

塔里木盆地为中国第一大盆地，面积560000 km^2，北以天山为界，南为昆仑山和阿尔金断裂所限（图2-2）。关于其基底性质，除个别学者（Hsu, 1988）认为其前身为弧后盆地以外，一般都认为是前寒武纪结晶-变质岩系。现有的地质资料表明，这些前寒武纪变质岩主要分布在盆地边缘，如阿克苏地区晚元古代蓝片岩，库鲁克塔格地区早-中元古代片麻岩和震旦纪结晶灰岩（图2-7）。最近，Guo等（2005）在塔里木盆地7000多米的钻孔中获得的花岗闪长岩$^{40}Ar/^{39}Ar$年龄为790.0±22.1~744.0±9.3 Ma，其岩相学具有岛弧岩浆岩的特征，因此被认为与阿克苏蓝片岩相关，并代表一个前寒武纪的俯冲碰撞带（Nakajima et al., 1990）。另外，现有的地质、地震和大陆钻探资料显示，塔里木盆地的基底构成在时、空两方面具有不均一性。其中时间的不均一表现在不同地区基底岩石由不同时代、不同岩性组成，空间上垂向的不均一体现在基底的双重结构（结晶基底和盖层），纵向上的分带性则表现为盆地南、北基底的差异（李锦轶等，1999）。

1.2. 准噶尔盆地基底性质

准噶尔盆地位于天山和阿勒泰山之间，为一个菱形盆地，总面积 13000 km^2，中、新生代沉积地层厚逾 10 km（Liu et al., 1990）。迄今为止，尚未在准噶尔盆地周缘发现前寒武纪地层，因而对准噶尔盆地基底的认识存在很大的争议。有学者认为，准噶尔古生代基底为一个残余弧后盆地（Caroll et al.,1990）。另外，Chen 等（2004）和 Jahn（2004）通过研究准噶尔周缘后碰撞花岗质岩石的$\varepsilon_{Nd}(T)$值，认为准噶尔基底是早古生代洋壳和岛弧杂岩。然而，另外一些学者通过对重力、航磁、地震等资料的分析，认为准噶尔基底属于前震旦纪大陆地壳（杨宗仁等，1986; 赵白等，1992；Sengör et al., 1993），李锦轶等（1999,2000）通过对东准噶尔卡拉麦里、西准噶尔克拉玛依古生代地层沉积物源区的分析，认为准噶尔盆地的基底性质应该属于陆壳而非洋壳。

1.3. 天山造山带构造基底及其时代

如图2-7所示，元古代基底在西天山分布十分普遍，其中木扎尔特群和那拉提群为天山造山带中出露最老的前寒武纪变质岩系（新疆地矿局，1993）。木扎尔特群出露在哈尔克山南坡木扎尔特达坂一带，其下亚群为条带状、眼球状混合岩和黑云斜长片麻岩；上亚群为绿泥斜长变粒岩、二云斜长片麻岩、浅变质的碳酸盐岩以及细粒碎屑岩等。那拉提群沿那拉提山主脊分布，主要岩性为角闪斜长片麻岩、黑云奥长片麻岩、条带状混合岩并夹少量绿片岩、石英岩和白云质大理岩等。陈义兵等（2000）对出露的独-库公路南侧的那拉提群变质岩系进行了U-Pb同位素测年工作，得到882±33Ma的年龄。出露在博乐以西的温泉群属于下元古界（新疆地矿局，1993），其上部为大理岩、结晶灰岩、绢云母石英片岩，下部为斜长角闪岩、黑云母斜长片麻岩、黑云母石英片岩、白云母石英片岩及石墨化大理岩等，Sm-Nd年代学研究表明其下限年龄为1700～1800Ma（胡霭琴等，1998）。另外，在托木尔峰地区图拉苏冰川-汗亚依拉克一带，前寒武纪变质岩系的Rb-Sr全岩等时线年龄为729Ma（杨学昌，1985），该区同类型变质岩Sm-Nd年龄为1570Ma（王宝瑜等，1994）。胡霭琴等（1998，2000）通过对天山造山带中元古代基底岩石Nd同位素的研究，认为这些基底岩石形成于1800Ma 前，基底变质岩系的母岩物质来源于长期亏损的地幔源区，推断它们处于古岛孤的构造环境，并与塔里木北缘地块截然不同。

2. 西天山蛇绿混杂岩带及其时代

前人经过几十年的研究，逐渐在天山地区发现了大量的蛇绿混杂岩。关于这些蛇绿混杂岩形成时代和构造属性的认识，至今仍有争议，对东、西天山蛇绿混杂岩之间的相互联系，也存在不同的认识。目前，人们基本上认为，在西天山主要存在三条蛇绿岩带，即北部巴音沟蛇绿岩带、中部哈尔克山北缘-库米什蛇绿岩带和南部霍拉山-额尔宾山蛇绿岩带。

2.1. 巴音沟石炭纪蛇绿岩带

巴音沟蛇绿岩位于独山子南部30km处，向西与莫托沙拉沟蛇绿岩（李生虎等，1994）相连，向东延伸到玛纳斯上游（肖序常等，1992）。该段蛇绿岩可能代表一个有限洋盆（肖序常等，1992；李生虎等，1994），其中硅质岩含有晚泥盆世-早石炭世的放射虫化石，因此该蛇绿岩带被认为是华里西中期北天山缝合带（肖序常等，1992；Windley et al., 1990；Allen et al., 1992；Gao et al., 1998）。在东天山北部，蛇绿岩主要分布在东天山卡拉麦里、巴里坤和康古尔一带，但它们可能代表晚古生代弧前、弧间盆地（马瑞士等，1993，1997；Shu et al., 2000, 2002），与巴音沟蛇绿岩带并不完全一致。

2.2. 哈尔克山北缘-米什沟志留-晚泥盆世蛇绿岩带与高压变质岩带

该带蛇绿岩主要分布在西天山哈尔克山北坡的长阿吾孜、穹库什太一带，向东经拉尔墩达坂，延伸到干沟-米什沟一带，该蛇绿岩带被认为是加里东晚期缝合带（肖序常等，1992）。在哈尔克山北麓，镁铁岩与超镁铁岩沿尼古拉耶夫构造线分布，并与高压变质的蓝片岩-绿片岩带共生。对高压变质岩的年代学研究表明，蛇绿岩所代表的洋壳可能存在于420Ma左右，而高压/超高压变质作用则发生在350Ma左右（高俊等，1994；汤耀庆等，1995；Gao et al., 1995, 1998, 2000, 2003；Klemd et al., 2005）。在米什沟，混杂堆积岩中的基质砂岩和复理石也发生了低绿片岩相变质和韧性变形，堆积层序中的辉长岩Rb-Sr年龄为468Ma（车自成等，1994）。Gao et al.（1995，2003）和汤耀庆等（1995）提出，科克苏变质火山岩形成于洋盆或海山环境。该带延伸到东天山可能与尾亚蛇绿岩相连，在尾亚一带，镁铁岩发生了麻粒岩化（舒良树等，2000），其中斜长石+辉石+全岩Sm-Nd等时线年龄为 538±24Ma，而从辉石退变质形成的角闪石$^{40}Ar/^{39}Ar$坪年龄值为432±1Ma（Shu et al., 2004）。麻粒岩地球化学特征表明其原岩形成于洋岛环境（Shu et al., 2004）。

2.3. 霍拉山-额尔宾山晚泥盆-早石炭世蛇绿岩带

在天山最南部的蛇绿岩分布在哈尔克山南坡黑英山、霍拉山色日克牙伊拉克、库勒湖和额尔宾山乌瓦门及库米什地区。王作勋等（1990）认为，乌瓦门地区蛇绿岩与库米什地区蛇绿岩可能属于两个不同时代的缝合带。肖序常（1992）等将西天山南部蛇绿岩带的时代归为华里西早期。另外，黑英山、库勒湖蛇绿岩和库米什铜花山等地蛇绿岩中的硅质岩含有晚泥盆世-早石炭世的放射虫化石（汤耀庆等，1995；Gao et al., 1998；Liu Y et al., 2001；Laurent-Charvet, 2001）。库勒湖蛇绿岩石英片岩基质中黑云母$^{40}Ar/^{39}Ar$年龄为370±4.8Ma（蔡东升等，1996）。榆树沟高压变质麻粒岩中锆石U-Pb年龄为392±7Ma（Zhou DW et al., 2004）。该带向东延伸可能与东天山红柳河蛇绿岩相连，其中辉长岩的锆石U-Pb年龄为425.5±2.3 Ma（于福生等，2006）。高俊等（1995）和王学潮等（1995）认为，霍拉山-额尔宾山一带蛇绿岩形成于有限洋盆的弱扩张脊环境，董云鹏等（2005）认为，乌瓦门蛇绿岩代表初试扩张的弧后盆地。另外，榆树沟变质镁铁岩具有MORB和OIB亲缘性（董云鹏等，2001），可能形成与洋岛环境（Shu et al., 2004）。

第三节 天山古生代构造演化的不同模式

自上世纪 30 年代，前苏联地质学家穆什凯托夫提出“天山运动”的概念，并划分出早石炭世末和晚石炭世末两期造山运动以来，天山古生代大地构造与构造演化成为中外地质学家研究的热点。黄汲清于 1954 年和 1984 年最早提出多旋回造山的概念。王作勋（Wang et al., 1988）利用板块构造理论，提出了天山手风琴式的造山过程。在多期开、合与多旋回造山等思想的指导下，上世纪 90 年代以来，中外地质学家对天山造山带古生代的构造演化提出了多种不同的动力学模式，这些模式之间互有借鉴之处，但也有明显的差别。

1. 阿勒泰造山模式

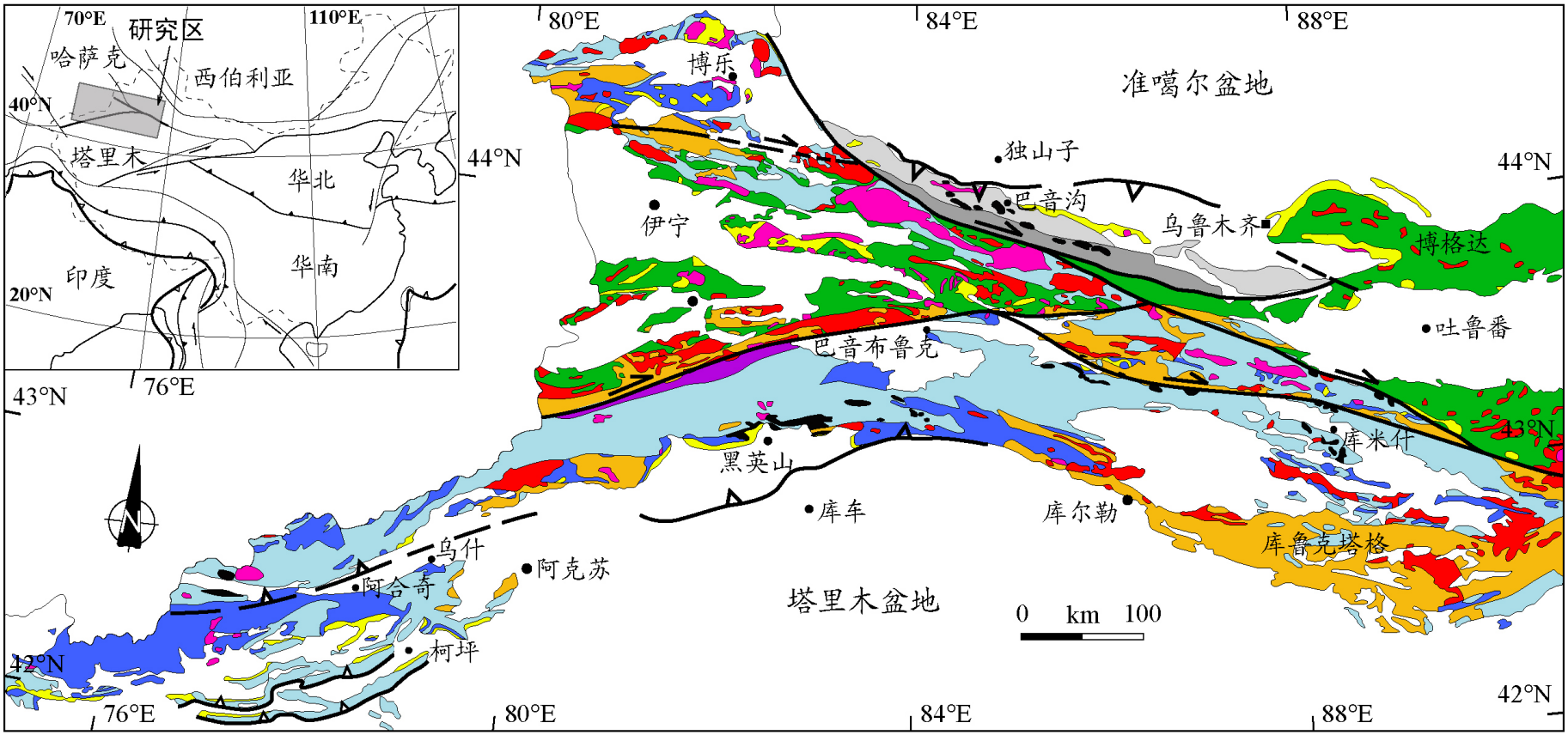

图 2-7 中国西天山地质构造简图

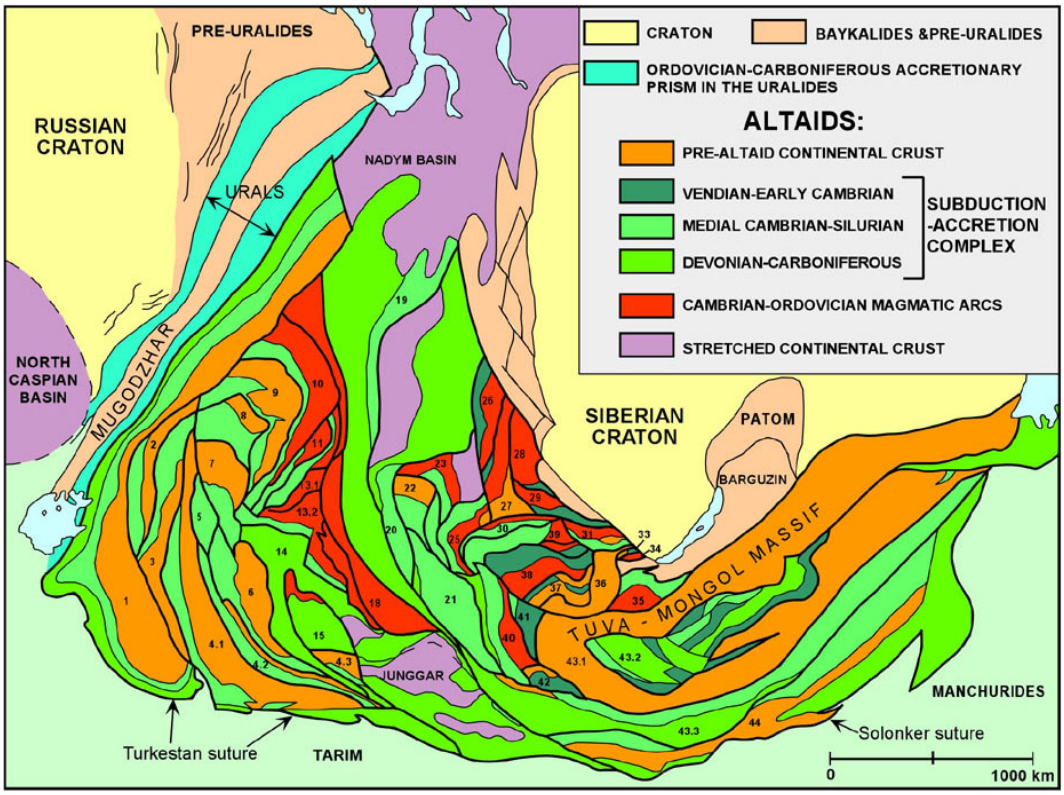

图 2-8 阿勒泰剪切造山带构造简图（据 Şengör and Natal'in, 1996）

Sengör et al.（1993，1996）认为，天山造山带属于阿勒泰造山带的一部分，后者是中亚地区一个由众多地质块体聚合而成的造山拼贴带（图 2-8）。20 多个岩浆岛弧主要由走滑断裂作用形成，并最后沿这些走滑断层再次拼合到一起。这种拼贴过程主要发生在中古生代期间。该模式强调了区域走滑事件对造山作用的影响，而在造山之后，区域走滑作用再次对造山带进行改造，并发生陆内变形。

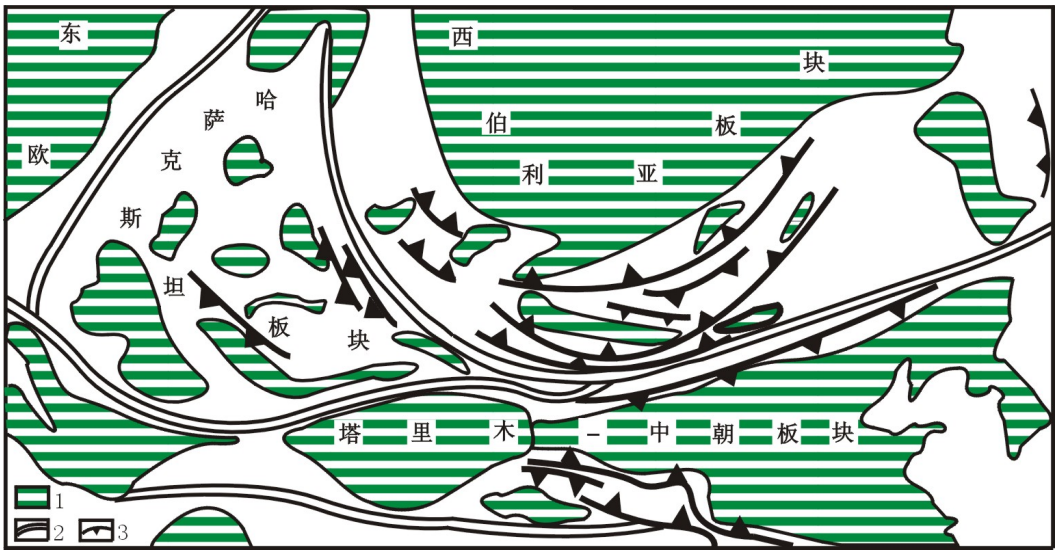

图 2-9 中亚地区古生代板块构造模式图(据李春昱等, 1982; 1,古大陆块体; 2,古大陆缝合带; 3,古俯冲带)

2. 西太平洋型岛弧增生模式

Shi et al.（1994）和 Shu et al.（2000）研究提出，中亚地区古生代构造格局为两大陆块（西伯利亚板块和塔里木-中朝板块）之间夹一大洋盆（天山大洋），而洋盆中分布多个地体

构造，其构造框架与现今的西太平洋布局十分相似（如图 2-9）。因此，天山造山带是一个晚古生代复杂地体的拼贴带，由散布在天山洋中的裂解陆块、地层块体、海山和火山弧以及彼此之间的小洋盆，经过俯冲、碰撞，最后在石炭纪末-二叠纪初增生拼贴到西伯利亚板块南缘和塔里木-中朝板块的北缘，并导致强烈的推覆作用，而诸多洋壳则形成蛇绿岩残片分布在天山造山带中。

3. 多期洋-陆（岛）俯冲和陆-陆（岛）碰撞模式

关于天山造山带的构造演化，更多的学者提出了多期洋-陆、洋-岛俯冲以及随后的陆-陆、岛弧-大陆之间的碰撞造山模式（Windley et al., 1990；Allent et al., 1992；Gao et al., 1998；Chen CM et al., 1999；Laurent-Charvet, 2001；Guo J. et al., 2002；Xiao et al., 2004）（图 2-10，2-11，2-12）。这些模式均大同小异，相同的是他们均强调，天山的造山过程以俯冲、碰撞为主，天山地区曾存在一个主要的大洋，其洋壳向大陆或岛弧的俯冲作用形成新的岛弧和大陆和/或岛弧之间新的洋壳，如此反复的俯冲过程最终在古生代末结束，所有的大陆和岛弧全部会聚在一起形成统一的大陆地壳。

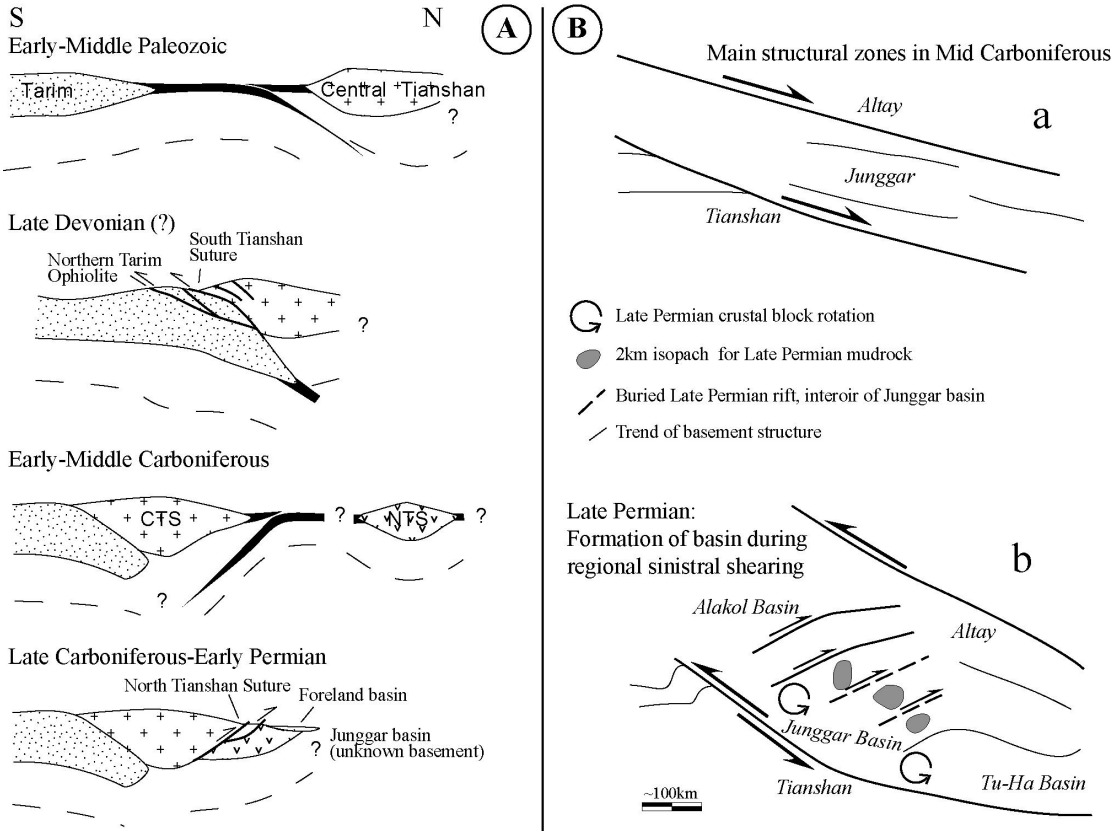

图 2-10 （A）西天山古生代构造演化（据 Allen et al., 1992）；

（B）阿勒泰剪切系北天山-准噶尔晚古生代演化（据 Allen et al., 1995）

然而，各种模式之间也存在明显的差异，主要表现在洋壳的俯冲方向和俯冲、碰撞的时代约束上。Windley 和 Allen 等（Windley et al., 1990；Allen et al., 1992）认为，天山洋在早-中古生代向北俯冲形成中天山岛弧，晚泥盆世关闭。北天山洋盆在早-中石炭世期间向南俯冲，使中天山再次成为活动大陆边缘，晚石炭世-早二叠世洋盆关闭（图 2-10）。Chen et al.（1999）则提出了南天山洋盆的形成机制，认为是由于晚寒武世-奥陶纪伊犁微地块从塔里木板块裂解过程中形成。南天山洋盆继而在志留纪-中泥盆世期间向北俯冲在伊犁地块之下，形成中天山早古生代岛弧。南天山洋盆剪刀式的关闭过程，在其西部形成了南天山残余洋盆，该洋盆在晚泥盆世-早石炭世期间继续向北俯冲，形成伊犁晚古生代活动大陆边缘。伊犁和

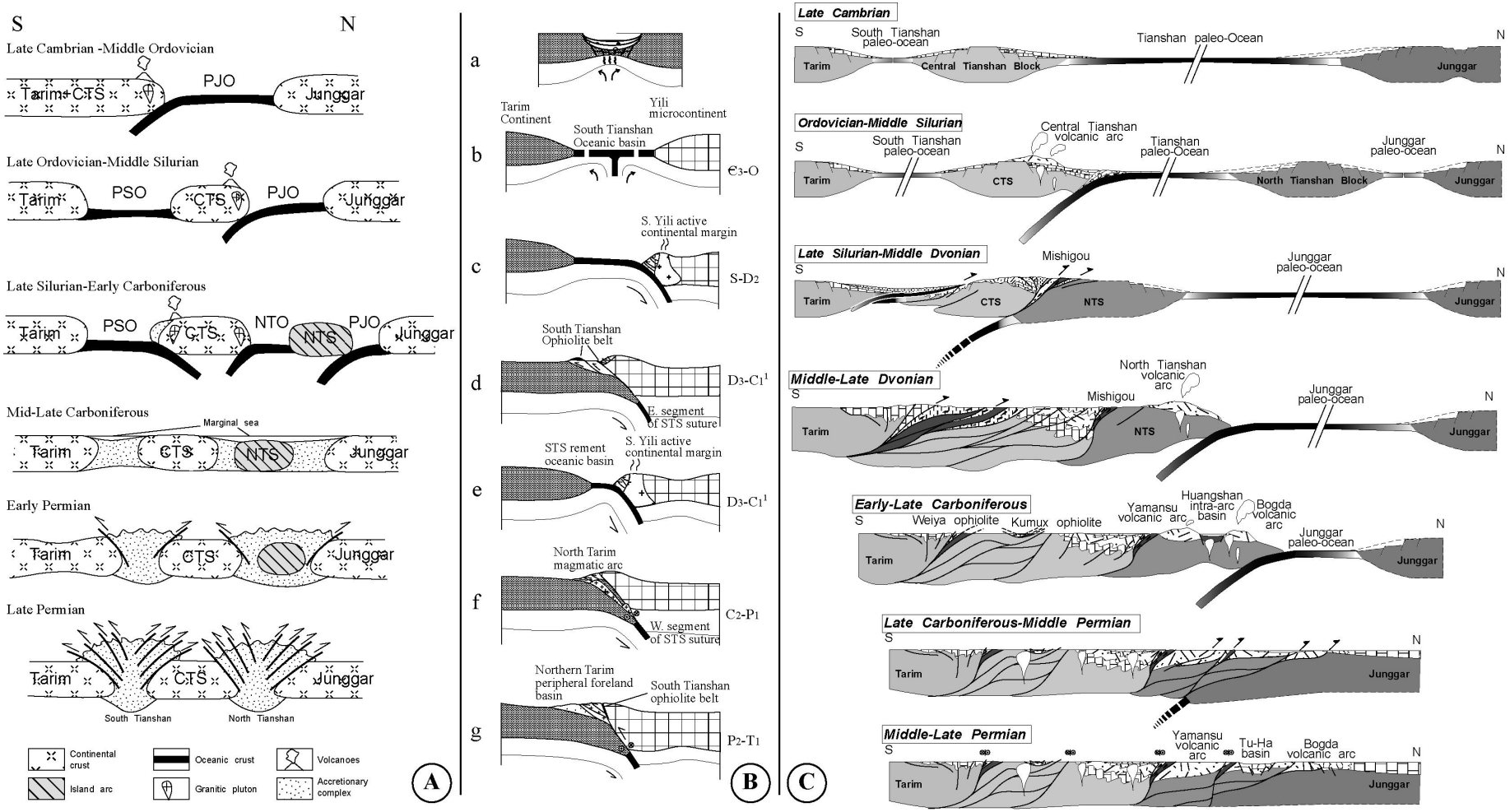

图 2-11 天山古生代构造演化(A 据 Gao et al., 1998; B 据 Chen et al., 1999；C 据 Laurent-Charvet, 2001)

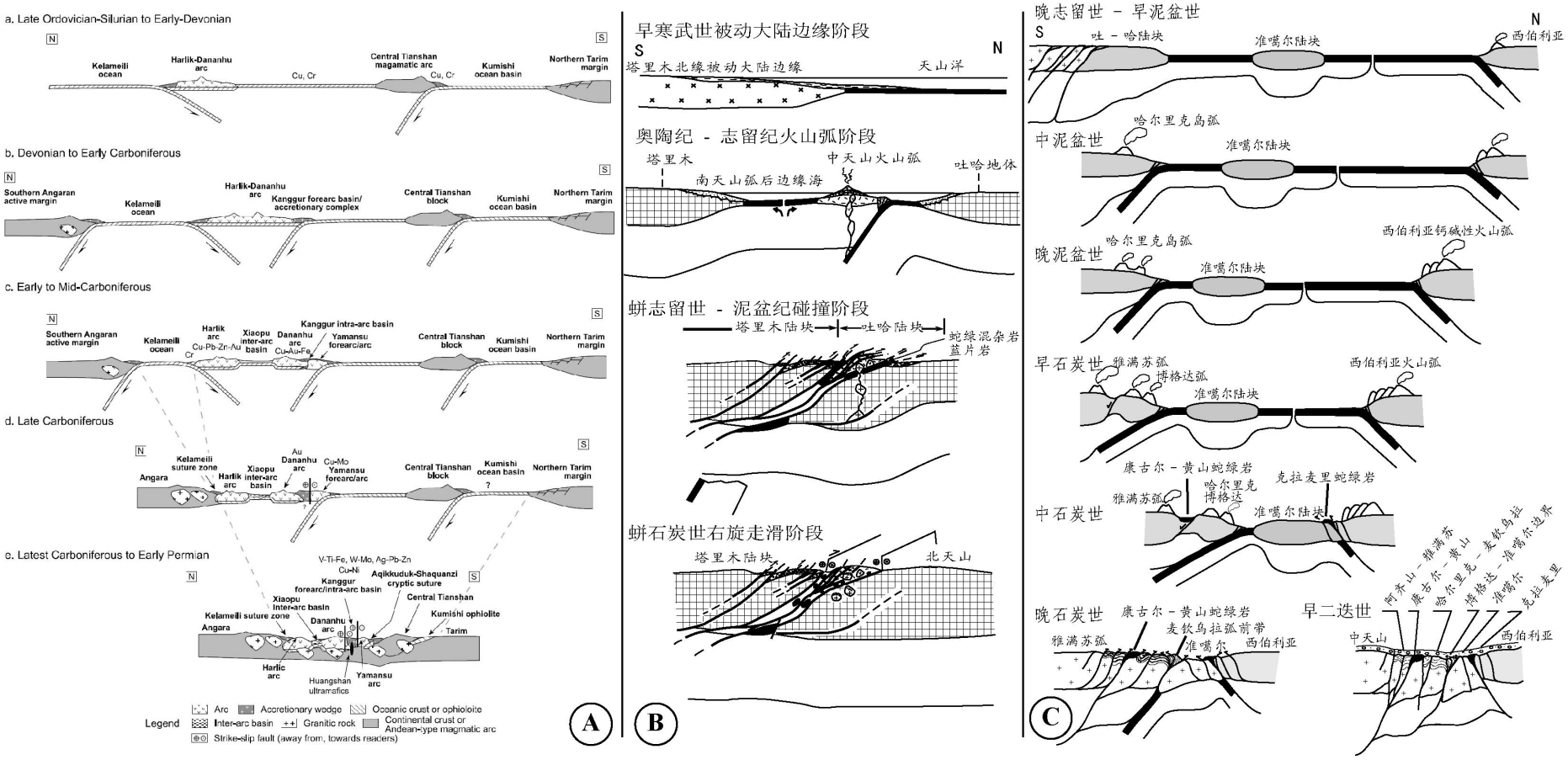

图 2-12 东天山古生代构造演化（A 据 Xiao et al., 2004；B,C 据舒良树，2004 内部地质报告）

塔里木板块在晚石炭世-早二叠世发生斜向碰撞，并导致走滑剪切作用（图 2-11B）。

Gao et al.（1998）和 Laurent-Charvet（2001）均认为古准噶尔洋在天山造山过程中起主导作用。前者认为，古准噶尔洋在晚寒武-中奥陶世期间向南俯冲，形成中天山早古生代岛弧以及古南天山洋（边缘海），使中天山-伊犁地块从塔里木板块裂解出来。南天山洋在晚志留-早石炭世期间开始向北消减，在伊犁-中天山南缘形成活动陆缘。而与此同时，准噶尔洋继续向南俯冲，并形成北天山大洋岛弧，从而在天山地区出现了一系列狭小的洋盆（图 2-11A）。这些洋盆分别向伊犁-中天山和北天山俯冲，在中-晚石炭世时全部关闭、碰撞造山。与之不同的是，Laurent-Charvet（2001）在运动学研究的基础上，对东天山的构造演化提出如下认识：古准噶尔洋与古南天山洋在晚寒武世即已存在，古准噶尔洋在奥陶纪-中志留世向南俯冲形成早古生代中天山岛弧，并使北天山“地块”从准噶尔裂解出来。晚志留世-中泥盆世，中天山与北天山发生碰撞，同时南天山洋也向南俯冲并关闭，从而北天山、中天山和塔里木已增生为一个整体。在中-晚泥盆世时，只有准噶尔洋继续向南俯冲，在北天山形成火山岛弧，如博格达、黄山和雅满苏岛弧等（图 2-11C）。最终的碰撞发生在晚石炭世-中二叠世。晚二叠世时天山地区普遍发生右旋走滑事件。

对于东天山的构造演化，Xiao et al.（2004）、舒良树（2004 内部地质报告）也提出了类似的模式，两模式均以准噶尔和天山洋的反向俯冲为特征，而前者以新洋壳的形成（图 2-12A）不同于后者洋壳的持续消减过程（图 2-12B-C）。总体来讲，这些演化模式在俯冲方式和时代上仍存在很多争议的地方，而且在东、西天山的对比中，俯冲方式更是差异甚大。因此，关于天山古生代构造演化的模型，尚需要进一步的研究、探讨，以期取得统一的认识。

第四节 小结

1．天山造山带位于准噶尔与塔里木盆地之间，是中亚造山带的主要组成部分，在欧亚大陆形成过程中发挥了重要作用。伊犁地块就处在西天山南、北两支之间，其构造属性与地球动力学演化是理解天山古生代造山过程的关键因素之一。

2．塔里木盆地构造基底为前寒武纪结晶-变质岩系，为中亚地区重要的大陆板块之一。塔里木板块基底在形成时代和空间分布上，存在不均一性。关于准噶尔盆地构造基底的认识目前尚存在争议。虽然不能排除它曾经是洋壳的可能，但地球物理研究发现，在盆地的中、新生代盖层之下发育有数十公里厚的古生代地层。因此，本论文在研究准噶尔对伊犁及西天山古生代构造演化的地质影响时，将其作为一个大陆块体。前寒武纪结晶基底广泛分布在天山地区，它们的形成环境和时代是划分天山大地构造单元和认识各单元构造属性的基本依据。

3．西天山地区发育多处蛇绿混杂岩，它们属于三条不同时代、不同构造属性的蛇绿混杂岩带，分别位于北天山巴音沟、中天山北缘米什沟-哈尔克山北麓穹库什太一带和南天山黑英山-库勒-库米什一带。巴音沟蛇绿混杂岩形成于晚古生代，代表一个有限洋盆；米什沟-穹库什太蛇绿混杂岩形成于早古生代，与洋盆扩张或洋岛活动有关；而南天山蛇绿混杂岩的时代为中-晚古生代，一般认为其形成于弱扩张的洋盆或弧后盆地环境。这些蛇绿混杂岩带在构造背景与形成时代上，与东天山蛇绿混杂岩的对应关系目前仍没有统一的认识。

4．现有的天山构造演化模式表明，天山是由多个地块及周围洋盆在古生代期间经过多期俯冲、碰撞造山作用形成的，在造山作用后期发生了区域走滑剪切事件。但不同的演化模式中，关于洋壳俯冲方向、俯冲-碰撞时代的认识尚有争议。另外，天山的构造演化在东、西天山相互联系上也存在类似的问题。

第三章 伊犁晚古生代活动大陆边缘

在伊犁盆地的周缘，广泛分布有石炭纪和二叠纪的火山岩（新疆地矿局，1993），这些火山岩的构造环境对认识天山造山带的形成与演化具有重要意义。近 30 年来，前人对该地区部分剖面的火山岩进行了岩石学和地球化学研究，划分出两类不同成因环境的火山岩系，一类为钙碱性岛弧火山岩，另一类为双峰式裂谷火山岩。然而，对不同成因类型火山岩的形成时代和构造意义仍存在争议，即石炭纪火山岩为岛弧型而二叠纪火山岩为裂谷型（姜常义等，1995；Gao et al., 1998；朱永峰等，2005；李注苍等，2006），或者石炭纪-二叠纪火山岩均为双峰式裂谷型（车自成等，1994，1996；Xia et al., 2003; 2004；夏祖春等，2005）。对这些火山岩构造属性认识的差异，导致对北天山及伊犁陆块晚古生代构造演化完全不同的解释。另外，由于缺少关于伊犁地区火山岩的精确定年数据，因此以往的研究通常以新疆地区不同比例尺地质图为依据来确定地层时代。最近，有研究者通过对伊犁南部原石炭纪火山岩的锆石 U-Pb SHRIMP 定年发现，有些火山岩的年龄老于石炭纪下限年龄（翟伟等，2006），而有些下石炭统火山岩的年龄为晚石炭世（朱永峰等，2005，2006），因此提出解体部分岩组的认识（朱永峰等，2006）。迄今为止，很少有研究者将该地区火山岩与侵入岩结合起来研究，也较少从岩石地球化学、同位素地球化学和年代学等方面进行系统的研究，同时也很少对与岩浆岩相伴生的沉积岩进行分析研究。本论文选择了伊犁地区 6 条典型的剖面，对石炭纪沉积岩、火山岩和侵入岩进行了岩相学、岩石地球化学、同位素地质学和放射性年代学研究，旨在探讨火成岩的物质来源与构造环境、岩浆岩的形成时代以及大地构造意义。

第一节 石炭纪火山岩浆与沉积序列

1．剖面描述

本论文所选择的六个剖面为：伊宁阿希金矿、尼勒克-唐布拉、玉希-那拉提、昭苏、特克斯和新源剖面（图 3-1）。

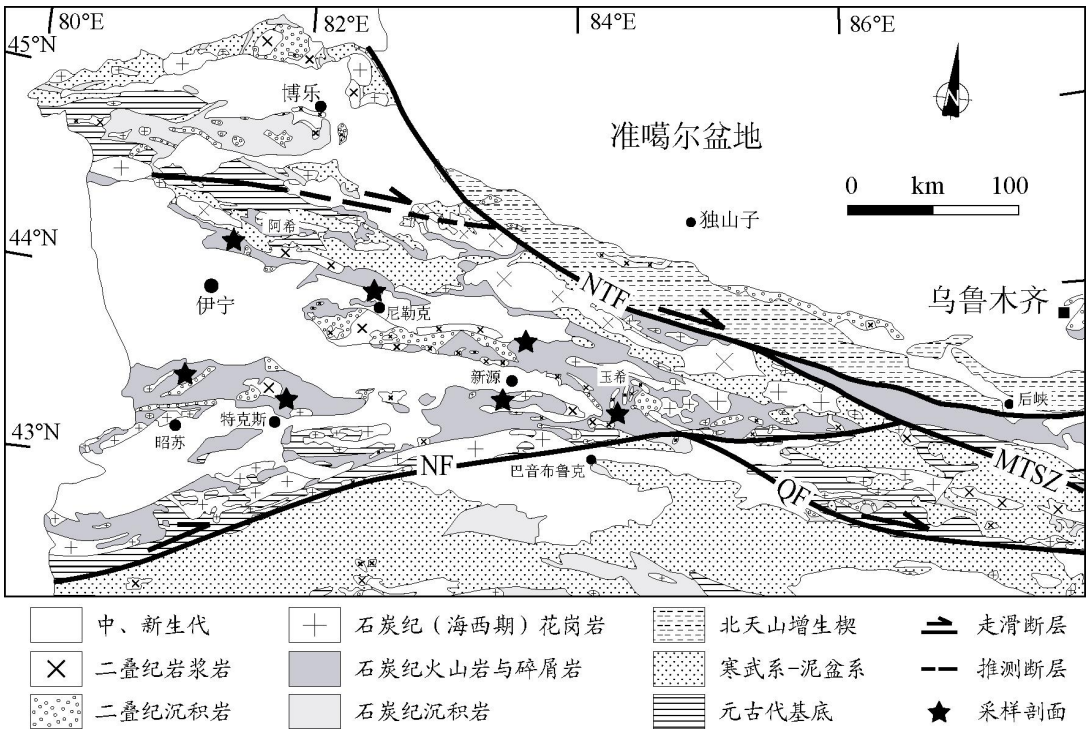

图 3-1 伊犁地区石炭纪地层分布图及主要剖面位置图

NTF，北天山断裂；NF，那拉提断裂；MTSZ，天山主断裂；QF，青布拉克断裂

1.1. 伊宁阿希金矿剖面

该剖面位于伊宁县北 30km 处，沿阿希金矿公路分布，脆性断裂发育，各时代地层多以断层接触。剖面总体上为一背斜构造，核部为奥陶系-志留系薄层灰岩、泥质砂岩和硅质岩；背斜的南翼由下石炭统大哈拉军山组（C_1d）、上石炭统脑盖图组（C_2n）和奥依曼布拉克组（C_2o）组成（新疆地质矿产局，1993；姜晓玮等，2002），北翼则只发育下石炭统 C_1d，上石炭统缺失。C_1d 主要由上部的凝灰砾岩、安山质角砾熔岩与下部的中-酸性火山碎屑岩、中-基性熔岩组成。C_2n 为中-酸性火山碎屑岩夹砂岩和砂砾岩。C_2o 下部主要为中-酸性熔岩、火山碎屑岩、凝灰质砂岩；上部主要为砂岩、薄层灰岩（图 3-2a）。石炭纪火山-沉积岩序列厚达 3000m。在 C_2o 中产有石炭纪蜓类（Fusulinella sp.）和珊瑚（Timania）化石。另外，李华芹等（1998）在 C_1d 的安山岩中得到 345.9±9Ma 的辉石 Rb-Sr 年龄和 325.1±0.6 Ma $^{40}Ar/^{39}Ar$ 坪年龄。剖面以北，石炭纪地层不整合于上奥陶统呼独克达坂组（O_3h）灰岩之上，或者与前寒武纪结晶基底青白口系（Qn）、蓟县系（Jx）和震旦系凯拉克提群（Zkl）叠层石大理岩断层接触（图 3-2a）。剖面的南侧，二叠纪砾岩、砂岩和粉砂岩不整合覆盖在石炭纪地层之上，三叠纪-侏罗纪陆源碎屑岩极为发育并含有煤层。

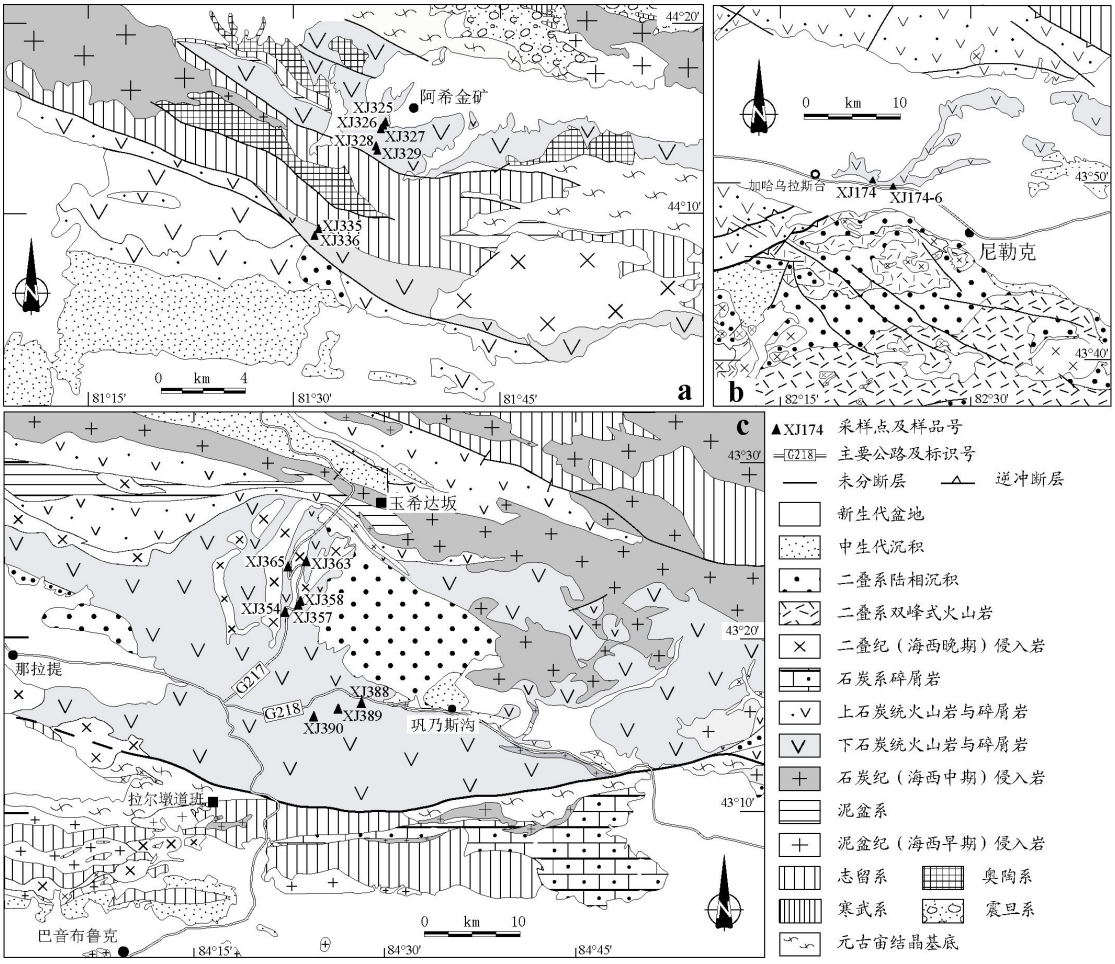

图 3-2 伊宁（a）、尼勒克（b）和那拉提（c）地区地质图

1.2. 尼勒克-唐布拉剖面

该剖面分尼勒克段和唐布拉段。前者位于尼勒克县城与加哈乌拉斯台之间的 315 公路和加哈乌拉斯台以北东 20km 处（图 3-2b）。石炭纪地层为美洛卡河组（C_1m）、阿恰勒河组（C_1a）和东图津河组（C_2d）。C_1m 由凝灰质火山熔岩、火山碎屑岩以及少量英安斑岩组成，主要发育在加哈乌拉斯台以北的博罗科努山南坡。C_1a 主要由中-酸性火山碎屑岩和薄层灰岩、砂岩与砂砾岩组成，在砂岩和灰岩中存在芦木（Calamites sp.）等化石（新疆地矿局，1980）。C_2d

则主要包括凝灰岩、凝灰质粉砂岩、砂岩、砾岩，主要分布在尼勒克县城以西的阿吾拉勒山。可能受二叠纪岩浆热液作用影响，C_2d 中断层、裂隙发育并被石膏层充填。C_1a 以底部砾岩不整合于 C_1m 之上，与 C_2d 的接触关系在野外不易观察。其中，下石炭统地层厚度达 3000m，上石炭统约 1000m 左右。

唐布拉段位于尼勒克县东 90km 的喀什河谷（图 3-1），下石炭统阿吾拉勒组（C_1aw）被上石炭统吐尔拱组（C_2t）不整合覆盖，前者包括安山玢岩、安山岩、中性凝灰岩、流纹斑岩、霏细斑岩、生物碎屑灰岩、砂屑灰岩和钙质粉砂岩，后者则主要由石英钠长斑岩、杏仁状安山玢岩、橄榄玄武岩、火山角砾岩和凝灰质砂砾岩等组成（新疆地矿局，1975）。二者均被侏罗纪煤系地层所覆盖。

1.3. 玉希−那拉提剖面

该剖面可分为两段，第一段从拉尔墩道班沿 217 国道至玉希达坂，由大量上石炭统吐尔拱组（C_2t）碎屑凝灰岩、安山玢岩、霏细斑岩、英安斑岩、石英钠长斑岩和玄武质熔岩等组成，底部发育有少量紫红色凝灰质砂岩，岩相学特征与唐布拉地区的同一岩组类似，岩层厚度约 2500m。大量红色花岗岩、花岗闪长岩侵入到火山岩中。第二段沿 218 国道分布于那拉提镇至巩乃斯牧场之间，为下石炭统雅满苏组（C_1y），岩性主要由巨厚层（>4000m）安山岩、杏仁状安山玢岩、少量玄武玢岩和中-酸性晶屑、岩屑凝灰质火山岩组成，凝灰岩中含有珊瑚和腕足类化石（新疆地矿局，1993）（图 3-2c）。朱永锋等（2005）从 C_2t（原文指 C_1d）粗面安山岩获得锆石 U-Pb SHRIMP 年龄为 312.8±4.2 Ma。值得指出的是，C_2t 和 C_1y 的岩相学特征与出露在那拉提达坂南坡的上石炭统（C_2）地层完全不同，后者主要由肉红色灰岩、黄褐色粗砂岩、长石石英砂岩、碳质泥岩、粉砂岩等组成，含植物化石，未见任何火山碎屑成分。二者之间以那拉提断裂为界（图 3-1，图 3-2c）。

1.4. 昭苏剖面

在伊犁盆地中，乌孙山位于昭苏县北 10-60km 范围内，东西向展布（图 3-1），主要由石炭纪岩层组成。沿伊宁-昭苏公路，石炭系包括三个岩组：下石炭统大哈拉军山组（C_1d）、阿克沙克组（C_1a）和上石炭统伊什基里克组（C_2y）。C_1d 主要分布在乌孙山南坡，下部由底砾岩、钙质砂岩、薄层灰岩、凝灰质砂岩、安山集块岩组成；上部主要为杏仁状安山岩、安山玢岩以及少量流纹岩、霏细岩、英安斑岩、凝灰岩夹凝灰质砂岩。C_1a 主要为灰白色厚层状生物碎屑灰岩、薄层泥质灰岩、浅黄色砂砾岩和紫红色砂岩，夹有少量火山凝灰岩。C_2y 主要出露在乌孙山北坡。其下部的紫红色砾岩、砂砾岩和火山碎屑砂岩不整合覆盖于下石炭统的生物碎屑灰岩之上。这一不整合现象可以在昭苏县北安各列特达坂观察到。在砂砾岩之上，发育有厚层安山质凝灰岩、安山玢岩、砖红色流纹岩、流纹斑岩以及玄武岩岩墙。

据新疆地矿局（1993），C_1a 假整合于 C_1d 之上。经过对该剖面为期一周的反复考察，作者发现整个剖面由多个沉积-喷发旋回组成，每个旋回基本上以浅水相碎屑岩、火山碎屑岩和火山岩由底到顶依次分布（图 3-3a）。在剖面的最南端，即昭苏县北 3-5km 范围内，两期花岗岩体侵入到 C_1d 火山沉积岩当中，早期岩体为黑云母斜长石花岗岩，而晚期岩体则为紫红色钾长石花岗岩，后者同时也侵入于早期花岗岩体中（图 3-3a）。高俊（1993）从黑云母花岗岩中获得 345.6Ma 和 334.4Ma 的 Ar-Ar 年龄。钱青等（2006）认为，昭苏北部 C_1d 火山岩形成于具有元古代陆壳基底的活动大陆边缘弧后拉张环境。

整个剖面受后期构造作用影响，发育有一系列不同性质的断层，如在安各列特达坂，多条东西向直立的走滑断层和（或）正断层切割灰岩、砂岩和火山岩地层（图 3-3a），导致它们在平面上呈透镜状产出。鉴于这些走滑断层同时切割了不整合覆盖在石炭系之上的上二叠统红色砾岩，因此它们应该是中、新生代的构造事件，很可能与 NWW-SEE 向的尼勒克断层（Zhao et al., 2003）同属一个构造体系。在安各列特达坂的南北两侧，普遍发育逆冲断层（图 3-3a），可能与新生代陆内变形有关。

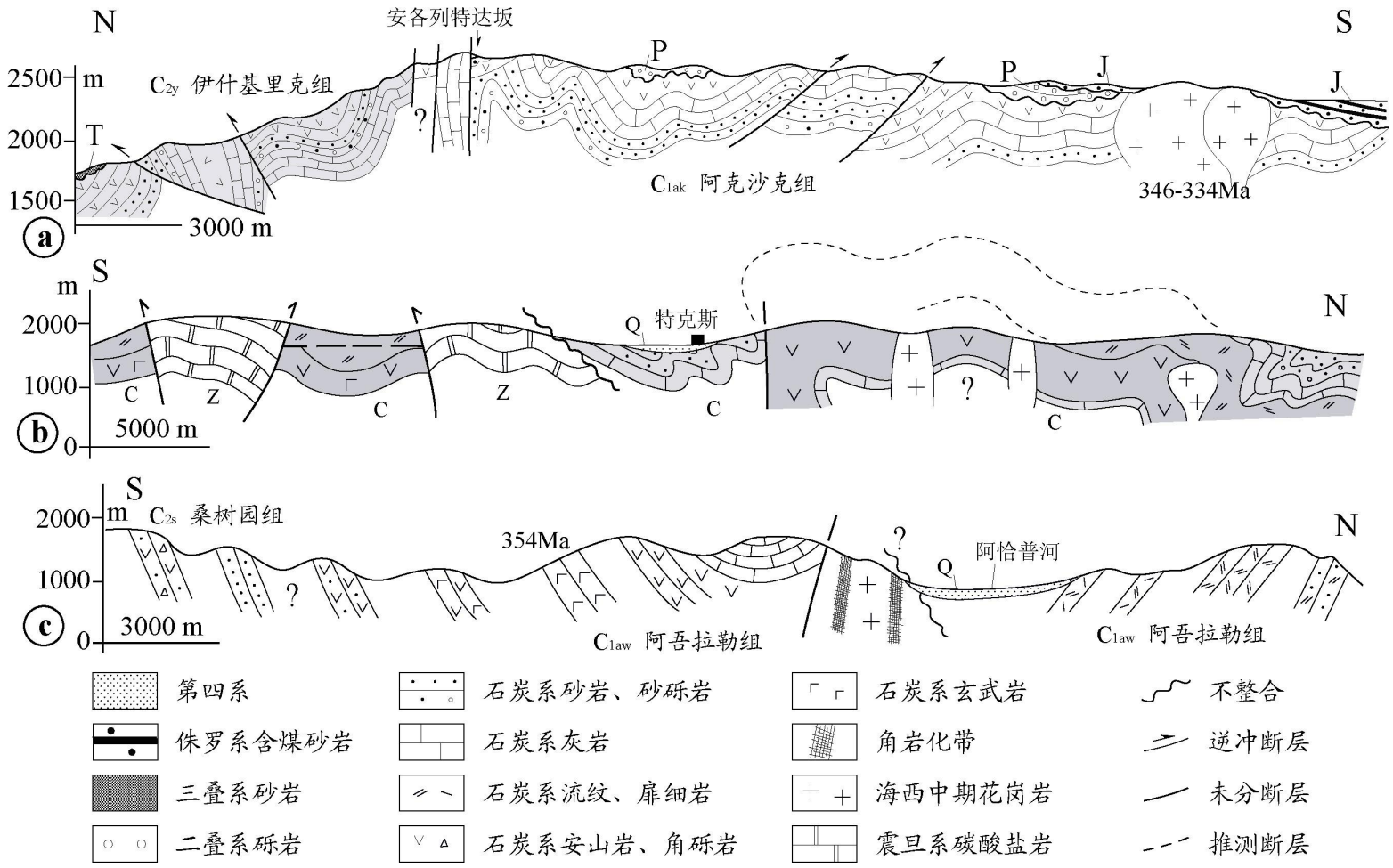

图 3-3 昭苏（a）、特克斯（b）和新源（c）地区地质剖面图

1.5. 特克斯剖面

该剖面分南北两段。其中北段位于特克斯县北的乌孙山，属于昭苏剖面的东延，岩组与岩性特征与昭苏剖面具有走向上的一致性。但不同的是，早石炭世陆源碎屑岩分布较少，仅在该段南侧和北侧分别出露有宽 1000m 和 300m 的灰岩、砂岩、砂砾岩等，且产状陡立，与本剖面北段主体部分的火山岩呈断层接触，上下层位关系不清（图 3-3b）。在剖面的北端，灰白色中层状灰岩中含有大量的生物化石，主要为海百合茎和贝类化石。在灰岩与火山岩接触带，安山质火山碎屑物附着于灰岩底部，二者之间紧密整合、逐渐过度，表明火山作用同时或稍早于灰岩沉积作用。火山岩主要包括玄武质安山岩、砖红色安山岩、紫红色流纹岩、火山碎屑岩等。其中流纹岩偶见典型的流纹构造，火山碎屑岩中也发育流动构造以及浆屑和岩屑，表明其形成于喷发高峰期。另外，与火山岩伴生有大量侵入岩体和次火山岩（图 3-3b）。

本剖面南段位于特克斯县南至哈尔克山北麓，石炭纪地层沿科克苏河下游出露。阿克沙克组（C_1a）砂岩、砂砾岩和薄层灰岩不整合覆盖于前寒武纪结晶基底之上，后者由震旦系特克斯群（Z_{tk}）、库什太群（Z_{qks}）和科克苏群（Z_{kks}）组成，岩石主要为叠层石灰岩、大理岩和白云岩（图 3-3b），类似于伊犁地块北缘赛里木湖地区震旦系凯拉克提群（Z_{kl}）（图 3-1）。在剖面的南侧，震旦系碳酸盐岩受后期构造作用，逆冲推覆于大哈拉军山组（C_1d）火山岩之上。C_1d 由上部的流纹岩、霏细岩和下部的安山岩、安山质硬砂岩、杏仁状安山岩、气孔状玄武安山岩组成。流纹岩的顶部有一不连续面，其上为团块状流纹岩，其下为褶皱变形的火山岩和火山碎屑岩地层（图 3-3b）。由于火山岩南、北界均被逆冲断层所限，并且不连续面上、下的流纹岩岩相学特征没有明显的区别，因而该不连续面可能为后期的局部构造推覆面。

1.6. 新源剖面

沿新源县以南的恰合普河谷两侧，由南向北分别发育上石炭统桑树园组（C_2s）和下石炭统阿吾拉勒组（C_1aw）地层（新疆地矿局,1993）。详细的野外调查表明，该剖面从南向北依次出露凝灰质砂岩、硬砂岩、生物碎屑灰岩、火山碎屑岩、杏仁状玄武岩、柱状橄榄玄武岩、辉石安山岩、英安质流纹斑岩、流纹质砂岩等。剖面长 30km, 地层厚度约 2000m。南侧火山碎屑岩和玄武质岩石的平均产状为 320°∠50°，北侧安山岩和流纹质砂岩地层的产状则明显不同，为 130°∠50°（图 3-3c）。二者之间的界限被古近纪山间盆地所覆盖，因而难以识别。从凝灰质沉积岩-玄武质火山岩-安山质火山岩-流纹质火山岩等在空间和层位上的演化来看，这一序列应该代表一个完整的喷发旋回，因此安山岩、流纹岩应归于玄武质火山岩的上覆岩层，二者之间的产状差异可能是由于喷发间隙的局部构造运动造成的不整合，也可能是后期构造作用引起的断层接触。朱永锋等（2005）从该剖面玄武岩中获得锆石 U-Pb SHRIMP 年龄为 353.7±4.5Ma。因此，该玄武岩以及下伏的凝灰质岩石应归为下石炭统而非上石炭统的桑树园组。在剖面北侧，黑云母斜长石花岗岩侵入到玄武质凝灰岩中，并在岩体周缘发生角岩化（图 3-3c）。

2．区域火山岩浆–沉积序列对比

由以上剖面介绍及图 3-4 中可以发现，伊犁地区石炭纪火山岩与沉积岩紧密伴生。火山岩以中性为主，酸性此之，基性仅出现在个别剖面的个别层位。沉积岩主要为浅水相碎屑岩，包括薄层状砂质灰岩、砂岩和砾岩等，未见同时代深水相沉积岩，如硅质岩。火山岩与沉积岩交互出现，呈互层产出。虽然在不同的剖面被划归为不同的岩组，但总体而言，伊犁地区至少从早石炭世开始，出现过多次沉积-火山喷发-再沉积-再次火山喷发的旋回，直至晚石炭世晚期，仍有少量的火山喷发记录。另外，火山岩与沉积岩均被海西中期（γ_4^2）的花岗质岩石侵入，构成完整的石炭纪岩浆-沉积岩序列。

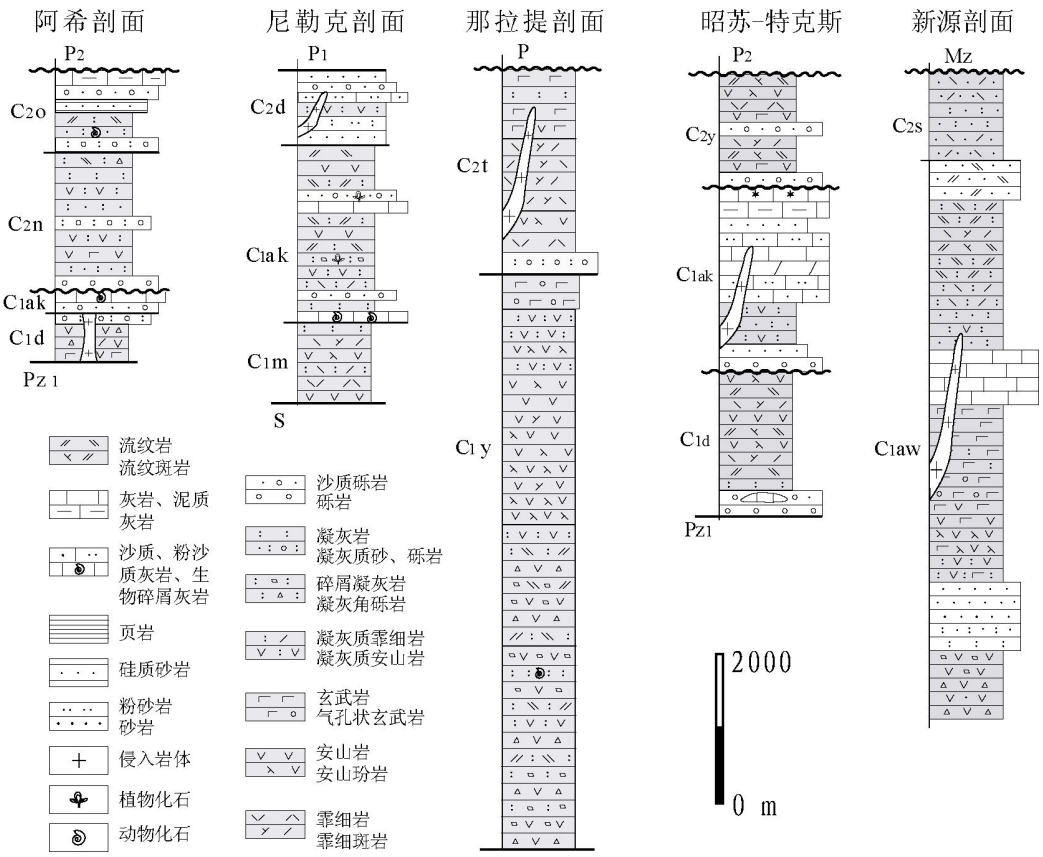

图 3-4 伊犁地区石炭系地层柱状图

第二节 石炭纪岩浆岩岩石、地球化学特征

笔者经过四年的野外考察，从以上 6 个剖面中采集了数百件火山岩和花岗岩样品。火山岩大多呈致密块状，微晶至细粒状，少数为粗粒状，可见长石或石英斑晶，如雅满苏组（C_1y）安山玢岩以粗大的中长石斑晶为特征，中长石粒径达 2~5 cm。多数岩石为暗紫红色或灰绿色。花岗岩主要为粗粒、等粒结构，无变形、未变质。采样中特别注意选取新鲜、未受风化、裂隙不发育以及蚀变程度尽可能低的手标本，对于那些局部发生蚀变的样品，在进行室内处理前，首先切除了受过蚀变或不纯净的部分。

1．岩石学特征

经过对岩石薄片的显微观察，发现所有岩石都具有明显的火山结构：大量长石斑晶分散于玻璃质或微结晶的基质中（图 3-5a~g），长石斑晶呈自形和半自形（图 3-5a,d,e,g）；在结晶基质中，长石多为针状（图 3-5c,e,g），少数具有自形特征（图 3-5c,g）。有些长石具有环带构造（图 3-5d）或者双晶（图 3-5a,e,g），部分长石矿物被后期交代为方解石或钠长石（图 3-5d）。在有些样品中可见气孔和杏仁构造，气孔通常被后期结晶的方解石或石英充填（图 3-5e）。在部分玄武岩和安山岩样品中可见辉石矿物斑晶（图 3-5c），其中个别辉石局部被蚀变为绿帘石或绿泥石（图 3-5b），或被氧化为铁的氧化物（图 3-5d）。

黑云母花岗岩主要由石英、斜长石、角闪石、黑云母组成，长石多见聚片双晶，黑云母解理发育，石英晶形完好（图 3-5h）。岩石大多具有等粒结构。钾长石花岗岩则主要含有钾长石、石英，偶见黑云母等暗色矿物，多为不等粒结构。花岗岩中含有 5%左右的不透明矿物，经扫描电镜观察，这些不透明矿物主要包括氧化物和硅酸盐、磷酸盐矿物如锆石、独居石等，它们可用来进一步研究这些花岗岩的年龄（见本章第五节）。

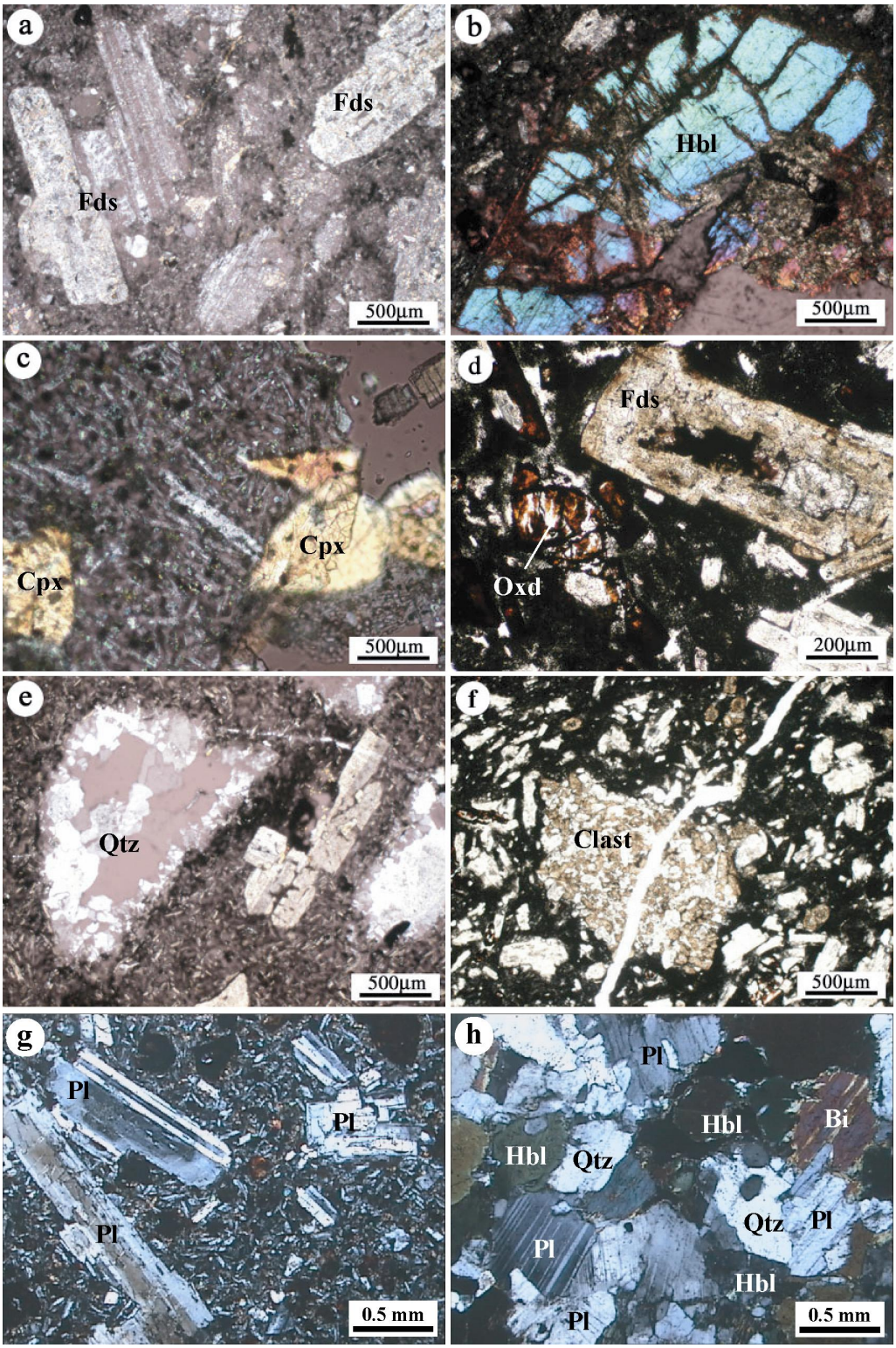

图 3-5 伊犁地区石炭纪岩浆岩显微照片

Bi，黑云母；Cpx,辉石；Fds,长石；Hbl,角闪石；Oxd，氧化物；Pl，斜长石，Qtz，石英

为了解样品的蚀变程度，对代表性火山岩进行了电子探针下的矿物成分测定。将样品切制成光薄片，并在南京大学内生矿床成矿机制国家重点实验室的 JEOL JXA-8800 M 型电子探针仪中进行测试。测试条件为 20 kV 电压和 2 x 10^{-8}A 电子束宽度，标定矿物包括自然与合成矿物。分析结果（表 3-1）表明，相当一部分长石矿物已被钠长石或方解石所替代，反映了后期低温条件下的重结晶作用。由此可见，虽然绝大多数样品在宏观和微观尺度均未发

现明显蚀变作用的痕迹，但它们仍经历了一定程度的矿物、化学成分的改变。

表 3-1 伊犁石炭纪火山岩矿物成分电子探针分析结果（%）

样品号	XJ325					XJ-354		XJ-388			XJ-390		
分析号	1	2	3	4	5	6	7	8	9	10	11	12	13
矿物	Ab(C)	Ab(C)		Sx(R)	Ab(C)	Ab(C)	Ab(C)	Hb(C)	Cal(C)	Hb(C)	Cal(R)	Ab(C)	Ab(C)
Na_2O	11.67	0.08	0.02	0.01	10.11	11.67	10.24	0.41	0.08	0.31	0.04	10.35	9.37
K_2O	0.12	0.02	1.83	0.03	0.24	0.07	0.27	0.02	0.00	-	0.02	0.58	0.69
MnO	0.00	0.30	-	-	0.02	-	0.01	0.09	2.18	0.15	1.45	0.09	-
MgO	0.91	1.76	8.89	0.15	1.53	0.00	0.06	13.39	0.39	14.69	0.41	0.06	0.08
TiO_2	0.04	0.14	0.92	0.08	0.04	0.01	-	0.78	0.01	0.48	-	0.09	0.02
FeO	0.46	0.80	5.58	3.65	0.63	0.06	0.31	7.88	0.45	7.20	0.33	0.63	0.71
Al_2O_3	22.09	0.62	31.18	0.44	20.91	20.55	21.54	5.99	0.16	4.14	0.15	21.83	22.22
CaO	0.44	52.54	0.28	-	3.48	2.20	0.34	22.01	56.58	21.74	56.74	0.59	0.62
SiO_2	65.48	3.24	41.61	93.36	62.84	66.63	67.13	48.70	1.32	49.72	0.38	66.70	66.00
Total	101.2	59.5	90.3	97.7	99.8	101.2	99.9	99.3	61.2	98.4	59.5	100.9	99.7

注：Ab，钠长石；Sx，燧石；Hb，角闪石；Cal，方解石；C，矿物中心；R，矿物边缘

2．地球化学特征

在研究岩石薄片的基础上，从 6 个剖面中选择蚀变微弱、具有代表性的 49 个火山岩（表 3-2）和 10 个花岗岩（表 3-3）样品进行了 XRF 主量元素分析和 ICP-MS（PE-Elan 6000 ICP-MS 分析仪）微量元素分析。为了对比数据的可靠性，这些样品被分为两部分，分别在中科院广州地球化学研究所和法国南锡实验室测试。主量元素分析误差为 1%~1.5%，绝大部分微量元素的分析误差为 0.7%-5%，个别样品 U 和 Th 的误差接近 10%。

2.1. 火山岩地球化学特征

2.1.1 主量元素

从表 3-2 可以看出，火山岩样品的挥发份（LOI）含量为 0.61%~10.84%，其中绝大部分（38/49）小于 5%，个别（7/49）大于 7%，说明大多数样品没有经受强烈的蚀变。绝大多数样品 SiO_2 含量介于 43.4%~69.1%之间（除了 XJ358 为 36.6%及 7 个样品 SiO_2>70%），并均匀分布。全碱（AK=Na_2O+K_2O）含量为 1.45%~10.2%（XJ358 为 0.32%），且大多数样品的 K_2O<Na_2O。由 SiO_2-AK 投影图（Le Bas et al., 1986；Le Maitre et al., 1989；Irvine et al., 1971）（图 3-6a）可以看出，伊犁地区 6 个剖面的火山岩均表现为从基性、中性到酸性的完整序列，由玄武岩、粗面玄武岩、苦橄玄武岩、碱玄岩、玄武安山岩、玄武质粗安岩、玄武粗面岩、粗面岩、粗面安山岩、安山岩、流纹岩、英安岩和粗面英安岩等组成。另外，阿希、昭苏、特克斯和新源剖面的火山岩均处于钙碱性系列范围，而尼勒克-唐布拉剖面的火山岩处于从钙碱性系列到碱性系列的过渡区域，而玉希-那拉提地区的火山岩则为碱性系列（图 3-6a）。

阿希和昭苏火山岩以及 8/10 特克斯火山岩、3/4 新源火山岩、4/8 尼勒克-唐布拉火山岩和 3/11 玉希火山岩的里特曼指数（$\sigma=AK^2/(SiO_2-43)$）小于 3.3，属于钙碱系列；4/8 尼勒克-唐布拉火山岩、5/11 玉希-那拉提火山岩、1/10 特克斯火山岩及 1/4 新源火山岩的 σ 处于 3.3~9 之间，为过渡系列；3/11 玉希-那拉提火山岩和 1/10 特克斯火山岩的 σ 大于 9，属于偏碱性系列。大部分火山岩含有较高的 Al_2O_3（64%的样品 Al_2O_3>10%），相应的铝饱和度 ASI（$=Al_2O_3/mol_{Al}$）/($Na_2O/mol_{Na}+K_2O/mol_K+CaO/mol_{Ca}$)） 为 0.74~1.25。这些火山岩 MgO 含量较低（<10%，除 XJ522 为 11.7%），同时，它们还有低 CaO 的特点（所有样品 CaO<10%，其中 39/49 样品的 CaO 含量小于 5%）。TiO_2 的含量变化较大，低钛火山岩（4/8 尼勒克火山岩、8/11 玉希火山岩和阿希火山岩）TiO_2 为 0.38~2.22%, 高钛火山岩（4/8 唐布拉火山岩、3/11 玉希火山岩及昭苏、特克斯火山岩）的 TiO_2 为 11.6~20.3%。

表 3-2 伊犁地区石炭纪火山岩主量元素地球化学分析结果（%）

样品号	SiO_2	TiO_2	Al_2O_3	Fe_2O_3	MnO	MgO	CaO	Na_2O	K_2O	P_2O_5	LOI	Total
尼勒克-唐布拉剖面												
XJ174	49.70	0.99	19.60	10.26	0.40	4.33	4.92	4.80	0.99	0.25	4.52	100.75
XJ174-1	50.61	0.93	19.02	9.74	0.22	3.94	7.19	4.12	1.22	0.24	2.72	99.95
XJ174-2	46.52	1.91	17.95	10.46	0.24	6.69	8.89	3.38	0.24	0.36	4.27	100.90
XJ174-6	66.54	0.71	15.86	4.30	0.14	1.29	1.16	5.36	4.01	0.16	1.21	100.72
XJ572	77.06	12.50	1.74	0.04	0.26	0.27	0.93	4.09	0.20	0.04	2.06	99.18
XJ575	63.28	15.45	5.86	0.11	1.61	3.24	4.35	2.69	0.59	0.19	2.06	99.43
XJ575A	73.33	13.46	2.36	0.04	0.48	2.64	3.13	2.05	0.18	0.05	2.38	100.08
XJ577	57.78	16.14	10.02	0.29	3.06	2.73	4.65	0.96	0.77	0.28	4.06	100.73
阿希剖面												
XJ325	53.42	0.84	16.54	8.21	0.12	3.13	6.83	3.05	0.60	0.16	8.39	101.29
XJ326	54.04	0.85	16.78	7.21	0.13	3.40	7.99	2.80	0.52	0.16	7.79	101.67
XJ327	53.18	0.94	17.20	7.94	0.13	5.98	3.32	5.21	0.22	0.18	5.96	100.26
XJ328	55.19	1.21	16.55	7.52	0.12	4.43	6.97	3.21	2.24	0.25	2.23	99.91
XJ329	59.21	0.90	16.32	5.58	0.10	3.30	3.51	3.32	2.97	0.18	4.42	99.79
XJ335	68.81	0.44	15.71	3.12	0.13	0.36	1.46	3.88	4.12	0.12	2.09	100.23
XJ335-1	67.42	0.38	14.15	1.91	0.19	0.41	5.06	1.55	3.49	0.11	5.98	100.64
XJ336	68.83	0.43	15.62	2.52	0.11	0.36	1.75	4.24	3.16	0.10	2.51	99.63
玉希-那拉提剖面												
XJ363	57.43	0.98	17.51	7.33	0.19	1.56	2.63	3.68	6.53	0.60	1.45	99.88
XJ365	68.71	0.89	13.00	4.18	0.13	0.69	1.12	2.82	6.58	0.19	0.89	99.20
XJ388	46.63	0.94	18.44	8.32	0.70	3.57	8.83	2.81	3.77	0.28	5.88	100.18
XJ389	46.56	0.90	17.28	8.96	1.18	2.67	6.55	2.66	6.27	0.23	6.45	99.69
XJ390	50.05	1.11	18.60	9.65	0.30	2.94	4.52	6.13	1.59	0.22	5.36	100.46
XJ354	56.15	0.85	17.63	8.49	0.20	1.95	1.81	3.11	7.05	0.54	1.73	99.50
XJ357	55.93	2.22	13.86	10.48	0.36	2.82	3.97	4.43	3.40	0.92	1.41	99.80
XJ358	36.55	1.80	26.61	24.62	0.15	0.02	0.26	0.10	0.22	0.58	9.44	100.36
XJ580	53.86	20.32	5.90	0.11	1.78	6.81	3.48	4.64	0.71	0.47	2.41	100.50
XJ582	46.17	16.00	11.40	0.25	7.48	6.62	1.54	5.00	1.62	0.47	3.99	100.54
XJ585-1	48.47	17.86	9.43	0.19	4.94	6.48	2.77	1.62	1.01	0.23	7.49	100.48
昭苏剖面												
XJ495-3	50.69	18.47	10.35	0.19	4.85	8.89	3.11	0.98	0.95	0.20	1.75	100.43
XJ495-4	76.65	12.30	2.39	0.03	0.14	0.72	5.42	1.16	0.29	0.06	0.83	99.98
XJ496	51.07	16.70	11.82	0.20	4.61	8.76	3.15	1.32	1.45	0.44	1.10	100.61
XJ497	49.52	18.70	10.43	0.19	3.66	7.78	4.24	1.56	1.28	0.37	2.57	100.30
XJ500	53.10	15.43	12.81	0.27	4.57	2.92	4.92	0.42	1.68	0.56	4.19	100.88
XJ502	48.81	19.02	11.30	0.29	3.48	9.50	3.43	0.74	1.63	0.30	2.38	100.88
XJ512	72.38	13.33	2.25	0.03	0.38	1.44	2.83	5.30	0.29	0.03	2.16	100.43
XJ516-2	50.11	16.01	7.89	0.12	4.98	7.89	1.87	2.90	0.85	0.26	7.85	100.72
特克斯剖面												
XJ517-1	61.02	18.10	5.16	0.11	1.55	2.40	5.20	2.95	0.67	0.27	2.08	99.51
XJ517-3	65.65	15.61	4.19	0.10	1.45	2.28	4.62	2.12	0.48	0.17	3.49	100.16
XJ517-2	64.40	16.33	5.12	0.11	1.49	1.64	5.53	1.96	0.62	0.24	2.32	99.75
XJ520-1	54.88	15.82	8.63	0.16	5.09	8.91	2.36	0.58	1.09	0.25	2.75	100.51
XJ520-2	54.21	15.71	9.35	0.18	5.94	8.17	2.34	1.43	1.10	0.24	1.94	100.61
XJ521	57.06	15.91	7.62	0.18	4.55	7.78	2.62	0.68	0.93	0.23	3.25	100.79
XJ522	43.41	15.70	8.65	0.15	5.36	11.73	2.76	0.94	1.09	0.22	10.84	100.86
XJ530	79.55	11.60	1.23	0.02	0.21	0.17	2.25	3.61	0.10	< L.D.	1.53	100.25
XJ537	71.02	13.99	3.24	0.05	0.39	1.68	3.19	4.59	0.45	0.10	1.40	100.11
XJ538	45.22	15.61	10.16	0.11	3.81	10.01	3.04	2.11	1.25	0.47	7.89	99.68
新源剖面												
XJ553-1	48.39	16.05	10.54	0.19	7.62	6.98	3.71	1.43	1.40	0.53	3.67	100.50
XJ553-2	47.71	16.70	10.03	0.25	8.35	6.61	3.70	1.20	1.31	0.45	4.40	100.69
XJ555	72.50	11.50	4.86	0.07	0.25	1.02	2.09	6.39	0.26	0.04	0.61	99.59
XJ554	46.47	16.61	11.58	0.23	6.28	9.29	2.98	1.81	1.64	0.72	2.64	100.25

LOI：烧失量（或挥发组分，loss of ignition）

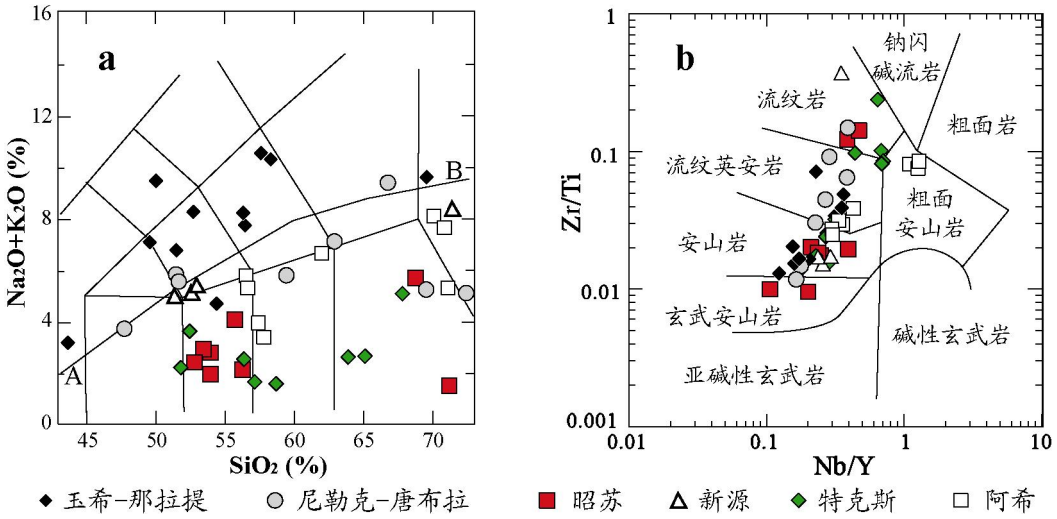

图 3-6 伊犁石炭纪火山岩 SiO_2-AK (TAS) 图解与 Nb/Y-Zr/Ti 图解

（a 中 AB 线之上为碱性系列，之下为钙碱性系列）

2.1.2 微量元素特征

由上文所述可以看出，大部分样品虽然没有经受显著的风化或蚀变，但却发生了低温条件下的矿物与化学成分改变。另外，部分样品含有较高的挥发组分，表明它们的主量元素成分在岩石形成过程中或成岩之后可能发生了的变化，至少部分地不能正确反映其岩浆特征和形成环境。相对于主量元素来说，微量元素在岩浆上升过程中和岩石形成以后，都比较稳定，不易受到大陆地壳混染和后期蚀变的影响，所以能更准确地反映岩浆来源和形成环境。在 Nb/Y-Zr/Ti 图解（Winchester et al., 1976）（图 3-6b）中，6 个剖面的火山岩主要为中性-酸性的安山岩、流纹岩、流纹英安岩和中酸性粗面安山岩，以及少量的偏基性玄武质安山岩。从图 3-6b 可见，火山岩从中基性-中性-中酸性-酸性表现为线性演化趋势，具有典型的钙碱性火山岩系列的特征。从单个剖面的火山岩来看，同样具有类似的演化趋势，但在各个剖面之间并不能观察到钙碱性与碱性系列的差异。

从表 3-3 可见，6 个剖面的火山岩具有不同的稀土元素总量。昭苏火山岩的稀土元素总量为 46~153 ppm，尼勒克-唐布拉火山岩为 66~184 ppm，玉希-那拉提火山岩为 63~202 ppm（除 XJ388 为 517 ppm），特克斯火山岩为 82~215 ppm，阿希火山岩为 85~218 ppm，新源火山岩为 101~152 ppm。这些火山岩稀土总量与玄武岩或中性火山岩的特征。所有火山岩的轻稀土元素都比重稀土元素富集，∑LREE/∑HREE (L/H) >3。另外，$(La/Yb)_N$ 值为 2.66~12.6，且大多数火山岩（38/49）的$(La/Yb)_N$<6，表明这些火山岩的稀土元素分配模式具有钙碱性火山岩的特征。所有火山岩的球粒陨石标准化稀土元素配分曲线均向右缓倾（图 3-7），其中阿希和特克斯剖面火山岩的配分曲线较其他稍陡。在单个剖面内部，火山岩的配分曲线大多比较协调一致、且较为集中，表明岩浆分异作用并不十分明显。新源剖面火山岩样品 XJ555 具有与众不同的配分曲线特征，即重稀土含量随原子量增加而增加，且轻、重稀土含量之比也较低（L/H=3），类似于玻安岩（boninite）的特征。由于该类岩石在本次研究中并不多见，因此缺乏统计比较，故不深入讨论其成因。

除了少数样品（2 个尼勒克、2 个昭苏和 1 个特克斯剖面的火山岩）具有弱的 Eu 正异常（δEu= 1.04~1.1），以及个别火山岩无 Eu 异常以外，其他火山岩样品均表现为中等或弱的 Eu 负异常（δEu=0.54~0.99），反映了不同地区岩浆经历了类似的长石结晶分异作用过程。样品 XJ530 具有很强的 Eu 负异常（δEu=0.09），与同一剖面其他火山岩明显不同，这一现象很可能为局部岩浆经过强烈的结晶分异作用而析出大量长石矿物所致，但也不能排除测试误差的可能性。

表 3-3 伊犁地区石炭纪火山岩稀土元素地球化学分析结果（ppm）

样品号	La	Ce	Pr	Nd	Sm	Eu	Gd	Tb	Dy	Ho	Er	Tm	Yb	Lu	Σ_{REE}	L/H	δEu
尼勒克-唐布拉剖面																	
XJ174	10.23	22.99	3.11	13.96	3.24	1.19	3.76	0.57	3.44	0.70	1.90	0.28	1.87	0.31	67.54	4.27	1.04
XJ174-1	10.18	22.28	2.98	13.48	3.26	1.13	3.65	0.56	3.35	0.67	1.86	0.29	1.90	0.31	65.91	4.23	1.00
XJ174-2	10.67	31.30	4.69	21.97	5.35	1.98	6.31	0.95	5.46	1.10	2.83	0.43	2.87	0.46	96.37	3.73	1.04
XJ174-6	36.72	73.64	8.31	32.66	6.59	1.52	6.90	1.05	6.18	1.27	3.62	0.57	3.88	0.66	183.57	6.61	0.68
XJ572	22.65	48.35	5.45	19.59	3.83	0.65	3.20	0.54	3.45	0.73	2.32	0.39	2.88	0.47	114.48	7.20	0.55
XJ575	16.77	35.32	4.29	17.06	3.73	1.08	3.53	0.58	3.59	0.76	2.21	0.35	2.46	0.39	92.11	5.65	0.89
XJ575A	14.39	25.97	2.67	9.67	1.90	0.47	1.85	0.30	1.89	0.41	1.25	0.21	1.53	0.26	62.75	7.16	0.76
XJ577	14.77	31.31	4.07	17.19	4.00	1.11	4.02	0.63	3.98	0.78	2.26	0.34	2.30	0.38	87.15	4.93	0.84
阿希剖面																	
XJ325	14.73	32.35	3.94	15.99	3.70	0.99	3.87	0.62	3.55	0.71	2.04	0.32	2.11	0.34	85.25	5.29	0.79
XJ326	15.17	34.03	4.20	17.42	3.88	1.05	4.00	0.64	3.77	0.75	2.09	0.32	2.21	0.37	89.89	5.36	0.81
XJ327	18.67	41.36	5.08	20.14	4.39	1.23	4.64	0.71	4.18	0.86	2.34	0.36	2.40	0.39	106.75	5.72	0.83
XJ328	23.11	50.95	6.22	25.38	5.51	1.31	5.68	0.90	5.27	1.06	2.92	0.44	2.95	0.48	132.18	5.71	0.71
XJ329	27.55	58.06	6.76	26.29	5.57	1.17	5.27	0.84	4.88	0.99	2.69	0.42	2.64	0.43	143.53	6.91	0.65
XJ335	49.49	93.61	10.19	35.51	6.02	1.18	4.92	0.81	4.62	0.92	2.61	0.40	2.81	0.48	213.57	11.16	0.64
XJ335-1	41.37	81.05	8.94	31.35	5.84	1.42	5.16	0.82	4.31	0.82	2.34	0.35	2.39	0.39	186.55	10.25	0.77
XJ336	50.25	95.04	10.63	36.66	6.23	1.16	5.13	0.83	4.69	0.95	2.69	0.43	2.94	0.49	218.13	11.01	0.61
玉希-那拉提剖面																	
XJ363	29.06	68.60	8.59	34.45	7.41	1.46	6.58	0.96	5.20	1.03	2.84	0.45	2.89	0.49	170.01	7.32	0.63
XJ365	26.29	62.48	8.56	39.06	9.73	2.72	11.17	1.66	9.90	1.97	5.42	0.80	5.31	0.86	185.93	4.01	0.80
XJ388	38.68	164.60	39.01	213.20	36.19	5.21	7.62	0.78	3.87	0.84	2.63	0.46	3.42	0.57	517.08	24.61	0.66
XJ389	37.54	79.44	10.51	42.66	8.47	1.72	7.15	1.03	5.48	1.09	3.07	0.45	3.07	0.50	202.18	8.26	0.66
XJ390	25.54	62.73	8.94	39.34	9.88	2.32	11.03	1.73	10.37	2.12	6.18	0.95	6.32	1.04	188.47	3.74	0.68
XJ354	19.29	37.59	4.79	20.68	4.86	1.30	4.89	0.72	4.11	0.82	2.18	0.34	2.22	0.36	104.14	5.66	0.80
XJ357	12.60	26.94	3.53	16.06	3.84	0.95	4.20	0.61	3.56	0.73	2.01	0.30	2.00	0.33	77.66	4.65	0.72
XJ358	10.73	25.06	3.54	15.63	4.05	1.34	4.92	0.78	4.79	1.00	2.80	0.45	2.90	0.48	78.44	3.33	0.91
XJ580	25.52	54.69	6.57	26.14	5.17	1.42	4.39	0.64	3.55	0.68	1.90	0.28	1.99	0.32	133.26	8.69	0.89
XJ582	14.45	35.97	4.99	22.16	5.34	1.76	5.27	0.81	4.96	0.97	2.71	0.40	2.64	0.41	102.84	4.66	1.00
XJ585-1	9.83	22.20	2.93	12.71	3.16	0.95	3.13	0.49	3.03	0.61	1.75	0.26	1.69	0.26	63.00	4.62	0.92
昭苏剖面																	
XJ495-3	6.94	16.44	2.24	10.25	2.86	1.05	3.10	0.52	3.27	0.67	1.94	0.29	1.98	0.31	51.84	3.30	1.07
XJ495-4	6.59	15.56	2.01	8.40	2.07	0.43	2.12	0.42	2.82	0.64	2.06	0.35	2.60	0.43	46.49	3.07	0.61
XJ496	19.76	43.29	5.46	23.43	5.64	1.64	5.62	0.91	5.62	1.12	3.21	0.47	3.24	0.51	119.93	4.79	0.88
XJ497	16.98	37.21	4.70	20.34	4.87	1.46	4.87	0.79	4.70	0.96	2.71	0.40	2.70	0.43	103.11	4.88	0.90
XJ500	17.57	45.94	6.29	28.00	6.95	1.90	6.91	1.11	6.80	1.41	4.09	0.60	4.11	0.64	132.30	4.16	0.83
XJ502	11.65	26.07	3.50	15.64	4.07	1.50	4.24	0.69	4.29	0.88	2.57	0.37	2.49	0.39	78.35	3.92	1.10
XJ512	31.21	66.14	7.51	27.94	5.38	0.92	4.24	0.63	3.63	0.70	2.07	0.31	2.22	0.36	153.26	9.82	0.57
XJ516-2	14.45	29.72	3.68	15.06	3.42	1.14	3.32	0.53	3.07	0.62	1.74	0.26	1.77	0.27	79.04	5.83	1.02
特克斯剖面																	
XJ517-1	35.83	78.85	9.06	34.56	6.86	1.62	6.10	0.94	5.64	1.12	3.25	0.49	3.35	0.53	188.21	7.79	0.75
XJ517-3	47.17	89.25	10.16	37.92	7.31	1.84	6.18	0.94	5.59	1.09	3.20	0.48	3.30	0.52	214.96	9.09	0.82
XJ517-2	39.43	81.42	9.40	35.74	7.00	1.46	6.00	0.92	5.44	1.09	3.23	0.51	3.46	0.54	195.64	8.23	0.67
XJ520-1	22.23	47.18	5.60	22.63	5.06	1.34	4.89	0.77	4.60	0.92	2.67	0.40	2.71	0.43	121.43	5.98	0.81
XJ520-2	21.52	47.26	5.73	22.98	5.11	1.40	5.02	0.78	4.64	0.94	2.75	0.41	2.73	0.44	121.71	5.87	0.83
XJ521	22.32	48.24	5.74	22.76	5.05	1.25	4.49	0.70	4.36	0.85	2.40	0.36	2.41	0.39	121.32	6.60	0.78
XJ522	13.35	29.98	3.85	16.20	4.06	1.20	4.11	0.68	4.13	0.82	2.41	0.36	2.41	0.39	83.94	4.49	0.88
XJ530	27.22	60.34	6.92	25.58	5.82	0.17	5.12	0.85	5.18	1.05	3.13	0.49	3.44	0.54	145.85	6.37	0.09
XJ537	29.90	62.14	7.06	26.16	5.09	1.06	4.05	0.62	3.62	0.72	2.14	0.35	2.37	0.38	145.66	9.22	0.69
XJ538	12.89	29.09	3.79	16.65	4.19	1.46	4.22	0.65	3.92	0.76	2.08	0.31	2.00	0.31	82.33	4.78	1.05
新源剖面																	
XJ553-1	19.22	44.46	5.78	24.70	5.66	1.78	5.38	0.82	4.88	0.97	2.72	0.40	2.67	0.40	119.84	5.57	0.97
XJ553-2	15.41	36.81	4.82	20.97	4.87	1.56	4.64	0.71	4.38	0.85	2.40	0.36	2.33	0.36	100.47	5.27	0.99
XJ555	19.37	46.56	5.71	23.57	6.27	1.11	6.09	1.22	8.61	1.90	6.20	1.07	7.89	1.24	136.81	3.00	0.54
XJ554	24.83	58.84	7.68	32.36	6.74	2.09	5.91	0.89	5.23	1.02	2.78	0.41	2.72	0.42	151.92	6.84	0.99

ΣREE：稀土元素总量；L/H：轻稀土元素总量与重稀土元素总量比值；

δEu（Eu 异常值）=Eu_N×2/（Sm_N+Gd_N），N 指球粒陨石标准化值。

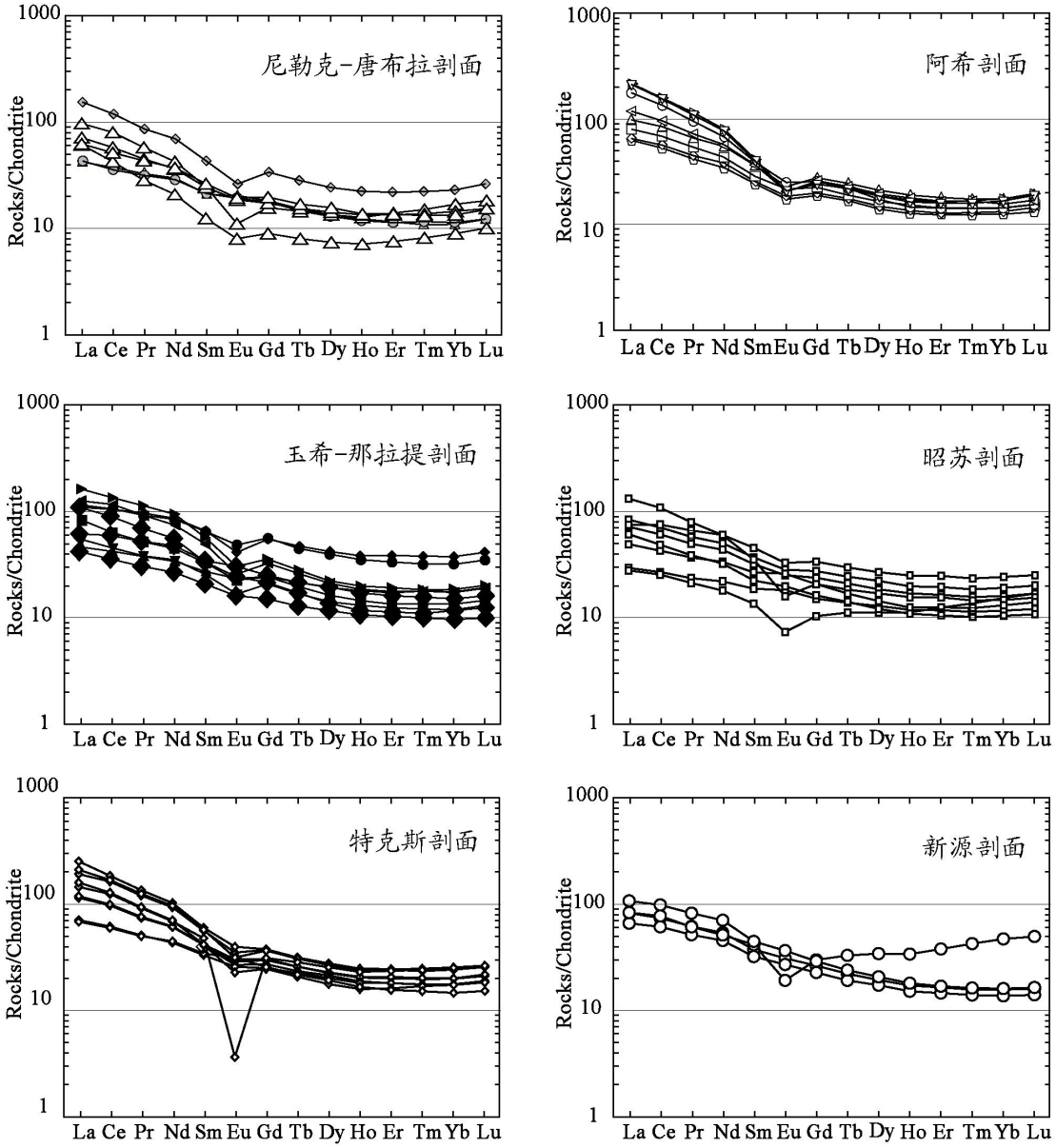

图 3-7 伊犁地区石炭纪火山岩球粒陨石标准化稀土元素配分曲线（标准化值据 Sun et al., 1989）

表 3-3 列出了火山岩的其他微量元素分析结果。从中可以看出，所有火山岩具有一个明显而共同的特征，即它们富集大离子亲石元素（LILE），如 Rb, Th 和 Ba 等。在正常洋脊玄武岩（N-MORB）标准化的微量元素蛛网图（图 3-8）上，K, Rb, Th 和 Ba 等元素在伊犁石炭纪火山岩中的含量明显高于它们在 N-MORB 中的含量。同时，这些火山岩不同程度地亏损高场强元素（HFSE），如 Nb, Ta, Zr, Hf 等。由图 3-8 中可见，HFSE 在伊犁石炭纪火山岩中的含量与在 N-MORB 中的含量比较接近或更低。结果，在图 3-8 中，所有火山岩在 Nb 和 Ta 处表现出一个明显的低谷区域，玉希-那拉提、昭苏和新源剖面的大部分火山岩和部分特克斯火山岩也在 Zr 和 Hf 处表现为另外一个低谷区域。然而，Zr、Hf 的下凹现象在其他火山岩中并没有明显的反映，相反，它们相对于相邻的 P、Ti 和稀土元素 Sm 表现出上凸特征。这一上凸现象实际上是由于 P 和 Ti 以氧化物形式析出而造成的 P、Ti 的亏损所造成的。另外，20 个火山岩样品的 Nb 含量均大于 3 ppm（除昭苏火山岩 XJ495-3 以外），接近大陆岛弧玄武岩的 Nb 含量（3.3±1.6 ppm），而明显大于大洋岛弧玄武岩的 Nb 含量（1.5±1.0 ppm），也大于 MORB 中 Nb 的丰度（2.8±1.6 ppm）（McCulluch and Gamble, 1991）。

表 3-4 伊犁地区石炭纪火山岩微量元素地球化学分析结果（ppm）

样品号	Sc	V	Cr	Co	Ni	Cu	Zn	Ga	Ge	Rb	Sr	Y	Zr	Nb	Ba	Hf	Ta	Th	U
尼勒克-唐布拉剖面																			
XJ-174	31.2	254	33.8	28.5	18.4	22.6	255	17.4	0.98	21.9	457	18.8	62.8	3.16	197	1.67	0.18	1.27	0.39
XJ-174-1	30.5	243	30.5	26.9	19	84.6	90.3	18.4	1.25	27.5	613	19.6	78.1	3.16	340	1.95	0.19	1.22	0.34
XJ-174-2	26.8	183	120	46.9	108	47.3	104	17.6	1.25	4.14	575	30.8	193	5.3	125	4.18	0.28	0.5	0.26
XJ-174-6	12.8	45.5	5.42	5.94	3.47	11.3	154	15.6	1.16	118	105	34.7	262	13.3	933	7.01	0.87	11.1	2.85
XJ572	37.7	21.7	463	4.5	247	10.5	46.5	15.1	1.76	127	45.7	22.6	174	8.73	637	5.07	0.95	15.7	4.42
XJ575	48.2	87.3	1715	19.2	555	24	50.8	16.9	1.48	74.4	435	22.7	155	5.98	656	3.96	0.49	6.26	1.74
XJ575A	24.6	16.5	694	7.36	360	10.7	17.3	14	1.13	78.1	602	12.8	96.3	3.63	542	2.53	0.45	6.7	2.02
XJ577	43.1	120	228	23.6	118	8.21	91.4	18.2	1.43	42.6	254	23.2	133	5.2	140	3.34	0.42	3.73	0.89
阿希剖面																			
XJ-325	23.5	130	62	18.7	21.5	20.8	64.5	17.1	0.88	24.1	195	19.3	125	5.98	576	3.44	0.44	4.02	1.04
XJ-326	24.1	180	65.1	20.5	22.8	71.5	56.9	18.3	0.96	22.9	202	21.1	135	6.4	180	3.52	0.45	4.13	1.14
XJ-327	27.3	230	95.3	26.2	33.1	174	69.1	23	1.27	5.84	124	23.3	165	8.12	26.4	4.16	0.57	5.9	1.56
XJ-328	22.6	197	62.2	21.6	41	60.3	71.2	19.1	1.25	86.8	463	30.8	220	10.4	354	5.41	0.7	7.99	1.99
XJ-329	16.7	130	74.1	17	32.1	70.4	57.6	19	0.97	126	194	26.2	209	11.1	538	5.74	0.87	10.9	3.12
XJ-335	3.55	18.6	3.01	4.17	2.52	5.42	70.7	18.8	1.09	142	146	26.9	209	34.4	638	5.83	2.34	23.9	4.15
XJ-335-1	2.98	21.3	2.76	2.22	4.62	16.1	74.7	17.4	1.47	141	86.7	25.3	190	31.5	99.7	5.01	2.09	20.7	4.92
XJ-336	3.02	15.8	5.73	3.54	4.75	5.83	110	18.8	1.26	111	129	29.2	211	32.5	442	5.58	2.19	22.2	4.51
玉希-那拉提剖面																			
XJ-363	13.9	102	10.6	12.7	7.68	157	135	17.7	1.43	263	222	28.4	222	10.3	928	4.81	0.67	16.1	3
XJ-365	26.5	170	2.7	17.3	2.95	9.1	173	18.5	1.68	163	338	54.5	238	9.42	772	5.96	0.61	6.43	1.98
XJ-388	24.7	573	50.9	13	17	22.4	46.4	32.9	2.2	9.57	4382	22.9	212	9.83	142	5	0.56	10.8	3.06
XJ-389	16.6	105	5.48	23.5	13.7	296	102	17.8	1.17	253	344	30.9	198	11	683	4.99	0.69	17.6	4.3
XJ-390	11.3	12.2	10.8	2.12	6.64	5.36	148	13.8	1.25	196	20	59.8	353	13.5	183	9.17	0.85	10.1	2.81
XJ-354	27.8	279	85.7	28.6	59.2	22	667	18.7	1.31	145	487	22.1	79.2	3.52	884	2.07	0.2	4.35	1.12
XJ-357	28.4	242	16.9	14.5	11.4	50	398	16	1.39	295	509	19.8	61.5	2.45	2235	1.69	0.15	2.88	1.06
XJ-358	22.3	231	10.8	32.9	21.7	34.8	159	17.7	0.86	84.6	307	27.8	113	4.3	108	2.8	0.26	1.97	0.55
XJ580	40.8	120	23.3	13.5	13.5	38.1	90.9	21.2	1.34	175	648	20.1	146	6.11	498	3.57	0.52	11.7	3.26
XJ582	62.4	226	235	40.4	131	19.9	170	18.6	1.56	179	986	28	159	5.66	1564	3.44	0.42	1.27	0.39
XJ585-1	54.5	251	94.6	30.8	36.3	21.6	123	21.1	1.13	59.5	241	17.1	82.8	3.02	265	2.2	0.24	2.3	0.53
昭苏剖面																			
XJ495-3	55.9	299	292	32.1	160	12.4	109	20.9	1.62	15.6	465	19.3	57.6	1.97	389	1.65	0.14	1.1	0.34
XJ495-4	49.4	27.4	694	6.17	371	17.7	15.7	7.13	1.13	22.4	311	19	216	7.28	605	5.54	0.63	9.67	2.8
XJ496	69.7	281	122	31.5	68	20.1	113	21.1	1.65	25.6	429	32.7	157	7.65	314	3.69	0.59	3.37	0.97
XJ497	58.9	248	144	28.8	78.1	19.5	123	22.1	1.65	30.5	690	27.8	135	6.55	435	3.17	0.51	2.98	0.8
XJ500	77.3	277	73.4	29.7	47.9	173	203	22.9	1.92	6.97	261	40.6	200	8.33	173	4.97	0.64	5.75	1.89
XJ502	54.5	318	54.3	31.2	34.9	52.4	96.9	20.2	1.37	4.96	543	24.6	92.7	4.84	208	2.22	0.37	1.39	0.38
XJ512	50.9	12.3	761	6.63	419	12.1	75.4	13.6	1.4	151	144	21.9	241	10.2	1041	6.6	0.93	17.3	3.82
XJ516-2	43.6	169	138	29.7	98.4	67.3	90	18.8	1.45	138	316	18.2	98.6	7.1	456	2.45	0.52	1.66	0.48
特克斯剖面																			
XJ517-1	67.5	34.6	396	8.8	216	7.42	183	20.7	1.43	102	432	32.6	330	23.3	835	7.61	1.76	11	2.55
XJ517-3	63.2	20.8	174	6.12	94.8	4.54	102	23.8	1.44	102	174	30.6	293	20.6	172	7.13	1.56	11.2	2.68
XJ517-2	68.2	25.6	493	8.81	261	8.29	119	17.2	1.79	55.8	307	31.6	316	22.3	695	7.6	1.72	10.9	2.52
XJ520-1	62.9	206	834	28.7	383	39	106	20.5	1.53	10.7	721	26.8	162	7.25	318	4.31	0.56	7.25	1.26
XJ520-2	63.6	214	497	29.3	197	30.3	106	21.1	1.68	29.2	407	27.1	164	7.23	426	4.34	0.55	7.08	1.16
XJ521	63.6	186	292	22.2	105	38.2	113	21.2	1.66	8.44	1014	24.6	180	7.79	708	4.68	0.64	8.89	1.85
XJ522	64.5	254	412	35.5	98.5	25.1	86.1	19.3	1.54	19.9	259	24	112	5.46	135	3	0.42	3.32	0.79
XJ530	31.1	5.59	202	2.2	106	11.9	39	17.3	1.5	171	14.1	33.2	144	21.3	108	5.29	2.12	20.6	4.23
XJ537	57	34.9	1150	11.5	599	19.2	40	16	1.64	155	205	22.6	265	9.91	752	6.53	0.89	13.3	3.21
XJ538	60.5	285	219	33.4	82.2	164	92.8	21.2	1.35	40	543	22	117	6.3	411	2.93	0.49	2.02	0.76
新源剖面																			
XJ553-1	64.2	239	267	37	126	22.9	168	18.2	1.35	63.4	587	28.7	141	6.75	716	3.13	0.44	1.06	0.43
XJ553-2	57.5	234	226	38.6	132	22.9	126	17	1.18	48.8	666	24.4	115	6.19	416	2.69	0.4	0.95	0.31
XJ555	108	34.4	1249	11.9	686	37.9	23.6	10.3	1.4	207	151	47.2	567	16.5	1014	13.3	1.45	17.2	3.93
XJ554	62.7	261	76.8	37.2	83.2	12.1	129	20.7	1.36	40.8	828	28.8	165	8.47	1596	3.7	0.57	1.68	0.54

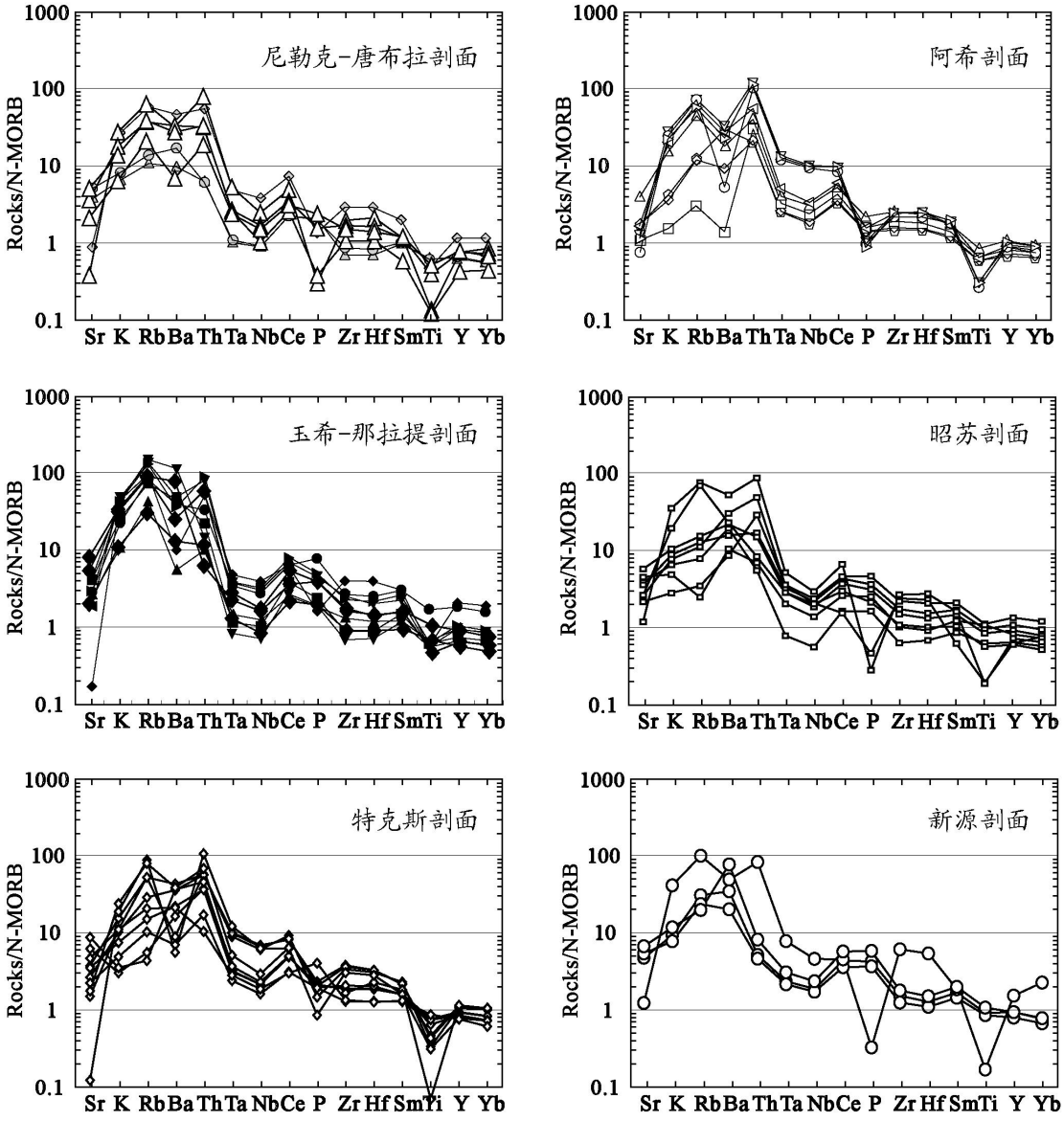

图 3-8 伊犁地区石炭纪火山岩微量元素蛛网图

2.2. 花岗岩地球化学特征

在本论文研究的 6 条剖面中，花岗质岩石与火山岩紧密伴生。在野外工作条件允许的情况下，在 5 条剖面中采集了与火山岩同时代的花岗质岩石 11 件，并对这些样品进行了地球化学全分析，其主量元素和微量元素化学成分见表 3-5。

所分析侵入岩的 SiO_2 含量为 52.3~75.2%，从中-基性、中性到酸性变化，但以酸性为主。在单个剖面中，也是中性与酸性侵入岩同时存在。所有样品全碱含量较低，AK=2.67~7.42%，其中 10 个样品的 AK<6%。另外，全部样品中 K_2O<<Na_2O，钾钠比值为 0.03~0.42。在 SiO_2-AK (TAS) 图解（图 3-9）（Cox et al., 1979；Wilson, 1989）中，只有玉希剖面的 XJ581 样品为碱性（正长闪长岩），其余样品全部投在钙碱性区域，分别辉石闪长岩、闪长岩、石英闪长岩和花岗岩。大部分样品中 Al_2O_3 中度富集，一般为 1.2~5.3%，少数大于 7%。CaO 的含量为 3~4.3%，较富集并比较一致，所有样品具有很低的铝饱和指数（ASI=0.09~0.74）。这些侵入岩同时还比较富集 Fe、Mg、Mn，FeO_t+MgO+MnO=1~7.3%，个别高达 10%，但其中全铁的比重较小，FeO_t/ (FeO_t+MgO)=0.02~0.07。由此可见，伊犁石炭纪侵入岩的主量元素特征与典型的低钾高钙含角闪石钙碱性花岗岩（ACG）的特征十分一致（Barbarin, 1999）。

表 3-5 伊犁地区石炭纪侵入岩地球化学分析结果

剖面	玉希-那拉提				昭苏		特克斯		阿希	尼勒克-唐布拉	
样品号	XJ581	XJ583	XJ701-1	XJ701-2	XJ515	XJ516-1	XJ535-2	XJ620	XJ693-1	XJ694	XJ695
SiO_2(%)	57.37	59.98	72.79	69.39	68.99	75.20	52.25	63.70	70.67	71.40	71.35
TiO_2	16.80	16.42	14.06	13.93	15.07	12.42	15.69	16.54	14.30	14.01	13.78
Al_2O_3	7.46	7.43	1.77	3.90	3.42	1.18	9.44	5.26	2.40	2.66	2.54
Fe_2O_3	0.14	0.13	0.05	0.08	0.08	0.04	0.15	0.13	0.08	0.05	0.06
MnO	1.72	3.09	0.51	0.49	1.26	0.20	3.97	1.75	0.59	0.10	0.09
MgO	3.59	6.61	2.09	2.03	3.25	0.96	5.90	5.40	1.36	0.88	0.80
CaO	4.33	3.33	3.72	4.02	3.53	3.12	4.19	3.06	3.88	3.90	3.78
Na_2O	6.44	1.87	3.30	3.72	3.53	4.92	2.87	2.98	3.96	5.75	5.65
K_2O	0.99	0.79	0.24	0.47	0.43	0.13	0.94	0.46	0.25	0.23	0.22
P_2O_5	0.61	0.16	0.08	0.12	0.11	0.02	0.45	0.20	0.09	0.04	0.05
LOI	1.41	0.90	0.78	0.66	0.87	1.14	4.19	0.67	1.13	0.29	0.33
Total	100.8	100.7	99.4	98.8	100.5	99.3	100.0	100.1	98.7	99.3	98.6
AK	7.42	2.67	3.53	4.19	3.97	5.05	3.81	3.44	4.22	5.98	5.87
ASI	0.38	0.74	0.14	0.28	0.27	0.09	0.71	0.48	0.17	0.16	0.15
σ	3.83	0.42	0.42	0.67	0.60	8.91	1.57	0.57	0.64	1.26	1.22
La(ppm)	37.62	15.34	18.35	33.00	27.99	24.04	23.19	18.69	26.08	52.07	54.77
Ce	82.86	33.93	37.36	71.59	54.81	45.86	51.62	36.43	49.85	103.60	106.20
Pr	10.01	4.17	4.22	8.93	5.90	4.60	6.64	4.04	5.16	11.69	12.11
Nd	39.82	17.56	15.48	35.96	20.25	14.68	27.96	15.24	17.20	42.58	43.49
Sm	8.20	4.11	3.36	8.30	3.89	2.75	6.17	2.91	3.04	6.42	6.32
Eu	1.65	1.11	0.64	2.32	0.83	0.32	1.80	0.88	0.77	0.47	0.47
Gd	6.73	4.29	3.05	7.65	3.31	2.26	5.13	2.45	2.53	4.37	4.10
Tb	0.99	0.71	0.50	1.24	0.55	0.40	0.72	0.38	0.41	0.65	0.57
Dy	5.65	4.43	2.91	7.54	3.29	2.47	3.99	2.25	2.48	3.59	3.17
Ho	1.08	0.90	0.57	1.48	0.63	0.49	0.73	0.45	0.51	0.68	0.59
Er	3.09	2.63	1.67	4.22	1.91	1.56	1.96	1.35	1.57	1.99	1.73
Tm	0.47	0.41	0.26	0.62	0.30	0.28	0.30	0.21	0.25	0.31	0.26
Yb	3.34	2.85	1.84	4.16	2.07	2.10	1.94	1.47	1.87	2.22	1.88
Lu	0.54	0.45	0.28	0.64	0.34	0.34	0.30	0.25	0.31	0.38	0.32
ΣREE	202.0	92.9	90.5	187.6	126.1	102.1	132.4	87.0	112.0	231.0	236.0
L/H	8.23	4.57	7.16	5.81	9.18	9.32	7.80	8.87	10.28	15.29	17.69
δEu	0.66	0.80	0.60	0.88	0.69	0.38	0.95	0.98	0.83	0.26	0.27
Sc(ppm)	74.33	62.03	-	-	36.96	18.22	55.99	37.22	-	-	-
V	121.8	174.5	18.0	14.9	48.5	8.5	289.9	80.7	16.9	1.6	1.9
Cr	9.36	27.12	10.65	7.22	8.90	-	226.10	8.35	8.57	5.86	9.21
Co	13.81	22.61	2.82	3.26	12.12	10.92	24.62	11.73	2.88	0.73	0.80
Ni	6.73	12.55	4.38	3.48	6.43	-	128.10	5.00	3.54	-	3.73
Cu	89.34	45.16	6.96	6.34	6.13	14.46	172.60	10.76	-	-	-
Zn	89.33	71.12	40.96	72.43	61.56	23.05	90.67	66.49	51.15	36.14	52.38
Ga	19.19	18.85	17.68	18.56	17.89	14.33	19.13	16.19	16.14	18.04	18.41
Ge	1.33	1.54	1.37	1.43	1.49	1.66	1.59	1.60	1.27	1.18	1.11
Rb	237.5	69.7	162.0	120.2	141.4	220.4	79.6	86.8	161.6	73.0	67.3
Sr	298.2	261.5	231.6	251.8	215.0	52.2	547.0	415.2	224.9	40.4	19.8
Y	32.34	26.70	18.06	43.30	20.04	15.24	21.49	13.56	15.26	18.13	15.93
Zr	296.8	192.9	110.7	533.8	157.1	85.3	104.0	124.0	136.3	410.7	414.5
Nb	11.76	4.98	8.13	11.58	14.76	25.55	3.82	5.29	14.09	8.56	8.77
Ba	593.4	319.0	330.3	1152.0	390.2	353.0	558.2	1010.0	550.1	134.3	124.6
Hf	6.93	4.88	3.21	10.56	4.16	3.18	2.63	3.11	3.71	9.49	9.55
Ta	0.96	0.50	1.45	1.21	1.36	4.06	0.28	0.45	1.56	0.85	0.61
Th	21.67	6.56	12.19	11.54	15.01	33.06	3.98	9.17	13.29	7.68	7.50
U	4.67	2.04	2.52	2.67	2.88	9.25	1.22	0.97	2.83	1.97	1.30

AK(全碱)= Na_2O+ K_2O; ASI(铝饱和指数)=$Al_2O_3/mol_{Al}/(Na_2O/mol_{Na}+K_2O/mol_K+CaO/mol_{Ca})$; σ(里特曼指数)=$AK^2/(SiO_2-43)$; ΣREE：稀土元素总量；L/H：轻稀土元素总量与重稀土元素总量比值；δEu（Eu异常值）=$Eu_N\times2/(Sm_N+Gd_N)$，N 指球粒陨石标准化值。

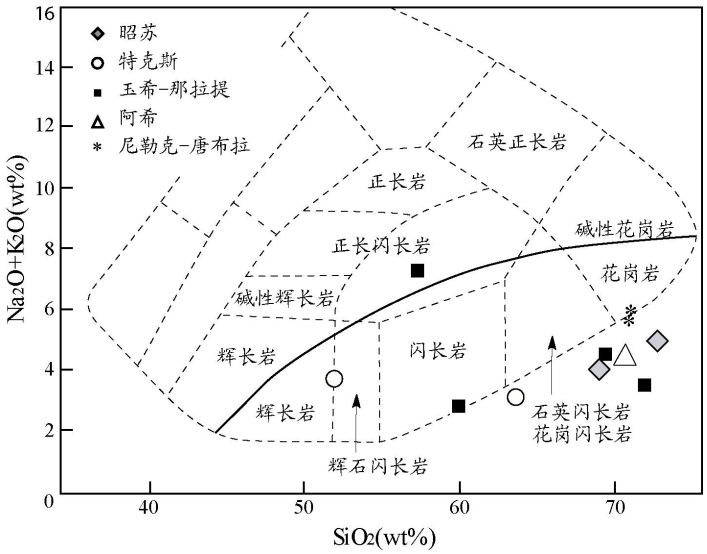

图 3-9 伊犁石炭纪花岗质岩石 SiO_2-AK (TAS) 图解

（黑实线之上为碱性系列，之下为钙碱性系列）

表 3-5 还列出了侵入岩的微量元素（包括稀土元素）含量。从中可以看出，所有样品的轻稀土元素较重稀土元素富集（∑LREE/∑HREE >4.5），稀土元素总含量较高（∑REE= 87~236 ppm）。这些侵入岩具有中等到弱的 Eu 负异常（δEu=0.60~0.98），少数具有较强的负异常（δEu=0.26~0.38）。从球粒陨石标准化稀土元素配分曲线（图 3-10a）可见，这些侵入岩与各自相应剖面的火山岩十分相似（图 3-7）。同时，不同剖面侵入岩的稀土配分曲线比较一致，且无明显分异，这一特点也类似于各剖面之间火山岩稀土配分曲线的特征。另外，这些侵入岩也具有与火山岩非常相似的正常洋脊玄武岩标准化微量元素蛛网图（图 3-10b），亏损的 Ta、Nb 和 Zr、Hf 值以及较富集的 K、Rb、Th 等元素表明，这些侵入岩与同一剖面的火山岩具有相同的岩浆源，且都来源于亏损的岩石圈地幔，同时经历了上地壳物质的混染。

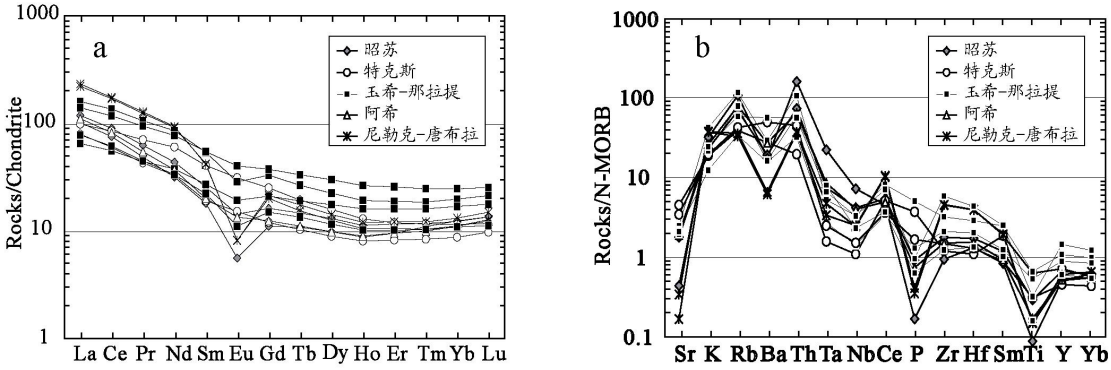

图 3-10 伊犁地区石炭纪侵入岩（a）球粒陨石标准化稀土元素配分曲线；

（b）正常洋脊玄武岩标准化微量元素蛛网图

第三节 石炭纪岩浆岩构造环境与岩浆成因讨论

从上文的论述可以看出，本章所研究的伊犁地区火山岩和花岗岩质岩石具有非常相似的地球化学特征：以中性为主、酸性次之、少量基性或中基性岩石，表现为钙碱性系列；全区喷发岩和侵入岩具有相同的稀土元素配分曲线和微量分布特征。野外地质考察表明，这些火山岩与花岗质岩石在空间上紧密伴生，时代上同期形成。因此，可以初步推断他们形成于同一个构造环境，来源于类似的岩浆库，但这些推论仍需进一步讨论。

1. 岩浆岩构造环境

伊犁地区石炭纪火山岩富集 LILE 和相对亏损 HFSE 的地球化学特征，同形成于俯冲带的火山岩特征（McCulloch and Gamble，1991）相当一致。其中 Nb, Ta 的显著亏损表明其岩浆来源于俯冲带熔融的上地幔或俯冲板片，而 Ba，Rb 和 Th 的相对富集则可能是由于这些岩浆在上升过程中被位于俯冲带之上地壳物质混染所致。

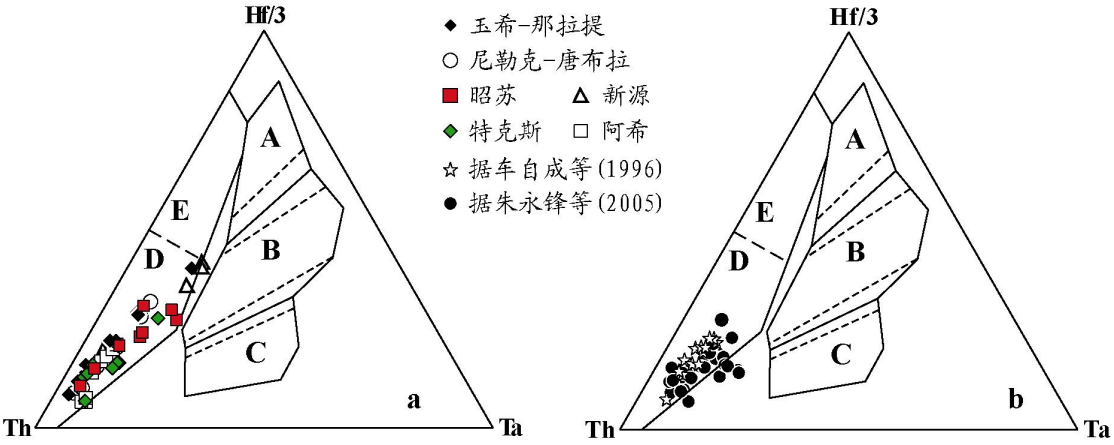

图 3-11 伊犁地区石炭纪火山岩的 Hf/3-Th-Ta 图解

A—洋脊玄武岩；B—富集洋脊玄武岩和板内拉斑玄武岩；C—板内碱性玄武岩；D—钙碱性玄武岩；E—岛弧拉斑玄武岩

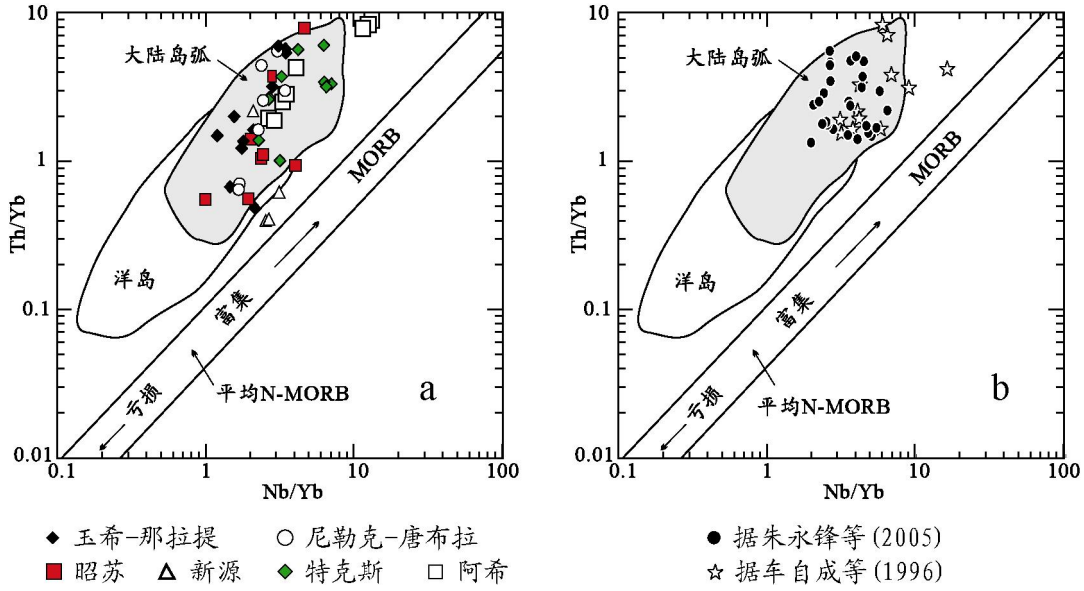

图 3-12 伊犁地区石炭纪火山岩 Th/Yb-Nb/Yb 图解

在 Hf/3-Th-Ta 三角图解（Wood et al., 1979）（图 3-11a）中，所有火山岩均投影于钙碱性玄武岩区域，并且每个剖面的火山岩均有从岛弧型拉斑玄武岩向钙碱性玄武岩演化的线性趋势。从区域上看，整个伊犁地区不同剖面的火山岩具有类似的演化趋势，而且这种趋势在不同剖面之间没有明显的差别。以上特征表明，这些火山岩可能形成于会聚板块边缘，即俯冲型火山岛弧环境。在不相容元素 Yb 标准化的 Th-Nb 坐标系（Pearce and Peate，1995）（图 3-12a）中，绝大多数样品（41/49）落在大陆岛弧火山岩区域，其中，多于 50%的火山岩样品仅投影于非重叠的大陆岛弧火山岩区域，少数样品则落在大陆岛弧与大洋岛弧火山岩的重叠区域，但也明显偏向大陆岛弧区域，表明这些火山岩更具有大陆火山岛弧亲缘性。另外，

阿希剖面的 3 个火山岩由于过高的 Th 含量而投影于自由区域，但仍偏向大陆岛弧火山岩。3 个新源剖面的火山岩、1 个昭苏剖面的火山岩及 1 个特克斯剖面的火山岩由于较低的 Th 含量而偏离大陆岛弧火山岩的区域（图 3-12a）。 Th 含量的变化可能是受到不同程度地壳物质混染的结果（Pearce and Peate，1995），同时也很可能由测量误差所致。

值得一提的是，前人所研究的新源地区火山岩（朱永锋等，2005）和特克斯、果子沟火山岩（车自成等，1996）也投在 Hf/3-Th-Ta 三角图解的钙碱性玄武岩区域（图 3-11b），这些火山岩具有比较接近的 Th 含量，因此分布比较集中，从岛弧型拉斑玄武岩向钙碱性玄武岩演化的线性趋势不十分明显。在 Th/Yb-Nb/Yb 投影图上（图 3-12b），这三个地区的火山岩中，多于 80%的样品唯一地投在大陆岛弧火山岩区域。这一结果与朱永锋等（2005）的认识一致，但不同于车自成等（1994，1996）和夏林圻等（2003，2004，2005）的认识。他们认为，伊犁地区石炭纪（和二叠纪）的火山岩形成于大陆裂谷环境，并可能与地幔柱活动有关。

另一方面，伊犁地区石炭纪火山岩同与之紧密伴生的花岗质岩石具有十分类似的地球化学特征。在 Y-Nb 图解（Pearce et al., 1984）中，所有侵入岩均落在火山岛弧花岗岩和同碰撞花岗岩区域（图 3-13a）。鉴于元素 Rb 在火山岛弧花岗岩和同碰撞花岗岩中具有不同特性，Y+Nb-Rb 图解（Pearce et al., 1984）可以用来区分这两类花岗岩。在图 3-13b 中，除 1 个阿希花岗岩和 1 个玉希花岗岩投在同碰撞花岗岩区域以外，其余花岗质岩石均在火山岛弧花岗岩区域中。对比与花岗质岩石伴生的火山岩的构造环境，可以推断这些花岗质岩石主要形成于火山岛弧环境，个别花岗岩可能形成于岛弧活动的晚期，即碰撞作用阶段。

以上所分析的火山岩均与同期的浅水相陆源沉积岩层相伴生或互层。如前所述，火山岩或覆于沉积岩之下，或伏于沉积岩之上，或呈夹层产于沉积岩之间反复出现，反映了火山岩浆不连续、多次喷发的过程。同时，花岗质岩石则侵入到同时代火山岩与沉积岩当中。这些地质证据和岩石地球化学分析结果一致表明，伊犁地区石炭纪火山岩和花岗质岩石形成于俯冲带之上的活动大陆边缘环境。

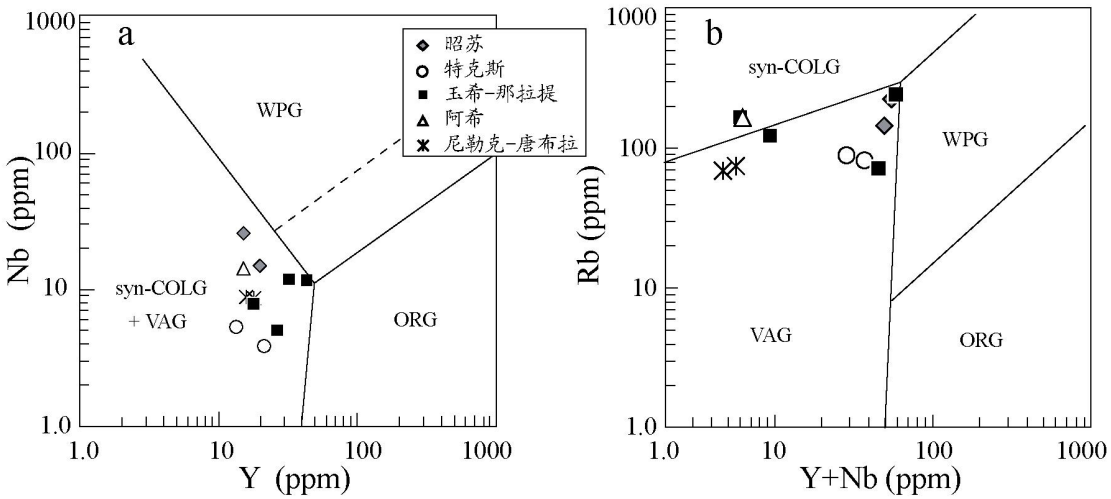

图 3-13 伊犁地区石炭纪花岗质岩石大地构造环境判别图解

VAG，火山岛弧花岗岩，syn-COLG，同碰撞期花岗岩，WPG，板内花岗岩，ORG，洋中脊花岗岩

2. Nd、Sr 同位素示踪

基于 Rb-Sr 同位素系统在大陆地壳和地幔中的不同特性，以及它们在岩浆形成与分异演化过程中的不同行为，Sr 同位素通常被用作地球化学示踪剂来研究火成岩物质来源，如富 Rb 贫 Sr 岩石中 $^{87}Sr/^{86}Sr$ 初始比值可以用来判别岩浆成因。另外，稀土元素 Sm-Nd 系统在岩石形成过程和形成以后发生的变化很小，因此能够反映岩石形成之初的物质成分，特别是那些较年轻的岩石。在实际应用中，Nd 和 Sr 同位素常被结合起来分析。本论文在岩石地球

化学分析的基础上，从关键剖面选择了代表性的火山岩和花岗岩样品，在法国南锡实验室进行了 Sm-Nd、Rb-Sr 同位素测定，测定结果见表 3-6。

表 3-6 伊犁地区火山岩与花岗岩同位素地球化学分析结果

样品	元素含量 (ppm)				$\frac{^{87}Sr}{^{86}Sr}$	$\frac{^{87}Rb}{^{86}Sr}$	$\frac{^{87}Sr}{^{86}Sr}_T$	εSr_T	$\frac{^{143}Nd}{^{144}Nd}$	$\frac{^{147}Sm}{^{144}Nd}$	$\frac{^{143}Nd}{^{144}Nd}_T$	εNd_T
	Rb	Sr	Sm	Nd								
昭苏火山岩与花岗岩（T=359Ma）												
XJ497	30.52	690.10	4.87	20.34	0.7056	0.0442	0.7054	18.7854	0.5127	0.2393	0.5122	-0.3165
XJ515	141.40	215.00	3.89	20.15	0.7188	0.6577	0.7154	161.0806	0.5128	0.1930	0.5123	3.0503
特克斯火山岩（T=340~359Ma）												
XJ522	19.91	259.20	4.06	16.20	0.7075	0.0768	0.7071	42.9009	0.5126	0.2509	0.5121	-2.9057
XJ537	155.00	204.80	5.09	26.16	0.7267	0.7568	0.7228	266.3099	0.5127	0.1946	0.5123	1.7399
博罗科努山火山岩与花岗岩（T=300Ma）												
XJ572	127.30	45.66	3.83	19.59	0.7393	2.7880	0.7271	325.7127	0.5126	0.1953	0.5122	-0.4915
XJ694	73.00	40.44	6.42	42.58	0.7145	1.8051	0.7069	39.4307	0.5126	0.1507	0.5123	1.6025
玉希火山岩与花岗岩（T=310~315Ma）												
XJ582	179.00	985.90	5.34	22.16	0.7075	0.1816	0.7067	36.2548	0.5128	0.2412	0.5123	1.0800
XJ583	69.69	261.70	4.11	17.56	0.7081	0.2663	0.7070	40.1718	0.5126	0.2341	0.5122	-1.6141

$\varepsilon Nd_T=[(^{143}Nd/^{144}Nd)_{rock(T)}/(^{143}Nd/^{144}Nd)_{CHUR(T)}-1]\times10^4$，其中$(^{143}Nd/^{144}Nd)_{rock(T)}=(^{143}Nd/^{144}Nd)_{rock(present)}-(^{147}Nd/^{144}Nd)_{rock(present)}\times(e^{\lambda T}-1)$，$(^{143}Nd/^{144}Nd)_{CHUR(T)}=(^{143}Nd/^{144}Nd)_{CHUR(present)}-(^{147}Nd/^{144}Nd)_{CHUR(present)}\times(e^{\lambda T}-1)$；$(^{143}Nd/^{144}Nd)_{CHUR(present)}=0.512638$，$(^{147}Nd/^{144}Nd)_{CHUR(present)}=0.1967$，$\lambda_{Nd}=6.54\times10^{-12}$，T 为岩石年龄。$\varepsilon Sr_T$ 计算过程类似，其中$(^{87}Sr/^{86}Sr)_{CHUR(present)}=0.7065$，$(^{87}Rb/^{86}Sr)_{CHUR(present)}=0.0827$。

从表 3-6 可以得出，各剖面火山岩和花岗岩的 Sm/Nd 比值为 0.15~0.24，与中、酸性岩浆的特征一致。Rb/Sr 比值为 0.04~2.8，表明 Rb 和 Sr 两元素受岩浆分异的影响比较明显，这一现象也表现在火山岩与侵入岩的 Rb 和 Sr 含量差异上。另一方面，火山岩的 Sr 同位素组成为 0.7054~0.7071 和 0.7228~0.7271，明显大于正常洋脊玄武岩（N-MORB）和富集洋脊玄武岩（E-MORB）的 Sr 同位素组成（0.7024~0.7033）（Saunders et al., 1988），同时也高于洋岛玄武岩（OIB）的 $^{87}Sr/^{86}Sr$ 比值（0.7027~0.7065）（Saunders et al., 1988；Chaffey et al., 1989；Gerlach et al., 1988；Cliff et al., 1991；White and Hofman, 1982；Storey et al., 1988；Stille et al., 1983）。其中低值区间与安第斯山的安山岩 Sr 同位素组成（0.7057~0.7095）十分相近（Hawkesworth et al., 1982）。

大部分花岗岩的 $^{87}Sr/^{86}Sr$ 比值为 0.7067~0.7070，明显低于 S 型花岗岩的 $^{87}Sr/^{86}Sr$ 比值（0.7094~0.8793），而与 I 型花岗岩的 $^{87}Sr/^{86}Sr$ 比值（0.7045~0.7301）比较接近（McCulloch and Chappell, 1982；Liew and McCulloch, 1985）。只有一个花岗岩（XJ515）（$^{87}Sr/^{86}Sr$ =0.7154）同时具有 S 型和 I 型花岗岩的特征。另外，火山岩和花岗岩 Sr 同位素组成的高值区间（0.7154~0.7271）也与上地壳物质的 Sr 同位素组成（0.7033~0.8405）和碎屑沉积岩的 Sr 同位素组成（0.7114~0.7892）非常一致（Davies et al., 1985；Allegre and Ben Othman, 1980）。

至于 Nd 同位素组成，火山岩 $^{143}Nd/^{144}Nd$ 比值范围为 0.5126~0.5127,明显小于 N-MORB 和 E-MORB 的 $^{143}Nd/^{144}Nd$ 比值（0.5130~0.5133）（Saunders et al., 1988），但与 OIB 的 $^{143}Nd/^{144}Nd$ 比值（0.5123~0.5130）比较接近（Saunders et al., 1988；Chaffey et al., 1989；Gerlach et al., 1988；Cliff et al., 1991；White and Hofman, 1982；Storey et al., 1988；Stille et al., 1983），而更接近于北美西部与俯冲有关的安山岩 $^{143}Nd/^{144}Nd$ 比值（0.51266~0.51284）（Norman and Leeman, 1990）。花岗岩 $^{143}Nd/^{144}Nd$ 比值范围为 0.5126~0.5127，与火山岩基本一致。

从表 3-6 可以看出，伊犁地区岩浆岩的ε_{Nd}值范围为-2.91~3.05，而且在每个剖面中，岩浆岩ε_{Nd} 值既负值，也有正值，表明这些岩浆岩的物质来源可能为一个在早期已产生过岩浆所留下的残余固相库（图 3-14），而且在岩浆上升、冷却结晶或喷发过程中，可能受到了上

地壳物质或碎屑沉积岩的混染。个别样品的ε_{Nd}值接近 CHUR 的值（表 3-6，图 3-14），类似俯冲带洋壳物质和深海沉积物再熔融的结果（Rollison, 1993；Wilson, 1989）。其中三个样品（图 3-14）具有明显偏高的 Sr 同位素比值，有可能是来自亏损地幔的岩浆受到受到了富 Ba, Sr 等的长英质岩浆的混染（朱永锋等，2006），或者是炽热的岩浆与尚未成岩的陆源沉积物反应的结果（Rollison, 1993；Wilson, 1989）。考虑到伊犁地区火山岩、花岗岩与碎屑沉积岩紧密伴生，因此后一种情况更适合于这些岩浆岩高 Sr 同位素比值的成因。

综合以上微量元素和同位素地球化学特征，伊犁地区石炭纪火山岩与其伴生的同期侵入岩可能经历了复杂的岩浆演化历史，由早期结晶分异的洋壳，在俯冲过程中，与洋壳沉积物一起熔融形成亏损岩浆，并在俯冲带之上受到了上地壳物质的混染（Hawkesworth et al., 1993）。因此，伊犁石炭纪岩浆岩代表一个活动大陆边缘环境。

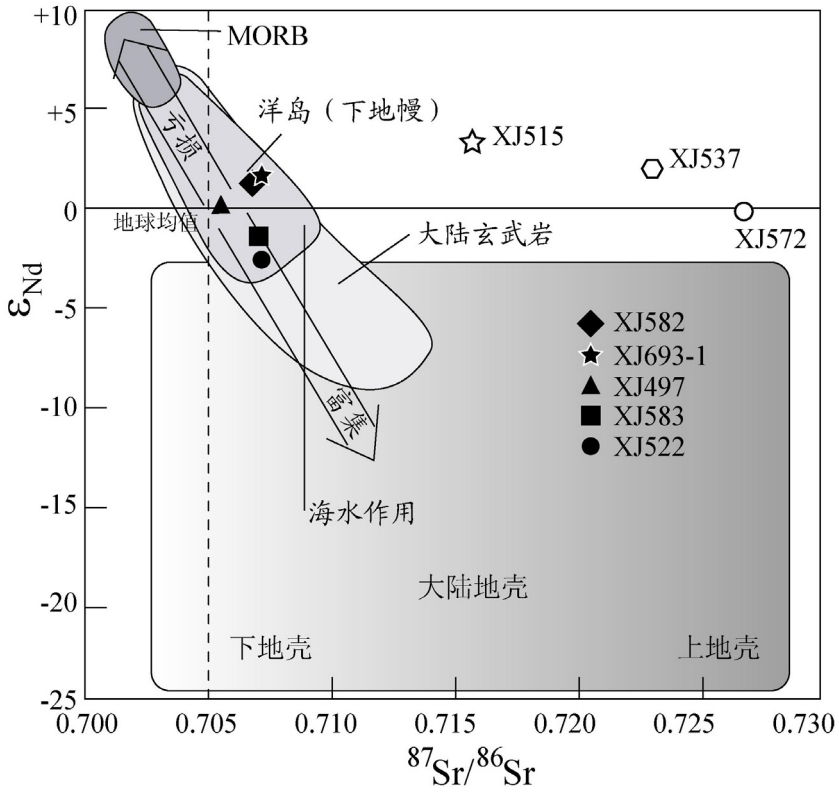

图 3-14 伊犁地区岩浆岩 $^{87}Sr/^{86}Sr$-ε_{Nd} 相关图（据 Depaoto and Wasserburg, 1979）

第四节 “石炭纪”岩浆岩锆石 U-Pb 年代学研究

伊犁地区石炭纪火山岩是一个地层概念，其地层时代通常都是利用与火山岩伴生的沉积岩中古生物证据来约束（新疆地矿局，1993）。最近，一些学者（李华琴等，1998；朱永锋等，2005；2006；朱志新等，2006；翟伟等，2006）陆续从这些火山岩中获得了一批年龄数据，并发现有些大哈拉军山组火山岩的年龄要比石炭纪下限年龄要老，也有些大哈拉军山组火山岩则属于上石炭统。因此，有研究者提出，大哈拉军山组需要解体（朱永锋等，2006）。由此可见，仅仅从地层学角度来约束伊犁地区原石炭纪地层的时代是远远不够的，而需要大量的精确年代学研究。作者在伊犁地区考察原石炭纪火山岩和侵入岩时，选择典型剖面，采集了新鲜的花岗质岩石样品。在研究其主量元素、微量元素和同位素地球化学特征的基础上，进一步筛选尽可能没有蚀变、Zr 含量大于 100ppm 以及结晶好的样品进行锆石 U-Pb 测年。岩石中锆石矿物一般分布在黑云母、角闪石等暗色矿物的边部，或以包体形态沿暗色矿物的解理方向生长。

表 3-7 伊犁北部花岗岩锆石 U-Pb ICPMS 测年数据

Plots	Ratios						Ages (Ma)						Disc.
	$^{207}Pb/^{235}U$	1σ	$^{206}Pb/^{238}U$	1σ	$^{207}Pb/^{206}Pb$	1σ	$^{207}Pb/^{235}U$	1σ	$^{206}Pb/^{238}U$	1σ	$^{207}Pb/^{206}Pb$	1σ	(%)
XJ626-1, Mean = 301±7 Ma 哈希勒根达坂南坡													
JA19E1	0.34	0.03	0.045	0.001	0.058	0.005	296	22	281	5	547	184	5
JA19E12	0.35	0.09	0.046	0.002	0.068	0.017	302	69	293	12	877	522	13
JA19E8	0.33	0.03	0.046	0.001	0.059	0.006	292	23	290	6	572	212	7
JA19E6	0.34	0.02	0.046	0.001	0.056	0.003	295	14	291	4	445	116	4
JA19E11	0.31	0.02	0.047	0.001	0.052	0.003	276	14	298	5	288	130	5
JA19E4	0.30	0.02	0.047	0.001	0.048	0.002	266	13	298	5	119	120	5
JA19E3	0.29	0.02	0.048	0.001	0.046	0.003	256	15	301	5	2	158	5
JA19E10	0.36	0.02	0.049	0.001	0.058	0.004	311	17	307	5	528	149	5
JA19E5	0.33	0.04	0.049	0.001	0.055	0.007	287	27	311	7	405	278	8
JA19E7	0.33	0.02	0.049	0.001	0.053	0.004	289	19	310	6	330	185	6
JA19E9	0.39	0.03	0.051	0.001	0.061	0.005	334	24	318	6	638	191	6
JA19E2	0.34	0.03	0.050	0.001	0.052	0.004	299	23	315	6	269	194	6
XJ581, Mean = 315±Ma 玉希望达坂南坡													
MA23C2	0.1044	0.01	0.0167	0.000	0.0480	0.0054	101	10	107	2.1	99	264	2.1
MA23C5	0.1541	0.00	0.0245	0.000	0.0449	0.0029	145	9	156	1.9	-61	159	1.9
MA23C11	0.1794	0.00	0.0247	0.000	0.0520	0.0029	168	8	157	2.4	284	126	2.4
MA23C7	0.3593	0.01	0.0482	0.000	0.0531	0.0016	312	8	303	2.4	332	69	2.4
MA23C8	0.3708	0.01	0.0482	0.000	0.0533	0.0027	320	14	303	5.4	342	115	5.4
MA23C12	0.3861	0.01	0.0489	0.000	0.0565	0.0016	332	8	306	3.4	471	61	3.4
MA23C9	0.3592	0.01	0.0490	0.000	0.0526	0.0019	312	9	309	2.6	311	83	2.6
MA23C3	0.3647	0.00	0.0494	0.000	0.0523	0.0013	316	6	311	2.1	300	57	2.1
MA23C6	0.3685	0.01	0.0502	0.000	0.0528	0.0014	319	8	316	2.4	320	62	2.4
MA23C10	0.3646	0.00	0.0510	0.000	0.0515	0.0014	316	7	321	2.4	263	61	2.4
MA23C4	0.3707	0.01	0.0515	0.000	0.0514	0.0021	320	11	324	3.2	261	93	3.2
MA23C1	0.3907	0.01	0.0532	0.000	0.0520	0.0021	335	11	334	3.5	285	93	3.5
XJ583, Mean =309 ± Ma 玉希望达坂南坡													
MA23M1	0.3494	0.02	0.0483	0.000	0.0537	0.0033	304	16	304	5.3	357	138	5.3
MA23M9	0.3560	0.02	0.0486	0.000	0.0540	0.0033	309	16	306	4.7	373	138	4.7
MA23M7	0.3673	0.02	0.0488	0.000	0.0558	0.0040	318	20	306	5.4	445	157	5.4
MA23M8	0.3342	0.02	0.0487	0.001	0.0530	0.0039	293	18	306	6.6	329	168	6.6
MA23M1	0.3612	0.02	0.0490	0.001	0.0551	0.0044	313	22	307	6.2	417	179	6.2
MA23M3	0.3588	0.02	0.0492	0.000	0.0565	0.0035	311	17	308	5.5	473	136	5.5
MA23M4	0.3832	0.02	0.0495	0.000	0.0578	0.0038	329	18	309	5.0	521	144	5.0
MA23M1	0.3306	0.02	0.0491	0.000	0.0513	0.0039	290	19	310	5.4	256	174	5.4
MA23M6	0.3662	0.02	0.0495	0.000	0.0560	0.0040	317	19	310	5.3	453	160	5.3
MA23M2	0.3953	0.02	0.0500	0.000	0.0594	0.0034	338	17	312	5.7	583	123	5.7
MA23M5	0.3250	0.02	0.0504	0.001	0.0502	0.0040	286	19	318	6.2	202	187	6.2
MA23M1	0.3705	0.02	0.0511	0.001	0.0574	0.0045	320	21	319	6.6	508	173	6.6
XJ693-1, Mean = 389±6 Ma 果子沟南													
JA19H10	0.45	0.02	0.058	0.001	0.059	0.003	380	17	362	7	582	126	7
JA19H11	0.44	0.04	0.060	0.001	0.054	0.005	368	27	374	8	387	204	9
JA19H5	0.50	0.06	0.061	0.002	0.066	0.009	415	43	382	13	812	286	14
JA19H8	0.47	0.03	0.061	0.001	0.058	0.003	392	19	379	6	530	114	6
JA19H3	0.43	0.02	0.061	0.001	0.053	0.002	366	14	380	5	322	105	5
JA19H12	0.46	0.03	0.061	0.001	0.057	0.003	381	19	383	6	503	133	7
JA19H2	0.44	0.02	0.062	0.001	0.053	0.003	369	14	390	5	308	109	5
JA19H6	0.45	0.02	0.063	0.001	0.053	0.002	379	13	392	5	349	93	5
JA19H7	0.47	0.02	0.063	0.001	0.056	0.002	388	12	396	5	439	87	5
JA19H9	0.46	0.02	0.063	0.001	0.054	0.003	387	17	395	5	382	121	6
JA19H4	0.49	0.02	0.065	0.001	0.058	0.002	402	12	403	5	531	86	5
JA19H1	0.48	0.02	0.065	0.001	0.056	0.003	401	15	409	6	471	104	6

Disc. (%) 为不协和百分比。

将选好的岩石首先压碎、清水淘洗后，经过重液和磁分选，最后在双目镜下挑选锆石单矿物颗粒 30 余颗，用于 U-Pb 同位素分析。锆石颗粒大多呈自形、无色（个别边部呈黄色）。

除少数颗粒外，一般没有分带和破裂纹，表明这些锆石主要为岩浆成因。从每个样品中选择颗粒较大、晶形好、透明度高的锆石颗粒 10 颗，在澳大利亚塔斯马尼亚（Tasmania）大学用 LA-ICPMS（Hewlett Packard HP 4500）方法进行 U-Pb 定年测试。质谱仪所配激光为 213nm NewWave Merchantek UP213 Nd-YAG，详细的测试过程参照 Meffre et al.（2004）。分析结果见表 3-7，3-8 和图 3-15，3-16 所示。

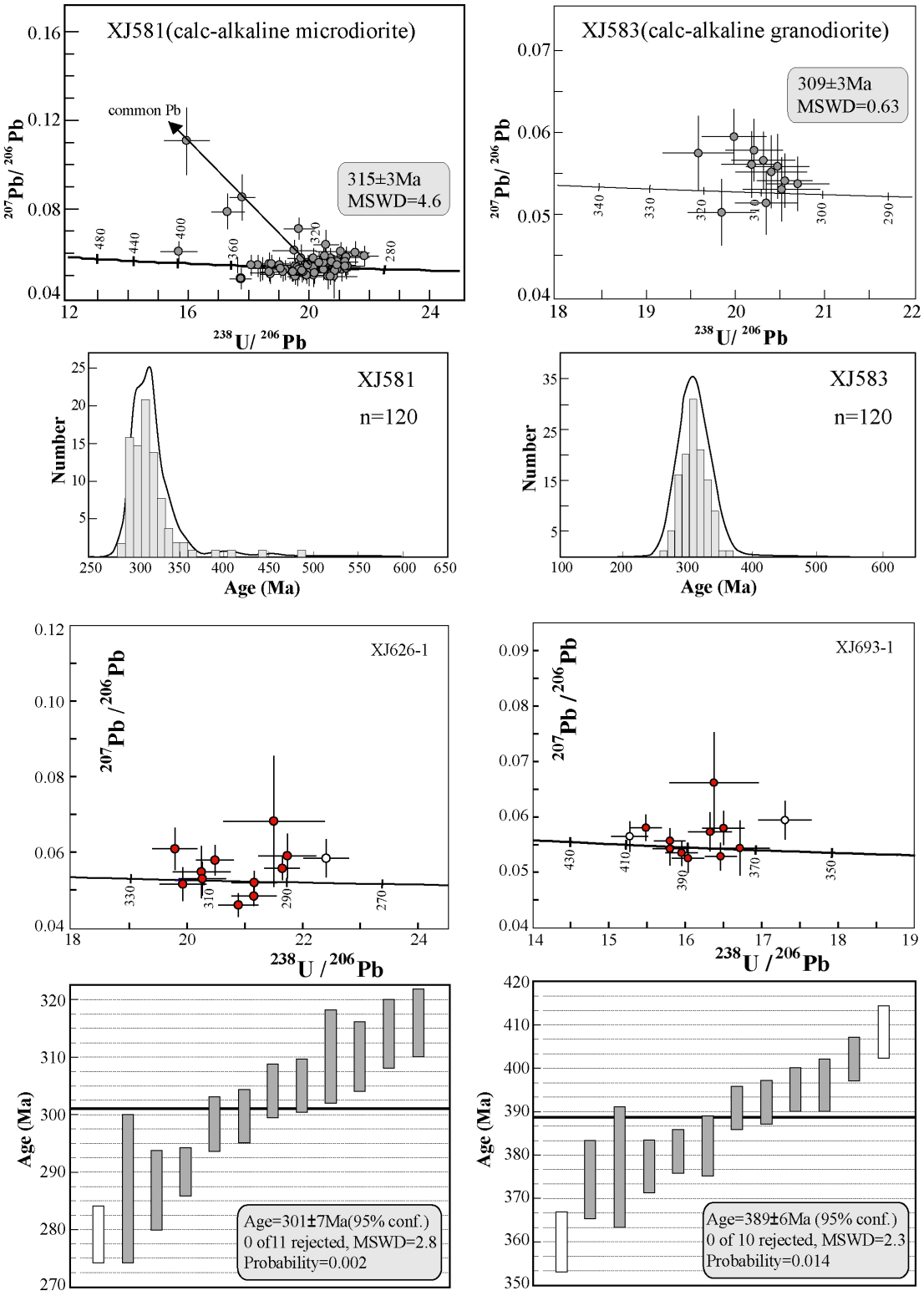

图 3-15 伊犁北部花岗岩锆石 U-Pb 测年的 $^{238}U/^{206}Pb$ 谐和图与年龄分布

表 3-8 伊犁南部花岗岩锆石 U-Pb ICPMS 测年数据

Plots	Ratios						Ages (Ma)						Disc.
	$^{207}Pb/^{235}U$	1σ	$^{206}Pb/^{238}U$	1σ	$^{207}Pb/^{206}Pb$	1σ	$^{207}Pb/^{235}U$	1σ	$^{206}Pb/^{238}U$	1σ	$^{207}Pb/^{206}Pb$	1σ	(%)
XJ515, Mean = 359±2.4 Ma				昭苏									
MA23L5	0.93	0.06	0.057	0.001	0.128	0.009	669	35	360	7.4	2071	122	8.5
MA23L9	0.52	0.02	0.056	0.000	0.068	0.002	424	11	353	2.5	863	66	2.7
MA23L10	0.51	0.01	0.057	0.000	0.066	0.002	421	10	358	2.6	811	61	2.8
MA23L4	0.41	0.02	0.056	0.001	0.056	0.003	352	15	354	3.6	465	109	3.7
MA23L8	0.44	0.03	0.057	0.001	0.058	0.004	371	20	355	5.4	515	137	5.6
MA23L11	0.44	0.01	0.057	0.000	0.057	0.002	369	9	355	2.6	478	63	2.7
MA23L12	0.45	0.01	0.058	0.000	0.056	0.002	376	10	364	2.7	466	68	2.8
MA23L3	0.45	0.01	0.058	0.000	0.056	0.002	374	9	365	2.4	454	62	2.5
MA23L1	0.48	0.01	0.060	0.000	0.059	0.002	396	10	373	2.5	577	71	2.6
MA23L7	0.46	0.02	0.060	0.001	0.057	0.002	386	11	373	3.8	505	80	3.9
MA23L2	0.45	0.02	0.060	0.001	0.058	0.003	377	15	375	3.9	545	98	4.1
MA23L6	0.45	0.02	0.061	0.001	0.055	0.002	378	13	380	3.9	402	91	4.0
XJ516, Mean = 357±6 Ma				昭苏									
MA23I6	0.61	0.04	0.036	0.000	0.121	0.007	485	24	229	1.8	1965	101	3.2
MA23I11	0.40	0.01	0.035	0.000	0.083	0.002	345	9	221	3.0	1275	46	3.1
MA23I8	0.51	0.02	0.056	0.001	0.066	0.003	417	16	350	4.4	791	91	4.6
MA23I9	0.43	0.01	0.055	0.000	0.057	0.001	362	7	348	2.9	474	51	3.0
MA23I2	0.42	0.02	0.056	0.001	0.057	0.002	360	13	350	3.7	500	86	3.8
MA23I12	0.50	0.03	0.056	0.002	0.067	0.003	409	17	353	9.7	823	101	9.7
MA23I5	0.46	0.02	0.057	0.001	0.059	0.002	387	11	356	3.4	576	74	3.5
MA23I4	0.44	0.02	0.057	0.001	0.056	0.002	368	12	358	4.0	451	90	4.2
MA23I7	3.84	0.25	0.082	0.002	0.318	0.014	1602	54	509	9.7	3562	67	20.4
MA23I1	0.44	0.01	0.060	0.001	0.054	0.002	372	11	374	3.3	355	75	3.4
MA23I10	0.46	0.01	0.061	0.001	0.055	0.002	384	9	382	3.8	406	65	3.9
MA23I3	0.53	0.02	0.064	0.001	0.060	0.002	429	11	398	3.4	609	68	3.6
XJ604, Mean = 341±6 Ma				科克苏									
MA23K9	0.89	0.05	0.054	0.001	0.118	0.007	647	30	341	5.5	1921	104	6.4
MA23K3	0.52	0.04	0.052	0.001	0.074	0.006	422	26	324	5.7	1029	153	6.0
MA23K11	0.37	0.02	0.052	0.001	0.051	0.003	317	16	327	4.1	250	135	4.3
MA23K5	0.39	0.02	0.053	0.001	0.055	0.004	332	18	334	4.4	409	148	4.6
MA23K12	0.45	0.02	0.054	0.001	0.061	0.003	378	17	339	4.2	624	113	4.3
MA23K2	0.40	0.03	0.054	0.001	0.056	0.004	345	19	342	4.7	437	143	5.0
MA23K10	0.42	0.02	0.055	0.001	0.055	0.003	354	17	343	5.2	422	137	5.4
MA23K4	0.40	0.03	0.055	0.001	0.053	0.004	340	22	342	4.8	315	171	5.1
MA23K6	0.41	0.03	0.055	0.001	0.055	0.004	346	20	346	4.9	400	146	5.1
MA23K8	0.42	0.02	0.056	0.001	0.056	0.003	356	15	350	3.8	454	120	4.0
MA23K1	0.50	0.02	0.056	0.001	0.064	0.003	412	17	354	4.2	757	104	4.4
MA23K7	6.76	0.37	0.117	0.004	0.471	0.029	2080	49	716	23.6	4153	93	47.9
XJ676, Mean = 338±8 Ma				科克苏									
DE10H12	0.34	0.02	0.041	0.001	0.057	0.002	295	12	257	6	510	87	6
DE10H2	0.37	0.01	0.042	0.001	0.063	0.002	317	7	263	3	702	56	3
DE10H6	0.46	0.04	0.046	0.001	0.070	0.007	381	29	292	9	939	194	9
DE10H8	0.43	0.03	0.048	0.001	0.062	0.004	367	19	301	8	677	129	8
DE10H5	0.34	0.04	0.048	0.002	0.050	0.007	296	34	300	13	212	315	14
DE10H3	0.41	0.05	0.053	0.002	0.068	0.009	350	36	334	11	864	268	12
DE10H10	0.49	0.02	0.054	0.001	0.066	0.003	406	16	338	8	821	94	8
DE10H1	0.44	0.04	0.054	0.001	0.058	0.006	370	30	340	8	515	216	8
DE10H11	0.53	0.06	0.055	0.002	0.064	0.007	432	42	345	13	739	241	13
DE10H9	0.52	0.03	0.056	0.001	0.068	0.003	428	17	351	8	862	92	8
DE10H7	0.48	0.02	0.061	0.001	0.054	0.002	396	16	385	6	388	102	6
DE10H4	0.51	0.04	0.063	0.002	0.058	0.004	422	25	394	12	546	161	12
XJ620, Mean = 313±4 Ma				穹库什太									
MA23J9	0.39	0.04	0.048	0.001	0.064	0.007	337	33	300	8.1	742	233	8.4
MA23J8	0.32	0.04	0.049	0.001	0.053	0.006	283	28	307	6.9	334	264	7.2
MA23J11	0.32	0.03	0.049	0.001	0.050	0.005	280	23	307	6.4	204	231	6.7
MA23J2	0.33	0.03	0.049	0.001	0.050	0.004	286	21	309	6.0	217	200	6.2
MA23JN3	0.37	0.03	0.050	0.001	0.056	0.004	322	20	312	5.0	438	160	5.2
MA23J7	0.33	0.03	0.049	0.001	0.052	0.005	287	26	311	5.7	274	242	6.1
MA23J3	0.40	0.03	0.050	0.001	0.060	0.004	340	22	316	5.0	588	160	5.3
MA23J10	0.35	0.02	0.050	0.001	0.053	0.004	306	18	314	4.6	326	160	4.8
MA23J6	0.37	0.02	0.050	0.001	0.057	0.004	320	18	315	4.8	485	152	5.0
MA23J12	0.40	0.03	0.051	0.001	0.060	0.005	345	23	319	5.6	607	168	5.9
MA23J5	0.30	0.06	0.051	0.001	0.050	0.009	269	44	318	8.9	194	410	9.5
MA23J4	0.30	0.03	0.051	0.001	0.044	0.004	267	21	323	5.6	-105	215	5.9

Disc. (%) 为不协和百分比。

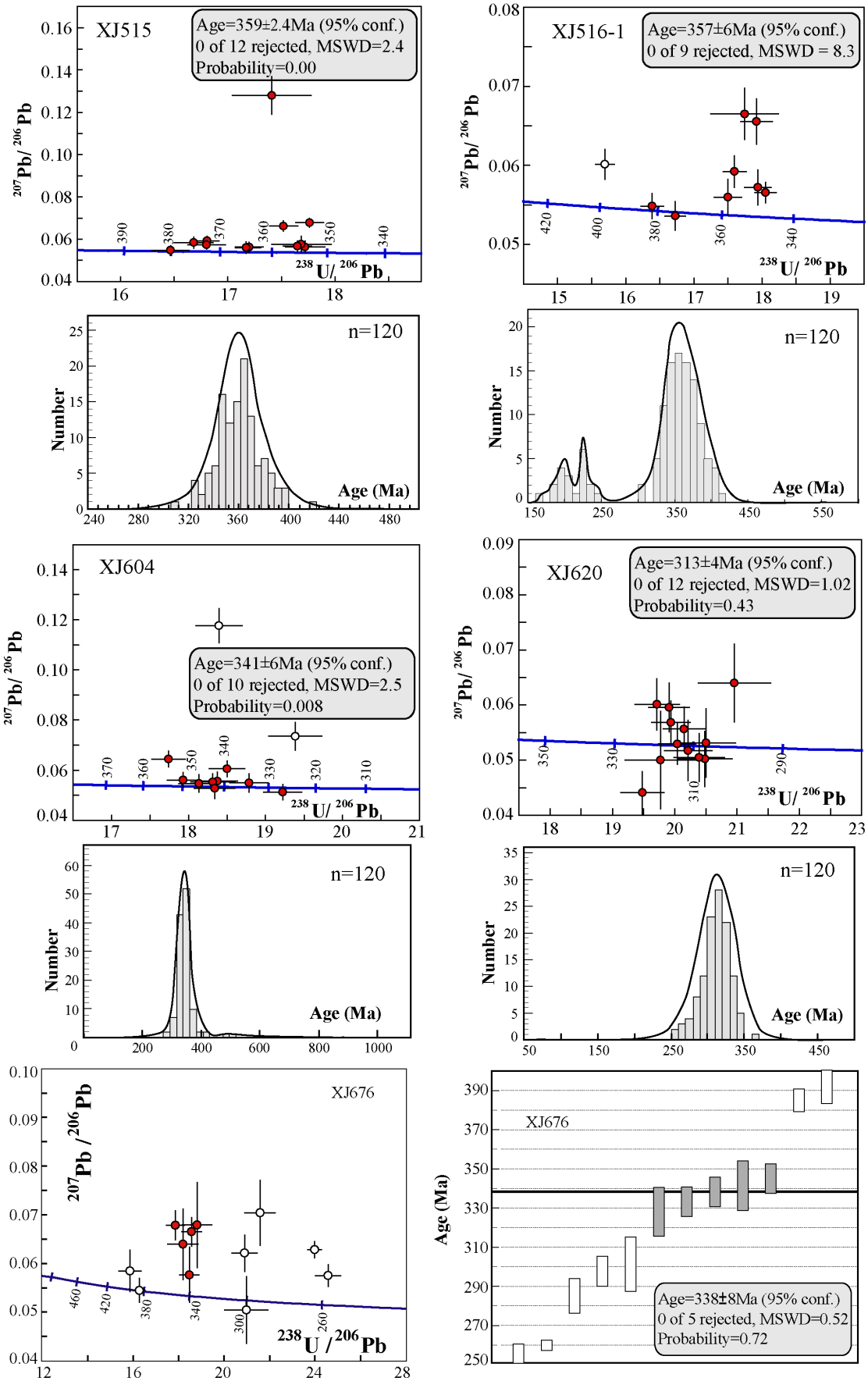

图 3-16 伊犁南部花岗岩锆石 U-Pb 测年的 $^{238}U/^{206}Pb$ 谐和图与年龄分布

岩石样品分为两组，表 3-7 和图 3-15 中所示为伊犁北部花岗岩的年龄。除了采自果子沟的样品 XJ693-1 年龄较老以外，其他三个采自独库公路玉希达坂和哈希勒根达坂一带的花岗岩年龄全为晚石炭世。样品 XJ581 中，个别分析点含有较高的普通铅，而一些分析点的年龄达 400 Ma 左右，可能代表捕获锆石的年龄，而其余分析点的年龄比较一致，谐和年龄 315±3Ma 代表岩浆结晶的年龄。样品 XJ626 中有一个测点的年龄明显小于其他测点的年龄，可能代表后期热液过程中再次结晶形成的锆石的年龄，而其他测点的谐和年龄为 301±7Ma，与样品 XJ583 基本一致。样品 XJ693-1 的一个测点年龄为 408±6Ma，可能来自捕获的碎屑锆石，另外一个测点的年龄 360±7Ma 与其他测点的年龄相差也比较大，而其余 10 个测点的谐和年龄为 389±6Ma，代表岩浆结晶成岩的时代。

表 3-8 和图 3-16 显示了伊犁南部昭苏和科克苏地区花岗岩的年龄。其中昭苏剖面黑云母花岗岩 XJ516-1 的谐和年龄为 357±6Ma，而侵入其中的钾长石花岗岩的谐和年龄为 359±2.4Ma。另外，在 XJ516-1 中，有一批分析点的年龄平均值为 396±3.6Ma，该年龄老于钾长石花岗岩的年龄，与果子沟的花岗岩 XJ693-1 的年龄接近，可能代表早期的岩浆作用。但是样品 XJ516-1 其他测点的年龄则集中在 360Ma 左右，与钾长石花岗岩的年龄一致，可能代表第二期岩浆活动中再次结晶的年龄。另外，科克苏地区红色钾长石花岗岩 XJ604 的 10 个测点产生一个谐和年龄为 341±6Ma，另外两个测点的年龄则相对较为年轻，分别为 317±6Ma 和 317±6.4Ma，与穹库什太地区黑云母花岗岩 XJ620 的谐和年龄 313±4Ma 比较接近。采自科克苏河的另外一个花岗岩 XJ676 产在韧性变形带和高压变质岩带的北侧（见第五章），该花岗岩与超糜棱岩化的辉长岩不同，并没有发生韧性变形。从该样品 U-Pb 谐和年龄图可以看出至少两期岩浆结晶作用，最早的锆石形成于 385~390Ma，高峰期岩浆作用年龄为 338±8Ma。至于其他高 U 锆石的年龄则从 250 到 300Ma，可能与后期构造、热事件造成的 Pb 丢失有关。

综上所述，伊犁地区花岗岩主要形成于 360~300 Ma 期间，而少数样品的年龄为 390Ma 左右。由此可以推断，伊犁地区与俯冲作用有关的岩浆活动最早可能发生在 390Ma 左右（中泥盆世晚期），而岩浆作用的高峰期则为石炭纪。这些花岗岩从老到新，从北向南在整个伊犁地区普遍存在。

第五节 小结

1．伊犁地区广泛分布有石炭纪火山岩与侵入岩。火山岩以中性安山岩类为主，酸性流纹岩类次之，少量中基性岩石。侵入岩以酸性的花岗岩为主，也有中基性辉长岩、中性闪长岩等。这些岩石与沉积岩紧密伴生，后者以浅水相陆源碎屑沉积为特征，没有深海相沉积岩发育。火山岩多与沉积岩呈互层出现，火山碎屑岩普遍发育，代表多期岩浆喷发-沉积作用。

2．本论文所研究的伊犁地区六个主要剖面火山岩具有典型的火山结构，岩石发生了中等程度的结晶作用。后期低温条件下的蚀变作用使这些岩石的矿物组成和地球化学成分发生了不同程度的改变。大多数火山岩具有富 Na, Al 低 Mg, Ca 的特点。主量元素和微量元素特征一致表明，这些火山岩属于钙碱性系列，不同剖面的火山岩具有类似的地球化学特征。所有剖面火山岩的轻稀土元素比重稀土元素相对富集，但稀土元素配分曲线比较平缓，单个剖面和不同剖面之间均没有明显的分异现象。大部分火山岩具有弱 Eu 负异常，个别样品表现有强负异常，而少数没有 Eu 异常。所有火山岩样品富集 Rb, Th, Ba 等大离子亲石元素，而亏损 Nb, Ta, Zr, Hf 等高场强元素，和形成于俯冲带之上的火山岩特征一致。大部分火山的 Nb 含量与大陆岛弧火山岩比较接近，而不同于大洋岛弧玄武岩和洋脊玄武岩。微量元素判别图中，所有火山岩均具有钙碱性玄武岩的特征，并属于大陆岛弧火山岩。

3．伊犁地区花岗质岩石具有低 K 富 Na、低 Al 富 Ca 和富集 Fe, Mg, Mn 的特点，与典型的低钾高钙含角闪石的钙碱性花岗岩（ACG）十分一致。这些花岗质岩石与火山岩具有

类似的微量元素特征，表现为轻稀土元素比重稀土元素富集，中等到弱的 Eu 负异常，以及富 Rb, Th, Ba 而亏损 Nb, Ta, Zr, Hf 等元素。不同地区花岗质岩石的地球化学特征均比较一致。微量元素判别图显示，这些花岗质岩石大部分属于火山岛弧花岗岩类型，个别可能形成于岛弧岩浆活动后期的碰撞环境。

4．伊犁地区石炭纪火山岩 Sr 同位素组成比洋脊玄武岩和洋岛玄武岩 Sr 同位素组成明显要高，但与安第斯山地区的安山岩比较一致。花岗质岩石 Sr 同位素组成与 I 型花岗岩比较接近，而明显低于 S 型花岗岩。一些火山岩和花岗质岩石的 Sr 同位素组成还与上地壳和碎屑沉积岩类似。同时，火山岩与花岗质岩石的 Nd 同位素组成非常一致，并明显小于洋脊玄武岩的 Nd 同位素组成，与洋岛玄武岩 Nd 同位素组成比较一致，但更接近于北美西部俯冲带安山岩。在所研究的每一个剖面，火山岩和花岗质岩石的$\varepsilon_{Nd(T)}$值既有负值也有正值。以上特征表明，伊犁地区火山岩和花岗质岩石源自亏损的地幔岩浆，可能由大洋地壳和洋底沉积物在俯冲带发生熔融形成，并在岩浆上升和结晶过程中，受到上地壳物质的混染。因而，这些岩浆岩代表一个活动大陆边缘环境。

5．花岗质岩石锆石 U-Pb ICPMS 定年结果表明，伊犁地区钙碱性花岗质岩石的形成年龄为 389~301Ma，但是大部分岩石的年龄小于 360Ma，表明与俯冲有关的岩浆活动最早可能发生在中泥盆世末，而岛弧岩浆作用的高峰期为 360~301Ma，既石炭纪。

第四章 伊犁地块北缘构造特征

伊犁地块北缘边界为北天山构造带，位于准噶尔盆地南缘（图 2-7）。一直以来，北天山被认为是一个晚古生代火山岛弧（Windley et al., 1990；Allen et al., 1992；肖序常等，1992；马瑞士等，1993；Gao et al., 1998）。该火山岛弧的形成曾经被解释为北天山洋盆朝北俯冲作用的产物。一般认为，北天山岛弧从西天山巴音沟一带向东延伸至博格达和东天山哈尔里克山（Windley et al., 1990；肖序常等，1992；马瑞士等，1993；孙家齐等，1994；王赐银等，1996；Gao et al., 1998；Laurent-Charvet, 2001）。但也有学者认为，北天山西段（乌鲁木齐以西地区）主要由复理石和蛇绿混杂岩组成（肖序常等，1992；高俊等，1997）。根据作者近 4 年来的考察，北天山可分为两个明显不同的构造地层单元：北天山构造缝合带与火山岛弧，二者之间的界限可以在后峡剖面中观察到（图 4-1）。 两个单元的构造属性对重新认识伊犁地块及天山造山带古生代构造演化具有重要意义。

第一节 北天山构造及变形特征分析

在博罗科努山北坡，一个长逾 300km，宽约 50km 的构造带沿 SEE-NWW 方向展布。该单元主要由石炭系浊积相复理石和蛇绿混杂岩组成，二者构成一俯冲杂岩带。根据浊积相复理石变形、变质程度的不同，可以将其再分为两个次级单元：北部未变质、弱变形带和南部韧性变形、高温变质带。后者被北天山断裂所限，为伊犁晚古生代岩浆岛弧（见第三章）的北缘边界（图 4-1）。

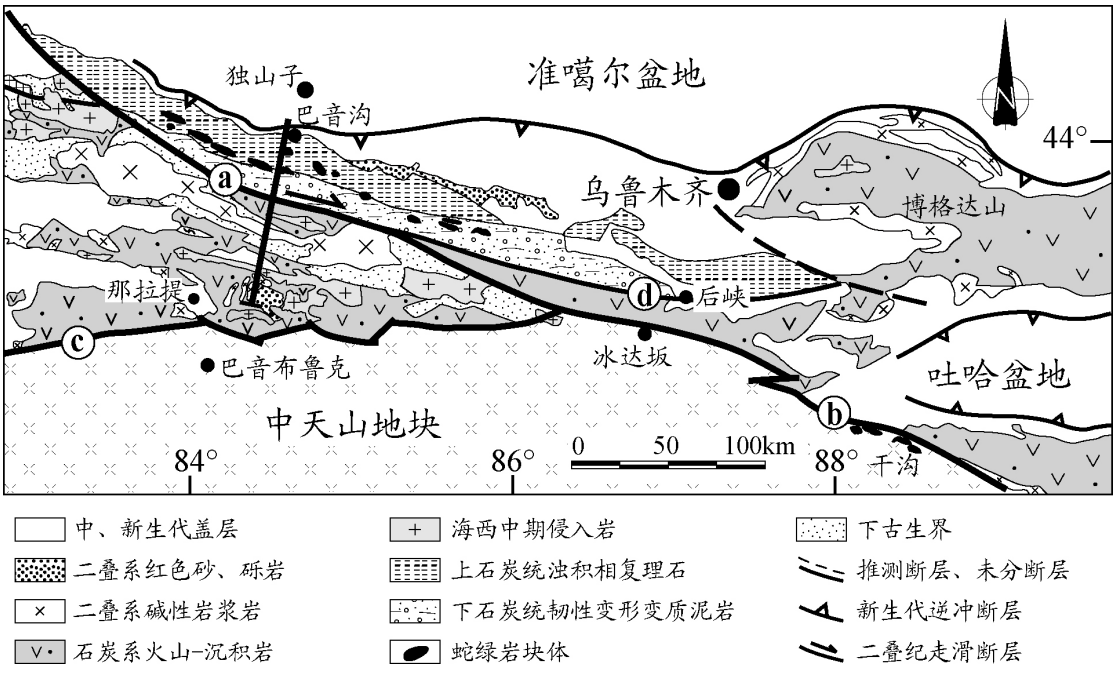

图 4-1 北天山及邻区地质构造简图

a, 北天山断裂；b, 天山主断裂；c, 那拉提断裂；d, 后峡断裂

1. 北天山构造地层特征

1.1. 石炭系弱变形浊积复理石带

由独山子向南 20km 的独库公里上，石炭系复理石向北逆冲推覆于新近系砂岩之上（图 4-2a）（Gao et al., 1998）。区域上，北天山复理石的北部亚单元被划归为上石炭统巴音沟组（C_2b）（新疆地矿局，1973；1993），主要由灰黑色凝灰质细砂岩、粉砂岩夹凝灰质泥岩、粉砂岩和少量硅质、泥质砂岩组成（图 4-2b,c,d,e）。砂岩中含有芦苇等植物化石及深水遗迹

化石，指示一种深海浊积扇沉积。岩层从薄、中到厚层状不等，单层厚度从几厘米到几米（图4-2b,c,d）。在一些剖面上还可见到典型的鲍玛层序（晋慧娟等，1989）。砂岩中岩屑颗粒包括陆缘沉积物、火山凝灰质碎屑岩、花岗岩碎屑、硅质岩碎屑和少量碳酸盐岩碎屑等（图4-2f）。岩石学分析表明，花岗质岩屑主要由花岗闪长岩、闪长岩和辉长岩组成，并具有钙碱性地球化学特征（晋慧娟等，1989）。岩层变形主要以褶皱和局部断裂为特征（图4-2b,c）。粒序层和层面重力印模等沉积构造比较常见，正常层序和倒转层序均有发育，二者具有近似的产状，指示同斜褶皱变形。同时，南倾的逆冲断层及伴生的破劈理指示从南向北的逆冲推覆作用。

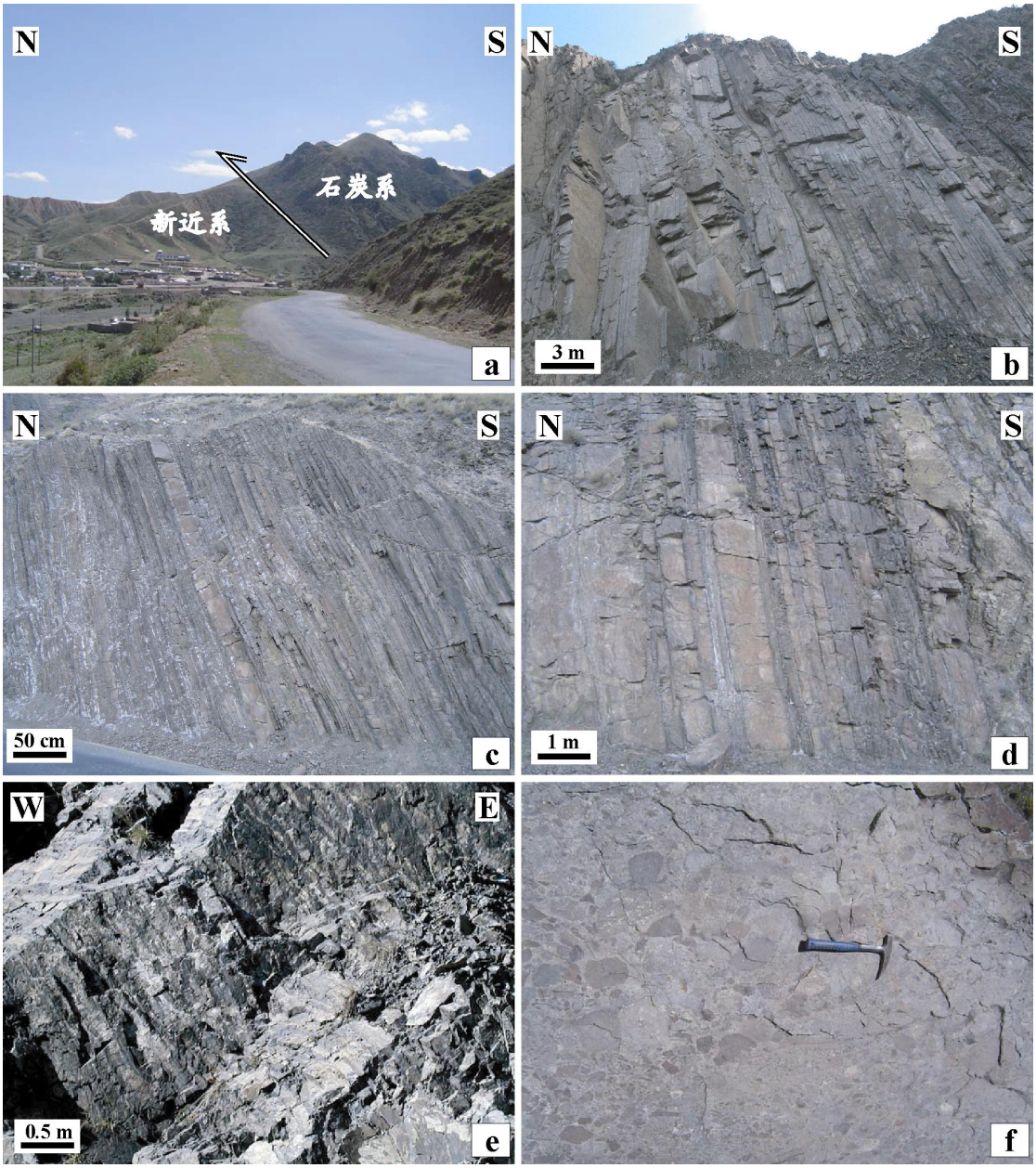

图4-2 北天山石炭系巴音沟组浊积复理石野外特征

1.2. 蛇绿混杂岩带

蛇绿混杂岩产出于浊积复理石中，呈不连续的块体分布在长250km，宽5~15km范围内（图4-1）。新疆地矿局（1973）将其作为一个地层单元划归为晚石炭世沙大王组（C_3s）。前人已经在该地区报道了多个蛇绿混杂岩剖面。在巴音沟地区，蛇绿岩主要包括蛇纹岩化橄榄

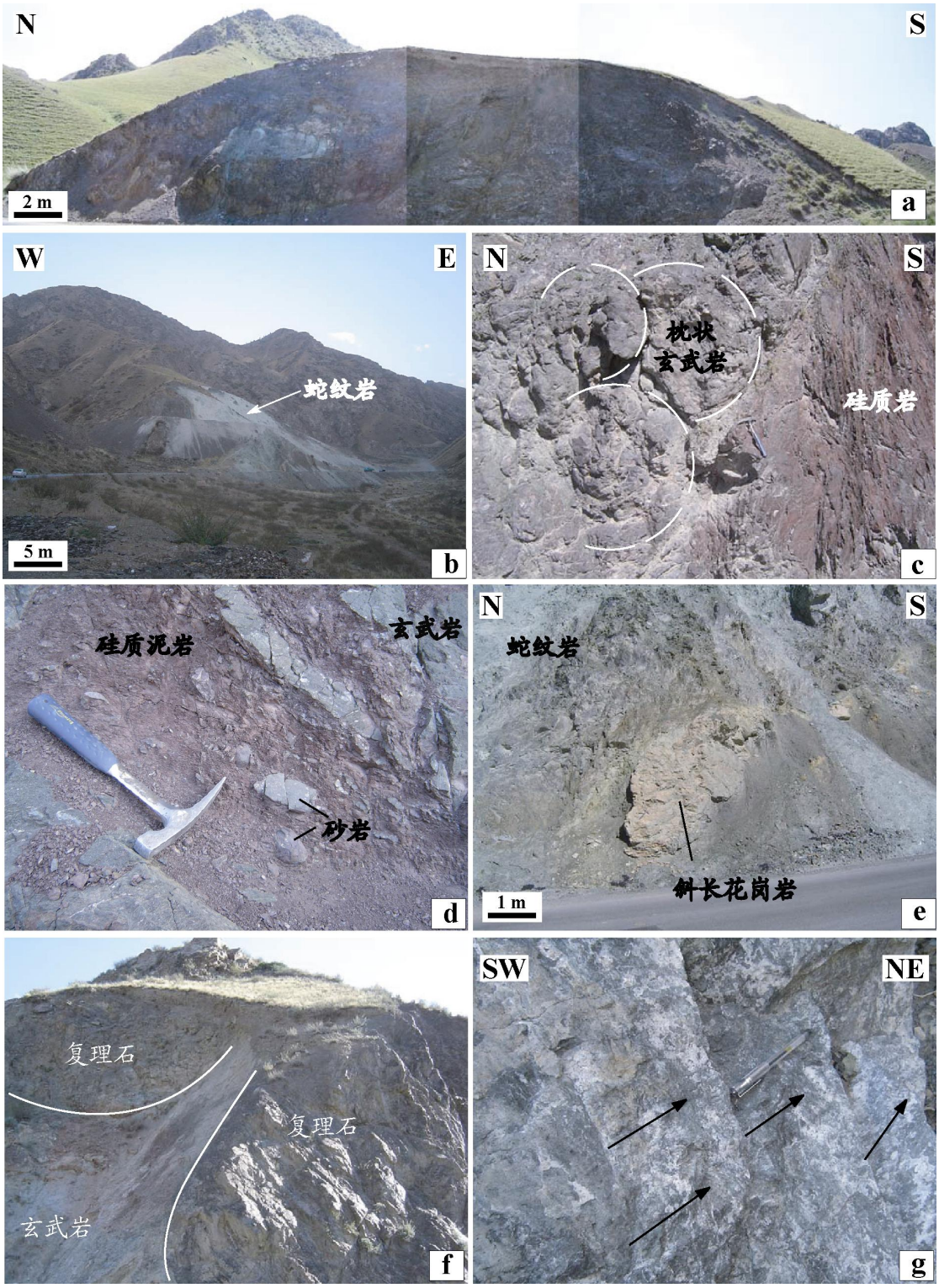

图 4-3 北天山巴音沟蛇绿混杂岩野外地质特征

岩（图 4-3a,b,e）、辉长岩、辉绿岩、（枕状）玄武岩（图 4-3c,d,f）、斜长花岗岩（图 4-3e）、硅质岩（图 4-3c,d）和少量灰岩（邬继易等，1989；肖序常等，1992；徐学义等，2005，2006）。同时，黑色、红色泥岩和浅黄绿色硬砂岩多被揉皱变形并环绕在其它蛇绿岩块周围。部分基性硬砂岩容易被误认为是辉长岩，但岩石学分析表明，该类岩石应为辉长质砂岩。野外观察表明，蛇绿岩主要以两种方式产出：（1）块状玄武岩、枕状玄武岩和上层泥质硅质岩呈连续的序列（图 4-3c），规模达数十米；（2）镁铁、超镁铁岩和沉积岩（主要为复理石和灰岩）

以单独的块体产出于强烈片理化的泥岩和复理石基质中，块体大小从数厘米到近 1km 不等（图 4-3d,f）。在第二种产状中，岩石块体没有任何的规律而随意分布在基质中。砂岩和玄武岩以透镜体镶嵌在强烈变形的泥岩中，表现为典型的破碎构造（图 4-3d）。基性岩块与沉

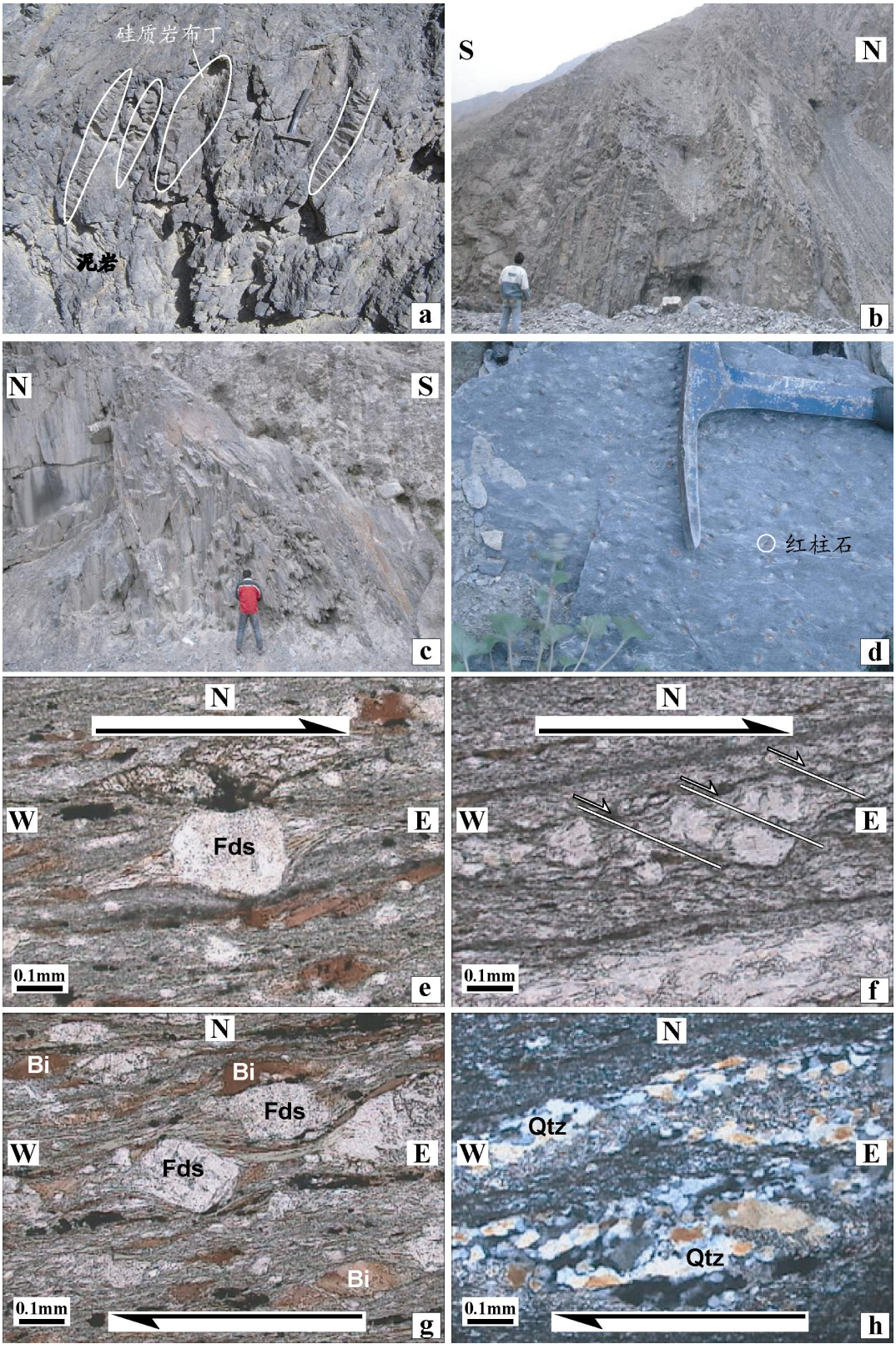

图 4-4 北天山断裂带绿片岩相变质泥岩野外特征和韧性剪切变形显微构造

Bi，黑云母；Fds，长石；Qtz，石英

积岩块有时呈断层接触，并共同被复理石基质所包围（图 4-3f）。

另外，据新疆地矿局（1973）的调查，在莫托沙拉沟-古尔图一带出露的蛇绿混杂岩体共有 21 处之多。沿莫托沙拉沟河谷可见大量红色深海硅质软泥以及与绿色镁铁岩的混杂岩滚石。河谷两侧的山体，由北向南、自上而下依次为中石炭世巴音沟组（C_2b）和沙大王组（C_3s），前者岩性主要由粉砂质、硅质泥岩、泥质或硅质粉砂岩、砂岩和火山凝灰岩组成，后者岩性则主要为含泥粉砂岩和凝灰岩等。镁铁、超镁铁岩体主要产于沙大王组中，出露在剖面起点南部约 12km 处（起点 GPS 坐标 N44°08’42”，E83°57’57”，终点 N44°08’06”，E83°58’30”）。露头上见到的蛇绿岩块体主要有蚀变橄榄岩、基性杂岩、基性熔岩、火山碎屑岩、远洋深海沉积硅质岩等（李生虎等，1994）。此外，含砾石泥岩（Pebbly mudstone）中包含角砾状辉长岩、玄武岩、砂岩、硅质岩和灰岩，可能代表火山岛弧前沿快速剥蚀、快速沉积的海沟浊积环境。出露在该剖面的蛇绿岩体基本上已被强烈构造肢解，未见完整的蛇绿岩套序列。各类岩块沿一系列逆冲断层和平移断层与基质呈构造接触，单个岩体一般呈块状，各岩体总体上沿 NWW-SEE 延伸、排列。在橄榄岩和玄武岩的表面，偶尔可以观察到具有透入性的拉伸线理构造（图 4-3g）。

1.3. 韧性变形复理石带

从蛇绿混杂岩带南侧至哈希勒根达坂北麓，复理石地层发生了明显的剪切变形。黑色硅质泥岩中发育硅质岩布丁构造（图 4-4a），布丁体呈透镜状、无根状近直立、断序排列，表明硅质泥岩经受了强烈的垂向剪切作用。硅质泥岩的南侧为强烈片理化并低绿片岩相变质的板岩、千枚岩和泥质片岩等。区域上，这些岩层被划归为中泥盆统拜辛德组（D_2b）（新疆地矿局，1973）。然而，对这些低绿片岩相变质岩的原岩分析表明，其沉积相与北部复理石无明显差别。在野外，没有观察到该岩层与蛇绿混杂岩北侧的复理石单元之间直接的接触关系。另外，由于该带南侧与“北天山断裂”（Zhou et al., 2001）或“博罗科努断裂”（Zhao et al., 2003）接触，并非常靠近沿断裂分布的海西晚期花岗岩（图 4-1），因而该单元不同于北侧复理石的变形、变质特征很可能是后期构造和岩浆热事件作用的结果，而并不代表其时代上的早晚差别。在板岩中，可见大量红柱石矿物，直径大小 0.1~1cm（图 4-4d），指示热接触变质作用，可能与海西晚期花岗质岩浆活动有关。该带南北宽度达 5 公里左右，呈 NNW-SSE 向延伸数百公里至后峡以南的冰达坂一带（图 4-1），受变形、变质的岩石主要为绿片岩、板岩和千枚岩。其中绿片岩原岩主要为凝灰质火山岩、凝灰岩和粉砂岩等。鉴于这些岩层发育在后峡剖面火山岩的南部，因此可能为北天山火山岛弧的组成部分（详见第二节）。

在哈希勒根达坂北麓的奎屯河谷，低绿片岩相变质的板岩、千枚岩和泥质片岩中发育 180°∠80°的 S_1 面理，并强烈改造了原生 S_0 面理（图 4-4b,c）。在 S_1 面理面上发育近水平、近 110°方向的拉伸线理构造。向东到冰达坂北坡，绿片岩 S_1 面理产状为 210°∠60°（~70°），近水平的矿物线理由拉长、定向排列的绿泥石、红柱石等（低）绿片岩相变质矿物组成。以上变形特征表明，该带为一个韧性剪切带，其运动学和年代学特征将在下文讨论。

2. 北天山多期变形分析

北天山位于天山造山带与准噶尔盆地的接合部位，在天山多旋回演化中，经历了多期构造变形。野外观察和区域构造分析表明，北天山主要经历了三期构造变形，从新到老依次为：北向逆冲推覆（D3），韧性走滑剪切（D2）和北向仰冲推覆（D1）作用（图 4-5）。

2.1. 北向逆冲推覆变形（D3）

在准噶尔盆地南缘，三叠系-新近系河流相陆源碎屑岩沉积序列厚达 10km 的（Liu et al., 1990），岩层普遍发生了褶皱变形。如图 4-2a 所示，石炭系地层向北逆冲推覆于中-新生代盆地之上，该推覆作用至少发生在新近纪以后。在石炭纪和中、新生代地层中，发育有一系列高角度脆性逆冲断层和向南倾斜的紧闭褶皱，指示南北向的挤压、缩短作用，断层两侧发

育的破劈理和拖曳褶皱显示从南向北的逆冲动向。地貌学和磁性地层学研究结果表明，这一挤压作用造成了南北向近 30km 的地壳缩短，可能与新生代印-藏碰撞作用向北的远距离效应有关（Avouac et al., 1993；Hendrix et al., 1994；Poupinet et al., 2002；Shu et al., 2005；Charreau et al., 2005）。

2.2. 韧性走滑剪切作用（D2）

在韧性剪切带中，绿片岩化或糜棱岩化岩石中普遍发育有不对称组构，如长石、石英σ或δ形斑晶，S-C 组构等，均指示右旋剪切动向。从定向样品的显微构造中可以观察到大量的运动学标志。一些长石斑晶局部被方解石替代，在斑晶的周围往往有黑云母形成的压力影构造（图 4-4e, g），σ形黑云母片形成云母鱼构造（图 4-4e, g），在长石斑晶周围或者岩石裂隙中常有石英动态重结晶现象，表现为石英亚颗粒的锯齿状边缘和波状消光，并斜向排列（图 4-4h）。S-C 组构在薄片中非常发育，一系列剪切带围绕在细小的长石或石英斑晶周围（图 4-4f）。所有这些运动学标志均显示右旋剪切作用。

该剪切带向东经米什沟到东天山阿奇库都克、尾亚一带，分别被称为“天山主韧剪带”（Main Tianshan Shear Zone, MTSZ）（Windley et al., 1990）和“阿奇库都克-尾亚带” (Shu et al., 1999，2002；Laurent-charvet et al., 2002, 2003)。韧性剪切作用使古生代基性火山岩发生强烈糜棱岩化，并形成一系列鞘状褶皱和反转褶皱，沿褶皱轴平行发育 N80°方向的水平拉伸线理。麻粒岩和变质辉长岩中书斜构造和辉石核幔构造等运动学标志以及石英 c 轴组构（Shu et al., 1999，2004；Laurent-charvet et al., 2001）统一指示右旋动向，与西天山运动学标志完全一致。

最新的 Ar-Ar 热年代学研究结果表明，哈希勒根达坂北坡和冰达坂北坡韧性剪切带糜棱岩化千枚岩和板岩中黑云母的年龄为 245~285Ma（详见下文）。同时，Shu et al.（1999）对米什沟二云片麻岩进行了白云母单矿物分步加热测试，分别得到 269.1±5.4Ma 的 K-Ar 坪年龄和 268.8±5.4Ma 的等时线年龄。另外在东天山，马瑞士等（1993）对位于中天山北缘阿奇山韧性剪切带中的云母片岩进行了 Rb-Sr 全岩定年，获得等时线年龄为 292±29Ma。而康古尔韧性剪切带中古生代糜棱岩化花岗岩 Rb-Sr 全岩年龄为 260±6Ma。这些测年结果非常一致地表明，在北天山从东到西的区域范围内存在一期 270Ma 左右的高峰构造热事件，该事件使相关岩石普遍发生了右旋韧性剪切变形。

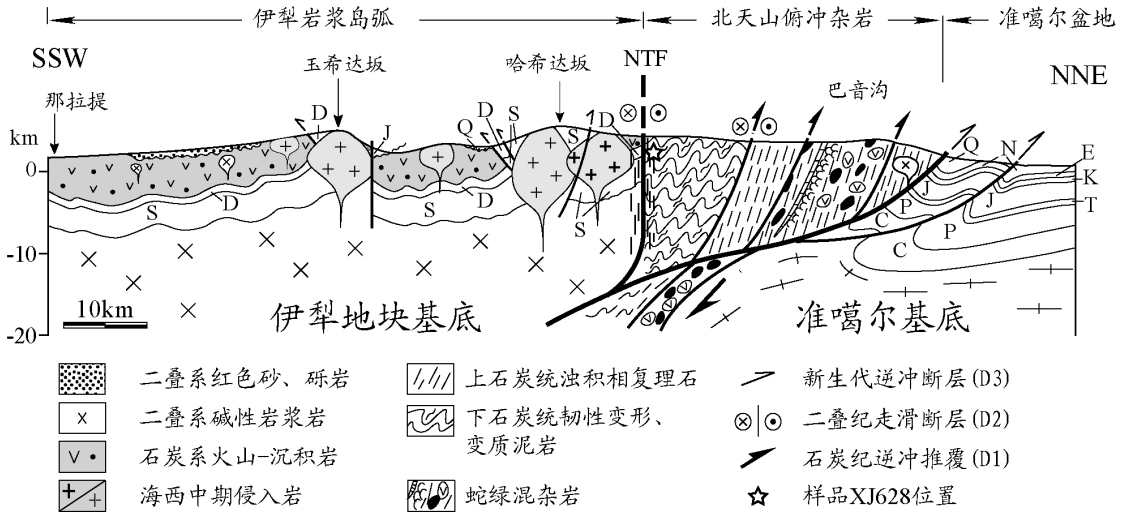

图 4-5 巴音沟-那拉提地质、构造解释剖面（剖面位置见图 4-1，地壳厚度根据 Liu et al., 1990）
S, 志留系；D, 泥盆系；C, 石炭系；P, 二叠系；T, 三叠系；J, 侏罗系；K, 白垩系；E, 古近系；N, 新近系；Q, 第四系；NTF, 北天山断裂

2.3. 北向仰冲推覆作用（D1）

在复理石单元中，一系列紧闭同斜褶皱和不对称褶皱指示从南向北的逆冲推覆作用。由于新生代南北向挤压作用的强烈改造，所以很难判断这些不对称褶皱发生在新生代还是更早。但在一些平行于层面的面理上，可以观察到绿泥石和伊利石构成的南北向擦痕或拉伸线理构造，并被低角度近东西向线理构造所切断，后者应与二叠纪走滑剪切作用有关，因而前者应该早于二叠纪。在蛇绿混杂岩带中，类似的剪切构造也比较常见。如图 4-3g 中所示，变质橄榄岩块的表面，发育有 NE-SW 向的透入性拉伸线理构造。在显微镜下，由于岩石重结晶作用非常强烈，运动学标志往往超出了拍摄尺度，但野外的构造要素（如阶步）指示从南向北的运动动向。保存于蛇绿混杂岩块中的这些韧性变形运动学要素可能直接与混杂岩的向北仰冲、侵位过程有关。也就是说，发生在二叠纪走滑剪切事件之前的蛇绿混杂岩构造变形作用，可能与洋壳俯冲消减和随后的碰撞所引起的南北向挤压和蛇绿混杂岩仰冲推覆作用有关。

表 4-1 北天山断裂韧性剪切带含黑云母变质泥岩 Ar-Ar 分析数据

Step	$^{40}Ar_{Atm}$	$^{39}Ar_K$ (%)	$^{37}Ar_{Ca}/^{39}Ar_K$	$^{40}Ar^*/^{39}Ar_K$	Age (Ma)
		XJ628-7	Whole Rock	J=0.00539635	
1	35.4	1.7	0.2	16.8	156.5 ± 3.7
2	8.1	0.9	0.1	23.4	214.1 ± 3.6
3	2.0	3.7	0.1	24.7	225.7 ± 1.5
4	1.1	9.1	0.1	27.4	248.4 ± 0.5
5	0.5	4.4	0.1	30.0	270.4 ± 0.9
6	0.3	5.6	0.1	31.3	281.3 ± 0.7
7	0.4	15.4	0.1	31.6	284.0 ± 0.5
8	0.5	24.1	0.1	30.4	274.1 ± 0.5
9	0.6	13.3	0.2	29.5	266.8 ± 0.5
10	1.0	12.1	0.2	28.3	256.6 ± 0.5
11	0.9	7.5	0.3	28.2	255.5 ± 0.7
12	2.9	1.8	2.4	27.2	246.9 ± 1.3
13	9.1	0.2	7.2	23.6	216.6 ± 9.0
fusion	65.5	0.2	4.5	11.0	103.7 ± 25.2
		XJ703	Whole Rock	J=0.00539543	
1	63.3	1.5	0.3	13.0	122.6 ± 3.3
2	17.5	1.7	0.1	17.2	160.1 ± 1.4
3	6.9	4.1	0.1	24.4	223.2 ± 1.8
4	1.1	7.5	0.1	28.2	255.6 ± 0.5
5	0.6	6.4	0.0	29.2	264.0 ± 0.5
6	0.5	6.5	0.0	29.7	268.3 ± 0.7
7	0.6	3.2	0.0	30.0	270.8 ± 0.9
8	0.5	9.7	0.1	30.2	271.9 ± 0.5
9	0.4	9.1	0.1	30.3	273.2 ± 0.5
10	0.7	11.9	0.1	29.9	269.7 ± 0.5
11	0.9	12.0	0.1	29.5	266.0 ± 0.6
12	1.0	9.8	0.1	29.3	265.0 ± 0.6
13	1.3	6.9	0.1	29.1	263.2 ± 0.7
14	1.5	8.1	0.1	29.0	262.5 ± 0.5
15	6.0	1.4	1.5	28.0	253.5 ± 2.0
fusion	25.2	0.2	6.3	29.1	263.3 ± 12.0

$^{40}Ar^*$为自然钾衰变过程中产生的放射成因 Ar；$^{40}Ar_{atm}$ 为大气成因 ^{40}Ar；$^{37}Ar_{Ca}$ 和 $^{39}Ar_K$ 分别为照射过程中有 Ca 和 K 形成的 Ar；J 为照射参数。

衰变常数 $^{40}K_{tot}$ = 5.543 x 10^{-10} a^{-1}；同位素丰度比值 $^{40}K/K$ = 0.01167 atom %（Steiger and Jäger, 1977）。

3. 北天山韧性走滑剪切带 Ar-Ar 年代学研究

分别从采自奎屯河谷和冰达坂北坡的定向样品中，选择富含黑云母矿物的糜棱岩化千枚岩样品 XJ628-7 和板岩样品 XJ703。将岩石研碎并清水洗涤、室温晾干后，在双目镜下挑选片状、富含黑云母的全岩颗粒 20 余个，颗粒大小为 0.3~2mm。全岩颗粒在法国 Rennes 大学激光探针中心用加拿大产 McMaster 反应堆连同透长石标样 TCR-2 一起照射 13 小时，最后用 $^{40}Ar/^{39}Ar$ 点熔激光探针(CO_2 Synrad®)和 Map215®质谱进行分析。详细的加热步骤和其他技术参数见 Ruffet（1991，1995）的描述。$^{40}Ar/^{39}Ar$ 分析数据见表 4-1。

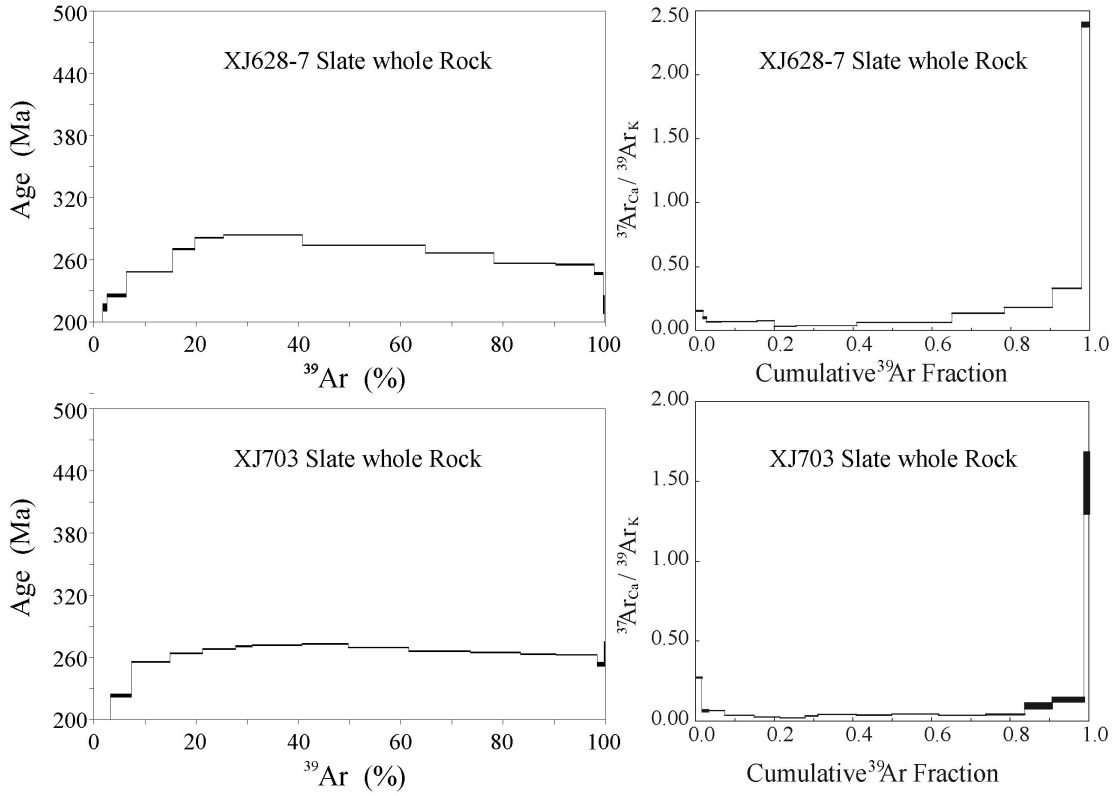

图 4-6 北天山断裂带韧性变形变质泥岩全岩 Ar-Ar 年龄谱

图 4-6 为 2 个样品全岩 $^{40}Ar/^{39}Ar$ 年龄谱图。从中可以看出，两个谱图均为不规则的穹隆形，在 90% Ar 释放的情况下，视年龄分别为 245~285 Ma（XJ628-7）和 255~275 Ma（XJ703）。从两个样品加热过程中 $^{37}Ar_{Ca}/^{39}Ar_K$ 比率的变化规律（表 4-1）可以看出，$^{37}Ar_{Ca}/^{39}Ar_K$ 均表现出 U 型的演变趋势，表明二者在化学成分上均为异源型，由多种不同的矿物组成。另外，$^{37}Ar_{Ca}/^{39}Ar_K$ 比率的变化趋势（表 4-6）正好与视年龄的变化呈负相关。在加热的初始阶段，$^{37}Ar_{Ca}/^{39}Ar_K$ 比值较高，可能与热蚀变过程中方解石和（或）绿泥石的形成有关。在加热最后阶段（最后 30%的氩气释放过程），较高的 $^{37}Ar_{Ca}/^{39}Ar_K$ 比值则可能是富 Ca 长石去气作用的结果。而中间过程则以低 $^{37}Ar_{Ca}/^{39}Ar_K$ 比率为特征，可能由富 K 云母（主要为黑云母）的去气作用所致。

尽管 2 个全岩样品穹隆型视年龄谱表现了样品中矿物成分和去气过程的复杂性，但其视年龄范围却相当一致。因此，这些岩石在走滑剪切带中靡棱岩化韧性变形作用发生在早-晚二叠世。从本节 2.2 部分的论述中可以看到，岩石发生了明显的动态重结晶，且部分岩石强烈细粒化。穹隆型视年龄谱的中间部分体现了在中子照射过程中富 K 云母向贫 K 矿物的回变过程，并在加热的最后阶段表现为富 Ca 长石的去气作用，表明在整个变形过程中均伴随有动态重结晶作用。在靡棱岩化作用引起的动态重结晶过程中，原有的同位素稳定体系被彻

底打破，而重新建立的同位素系统则反应的是动态重结晶过程的年龄。总之，这一年龄比较可靠地反应了走滑剪切作用的时代。该时代范围与前人在天山主断裂带和东天山走滑剪切带中获得的年龄基本一致（Shu et al., 1999，2002；Laurent-Charvet et al., 2002）。

第二节 北天山火山岛弧

在天山东段，北天山由围绕在吐-哈盆地周缘的几个火山岛弧组成，即博格达岛弧、哈尔里克岛弧、觉罗塔格岛弧和雅满苏岛弧（马瑞士等，1993；1997；孙家齐等，1994；王赐银等，1996；舒良树等，1997；王宗秀等，2003）。而在天山西段，北天山火山岛弧主要指博格达岛弧和觉罗塔格岛弧向西的延伸，主要发育在后峡与冰达坂之间（图 4-1）。需要指出的是，一些学者认为，博格达及邻区石炭系火山岩为大陆裂谷作用（车自成等，1996；Xia et al., 2003；2004）、“俯冲撕裂型”裂谷（顾连兴等，2001a；2001b；王银喜等，2005，2006）和地幔柱作用（夏林圻等，2004；2005）的产物。

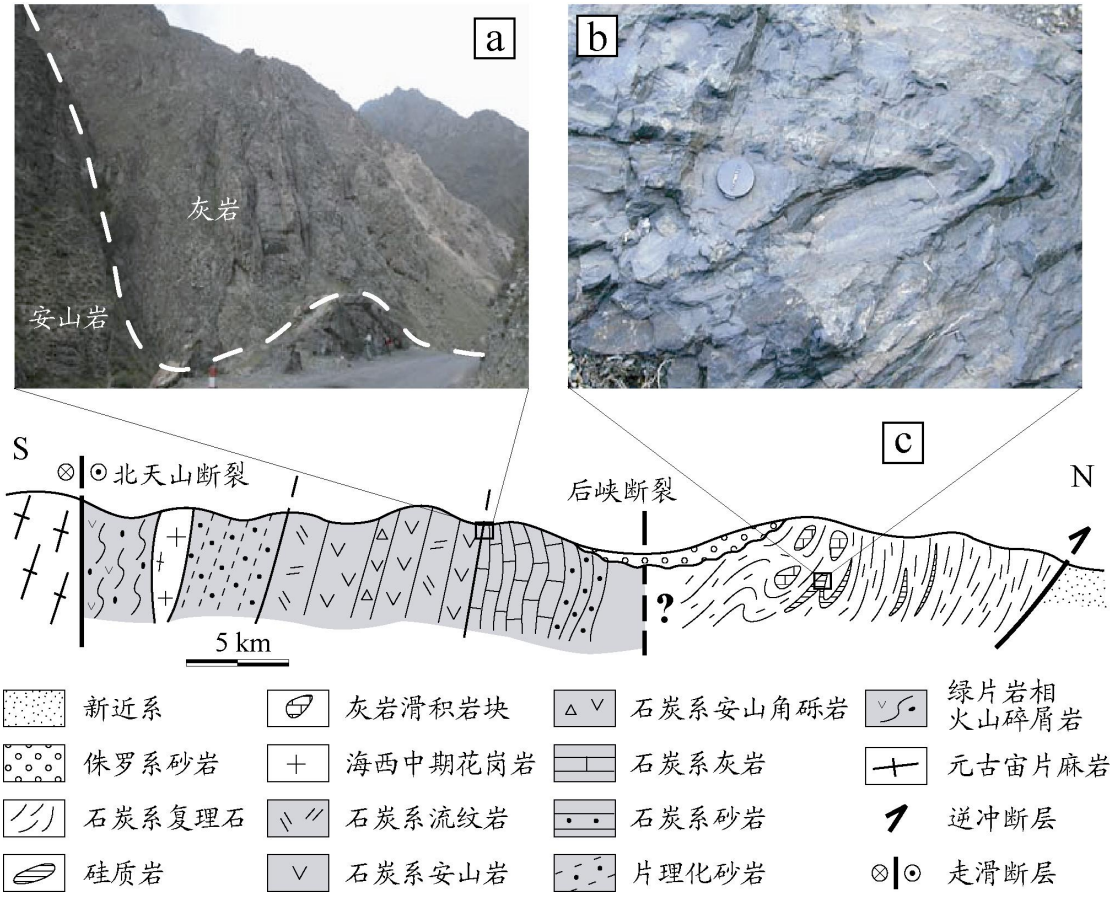

图 4-7 北天山后峡地质剖面图及野外地质照片

实际上，后峡剖面（图 4-7）的北段主要为石炭系复理石，沉积相和变形特征与巴音沟和莫托沙拉沟一带的复理石非常接近。一系列陡立、南倾的泥质砂岩中发育有硅质岩透镜体和硅质岩薄层紧闭褶皱（图 4-7b）。在复理石南部还有灰岩滑积岩块，指示强烈挤压变形造成的混杂堆积作用（图 4-7c）。虽然没有蛇绿混杂岩出露，但从巴音沟一带浊积复理石和蛇绿混杂堆积岩的区域分布特征来看，后峡北部的复理石和混杂岩应属于巴音沟的东延。在后峡剖面南段，岩性和变形特征发生明显改变，火山-沉积岩地层（图 4-1，图 4-7c）除产状比较陡立近垂直以外，没有明显的变形。由于后峡盆地被侏罗系含煤层砂岩和第四系所覆盖，复理石堆积岩和火山-沉积岩层之间的接触关系在野外无法直接观察到，但二者之间沉积相

表 4-2 后峡石炭系火山岩 ICPMS 全岩分析结果（符号简写同表 3-1。）

样品号	XJ595HX	XJ596HX	XJ597HX	XJ599HX	XJ600HX
SiO_2(%)	59.69	58.50	49.11	66.67	69.10
TiO_2	16.71	17.12	16.10	13.76	14.57
Al_2O_3	6.97	7.64	8.02	3.80	3.49
Fe_2O_3	0.15	0.12	0.14	0.17	0.14
MnO	3.27	2.65	3.57	0.97	0.78
MgO	3.81	4.07	9.95	4.71	2.73
CaO	4.19	4.32	3.48	3.22	4.16
Na_2O	1.50	2.05	1.62	2.78	2.41
K_2O	0.49	0.60	0.81	0.28	0.26
P_2O_5	0.30	0.22	0.19	0.11	0.11
LOI	2.86	2.56	7.53	3.76	2.39
Total	99.94	99.85	100.52	100.23	100.14
AK	1.99	2.65	2.44	3.06	2.67
ANKC	0.66	0.64	0.81	0.35	0.30
σ	0.24	0.45	0.97	0.39	0.27
La(ppm)	10.83	13.49	9.97	17.81	19.38
Ce	24.47	30.09	23.37	38.7	43.09
Pr	3.228	3.841	3.121	4.825	5.399
Nd	13.74	16	13.63	19.42	21.43
Sm	2.97	3.461	3.099	3.979	4.535
Eu	0.914	1.043	0.989	0.962	1.057
Gd	2.588	3.233	2.767	3.41	3.883
Tb	0.407	0.501	0.435	0.554	0.62
Dy	2.404	2.91	2.608	3.405	3.704
Ho	0.483	0.587	0.518	0.656	0.735
Er	1.421	1.768	1.543	1.98	2.24
Tm	0.215	0.267	0.233	0.316	0.358
Yb	1.518	1.913	1.568	2.215	2.536
Lu	0.25	0.311	0.256	0.36	0.412
ΣREE	65.44	79.42	64.11	98.59	109.38
L/H	6.05	5.91	5.46	6.65	6.55
dEu	0.985	0.938	1.011	0.779	0.751
Sc	28.492	40.714	43.051	28.954	31.285
V	49.01	141.3	192.5	32.23	24.75
Cr	403.3	890.6	315.9	1153	1027
Co	11.36	19.88	26.27	13.43	10.48
Ni	216.7	472.9	162.5	567.5	469.9
Cu	10.19	28.83	42.17	16.12	17.77
Zn	70.78	73.86	75.64	77.94	70.72
Ga	14.29	18.43	18.78	15.17	17.75
Ge	1.169	1.403	2.287	1.812	1.712
Rb	30.35	46.1	48.24	85.01	81.18
Sr	676.2	601.3	580	1031	465.7
Y	14.5	17.97	15.47	20.96	24.53
Zr	88.34	117.2	72.25	117.2	132.1
Nb	2.296	3.161	1.897	4.964	5.564
Ba	440.7	435.8	288.1	508.8	400.1
Hf	2.344	2.987	1.924	3.348	3.708
Ta	0.179	0.247	0.137	0.421	0.453
Th	2.663	3.942	1.869	5.719	6.528
U	0.956	1.291	0.888	1.736	1.942
Be	0.904	1.1	0.621	1.479	1.569
Cs	1.104	1.053	6.08	5.433	6.217
W	0.777	1.655	1.362	1.706	2.113
Mo	13.72	31.04	10.29	38.88	43.18
Sn	0.869	1.325	0.952	2.115	2.364
Pb	3.7405	3.4038	4.6931	9.3121	12.7833

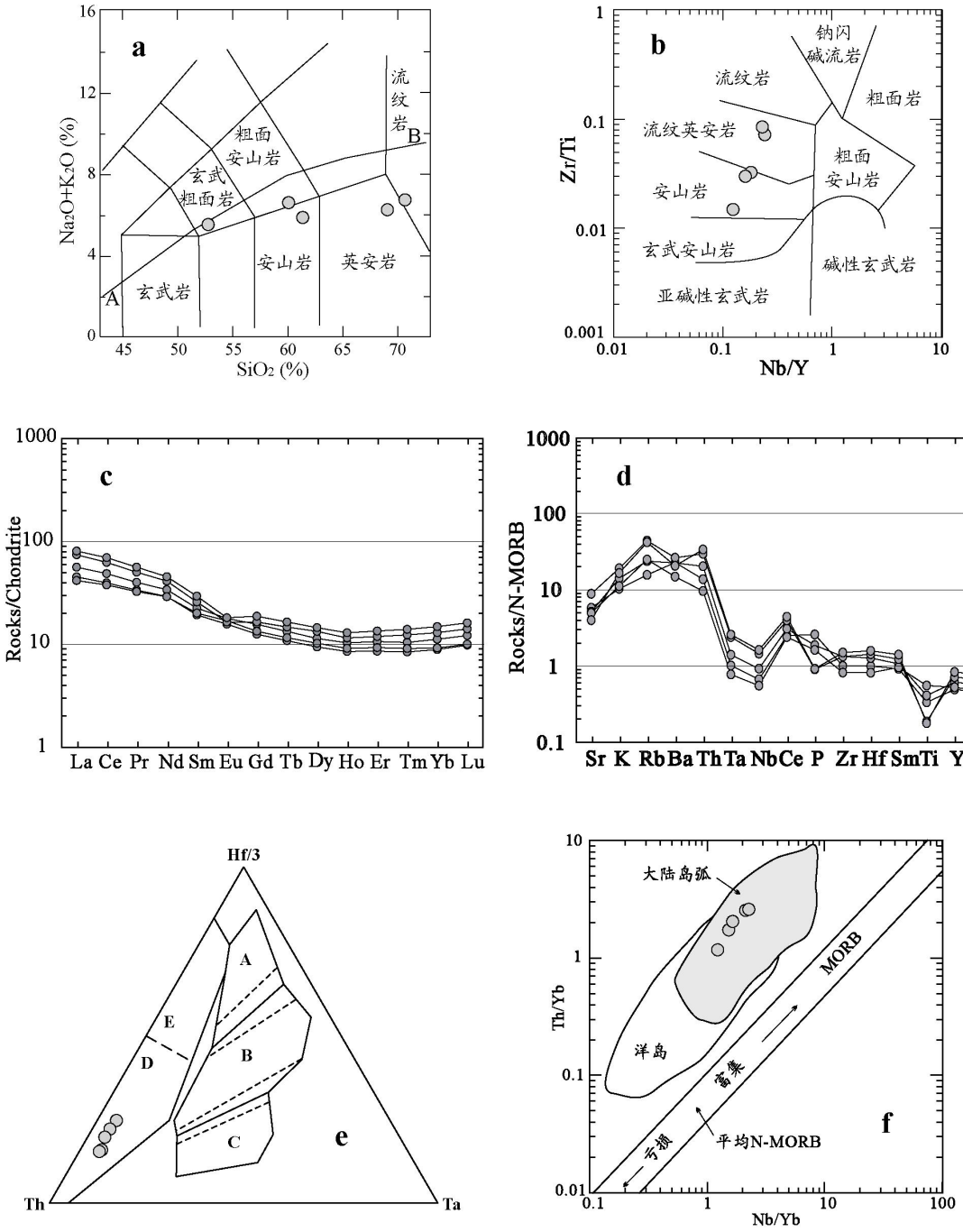

图 4-8 北天山后峡剖面石炭系火山岩岩石地球化学图解

（e 中简写符号同图 3-11）

和变形程度的明显差别表明，沿后峡盆地可能发育一条近东西向断裂（后峡断裂）（图 4-1，图 4-7c）。

在火山-沉积岩的南部，泥质砂岩和凝灰质、安山质砂岩发生了强烈片理化。板岩、千枚岩和绿片岩中发育陡立南倾的面理构造，变形运动学特征类似哈希勒根达坂北坡，其中富含黑云母的板岩 Ar-Ar 全年定年得到 255~275Ma（见本章第一节），表明该带为北天山断裂韧性右旋走滑剪切带的东延（图 4-1）。该走滑剪切带宽约数公里，向南在冰达坂与元古宙花岗片麻岩接触（图 4-1，图 4-7c）。

石炭系火山-沉积岩主要包括砂岩、灰岩、安山角砾岩、杏仁状安山岩和流纹岩，以及低绿片岩相变质、韧性剪切变形的火山碎屑岩（图 4-7c）。由于岩层陡立，且多发育局部断

层，因此火山岩与沉积岩上、下层位关系不明。作者在本剖面采集了 5 件新鲜火山岩样品，进行了 ICPMS 全岩分析，有关化学分析的信息详见第三章，分析结果见表 4-2。除 XJ597HX 的烧失量 LOI 比较高以外，其他样品的 LOI 均比较低（<3.8%），表明这些样品没有经受明显的后期蚀变。样品中 SiO2 含量从 49%到 69%，考虑到所采样品数量及其代表性，至少可以认为，火山岩从基性、中性到酸性连续分布，并且中性火山岩比较常见，并不是只有基性和酸性成分的“双峰式”系列（夏林圻等，2004；顾连兴等，2001）。全碱含量（2~3%）较低，属于亚碱性系列，而且所有样品中 Na_2O 大于 k_2O，具有中钾、钙碱性特征（表 4-2，图 4-8a）。

在 Nb/Y-Zr/Ti 投影图（图 4-8b）中，这些岩石主要为安山岩和流纹英安岩，并呈线性分布，基本与 TAS 图解（图 4-8a）的结果一致，表明主量元素在岩石形成以后并没有发生明显的变化。稀土元素低度富集，在中、酸性岩石之间没有发生明显的分异。轻稀土元素比重稀土元素轻度富集，相应的球粒陨石标准化配分曲线（图 4-8c）呈向右缓倾趋势。个别样品具有负弱 Eu 异常（0.75~0.78）。所有样品均亏损高场强元素 Nb, Ta, Zr, Hf 等，而相对富集大离子亲石元素 Th, Ba, Rb 等，一些样品还具有较低的 P 和 Ti 元素。以上特征共同表明，这些火山岩属于钙碱性系列，和形成于俯冲带之上的火山岩具有类似的地球化学特征。火山岩物质成分可能来自于地幔，同时受到地壳物质的混染。

在 Hf/3-Th-Ta 图解（图 4-8e）中，这些火山岩全部投在钙碱性玄武岩区域，并由中性到酸性相应地表现为从岛弧拉斑玄武岩向钙碱性系列呈线性过度的趋势，而与板内碱性玄武岩、板内拉斑玄武岩没有任何关系。因此这些火山岩形成的构造环境应该与俯冲作用形成的岛弧背景有关，而与板内的裂谷或洋中脊环境无关。Th/Yb-Nb/Yb（图 4-8f）图解显示，这些火山岩全部投在大陆岛弧和大洋岛弧的重叠区域，但从中性岩到酸性岩，它们逐渐远离洋岛区域，而向大陆岛弧中心区域靠近。同时，这些火山岩所有的地球化学特征与伊犁地区石炭系火山岩十分接近，且都与浅水相薄层状陆源碎屑岩（砂岩、灰岩等）伴生，未见深海硅质岩等与之共生。这些地质证据表明，后峡南部火山岩形成于与俯冲作用相关的活动大陆边缘环境。在后峡剖面的南部，花岗闪长岩与低绿片岩相变质岩石侵入接触，且岩体局部也被韧性走滑剪切作用影响而发生变形（图 4-8c）。虽然没有地球化学和年代学研究成果证实，但该花岗岩体很可能是与火山岩伴生的岛弧型侵入岩。

第三节 北天山缝合带及其构造属性

传统上“北天山缝合带”是指北天山巴音沟蛇绿混杂岩带和干沟-米什沟蛇绿混杂岩带（Windley et al., 1990；王作勋等，1990；Allen et al., 1992；肖序常等，1992；Gao et al., 1998；Xiao WJ et al., 2004）。然而，北天山巴音沟蛇绿混杂岩是否延伸到干沟-米什沟一带，是关系到天山大地构造和构造演化的重大科学问题（马瑞士等，1993；Laurent-Charvet, 2001）。另外，北天山蛇绿混杂岩的形成机制尚存在争议，一些学者将其作为一个原地完整的蛇绿岩套（王作勋等，1990；肖序常等，1992），而另有学者则认为是构造推覆体（高俊等，1997；Gao et al., 1998）。近年来，一些学者（夏林圻等，2005；徐学义等，2005a, 2005b, 2006）通过研究巴音沟蛇绿混杂岩中斜长花岗岩的地球化学和同位素组成，认为巴音沟蛇绿岩形成于大陆裂谷向大洋裂谷转化的构造环境，进而提出天山造山带晚古生代发生过“红海型”洋盆的认识。因此可见，北天山蛇绿混杂岩的构造属性仍然是一个争议的课题。

前人对巴音沟、莫托沙拉沟一带蛇绿混杂岩中镁铁岩的地球化学研究表明，这些洋壳岩石具有三种不同的地球化学亲缘性，即 MORB、OIB 和 IAT，显示一种有限洋盆的特性（王作勋等，1990；肖序常等，1992；李生虎等，1994；Wang ZH et al., 2003）。徐学义等（2006）对巴音沟蛇绿岩中辉长岩、辉绿岩和基性熔岩的研究结果显示，稀土元素球粒陨石标准化分配型式呈平坦型分布，$(Ce/Yb)_N$ = 0.63～1.36，$(Gd/Yb)_N$ = 1.02～1.41，近似于 N-MORB 分

配型式。另外他们对这些岩石 Sr 同位素的研究发现，其 $^{87}Sr/^{86}Sr$ 比值为 0.70306～0.70439，$\varepsilon_{Nd}(t)$ = 4.63～8.69，表明其岩浆主体来源于 N-MORB，但在形成过程中有 OIB 组分的加入。斜长花岗岩的$(Ce/Yb)_N$ = 0.67～0.88，$(Gd/Yb)_N$ = 0.63～0.73，$\varepsilon_{Nd}(t)$ = 8.36～8.52，$^{87}Sr/^{86}Sr(t)$ = 0.70365～0.70408，与镁铁质岩完全一致（徐学义等，2006）。因而，这些结果也支持蛇绿岩形成于洋盆环境的认识。

前人在巴音沟-莫托沙拉沟蛇绿岩带的硅质岩中发现了晚泥盆世法门期-早石炭世的放射虫和牙形刺等微体化石（王作勋等，1990；肖序常等，1992；李生虎等，1994；Gao et al., 1998）。徐学义等（2005a, 2005b）从巴音沟蛇绿岩中斜长花岗岩获得 324.8±7.1Ma 的锆石 U-Pb SHRIMP 年龄。这些证据表明，北天山巴音沟地区蛇绿混杂岩所代表的洋盆可能最晚存在于晚泥盆世-早石炭世期间，而洋盆关闭、碰撞的年龄则至少晚于 325Ma。考虑到在巴音沟蛇绿混杂岩中，包含有晚石炭世巴音沟组复理石岩块和片理化复理石基质，表明混杂岩的形成与巴音沟组时代同期或更晚，即晚石炭世末。

如本章第一节所述，虽然巴音沟蛇绿混杂岩中发育有典型蛇绿岩套的各种岩石组分，但却没有完整的蛇绿岩序列，洋壳岩石被彻底构造肢解并与沉积岩混杂堆积在一起。同时，蛇绿岩和沉积岩的块体边缘通常被剪切片理化的基质所围绕。这些构造现象是俯冲洋壳碎片的典型特征。在巴音沟、芦苇沟和莫托沙拉沟一带，通常可以见到镁铁-超镁铁岩块与辉长质砂岩、杂砂岩和红色泥质岩块混杂在一起，表明洋壳岩石可能经历了一个与橄榄岩、辉长岩底侵作用有关的板内构造事件，继而在洋底发生再沉积和混杂作用，最后，这些已经混杂堆积在一起的洋壳岩石在俯冲过程中被卷入到海沟带的浊积复理石中（Raymond，1984）。构造运动学研究（见第一节）表明，巴音沟蛇绿混杂岩中发育有从南向北的韧性剪切变形构造。因此，北天山巴音沟蛇绿混杂岩带可能代表一个向南俯冲的缝合带。该缝合带与伊犁、北天山岩浆岛弧在空间上具有很好的配比关系，而且北天山洋盆及其缝合时代与伊犁、北天山岩浆岛弧的活动时间也十分一致，因此可以推断，伊犁、北天山岩浆岛弧的形成与北天山洋盆向南的俯冲作用有关。

虽然干沟-米什沟蛇绿混杂岩与北天山巴音沟蛇绿岩沿天山主断裂分布，二者在空间上具有很好的连续性（图 4-1），但是，它们可能并不属于同一个蛇绿岩带。时代方面，干沟-米什沟蛇绿混杂岩被认为是一个早古生代的缝合带（马瑞士等，1993，1997；车自成等，1994；Laurent-Charvet，2001；Shu et al., 2002），明显早于巴音沟蛇绿混杂岩的形成时代。另外，尽管干沟-米什沟蛇绿混杂岩中变形特征（见第五章）与巴音沟蛇绿岩的变形特征一致，但其南侧并没有与伊犁地区相同的岛弧火山作用，相反，北天山岛弧却位于该蛇绿混杂岩带的北缘。同一个洋盆不可能在其西段朝南俯冲，而在东段朝北俯冲。因此干沟-米什沟蛇绿混杂岩不同于巴音沟蛇绿岩，而应属于另外一个缝合带（见第五章、第七章）。

由于在乌鲁木齐以东、博格达以北地区未见任何蛇绿混杂岩出露，因此，关于北天山缝合带的东延问题目前尚不清楚。考虑到伊犁晚古生代岩浆岛弧与博格达岛弧在空间、时间上的一致性，作者推测，这两个岛弧可能形成于同一个向南的洋壳俯冲作用。俯冲带向东可能一直延伸到哈尔里克岛弧以北，与向南俯冲的卡拉麦里俯冲带（马瑞士等，1993；舒良树等，1997；Shu et al., 2002；Charvet et al., 2002；Xiao WJ et al., 2004）同属于一个缝合带。值得提出的是，由于新生代陆内俯冲引起的大型逆冲推覆构造作用，使天山北缘数十公里宽的古生代地层发生了强烈的脆性变形，并形成巨大的推覆体向北逆冲在准噶尔中、新生代沉积盆地之上，向北的推覆作用造成了至少 30 km 的南北向地壳缩短（Avouac et al., 1993）。另外，博格达山在中生代以来的快速隆起（沈传波等，2006；朱文斌等，2006；马前等，2006）也可能使其北侧的蛇绿混杂岩遭到彻底的构造破坏而难以辨认。因此，作者认为，新生代推覆作用可能导致北天山缝合带在部分区段被大型推覆体所掩盖，如博格达以北地区，图 4-5 示意了这一后期构造变形对早期俯冲带的改造作用。

第四节 小结

1．伊犁地块北缘为北天山构造带，由蛇绿混杂岩带和北天山岩浆岛弧两个次级构造、地层单元组成。巴音沟地区蛇绿混杂岩和晚石炭世浊积复理石构成一个俯冲增生杂岩体，代表北天山缝合带。蛇绿岩包括变质橄榄岩、辉长岩、辉绿岩、枕状玄武岩、斜长花岗岩和硅质岩等，并呈团块状杂乱堆积在强烈片理化的泥质岩和复理石基质中。岩石学和地球化学特征表明，蛇绿岩可能形成于有限洋盆环境。硅质岩中放射虫化石时代和斜长花岗岩年龄表明，北天山洋盆至少存在于晚泥盆世-早石炭世末期间。晚石炭世复理石在蛇绿混杂岩中以岩块与基质的形态同时存在，因而，北天山洋盆关闭并发生碰撞的时代应为晚石炭世末。

2．在后峡与冰达坂之间，石炭系主要由基性-中性-酸性火山岩、火山碎屑岩、砂岩和灰岩组成，并有花岗闪长岩侵入到火山碎屑岩中。火山岩地球化学研究表明，它们属于富 Na 的钙碱性系列。稀土元素低度富集，稀土配分模式与典型钙碱性火山岩的特征一致，而且岩石之间分异程度弱，Eu 负异常不明显。这些火山岩还富集大离子亲石元素，并明显亏损高场强元素。微量元素判别图中，所有火山岩均与大陆岛弧玄武岩类似。这些火山岩在岩相学和岩石地球化学方面，与伊犁地区岛弧岩浆岩完全一致，因此，它们可能形成于俯冲带之上的大陆岛弧环境，既北天山岛弧。

3．详细的变形运动学分析表明，北天山构造带经历了石炭纪北向逆冲推覆（D1）、二叠纪韧性剪切（D2）和新生代北向逆冲推覆（D3）三期构造变形作用。其中，发育在变质橄榄岩表面的韧性变形要素指示从 SW 向 NE 的剪切推覆作用，代表石炭纪末蛇绿混杂岩构造侵位过程中的变形运动方向。因此，北天山缝合带可能形成于北天山洋盆向南的俯冲和碰撞作用。

4. 巴音沟蛇绿混杂岩带形成于石炭纪末，而干沟-米什沟蛇绿混杂岩带形成于早古生代，因此，二者属于两个不同的缝合带。伊犁、北天山岛弧与北天山缝合带在空间上的配比关系和时间上的一致性，表明它们的形成可能与北天山洋盆向南的俯冲作用有关。北天山火山岛弧向东延伸，可能与东天山博格达岛弧甚至哈尔里克岛弧相连，因而，北天山缝合带可能也向东延伸，经博格达山以北，到卡拉麦里蛇绿混杂岩带。中、新生代以来博格达山的快速隆升和天山陆内变形作用，形成了宽达数十公里的大型推覆体，并可能将北天山缝合带的东段彻底破坏，或者掩盖于推覆体之下。

5．二叠纪走滑剪切作用使晚石炭世复理石的南部和岛弧火山岩的南部均发生了强烈片理化和靡棱岩化变形，运动学标志显示右旋剪切动向。与走滑剪切作用共生的岩浆作用还使变形岩层发生了热接触低绿片岩相变质作用。韧性剪切变形岩石全岩 Ar-Ar 年代学研究表明，走滑事件发生在 285~245Ma 之间，走滑剪切变形的整个过程中伴随着强烈的矿物动态重结晶作用。

第五章 伊犁地块南缘构造特征

伊犁地块南缘以尼古拉耶夫构造线（王作勋等, 1990；Tagiri et al., 1995；Zhou et al., 2001）为界，其南侧的哈尔克山、额尔宾山和霍拉山一带，分布有高压变质杂岩和多处蛇绿混杂岩，因此，记录了大量有关伊犁及天山造山带构造演化的地质信息。前人将沿尼古拉耶夫构造线分布的高压变质岩和蛇绿混杂岩作为“南天山缝合带”（Windley et al., 1990；Allen et al., 1992；Gao et al., 1998；Chen et al., 1999; Zhou et al., 2001），并认为该缝合带为“南天山洋”向北俯冲、消减的产物，伊犁晚古生代大陆岛弧就是在“南天山洋”俯冲过程中形成的（汤耀庆等，1995；刘本培等，1996；Gao et al., 1998；Klemd et al., 2005; 朱永峰等，2005）。有学者还认为，位于“南天山缝合带”以南的蛇绿混杂岩带是前者向南仰冲作用形成的构造推覆体或飞来峰（Allen et al., 1992；高俊等，1997）。一些研究者通过研究榴辉岩相高压变质岩 PTt 轨迹和年代学，提出高压变质作用的峰值年龄为 345Ma 左右，即早石炭世早期，代表南天山洋俯冲的时代（Gao et al., 2000；2003；klemd et al., 2003；2005）。作者经过数年的野外地质考察，从构造地质学、运动学、年代学等角度，对天山南部几个关键剖面进行了详细分析。

第一节 科克苏-黑英山剖面构造特征

西天山整体海拔高度远高于东天山，特别是天山西南部的哈尔山更是崇山峻岭，平均海拔高度达 4000m 左右，因而给地质考察带来了很多困难。独库公路贯穿越天山南部，给地质工作者提供了一个认识西南天山大地构造的窗口，王宝瑜等（1997）和 Zhou Da 等（2001）对该剖面地质现象进行了系统描述。在平行于独库公路的西侧约 150km 处，科克苏-黑英山剖面跨越了伊犁地块南缘、哈尔克山高压变质带、中天山地块、南天山蛇绿混杂岩带和塔里木板块北缘（图 5-1），因此是研究伊犁和天山古生代构造演化的理想场所。该剖面由科克苏（北）段和黑英山（南）段组成，前者沿科克苏河上游向北至特克斯，后者位于黑英山北西 40km 处。

1. 科克苏河多期构造变形带

科克苏段从北向南包括：伊犁晚古生代岩浆岛弧、伊犁地块结晶基底、高压变质杂岩和中天山地块（图 5-1，图 5-2）。该地区经历了复杂的构造变形。

1.1. 科克苏河段地质特征

1.1.1. 伊犁岛弧

在科克苏河剖面的北段，从特克斯到温泉北（图 5-1，图 5-2），出露的地层主要为石炭系大哈拉军山组（C_1d）和阿克沙克组（C_1a）火山岩和陆源碎屑岩（新疆地矿局，1979，1993）。火山岩主要由中基性玄武安山岩、中性安山岩、粗面安山岩和酸性流纹岩、英安岩等组成，并伴有大量同时代侵入岩。侵入岩主要为糜棱岩化辉长岩、花岗闪长岩、英云闪长岩和部分未变形钾长石花岗岩和花岗质岩脉（图 5-3a,b,c）。沉积岩则主要为火山碎屑砂岩、粉砂岩、砂砾岩、薄层灰岩和泥质岩。前文（第三章）已从岩石学、地球化学、同位素地质学和地质年代学等方面论证了这些火山岩的大地构造背景和年龄，认为伊犁地块在中泥盆世晚期-石炭纪期间为活动大陆边缘环境。

1.1.2. 伊犁地块前寒武纪结晶基底

震旦系碳酸盐岩与岛弧火山-沉积岩层呈断层接触，局部被后者不整合覆盖（图 5-1）。碳酸盐岩主要为结晶灰岩、大理岩和白云岩，灰岩中富含叠层石化石（新疆地矿局，1979）。这些岩层区域上被划归为穹库什太群和特克斯群，与出露在伊犁北部赛里木湖地区（图 2-7）的震旦系非常相似。另外，元古代片麻岩也广泛分布于特克斯地区，并向南到温泉一带，都有零星分布（图 5-1，图 5-2），向东则断续延伸至那拉提南侧拉尔墩达坂（图 2-7）。

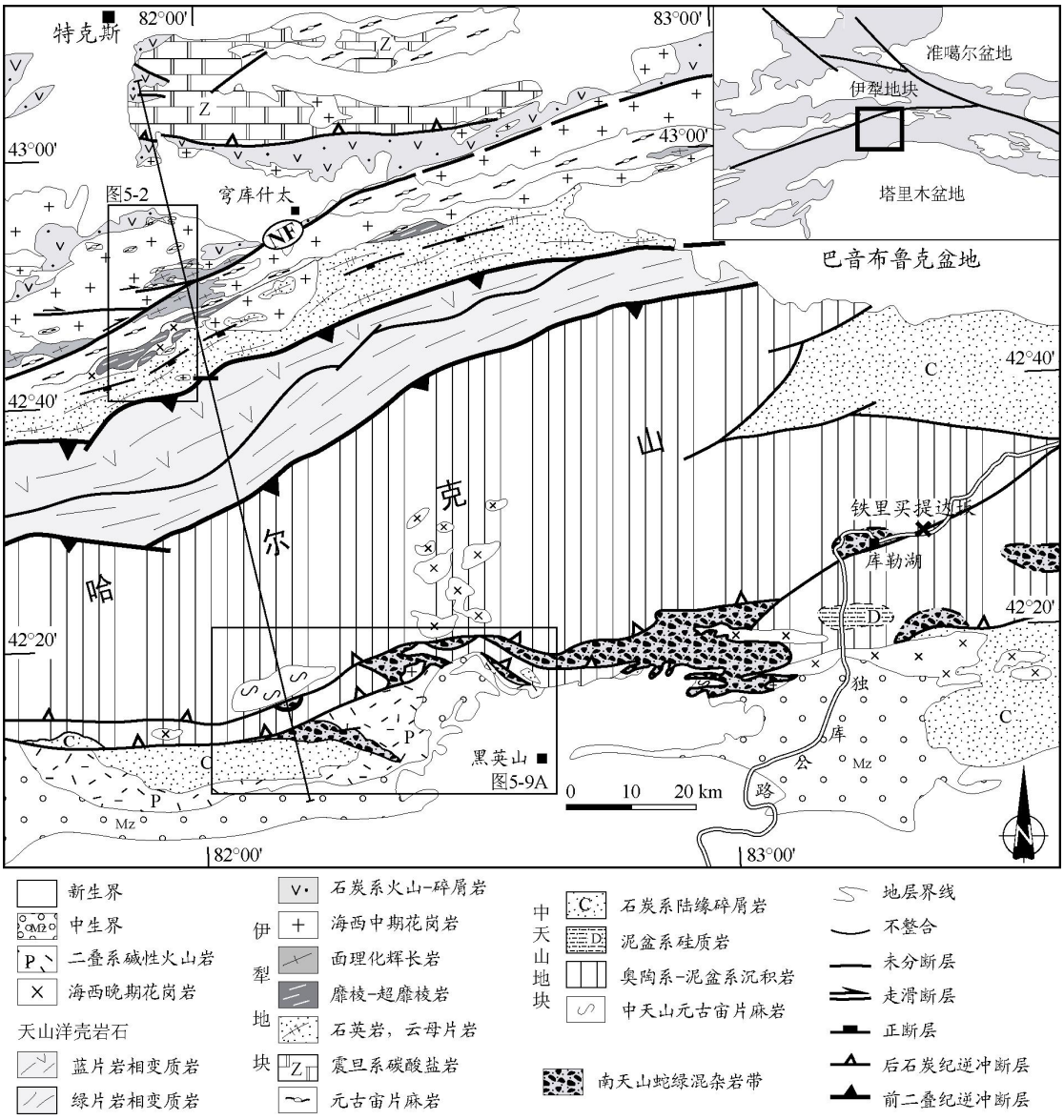

图 5-1 科克苏-黑英山剖面地质简图（据新疆地矿局，1979，1983，1993；高俊等，1995，2000，2003 改编）

NF, 那拉提断裂的西延

另外，沿科克苏河地质点 N42°45’以南，发育有二云母片岩、含云母石英岩和黑云母片麻岩（新疆地矿局，1979；Gao et al., 1995；汤耀庆等，1995）。部分片麻岩中可见眼球状长石斑晶和椭球体状黑云母残留体（图 5-3e），表明花岗质岩石曾经侵入到碎屑岩中，并发生了角闪岩相变质作用。这些岩石可能为伊犁晚古生代岛弧南缘早古生代基底，在后期经历了多期强烈、韧性变形作用（多期变形分析见下文），并局部发生了超糜棱岩化（图 5-3d）。

1.1.3. 高压变质杂岩体

在元古代-早古生代角闪岩相变质带南侧，蓝片岩-榴辉岩相变质岩发育在一个宽约 20km，长近 200km 的绿片岩带中（图 5-1）（Gao et al., 1995；汤耀庆等，1995；Gao et al., 1998；2000；2003；Klemd et al., 2002；2003；2005；Zhang et al., 2002，2003a；2003b；Wei et al., 2003；黄德志等，2004）。该带向西延伸到长阿吾孜、阿克雅孜一带（Klemd et al., 2002；2003；Zhang et al., 2002，2003a；2003b），并出境到哈萨克斯坦（Dobretsov et al., 1987；Tagiri et al., 1995）和塔吉克斯坦（Volkova and Budanov, 1999），向东则至巴音布鲁克盆地西侧消失（图 5-1）。根据前人对该带变质岩矿物学、地球化学的研究结果和其原岩性质的确定（Gao et al., 1995；汤耀庆等，1995），该变质带可分为两个亚单元：北部蓝片岩相带和南部绿片岩相带

（图 5-1）。蓝片岩相带主要由云母片岩、含云母石英片岩以及高压变质的基性岩石和大理岩组成。蓝片岩主要以数米级大小的块体、透镜体、薄层和布丁构造产出于绿片岩相退变质的泥质岩层中。在长阿吾孜一带还发育有榴辉岩相变质岩（Gao et al., 1995, 2000; Gao and Klemd, 2003）。绿片岩带主要由绿片岩、石英片岩和少量大理岩组成，没有蓝片岩发育。

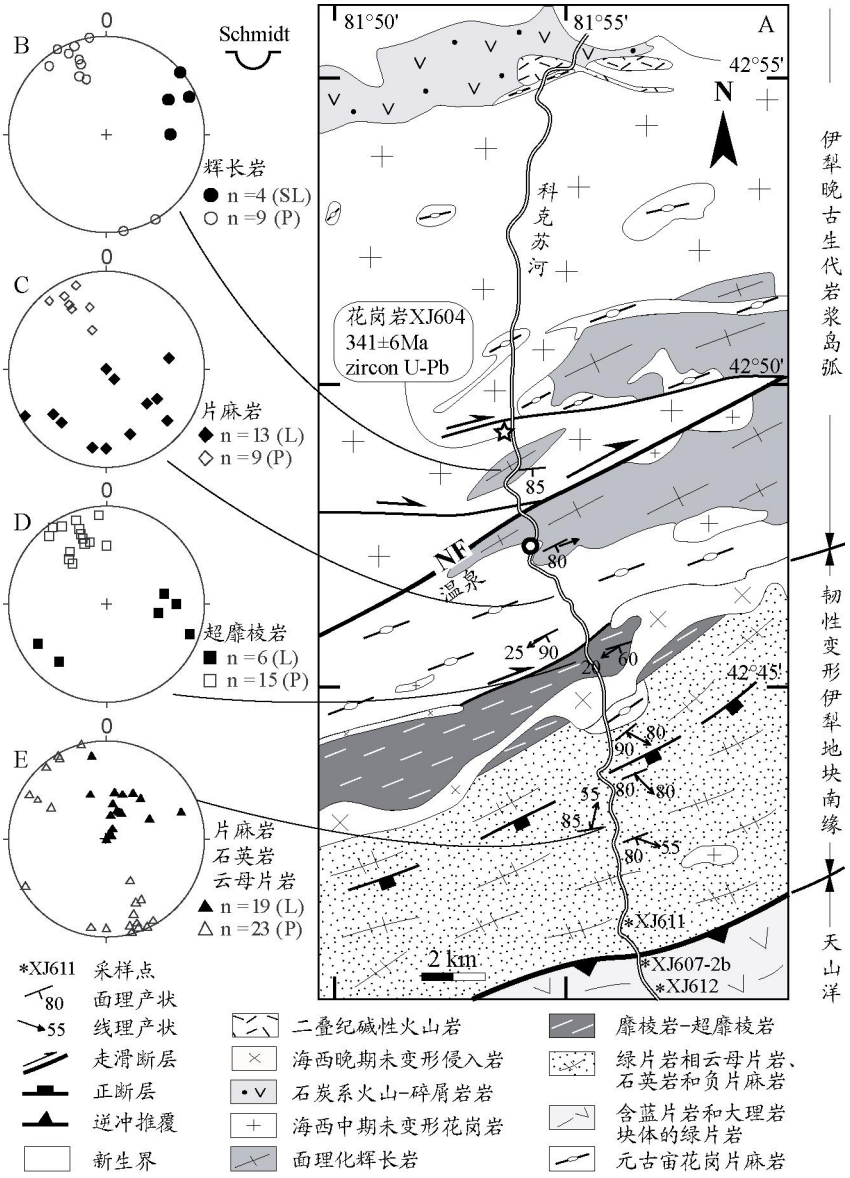

图 5-2（A）科克苏河上游地质构造简图（据新疆地矿局，1979 和高俊等，2000 改编）
（B-E）韧性变形岩石中线状和面状要素的史蜜特网下半球投影图
NF, 那拉提断裂的西延，同图 5-1

高压变质岩经历了 2.0±0.1 Gpa 和 550±50°C 的高峰变质作用过程（Klemd, 2003；Klemd et al., 2002；Gao et al., 2003）。然而，Wei et al .（2003）认为，蓝片岩和榴辉岩经历了不同的高峰变质条件，进而提出了发生在 2.5 Gpa 甚至 5.0 Gpa 的超高压变质作用（Wei et al., 2003; Zhang et al., 2003a, 2003b）。

在科克苏河一带，蓝片岩相变质岩经历了绿片岩相退变质作用的改造（Gao et al., 2003; Klemd et al., 2005）。在绿片岩相带和蓝片岩相带中，变质沉积岩具有相似的原岩特征，原岩主要为泥质粘土岩、钙质-硅质页岩、硅质岩和火山碎屑杂砂岩等（Gao et al., 1995；汤耀庆等，1995）。变质基性岩的岩石学、地球化学研究表明，其原岩与洋中脊玄武岩和洋底拉斑

玄武岩相似。另外，由于变质基性火山岩同时还具有洋岛拉斑玄武岩的特征，因此一些学者还提出了一种类似海山的构造环境（Gao et al., 1995；Volkova et al., 1999）。由此可见，这些高压变质的岩石既包括洋壳物质，也包括洋底深海沉积物，因而代表一个洋盆环境，该洋盆被称为“南天山洋”（肖序常等，1992；Gao et al., 1995；1998；汤耀庆等，1995；高俊等，1997）。有学者将高压变质带作为“南天山缝合带”（Windley et al., 1990；Allen et al., 1992；肖序常等，1992）。为避免在下文讨论的天山南部蛇绿混杂岩时在空间上引起混乱，本文将其改称为“天山洋”和“天山洋缝合带”。鉴于高压变质带与伊犁岩浆岛弧在空间上的匹配关系，一些学者认为天山洋向北的俯冲作用形成了伊犁活动大陆边缘（Gao et al., 1995, 1998；Gao and Klemd, 2003；朱永峰等，2005）。然而，下文所要论述的运动学标志并不支持天山洋向北的俯冲作用。

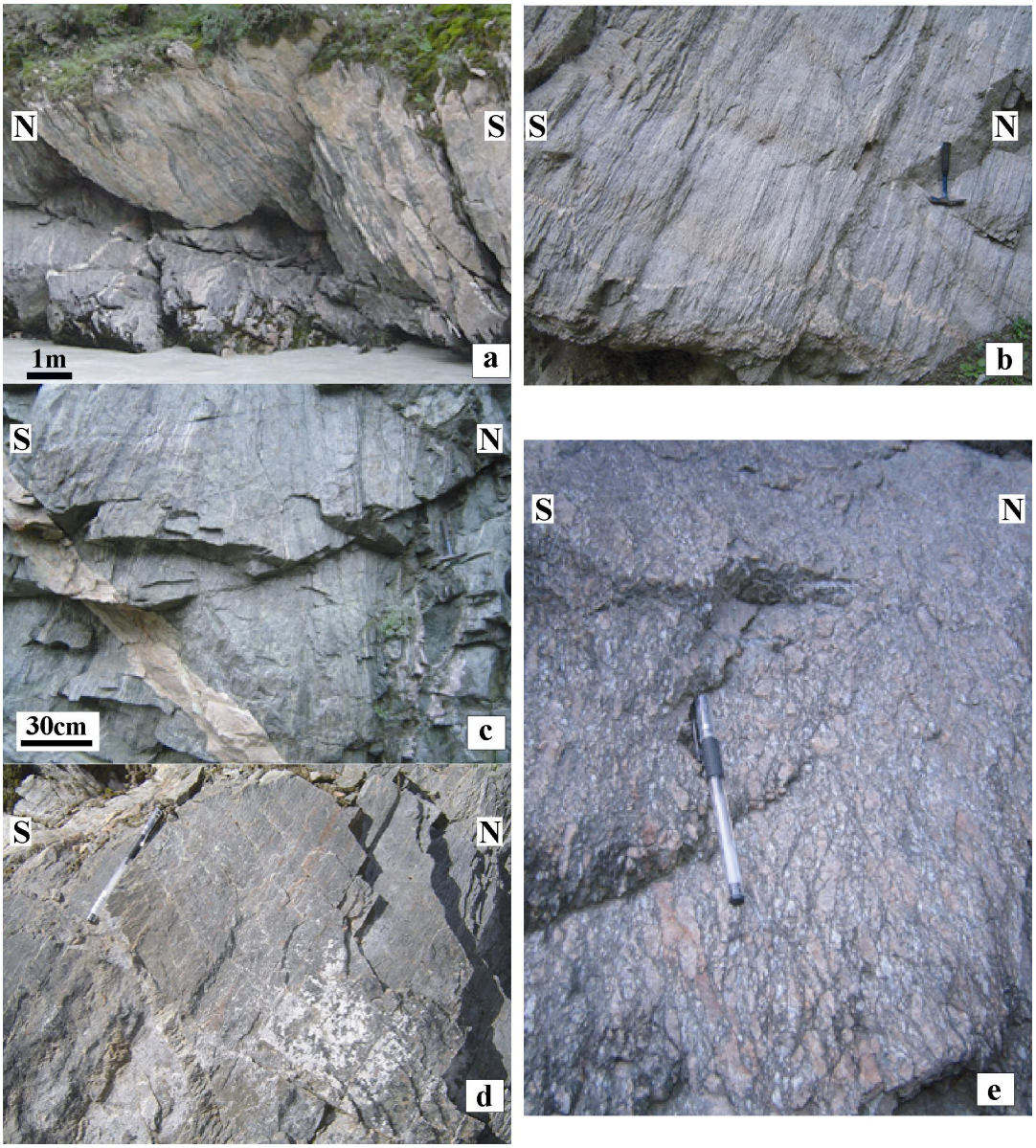

图 5-3 科克苏河剖面韧性变形岩石野外地质特征

1.2. 科克苏河段多期构造变形分析

在科克苏河剖面，伊犁地块南缘基底和天山洋壳岩石经历了复杂的多期构造变形作用。经过详细的野外地质调查，分析出了三期主要的古生代构造变形事件，从新到老依次对应于三个主要的韧性变形带：右旋走滑剪切断层，朝南的韧性正断层和朝北的逆冲推覆带。

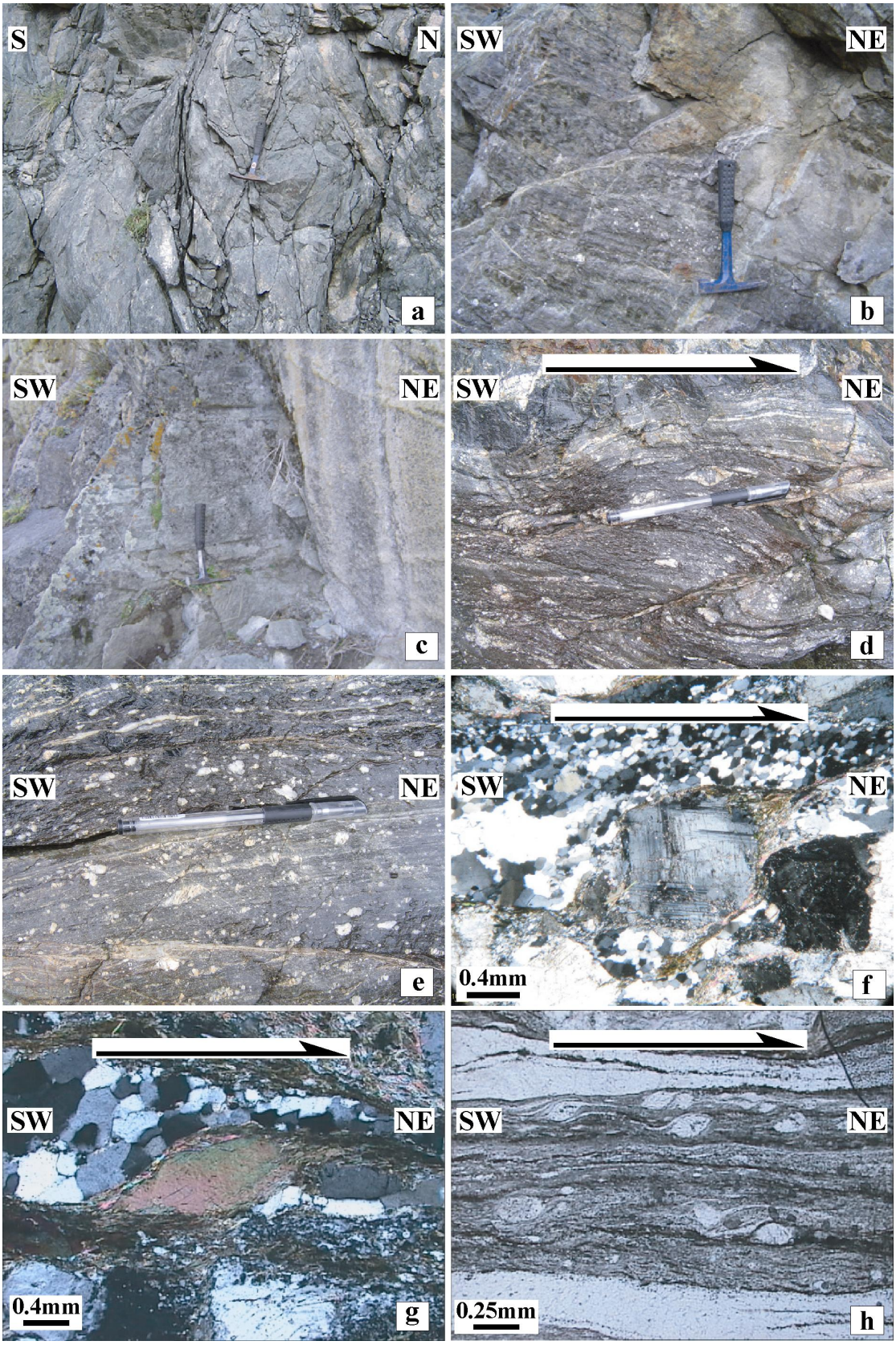

图 5-4 科克苏河地区右旋走滑剪切带野外地质和显微构造特征

1.2.1 右旋走滑剪切带

在温泉附近（从 N 42°55’ 到 N42°45’范围内），发育有大量花岗岩、花岗闪长岩和辉长岩，它们可能代表伊犁晚古生代岩浆岛弧（图 5-1，5-2）。在剖面北侧，这些岩石以脆性的

破裂变形为主。透镜体状岩块被一系列近垂直的剪切面所分隔（图 5-4a），在这些剪切面上发育有近水平、N80E 向延伸的擦痕。随着变形程度的加深，这些岩石在剖面南部，发生了糜棱岩化甚至超糜棱岩化作用（图 5-3c，图 5-4d,e）。在糜棱岩化岩石中，向 SE 方向陡立倾斜的剪切面上发育有 ENE-WSW 方向延伸的拉伸线理和矿物线理构造（图 5-4b；图 5-2B,D），其中后者主要由肠状辉石、拉长的长石条带等组成。在糜棱岩化辉长岩中，侵入有钾长石花岗质岩脉（图 5-3c），其中部分岩脉被布丁化呈香肠状平行剪切面理排布（图 5-3a），另一些岩脉则被褶皱变形，褶皱轴面平行于剪切面理（图 5-3b）。在应力椭球的 XZ 面，即平行于线理而垂直于面理方向的平面上，拖曳褶皱（图 5-4d）和不对称长石斑晶（图 5-4d,e）指示右旋剪切动向。在显微镜下，原位定向的样品中含有σ型长石、辉石斑晶（图 5-4f），斑晶周围发育有黑云母压力影、云母鱼（图 5-4g）以及拉长、斜向排列的石英亚颗粒（图 5-4f,g），这些亚颗粒具有锯齿状边界，并波状消光，由动态条件下重结晶形成。

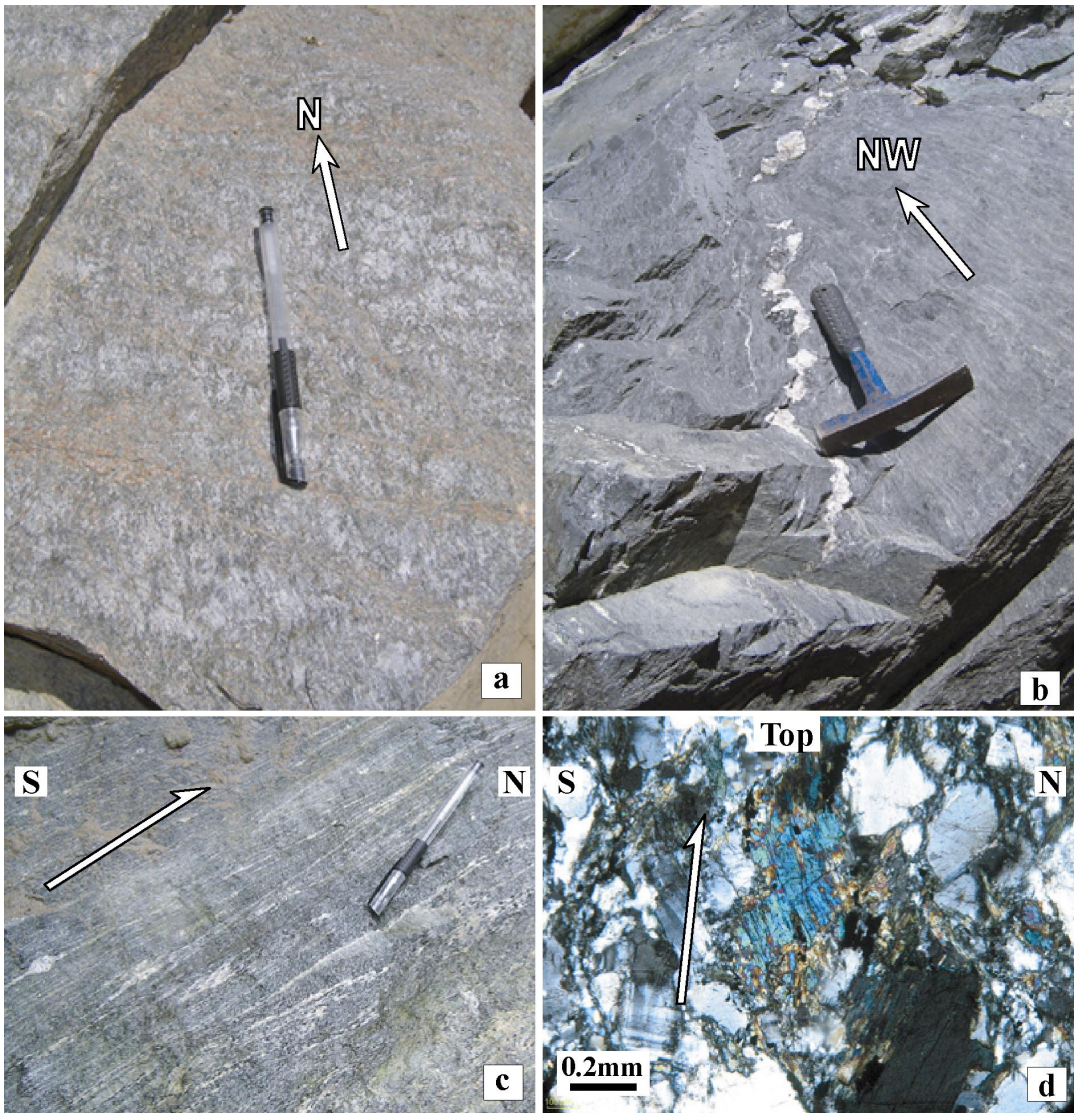

图 5-5 科克苏河地区逆冲推覆带片麻岩和糜棱岩运动学特征

该韧性变形带属于那拉提断裂右旋剪切带的西延（图 5-1）。在巴音布鲁克北的拉尔墩达坂（图 2-7），花岗质岩石在 50m 范围内发生了强烈的韧性变形，在 E-W 或 NE-SW 向延伸、近垂直的糜棱面理上发育有近直立的拉伸线理，显微构造中σ和δ型组构显示了右旋剪切动向（图 5-4h），与科克苏地区完全一致。这些观察与 Yin et al.（1996）的结果一致，但不同于 Bazhenov et al.（1999）和 Zhou et al.,（2001）的认识，他们认为，那拉提断裂为一

左旋走滑断层。鉴于此，Yin et al.（1996）提出，该断裂早期可能为左旋走滑，之后经受了后期右旋走滑的改造。然而，作者在科克苏和拉尔墩地区构造变形研究中，没有观察到任何与左旋有关的运动学标志。另外，最新的古地磁研究结果（见第六章）表明，从晚石炭世到晚二叠世期间，伊犁-准噶尔地块一起相对于塔里木发生了 46°逆时针旋转，该旋转在地质上表现为沿板块边界的右旋走滑作用。在拉尔墩北，超糜棱岩中黑云母 $^{40}Ar/^{39}Ar$ 年龄为 250

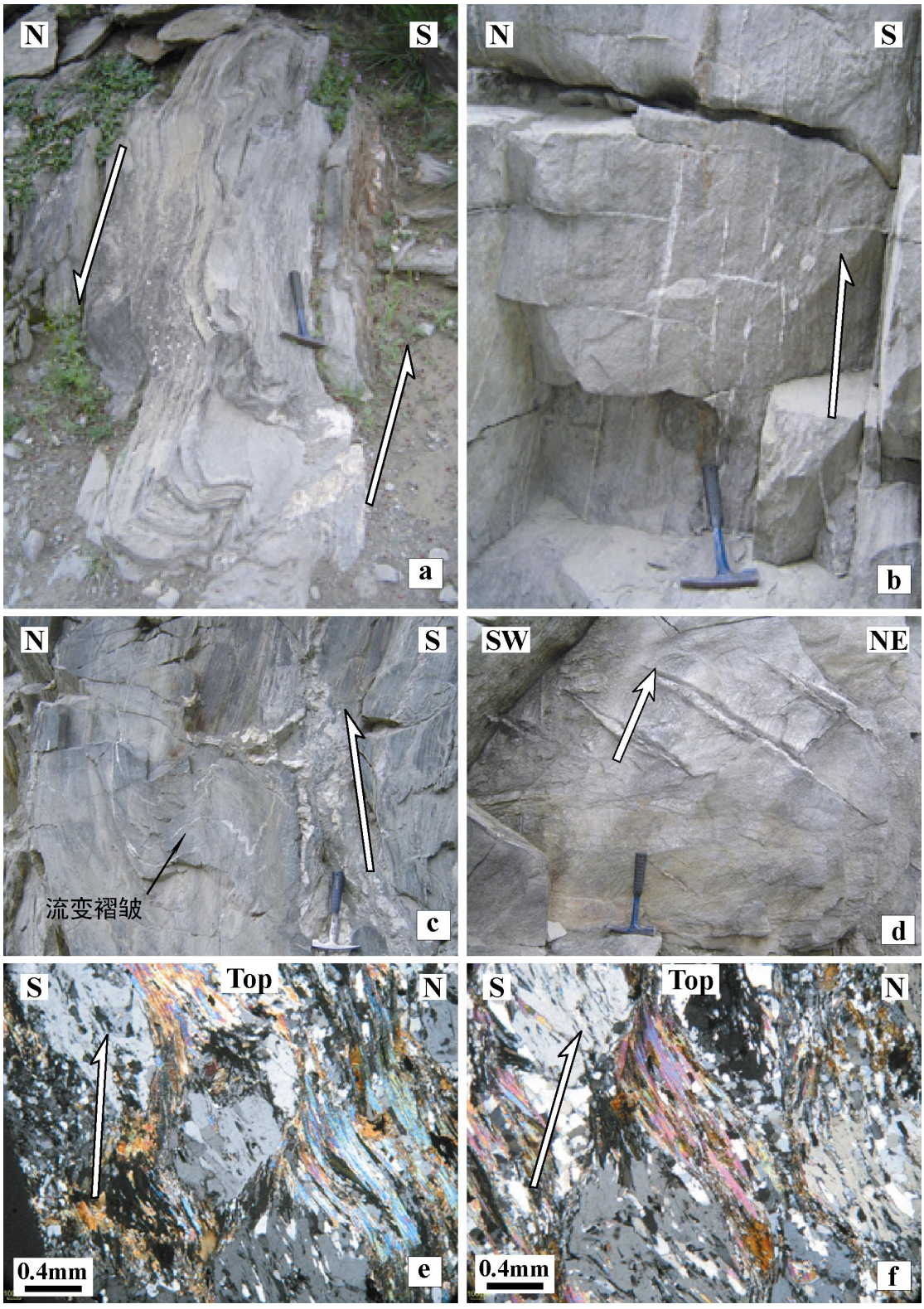

图 5-6 科克苏地区绿片岩相变质岩变形特征与逆冲推覆运动学标志

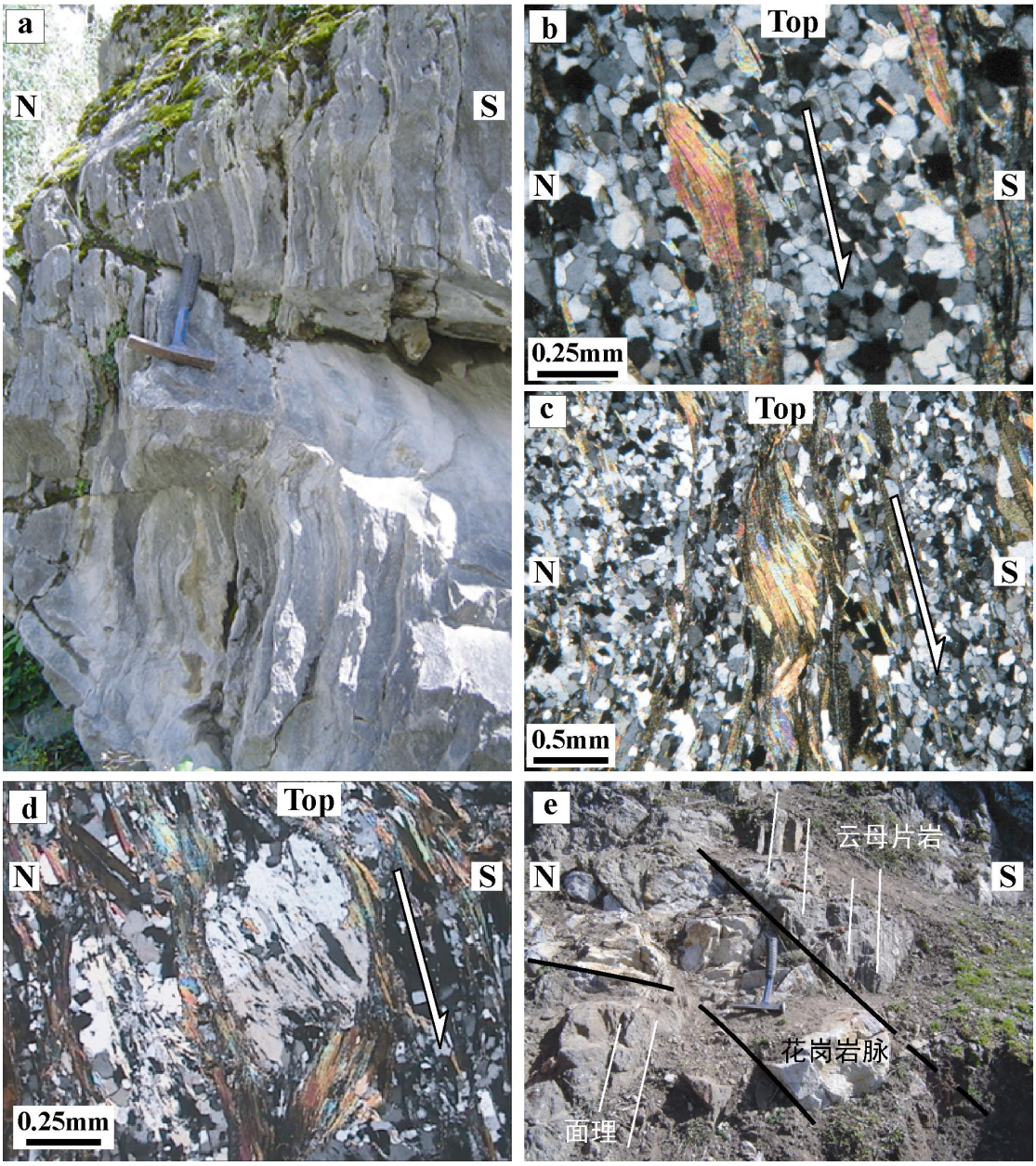

图 5-7 科克苏地区石英岩变形特征和韧性正断层运动学及后期热液活动标志

±7.9 Ma（蔡东升等，1996），而面理化花岗岩中黑云母和钾长石 $^{40}Ar/^{39}Ar$ 年龄分别为 285Ma 和 270Ma（Zhou et al., 2001），表明右旋走滑剪切事件发生在中-晚二叠世。

1.2.2 北向逆冲推覆作用

在右旋走滑剪切带南侧，糜棱岩化辉长岩、片麻岩、云母片岩和石英片岩中，发育有 SE 向倾斜、陡立的剪切面理。面理面上，近 N-S 向、NW-SE 或 NE-SW 向延伸的拉伸线理和矿物线理（图 5-5a,b,c）指示一期完全不同于走滑剪切的变形作用。在花岗片麻岩中，钾长石斑晶和黑云母集合体构成主要线形构造，线理倾伏角从 20°到 60°不等，大部分为 50°左右，少数达 80°（图 5-2C）。类似的线状构造要素也常见于超糜棱岩化辉长岩中（图 5-5c；图 5-2D）。辉长岩中不对称的斜长石布丁构造指示从南向北逆冲的运动动向（图 5-5c）。在显微组构中，S 型辉石解理也指示南侧向上、北侧向下的运动学方向（图 5-5d）。伊犁地块南缘基底云母石英片岩和含黑云母花岗片麻岩也受到了该期变形作用的影响，发育有向南陡倾的面理和近南北向的线理构造（图 5-5a,b），但由于岩石重结晶程度高，在显微尺度不易

观察其运动学特征。

另外，前人在高压变质带中也识别出了朝北的剪切运动标志（Gao et al., 1995；汤耀庆等，1995）。不同的是，该剪切作用被解释为高压变质岩在折返过程中向北的滑脱作用。在绿片岩相变质沉积岩和基性岩中，常见层间 A 型褶皱、流变褶皱、布丁状石英脉等构造（图 5-6a,b,c），其中褶皱轴面平行于面理，从褶皱形态可以推断出南上北下的剪切应力方向。布丁状和 S 型石英脉指示了自南向北的运动动向（图 5-6b,c）。钠长石-黑云母片岩和云母石英片岩中发育 NE-SW 向陡立的面理和近垂直线理构造（图 5-6d），而面理和线理均被后期的拉张裂隙所切割（图 5-6b,d），拉张裂隙近垂直于面理，可能跟后期南北向积压或垂向拉张应力作用有关。在显微镜下，已交代蚀变的不对称长石斑晶以及环绕周围的云母尾和 S 型云母鱼构造（图 5-6e,f）也指示了南部向上、北部向下的运动动向。

虽然这些面理陡立，线理 S-N 向延伸，并指示南上北下的运动方向，但是单从高压变质岩的构造形态很难判断这些运动学要素代表向北的逆冲或者是向北的滑脱。考虑到高压变质岩中的运动动向与糜棱岩和片麻岩中的动向非常一致，且在空间上具有连续性，同时从糜棱岩-片麻岩到高压变质岩，面理产状从向南缓倾（50°~60°）渐变到陡立（80°~90°），因此作者认为，这些岩石中运动学指示从南向北的逆冲推覆更为合理。此外，年代学研究的结果表明，该期构造变形作用发育在未退变质或弱退变质的岩石中，而那些发生了强烈退变质的岩石则表现为完全相反的构造变形特征（见下文），后者显然要晚于前者。由此可以推断，这一从南向北的逆冲推覆作用应该与高压变质岩的侵位有关。关于高压变质岩的侵位时代，目前尚存在争议。虽然 Zhang 等（2002a，2002b；2003a）从榴辉岩相变质岩中得到的锆石 SHRIMP 年龄小于 310Ma 甚至小于 250Ma，但是将其解释为榴辉岩相变质作用的年龄是很难令人相信的。肖序常等（1992），Gao et al.和 Klemd et al.（2000，2003，2005，2006）对蓝片岩中多种变质矿物进行了 Ar-Ar, K-Ar 和 Rb-Sr 定年研究，得到了大量不同阶段的年龄数据，从而认为，高压变质的高峰期发生在 345Ma 左右。这一认识与野外地质事实相一致，在高压变质带北侧，年龄为 341±6 Ma（锆石 U-Pb ICPMS，见第三章）的伊犁岛弧钾长石花岗岩没有发生与该高压变质作用有关的变形（图 5-2A）。

1.2.3 南向韧性正断层

在接近高压变质岩带的地区，伊犁地块南缘基底岩石发生了强烈变形，其中石英岩和片麻岩中陡立的面理发生了褶皱变形（图 5-7a），褶皱轴面平缓，有时可见近水平的滑动劈理构造，表明可能存在垂向缩短作用。面理上发育密集的拉伸线理和矿物线理，在平行于线理而垂直与面理的切面（应变椭球体 XZ 面）上，发育有丰富的显微构造，如 S 型白云母、倾斜排列的动态重结晶石英颗粒（图 5-7b,c）以及不对称长英质矿物集合体和云母压力影构造（图 5-7d）等。它们共同指示南下北上的运动动向，与发生在糜棱岩、片麻岩和高压变质岩带中的运动学标志完全相反，因而属于另一期完全不同的构造变形事件。类似地，对这一运动学特征也有两种可能的解释，即它可能代表从北向南的逆冲推覆，也可能代表从北向南的滑脱作用。在野外观察和薄片研究发现，这期变形构造仅仅发育在绿片岩相变质的石英岩中，而且石英岩可能经历过垂向缩短变形。同时，下文的研究表明，石英岩形成于强退变质条件下，其中变质白云母的年龄晚与弱退变质蓝片岩相岩石中白云母的年龄。因此，这期变形应该为从北向南的韧性滑脱作用，可能与高压变质岩带的隆升折返作用有关。由于野外条件的限制，该期构造变形只在局部可以观察到，尚需要在区域上进一步研究、验证。值得提出的是，在高压变质岩中发育有一系列花岗质岩石的脉体，并切割陡立的面理构造（图 5-7e），可能为高压变质岩折返伸展过程中岩浆、热液活动的标志。

1.3. 高压变质岩 Ar-Ar 年代学

1.3.1 现有的同位素年代学结果

在过去的 20 年中，特别是近 5 年来，前人在西天山高压变质岩带中获得了大量的同位

素年龄数据（表 5-1）。肖序常等（1992）从长阿吾孜高压变质岩中蓝闪石获得了 350.9±2.0Ma 的 $^{40}Ar/^{39}Ar$ 年龄。Gao et al.（1995）从科克苏河蓝片岩中的多硅白云母得到 $^{40}Ar/^{39}Ar$ 坪年龄为 345.5±7 Ma。同一个剖面的榴辉岩绿辉石、石榴石、蓝闪石及全岩 Sm-Nd 等时线年龄为 343±44 Ma，其中石榴石-蓝闪石的 Sm-Nd 等时线年龄 346±3Ma 与青铝闪石的 $^{40}Ar/^{39}Ar$ 坪年龄 343.7 ± 1.3Ma 基本一致（Gao and Klemd，2003）。由此，Gao et al.（2003）和 Klemd et al.（2003；2005）将 345Ma 解释为榴辉岩相变质作用的年龄。

表 5-1 西天山高压变质岩带同位素年龄一览表

地点	矿物	岩石	方法	年龄（Ma）	作者
长阿吾孜	多硅白云母	蓝片岩	Ar-Ar	315	Jia, 1996
长阿吾孜	蓝闪石	蓝片岩	Ar-Ar	350.9±2	肖序常等, 1992
哈萨克斯坦	-	蓝片岩	-	410±15	Dobretsov et al., 1987
穹库什太	多硅白云母	蓝片岩	Ar-Ar	415.4±2.3	高俊, 1993
穹库什太	多硅白云母	蓝片岩	Ar-Ar	419.6±3.9	高俊, 1993
科克苏	多硅白云母	蓝片岩	Ar-Ar Plateau	345.4±6.5	Gao et al., 1995
科克苏	石榴石, 蓝闪石等	榴辉岩	Sm-Nd 全岩	346±3	Gao and Klemd, 2003
科克苏	多硅白云母	蓝片岩	Ar-Ar Plateau	344±1~331±2	Gao and Klemd, 2003
科克苏	钠闪石	榴辉岩	Ar-Ar Plateau	401±1	Gao et al., 2000
科克苏	多硅白云母	榴辉岩	Ar-Ar Plateau	381±1	Gao et al., 2000
科克苏	钠闪石	蓝片岩	Ar-Ar Plateau	370+1	Gao et al., 2000
科克苏	多硅白云母	蓝片岩	Ar-Ar Plateau	364+1	Gao et al., 2000
科克苏	白云母	蓝片岩	K-Ar	327±9~309±9	Klemd et al., 2005
科克苏	白云母	蓝片岩	Ar-Ar	328±0.5~311±5	Klemd et al., 2005
科克苏	白云母	蓝片岩	Rb-Sr isochron	313±4~302±3	Klemd et al., 2005
科克苏	白云母	蓝片岩	Ar-Ar Plateau	316.3±2.2	本文
科克苏	白云母	蓝片岩	Ar-Ar Plateau	330.7±0.3	本文
科克苏	白云母	绿片岩	Ar-Ar	322.8±0.4	本文

同时，有些学者还从西天山高压变质岩中得到了一些更老的年龄，如穹库什太（图 5-1）蓝片岩中多硅白云母具有穹隆形的 $^{40}Ar/^{39}Ar$ 年龄谱图（高俊，1993；汤耀庆等，1995），其中坪年龄为 415.4±2.3Ma。在科克苏河西南方向的阿克雅孜地区，榴辉岩残核边部的钠闪石和多硅白云母 $^{40}Ar/^{39}Ar$ 年龄分别为 415.4±2.3Ma 和 380.7±1.2Ma，而榴辉岩的蓝片岩相基质中钠闪石和多硅白云母 $^{40}Ar/^{39}Ar$ 年龄分别为 370.4±1.2Ma 和 363.9±0.5Ma（Gao et al., 2000）。另外，在哈萨克斯坦，Atbashy 蓝片岩全岩 K-Ar 年龄为 410~350 Ma（Dobretsov et al., 1987）。虽然这些年龄可能意味着天山洋早期的俯冲-增生变质作用，如中亚地区早古生代造山带俯冲事件（de Jong et al., 2006），但是作者通过对以上年龄数据的研究发现，这些年龄中至少有部分是不可靠的。如高俊（1993）和汤耀庆等（1995）所得到的穹隆形年龄谱，根据 Wijbrans and McDougall（1986）和 de Jong（2003）的解释，很可能是由于混合相中的去气作用造成的。因而，415.4±2.3Ma 的年龄可能没有实际地质意义。另外，Klemd et al.（2005）提出，Gao et al.（2000）发表的 401~364Ma 的 $^{40}Ar/^{39}Ar$ 年龄数据可能含有过剩的 Ar。实际上，从其年龄谱和 $^{37}Ar/^{39}Ar$ 与 $^{38}Ar/^{39}Ar$ 比值可以看出，钠闪石极其富 K，白云母也过度富 Ca，表明这些样品并不纯净。因此，Gao et al.（2000）所报导的偏高的年龄（381~364Ma）很可能是由于较老的富 Ca 相混染的结果。另外，Dobretsov 等（1987）的 K-Ar 年龄则有可能是全岩样品中多矿物继承特性的反映，其可靠性仍需要进一步探讨。

根据上文论述，西天山俯冲增生有关的蓝片岩相变质作用年龄为 350Ma 左右，即早石炭世早期。但是，Zhang 等（2002a, 20002b）认为，西天山存在超高压榴辉岩相变质作用（500-600°C, 2.6-2.7 Gpa），而绿帘石蓝片岩则代表发生在高压条件（500-530°C, 1.0-1.2 Gpa）

下的退变质作用。虽然 Klemd et al.（2003）对该认识提出了异议，但 Wei et al.（2003）指出，榴辉岩至少部分地经历了与蓝片岩不同的变质条件。因而不能排除西天山榴辉岩相变质作用早于蓝片岩相变质作用，即大于 350Ma。

另外，Gao et al.（2003）从青铝闪石伴生的多硅白云母中获得了 331.0±2.0Ma 的 $^{40}Ar/^{39}Ar$ 坪年龄，该年龄被解释为蓝片岩从高压条件下转换到较高构造位置过程的时代。在经历了从榴辉岩相到绿辉石蓝片岩相甚至绿片岩相退变质作用的岩石中，Klemd et al.（2005）测定了多硅白云母和钠云母的 Rb-Sr 年龄和 $^{40}Ar/^{39}Ar$ 年龄分别为 313.0~301.6Ma 和 310.9~311.6Ma。这些退变质白云母的年龄比蓝片岩相变质作用的时代要晚 50~35Ma。目前尚无可靠的年龄数据来约束榴辉岩相变质作用的时代，Zhang et al.（2002b,2003a）从榴辉岩中所得到的锆石 SHRIMP 年龄和 Tagiri et al.（1995）在吉尔吉斯坦榴辉岩中所得到的 Rb-Sr 等时线年龄均为二叠纪，这些年龄与之前所得的退变质作用的年龄相差甚远，它们可能代表退变质过程或之后的流体活动的年龄。

1.3.2 Ar-Ar 测年样品岩石学特征

作者在前人研究的基础上，针对性地从科克苏河剖面蓝片岩相高压变质带和伊犁地块南缘变形变质基底（图 5-1）中采集了三件变质岩样品，用来 $^{40}Ar/^{39}Ar$ 测年。

样品 XJ607-2b 采自 42°40.6’N, 81°56.9’E（GPS 坐标）（图 5-2A），为一强烈面理化和线理化含石榴石蓝片岩。主要矿物有蓝闪石、绿泥石和白云母以少数绿帘石（图 5-8a）。其中蓝闪石和绿帘石排列方向多变，但在数毫米尺度上其优选的排列方向表现为明显的面理构造。蓝闪石一般大小为 0.2~1mm 长的晶体，具有深蓝色到苍白、紫色等多色性，并通常形成捆绑状集合体（图 5-8a）。蓝闪石晶体通常由于颜色的差别出现环带构造，核部呈深兰色，边缘呈苍白色，在含有石榴石包体的情况下，其核部则呈暗兰色或紫色（图 5-8a）。蓝闪石边部往往与绿泥石交错生长，或完全被绿泥石替代，大多数绿泥石则集中分布于裂开的钠长石之间，表明样品经历了明显的退变质作用。单晶体白云母通常出现在绿泥石集中的位置，有时包含有蓝闪石的残留体，而白云母集合体则往往表现出交错结构，有些白云母也偶尔出现在角闪石的位置。

样品 XJ612 产于 42°40.2’N, 81°57.4’E（图 5-2A），线理和面理构造十分发育。主要矿物为蓝闪石和绿帘石，二者强烈定向排列，优选方向非常明显，白云母和绿泥石沿着蓝闪石线状构造分布（图 5-8b）。类似于样品 XJ607-2b，蓝闪石长条状晶体常常具有核部深色、边部浅色的分带现象。一些蓝闪石已被绿泥石和纳长石所交代甚至被部分替代。数毫米大小的单斜辉石斑晶含有蓝闪石的包体，蓝闪石表现出与外部面理一致的定向性。在样品中，常见被方解石充填的拉张裂隙，并切割面理和线理构造（图 5-8b）。白云母往往沿岩石主要面理和线理分布，部分白云母与绿泥石沿其解理方向交错生长，而另一些白云母和绿泥石交错生长形成的集合体局部地切割了蓝闪石-绿帘石构成的主要线理构造。相对而言，该样品也发生了一定的退变质作用，但较样品 XJ607-2b 退变质程度要低。

样品 XJ611 采自 42°41.1’N, 81°56.3’E（图 5-2A），为一不等粒状含石榴石的绿泥石云母石英片岩，属于绿片岩相变质的伊犁南缘基底。岩石面状和线状构造不明显（图 5-8c）。次等粒状石英颗粒具有锯齿状边界，表现为波状消光，由动态条件下重结晶形成。白云母以 0.05~1mm 长的晶体分布于石英颗粒之间（图 5-8c），有时也沿绿泥石的主劈理方向发育而形成较大的斑晶。岩石中含有较多的石榴石矿物，其中不含蓝闪石包体，没有绿泥石化作用。岩石偶尔还发育较大的方解石晶体，并充填于基质中。

1.3.3 Ar-Ar 测年结果

将变质岩样品压碎成 500μm 以下的颗粒，用清水冲洗、低温（40°C）烘干后，在双目镜下手挑选出 0.3-2mm 大小的白云母单颗粒，在 $^{40}Ar/^{39}Ar$ 激光探针(CO_2 Synrad®)中分步加热分析。实验中，白云母颗粒封装在 11 mm × 11 mm × 0.5 mm 大小的铝箔封袋中，封袋排

列放置在固定的照射装置中，并且在每 8-10 个样品之间放置一个电通量控制器。控制器中的标样 TCR-2 年龄为 28.34 Ma（Renne et al., 1998）。样品和标样一起放在 McMaster 反应堆（加拿大 Hamilton）中照射 13.33 小时，总通量为 1.7×10^{18} n×cm^{-2}。详细的分步加热过程见 Ruffet 等（1991, 1995）。样品测试在 Map215®质谱仪中进行。

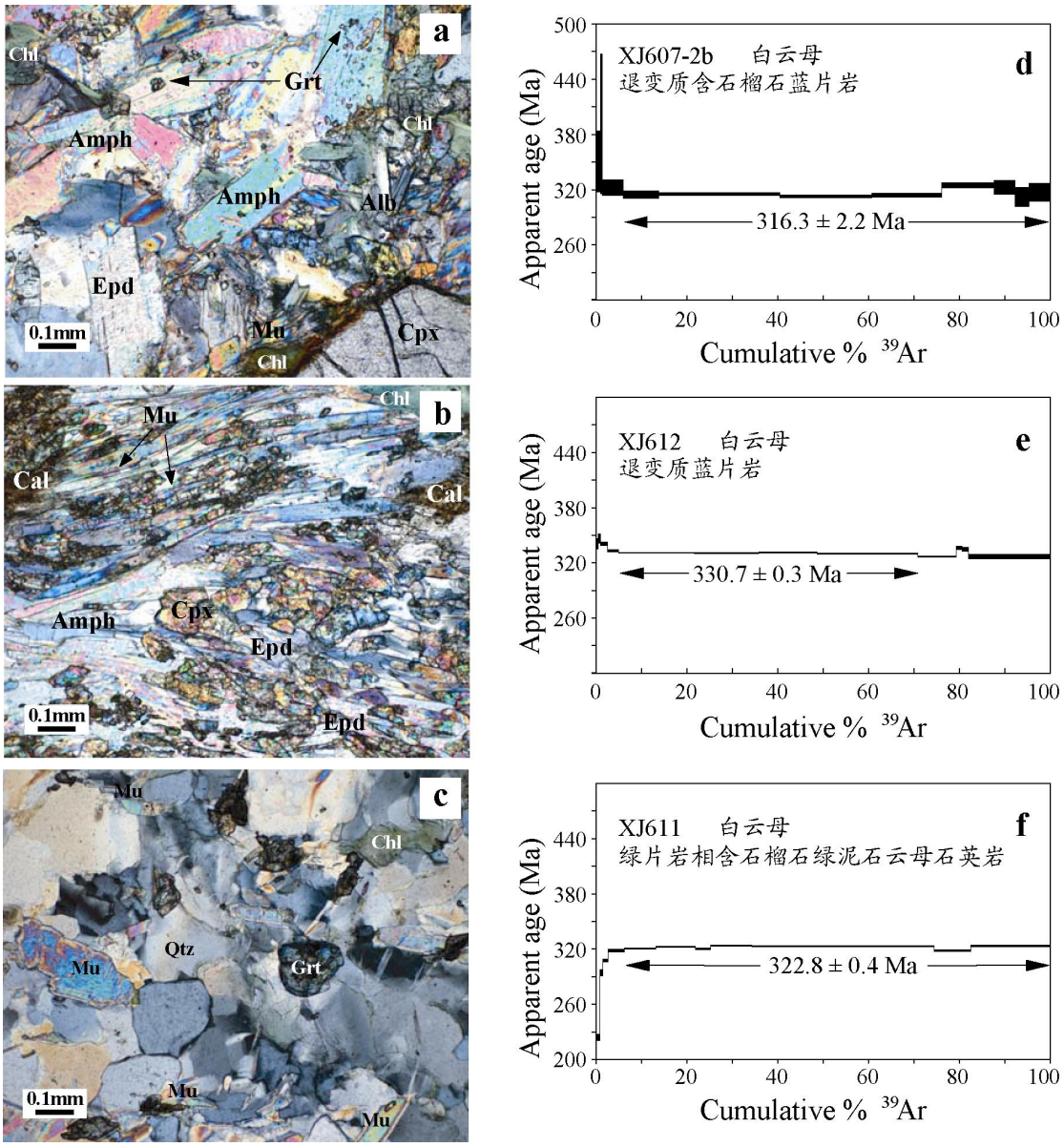

图 5-8 科克苏剖面高压变质岩岩石学特征和 Ar-Ar 坪年龄谱图

Alb，钠长石；Amph，角闪石（主要为蓝闪石）；Cal；方解石；Chl，绿泥石；Epd，绿帘石；Grt，石榴石；Mu，白云母；Qtz，石英

样品 $^{40}Ar/^{39}Ar$ 分析结果见表 5-2。在连续的三步以上加热过程中 $^{39}Ar_K$ 释放达到 70%以上，且其中单步年龄控制在 1σ或 2σ水平时，方可计算出坪年龄。否则，低于 70%的 $^{39}Ar_K$ 释放则只能计算出似坪年龄。在此基础上，有关分析数据对应的年龄谱见图 5-8d-f。所有的误差控制在 1σ水平。然而，所有样品在分步加热中所形成的气体溢出相对应的坪年龄则在 1σ的置信水平上是不一致的。通过计算，得出样品 XJ607-2b 中白云母的坪年龄为 316.3 ± 2.2 Ma，样品 XJ612 中白云母的坪年龄为 330.7 ± 0.3 Ma，而绿片岩相变质岩 XJ611 中白云母的坪年龄为 322.8 ± 0.4 Ma（图 5-8d,e,f）。

1.3.4 Ar-Ar 年龄地质意义

表 5-2. 科克苏河剖面变质岩中白云母单颗粒激光探针分步加热 $^{40}Ar/^{39}Ar$ 分析数据

步骤	$^{40}Ar_{Atm}$(%)	$^{39}Ar_K$(%)	$^{37}Ar_{Ca}/^{39}Ar_K$	$^{40}Ar^*/^{39}Ar_K$	年龄 (Ma)
XJ607-2b, 含石榴石退变质蓝片岩中白云母(J=0.00539485)					
1	57.0	0.9	0.000	39.79	350.8 ± 33.3
2	26.6	0.5	0.265	44.96	391.8 ± 75.8
3	24.8	4.5	0.131	36.27	322.4 ± 8.4
4	20.3	7.8	0.155	35.32	314.6 ± 4.2
5	12.6	26.7	0.109	35.38	315.1 ± 1.6
6	11.8	20.2	0.120	35.12	313.0 ± 1.6
7	13.9	15.4	0.176	35.24	313.9 ± 2.3
8	11.7	11.6	0.643	36.57	324.8 ± 3.2
9	6.8	4.6	1.847	36.31	322.7 ± 7.7
10	5.6	3.1	0.916	35.03	312.2 ± 10.3
Fusion#	1.6	4.7	0.515	35.62	317.1 ± 9.6
XJ611, 绿片岩相含石榴石、绿泥石、云母石英片岩中白云母(J=0.00539318)					
1	11.4	0.9	0.128	24.49	223.8 ± 3.4
2	0.6	0.6	0.000	32.86	294.4 ± 3.7
3	0.6	1.3	0.000	34.50	307.8 ± 1.6
4	0.5	1.9	0.013	35.80	318.5 ± 1.4
5	1.3	1.7	0.061	35.81	318.5 ± 1.5
6	1.0	6.9	0.031	36.08	320.7 ± 0.6
7	0.7	8.7	0.031	36.30	322.5 ± 0.6
8	0.9	3.3	0.060	36.04	320.4 ± 0.8
9	0.7	9.0	0.018	36.44	323.6 ± 0.6
10	0.5	40.2	0.023	36.35	322.9 ± 0.7
11	0.8	8.0	0.039	35.81	318.5 ± 0.8
fusion	1.1	17.5	0.061	36.42	323.5 ± 0.9
XJ612, 退变质蓝片岩中白云母 (J=0.00539568)					
1	13.3	0.5	0.415	38.51	340.6 ± 5.7
2	4.3	0.5	0.080	39.22	346.3 ± 5.1
3	5.1	1.5	0.001	38.54	340.9 ± 1.8
4	5.0	2.4	0.072	37.62	333.4 ± 1.3
5	1.9	16.6	0.014	37.32	331.0 ± 0.6
6	1.0	14.2	0.018	37.29	330.8 ± 0.6
7	1.0	12.8	0.016	37.34	331.2 ± 0.6
8	0.8	22.2	0.019	37.23	330.2 ± 0.6
9	0.8	8.5	0.039	36.82	326.9 ± 0.6
10	2.3	1.3	0.025	37.96	336.2 ± 1.8
11	3.0	1.4	0.056	37.83	335.1 ± 2.2
fusion	1.5	18.1	0.022	36.81	326.9 ± 2.5

#fusion 为加热最后一步，在激光束汇焦时获得； $^{40}Ar^*$为 K 自然衰变过程中形成的放射成因 Ar； $^{40}Aratm$ 为大气中的 ^{40}Ar； $^{37}Ar_{Ca}$ 与 $^{39}Ar_K$ 分别为 Ca 和 K 在照射过程中释放的 Ar；J 为照射参数。衰变常数和同位素丰度比值：$^{40}K_{tot}$ = 5.543 × 10-10 a-1; $^{40}K/K$ = 0.01167 atom %（Steiger and Jäger, 1977）。

从上文 Ar-Ar 测年结果可以看出，三个退变质的岩石 $^{40}Ar/^{39}Ar$ 年龄范围为 330-316 Ma，比高压变质的蓝片岩年龄（肖序常等，1992；Gao et al., 1995；Gao and Klemd，2003）（表 5-1）小了约 30Ma。这些岩石中退变质作用特征矿物绿泥石-钠长石-白云母等矿物组合和它

们的结构、构造表明，样品 XJ607-2b 和 XJ612 中白云母形成于蓝片岩退变质作用过程中。退变质作用相对较强的样品 XJ607-2b 的坪年龄（316.3 ± 2.2 Ma）比退变质较弱的样品 XJ612 的坪年龄（330.7 ± 0.3 Ma）更小。同时，绿片岩相的石英岩样品 XJ611 中白云母坪年龄（322.8 ± 0.4 Ma）与退变质作用的年龄一致。这些年龄与位于采样剖面西侧 80km 处退变质的蓝片岩白云母 Rb-Sr 和 $^{40}Ar/^{39}Ar$ 年龄（Klemd et al., 2005）也基本一致。因此，这些年龄代表白云母在退变质作用过程中结晶的年龄，而从蓝片岩相退变质到绿片岩相的过程，则应该与高压变质岩的折返抬升作用有关。

由此可见，高压变质岩退变质作用的年龄明显比伊犁岩浆岛弧作用的最晚年龄（301Ma，见第三章）要晚，即在伊犁岩浆岛弧活动的晚期，伊犁南缘处于拉张环境。这一结果表明，伊犁岩浆岛弧的形成与天山洋的俯冲作用没有直接关系。

2. 黑英山蛇绿混杂岩及其构造基底与盖层

黑英山剖面位于拜城县北东 60 km 的梅斯布拉克上游与阿尔腾卡什河一带（图 5-1）。在梅斯布拉克上游，古生代可分为三个构造-地层单元：北带下部单元为中天山地块早古生代低绿片岩相变质变形带，中部为南天山晚古生代蛇绿混杂岩带，南带上部单元为塔里木北缘晚古生代未变质弱变形带（图 5-9A,B）。其中北带与混杂岩带以断层接触，前者逆冲于后者之上，可能是造山后期中、新生代陆内挤压变形的结果。南带下石炭统不整合覆盖在混杂岩带之上，局部以断裂接触（图 5-9）。

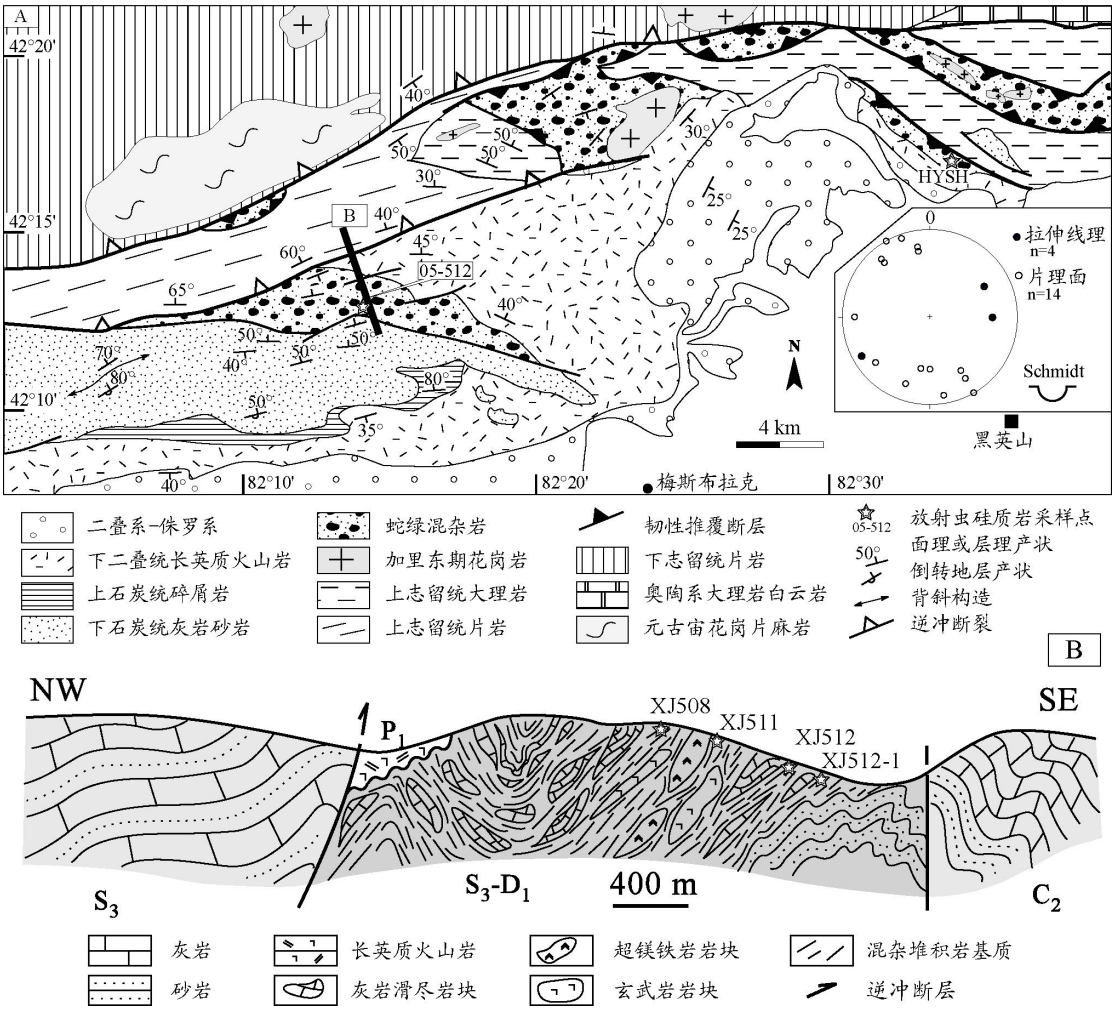

图 5-9 西南天山黑英山地区地质简图（A）与剖面图（B）（据新疆地矿局，1983）

2.1. 中天山早古生代变形带

低绿片岩相带主要由下-中志留统合同沙拉群($S_{1-2}ht$)，晚志留统穹库什太组(S_3q)，阿克雅孜组（S_3a）和乌帕塔尔坎组（S_3w）组成（新疆地矿局，1983）。其中 $S_{1-2}ht$ 主要为大理岩、变粒岩和片岩，S_3q 由强烈片理化的碎屑岩、大理岩和火山碎屑岩组成，S_3a 以砂岩为主，而 S_3w 则主要为碳酸盐岩（图 5-9A）。志留纪灰岩中富含珊瑚类、腕足类、腹足类、层孔虫类和三叶虫等化石。片理化大理岩中发育 NE-SW 向延伸的劈理构造，劈理面向北陡倾（图 5-10f），局部还见糜棱岩化作用，其岩相和变形特征与库勒湖以南地区志留系-泥盆系（图 5-1）变形特征十分一致（Zhou et al., 2001；Laurent-Charvet, 2001），同时也与别迭勒剖面超糜棱岩化大理岩及库米什北西方向吾拉斯台的大理岩（见下文）比较相似。

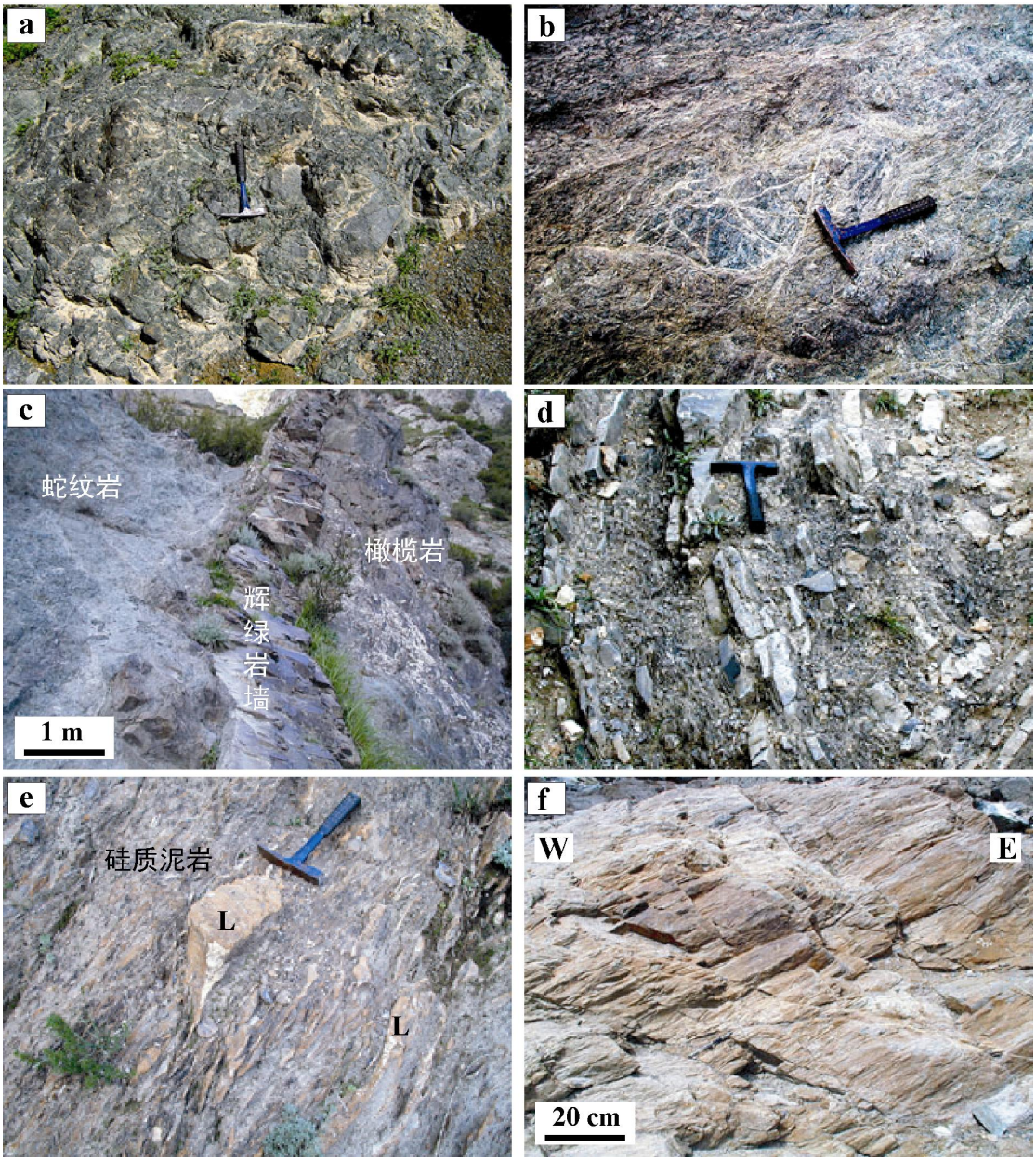

图 5-10. 黑英山蛇绿混杂岩（a-e）及构造基底岩石（f）地质特征（e 中 L 指灰岩）

该低绿片岩相带的变形程度向北逐渐减弱。在科克苏河上游和梅斯布拉克上游之间的哈尔克山主脊一带，奥陶-志留系灰岩变形特征与黑英山低绿片岩相变质岩和科克苏河高压变质岩的变形特征完全不同（新疆地矿局，1979；1983；1993）。未变质、微弱褶皱变形的灰岩向北逆冲推覆在高压变质带之上，向南也发育一系列北倾的逆冲断层，并将其与南侧片理

化岩石隔开（图 5-9）。由于野外条件限制，关于该段剖面的详细野外资料至今仍十分有限。但在该剖面东侧近 200km 的独库公路上（图 5-1），发育有同一地层单元的野外露头。在铁里买提达坂北坡，志留系主要由浊积相复理石、火山碎屑岩及灰岩组成。铁里买提达坂以南，志留系岩石主要为陆坡相灰岩及层间砾岩，其中灰岩发生重结晶作用。在志留系之上，覆盖有泥盆系砾岩、砂岩、灰岩和条带状硅质岩（新疆地矿局, 1993；王宝瑜等，1997；Zhou et al., 2001；Laurent-Charvet, 2001）。在巴音布鲁克西南方向，下石炭统未变质、弱褶皱变形的砾岩、砂岩和碳酸盐岩不整合覆盖于加里东晚期-海西早期的花岗岩之上，该花岗岩中锆石 U-Pb 年龄为 378 Ma（Hu et al., 1986）。在二乡桥南侧，石炭系结晶灰岩不整合覆盖在泥盆系砂岩之上（Zhou et al., 2001）。需要强调指出的是，石炭系地层均没有发生明显变形，且没有火山物质的加入，同期的侵入岩体也不发育，与其北侧伊犁地块石炭系岩相学特征完全不同。

此外，在梅斯布拉克上游河谷，可以见到很多花岗片麻岩滚石，这些滚石应该来源于哈尔克山主脊，可能为元古代基底岩石。因此，沿哈尔克山主脊分布的早古生代地层形成于两种构造环境，奥陶-早志留世为稳定陆坡沉积，晚志留世出现火山活动，可能为活动陆缘环境，泥盆纪开始再次成为被动陆缘沉积环境，并在其南部甚至出现半深海环境。

在西天山，位于高压变质带以南、黑英山蛇绿混杂岩带以北的区域，一直被当作南天山构造带的一部分（Allen et al., 1992; Gao et al., 1998; Zhou et al., 2001 以及所引文献）。但实际，该单元与中天山巴音布鲁克以东地区具有相似的构造-地层-岩石特征，而与南天山蛇绿混杂岩带及其以南地区在变质变形与沉积序列上却完全不同（见下文）。因此，本文将高压变质带与南天山蛇绿混杂岩带之间的区域划为“中天山”，它代表一个具有元古代变质基底的大陆块体，处于伊犁地块和塔里木板块之间，对于伊犁地块及天山造山带的构造演化起着关键作用。

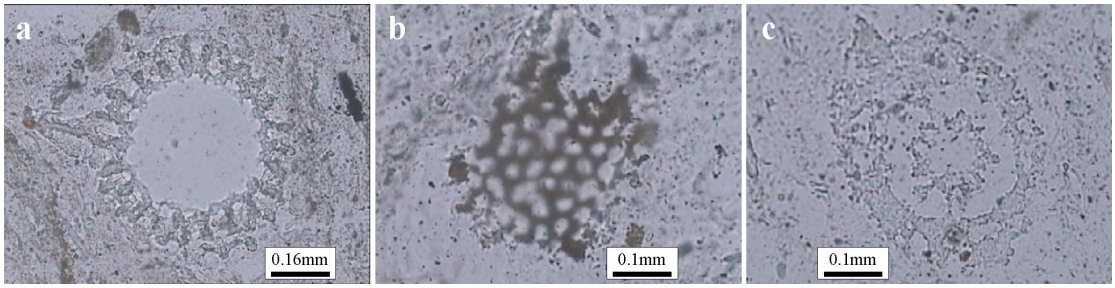

图 5-11. 黑英山蛇绿混杂岩基质中含放射虫硅质岩显微照片

2.2. 南天山晚古生代蛇绿混杂岩带

2.2.1 蛇绿混杂岩地质特征

上志留-下泥盆统阿尔腾柯斯组（S_3-D_1）为混杂堆积岩带，岩组由形状各异、大小不均的块体与基质构成混杂堆积序列（图 5-9B）。构造岩块包括灰岩、砂岩、硅质岩和镁铁质-超镁铁质岩，镁铁岩-超镁铁岩主要由玄武岩、枕状玄武岩（图 5-10a）、辉长岩和变质橄榄岩（图 5-10b）及辉绿岩脉（图 5-10c）等组成。其中辉长岩呈粗粒状，结晶程度好，而橄榄岩不同程度地发生了蛇纹岩化作用，并被大量不规则的方解石脉所穿插。这些岩块小则几十厘米，大到几百米，因而很容易被误认为是原地的地层单元。从整体来看，这些岩石块体均为透镜体状、无根状产出，表明曾经经受过强烈的构造剪切变形。岩块内部变形较弱，如在灰岩、砂岩和硅质岩块体中可见清晰、规则的层理和顶底关系。岩块与周围的基质不规则接触，基质由硅质复理石和硅质岩组成（图 5-10d）。与岩块不同的是，大部分基质发生了强烈的褶皱变形和片理化，在基质内部，可见倒转层序和复褶皱等变形构造。在与岩块接触带，基质复理石的初始层面或硅质泥岩基质的片理面往往环绕灰岩剪切块体（图 5-10e），表明该变形为同沉积变形，因而，基质年龄应代表混杂堆积岩形成的时代。经过对多处基质复

理石的层面和片理面的测量统计，估算出混杂堆积岩的总体走向为 N40E（图 5-9A 插图），层面和片理面近平行。

蛇绿混杂岩与北侧强烈片理化大理岩和片岩呈断层接触，朝北高角度倾斜的逆断层指示片岩与大理岩逆冲在蛇绿混杂岩之上。由于类似的变形普遍发育在该剖面晚古生代-中生代地层中，并均以脆性变形为特征，因此这些逆冲推覆作用为新生代陆内变形的结果。相反，在强烈片理化的大理岩中，破劈理指示从南向北的韧性剪切作用。由于大理岩重结晶程度较高，很难观察到其他运动学标志，但在黑英山西南方向的乌什地区，一系列变形运动学标志（见下文）也指示从南向北推覆的运动动向。前人（Windley et al., 1990；Allen et al., 1992）认为，南天山蛇绿混杂岩是从天山洋缝合带向南推覆形成的飞来峰或构造推覆体，因而不代表一个单独的构造缝合带。然而，本文的运动学研究认为，天山洋缝合带（如科克苏河高压变质带，见上文；干沟-米什沟蛇绿混杂岩带，见本章第三节）和南天山蛇绿混杂岩（参见本章第二-三节）的变形运动学并不支持从北向南的推覆作用。

2.2.2 蛇绿混杂岩时代

2.2.2.1. 古生物地层学证据

关于该蛇绿混杂岩的形成时代，新疆地质矿产局（1983）在 1：20 万地质填图工作中，将梅斯布拉克蛇绿岩和阿尔腾柯斯中游超镁铁岩带划归为华里西早期（早泥盆世）。肖序常等（1992）根据新疆维吾尔自治区 1：200 万地质图中超镁铁岩侵位于泥盆系或逆冲于石炭系之上的产状关系，认为黑英山蛇绿混杂岩带形成于晚古生代早期。王作勋等（1990）通过对比该蛇绿混杂岩带与哈尔克山蛇绿混杂岩带硅质岩中放射虫化石，将其时代归为早古生代晚期。郝杰等（1993）认为南天山蛇绿岩形成于志留纪，泥盆纪-石炭纪时发生俯冲而构造变形。最近，Liu Yu（2001）在黑英山以北（图 5-9A）阿尔腾柯斯尔组蛇绿岩带中发现了大量保存完好的晚泥盆世-早石炭世放射虫，进而认为该蛇绿岩形成于石炭纪。这一结果与库勒湖蛇绿混杂岩带硅质岩中晚泥盆世-早石炭世放射虫和牙形刺微古化石的时代（汤耀庆等，1995；Gao et al., 1998）完全一致。然而，Li YJ et al.（2002，2005）先后在西南天山阿合奇以西 60~80 km 处的上石炭统艾克提克群（C_2ak）和志留系乌帕塔尔坎组（S_3w）中发现了早石炭世-晚二叠世的放射虫化石，提出南天山残留洋直至二叠纪末才关闭的认识。由此可见，西南天山蛇绿混杂岩带的形成时代仍然是一个尚存争议的问题。

如上文所述，前人在阿尔腾柯斯组的灰岩中，发现了大量的志留纪-泥盆纪珊瑚、腕足类、腹足类和海百合茎化石（新疆地矿局，1983），因而长期以来，该混杂堆积岩的时代被定为是晚志留世-早泥盆世（S_3-D_1）。然而，含有丰富化石的灰岩并非原地沉积形成的，而是以团块状或透镜体状与砂岩、硅质岩以及镁铁-超镁铁岩的块体混杂堆积在一起，同复理石和硅质泥岩基质一起形成构造混杂堆积岩。因此，这些灰岩团块中的化石不能代表混杂堆积岩的形成时代，而仅代表灰岩的年龄。构造混杂岩的形成应该晚于各构造岩块的年龄，而与基质的年龄同时。另外，关于用硅质岩中放射虫来约束蛇绿岩形成时代的问题，王玉净等（2001）提出，只有产于蛇绿岩套上部单元，即枕状熔岩之上的放射虫硅质岩才能真正代表残余洋壳的年龄。因而在放射虫硅质岩研究中，应该特别注意硅质岩与枕状熔岩之间的接触关系，如新疆巴音沟蛇绿混杂岩带（肖序常等，1992）和卡拉麦里蛇绿岩带（舒良树等，2001）中红色硅质岩紧临并覆盖于枕状熔岩之上，故而其中所保存的放射虫化石能够较可靠地反映蛇绿岩形成的上限年龄及混杂岩形成的下限年龄。以构造岩片、无根透镜体等形式产出于混杂岩中的硅质岩，其时代具有多义性，即这种硅质岩块体有可能是蛇绿岩套的一部分，也可能是被构造混杂作用卷入到蛇绿混杂岩中的早期硅质岩，还可能是由于蛇绿混杂岩形成以后构造跨塌作用卷入的更年轻的硅质岩（郭令智等，1996；王博等，2001），而这些被构造卷入的含放射虫硅质岩则不一定形成于洋盆环境。

鉴于以上原因，作者最近对黑英山梅斯布拉克蛇绿混杂岩剖面进行了野外考察，并系统

采集了 10 余件混杂岩基质中的泥质硅质岩、硅质泥岩、薄层状硅质灰岩样品，旨在获取一些微体古生物化石，进一步探讨构造混杂岩的形成时代。样品均采自黑英山西约 35 km 处、梅斯布拉克上游河谷中，采样点位于（N42°14.09’，E82°12.52’）与（N42°12.68’，E82°12.66’）之间（图 5-9）。这些样品均未经受强烈的变形，其中泥质硅质岩呈灰黑色、薄层块状、坚硬、很少发育裂隙与方解石脉体，新鲜面可见一系列白色斑点，疑为放射虫化石。硅质泥岩为淡绿色、薄层状、微粒并具有纹层、条带，岩石微弱变形并较破碎，表面分布密集的深色点状物。

对初选的 9 个样品进行磨片并用放大镜观察，进一步选择可能含有放射虫化石的 6 个样品切制薄片。镜下观察发现，泥质硅质岩致密、含有大量生物碎屑，主要为环形构造的放射虫化石，保存十分完整，壁状结构清晰可见（图 5-11a）。硅质泥岩中也可见到类似于环状构造的生物碎屑，但大部分结构较为模糊不清（图 5-11b,c）。将保存有完整放射虫化石的硅质岩样品 XJ512 送交南京古生物研究所经王玉净研究员分析后，鉴别出大量放射虫化石，主要有 *Archocyrtium cf. procerum Cheng, Archocyrtium venustum Cheng, Archocyrtium cf. ludicrum Deflandre, Archocyrtium cf. mirousi Gourmelon, Trilonche almae (Won), Stigmosphaerostylus Pantotolma Braun, Stigmosphaerostylus vulgaris Won, Stigmosphaerostylus wuppertalensis Won), Stigmosphaerostylus cf. Tortispina Ormiston et Lane, Holoeciscus foremanae sp., Albaillella paradoxa sp.*等。这些微体化石为晚泥盆世法门期和早石炭世杜内期 *Holoeciscus foremanae* 和 *Albaillella paradoxa* 组合中常见的化石分子，因此认为，硅质岩基质形成的时代为晚泥盆世-早石炭世。这一结果与黑英山以北蛇绿岩剖面（图 5-9A）中放射虫的时代（Liu Y, 2001）完全一致，同时也与库勒湖蛇绿混杂岩带（图 5-1）中放射虫的时代（汤耀庆等，1995；Gao et al., 1998）相同。另外，放射虫时代与库勒湖蛇绿混杂岩中石英片岩的黑云母 $^{40}Ar/^{39}Ar$ 年龄（370±4.8Ma）也十分吻合，其中石英片岩产出在基质中，形成于蛇绿混杂岩构造侵位过程中的强烈韧性剪切作用（蔡东升等，1996）。王学潮等（1995）从库勒湖蛇绿混杂岩的辉长岩中获得斜长石 $^{40}Ar/^{39}Ar$ 年龄为 330~335 Ma，该年龄可能是在蛇绿混杂岩仰冲剪切推覆中，斜长石同位素系统被重置的结果。因此，南天山黑英山-库勒湖一带蛇绿混杂岩的形成时代应为晚泥盆世-早石炭世。

表 5-3 黑英山蛇绿混杂岩带中辉长岩锆石 U-Pb ICPMS 分析数据

Plots	元素含量				原子比值						年龄 （Ma）						Disc.
	U ppm	1σ	Pb ppm	1σ	$^{206}Pb/^{238}U$	1σ	$^{207}Pb/^{235}U$	1σ	$^{207}Pb/^{206}Pb$	1σ	$^{206}Pb/^{238}U$	1σ	$^{207}Pb/^{235}U$	1σ	$^{207}Pb/^{206}Pb$	1σ	(%)
JA19D2	170	10	16	1	0.061	0.001	0.45	0.03	0.056	0.004	381	6	374	21	451	146	6
JA19D12	348	16	32	2	0.062	0.001	0.44	0.02	0.056	0.002	386	4	373	14	460	98	4
JA19D1	306	15	28	1	0.062	0.001	0.47	0.02	0.059	0.003	389	4	390	17	564	113	4
JA19D5	210	10	22	1	0.063	0.001	0.47	0.03	0.059	0.003	394	5	393	19	559	122	5
JA19D11	320	17	28	2	0.063	0.001	0.45	0.03	0.056	0.004	395	5	380	20	451	140	5
JA19D8	459	34	41	3	0.064	0.001	0.51	0.04	0.062	0.004	399	5	420	24	657	152	6
JA19D9	417	18	37	2	0.064	0.001	0.51	0.03	0.062	0.003	402	5	420	18	665	114	5
JA19D10	358	18	33	2	0.064	0.002	0.46	0.04	0.054	0.005	398	10	386	26	386	201	10
JA19D7	601	27	65	3	0.064	0.001	0.46	0.02	0.056	0.002	401	4	381	12	446	84	4
JA19D3	441	20	43	2	0.067	0.001	0.48	0.02	0.056	0.002	419	4	398	14	446	87	4
JA19D6	269	12	21	1	0.070	0.001	0.52	0.03	0.057	0.003	434	6	422	18	482	108	6

Disc. (%) 为不协和百分比。

2.2.2.2. 辉长岩锆石 U-Pb 测年

黑英山蛇绿混杂岩的形成年龄代表俯冲洋壳最终缝合的年龄，然而，洋壳存在的时代则需要由混杂岩带中蛇绿岩的年龄来约束。作者在野外考察中，从黑英山蛇绿混杂岩中采集了

一件 5 kg 重的辉长岩样品，岩石为粗晶等粒结构，主要由 1-1.5 cm 大小的辉石和长石组成。岩石经过压碎、清水涛洗、重液和磁分选后，在双目镜下选出锆石单矿物颗粒 30 余颗。锆石颗粒大多呈自形、无色，没有分带和破裂纹，表明这些锆石主要为岩浆成因。选择颗粒较大、晶形好、透明度高的锆石颗粒 10 颗，在澳大利亚塔斯马尼亚（Tasmania）大学用 LA-ICPMS 方法进行了 U-Pb 定年测试，有关仪器工作参数和其他详细的测试过程参照第三章和 Meffre et al.（2004）。分析结果见表 5-3 所示。

由 U-Pb 分析结果可以看出，11 个测点中 9 个点可以得出一个协和年龄：392±5Ma (MSWD=1.8)（图 5-12），该年龄可以解释为锆石结晶的年龄，即蛇绿岩形成的年龄，表明在 390 Ma，也就是中泥盆世时，在南天山存在一个洋壳。另外两个测点则给出了相对偏老的年龄，分别为 420Ma 和 433Ma，可能来自个别较老的捕获锆石，可能代表洋壳早期拉张阶段的岩浆结晶作用。

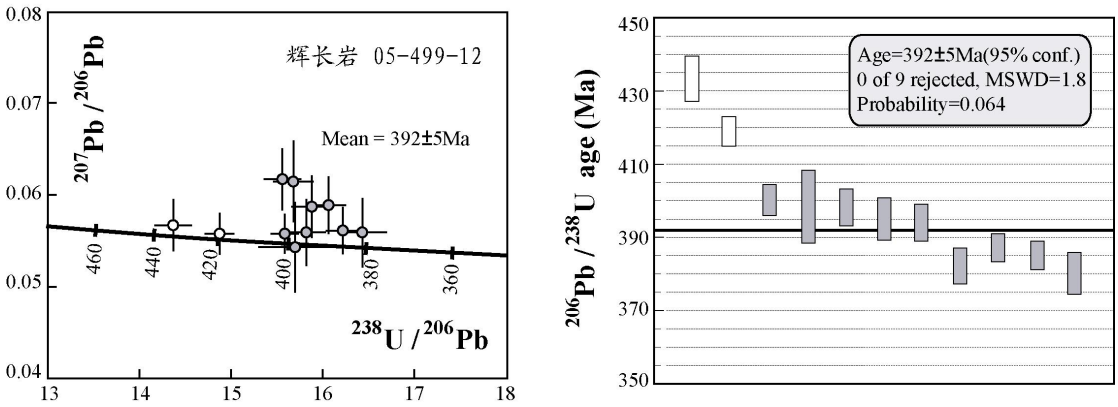

图 5-12 黑英山蛇绿混杂岩带中辉长岩锆石 U-Pb 测年结果

关于该蛇绿岩所代表的构造环境，前人已从岩石学、地球化学的角度对该混杂岩带中的变质超镁铁岩、镁铁岩（包括辉长岩、玄武岩、玄武安山岩、斜长角闪岩等）进行了研究。结果显示，黑英山蛇绿岩中镁铁岩形成于残留洋盆环境（刘本培等，1996）、洋中脊环境（王学潮等, 1995）或者小洋盆中不成熟岛弧环境（汤耀庆等，1995；高俊等，1995）。

2.3. 塔里木北缘前陆变形带

在蛇绿混杂岩以南，晚古生代地层主要包括下石炭统干草湖组（C_1g）、野云沟组(C_1y)，中（上）石炭统卡拉苏组（C_2k），上石炭统康克林组（C_3k），下二叠统小提坎力克组（P_1x）、库尔干组（P_1k）和上二叠统比尤勒包谷孜组（P_2b）（图 5-9）。下石炭统不整合于蛇绿混杂岩（S_3-D_1）之上，如 C_1y 与 S_3-D_1 之间的不整合（新疆地矿局，1983，1993）。但在野外，由于条件限制，这些不整合接触关系并不容易观察到。下石炭统以砾岩、砂岩、粉砂岩和砂质灰岩为主，富产微古植物化石；上石炭统则以生物碎屑灰岩为主，夹有砂岩、粉砂岩和泥岩。灰岩中产大量腕足类、珊瑚和少量腹足类化石。P_1x 由酸性和基性为主的双峰式火山岩、火山碎屑岩组成。P_1k 和上二叠统，以及中、新生代地层均为陆源碎屑岩，含大量植物和动物化石（新疆地矿局，1983）。所有以上地层均没有发生变质，变形仅以褶皱、脆性断裂构造为特征。一系列逆断层切隔了中生代以前的地层，并使老的地层向南逆冲覆盖到新地层之上，该期变形与新生代印藏碰撞引起的塔里木-天山陆内俯冲作用有关（Molnar and Tapponnier, 1975; Tapponnier and Molnar, 1979; Nelson et al., 1987; Avouac et al., 1993；Allen et al., 1999）。南侧梅斯布拉克下游，一系列中、新生代褶皱变形发育在天山与塔里木山-盆交接地带，著名的塔里木油田克拉二井就位于其中。该带属于塔里木北缘前陆变形带，其北界以南天山蛇绿混杂岩带与中天山相隔（图 5-1）。

3. 科克苏-黑英山综合解释剖面图

根据以上地质学、运动学、年代学等综合分析，科克苏-黑英山剖面跨越了伊犁地块、天上洋缝合带、中天山地块、南天山蛇绿混杂岩带和塔里木北缘前陆变形带。图 5-13 是一个综合地质解释剖面，表示了各个单元及其相互之间的关系。剖面的北部为伊犁晚古生代岩浆岛弧，其元古宙片麻岩基底和早古生代盖层出露于伊犁地块的南缘，并经历了至少两期韧性变形事件。早期（早于 350 Ma）天山洋俯冲作用引起的南北向挤压造成了从南向北的剪切逆冲推覆作用，晚期（二叠纪）走滑剪切断层（那拉提断裂）使伊犁地块岩浆岛弧南缘及其构造基底再次发生韧性变形。

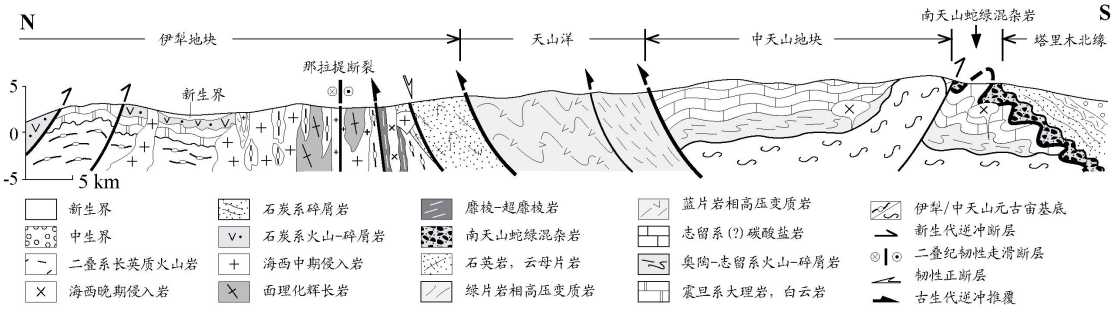

图 5-13 科克苏-黑英山综合解释剖面图

伊犁地块的南界为高压变质岩带，其原岩由洋壳玄武质岩石和海底沉积物组成，代表一个古生代的洋盆，即天山洋。该洋盆在 350Ma 左右或更早即已关闭、碰撞，形成了高压变质岩，并向北推覆至伊犁地块南缘之上，使伊犁元古代基底和早古生代盖层发生了变质变形作用。在 330~310Ma 期间，高压变质岩发生折返抬升及相应的向南韧性滑脱作用。

中天山为一个具有元古代片麻岩构造基底的微地块，主要由奥陶系-泥盆系碳酸盐岩和少量志留系火山碎屑岩组成，其北部大理岩逆冲推覆到高压变质岩之上，南部则发生了强烈的片理化作用。南天山蛇绿混杂岩代表一个中泥盆世的洋盆在晚泥盆世-早石炭世俯冲关闭，洋壳残片逆冲推覆到中天山南缘之上，造成了中天山南缘早古生代地层的韧性变形作用。下石炭统碎屑岩地层不整合覆盖于蛇绿混杂岩和中天山前石炭纪地层之上。在塔里木北缘盆山交接带，古生代-中生代地层发生了脆性褶皱变形，并形成一系列向南的逆冲推覆断层。

第二节 乌什–阿合奇剖面构造变形特征

沿天山南缘，南天山蛇绿混杂岩带向西南延伸至乌什-阿合奇一带（图 2-7）。在阿合奇地区，一些学者从硅质岩中发现了晚二叠世的放射虫（Li YJ et al., 2002；2005），这一结果与以往对天山造山带构造演化的认识有所不同。为了对比该蛇绿混杂岩与黑英山及以东地区的蛇绿混杂岩特征，作者在乌什和阿合奇地区进行了野外地质考察。

1. 乌什别迭勒剖面

别迭勒剖面位于乌什县北西方向 60 km 处的别迭勒河谷。剖面的南侧为近 3000 m 厚的二叠系砂岩、碳质砂岩和砾岩，岩层向北陡倾（50°~70°）。层面印摸和粒序层等沉积构造表明，该地层中发育频繁的紧闭同斜褶皱，褶皱形态指示从北向南的挤压推覆作用。在二叠系以北，泥盆系大理岩高角度逆冲在二叠系地层之上（图 5-14a）。据正在执行新疆 1:5 万乌什幅填图项目的青海地调队杨延兴总工介绍，在临近的剖面中，石炭系主要由灰岩和砂岩组成，且逆冲在二叠系之上，偶尔也见二叠系不整合于石炭系之上。泥盆系也逆冲推覆在石炭系之上。石炭系和二叠系岩层主要以脆性褶皱变形作用为主，表现为一系列紧闭的不对称褶皱和逆冲断层及伴生的破劈理构造（图 5-14b,c,d）。这些变形特征与黑英山剖面南端石炭纪-中生代地层的变形特征十分一致。前石炭纪地层主要包括泥盆系和志留系，均发生了强烈的韧性

变形，如志留系碎屑岩和火山碎屑岩则发生了强烈的片理化（图 5-14e），泥盆系大理岩发生了超糜棱岩化（图 5-14f）。在这些韧性变形的岩石中，面理（S_1）呈不同角度向北倾斜，并发生了不同程度的褶皱变形（S_2）和局部错动（图 5-14e），褶皱和断错形态显示从北向南逆冲推覆作用。在 S_1 面理上，可以识别出 S-N 向或 SE-NW 向拉伸线理构造，指示韧性剪切作用。大理岩发生了明显的重结晶作用，但仍可以在垂直面理和平行线理的切面上，见到布丁状零星分布的不对称球状吐起，可能是不均一重结晶作用中留下的灰岩残斑，在韧性剪切过程中发生变形，其不对称形态也显示从南向北的运动动向。同时，在片理化的碎屑岩和火山碎屑岩中，可以观察到可靠的显微运动学标志（图 5-15）。如长石、石英和绿泥石等矿物的颗粒发生绕曲排列形成 S-C 组构（图 5-15a）；绿泥石、云母类矿物围绕石英重结晶矿物集合体形成δ型组构（图 5-15b）；泥质岩石中发育的σ型和δ型不对称组构、拖曳褶皱（图 5-15c,d,e）以及黄铁矿石英压力影构造等（图 5-15f）。这些运动学标志统一指示从南向北的韧性剪切作用，与发育在这些岩石中从北向南的脆性逆冲变形完全不同。

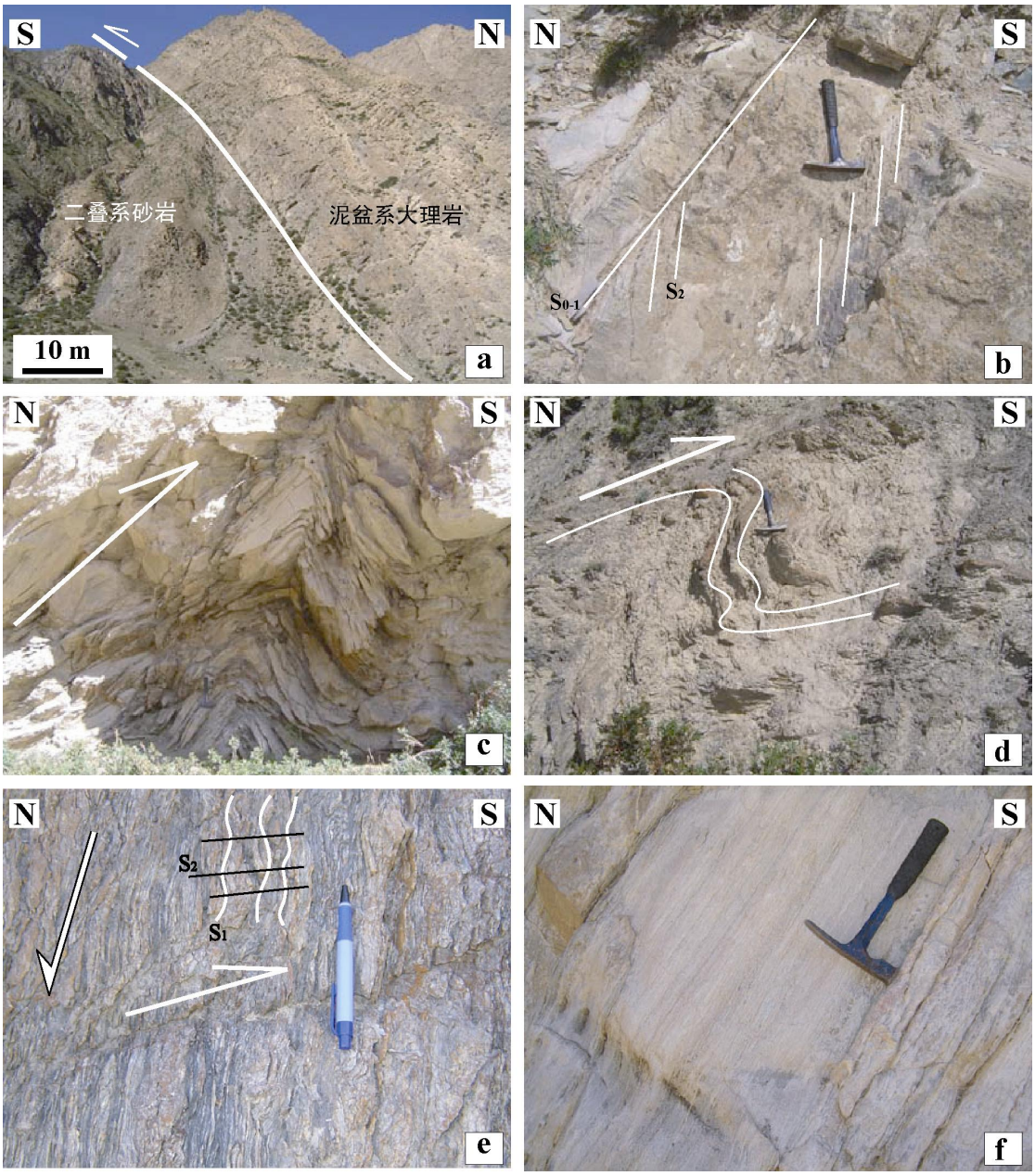

图 5-14 乌什县别迭勒剖面古生代地层变形特征

这些前石炭纪岩层的变形特征与黑英山蛇绿混杂岩北侧片理化碳酸盐岩中的变形非常相似，因此作者认为它们属于同一期变形作用。在别迭勒剖面中，未见蛇绿混杂岩单元。但据青海地调队杨延兴介绍，在别迭勒剖面的西侧约 5 km 处，出露有蛇绿岩岩块，并被下石炭统砂岩和灰岩不整合覆盖。因此，作者推断，别迭勒沟蛇绿混杂岩和石炭系地层的“缺失”，可能是由于新生代逆冲推覆作用，使它们被掩盖于前石炭纪地层的推覆体之下（图 5-16）。

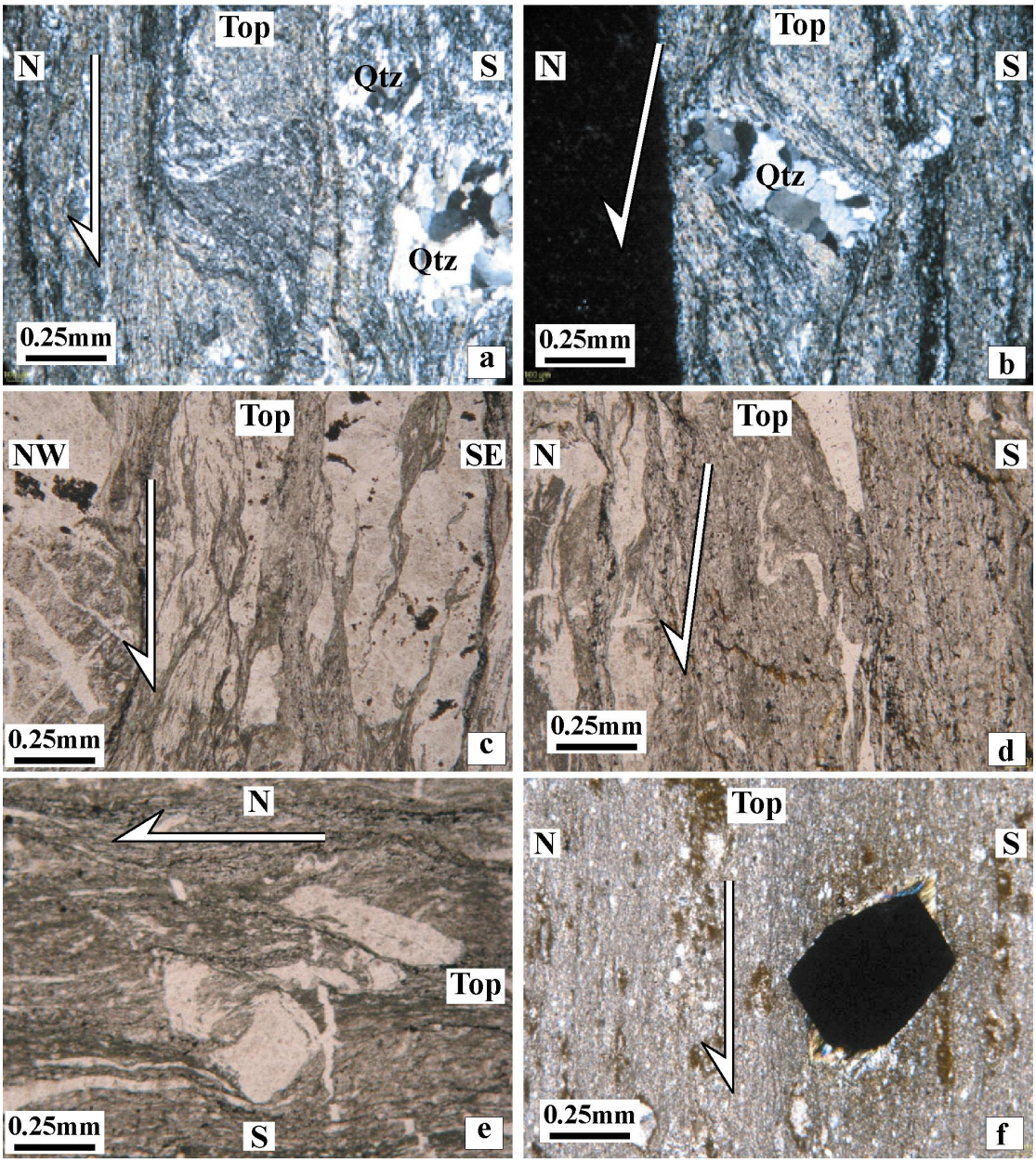

图 5-15 乌什县别迭勒剖面韧性变形岩石显微运动学特征

在乌什县南东方向，下石炭统泥岩、砂岩和浊流相砾岩不整合覆盖在寒武系-泥盆系之上，这些早-中古生代的地层均为碎屑岩，属于塔里木被动大陆边缘沉积。塔里木震旦纪和早、中元古代基底岩石出露在阿克苏地区（图 2-7；图 5-16）。前人的研究表明，震旦系-新近系岩石均被卷入到一系列从北向南的逆冲推覆体中（Allen et al., 1999；曲国胜等，2003），即柯坪塔格前陆推覆带（图 5-16）。现有的地震资料显示，沿托什干河发育一条活动断裂，即“南天山断裂”（Allen et al., 1999；Zhao et al., 2003），并将天山造山带与塔里木盆地及其北缘逆冲变形带分开（图 5-16）。

野外观察表明，塔里木北缘褶皱带泥盆系与别迭勒剖面泥盆系的岩相学和变形特征明显

不同，前者主要为红色砂岩和泥岩，没有发生明显的变形，而后者则为超糜棱岩化大理岩。鉴于南天山蛇绿混杂岩从南向北推覆于韧性变形的泥盆系碳酸盐岩之上，因此，南天山蛇绿混杂岩带为这两个沉积-构造单元的分界线，北部单元属于中天山地块，而南部单元属于塔里木板块。蛇绿混杂岩根部很可能位于南天山断裂带内，也就是说，南天山断裂为一条古生代构造缝合带，在新生代陆内变形过程中，再次活动。

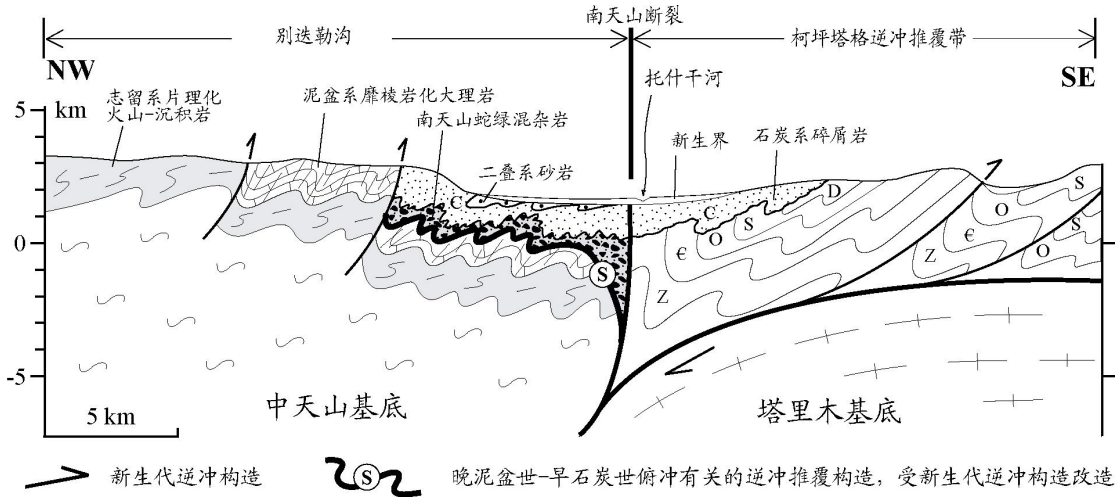

图 5-16 乌什别迭勒韧性变形带-柯坪塔格前陆推覆带地质剖面图

Z，震旦系；€，寒武系；O，奥陶系；S，志留系；D，泥盆系；C，石炭系

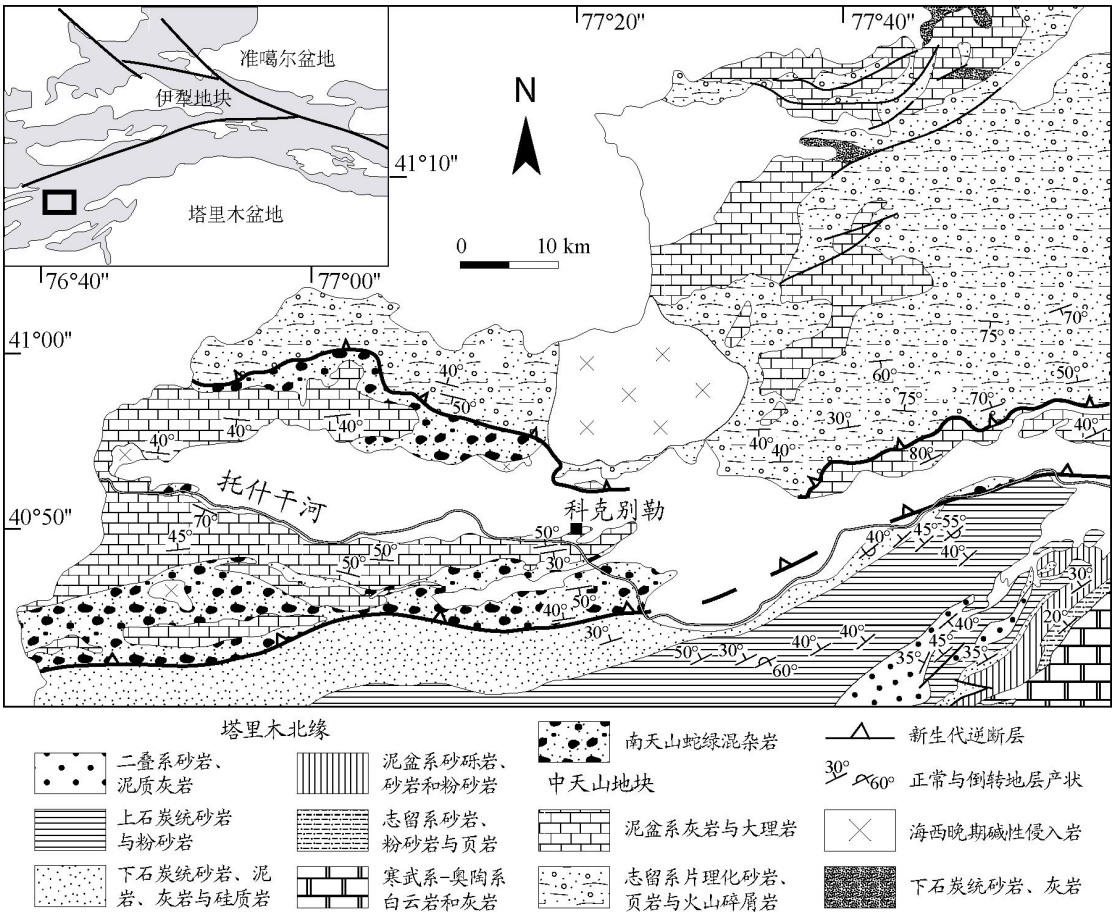

图 5-17 阿合奇科克别勒地区地质构造简图（据新疆地矿局（1961）改编）

2. 阿合奇科克别勒剖面

科克别勒剖面位于阿合奇县城南西方向 40 km 左右的托什干河畔（图 5-17），离乌什县约 150 km 左右。在该剖面北侧接近中哈边界的地区，变质基性岩、条带状硅质岩等蛇绿岩和灰岩呈数米到 1km 宽的块体产出于片理化灰绿色泥岩和硅质岩基质中（据新疆地矿局，1961）。在该蛇绿岩以北，志留系主要由强烈片理化砂岩、页岩和火山碎屑岩组成，泥盆系以大理岩与灰岩为主，下石炭统砂岩与灰岩不整合覆盖在志留系-泥盆系之上（图 5-17）。

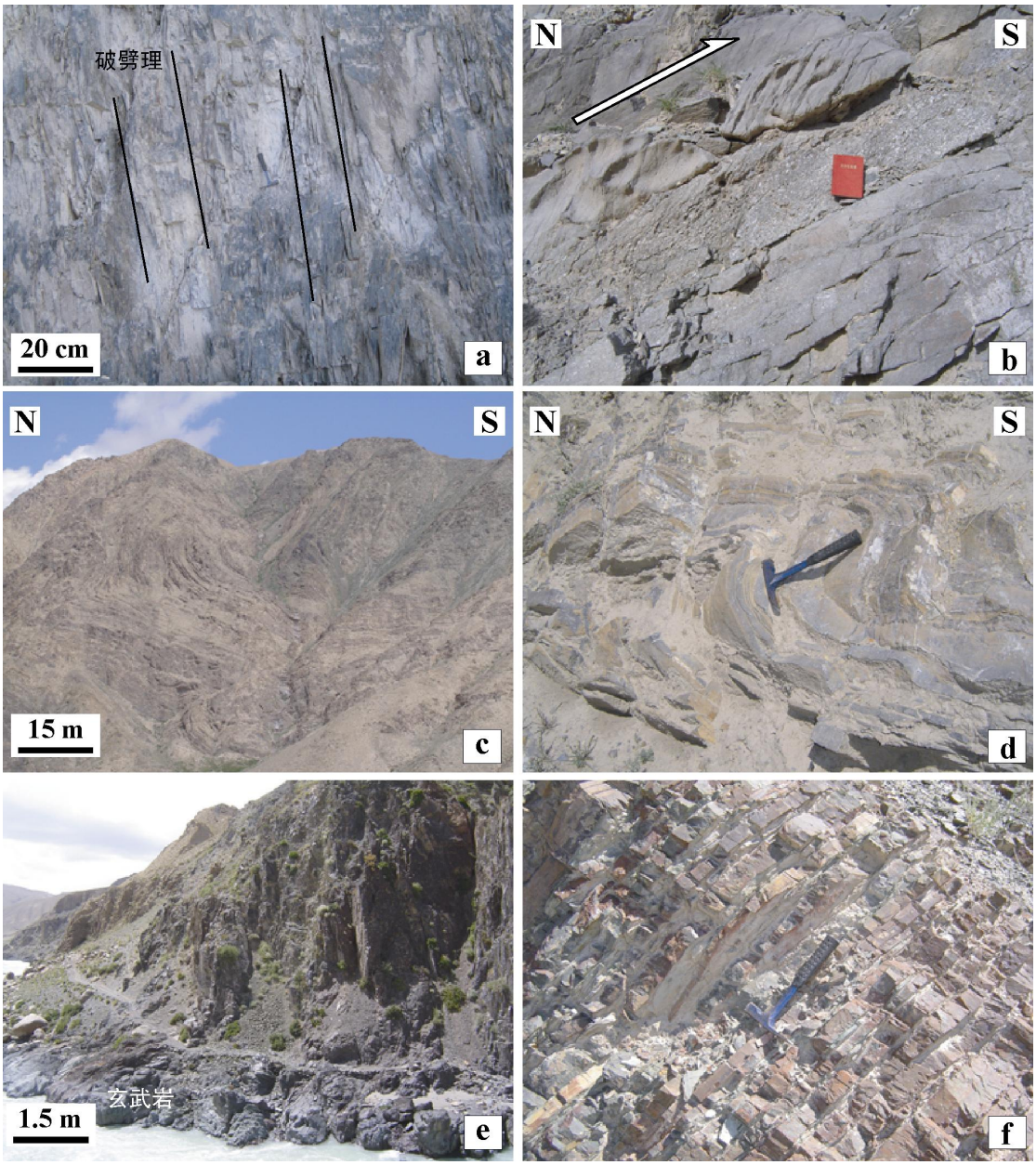

图 5-18 阿合奇剖面石炭系（a-b）和混杂岩带（c-f）变形特征

区域上，科克别勒南侧的地层单元被划归为乌帕塔尔坎群（S-D_2 *wu*），主要由巨厚的灰岩、复理石、硅质岩、凝灰岩和火山岩组成（新疆地矿局，1961）。但在沿托什干河 5 km 长的剖面上，仅观察到了一处基性火山岩的块体（图 5-18e），与硅质复理石呈不连续过度关系。硅质复理石主要为薄层状砂岩、灰岩（图 5-18f），且通常发生了褶皱变形（图 5-18c,d）。从褶皱形态分析可知，这些变形形成于南北向挤压作用，并指示从北向南的挤压应力方向，与别迭勒剖面泥盆系-志留系岩层中的脆性褶皱变形相吻合，因而属于新生代变形作用的产物。

强烈片理化泥岩的劈理总体走向为 N50°E，而与基性岩接触的复理石（图 5-18e,f）平层理均走向为 N70°E，这些面状要素整体上比较接近，并与黑英山蛇绿混杂岩基质的特征相

一致（图 5-9）。鉴于复理石、灰岩等的块体一般都非常大（几十米到 1km 宽），很容易被当成原地地层来处理。但不同岩块之间的接触关系很不规则，变形也不连续，因此它们属于混杂岩块。由于新生代构造变形改造强烈，因而很难识别出混杂岩带中早期的韧性变形要素。

Li YJ et al.（2002；2005）从该剖面硅质岩中发现了早石炭世-晚二叠世的放射虫化石。笔者对采自该剖面的两块灰绿色条带状硅质岩进行薄片鉴定，发现其中含有大量结构模糊的生物碎屑，疑似放射虫化石。经南京古生物所王玉净研究员分析处理后，这些化石难以辨别种属，故不能确定其时代，但认为是二叠纪放射虫的可能性不大。

在阿合奇混杂岩以南，上石炭统生物碎屑灰岩整合覆盖在下石炭统红色砂岩、粗粒砂岩和砾岩互层（图 5-18b）之上。这些岩石没有发生任何韧性变形和变质作用，但均受到了向南挤压推覆作用的影响，层内和层间破劈理十分发育（图 5-18a,b）。

第三节 干沟-库米什剖面构造变形特征

在天山造山带南部，蛇绿混杂岩带由阿合奇、黑英山一带向东经库勒湖、乌瓦门一直延伸到榆树沟、库米什地区（图 2-7）（张池等，1981；王作勋等，1990；肖序常等，1992；汤耀庆等，1995；刘本培等，1996；Gao et al., 1998；Chen et al., 1999；姜常义等，2001；李向明等，2002；Xiao et al., 2004）。天山主断裂以南的干沟-库米什地区（图 5-19），跨越了北天山、中天山和南天山以及它们之间的构造界线（Windley et al., 1990；Allen et al., 1992；Laurent-Charvet, 2001；Shu et al., 2002，2004；Xiao et al.,2004），是认识天山大地构造的一个关键剖面。

1. 干沟-米什沟蛇绿混杂岩带

干沟和米什沟剖面分别位于乌鲁木齐-库尔勒公路的东侧和西侧（图 5-19）。蛇绿岩主要由蛇纹岩、辉长岩、大理岩和硅质岩组成，并呈不规则块体产出于杂色的片理化基质中（Allen et al., 1992; Laurent-Charvet, 2001）。蛇绿岩块体和基质中均普遍发育有面理和线理构造，面理近垂直，而线理近水平，呈 SE-NW 向延伸。运动学分析表明，这些变形构造与右旋走滑作用，即天山主断裂带有关（图 5-19）（Shu et al., 1999；Laurent-Charvet, 2001，Laurent-Charvet et al., 2002，2003），该带向西与北天山断裂右旋走滑剪切带相连（图 2-7，4-1）。Ar/Ar 年代学表明，该期走滑事件发生在二叠纪（见第四章；Shu et al., 1999；Laurent-Charvet et al., 2002，2003）。

在米什沟南部，蛇绿混杂岩基质中发育剪切逆断层与破劈理构造，并指示从南向北的挤压运动动向。另外，野外地质观察表明，奥陶系火山-沉积岩序列从南向北逆冲推覆于米什沟蛇绿混杂岩之上（Laurent-Charvet, 2001）。同时，在乌-库公路上，志留系复理石发育有从南向北挤压的褶皱变形和水平剪切带（图 5-20b）（Laurent-Charvet, 2001）。由此可见，干沟-米什沟蛇绿混杂岩带虽然受到了二叠纪右旋走滑事件的改造，但仍然保留了早期与蛇绿混杂岩构造侵位有关的变形构造。一直以来，前人将干沟-米什沟蛇绿混杂岩作为北天山缝合带的一部分，向西经冰达坂延伸到巴音沟（Windley et al., 1990；Allen et al., 1992；Gao et al., 1995, 1998；Zhou et al., 2001）。然而，如第四章所述，巴音沟和干沟-米什沟蛇绿混杂岩带虽然具有相同的变形运动学特征，但属于两个不同时期的构造缝合带。

车自成等（1994）从蛇绿混杂岩带中得到辉长岩 Rb-Sr 全岩年龄为 468 Ma，而变形玄武岩的年龄为 422 Ma。同时，大量未变形的伟晶花岗岩侵入到奥陶系、志留系和蛇绿混杂岩中（图 5-19），虽然这些花岗岩的确切年龄目前尚不清楚，但新疆地矿局（1959）将其归为海西早期，即泥盆纪。花岗岩与奥陶-志留系均被石炭系不整合覆盖（图 5-19）。因此，该蛇绿混杂岩形成的年龄至少早于晚泥盆世-早石炭世。因而，干沟-米什沟蛇绿混杂岩虽然与北天山岛弧在空间上毗邻，但无论在运动学还是年代上，都没有直接的关系。鉴于：1）干

沟-米什沟蛇绿混杂岩与西天山科克苏地区高压变质带具有相似的运动学特征（本章第一节）；2）各自所代表的碰撞时代都早于 350 Ma；3）该带南侧的中天山地块发育奥陶纪-早志留世火山岩和火山碎屑岩，因此干沟-米什沟蛇绿混杂岩与科克苏高压变质岩很可能同属于一个缝合带，由天山洋俯冲作用形成。

青布拉克断裂一直被认为是“南天山缝合带”（Windley et al., 1990; Allen et al., 1992；Gao et al., 1998；Chen et al., 1999），但实际上该断裂为一个韧性走滑断层。如图 5-19 所示，沿青布拉克断裂出露有元古代花岗片麻岩，其中发育陡立南倾的面理构造，在 XZ 面上，粗粒状不对称长石眼球构造显示右旋剪切动向。该剪切带运动学特征与那拉提断裂一致，可能为那拉提断裂的东延。运动学和年代学研究表明，该断裂是一个发生在二叠纪的右旋韧性剪切带（Allen et al., 1992；Yin and Nie, 1996；Laurent-Charvet, 2001；Laurent-Charvet, 2002）。沿韧性走滑剪切带，二叠纪花岗岩（锆石 U-Pb 年龄 252±4Ma；见第七章）零星分布并侵入到元古代花岗片麻岩中（图 5-19）。

值得提出的是，有学者将天山主断裂和青布拉克断裂之间的区域划归为“伊犁-中天山地块”（肖序常等，1992；Gao et al., 1998）。然而，该区域古生代地层与伊犁地块相应地层（见第三章）具有十分明显的差别。本区内奥陶系岩石主要包括玄武岩、安山岩、英安岩、凝灰岩、火山碎屑岩和硬砂岩（新疆地矿局，1959；1993），而伊犁北部奥陶系为陆缘沉积岩；本区石炭系主要为砾岩、砂岩和浅水相灰岩沉积，不含任何火山碎屑沉积物和火山岩，石炭系不整合覆盖在奥陶系火山-沉积岩和志留系复理石之上（图 5-19）（新疆地矿局，1959；Laurent-Charvet, 2001）。另外，在巴音布鲁克北侧，石炭系灰岩和粗砂岩不整合覆盖在志留系含铜矿安山岩之上（新疆地矿局，1969；Wang ZL et al., 2004）。然而，在伊犁地块和北天山岛弧带，石炭系主要为火山岩-沉积岩的互层并伴生有大量侵入岩体（见第三、四章）。由此可见，伊犁和中天山在古生代期间处于完全不同的构造环境。本论文将天山主断裂和青布拉克断裂之间、从干沟南到巴音布鲁克北的区域作为中天山地块的一部分，认为其向西与哈尔克山、铁里买提一带（见本章第一节），同属一个构造单元。另外，沿青布拉克断裂分布的元古代片麻岩与出露在黑英山蛇绿混杂岩北侧的花岗片麻岩具有一致的岩相学特征，同时也与乌瓦门蛇绿岩以北巴伦台元古代片麻岩地区以及冰达坂南坡的元古代花岗片麻岩十分相似（图 2-7），应该同属于中天山地块的结晶基底。在青布拉克断裂以南乌拉斯台地区，糜棱岩化大理岩和云母片岩被海西早、中期花岗岩侵入（图 5-19，图 5-20a）（新疆地矿局，1959；1960），因此大理岩和片岩时代应为晚志留世或泥盆纪。这些片岩和大理岩的岩相学和构造变形特征与西天山库勒湖、黑英山和别跌勒一带志留-泥盆系韧性变形的火山碎屑岩和大理岩非常相似，因此，作者认为，库米什与青布拉克断裂之间的区域属于中天山南缘韧性变形带。

2. 库米什–榆树沟蛇绿混杂岩带

在库米什西南侧，蛇绿混杂岩出露 50 km 长，30 km 宽的范围内，分布于硫磺山、铜花山和榆树沟一带（图 5-19A）。在硫磺山、铜花山地区，大量不同规模的大理岩、放射虫硅质岩、蛇纹岩、玄武岩和辉长岩呈块状产出于强烈片理化的基质中，基质岩石包括泥岩、含海百合茎灰岩、变质砂岩和变形砾岩等（Laurent-Charvet，2001）。在大理岩块中，含有大量晚奥陶-晚志留世腕足类和珊瑚化石（新疆地矿局，1959），在硅质岩块体中含有早-中泥盆世的放射虫化石（Gao et al., 1998），基质中包含海百合茎灰岩，同时，石炭系碎屑岩不整合覆盖在蛇绿混杂岩之上（图 5-19），因此该蛇绿混杂岩最终形成的时代可能为早石炭世。在榆树沟地区，蛇绿岩包括蛇纹岩残块、强烈变形的堆积辉长岩、角闪岩和麻粒岩，基质由强烈剪切破碎的变质泥岩和变质砂岩组成。该蛇绿混杂岩也出露在库米什北西侧，紧临青布拉克断裂带的位置（图 5-19）。在库米什盆地边缘，一系列向南逆冲的断层将蛇绿混杂岩推

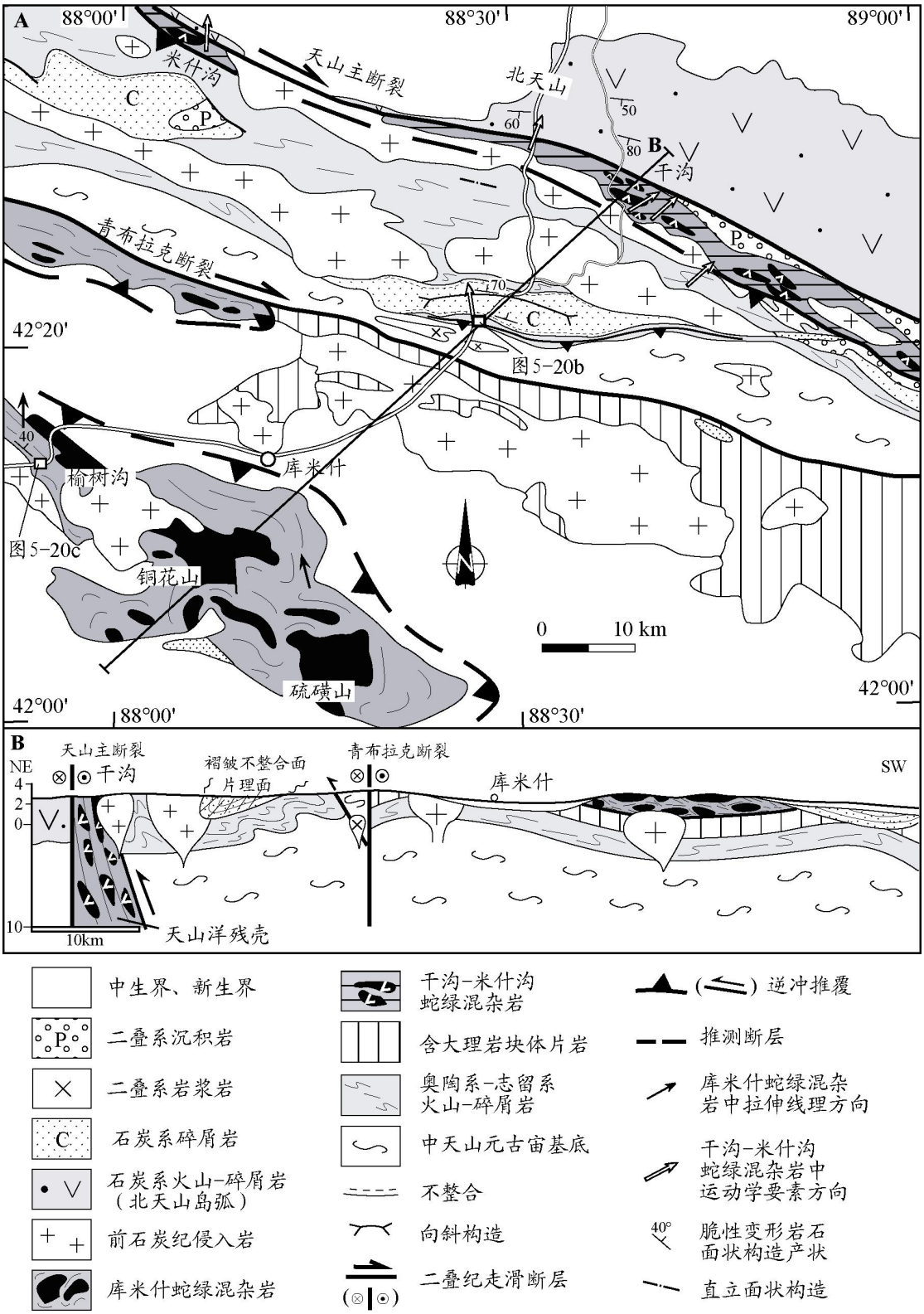

图 5-19 干沟-库米什剖面地质构造简图

（据新疆地矿局，1959；Allen et al., 1992；Laurent-Charvet, 2001；Shu et al., 2004）

覆在中、新生代沉积岩层之上。库米什-榆树沟蛇绿混杂岩曾经被解释为从青布拉克缝合带向南逆冲推覆而形成的构造推覆体（Allen et al., 1992）。但在蛇绿混杂岩中，韧性剪切作用在基质中形成了较平缓的面理构造和中等倾伏的线理构造，硅化的变质泥岩和砂岩发育有大量的不对称运动学组构，如 S 型石英脉（图 5-20c）、S-C 剪切带和压力影构造等

（Laurent-Charvet，2001），它们指示从南向北的运动动向，因而并不支持库米什-榆树沟蛇绿混杂岩从北向南的推覆运动。实际上，这一构造变形作用与黑英山蛇绿混杂岩的变形特征完全一致，蛇绿混杂岩从南向北推覆在中天山南缘志留系-泥盆系片岩和大理岩之上，使其发生韧性变形。因此，本文认为，库米什-榆树沟蛇绿混杂岩与西侧黑英山一带的蛇绿混杂岩一起，构成南天山蛇绿混杂岩带，该带还包括了阿合奇、库勒湖、乌瓦门一带的蛇绿混杂岩（图 2-7）。

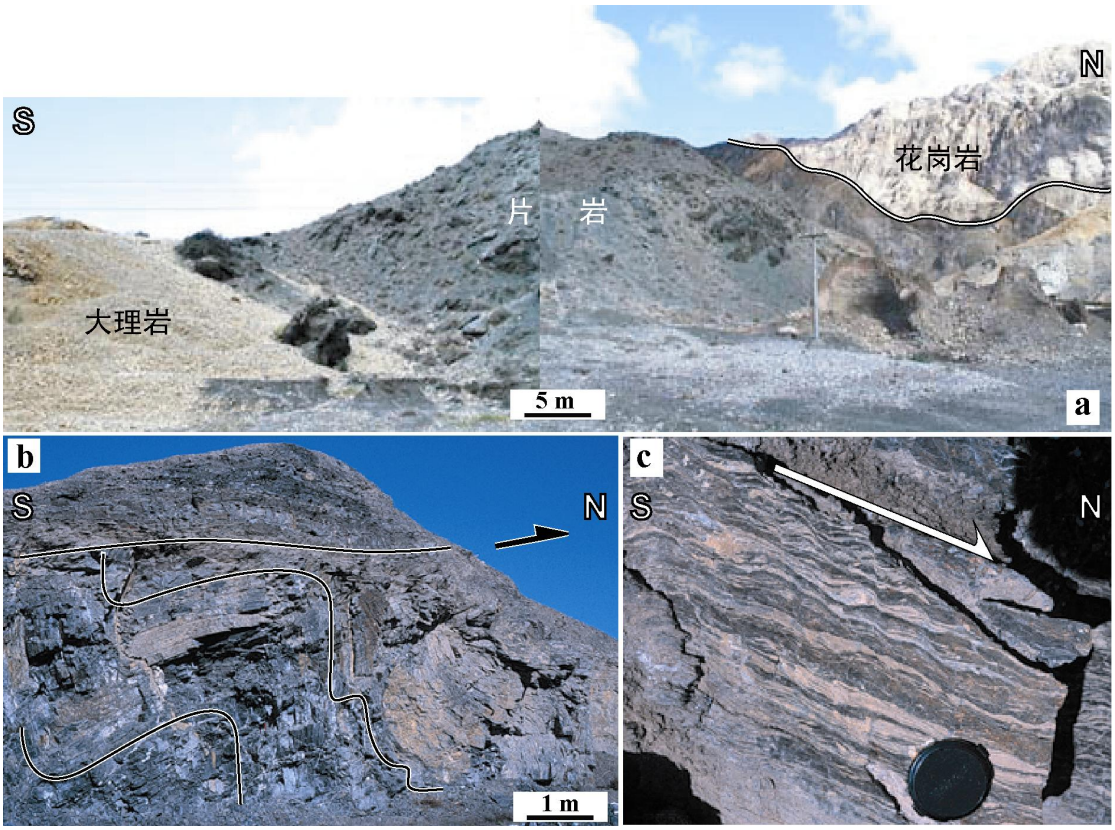

图 5-20 乌拉斯台混杂岩（a）与库米什（b）-榆树沟（c）剖面岩石变形特征

从南向北推覆的运动学特征表明，南天山蛇绿混杂岩带并不是源于天山洋缝合带的构造推覆体或飞来峰，而是代表一个洋盆向南的俯冲作用形成的缝合带。马瑞士等（1990）和吴文奎等（1992）从硫磺山辉石角闪岩和玄武岩中获得 Rb-Sr 全岩年龄分别为 452±19 Ma 和 340±4 Ma。张良臣等（1985）从铜花山辉长岩中获得角闪石 K-Ar 年龄为 420±14 Ma，而榆树沟堆积辉长岩的 K-Ar 年龄为 437 Ma。另外，周鼎武等（2004）从榆树沟麻粒岩中的锆石获得 390±11Ma~392±7Ma 的 U-Pb SHRIMP 年龄，而榆树沟辉长岩中锆石的 U-Pb 年龄为 378±6 Ma（姜常义等，2000）。这些年龄与黑英山蛇绿混杂岩中辉长岩锆石 U-Pb ICPMS 年龄（392±5Ma）基本一致（见本章第一节）。由此可以推断，南天山蛇绿混杂岩带所代表的洋盆形成于晚奥陶世（~450 Ma），中泥盆世（~390 Ma）开始俯冲关闭，最终在晚泥盆世-早石炭世缝合，形成蛇绿混杂岩。

第四节 小结

1．伊犁地块南缘边界是一个多期构造变形带。1）在科克苏河地区，伊犁晚泥盆世-石炭纪岛弧花岗质岩石发生了超糜棱岩化和面理化韧性变形，宏观和微观运动学标志指示右旋走滑剪切作用。该剪切带沿那拉提断裂向东延伸，经过拉尔墩达坂至青布拉克断裂带，前人对剪切变形岩石的热年代学研究表明，该剪切作用发生在二叠纪；2）走滑剪切带以南，伊

犁岛弧花岗质岩石、伊犁早古生代变质盖层、元古代片麻岩以及高压变质岩均发育有向南陡倾或近垂直的面理和近南北向线理等韧性变形构造。野外和显微运动学分析表明，这些岩石经历了从南向北的韧性剪切变形。高压变质岩从南向北的剪切推覆和伊犁基底南缘的韧性变形反映了天山洋向南的俯冲作用和洋盆关闭之后的陆陆碰撞作用。前人对蓝片岩相变质岩的同位素测年表明，高压变质作用的峰值年龄为 350Ma 或更早。因此，与天山洋俯冲碰撞有关的朝北剪切作用发生在晚泥盆世末-早石炭世初；3）在部分退变质绿片岩相变质岩中，变形运动学标志显示从北向南的剪切变形，鉴于这些退变质岩石还发育有垂向压缩变形构造，因此它们可能经历了一期南北向拉张环境下的变形作用，也就是说，从北向南的剪切作用可能代表高压变质岩隆升折返过程引起的韧性滑脱作用。退变质绿片岩 $^{40}Ar/^{39}Ar$ 坪年龄为 331~316Ma，为该期滑脱剪切变形的年龄。

2．在伊犁地区，岛弧岩浆作用持续到石炭纪末（301Ma），而科克苏地区蓝片岩相高压变质作用发生在 350Ma 以前，高压变质岩中的韧性剪切指示天山洋向南的俯冲碰撞作用。退变质蓝片岩相变质岩中白云母的 $^{40}Ar/^{39}Ar$ 坪年龄为 331~316Ma，而绿片岩相石英岩中白云母 $^{40}Ar/^{39}Ar$ 坪年龄为 323Ma，并发育有从北向南的滑脱剪切作用，表明高压变质岩于 331~316Ma 期间在拉张背景下折返并发生退变质作用。因此，伊犁岩浆岛弧与天山洋缝合带在时代和运动学上没有直接关系。

3．在干沟-米什沟一带，蛇绿混杂岩受到了天山主断裂的强烈改造，发育有明显的近垂直面理和水平线理构造，运动学标志指示右旋走滑剪切作用。但在蛇绿混杂岩带的局部，仍然保留了早期南北向挤压剪切的变形运动学标志，并指示从南向北的剪切推覆作用。该变形运动学特征与科克苏河地区高压变质岩中的剪切动向完全吻合。另外，干沟-米什沟蛇绿岩的年龄为奥陶纪-中志留世，与北天山巴音沟蛇绿岩年龄相差较大。蛇绿混杂岩与泥盆纪花岗质岩体呈侵入接触关系，二者均被石炭纪沉积岩所覆盖，由此推断干沟-米什沟蛇绿混杂岩构造侵位年龄的上限为晚泥盆世，与科克苏高压变质作用的时代（~350Ma）比较一致。因此，干沟-米什沟蛇绿混杂岩与北天山巴音沟蛇绿混杂岩不同，它不属于北天山缝合带，而可能与科克苏一带高压变质岩属于同一条缝合带，是天山洋向南俯冲、碰撞作用的产物。

4．在黑英山地区，蛇绿混杂岩中辉长岩锆石 U-Pb 年龄为 392Ma，与库米什-榆树沟地区蛇绿岩同位素年龄和硅质岩中放射虫时代一致。黑英山与库勒湖蛇绿混杂岩基质中放射虫硅质岩的时代为晚泥盆世-早石炭世，与库勒湖蛇绿混杂岩的片岩基质中黑云母 $^{40}Ar/^{39}Ar$ 年龄吻合。同时，该带蛇绿混杂岩普遍被石炭纪碎屑岩不整合覆盖。阿合奇-别迭勒-黑英山-榆树沟-库米什一带蛇绿混杂岩中变形运动学均显示从南向北的剪切推覆作用，与其北侧志留纪火山碎屑岩和泥盆纪大理岩的韧性变形运动学完全一致。因此，该蛇绿混杂岩带不是天山洋缝合带从北向南的构造推覆体，而是一个不同的构造缝合带。前人对该带蛇绿岩的地球化学研究表明，它们形成于类似于弧后盆地的有限扩张洋盆环境。

5．在科克苏高压变质带以南至黑英山蛇绿混杂岩以北地区，古生代地层包括奥陶纪-泥盆纪碳酸盐岩、陆源碎屑岩和火山碎屑岩。其中晚奥陶-中志留世火山碎屑岩也发育在巴音布鲁克和米什沟以南地区。在乌什别迭勒剖面、黑英山北部、巴伦台南部和乌拉斯台以北地区，该火山碎屑岩与泥盆纪大理岩发生了强烈韧性变形、局部超糜棱岩化作用。部分地区，如库勒湖以南，发育有泥盆纪半深海相条带状硅质岩，可能与南天山弧后盆地拉张作用有关。元古代片麻岩分布在黑英山以北、巴伦台和青布拉克断裂一带。石炭纪陆源碎屑岩中没有火山碎屑物质，且在巴音布鲁克、巴伦台和干沟一带不整合覆盖在早古生代地层和元古代基底片麻岩之上。因此，位于天山洋缝合带和南天山蛇绿混杂岩带之间的区域具有统一的元古代结晶基底，古生代以来处于相同的大地构造环境，经历了类似的构造变形，所以本文将该单元称为中天山地块。

6．在南天山蛇绿混杂岩带以南的阿合奇、乌什和黑英山地区，古生代地层以碎屑沉积

岩为主，以发育脆性褶皱变形为特征，并没有发生变质作用，因而与蛇绿混杂岩带以北同时代地层在岩相学和构造变形方面完全不同，属于塔里木北缘前陆变形带。由于新生代强烈的挤压、褶皱、断裂作用，天山南缘古生代地层往往高角度逆冲推覆在中、新生代塔里木盆地之上。

第六章　伊犁地块晚古生代地层古地磁研究

如上文所述，基于现有的地质证据，地质学家对天山古生代造山作用提出了不同的解释。虽然大部分学者认为，天山山脉由众多微陆块和火山岛弧经过多期俯冲-碰撞造山作用形成（Coleman, 1989; Windley et al., 1990; Allen et al., 1992; 肖序常等, 1992; 马瑞士等, 1993; Shi et al., 1994; Gao et al., 1998; Chen et al., 1999; Shu et al., 2000, 2002; Laurent-Charvet, 2001），但另有一些学者则把天山作为阿勒泰拼贴造山带的一部分，认为其造山过程主要为走滑-拼贴为主（Sengör et al., 1993; Sengör and Natal'in, 1996）。另外，最近有些研究者提出，伊犁地区石炭纪-二叠纪时为大陆裂谷，巴音沟蛇绿岩为“红海型”洋盆地质过程的记录（夏林圻等，2004，2005；徐学义等，2005a；2005b；2006a；2006b），因此在伊犁、北天山和准噶尔之间存在二叠纪以后的洋盆消减和板块会聚过程。同时，一些学者（Li YJ et al., 2002; 2005）还从南天山混杂岩带中发现了石炭纪-晚二叠世的放射虫化石，进而认为，南天山洋壳至少到晚二叠世还存在，也就是说，它的消减闭合作用发生在晚二叠世之后。这些最新发表的研究结果均不同于以往被广泛接受的认识，即天山古生代俯冲、碰撞造山作用在晚二叠世全部结束，二叠纪已进入后碰撞构造阶段，并以区域性陆相红层沉积作用、大型走滑-剪切带和广泛分布的双峰式火山-岩浆作用为特征。因此，高俊等（2006）坚持认为，天山属于一个晚古生代的造山带。本章尝试用古地磁学方法来检验以上不同的学术观点。

古地磁学以板块构造理论为基础，以板块刚体假设为前提，通过对已知年龄、未变形变质的岩石进行测量，获取其原生剩磁，计算岩石形成时所处的古纬度，从而可以得知岩石所在板块发生的古纬度变化。由岩石剩磁计算可得板块的古磁极方向，因此通过对比不同板块相同时代的古磁极方向，可以了解不同板块之间在特定的地质历史时期所发生的相对运动（包括纬度上的相对运动和相对旋转）（Tarling, 1971；Butler, 1998）。

在天山及其邻区，塔里木盆地古地磁学研究程度最高，积累了大量元古代至第四系的古地磁数据。相比而言，准噶尔盆地研究成果不多，仅有少数古生代古地磁数据发表，而且这些数据在时代上不够连续，空间上分布也不均匀。伊犁虽然被认为是一个具有前寒武纪结晶基底的微大陆地块，但迄今为止，在伊犁地区尚无任何古地磁学的研究成果。这一空白很大程度上影响了人们对该地区古生代板块构造与动力学演化过程的认识。类似地，“中天山”也是一个具有元古代变质基底的微陆块，它在天山造山过程中发挥了非常重要的作用，但由于该单元经历了复杂的构造演化，多期变形作用显著，因此在中天山地区至今也没有开展古地磁学研究。为了了解伊犁及其相邻陆块古生代期间的相对关系，本论文对伊犁及其邻区典型剖面古生代地层进行了古地磁学研究。

第一节 古地磁采样与测量

伊犁地区早古生代地层主要出露在伊犁盆地北缘的博罗科努山，如赛里木湖地区（图 2-7，图 3-1），寒武系-奥陶系主要由硅酸盐岩、碳酸盐岩和陆源碎屑岩组成，志留纪则主要为复理石沉积。由于这些地层出露于西天山北支的变形带，大多地层不适合于古地磁采样。在伊宁北部阿希剖面（图 3-1），奥陶系主要由奈楞格勒组黑色泥质灰岩和红色泥质岩组成，变形较弱，也未见火山岩和花岗岩的烘烤痕迹，因此在该地层中采集了 8 个点的古地磁样品（见表 6-1）。石炭纪沉积-火山岩序列在伊犁地区广泛分布（见第三章），本论文选择昭苏、新源和玉希剖面，采集了石炭系红色砂岩、安山凝灰质砂岩、流纹质砂岩、安山岩和玄武岩的古地磁样品（表 6-1）。另外，在博乐地区采集了石炭系阿恰勒河组和东图津组砂岩，在北天山后峡地区采集了石炭系砂岩和玄武岩，在中天山地块巴音布鲁克地区采集了下石炭统雅满苏组灰岩和上石炭统石英砂岩。二叠纪古地磁样品采自巩留地区原晚二叠统晓山萨依组红色砂岩。其他采样信息详见表 6-1。

表 6-1 伊犁及其邻区古地磁采样表

剖面	GPS 坐标	点号	岩　性	岩石年龄	地层名称	产状（走向/倾角）	n/N*
博乐	44.9°N, 81.3°E	501	浅黄色砂岩	C_2	东图津组	25°/50°	7/8
	44.9°N, 81.3°E	502	浅黄色砂岩	C_2	东图津组	25°/50°	8/8
	44.9°N, 81.3°E	503	浅黄色砂岩	C_2	东图津组	25°/45°	9/10
	44.9°N, 81.3°E	504	浅黄色砂岩	C_2	东图津组	45°/50°	7/8
	44.9°N, 81.3°E	505	浅黄色砂岩	C_2	东图津组	35°/65°	7/9
	44.8°N, 81.1°E	506	泥质砂岩	C_1	阿恰勒河组	50°/75°	7/11
	44.8°N, 81.1°E	507	泥质砂岩	C_1	阿恰勒河组	25°/75°	9/9
	44.8°N, 81.1°E	508	泥质砂岩	C_1	阿恰勒河组	345°/75°	8/8
	44.8°N, 81.1°E	509	浅黄色砂岩	C_1	阿恰勒河组	315°/75°	8/11
阿希	44.2°N, 81.5°E	510	灰色泥岩	O_2	奈楞格勒组	290°/40°	9/9
	44.2°N, 81.5°E	511	灰色泥岩	O_2	奈楞格勒组	260°/77°	10/10
	44.2°N, 81.5°E	512	灰色泥岩	O_2	奈楞格勒组	285°/78°	7/8
	44.2°N, 81.5°E	513	灰色泥岩	O_2	奈楞格勒组	80°/72°	7/8
	44.2°N, 81.5°E	514	灰色泥岩	O_2	奈楞格勒组	255°/80°	6/7
	44.2°N, 81.5°E	515	黑色灰岩	O_2	奈楞格勒组	320°/58°	7/7
	44.2°N, 81.5°E	516	黑色灰岩	O_2	奈楞格勒组	320°/58°	8/8
	44.2°N, 81.5°E	517	红色泥岩	O_2	奈楞格勒组	320°/45°	6/8
昭苏	43.5°N, 81.1°E	518	红色砂岩	C_2	伊什基里克组	270°/18°	6/8
	43.5°N, 81.1°E	519	红色砂岩	C_2	伊什基里克组	305°/22°	6/8
	43.4°N, 81.1°E	520	砂岩	C_2	伊什基里克组	270°/20°	6/10
	43.4°N, 81.1°E	521	砂岩	C_2	伊什基里克组	280°/15°	6/8
	43.4°N, 81.1°E	522	砂岩	C_1	伊什基里克组	250°/12°	6/9
	43.3°N, 81.0°E	523	红色安山质砂岩	C_1	阿克沙克组	110°/12°	6/8
	43.3°N, 81.0°E	524	红色砂岩	C_1	阿克沙克组	245°/25°	6/8
	43.3°N, 81.0°E	525	砂岩	C_1	阿克沙克组	255°/26°	6/9
	43.3°N, 81.6°E	526	黄色砂岩	C_1	阿克沙克组	230°/78°	7/10
巩留	43.4°N, 82.5°E	527	红色砂岩	P_2	晓山萨依组	93°/40°	6/8
	43.4°N, 82.5°E	528	红色砂岩	P_2	晓山萨依组	93°/45°	6/8
	43.4°N, 82.5°E	529	红色砂岩	P_2	晓山萨依组	95°/48°	6/7
	43.4°N, 82.5°E	530	红色砂岩	P_2	晓山萨依组	92°/49°	6/8
	43.4°N, 82.5°E	531	红色砂岩	P_2	晓山萨依组	100°/41°	6/9
新源	43.3°N, 83.3°E	532	凝灰质砂岩	C_1	阿吾拉勒组	287°/48°	9/9
	43.3°N, 83.3°E	533	泥质砂岩	C_1	阿吾拉勒组	285°/51°	8/8
	43.3°N, 83.3°E	534	灰色砂岩	C_1	阿吾拉勒组	292°/52°	8/9
	43.3°N, 83.3°E	535	凝灰质砂岩	C_1	阿吾拉勒组	268°/45°	8/8
	43.3°N, 83.3°E	536	凝灰质砂岩	C_1	阿吾拉勒组	272°/48°	9/9
	43.3°N, 83.3°E	537	玄武岩	C_1	阿吾拉勒组	240°/47°	8/9
	43.3°N, 83.3°E	538	玄武质凝灰岩	C_1	阿吾拉勒组	237°/49°	8/8
	43.3°N, 83.3°E	539	玄武岩	C_1	阿吾拉勒组	237°/49°	8/8
	43.3°N, 83.3°E	540	玄武岩	C_1	阿吾拉勒组	237°/49°	12/12
	43.4°N, 83.3°E	541	红色流纹质砂岩	C_1	阿吾拉勒组	38°/48°	6/7
	43.4°N, 83.3°E	542	红色流纹岩砂岩	C_1	阿吾拉勒组	29°/47°	6/7
巴音布鲁克	43.1°N, 84.8°E	543	黄色粗砂岩	C_2	-	192°/14°	6/8
	43.1°N, 84.8°E	544	黄色粗砂岩	C_2	-	192°/14°	6/10
	43.1°N, 84.8°E	545	黄色粗砂岩	C_2	-	290°/5°	6/9
	43.1°N, 84.8°E	546	黄色粗砂岩	C_2	-	290°/5°	6/9
	43.1°N, 84.8°E	547	肉红色灰岩	C_1	雅满苏组	59°/26°	7/8
	43.1°N, 84.8°E	548	肉红色灰岩	C_1	雅满苏组	58°/28°	10/10
玉希	43.4°N, 84.4°E	549	安山岩	C_2	图尔拱组	54°/15°	6/7
	43.4°N, 84.4°E	550	安山岩	C_2	图尔拱组	54°/15°	6/7
	43.4°N, 84.4°E	551	安山岩	C_2	图尔拱组	54°/15°	6/7
	43.4°N, 84.4°E	552	紫红色砂岩	C_2	图尔拱组	54°/15°	6/9
	43.4°N, 84.4°E	553	安山岩	C_2	图尔拱组	54°/15°	6/7
	43.4°N, 84.4°E	554	安山岩	C_2	图尔拱组	54°/15°	6/8
后峡	43.1°N, 87.1°E	555	安山质玄武岩	C_2?	天格尔组	327°/82°	7/8
	43.1°N, 87.1°E	556	安山质玄武岩	C_2?	天格尔组	327°/82°	6/10
	43.1°N, 87.1°E	557	安山质玄武岩	C_2?	天格尔组	327°/82°	6/6
	43.1°N, 87.1°E	558	红色砂岩	C_2?	天格尔组	327°/82°	7/8
	43.1°N, 87.1°E	559	红色砂岩	C_2?	天格尔组	327°/82°	6/6
	43.1°N, 87.1°E	560	玄武岩	C_2?	天格尔组	327°/82°	6/7
	43.1°N, 87.1°E	561	玄武岩	C_2?	天格尔组	327°/82°	6/8

* n, 测试样品数; N, 采集样品数

从以上 8 个剖面的 61 个采点中，共采集了 561 个岩芯。野外采样使用美国产手持式汽油钻机。根据地层厚度情况，从每个采点中钻取 6-12 个岩芯，每个岩芯均在原地采用普通

罗盘和太阳罗盘（在天气情况允许时）定向。太阳方位角与地理方位角之间的平均差值为4.0°±3.4°，该差值用来矫正那些仅用普通罗盘定向的样品。

在测量前，所有岩心均被切制成 1~2 个直径 2.5cm、高 2.2cm 的圆柱体。对岩芯的测量实验分为两部分：岩石磁学实验和剩磁清洗实验。以下方法和仪器用于岩石磁学实验：（1）居里温度点热磁学实验使用 AGICO KLY-3S 型磁化率仪及附带的 CS3 加热炉；（2）等温剩磁实验（IRM）使用 IM30+磁化仪；（3）岩石磁组构实验（AMS）使用 KLY3 型磁化率仪；（4）粘滞剩磁（磁滞回归曲线）实验使用 Gaussmeter Model 7303。其中居里温度点、IRM 和 AMS 实验在法国奥尔良地球科学研究所岩石磁学实验室进行，而粘滞剩磁实验在巴黎全球物理研究所（IPGP）St Maur 磁学研究中心进行。从每个采点选择 6 个或以上的岩芯进行热退磁和（或）交变（AF）退磁，自然剩磁（NRM）较弱的样品使用 IPGP 的 2G 横式三轴 AF 超导磁化率仪进行交变退磁并测量磁化强度，NRM 较强的样品通过热退磁，并由 JR-5A 自动调控磁化率仪或 2G 竖式四轴超导磁化率仪测量磁化强度。热退磁过程分为约 15 步，每步之间的间隔从 20°C 到 150°C 不等。交变退磁过程则分为 10~11 步，每步间隔为 1~20mT。

使用多种计算程序对测量数据进行分析，其中剩磁方向采用 Kirschvink（1980）的主分量分析程序；样品、采点、剖面和年龄尺度的平均剩磁方向由两个不同程序进行计算，包括 Cogné（2003）提供的古地磁分析软件中的 Fisher（1953）统计和基于 PC Windows 的 PMGSC（4.2 版）古地磁分析软件（R. Enkin，未发表）。

第二节 伊犁地块及邻区古地磁测量结果

从绝大多数热退磁和交变退磁曲线中，都可以分析出两个分量：（1）低温分量（LTC）一般从 20°C（室温，NRM）到 250°C，软磁分量（SAF）一般从 1mT 到 15mT，二者一般都不趋向于 Zijderveld（1967）正交坐标的原点；（2）高温分量（HTC）从 250°C 到 580°C 甚至 680°C，硬磁分量（HAF）则从 20mT 到 90 或 100mT，它们一般都趋向原点。低温、软磁分量的平均方向十分接近于现代地磁场（PEF），而从热退磁和交变退磁曲线中分离出的特征剩磁则原离 PEF。在绝大部分样品中剩磁载体主要为磁铁矿和赤铁矿（见下文详述），实验表明，热退磁更能有效的清洗剩磁，因而后者用于大多数样品的退磁方法。下面将分剖面介绍具体的测量结果。

1．测量结果

1.1 昭苏剖面

如表 6-1 所示，昭苏剖面古地磁样品主要为下石炭统阿克沙克组（C_1ak）砂岩、安山质砂岩和上石炭统伊什基里克组（C_2y）红色砂岩。采样剖面位于昭苏县以北 20km（见图 3-1 和图 3-3a）。

1.1.1 阿克沙克组（C_1ak）

从代表性样品的等温剩磁曲线（图 6-1c 中 523-198，526-220）可以看出，随瞬间磁场的升高，磁化率快速升高并在 200mT 时接近饱和，表明样品中剩磁载体主要为低矫顽力磁性矿物。居里温度曲线（图 6-2f，g）显示，砂岩和安山质砂岩的磁化率在加热到 580°C 左右快速下降，表明样品中含有低钛磁铁矿。从绝大多数样品（22/25）中可以分析出两个主要剩磁分量，其中低温（20~150°C）分量比较分散，体现了粘滞磁性特征。高温分量从 200-300°C 到 580°C（图 6-4a），表明样品中磁铁矿的存在。在产状校正前的退磁曲线正交矢量投影图（Zijderveld, 1967）中，采点 523 和 526 相对于采点 524 和 525 具有较低的磁倾角（<45°）（图 6-4b），而且采点 526 的磁偏角方向明显西偏，但在校正后的 Zijderveld 图中，所有 4 个采点的剩磁方向变得非常一致（图 6-4c）。这一现象可能由于采点分布于不对称褶

皱所致（见表 6-1 产状）。从这 4 个阿克沙克组的采点计算出平均特征剩磁方向为：Dg=207.3°, Ig =-57.8°, k=10.5, α_{95}g=29.8°（校正前）；Ds=180.2°, Is=-40.9°, k=46.9, α_{95}s=13.6°（校正后）（表 6-2）。Enkin（2003）DC 褶皱检验结果为正检验，最大精度参数 k=74.4% ± 49.7%。

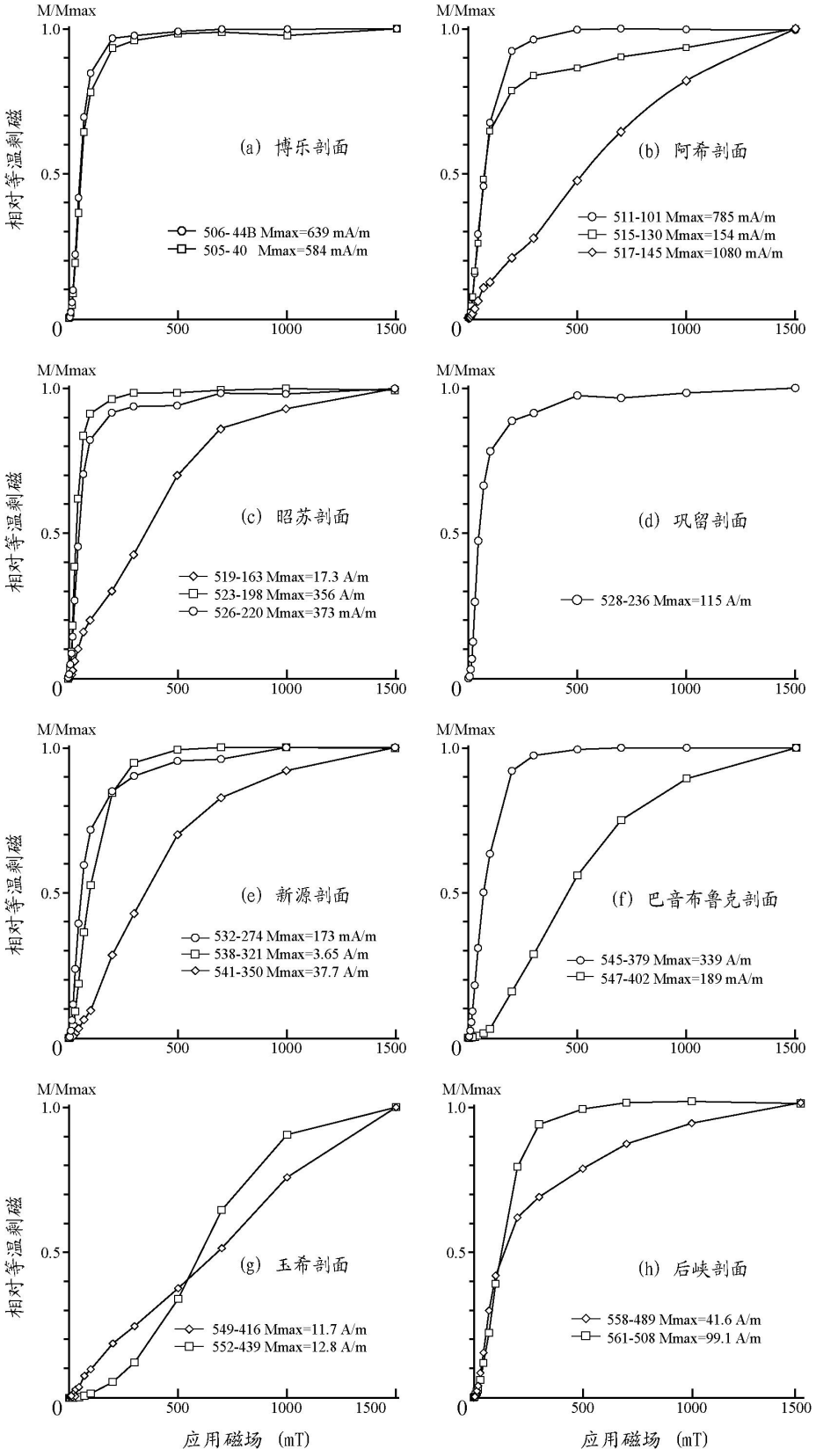

图 6-1 伊犁及邻区代表性岩石等温剩磁曲线

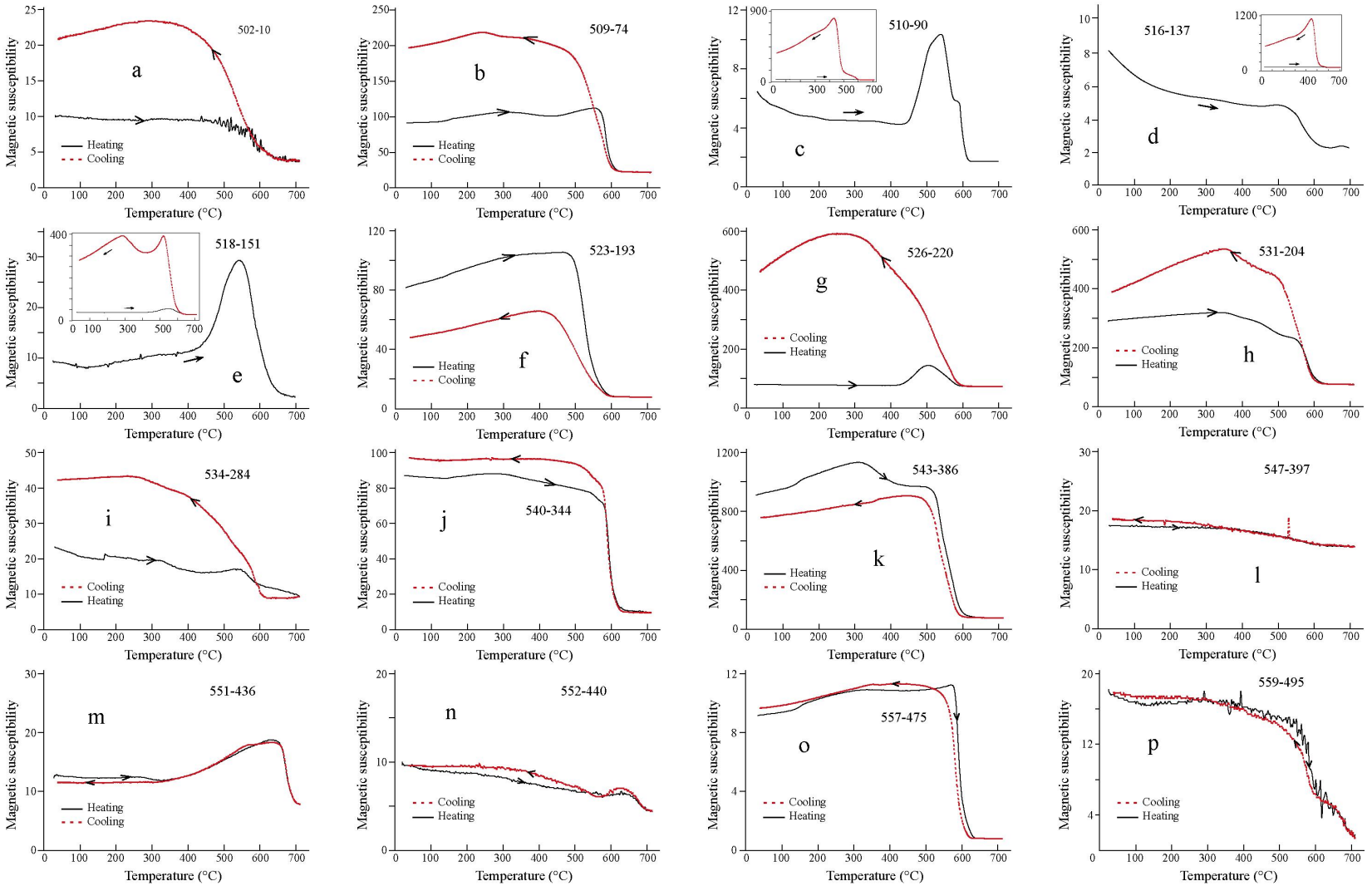

图 6-2 伊犁及邻区代表性岩石居里温度曲线

.1.2. 伊什基里克（C_2y）

采点 518-522 的样品采自昭苏剖面北段（图 3-3a），采样地层厚约 200m。从等温剩磁曲线（图 6-1c）中可以看出，瞬间磁场从 1mT 到 150mT 磁化率增加较快，达 20%饱和度，之后磁化率近线性增加，至 700mT 时达到 80%饱和度，然后缓慢增加直至 1500mT 达到饱和。这一过程表明，样品中低矫顽力和高矫顽力磁性矿物同时存在。图 6-3a 中磁滞回归曲线形态证实了软磁性和硬磁性矿物在样品中的共生关系。另外，退磁过程的相对磁化强度曲线（图 6-4f）显示了两个阻止温度点，磁化强度在 580°C 附近迅速下降至 50%，之后几乎保持稳定，而在 680°C 左右时再次快速下降并基本消减至零。居里温度曲线（图 6-2e）显示，样品在加热到 550~620°C 时磁化率显著并快速下降，但在冷却过程中，磁化率明显增加，表明在样品热退磁过程中磁性矿物会被氧化。然而，从退磁曲线（图 6-4d,e）可以看出，两个连续温度谱区间（250°C~580°C 和 580°C~660-680°C）的磁化方向均非常稳定而且相互一致，表明在样品热退磁过程中磁性矿物的氧化现象并没有扰动剩磁方向。由此可见，伊什基里克组红色砂岩中的磁性矿物主要为磁铁矿和赤铁矿，二者记录了同一个磁场方向，均表现为反极性。由此，计算出伊什基里克组中 5 个采点的平均特征剩磁方向为：Dg=151.6°, Ig=-61.2°, kg=48.0, α_{95}g=11.2°（校正前）；Ds=164.7°, Is=-47.4°, ks=50.7, α_{95}s=10.9°（校正后）（表 6-2）。虽然校正后的精度参数 k 稍微优于校正前，但由于样品均采自单斜地层（表 6-1 产状），因而无褶皱检验。

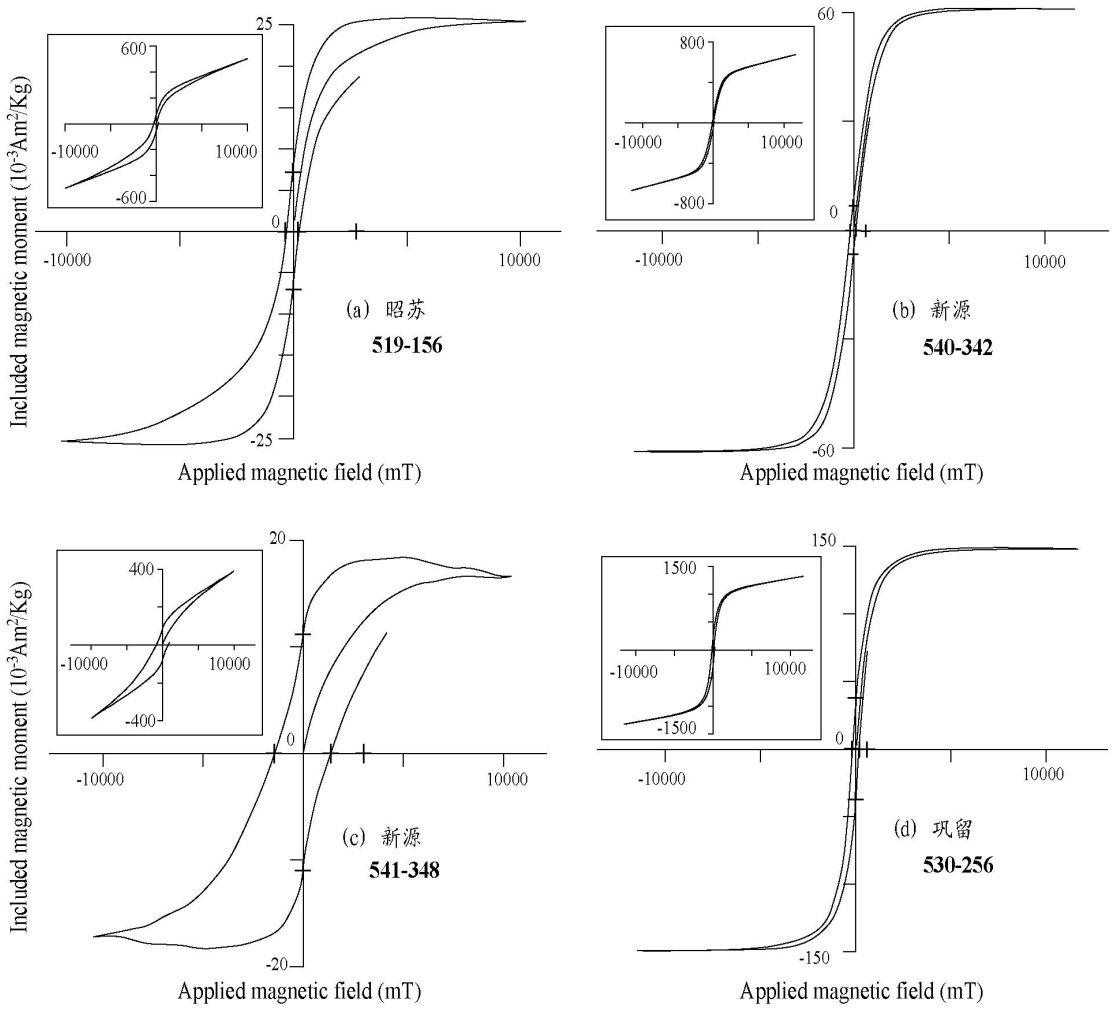

图 6-3 伊犁地区代表性岩石磁滞回归曲线

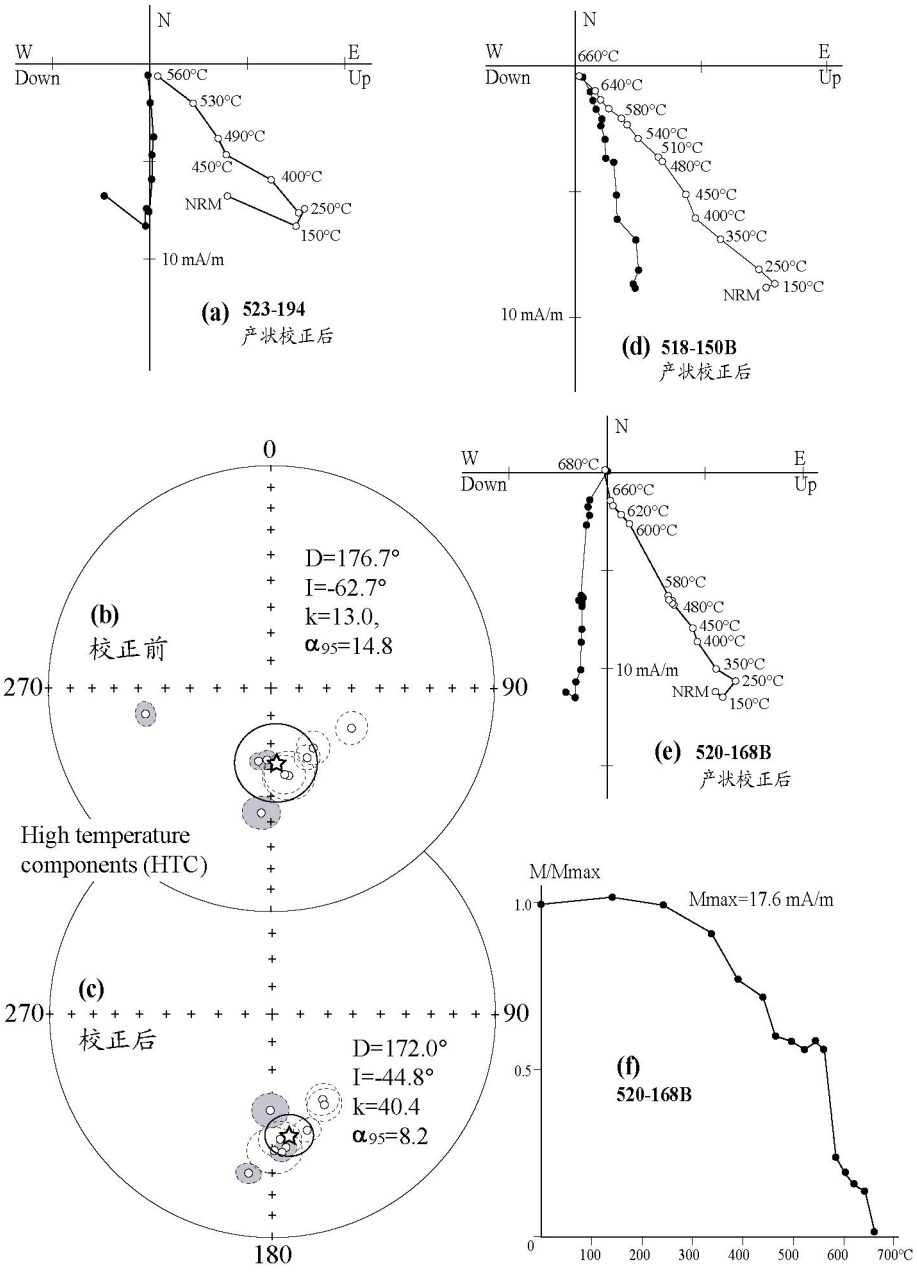

图 6-4 昭苏剖面石炭纪岩石代表性退磁曲线正交矢量投影图（a,d,e）、吴氏网投影图（b,c）与相对磁化强度曲线（f）（b 和 c 中五角星代表全部采点的平均特征剩磁方向；阴影表示的置信椭圆代表阿克沙克组的点平均剩磁方向，其余代表伊什基里克组的点平均剩磁方向）

1.2. 新源剖面

新源剖面古地磁样品主要包括下石炭统阿吾拉勒组（C_1aw）凝灰质砂岩、凝灰岩、玄武岩和流纹质砂岩（图 3-3c）。凝灰质和玄武质岩石的等温剩磁强度在瞬间磁场为 200mT 时即达到饱和（图 6-1e），而磁化率在居里温度点 580°C 左右明显下降（图 6-2i,j），另外玄武岩具有典型的窄长型磁滞回归曲线（图 6-3b）。这些现象表明，凝灰质和玄武质岩石中剩磁载体主要为低矫顽力磁性矿物(低钛磁铁矿)。在个别凝灰质岩石中，磁化率在 160°C 和 350°C 左右也出现显著的下降（图 6-2i），表明样品中也存在其他低矫顽力磁性矿物（如磁黄铁矿、磁赤铁矿等）。

流纹质砂岩（样品 541-350）的等温剩磁曲线（图 6-1e）则表现为近线性上升趋势，瞬间磁场为 700mT 时相对剩磁强度达 80%的饱和度，之后缓慢增加直至 1500mT 时达饱和。

另外，流纹质砂岩还具有典型宽腰型磁滞回归曲线（图 6-3c）。因此，在流纹质砂岩中，低矫顽力和高矫顽力磁性矿物同时存在。

表 6-2 伊犁地区奥陶系、石炭系与二叠系岩石特征剩磁方向

剖面	采点	n/N	极性	年龄	Dg	Ig	Ds	Is	k	α_{95}
昭苏	523	6/6	R	$C_2(C_1)^{\#}$	185.1	-43.5	181.1	-55.0	140.7	6.5
	524	6/6	R	$C_2(C_1)$	190.4	-63.0	174.0	-40.3	354.9	3.2
	525	6/6	R	$C_2(C_1)$	184.0	-63.7	176.1	-38.4	324.7	3.7
	526	6/6	R	$C_2(C_1)$	258.6	-41.8	188.6	-29.2	220.0	4.1
	Mean	**4**	**R**	**$C_2(C_1)$**	**207.3**	**-57.8**			**10.5**	**29.8**
							180.2	**-40.9**	**46.9**	**13.6**
	518	6/6	R	C_2	153.1	-61.8	163.1	-45.3	197.6	4.8
	519	6/6	R	C_2	116.3	-57.5	149.0	-54.0	66.7	6.0
	520	6/6	R	C_2	169.1	-57.2	179.0	-39.1	43.1	9.3
	521	6/6	R	C_2	171.6	-57.9	176.4	-43.4	84.4	7.3
	522	6/6	R	C_2	145.7	-63.5	149.7	-51.8	80.4	6.2
	Mean	**5**	**R**	**C_2**	**151.6**	**-61.2**			**48.0**	**11.2**
							164.7	**-47.4**	**50.7**	**10.9**
	Mean	**9**	**R**	**C_2**	**176.7**	**-62.7**			**13.0**	**14.7**
							172.0	**-44.8**	**40.4**	**8.2**
新源	532	7/7	N	? (C_1)	93.4	80.7	28.7	39.2	5.8	27.4
	533	4/7	N	? (C_1)	330.6	70.2	360	23.8	27.2	18.0
	534	4/8	N	? (C_1)	323.6	75.9	8.2	29.8	13.9	25.5
	535	11/11	N	? (C_1)	331.3	61.5	344.9	18.6	3.8	26.9
	536	10/10	N	? (C_1)	14.0	59.5	8.2	12.0	5.8	21.9
	537	7/8	R	$C_2(C_1)$	181.5	-24.0	179.9	16.9	6.1	21.2
	538	8/8	R	$C_2(C_1)$	167.9	-27.4	166.6	18.9	35.9	7.7
	539	8/8	R	$C_2(C_1)$	156.2	-30.5	155.4	18.0	11.2	14.3
	540	8/8	R	$C_2(C_1)$	160.5	-36.6	216.7	-64.4	35.0	7.8
	541	8/8	R	$C_2(C_1)$	149.0	-5.2	160.8	-48.7	289.7	3.9
	542	8/8	R	$C_2(C_1)$	145.5	-9.5	161.5	-49.2	187.6	4.9
	Mean*	**6**	**R**	**$C_2(C_1)$**			**165.3**	**-36.4**	**37.7**	**11.0**
	Mean**	**15**	**R**	**C_2**			**169.1**	**-41.5**	**36.6**	**6.4**
巩留	527	6/6	R	P_2	186.5	-17.7	189.5	-59.3	11.0	14.1
	528	6/6	R	P_2	194.9	-6.2	201.6	-49.8	8.7	14.9
	529	6/6	R	P_2	187.5	-14.6	190.3	-62.5	38.7	10.9
	530	6/6	R	P_2	187.7	-25.6	200.9	-73.9	74.3	7.8
	531	6/6	R	P_2	189.4	-16.6	189.4	-57.6	123.4	5.8
	Mean	**5**	**R**	**P_2**	**189.3**	**-16.2**			**111.7**	**7.3**
							194.1	**-60.7**	**76.1**	**8.8**
玉希	549	6/6	R	C_2	214.4	-35.7	225.7	-39.3	380.6	3.4
	550	6/6	R	C_2	212.0	-35.3	223.1	-39.6	411.8	3.3
	551	6/6	R	C_2	213.0	-37.5	225.1	-41.4	64.7	8.4
	552	6/6	R	C_2	207.3	-39.1	220.0	-44.4	60.0	8.7
	553	6/6	R	C_2	216.9	-32.6	226.9	-35.7	179.2	5.0
	554	6/6	R	C_2	204.9	-38.0	217.0	-44.0	124.9	4.1
	Mean	6	R		211.5	-36.4			354.3	3.6
							223.1	-40.8	350.1	3.6
阿希	Mean	28/62#	R	O_2	265.0	-61.2			4.3	15.0
	(510-517)						230.4	-28.5	7.9	10.4

#,括弧中时代代表岩石年龄；

*，由 4 个采点（537-540）校正前方向和 2 个采点（541-542）校正后方向计算所得的平均剩磁方向；

**，由昭苏和新源石炭纪样品的特征剩磁方向计算所得的 C_2 剩磁方向。

Dg，Ig 分别为校正前磁偏角和磁倾角；Ds，Is 分别为校正后磁偏角和磁倾角；k 为最佳估计精度参数；α_{95} 为 95%置信区间半径；N 为退磁样品数；n 为用来计算平均剩磁方向的样品数。

该剖面前 5 个采点（532-536）中凝灰质砂岩的自然剩磁强度非常弱，通常小于 1 mA/m。退磁过程表明，大部分样品的剩磁在 350°C 时即可清洗干净（图 6-5a, b），代表粘滞剩磁分量，与现代地磁场十分接近（图 6-5a）。去除粘滞分量后，绝大部分样品由于剩磁强度太弱，因而剩磁方向相当不稳定，只有个别样品具有较稳定的剩磁方向，但仍与现代地磁场相似（图 6-5b）。各采点的平均剩磁方向的α_{95}值很高（18~27）、而 k 值很低（表 6-2），因而，这些方向可信度较低，不能用作下一步剩磁方向分析。

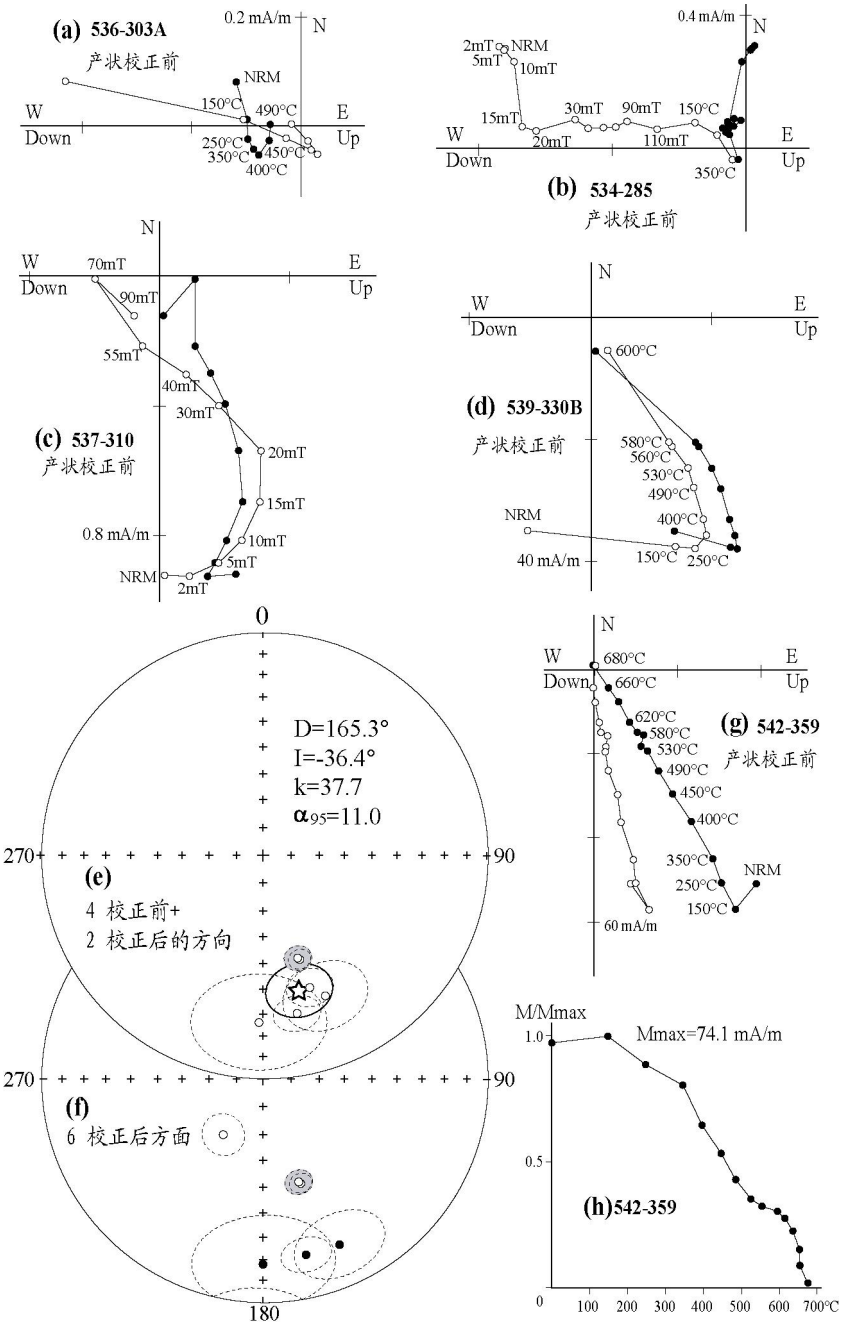

图 6-5 新源剖面岩石代表性退磁曲线正交矢量投影图（a-d,g）、吴氏网投影图（e,f）和相对磁化强度曲线（h）（e 和 f 中五角星代表平均特征剩磁方向；阴影表示的置信椭圆代表流纹砂岩的点平均剩磁方向，其余置信椭圆代表玄武岩的点平均剩磁方向；置信椭圆中心的空心点代表反极性，实心点代表正极性）

玄武岩样品（采点 537-540）的自然剩磁强度从几 mA/m 到几十 mA/m 不等，具有相对稳定且比较一致的磁性特征。样品剩磁在 90~100mT 或 580°C 时基本清除（图 6-5c, d），

表明玄武岩中主要磁性矿物为低钛磁铁矿。从绝大多数测试样品中，由热退磁和交变退磁分别分离出高温分量（250°C~600°C）和硬磁分量（20~90mT），这些分量在产状校正前显得比在产状校正后更集中（图 6-5e, f）。在野外，玄武岩产出于火山碎屑岩中，其产状受上覆和下伏沉积岩产状控制（表 6-1；图 3-3c），但这些沉积岩的产状在区域上基本一致，因而没有严格的褶皱检验。然而，产状校正前后的精度参数比值 k_g/k_s=16.67，表明产状校正前的剩磁方向具有更高的可信度，并可能代表玄武岩的特征剩磁方向（见下文讨论）。

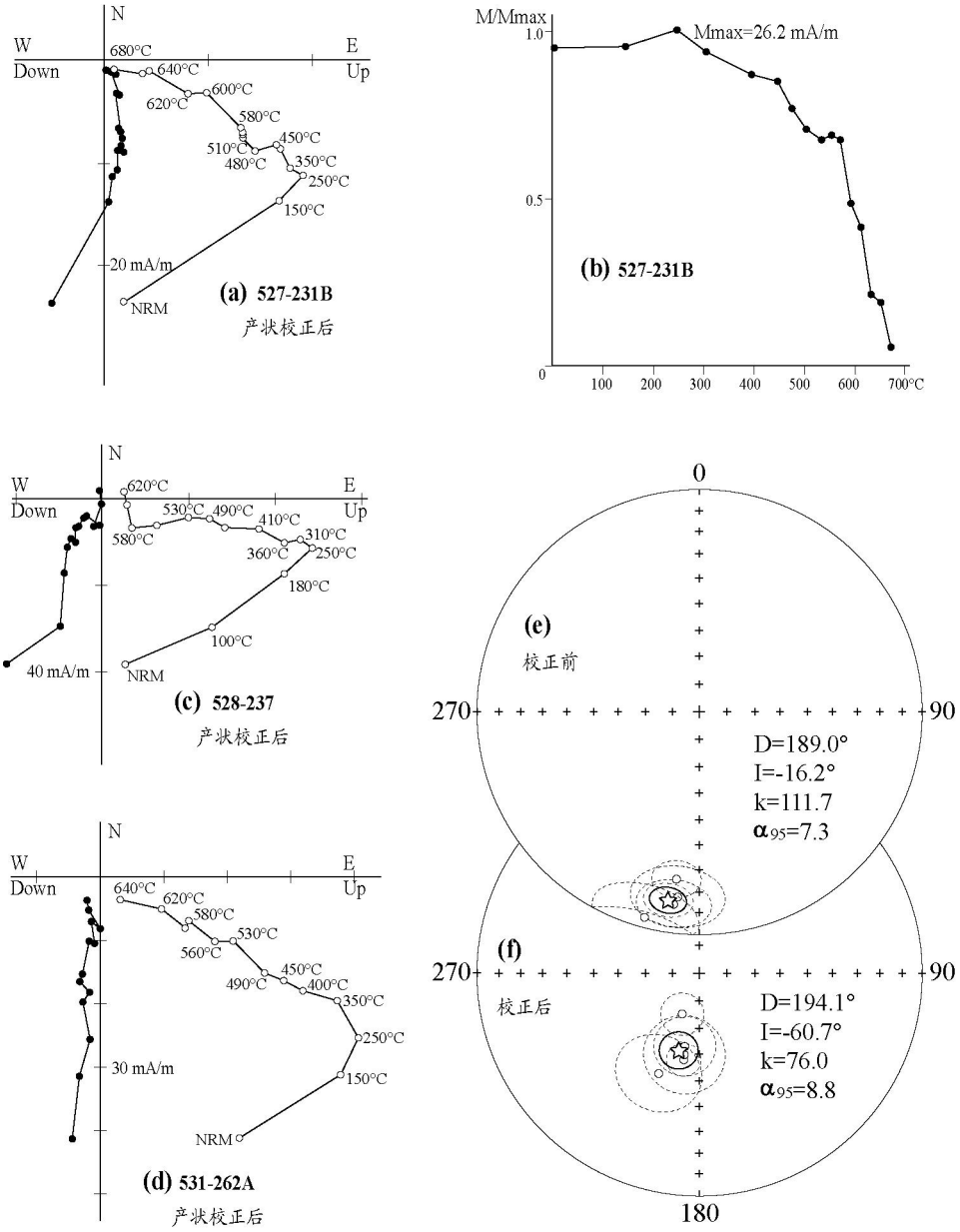

图 6-6 巩留剖面岩石代表性退磁曲线正交矢量投影图（a,c,d）、吴氏网投影图（e,f）和相对磁化强度曲线（b）（e 和 f 中五角星代表平均特征剩磁方向）

流纹质砂岩样品（采点 541-542）的热退磁曲线（图 6-5g）和相对磁化强度曲线（图 6-5h）显示，岩石磁化率在 580°C 和 680°C 时均出现快速减弱的现象，而且从两个连续温度谱区间（150°C~580°C 和 600°C~680°C）分离出的剩磁分量十分一致，表明样品中两种主要剩磁载体——磁铁矿和赤铁矿记录了相同的剩磁方向。由于两个采点的地层产状相同，因而没有褶皱检验。但是，产状校正后的剩磁方向比校正前的方向更接近于玄武岩的特征剩磁方向（产状校正前的方向）。于是，由校正后的 2 个流纹质砂岩点平均剩磁方向与校正前的 4 个玄武

岩点平均剩磁方向计算得出，新源剖面下石炭统岩石的平均剩磁方向为 D=165.3°，I=-36.4°，k=37.7，α_{95}=11.0（详见下文讨论）。

1.3. 巩留剖面

在巩留县东南，沿特克斯河向恰西方向去的公路上发育有一个长约 10km，地层厚度约 2km 的二叠系红层剖面。区域上，该红色属于原晚二叠统晓山萨依组（P_2x）（新疆地矿局，1979；1993），岩性主要为红色砂岩、粉砂岩、砂砾岩等。地层时代由丰富的植物化石所确定。在晓山萨依组的底部，红色砾岩中含有大量滚圆砾石，砾石大小 1~100cm，并与下层位的早二叠世碱性火山岩呈不整合接触关系。穿越地层走向采集古地磁样品，采样剖面长约 300m，地层厚度逾 100m。图 6-1d 显示，红色砂岩等温剩磁在瞬间磁场为 200mT 时达到 90%饱和度，并在 500mT 即达饱和。居里温度曲线（图 6-2h）也显示磁化率在 580°C 时显著快速下降。同时，这些样品还具有典型的窄长型磁滞回归曲线（图 6-3d）。这些现象共同表明，磁铁矿是红色砂岩中主要的剩磁载体。另外，等温剩磁在 200-500mT 之间的磁滞现象表明，样品中还存在少量赤铁矿。居里温度曲线也显示，在约 300°C 和 400°C 时，磁化率也出现了一定程度的下降，表明样品中含有少量的低矫顽力磁性矿物（如磁黄铁矿、磁赤铁矿等）。此外，在热磁实验的冷却阶段，样品磁化率明显升高（图 6-2h），表明加热过程中磁性矿物发生氧化作用。但磁性矿物的氧化转换似乎并没有明显地干扰到退磁过程，因为热退磁曲线在 580°C 处没有发生重要的转折（图 6-6a, c, d），磁铁矿和赤铁矿所记录的剩磁方向非常一致。从所有的测试样品都可以分离出两个剩磁分量，其中由高温分量计算出 5 个采点的平均剩磁方向为 Dg=189.3°, Ig=-16.2°, kg=111.7, α_{95}g=7.3°（校正前）；Ds=194.1°, Is=-60.7°, ks=76.1, α_{95}s=8.8°（校正后）（表 6-2）。由于采样地层为单斜构造，且产状非常一致（表 6-1），故没有褶皱检验。

1.4. 玉希剖面

玉希剖面位于那拉提以东从零公里向玉希达坂的 207 国道上（图 3-2c），采样剖面厚度约 15m，所采样品为上石炭统图尔拱组（C_2t）紫红色安山岩与杂色砂岩（表 6-1），砂岩的结构、构造显示其形成环境可能为蒸发相内陆湖泊。近线性等温剩磁曲线（图 6-1g）体现了典型的高矫顽力磁性矿物的特征。居里温度曲线（图 6-2m, n）显示，磁化率在 680°C 明显下降，表明安山岩和砂岩中磁性矿物主要为赤铁矿。所有样品都具有高温特征剩磁分量，且非常稳定，分量方向也非常一致。全部 6 个采点的平均剩磁方向为：Dg=211.5°, Ig=-36.4°, kg=354.3, α_{95}g=3.6°（校正前）；Ds=223.1°, Is=-40.8°, ks=350.1, α_{95}s=3.6°（校正后）（表 6-2）。安山岩的产状受砂岩产状约束，而砂岩产状稳定且非常平缓（15°，见表 6-1），因此精度参数和α_{95}在产状校正前后没有明显的变化，故没有褶皱检验。

1.5. 阿希剖面

为了获取石炭纪以前的古地磁数据，作者还在伊宁县以北 30km 处，沿阿希金矿公路（见图 3-2a）采集了中奥陶统奈楞格勒达坂组泥质灰岩、砂质泥岩等样品。不同岩性的等温剩磁实验显示三种类型的曲线（图 6-1b）：1）灰色泥岩的相对等温剩磁强度在 200 mT 时即达到饱和，表明样品中剩磁载体为低矫顽力磁性矿物（低钛磁铁矿）；2）黑色泥质灰岩的相对剩磁强度在低瞬间磁场中迅速增加，200mT 时达到 80%的饱和度，之后继续缓慢增加，至 1500mT 时达最大磁化强度，表明样品中低矫顽力和高矫顽力磁性矿物同时存在；3）红色砂质泥岩的相对剩磁强度线性变化，在瞬间磁场为 100mT 达最大磁化强度，体现了高矫顽力磁性矿物的特征。热磁学实验表明，灰色泥岩和泥质灰岩的磁化率在 580°C 时快速下降（图 6-2c, d），表明岩石中主要的磁性矿物为低钛磁铁矿，而且样品在加热过程中，磁性矿物普遍被氧化。各类岩性的自然剩磁强度均非常低，一般为 0.096~6.98mA/m，大部分样品为 0.25 mA/m 左右。超导磁力仪交变退磁和热退磁过程显示，绝大部分样品仅表现出粘滞剩磁，很难分析出稳定的特征剩磁分量。从所有 8 个采点的 62 个样品中，只有 28 个样品可以分析出

硬磁分量或高（中）温分量，从而求得所有样品的平均剩磁方向为：Dg=265.0°, Ig=-61.2°, kg=4.3, α_{95}g=15.0（校正前）；Ds=230.4°, Is=-28.5°, ks=7.9, α_{95}s=10.4（校正后）（表 6-2）。

表 6-3 伊犁邻区石炭系岩石古地磁分析结果

剖面	采点	n/N*	极性	年龄	Dg	Ig	Ds	Is	k	α_{95}
博乐	501	7/7	R	C_2	198.1	-55.2	244.4	-41.8	448.6	2.9
	502	6/7	R	C_2	196.6	-54.2	242.6	-42.0	81.9	7.4
	503	8/8	R	C_2	198.3	-50.7	242.6	-36.3	144.2	4.6
	504	5/6	R	C_2	158.4	-83.4	310.1	-45.9	38.3	12.5
	Mean	4	R	C_2	195.5	-61.1			25.9	18.4
							257.2	-45.0	11.6	28.2
	505	5/6	R	C_1	237.4	-56.1	276.6	-9.9	31.7	13.8
	506	8/8	R	C_1	189.8	-50.8	281.8	-35.9	57.7	7.4
	507	7/8	R	C_1	176.1	-70.4	275.2	-23.3	141.0	5.1
	508	8/8	R	C_1	96.7	-68.5	253.5	-39.8	32.6	9.8
	509	10/10	R	C_1	28.0	-70.0	230.5	-33.1	39.4	7.8
	Mean	5	R	C_1	181.7	-77.3			8.5	27.9
							264.5	-29.8	13.8	21.3
巴音布鲁克	Mean	16/24	N	C_2	149.9	14.1			2.6	29.1
	(543-546)						150.3	18.0	2.5	29.4
	Mean	7/12	R	C_1	148.2	-43.2			5.8	27.3
	(547-548)						147.4	-69.7	5.9	27.0
后峡	555	4/7	R	C_2	36.2	-29.0	277.3	-61.3	51.1	13
	556	5/6	R	C_2	58.3	-45.0	235.5	-53.0	384.5	3.9
	557	9/9	R	C_2	75.5	27.5	83.0	-50.3	4.4	27.7
	558	7/7	R	C_2	58.6	-36.5	234.3	-61.4	6.1	26.5
	559	5/6	R	C_2	83.5	15.5	105.2	-54.8	9.5	26.1
	560	9/9	N	C_2	195.6	5.5	147.8	48.8	162.1	4.1
	561	3/6	N	C_2	194.5	6.3	146.5	47.8	167.7	9.6
	Mean	34/50	R	C_2	49.9	-48.8			2.5	15.4
	(555-561)						244.1	-48.8	2.8	18.1

* N 为退磁样品数，n 为用来计算平均剩磁方向的样品数。

其他简写符号同表 6-2。

1.6. 博乐剖面

博乐剖面位于伊犁地块北部边缘、沿博乐到赛里木湖的公路上（图 2-7，图 3-1）。博乐地区石炭纪地层主要陆源碎屑沉积岩，没有任何火山碎屑成分（新疆地矿局，1992，1993），与伊犁地区石炭系具有完全不同的岩相学特征。因此，博乐剖面所在的大地构造位置可能不属于伊犁地块，在石炭纪期间与伊犁地块处在不同的大地构造环境。所采古地磁样品为上石炭统东图津组（C_2d）的浅黄色砂岩、粗砂岩和下石炭统阿恰勒河组（C_1a）泥质、粉砂质砂岩（表 6-1）。等温剩磁曲线（图 6-1a）显示了典型的低钛磁铁矿的特征。居里温度曲线（图 6-2a, b）显示磁化率在 580°C 明显下降，表明磁铁矿是 C_1a 和 C_2d 砂岩中剩磁的主要载体，同时，在加热过程中，样品中磁性矿物发生了部分氧化现象。在剩磁清洗实验中，大多数样品均可分离出两个剩磁分量。在单个采点内，高温或硬磁分量往往比较一致，且均为负极性（表 6-3），然而在相邻的采点之间，点平均剩磁方向却十分分散。从表 6-3 可以看出，对于下石炭统而言，除点 505 以外，其他 4 个采点校正后的磁倾角比较一致，而磁偏角则相差较大，计算得平均剩磁方向为：Dg=181.7°，Ig=-77.3°，kg=8.5，α_{95}g =27.9（校正前）；Ds=264.5°，Is=-29.8°，ks=13.8，α_{95}s=21.3（校正后）。上石炭统砂岩也具有类似的情况，C_2d 的平均剩磁方向为：Dg=195.5°，Ig=-61.1°，kg=25.9，α_{95}g=18.4（校正前）；Ds=257.2°，Is=-45，ks=11.6，α_{95}s=28.2（校正后）。

1.7. 巴音布鲁克剖面

在那拉提断裂南侧的中天山地块，石炭纪地层主要为稳定陆缘浅水相沉积的碎屑岩（新

疆地矿局，1969）。在巴音布鲁克镇北东方向 50km 左右的剖面上（图 3-2c），从下石炭统肉红色灰岩和上石炭统粗砂岩地层中采集了古地磁样品（表 6-1）。等温剩磁曲线（图 6-1f）显示，灰岩样品中磁性矿物以高矫顽力为特征的赤铁矿为主，而砂岩中则以低矫顽力为特征的磁铁矿为主，同时还有少量赤铁矿。灰岩的磁化率在加热过程中，变化不太明显，但从居里温度曲线中仍可以观察到磁化率在 400°C~600°C 之间微弱下降（图 6-2*l*）。砂岩的居里温度曲线则在 580°C 时出现明显的转折，磁化率迅速下降到最小值（图 6-2k），表明该样品中主要的磁性矿物为低钛磁铁矿。砂岩的自然剩磁非常强，而灰岩的自然剩磁却异常微弱，二者退磁结果显示，大多数样品的高温或硬磁分量都非常不稳定，很难计算点平均剩磁方向。在剩磁分析过程中，通常把同一时代同类岩性的有效剩磁分量放在一起，但由于各分量方向十分分散，且既有正极性，也有负极性，由此计算所得的年龄平均剩磁方向可靠性很低，没有实际意义（表 6-3）。

1.8. 后峡剖面

后峡剖面属于北天山构造单元，位于后峡和冰达板之间（图 3-1，图 4-1）。所采样品主要为上石炭统天格尔组红色砂岩、玄武岩、安山质玄武岩（表 6-1）。等温剩磁曲线（图 6-1h）表明，玄武岩（561-508）中剩磁载体主要为低矫顽力磁性矿物，而红色砂岩（558-489）中既有低矫顽力磁性矿物也有高矫顽力矿物磁性矿物。热磁实验（图 6-2o, p）显示，安山质玄武岩（557-475）的居里温度曲线在 580°C 左右发生转折，磁化率迅速下降，为磁铁矿的典型特征。砂岩（559-495）的居里温度曲线除在 580°C 时明显转折，同时磁化率在 680°C 时也有较明显的下降，表明砂岩中既含有磁铁矿，也含有赤铁矿。从大部分样品的热退磁过程中可以分离出两个剩磁分量，低温剩磁分量与现代地磁场比较接近，而高温剩磁分量则比较分散，而且在一些采点（557-559）内，不同样品的剩磁方向差别也比较大，表现为很大的α_{95}值与低的精度参数 k 值（表 6-3）。各点平均剩磁方向在产状校正后磁倾角比较接近，磁极有正有负，但磁偏角相差非常大。表 6-3 列出了由 34 个单独样品特征剩磁方向计算出的平均值，但精度参数和α_{95}值均不理想。

2. 数据可靠性与剩磁年龄讨论

2.1. 磁组构研究

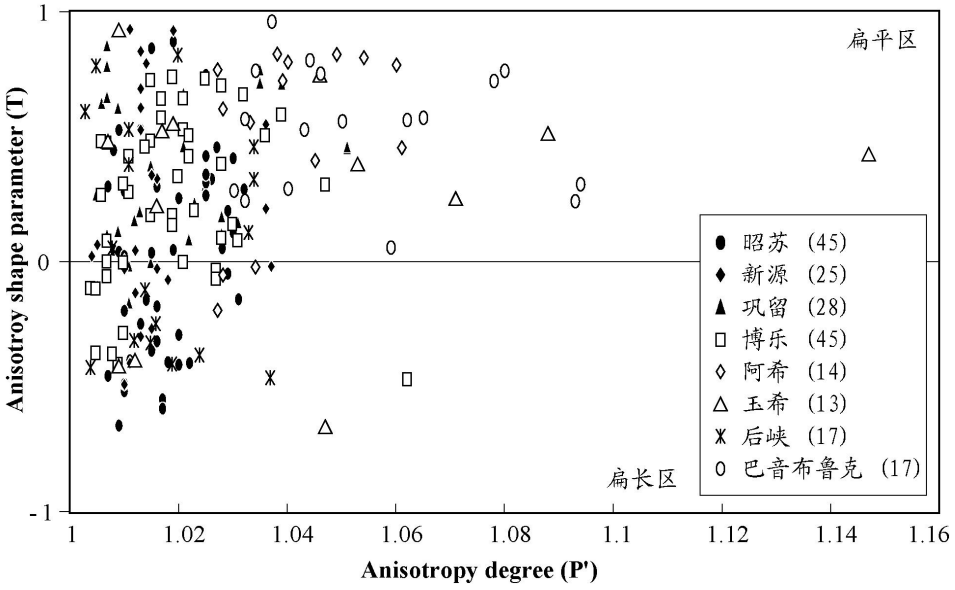

图 6-7 伊犁及其邻区古生代岩石磁化率椭球形态参数(T) 与各向异性度 (P') 投影图
$P' = \exp\{2[(\ln K1-\ln Km)^2+(\ln K2-\ln Km)^2 + (\ln K3-\ln Km)^2]^{1/2}\}$, $T=2\ln(K2/K3)/\ln(K1/K3)-1$, 其中 K1, K2 与 K3 磁组构主轴，Km 为三者平均值。

前文已有论述，天山造山带自古生代以来经历了多期构造变形。为了了解构造变形事件对以上古地磁采样剖面的影响程度，对选自不同剖面的样品（样品数见图 6-7）进行了磁组构测试。结果显示，各个剖面的绝大多数样品具有较弱的各向异性度（P'<1.1），而且除了玉希和巴音布鲁克剖面的少数样品外，大部分样品的各向异性度通常小于 1.06，只有玉希剖面的个别样品 P'达 1.15。因此可以认为，这些样品并没有经受明显的构造变形。另外，各个剖面中超过一半的样品具有正的磁化率椭球形态参数（T），从而投在扁平区域（图 6-7）。

2.2. 剩磁方向可靠性

除了阿希剖面泥质岩和巴音布鲁克剖面灰岩以外，所测样品大部分都显示了两个不同的剩磁分量：粘滞性剩磁分量和特征剩磁分量。将所有低温和软磁剩磁分量放在一起，计算出一个平均值：Dg=348.4°, Ig=67.1°, kg=15.9, α_{95}g=3.1°（校正前）；Ds=350.2°, Is=52.9°, ks=3.3, α_{95}s=7.9°（校正后）（n=185），并在区域上具有负检验。该平均值十分接近于现代地磁场的方向。岩石磁学和退磁过程表明，低钛磁铁矿和赤铁矿是大部分岩石中剩磁的主要载体，而且当二者同时存在于同一个样品中时，它们所记录的特征剩磁方向十分一致，并明显区别于现在地磁场，也不同于其他中、新生代的磁场方向（Chen et al., 1992）。

由于阿希和巴音布鲁克剖面大部分样品的自然剩磁强度很弱，因而无法得到有效、稳定的剩磁方向。从少数自然剩磁较强的样品中获得的剩磁方向却特别分散，即使将所有单独样品的剩磁方向放在一起，结算所得平均剩磁方向的精度也很低（见表 6-2 和表 6-3）。因此从这两个剖面所得的剩磁方向不能用于下一步构造解释。

关于博乐剖面，虽然 C_2 砂岩的平均剩磁方向显示负的褶皱检验，然而磁倾角在产状校正后比校正前更集中（表 6-3），但同时相应的磁偏角却变得更为分散。对于 C_1 的泥质砂岩，其平均剩磁方向显示正的褶皱检验，除了采点 505 以外，其余 4 个采点校正后的磁倾角比较接近，且不同于 C_2 砂岩的磁倾角，但磁偏角方向也特别分散。从图 2-7 可见，博乐地块与伊犁地块的边界可能为一走滑构造带。虽然磁组构研究结果表明，这些岩石并没有发生单个样品尺度上的明显变形作用，但在各采点之间，磁倾角比较一致而磁偏角相差较大，这可能是由于发生在采点尺度上的构造变形所致。考虑到该局部构造变形作用的影响，这些剩磁方向不能用来代表博乐地块的古地磁方向。

后峡剖面的情况与博乐剖面类似。虽然全部样品的有效剩磁分量具有负的褶皱检验，但在野外，地层产状近直立且走向一致。值得一提的是，有两个采点的平均剩磁方向为正极性（表 6-3），将其极性倒转后，在地层坐标系下，磁倾角与其他采点的磁倾角十分接近，但它们的磁偏角差别却增大。鉴于采样剖面位于北天山断裂和后峡断裂之间，其中北天山断裂为一大型走滑韧性剪切带，因此这些样品偏角的漂移现象可能与沿两断裂带的构造变形有关。变形应该发生在采样点之间，而单个样品并没有受到该变形作用的影响。

新源剖面的前 5 个采点由于自然剩磁强度太弱，少数有效剩磁方向彼此十分分散，因此无法计算具有构造意义的平均剩磁方向。其余 6 个采点的剩磁方向则比较稳定，而且相互之间可以对比。另外，昭苏剖面石炭系样品以及巩留地区二叠系样品的剩磁方向也比较稳定，同时，采样点位于伊犁地块内部而远离构造变形带，因此这些剩磁方向可以代表伊犁地块的古地磁方向，其时代和构造意义将在下文讨论。

玉希剖面的 6 个点平均剩磁方向非常一致，且均为负极性。由于地层平缓且产状一致，因为没有褶皱检验。这些剩磁方向的磁倾角与昭苏、新源剖面的剩磁倾角非常一致，但是磁偏角却差别非常大。由图 2-7 和图 3-1 可以看出，玉希剖面位于那拉提和北天山走滑剪切带之间，后期走滑剪切作用可能导致玉希剖面石炭纪岩层发生变形和局部旋转，从而使该剖面样品的剩磁偏角发生相对偏移。因此，下文的构造分析将不考虑该剖面的古地磁方向。

2.3. 剩磁年龄

从表 6-2 可见，伊犁及其邻区石炭系和二叠系岩石特征剩磁方向均具有负极性，与石炭

-二叠纪反极性区间（PCRS，或 Kiaman 反极性区间）（Hounslow et al., 2004）十分吻合。但由于伊犁地区采样剖面往往发育有大量后期火山岩和花岗岩，因此在进行构造解释之前，需要先讨论其剩磁年龄。

如上文所述，巩留剖面红色砂岩中含有大量植物化石，同时其底部砾岩不整合覆盖在早二叠世火山岩之上，新疆地矿局（1979）将其时代归为晚二叠世。根据最新的国际地层表，虽然二叠纪已经划分为早、中、晚二叠世，但实际上，晚二叠世的时代范围仍与原来的二分方案一致，既 260~250Ma。因此该红层的时代为晚二叠世应没有问题，但本论文为了统一地层代号，仍延用 P_2 标识（表 6-1，6-2，6-4）。虽然平均剩磁方向的精度参数 k 值在产状校正后减小，但采样剖面的单斜构造不能提供有效的褶皱检验。对比 PCRS，该剖面单一负极性特征剩磁方向表明，岩石剩磁应该在 250 Ma（PCRS 的上限年龄）之前获得，即该剩磁代表晚二叠世沉积过程中形成的原生剩磁。于是，从该剖面平均剩磁方向计算获得伊犁地块晚二叠世的古地磁极：λ=79.7°N, ϕ=172.0°E, A95=11.3°（n=5）（表 6-4）。

昭苏剖面下石炭统阿克沙克组 4 个采样点的剩磁方向通过了正的褶皱检验，且均具有负极性。鉴于早、晚石炭世的界限（325Ma）与 PCRS 的下限年龄比较一致，考虑到采样的代表性，这些样品应该有一部分具有正极性剩磁方向。然而事实相反，因此可以推断，这些下石炭统岩石的剩磁并非早石炭世获得。另一方面，早二叠世陆内碱性火山岩区域上不整合覆盖在褶皱变形的石炭系地层之上（新疆地矿局，1993；Allen et al., 1995；Shu et al., 2003），表明褶皱作用发生在早二叠世之前，因而可以排除早二叠世的重磁化作用。此外，下石炭统岩石剩磁方向与上二叠统砂岩的剩磁方向明显不同（表 6-2），因此该特征剩磁方向也不是晚二叠世重磁化的结果。鉴于下石炭统与上石炭统岩石的剩磁方向非常一致（表 6-2），并且昭苏剖面早、晚石炭世沉积地层与同时代火山岩地层交互产出，并伴有大量海西中期的花岗质岩石，锆石 U-Pb 年代学研究表明，这些岩浆岩的年龄从 361Ma 到 309Ma（详见第三章），表明与伊犁岩浆岛弧有关的热事件一直持续到晚石炭世中晚期。这一显著的热事件很容易使早期（比如早石炭世）形成的岩石在后期（晚石炭世）岩浆作用过程中发生热重磁化。下石炭统岩石剩磁方向的正褶皱检验可以解释为发生在重磁化之后的褶皱作用，实际上，在野外可以观察到沉积岩和火山岩共同的褶皱层面（图 3-3a），褶皱时间应晚于岩浆作用，但早于早二叠世。因此，有理由认为，伊犁地区下石炭统和上石炭统岩石最终共同记录了晚石炭世剩磁方向。由此可以计算出石炭系全部 9 个采点的平均特征剩磁方向为：Dg=176.7°, Ig=-62.7°, kg=13.0, α_{95g}=14.7°（校正前） Ds=172.0°, Is=-44.8°, ks=40.4, α_{95s}=8.2°（校正后）（表 6-2；图 6-4b, c）。

类似的情况也出现在新源剖面。玄武岩（采点 537-540）形成于早石炭世（锆石 U-Pb 年龄为 354±5Ma，据朱永锋等，2005），但所有可靠的剩磁方向在地理坐标系中均具有负极性，并且显示负的褶皱检验（图 6-5e, f），表明这些剩磁方向应为重磁化的结果，而不是早石炭世的原生剩磁。考虑到在采样地区存在 313±4 Ma（朱永锋等，2005）和 315±3~309±3Ma 的花岗岩（见第三章），因而下石炭统玄武岩的特征剩磁为晚石炭世（~310Ma）岩浆热事件重磁化的结果。至于剩下的两个流纹砂岩采点，其平均剩磁方向也具有负极性，但它们在地层坐标系下更接近于玄武岩在地理坐标系下的剩磁方向，并且与昭苏剖面的平均剩磁方向一致。虽然流纹砂岩被划归为下石炭统阿吾拉勒组（新疆地矿局，1975；1993），然而其时代仍有疑义。从区域构造和地层关系来看，流纹质火山碎屑岩的形成应晚于早石炭世的玄武岩，因而很可能属于上石炭统（见第三章论述）。基于以上讨论，由 4 个玄武岩采点校正前的剩磁方向和 2 个流纹砂岩校正后的剩磁方向计算出一个平均剩磁方向：D=165.3°, I=-36.4°, k=37.7, α_{95}=11.0°（图 6-5e, f，表 6-2）。

综上所述，位于伊犁地块内部的昭苏、新源剖面石炭系岩石均记录了晚石炭世剩磁方向，从而由两个剖面所有采点的有效点平均剩磁方向可以计算出伊犁地块晚石炭世的古地磁极：

λ=68.6°N, ϕ=290.6°E, A_{95}=6.1°（n=15）（表 6-4）。

第三节 伊犁地块及邻区古地磁数据对比

过去 60 年来，古地磁学被广泛应用于大地构造研究。近几十年来，很多古地磁学家研究了塔里木等中亚地区主要陆块，发表了大量古地磁数据。但迄今为止，没有任何关于伊犁地块的古地磁数据发表。Bazhenov 等（1993；1999；2003）对哈萨克斯坦境内“北天山构造带”中奥陶系、石炭系和二叠系岩石进行了古地磁研究，结果发现，该地区不同时代地层古地磁方向的磁偏角相对于参考陆块（西伯利亚和塔里木）发生了明显的西偏现象。由于研究区域十分靠近天山构造变形带，因而磁偏角的西偏现象被认为是由于造山带内走滑断裂作用所致，而与任何刚性块体的旋转无关（Bazhenov et al., 1999）。事实上，伊犁地块是一个具有前寒武纪结晶基底的微大陆块块（Allen et al., 1992；Coleman, 1994；Gao et al., 1998；Chen et al., 1999），其西部延伸至哈萨克斯坦，东部以天山南、北两支为界（图 2-7）。虽然伊犁地块的边界为强烈变形的造山带，但其内部并没有发生明显的变形，最直接的证据是，昭苏和新源剖面相隔 200km，但两地同时代岩石具有非常一致的晚石炭世剩磁方向。因此，从伊犁地块内部的昭苏、新源和巩留地区获得的剩磁方向，可以用来计算代表整个伊犁地块的古地磁极（表 6-4）。

表 6-4 伊犁地块及邻区晚石炭世和晚二叠世古地磁极对比表

陆块	研究区域	年龄	Slat	Slong	N	Plat	Plong	A_{95}	参考文献
伊犁	巩留	**P_2**	**43.4**	**82.5**	**5**	**79.7**	**172.0**	**11.3**	本文
	昭苏	C_2	43.3	81.1	9	72.0	287.1	8.9	本文
	新源	C_2	43.3	83.3	6	63.9	296.0	9.8	本文
	Mean	**C_2**			**15**	**68.6**	**290.6**	**6.1**	本文
塔里木	阿克苏	P_2	40.2	79	21	65.6	181.2	3.9	Li et al., 1988
	南西部	P	37	80	8	65.4	170.5	8.5	Gilder et al., 1996
	-	P_2	40.8	79.8	24	62.9	190.7	6.3	程国良等，1983
	-	P_2			20	66.0	188.8	6.3	孟自芳, 1991
		P_2	42.1	83.4	10	73.2	191.0	7.3	McFadden et al., 1988
	Mean	**P_2**				**66.8**	**184.1**	**4.9**	
	南西部	C_2	37	80	7	60.2	165.4	11.1	Gilder et al., 1996
	阿克苏	C_2	40.3	79.5	44	52.2	179.5	8.6	Bai et al., 1987
	阿克苏	C_2	40.6	79.5	9	46.5	168.0	4.6	Fang et al., 1990
	-	C_2	40.5	78.8	3	41.0	160.0	4.0	Zhai, 1988
	-	C_2			44	61.3	174.0	4.0	孟自芳等, 1990
	-	C_2			22	46.6	170.2	4.5	方大钧等, 1996
	Mean	**C_2**				**51.5**	**169.1**	**7.7**	
西伯利亚	-	P_2			5	50.0	160.0	7.0	Van der Voo, 1993
	-	C_2			17	41.0	169.0	3.0	Van der Voo, 1993
准噶尔	天池	**P_2**	**44**	**88.1**	**7**	**76.0**	**193.0**	**4.6**	Nie et al., 1993
	乌鲁木齐[a]	P_2	43.8	87.7	78*	77.7	0.4	5.5	Sharps et al., 1992
	乌鲁木齐[b]	C_2-P	47.2	86.6	26	69.0	350.0	7.5	Li et al.,1991
	乌鲁木齐[b]	C_2-P	45.6	83.2	23	78.0	238.7	7.9	Li et al.,1989
	乌鲁木齐[b]	C_2-P	43.8	87.8	4	69.0	231.0	13.7	Li et al.,1991
	乌鲁木齐[b]	C_2-P	43.8	87.8	7	55.0	172.0	15.1	Li et al.,1991
	北西部	**C_2**	**46.7**	**86.1**	**15**	**70.0**	**299.0**	**6.4**	Li et al., 1991

a, 剩磁方向以粘滞磁性为主, 全部 78 个样品中只有 4 个采点的 26 个样品可分离出稳定剩磁方向，但彼此相对比较分散。其它分量由大圆弧方法分析获得。

b, 剩磁年龄不确定，并可能经受后期热重磁化作用。

* 指单个样品数目。

为了对比晚石炭世-晚二叠世期间伊犁地块与相邻陆块之间的相对运动，表 6-4 还列出了前人所获得的塔里木、准噶尔和西伯利亚地块同时代古地磁极。塔里木板块晚石炭世和晚二叠世的古地磁数据可靠性比较高（低 A_{95}），且同时代古地磁极比较一致（程国良等，1983；Bai et al., 1987；Li et al., 1988；McFadden et al., 1988；Zhai, 1988；Fang et al., 1990；孟自芳等, 1990；孟自芳, 1991；Gilder et al., 1996；方大钧等, 1996），因此求得平均值分别为λ=51.5°N, ϕ=169.1°E, A_{95}=7.7°和 λ=66.8°N, ϕ=184.1°E, A_{95}=4.9（表 6-4）。Van der Voo（1993）报导了西伯利亚板块晚石炭世和晚二叠世的古地磁极分别为λ=41.0°N，ϕ=169.0°E，A_{95}=3.0°和λ=50.0°N，ϕ=160.0°E，A_{95}=7.0°（表 6-4）。

关于准噶尔地块，到目前为止，古地磁数据还不多。一些学者从准噶尔南缘和北西缘石炭纪-二叠纪中获得了一些古地磁数据（Li et al.,1989；Li et al., 1991；Sharps et al., 1992；Nie et al., 1993）（表 6-4）。但是这些数据一般比较分散，而且大部分剩磁方向的年龄不够明确。例如 Li et al.（1991）从准噶尔南缘和北西缘获得的古地磁数据非常不一致，而后期的重磁化可能是导致不一致的重要原因，另外，剩磁的年龄也粗略的确定为晚石炭世到二叠纪。因而，这些数据不适合同其它地区古地磁数据进行对比。尽管如此，Li et al.（1991）还报导了一个晚石炭世的古地磁极，由于数据精确可靠性比较高，剩磁年龄也比较确切，因而用来代表准噶尔地块晚石炭世的古磁极（λ=70.0°N, ϕ=299.0°E, A_{95}=6.4°，表 6-4）。

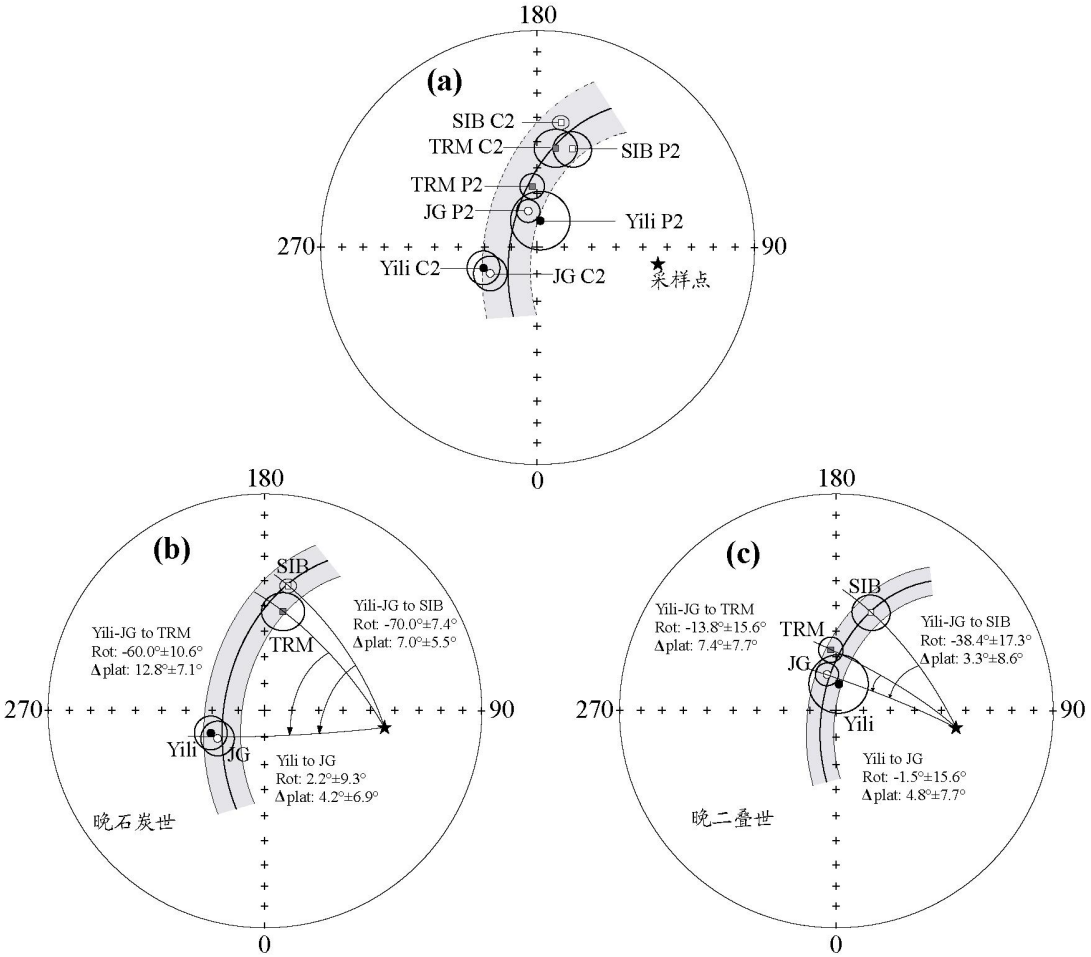

图 6-8 伊犁及其相邻地块晚石炭世、晚二叠世古地磁极吴氏网等面投影图

TRM，塔里木板块；JG，准噶尔地块；SIB，西伯利亚板块，Yili，伊犁地块；Rot，板块之间相对角旋转量，负值表示逆时针旋转；Δplat，板块之间纬度上的相对运动量（角度），正值表示会聚。

Sharps 等（1992）和 Nie 等（1993）分别从乌鲁木齐和天池地区获得了两个晚二叠世的

磁极，但如表 6-4 所示，前者全部 78 个分析样品中仅有 4 个采点的 26 个样品具有稳定的剩磁方向，其余样品的剩磁方向均有大圆弧方法分析获得，且显示很高的α_{95} 值。另外，这些剩磁方向在点内和点间均比较分散，而平均古磁极方向也是用所有单个样品的剩磁方向计算得来的。相比而言，从天池地区所得的古地磁方向比较稳定，且通过了正的褶皱检验，由此计算出的古地磁极（λ=76.0°N, ϕ=193.0°E, A95=4.6°）可以用来代表准噶尔地块晚二叠世的古磁极。

图 6-8 显示了伊犁及其相邻主要地块晚石炭世和晚二叠世磁极的吴氏网等面投影，从中可以看出，自晚石炭世以来，4 个陆块之间在纬度上已经没有明显的相对运动，但他们之间存在明显的角距离。在晚石炭世，伊犁地块与准噶尔地块非常接近，只有 7.7°±6.6°的角度距离，而与塔里木和西伯利亚板块相距较远，它们之间的角距离分别为 120.5°±7.0°和 119.0°±5.1°（图 6-8b）。以采样点为圆心的小圆弧显示，伊犁与准噶尔之间晚石炭世时存在 4.2°±6.9°的纬度距离，而与塔里木之间的纬度距离为 12.8°±7.1°，与西伯利亚之间的纬度距离为 7.0°±5.5°。这些纬度上的角度距离在误差范围内非常微小。但伊犁地块与其他地块之间经度上的角距离则非常大。伊犁与准噶尔之间自晚石炭世以来只有 2.2°±9.3°的相对旋转，鉴于旋转量远比误差值小，因而旋转的方向已没有实际意义。伊犁相对于塔里木具有 60.0°±10.6°的逆时针旋转，相对于西伯利亚具有 70.0°±7.4°的逆时针旋转（图 6-8b）。晚二叠世时，伊犁、准噶尔和塔里木的磁极基本一致，其角度距离小于 12.1°±9.9°。而三者与西伯利亚之间仍存在较大的距离（>24.1°±6.8°）（图 6-8c）。自晚二叠世以来，伊犁相对于准噶尔、塔里木和西伯利亚在纬度上的角距离分别为 4.8°±7.7°, 7.4°±7.7°和 3.3°±8.6°，而相对旋转量分别为-1.5°±15.6°, -13.8°±15.6°和-38.4°±17.3°，负值表示逆时针旋转。

第四节 古地磁数据的大地构造意义

从上文分析可见，伊犁地块与准噶尔、塔里木和西伯利亚地块之间在晚石炭世和晚二叠世时，纬度上的角距离非常微小，且往往小于误差值，表明自晚石炭世以来，4 者之间基本没有发生明显的纬度上的相对运动。这一结果与地质上的认识完全吻合，即以塔里木、伊犁和准噶尔等陆块会聚、碰撞为主的天山造山作用在晚石炭世末期基本结束（Windley et al., 1990；Allen et al., 1992；Gao et al., 1998）。自晚石炭世或晚二叠世以来，伊犁地块与其他相邻地块在纬度上的相对运动实际上对应于新生代塔里木和准噶尔盆地朝天山的陆内俯冲作用和相应的南北向地壳缩短（Tapponnier et al., 1979；Chen et al., 1992；Avouac et al., 1993；Cunningham et al., 1996；Burchfiel et al., 1999；Shu et al., 2003；Charreau et al., 2005）。

自晚石炭世以来，伊犁地块和准噶尔地块的磁极一直非常接近，表明这两个陆块在晚石炭世末期已拼合到一起，也就是说，从古地磁角度已无法识别两地块之间微小的相对运动，因而二者可以被看作一个整体。如上文所述，伊犁地块古地磁极与塔里木和西伯利亚同时代古地磁极之间的角距离揭示了伊犁-准噶尔块体相对其它两个大陆块体的逆时针旋转。由此可以分别计算出自晚石炭世和自晚二叠世以来，伊犁-准噶尔相对于塔里木和西伯利亚的相对旋转量（图 6-8）。通过从晚石炭世以来的相对旋转量减去晚二叠世以来的相对旋转量，可以得到晚石炭世-晚二叠世期间的相对旋转量。于是，从晚石炭世到晚二叠世期间，伊犁-准噶尔块体相对于塔里木板块逆时针旋转了 46.2°±15.1°，相对于西伯利亚板块旋转了 31.6°±15.1°。从图 6-8c 可见，自晚二叠世以来，伊犁-准噶尔相对于塔里木的逆时针旋转（13.8°±15.6°）在误差范围内已经变得微不足道，然而相对与西伯利亚仍然有 38.4°±17.3°的逆时针旋转。

由于自晚石炭世以来，4 个地块已经会聚到一起，因此地块之间的相对旋转主要表现为沿地块边界的走滑剪切作用以及相应的侧向位移。如图 2-7 所示，伊犁地块南、北边界发育两条韧性走滑剪切带。其中北部边界为北天山断裂（Sengör et al., 1993；Zhou et al., 2001；

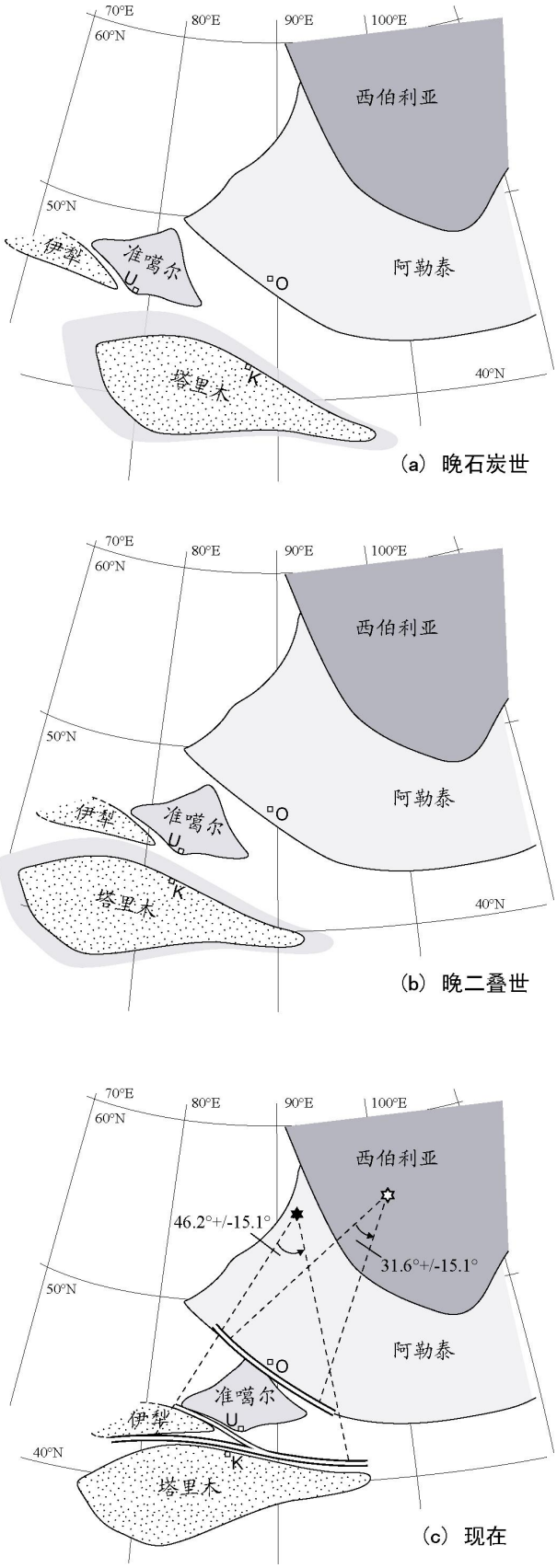

图 6-9 中亚地区主要板块之间晚石炭世-晚二叠世期间相对旋转和走滑作用简易重建图
（塔里木板块周缘阴影区域表示新生代板内俯冲过程中消减的塔里木大陆边缘）
K，库尔勒；U，乌鲁木齐；O，乌列盖（蒙古国）

Zhao et al., 2003），向东并入天山主断裂（MTSZ；Shu et al., 1999；Laurent-Charvet et al., 2002, 2003）。运动学研究显示，北天山断裂和天山主断裂均为右旋走滑剪切带（见第四章；Laurent-Charvet et al., 2002, 2003）。伊犁南部边界为那拉提断裂（Zhao et al., 2003），向东为青布拉克断裂（Windley et al., 1990；Allen et al., 1993；Laurent-Charvet et al., 2001），二者也为右旋走滑断层（第五章）。南、北两条断裂带近东西向延伸，向东天山彼此接近平行（Shu et al., 1999；Laurent-Charvet et al., 2002, 2003）。

为了解释古地磁和运动学证据，图 6-9 显示了一个板块间相对旋转的古地理重建简图，该重建图将西伯利亚板块固定在现今的地理位置，根据陆块间的相对运动，来恢复它们之间原来的相对位置。为了定量估算伊犁-准噶尔地块相对于塔里木、西伯利亚板块的相对侧向位移，图 6-9 定义了一个相对旋转的欧拉极。一个板块围绕欧拉极相对于另一个板块沿一主断裂发生旋转。在天山造山带中，两条接近平行的右旋走滑剪切带形成一个弧形断裂带（图 6-9c）。通过这一弧形的最优小圆弧的圆心即是伊犁-准噶尔相对于塔里木的欧拉极位置：55°N, 92°E，小圆弧半径为 13°。由此，从晚石炭世到晚二叠世，伊犁-准噶尔相对于塔里木的逆时针旋转（46.2°±15.1°）导致两大块体之间沿天山走滑带发生了 1160±380 km 的侧向位移（图 6-9a, b）。该位移量实际上由伊犁-准噶尔和塔里木沿天山走滑带发生的反方向旋转的总和。在此期间，伊犁-准噶尔相对于西伯利亚向东运动了 670±320 km，而塔里木则相对于西伯利亚西向运动了 360±270 km。值得提出的是，图 6-9 没有考虑位于伊犁和塔里木之间的中天山地块。

类似地，伊犁-准噶尔块体相对于西伯利亚的逆时针旋转，地质上表现为沿阿尔泰造山带中额齐斯断裂带的左旋走滑剪切作用（Laurent-Charvet et al., 2002, 2003）。由弓形的剪切带可以估算出另一个欧拉极的位置：56°N, 101°E，其中小圆弧半径为 11°（图 6-9c）。晚石炭世-晚二叠世期间，伊犁-准噶尔相对于西伯利亚的逆时针旋转（31.6°±15.1°）导致准噶尔沿额齐斯走滑带向东发生了 670±320 km 的侧向位移，而晚二叠世以来的逆时针旋转（38.4°±17.3°）则导致准噶尔继续向东运动了 820±370 km。这意味着二叠纪以后，伊犁、准噶尔和塔里木一起，相对于西伯利亚向东运动（图 6-9b, c）。鉴于塔里木和西伯利亚的白垩纪古地磁极已经非常一致（Chen et al., 1992），因此这一逆时针旋转及其相应的东向位移应该发生在晚二叠世和早白垩世之间。

Ar-Ar 热年代学研究（见第四章）表明，天山地区右旋走滑事件发生在 290~245 Ma（Yin et al., 1996；蔡东升等，1996；Shu et al., 1999；Zhou et al., 2001；Laurent-Charvet et al., 2002, 2003），而额齐斯左旋走滑事件则从 290 Ma 到 240 Ma（Laurent-Charvet et al., 2003），并持续到三叠纪-早侏罗世（Allen et al., 1995）。同时发生在两条反旋向走滑带之间的大规模侧向位移，可能代表伊犁-准噶尔块体在晚石炭世末期的碰撞事件之后，整体向东挤入到塔里木和西伯利亚板块之间。

第五节 小结

1．伊犁地区古生代地层的古地磁学研究至今尚为空白。本论文选择伊犁地块及其邻区 8 个剖面，采集了奥陶系、石炭系和二叠系的沉积岩和火山岩样品共 61 个点 561 个岩芯，进行了系统的岩石磁学和古地磁学研究。等温剩磁、居里温度、磁滞回归曲线等岩石磁学研究及热（交变）退磁过程表明，所有样品中主要的磁性矿物为磁铁矿和（或）赤铁矿。

2．退磁过程从大部分样品中分离出两个剩磁分量。所有低温或软磁分量的平均剩磁方向与现代地磁场非常接近。阿希剖面奥陶系岩石和巴音布鲁克下石炭统灰岩样品的自然剩磁非常弱，因而没有获得有效剩磁方向。巴音布鲁克上石炭统砂岩和博乐剖面部分上石炭统砂岩样品的剩磁方向非常不稳定，而且在采点内和点间均特别分散，因此没有求得有效的平均剩磁方向。新源剖面下石炭统基性火山碎屑岩的剩磁方向与现代地磁场相似，因而可能是近

代重磁化的结果。博乐石炭系砂岩、后峡上石炭统砂岩和火山岩以及玉希上石炭统砂岩、火山岩样品均具有稳定的特征剩磁方向，但是，各剖面各时代样品的剩磁方向非常分散。虽然磁组构研究表明，绝大部分测试样品并没有发生明显的构造变形，但是由于这些采样剖面与后期走滑断裂带非常接近，因此这些剖面内的岩层可能发生了变形作用和局部旋转，从而使这些样品特征剩磁的磁偏角发生了明显的漂移。但是这些变形作用并没有发生在单个样品的尺度范围内。

3．从昭苏和新源地区下石炭统和上石炭统岩石中获得了稳定的有效特征剩磁，并且在剖面和时代范围内非常一致，所有剩磁方向均为负极性。昭苏下石炭统岩石平均剩磁方向通过正的褶皱检验。新源下石炭统玄武岩平均剩磁方向则显示负褶皱检验。鉴于伊犁晚古生代岛弧岩浆作用一直持续到晚石炭世末，因而，所有下石炭统和上石炭统岩石都被最晚的岩浆热事件重磁化，结果它们共同记录了晚石炭世末的剩磁方向。通过计算昭苏、新源石炭系岩石中获得的剩磁方向，求得伊犁地块晚石炭世古地磁极为λ=68.6°N, ϕ=290.6°E, A_{95}=6.1°（n=15）。

4．巩留剖面晚二叠统红层具有非常稳定、一致的特征剩磁方向。由于样品采自单斜地层，因而没有褶皱检验。但产状校正后精度参数有所提高，因此该剩磁方向代表晚二叠统红层的原生剩磁，并由此计算得到伊犁地块晚二叠世的古地磁极：λ=79.7°N, ϕ=172.0°E, A_{95}=11.3°（n=5）。

5．通过对比伊犁地块与准噶尔、塔里木和西伯利亚板块同时代的古地磁极，发现自晚石炭世和晚二叠世以来，四个陆块之间在纬度上没有明显的相对运动，表明晚石炭世以后，准噶尔、伊犁和塔里木之间没有发生重要的离散和会聚作用。另外，从晚石炭世到晚二叠世期间，伊犁地块相对于准噶尔没有发生重要的相对旋转，但伊犁-准噶尔一起相对于塔里木板块逆时针旋转了 46.2°±15.1°，相对于西伯利亚逆时针旋转了 31.6°±15.1°。前者导致伊犁-准噶尔相对于塔里木沿天山右旋走滑剪切带发生了 1160±380 km 的侧向位移，后者导致伊犁-准噶尔沿阿勒泰额齐斯左旋剪切带相对于西伯利亚发生了 670±320 km 的侧向位移。地质年代学表明，这些走滑事件同时发生在 290~245Ma 之间。因此，伊犁-准噶尔沿天山和额齐斯剪切带的走滑运动，使其在二叠纪期间向东挤入到塔里木和西伯利亚两大板块之间。

第七章 伊犁及西天山古生代地球动力学演化

天山造山带经历了从古生代到新生代的多期造山和构造变形作用。古生代洋陆转换和俯冲、碰撞造山作用形成了古天山的雏形，晚古生代末区域大型走滑事件和中、新生代以来的陆内变形、再造山作用强烈叠加、改造了古生代构造带，给人们认识和恢复天山古生代构造演化带来了很多困难和误导。为了合理解释天山造山带古生代地球动力学演化机制，必须剔除后期构造作用对古生代造山带的改造。本研究在分析天山中、新生代构造变形和晚古生代后碰撞构造作用的基础之上，尽可能寻找与古生代构造作用有关的直接证据，从而提出了关于伊犁及相邻地块之间地球动力学演化的二维模式，以供与专家、同行探讨。

第一节 现今的构造

现今的天山山脉是新生代欧亚板块与印度板块碰撞作用引起的陆内再造山作用的结果（Molnar and Tapponnier, 1975; Tapponnier and Molnar, 1979; Nelson et al., 1987; Avouac et al., 1993; Hendrix et al., 1994; Burchfiel, et al., 1999; Poupinet et al., 2002; Shu et al., 2003），跨越天山南北的地壳缩短、增厚作用反映了中亚地区典型的陆内俯冲和盆山藕合作用（Allen et al., 1999; Vinnik et al., 2004）。塔里木板块向北俯冲在天山造山带之下，导致天山-塔里木山盆交接带古生代-中、新生代地层发生了褶皱变形，并向南推覆到塔里木盆地之上（Allen et al., 1999）（图 7-1）。沿托什干河，南天山断裂代表现今天山造山带与塔里木盆地之间的边界。地震资料（Zhao et al., 2003；Wang et al., 2004a）显示，南天山断裂向深部可能延伸至塔里木俯冲下插的地壳基底。由上文（第五章）论述可知，南天山断裂两侧古生代地层岩相学和变形特征存在明显差异，表明该断裂可能代表一个活化的古生代构造缝合带。

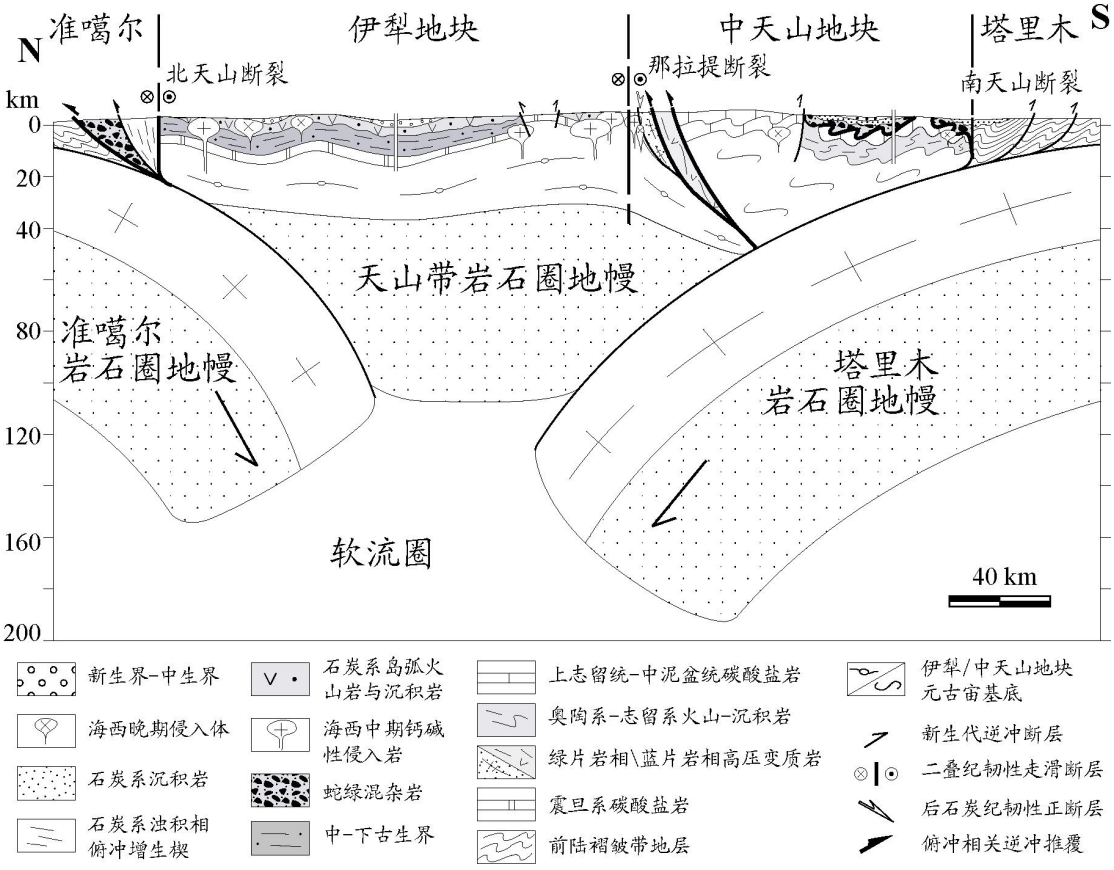

图 7-1 伊犁及相邻大陆地块岩石圈尺度综合剖面图

（深部构造根据 Zhao et al., 2003；Wang et al., 2004a，并修改）

类似地，天山北缘与准噶尔盆地交接的地带为一个向北逆冲的新生代推覆变形带，厚达10~12 km 的三叠纪-新近纪沉积岩地层发生了脆性褶皱变形（图 7-1）。同时，北天山石炭纪浊积相复理石和蛇绿混杂岩也被卷入到该推覆体中，逆冲在中-新生代地层之上。大型的构造推覆作用吸收了近 30km 的南北向地壳缩短（Avouac et al., 1993），也使古生代地层之间原有的构造关系发生了强烈的破坏（郭召杰等，2006）。新生代以来的活动构造在天山内部也有明显的反映，如在伊宁盆地、库米什盆地、巴音布鲁克盆地边缘，多见古生代构造地层、甚至元古代构造基底逆冲推覆在中、新生代盆地之上（图 7-1）。

第二节 二叠纪后碰撞构造与岩浆作用

Liegeois（1998）及其他研究者曾论述了俯冲造山带后碰撞的主要特征，即区域走滑事件、碱性岩浆作用和拉分盆地构造。这三个特征在新疆北部都有体现，Allen et al.（1993，1995）认为，吐哈盆地和准噶尔盆地为二叠纪侧向剪切作用形成的拉分盆地（图 2-10B）。另外，在乌鲁木齐以南的白杨沟地区和吐鲁番以西的托克逊阿拉沟地区（图 2-7），二叠系混杂堆积的灰岩、砂岩、硅质岩和双峰式火山岩呈滑积岩块产于陆源碎屑和硅化基质中，显示一种快速沉降和混浊沉积的盆地环境，并伴随有碱性岩浆的喷发作用（Allen et al., 1995；舒良树等，2005）。虽然位于西天山的伊宁盆地、昭苏盆地、库米什盆地、巴音布鲁克盆地和博乐盆地也具有拉分盆地的特征，但至今还没有这方面的研究成果。在伊犁地块南北两侧，发育数条近 E-W 向延伸的大型走滑断层，如北天山断裂、天山主断裂、那拉提断裂、青布拉克断裂等（图 7-2），运动学（见第四、五章）和古地磁学（第六章）研究表明，这些断裂带属于发生在 290 Ma~245 Ma（表 7-1）期间的右旋韧性剪切带（Cai et al., 1996; Yin et al., 1996；Bazhenov et al., 1999; Shu et al., 1999; Zhou et al., 2001; Laurent-Charvet et al., 2002, 2003）。Sengör et al.（1993）和 Allen et al.（1995）认为，侧向走滑剪切作用在整个中亚地区十分普遍，并且在中亚造山作用中扮演十分重要的角色。伊犁地区石炭-二叠系岩石古地磁研究结果表明，在晚石炭世-晚二叠世期间，伊犁地块和准噶尔地块一起，相对于塔里木沿天山韧性走滑剪切带发生了 1000 km 左右的右旋侧向位移。

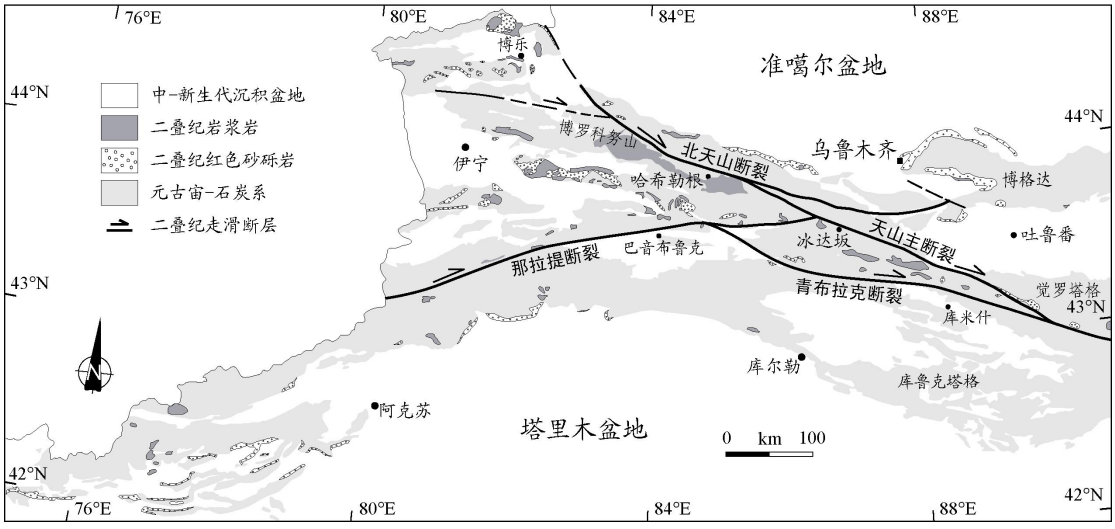

图 7-2 伊犁及西天山地块二叠纪构造、岩浆作用示意图

二叠纪岩浆岩遍布于整个西天山地区，但是大部分岩浆岩主要沿走滑剪切带分布（图 7-2）。在伊犁北缘的博罗科努山，钾长石花岗岩锆石 U-Pb 年龄为 290~260 Ma（表 7-1），与 Rb-Sr 和 Ar-Ar 年龄基本一致，岩石没有发生变形，表明花岗岩没有受到走滑断裂作用的影响。从表 7-1 可以看出，该花岗岩体的年龄与北天山韧性剪切事件的时代十分接近，表明花

岗岩的形成可能与韧性剪切作用有关。在库米什北，未变形粗粒花岗岩沿青布拉克侵入到元古代片麻岩中，花岗岩锆石 U-Pb 年龄为 252±4 Ma。科克苏地区云母片岩中发育后期热液活动的石英脉和钾长石花岗岩，这些花岗岩有的受那拉提断裂剪切作用的影响而发生韧性变形，也有的没有发生变形，其中一未变形花岗岩的锆石 U-Pb 年龄为 277±3 Ma。在乌鲁木齐东南方向的白杨沟剖面，拉斑玄武岩中锆石 U-Pb SHRIMP 年龄为 289±5Ma（舒良树等，2005）。另外，博乐地区普遍发育二叠纪长英质火山岩和花岗岩，陈江锋等（1994；2000）从这些岩石中获得 280~270 Ma 的 K-Ar 和 $^{40}Ar/^{39}Ar$ 年龄。

表 7-1 伊犁地块及邻区二叠纪构造、岩浆作用年代学数据

地质事件	地 点	岩石	矿物	方法	年龄（Ma）	作 者
北天山断裂	博罗科努山	变形花岗岩	黑云母	Ar-Ar	260.1±3.4	Yin et al., 1996
北天山断裂	哈希勒根达坂	变形花岗岩	黑云母	Ar-Ar Plateau	267.7±1.8	Zhou et al., 2001
北天山断裂	哈希勒根达坂	变形花岗岩	黑云母	Ar-Ar Plateau	275.3±1.9	Zhou et al., 2001
北天山断裂	哈希勒根达坂	板岩	全岩	Ar-Ar	285-245	本文
天山主断裂	冰达坂北	板岩	全岩	Ar-Ar	275-255	本文
天山主断裂	冰达坂	片麻岩	黑云母	Ar-Ar	290-245	Laurent-Charvet et al., 2003
那拉提断裂	巴音布鲁克	变形花岗岩	钾长石	Ar-Ar Plateau	265.3±2.4	Zhou et al., 2001
那拉提断裂	巴音布鲁克北	靡棱岩	黑云母	Ar-Ar	250±7.9	蔡东升等，1996
二叠纪岩浆活动	博罗科努山	花岗岩	全岩	Rb-Sr	292±15	王作勋等，1990
	博罗科努山	花岗岩	黑云母	Ar-Ar	254.5±4.8	Yin et al., 1996
	博罗科努山	花岗岩	锆石	U-Pb ICPMS	272±6	本文
	博罗科努山	花岗岩	锆石	U-Pb ICPMS	266±6	本文
	哈希勒根达坂	花岗岩	锆石	U-Pb ICPMS	280±5	本文
	哈希勒根达坂	花岗岩	锆石	U-Pb ICPMS	294±7	本文
	巴音布鲁克北	花岗岩	钾长石	Ar-Ar Plateau	274.8±0.4	Wang et al., 2004
	乌鲁木齐西	花岗岩	-	K-Ar	285	新疆地矿局，1993
	乌鲁木齐东	花岗岩	黑云母	K-Ar	265.5	Hu et al., 1986
	乌鲁木齐东	花岗岩	黑云母	K-Ar	256.3	Hu et al., 1986
	乌鲁木齐南	拉斑玄武岩	锆石	U-Pb SHRIMP	289±5	舒良树等，2005
	觉罗塔格	花岗岩	-	K-Ar	292	王作勋等，1990
	觉罗塔格	花岗岩	-	K-Ar	293	新疆地矿局，1993
	库尔勒北	花岗岩	黑云母	Ar-Ar	286	Yin et al., 1996
	库尔勒北	花岗岩	角闪石	Ar-Ar	262	Yin et al., 1996
	库米什	花岗岩	锆石	U-Pb ICPMS	252±4	本文
	科克苏	花岗岩	锆石	U-Pb ICPMS	277±3	本文

前人的研究表明，二叠纪岩浆岩属于碱性系列，火山岩具有双峰式特点，地球化学显示板内岩浆活动的构造环境（Allen et al., 1992；Chen et al., 1999；陈江锋等，1994, 2000；Shu et al., 2005）。二叠纪岩浆岩主要沿韧性剪切带分布，其成因可能与走滑剪切作用有关，二者在天山构造演化中，是一期重要的构造热事件，它很可能使早期的构造、变质事件发生部分热改造。例如，库勒湖和长阿吾孜一带的云母片岩中黑云母 $^{40}Ar/^{39}Ar$ 年龄为 259±3.3 Ma 和 245±0.3 Ma（蔡东升等，1995；郝杰等，1993）。

值得提出的是，从图 7-2 可以看出，二叠纪红色砂岩、砾岩在整个天山地区也普遍发育（新疆地矿局，1993；Caroll et al., 1995；Allen et al., 1995；崔智林等，1996）。其中砾岩中

含有不同岩性成分的河流相砾石，作为红色“磨拉石”沉积的底部不整合在前二叠纪的地层之上，表明二叠纪时，天山会聚造山作用已经结束，整个天山进入陆内演化阶段。

第三节 伊犁及其邻区大地构造划分

1. 构造缝合带及其时代讨论

如前文所论述，西天山发育数条蛇绿混杂岩带和高压变质岩带，它们主要分布在巴音沟、干沟-米什沟、长阿吾孜-科克苏-穹库什太、阿合奇、黑英山、库勒湖、乌瓦门和榆树沟-库米什等地（图 2-7）。一直以来，巴音沟和干沟-米什沟蛇绿混杂岩带被认为是北天山缝合带（Windley et al., 1990; Allen et al., 1992; Gao et al., 1998; Zhou et al., 2001），但是，考虑到：1）巴音沟蛇绿岩中放射虫硅质岩时代为晚泥盆世-早石炭世，而混杂岩中有晚石炭世的复理石块体，因而该蛇绿混杂岩最终形成的时代应为晚石炭世末。现有的地层学和同位素年代学证据表明，干沟-米什沟蛇绿岩的时代为晚奥陶世-志留纪；2）巴音沟蛇绿混杂岩带以南为伊犁晚中泥盆世-石炭纪岩浆岛弧，干沟-米什沟蛇绿混杂岩带以南则发育奥陶纪-志留纪中天山岛弧火山岩，而北天山石炭纪火山岛弧发育在两条蛇绿混杂岩带之间（见第四、五章）。因此，本论文认为，巴音沟和干沟-米什沟蛇绿混杂岩带属于两个不同时代、不同构造位置的缝合带，其中巴音沟蛇绿混杂岩带为北天山缝合带，代表北天山洋盆（肖序常等，1992）向南的俯冲消减作用，并与伊犁岩浆岛弧的形成有关。北天山-博格达石炭纪火山岛弧的形成也可能与该缝合带有关，但由于受新生代推覆作用的影响，北天山蛇绿混杂岩与北天山-博格达岛弧火山-碎屑岩向北逆冲在准噶尔中-新生代沉积盆地之上，导致北天山蛇绿混杂岩带在东天山可能被掩盖在推覆体之下而没有出露。在图 7-3 中，北天山缝合带被表示为 S3，为天山造山带中形成时间最晚（晚石炭世末）的一条缝合带。

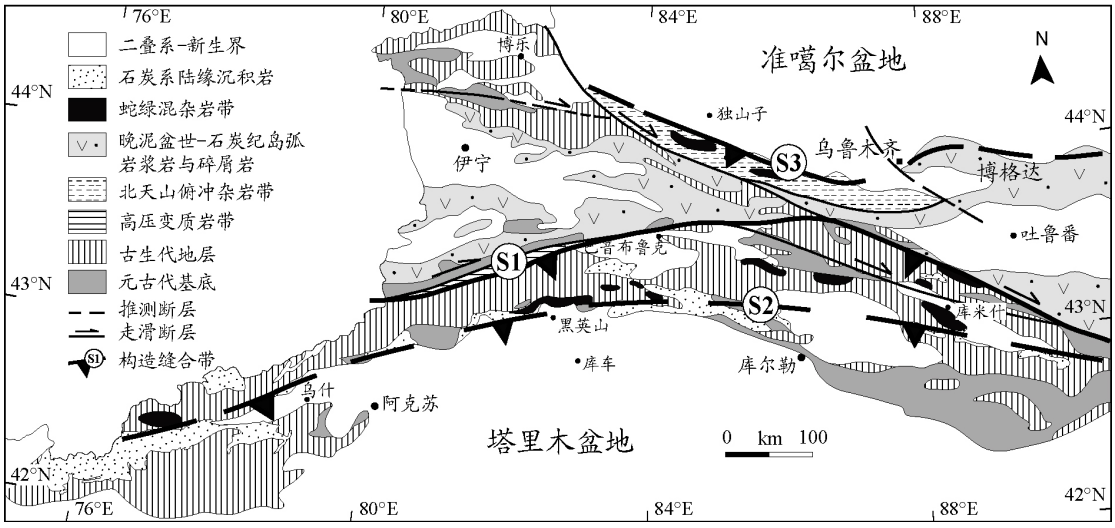

图 7-3 西天山构造简图

（S1，早-中古生代天山洋缝合带；S2，南天山晚泥盆世-早石炭世缝合带；S3，北天山晚石炭世缝合带）

除巴音沟和干沟-米什沟蛇绿混杂岩以外，西天山其它蛇绿混杂岩曾被当作同一个构造缝合带，即“南天山缝合带”（Windley et al., 1990; Allen et al., 1992）。前人认为，“南天山缝合带”的构造位置从科克苏高压变质岩到青布拉克断裂一带，而位于其南部的蛇绿混杂岩则属于从“南天山缝合带”向南的构造推覆体或飞来峰。“南天山缝合带”因此被认为代表一个朝北的洋壳俯冲带，并与伊犁岩浆岛弧的形成有关（Gao et al., 1998；Klemd et al., 2005；朱永锋等，2005）。

实际上，长阿吾孜-穹库什太一带的蛇绿岩年龄为 410-440 Ma，与干沟-米什沟蛇绿混杂

岩的时代比较一致。蓝片岩相高压变质岩的时代为 350-330 Ma（Gao et al., 2000; Gao and Klemd, 2003；Klemd et al., 2005），其中榴辉岩相高压变质作用可能早于 350 Ma，绿片岩相退变质作用的时代为 330-316 Ma（见第五章），这些年龄比伊犁岛弧岩浆岩的年龄（389 Ma ~ 310 Ma）更为年轻，表明高压变质岩与伊犁岛弧岩浆活动之间没有直接联系。另一方面，科克苏高压变质岩和干沟-米什沟蛇绿混杂岩中运动学标志均指示从南向北剪切推覆的运动动向（第五章）。同时，奥陶纪-志留纪钙碱性火山岩、火山碎屑岩零星出露在米什沟蛇绿混杂岩以南、那拉提断裂以南和乌什以北地区。因此，科克苏高压变质岩和干沟-米什沟蛇绿混杂岩可能代表同一个洋壳的残片（即前人所谓“南天山洋”，本论文改称“天山洋”）。在奥陶纪时，天山洋开始向南俯冲，并最终在晚泥盆世-早石炭世关闭，形成天山洋缝合带，该缝合带为天山地区最早的一个缝合带，图 7-3 中用 S1 表示。

最后，出露在天山南部阿合奇、黑英山、库勒湖、乌瓦门和榆树沟-库米什一带的蛇绿混杂岩，从时代上，它们的基质均形成于晚泥盆世-早石炭世（第五章），基质中包含的辉长岩年龄为 400~380 Ma；在运动学上，大部分蛇绿混杂岩中发育有韧性变形构造，且指示从南向北的剪切推覆动向，与普遍发育在该蛇绿混杂岩北侧志留系-泥盆系片岩和大理岩中的运动学标志完全一致。这些变形特征不支持该蛇绿混杂岩是北部天山洋缝合带构造推覆体的认识。董云鹏等（2005）对乌瓦门蛇绿岩的地球化学研究表明，这些洋壳物质形成于弧后盆地环境，与科克苏-干沟一带蛇绿岩的洋中脊环境不同。因此，作者认为，位于天山南部的蛇绿混杂岩可能代表一个与天山洋缝合带完全不同的单独的缝合带，它代表一个形成于早-中泥盆世的弧后盆地，在中泥盆世向南俯冲，并在晚泥盆世-早石炭世最终关闭。在图 7-3 中，该缝合带表示为 S2。南天山蛇绿混杂岩带是该缝合带在南北向挤压作用下不断向北推覆形成的，而真正的缝合带位于南天山断裂一带，向东则被掩盖于塔里木盆地北缘中-新生代沉积物之下。在库尔勒以东，它位于库鲁克塔格地区塔里木基底以北，并经过库米什以南，延伸到东天山。

2. 天山造山带前二叠纪构造单元划分

经过对后石炭纪地质事件和构造变形的分析与剔除，图 7-4 描述了前二叠纪天山造山带的构造轮廓，即上文所讨论的三个缝合带和它们所分隔的的主要构造单元：准噶尔、（北天山）、伊犁、中天山和塔里木。

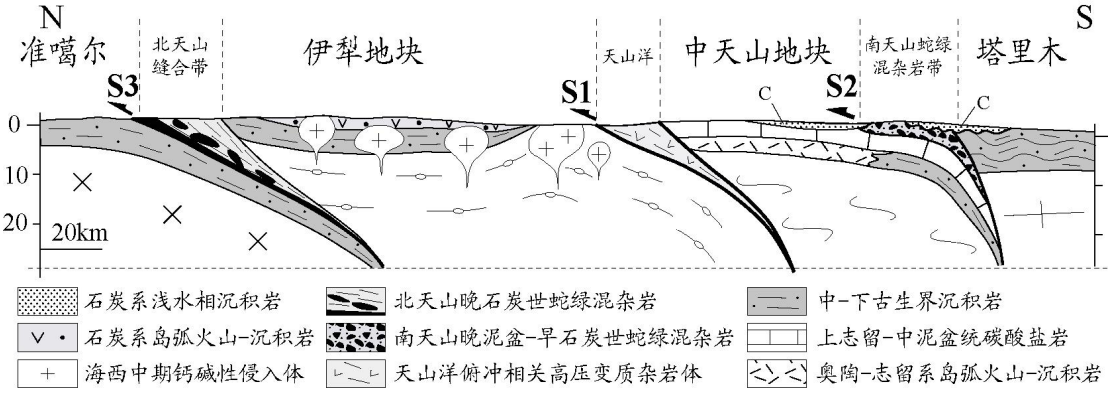

图 7-4 西天山前二叠纪构造恢复图

关于准噶尔和塔里木的构造属性，前文（第二章）已有论述，塔里木属于一个具有元古代基底的大陆板块已为众所周知，虽然准噶尔盆地构造基底的性质目前仍存在较大争议，但本论文主要研究伊犁晚古生代构造演化，因此将准噶尔作为一个早古生代的大陆地块。在北天山缝合带（S3）以北，北天山构造带主要为一个晚石炭世俯冲杂岩体，由浊积复理石和蛇绿混杂岩组成，向东，北天山为石炭纪火山岛弧，发育在博格达和后峡地区。伊犁地块

是一个具有元古代结晶基底的早古生代被动大陆边缘，以寒武纪-志留纪大陆坡沉积为特征，在晚古生代（晚中泥盆世-石炭纪）时，由于北天山洋盆的俯冲，转变为一个活动大陆边缘，表现为岛弧岩浆作用和陆源碎屑沉积作用。虽然伊犁地块以北天山断裂为界，但没有证据显示，北天山断裂在前二叠纪时已经存在。因此，伊犁地块的真正北界应为北天山俯冲杂岩（蛇绿混杂岩带）。北天山-博格达岛弧的基底性质虽然目前尚不清楚，但是它很可能与伊犁岛弧共同以北天山俯冲杂岩为北界，与北天山洋盆的俯冲作用有关，而现今的构造位置则可能是二叠纪走滑事件以及新生代陆内再造山作用的结果。

中天山位于天山洋缝合带（S1）和南天山蛇绿混杂岩带（S3）之间，其元古代基底出露于巴伦台-青布拉克一带以及黑英山地区，属于一个大陆微地块。奥陶系-志留系火山岩和火山碎屑岩组合表明，中天山在早古生代为一个活动大陆边缘，其成因可能与位于伊犁地块和中天山微地块之间的天山洋向南的早期俯冲作用有关。在中天山北缘，未变质的志留系复理石褶皱变形特征以及 S1 高压变质带与蛇绿混杂岩带中的韧性变形运动学显示从南向北的剪切推覆作用。在中天山南缘，中泥盆世条带状硅质岩显示沉积环境由浅海向半深海的转变。志留系火山碎屑岩与泥盆系大理岩发生了强烈韧性变形，可能与南天山蛇绿混杂岩推覆体从南向北的剪切推覆作用有关。下石炭统陆缘碎屑岩和砾岩不整合覆盖在早古生代地层和蛇绿混杂岩之上。石炭系中没有任何火山活动的迹象，因此，中天山地块早古生代和晚古生代所处的构造环境明显不同于伊犁地块。

中天山南缘边界以蛇绿混杂岩为主，本文将其归为南天山，即南天山蛇绿混杂岩带，其根部为中天山地块与塔里木板块之间的缝合带（S2）。蛇绿混杂岩带中镁铁岩的地球化学和年代学表明，该缝合带可能代表天山洋早期俯冲过程中形成的南天山弧后盆地（边缘海）。南天山蛇绿混杂岩形成的时代为晚泥盆世-早石炭世，代表弧后盆地最终关闭的时间。南天山蛇绿混杂岩带以南的早古生代地层主要以陆源沉积为主，以褶皱变形作用为特征，在岩相学和变形特征上明显不同于中天山南缘韧性变形带，而属于塔里木北缘前陆褶皱带。值得提出的是，在塔里木北缘志留纪-泥盆纪地层中未见任何与南天山弧后盆地俯冲作用有关的火山物质和侵入岩体，可能与南天山弧后盆地洋壳规模较小、扩张时间较短以及快速俯冲作用等因素有关。

第四节 伊犁及相邻地块古生代地球动力学演化模式

在上述讨论的基础上，本文提出了一个关于伊犁地块及西天山古生代构造演化的二维剖面模式（图 7-5），该模式没有表示出二叠纪近东西向走滑剪切作用对造山带的改造作用，而以南北向洋陆会聚造山作用为主。

在奥陶纪-早志留世，中天山和塔里木为一个整体，在伊犁地块和中天山-塔里木板块之间存在一个大洋地壳，即天山洋。天山洋在晚奥陶世-中志留纪世向中天山-塔里木板块发生初始俯冲，形成中天山早古生代火山岛弧。由于天山洋的俯冲作用，在中天山岛弧南缘形成弧后拉张作用，南天山弧后盆地开始形成，中天山微地块从塔里木板块开始裂解。此时，伊犁地块处于被动大陆边缘环境。在中志留-中泥盆世期间，天山洋持续俯冲，南天山弧后盆地逐渐拉开，并在中天山南缘形成半深海环境。与此同时，在伊犁和准噶尔地块之间，存在一个洋盆，即北天山洋盆。中泥盆世晚期-晚泥盆世末-早石炭世初，天山洋快速俯冲、关闭，导致伊犁地块和中天山地块发生碰撞，拼合为一个整体，并发生高压变质作用。此时南天山弧后盆地开始向南快速俯冲并在早石炭世初关闭，形成南天山蛇绿混杂岩带，伊犁-中天山再次与塔里木板块拼合。与此同时，北天山洋盆从中晚泥盆世开始向南俯冲，伊犁地块转变为活动大陆边缘。早石炭世，北天山洋盆继续俯冲，在伊犁南部和天山洋缝合带地区造成弧后拉张作用，引发高压变质岩开始折返，发生退变质作用。晚石炭世末，北天山洋盆最终关闭，伊犁岛弧岩浆活动结束，晚石炭世复理石增生楔与洋壳碎片混杂堆积到一起，形成北天

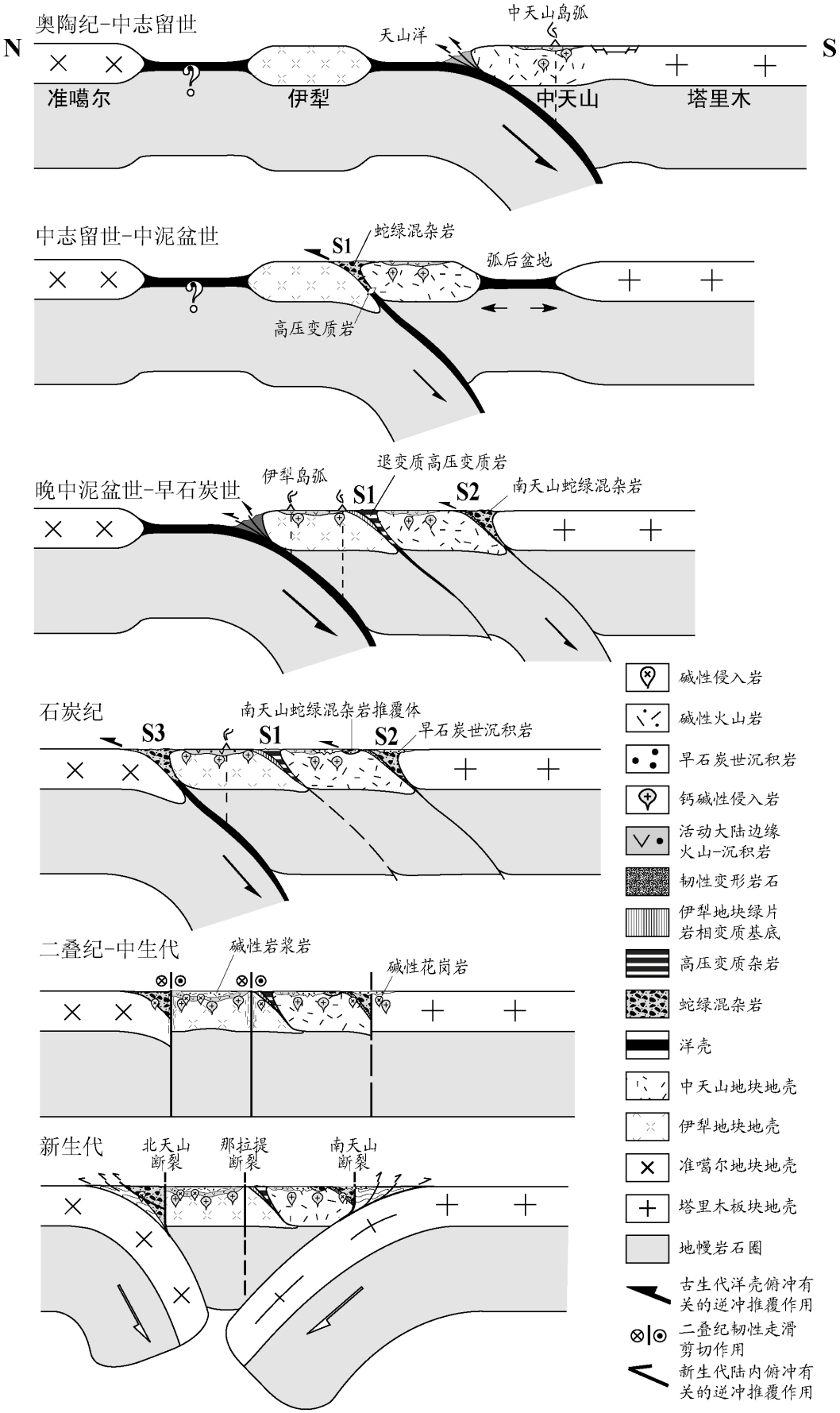

图 7-5 伊犁及邻区地块古生代地球动力学演化二维模式

山蛇绿混杂岩。晚石炭世末，西天山俯冲、碰撞造山作用完成，各陆块完全会聚、拼合到一起，此时各地块中岩石获得的古地磁极已基本一致。

西天山晚古生代地块之间的俯冲、碰撞作用可能是斜向的，从而使这些碰撞在垂直方向上的分量减小，成为软碰撞，而侧向分量增加。碰撞作用的侧向分量则表现为碰撞后陆块之间沿构造带发生走滑剪切作用。晚石炭世末-晚二叠世期间，伊犁、准噶尔和塔里木之间相对逆时针旋转正是这种侧向走滑剪切作用的体现。二叠纪期间，发生在天山内部的右旋走滑位移达 1000 km 左右，导致天山造山带内原始的构造关系发生了明显改变。新生代期间，作为印度板块和欧亚板块之间陆陆碰撞作用的远距离响应，塔里木和准噶尔盆地分别向天山发生了陆内俯冲作用，从而使天山造山带内古生代构造带被再次改造，最终形成现今巍峨壮观的天山山脉。

第八章 主要结论

1. 天山后造山多期构造叠加事件对古生代造山带造成强烈改造和破坏

天山是一个古生代造山带，并经后碰撞走滑剪切和新生代陆内造山作用强烈叠加、改造。现有的研究结果表明，新生代以来天山地壳缩短和快速隆升作用在其南、北缘造成了强烈的双向逆冲推覆作用，使古生代构造带被再次变形，甚至被宽达数十公里的推覆体所掩盖。古地磁研究表明，在晚石炭世-晚二叠世期间，伊犁-准噶尔相对于塔里木板块发生的近 50°逆时针旋转，地质上表现为沿天山主要韧性剪切带的右旋走滑，走滑距离达 1000 km。如此大的剪切位移很可能使原有的构造界线受到破坏，地块间相对位置发生变化。因此，研究天山大地构造和构造演化，不仅需要剔除新生代构造变形的影响，还需要考虑到后碰撞剪切走滑作用对古生代造山带的改造，而后者在以往的研究中估计不够。

2. 以俯冲-碰撞为主的天山造山作用在晚石炭世末基本结束

构造地质学、年代学和古地磁学结果表明，天山大型走滑剪切带的变形年龄小于 300Ma，推覆剪切变形的时代以及与造山作用有关的蛇绿混杂岩及岩浆岩的年龄多早于 300Ma，岩石学和构造地质学证据不支持区域走滑的造山模型。古地磁数据表明，自晚石炭世以来，天山地区主要陆块（准噶尔、伊犁和塔里木）之间已经没有纬度上的差异，并且在晚石炭世-晚二叠世期间以及晚二叠世以来，各陆块之间也没有发生明显的开、合事件，表明各陆块及周围洋盆的会聚造山作用至少在晚石炭世末已经结束，因而不支持三叠纪碰撞造山的认识。

3. 伊犁为石炭纪活动大陆边缘而非大陆裂谷

伊犁地区原石炭系火山岩和海西期侵入岩形成的时代为 389~301Ma，其中岩浆活动高峰期为 359~301Ma，且在伊犁地块南、北部表现一致。这些岩浆岩的地球化学具有俯冲带钙碱性岩浆岩的特征，而同位素组成表明它们来自亏损的地幔岩浆，并经受了上地壳或陆源沉积物的混染作用。结合岩石学、火山岩喷发序列及与之伴生的陆源碎屑岩岩相特征等，本文认为，伊犁地块在中泥盆世末-石炭纪末期间为活动大陆边缘环境。分布在后峡以南的北天山石炭系火山岩具有与伊犁岛弧火山岩一致的岩相学和地球化学特征，因此二者可能属于同一个火山岛弧，它们现今的相对位置可能主要是二叠纪右旋走滑剪切作用的结果。

4. 北天山缝合事件形成伊犁岛弧并可能向东天山延伸

鉴于干沟-米什沟蛇绿岩时代为奥陶-志留纪，且位于北天山岛弧以南，而北天山巴音沟蛇绿岩时代则为中、晚泥盆世-早石炭世，且位于伊犁和北天山岛弧以北，据此认为 2 条蛇绿混杂岩带分别属于 2 个不同的缝合带。巴音沟蛇绿混杂岩中晚石炭统复理石以构造岩块和基质同时出现，表明混杂岩形成的时代应为晚石炭世末，而混杂岩中的变形运动学特征指示北天山洋盆向南的俯冲作用，并与伊犁和北天山岛弧的形成有关。由于北天山岛弧向东经博格达至东天山，因此本论文推断，北天山缝合带可能经博格达山以北向东延伸。目前在博格达及以东未见蛇绿混杂岩的露头，分析认为是由于博格达山在中、新生代以来快速隆升，造成大型推覆体，并将该缝合带的东延部分掩盖。

5. 天山洋在奥陶纪向南俯冲，晚泥盆世末关闭碰撞，与伊犁岛弧无关

长阿吾孜-科克苏河一带的蛇绿岩年龄与干沟-米什沟蛇绿岩时代一致，科克苏河退变质的蓝片岩和退变质绿片岩相石英岩的 Ar/Ar 年龄为 330~315Ma, 前人所得蓝片岩的变质年龄为 345~350Ma，因而与俯冲、碰撞有关的高压（或超高压）变质作用至少发生在 350Ma 以前，这些年龄均比伊犁岩浆岛弧活动的最晚时代明显要老。此外，科克苏地区高压变质带、伊犁南缘基底韧性变形带以及干沟蛇绿混杂岩带中的变形运动学均指示天山洋向南俯冲，因而与伊犁岩浆岛弧的形成无关。在长阿吾孜-科克苏-干沟-米什沟以南，奥陶-志留纪地层中发育岛弧火山岩和火山碎屑岩，表明天山洋在奥陶纪开始向南俯冲形成火山岛弧，晚泥盆世末关闭并发生碰撞。

6. 南天山蛇绿混杂岩带是中天山地块南缘中古生代弧后边缘海

在天山最南部的阿合奇-黑英山-库勒湖-乌瓦门-库米什一带，蛇绿混杂岩中镁铁岩年龄为晚志留-中泥盆世，而基质年龄为晚泥盆-早石炭世，蛇绿混杂岩及其构造基底的变形运动学反映从南向北的推覆运动方向，指示该区曾发生过一期从北向南的洋壳消减过程，因此该蛇绿混杂岩带应代表南天山缝合带。前人对蛇绿岩的地球化学研究表明，该缝合带可能为天山洋向南俯冲时形成的弧后盆地或边缘海。位于天山洋缝合带与南天山缝合带之间的早古生代火山岛弧，属于中天山微地块，其前寒武纪基底主要出露在黑英山、巴伦台和冰达坂一带。

致　谢

本论文是在导师舒良树教授、Michel Faure 教授、Dominique Cluzel 教授、陈岩教授和 Jacques Charvet 教授的悉心指导下完成的。首先感谢我的中方导师舒良树教授 8 年来对我的辛勤培养，恩师严谨的治学风范、一丝不苟的工作精神、真诚热情的为人处事态度是我终生学习的楷模。多年来，舒老师对我在学习上耐心的指导、学业上精心周密的安排和生活上无微不至的关怀与帮助，都使我无比感动并将铭记于心。8 年来，我在学业上的任何进步，都倾注了舒老师大量的心血和汗水。另外，还要由衷地感谢他对我的推荐，才使我有机会到法国去学习。感谢我的法方导师 Faure 教授、Cluzel 教授、陈岩教授和 Charvet 教授，他们渊博的专业知识、深厚的学术造诣、敏锐的学术思想、以及野外工作期间给我耐心细致的讲解，都使我受益匪浅，也将对我今后的学术生涯产生深远的影响。也感谢他们带我参观、学习 Alps、Massif Central 和 Corbiere 等地区的地质概况。在我旅法学习期间，陈岩老师对我在工作上给予了大力支持、启发和引导，生活上提供了热情的帮助和便利，以及体育锻炼方面的培养，使我不仅顺利地度过了在法学习的时间，还让我增加了很多社会经验。三年来，良师般的教诲、长辈般的关怀和朋友般的帮助，都使我终生难忘。

感谢地科系卢华复老师、周新民老师、孙岩老师、张庆龙老师、王良书老师、杨振宇老师、贾东老师、朱文斌老师、邱检生老师、张文兰老师等在专业和实验上对我的指导和帮助。解国爱博士、孙涛博士和王胜利博士也在工作中给予了诸多便利。感谢王淑君老师、刘宪华老师、张孝琴和张晓茜老师对我在学习和生活上的帮助。

特别感谢法国奥尔良大学 O. Monod, M. Vidal, N. Lebreton, R. Augier 在野外和专业知识方面的帮助，另外，J.G. Badin, S. Janiec, M. Hatton, N. Pothier 等在实验和资料方面给予了很大帮助。湛胜在一同旅法期间，在学习和生活等方面提供了帮助。有幸先后与 C. Cartier, J.Y. Talbot, P. Trap, A. Joly 分享办公室，他们给了我学习、论文和语言上的很大帮助。J. Charreau, Eric Gloaguen, M. Duguet, E. Be, J. Tuduri, N. Volland-Tuduri, N. Charles, M. Essalhi 和 S. Drouin 等在论文工作中给予热情帮助。感谢 K. De Jong 在 Ar/Ar 定年方面给予的帮助。

感谢师弟马前在野外工作期间的全力帮助。另外，闵斌、陈竹新、王淼、王彬及其他没有提到名字的同学都对我的论文工作给予了帮助和鼓励。

新疆自治区国家 305 办公室的马映军主任、王宝林主任、王金良主任、徐新主任、王煜处长、朱炳玉处长、郭红处长等领导和其他工作人员为论文野外工作给予了大力支持和热情帮助，《新疆地质》编辑部的李强老师、崔曦老师等帮助作者查阅资料。法国南锡实验室、中科院广州地化所、巴黎全球物理研究所古地磁实验室、奥尔良磁学实验室、南京大学成矿作用重点实验室、澳大利亚 Tasmania 大学 Meffre 教授、法国 Rennes 大学 Ruffet 教授等为分析测试给予了帮助，法国奥尔良地矿所（BRGM）对资料文献查阅提供了方便，在此一并致谢。

最后，永远不会忘记父母对我的理解与支持。特别感谢我的姐姐、姐夫和哥哥，多年来在学习上不倦的鼓励和物质上全力的支持，才使我有机会完成今天的学业。感谢我的爱人薛春燕对我学习上一贯的激励和支持，特别是论文期间时间紧迫的情况下，全力支持我完成论文。

参考文献

[1] Allègre, Claude J., Dalila Ben Othman, 1980. Nd−Sr isotopic relationship in granitoid rocks and continental crust development: a chemical approach to orogenesis. Nature, 286: 335 - 342.

[2] Allen M B, Windley B F, Zhang Chi, et al. 1993. Evolution of the Turfan basin, Chinese central Asia. Tectonics, 12(4): 889-896.

[3] Allen M.B., Windley B.F., Zhang C., 1992. Paleozoic collisional tectonics and magmatism of the Chinese Tien Shan, Central Asia. Tectonophysics, 220: 89-115.

[4] Allen, M.B., Sengör, A.M.C., Natal'in, B.A., 1995. Junggar, Turfan and Alakol basins as Late Permian to ?Early Triassic extensional structures in a sinistral shear zone in the Altaid orogenic collage, Central Asia. Journal of Geological Society of London, 152: 327-338.

[5] Allen, M.B., Vincent, S.J., Wheeler, P.J., 1999. Late Cenozoic tectonics of the Kepingtage thrust zone: Interactions of the Tien Shan and Tarim basin, northwest China. Tectonics, 18 (4): 639-654.

[6] Allen, M.B., Windley, B.F., Zhang, C., et al., 1993. Evolution of the Turfan basin, Chinese central Asia. Tectonics, 12 (4): 889-896.

[7] Avouac, J.P., Tapponnier, P., Bai, M., et al., 1993. Active thrusting and folding along the northern Tien Shan and Late Cenozoic rotation of the Tarim relative to Dzungaria and Kazakhstan. Journal of Geophysics Research, 98 (B4): 6755-6804.

[8] Bai, Y.H., Cheng, G.L., Sun, Q.G., et al., 1987. Late Paleozoic polar wander path for the Tarim platform and its tectonic significance. Tectonophysics, 139: 145-153.

[9] Barbarin, B., 1999. A review of the relationships between granitoid types, their origins and their geodynamic environments. Lithos., 46: 605-626.

[10] Bazhenov, M.L., Burtman, V.S., Dvorova, A.V., 1999. Permian paleomagnetism of the Tien Shan fold belt, Central Asia: Post-collisional rotation and deformation. Tectonophysics, 312 (2-4): 303-329.

[11] Bazhenov, M.L., Chauvi, A., Audibert, M., et al., 1993. Permian and Triasic paleomagnetism of the southwestern Tien Shan: timing and mode of tectonic rotations. Earth and Planetary Sciences Letters, 118: 195-212.

[12] Bazhenov, M.L., Collins, A.Q., Kirill E.D., et al., 2003. Paleozoic northward drift of the North Tianshan (Central Asia) as revealed by Ordovician and Carboniferous paleomagmatism. Tectonophysics, 366: 113-141.

[13] Brookfield, M.E., 2000. Geological development and Phanerozoic crustal accretion in the western segment of the southern Tien Shan (Kyrgyzstan, Uzbekistan and Tagikistan). Tectonophysics, 328 : 1-14.

[14] Buckman, S., Aitchison J.C., 2004. Tectonic evolution of Paleozoic terranes in West Junggar, Xinjing, NW China, in Aspects of the tectonic evolution of China, edited by J. Malpas, C.J.N. Fletcher, J.R. Ali, and J.C. Aitchison, Geol. Soc., London, Spec. Publ., 226: 101-129.

[15] Bump, H.A., Sheehan, A., 1998. Crustal thickness variations across the northern Tien Shan from teleseismic receiver functions. Geophysica Research Letters, 25 (7): 1055-1058.

[16] Burchfiel, B.C., Brown, E.T., Deng, Q.D., et al., 1999. Crustal shortening on the Margins of the Tien Shan, Xinjiang, China. International Geology Review, 41: 665-700.

[17] Burtman, V.S., 1975. Structural geology of variscan Tien Shan, USSR, American Journal of Sciences, 275 (A): 157-186.

[18] Buslov, M.M., Fujiwara, Y., Iwata, K., et al., 2004. Late Paleozoic-Early Mesozoic Geodynamics of Central Asia. Gondwana Research, 7 (3): 791-808.

[19] Butler, R.F., 1998. Paleomagnetism: magnetic domains to geologic terrains, Electronic edition. Department of Geosciences, University of Arizona, Tucson, Arizona, USA.

[20] Carroll, A. R., Liang, Y., Graham, S., et al., 1990. Junggar basin, NW China: trapped late Paleozoic ocean. Tectonophysics, 186: 1-14.

[21] Carroll, A.R., Graham, S.A., Hendrix, M.S., et al., 1995. Late Paleozoic tectonic amalgamation of NW China: sedimentary records of the northern Tarim, northwestern Turpan, and southern Junggar basins. Bull. Soc. Am., 107: 571-594.

[22] Chaffey, D.J., Cliff, R.A., Wilson, B.M., 1989. Characterization of the St Helena magma source. In: Saunders, AD & Norry, MJ (eds) Magmatism in the Ocean Basins. Geological Society, London, Special Publications 42: 257–276.

[23] Charreau, J., Chen, Y., Gilder, S., et al., 2005. Magnetostratigraphy and rock magnetism of the Neogene Kuitun He section (northwest China): implications for Late Cenozoic uplift of the Tianshan mountains. Earth and Planetary Science Letters, 230 (1-2): 177-192.

[24] Charvet, J., Laurent-Charvet, S., Shu, L.S., et al., 2001. Paleozoic Continental Accretions in Central Asia Around Junggar Block: New Structural and Geochronological Data. Gondawana Research, 4 (4): 590-592.

[25] Chen, Chuming, Lu, Huafu, Jia, Dong, et al., 1999. Closing history of the southern Tianshan oceanic basin, western China: an oblique collisional orogeny. Tectonophisics, 302: 23-40.

[26] Chen, Jiangfeng, Zhou, Taixi, Xie, Zhi, 2000. Formation of positive εNd(T) granitoids from the Alataw Mountains, Xinjiang, China, by mixing and fractional crystallization: implication for Phanerozoic crustal growth. Tectonophysics, 328: 53-67.

[27] Chen, Y., Cogné, J.P., Courtillot, V., 1992. New Cretaceous paleomagnetic poles from the Tarim Basin, Northwestern China. Earth and Planetary Science Letters, 114: 17-38.

[28] Cliff, R.A., Baker, P.E., Mateer, N.J., 1991. Geochemistry of inaccessible island volcanics. Chem., Geol., 92: 251-260.

[29] Cogné, J.-P., 2003. A MacintoshTM application for treating paleomagnetic data and making plate reconstructions. Geochem. Geophys. Geosyst., 4 (1): 10.1029/2001GC000227.

[30] Coleman, R.G., 1989. Continental growth of northwest China. Tectonics, 8 (3): 621-635.

[31] Coleman, R.G., 1994. Terrains (units) in the Western half of the geodynamic map. In: Stanford-China Geosciences industrial affiliates program annual review, Stanford University, Palo Alto, USA, 1-8.

[32] Cox K.G., Bell J.D., Pankhurst R. J., 1979. The Interpretation of igneous rocks. George Alien & Unwin, London, 450.

[33] Cunningham, W.D., Windley, B.F., Dorjnamjaa, D., et al., 1996. A structural transect across the Mongolian Western Altai: Active transpressionnal mountain building in central Asia. Tectonics, 15 (1): 142-156.

[34] Davies, G.R., Gledhill, A., Hakesworth, C., 1985. Upper crustal recycling in southern Britain: evidence from Nd and Sr isotopes. Earth Planet. Sci. Lett., 75: 1-12.

[35] De Jong, K., 2003. Very fast exhumation of high-pressure metamorphic rocks with excess 40Ar and inherited 87Sr, Betic Cordilleras, southern Spain. Lithos, 70: 91-110.

[36] De Jong, K., Xiao, W.J., Windley, B.F., et al., 2006. Ordovician 40Ar/39Ar phengite ages from the blueschist-facies Ondor Sum subduction-accretion complex (Inner Mongolia) and implications for the early Paleozoic history of continental blocks in China and adjacent areas. Am. J. Sci., in Press.

[37] Dobretson,N,L., Buslon, M.M., 2004. Serpentinitie Mélanges Associated with HP and UHP Rocks in Central Asia. International Geology Review, 46: 957-980.

[38] Dobretsov, N.L., Coleman, R.G., Liou, J.G., et al., 1987. Blueschist belt in Asia and possible periodicity of blueschist facies metamorphism. Ofioliti, 12: 445-456.

[39] Enkin, R.J., 2003. The direction-correction tilt test: An all-purpose tilt/fold test for paleomagnetic studies. Earth Planet. Sci. Lett., 212: 151–166.

[40] Fang, D.J., Chen, H.L., Jin, G.H., et al., 1990. Late Paleozoic and Mesozoic paleomagnetism and tectonic evolution of Tarim terrane, in: Wiley, T.J., D.G. Howell, F.L. Wong (eds.), Terrane analysis of China and the Pacific rim, Houston (USA), Circum-Pacific Council for Energy and Mineral Resources Earth Science Series, 13: 251-255.

[41] Fisher, R., 1953. Dispersion on a sphere. Proc. R. Soc. London, Ser. A 217: 295–305.

[42] Gao, J., Klemd, R., 2000. Eclogite Occurrences in the Southern Tianshan High-Pressure Belt, Xinjiang, Western China. Gondwana Res., 3(1): 33-38.

[43] Gao, J., Klemd, R., 2003. Formation of HP-LT rocks and their tectonic implications in the western Tianshan Orogen, NW China: geochemical and age constraints. Lithos., 66:1–22.

[44] Gao, J., Zhang, L., Liu, S., 2000. The 40 Ar/39Ar age record of formation and uplift of the blueschists eclogites in the western Tianshan Mountains. Chinese Science Bulletin, 45 (11): 1047-1051.

[45] Gao, Jun, He, Guoqi, Li, Maosong, et al., 1995. The mineralogy, petrology, metamorphic PTDt trajectory and exhumation mechanism of blueschists, south Tianshan, northwestern China. Tectonophysics, 250: 151-168.

[46] Gao, Jun, Li, Maosong, Xiao, Xuchang, et al., 1998. Paleozoic tectonic evolution of the Tianshan orogen, northwestern China. Tectonophysics, 287: 213-231.

[47] Gerlach, D.C., Cliff, R.A., Davies, G.R., et al., 1988. Magmasources of the Cape Verdes archipelago: isotopic and trace element constraints. Geochim. Acta, 52: 2979-2992.

[48] Gilder, S., Zhao, X.X., Coe, R.S., et al., 1996. Paleomagnetism and tectonics of the southern Tarim basin, northwestern China. Journal of Geophysical Research, 101: 22,015-22,031.

[49] Guo, Jian, Shu, L.S., Charvet, J., et al., 2002. Geochemical Features of the Two Early Paleozoic Ophiolitic Zones and Volcanic Rocks in the Central-Southern Tianshan Region, Xinjiang.Chinese Journal of Geochemistry, 21(4): 308-321.

[50] Guo, ZhaoJie, Yin, An, Robinsonb, Alexander, et al., 2005. Geochronology and geochemistry of deep-drill-core samples from the basement of the central Tarim basin. Journal of Asian Earth Sciences, 25 (1): 45-56.

[51] Hawkesworth, C. J., Hammill, M., Gledhill, A. R., et al., 1982. Isotope and trace element evidence for late-stage intra-crustal melting in the High Andes. Earth and Planetary Science Letters, 58 (2): 240-254.

[52] Hawkesworth, C.J., Gallagher, K., Hergt, J.M., 1993. Mantle and slab contributions in arc magmas. Annu. Rev. Earth Planet. Sci., 21: 175-204.

[53] Hawkesworth, C.J., Turner, S., Gallagher, K., et al., 1995. Calc-alkaline magmatism, lithospheric thinning and extension in the Basin and Range. Journal of geophysical research, 100 (B7): 10 271-10 286.

[54] Hendrix, M.S., Dumitru, T.A., Graham, S.A., 1994. Late Oligocene-Early Miocene unroofing in the Chinese Tian Shan: An early effect of the India-Asia collision. Geology, 22: 487-490.

[55] Heubeck, C., 2001. Assembly of central Asia during the middle and late Paleozoic. Geological Society of America, Memoir 194: 1-22.

[56] Hounslow, M.W., Davydov, V.I., Klootwijk, C.T., et al., 2004. Magnetostratigraphy of the Carboniferous: a review and future prospects, Newsl. Carbonif. Stratigr. 22: 35-40.

[57] Hsu, K. J., 1988. Relict back-arc basins: principles of recongnition and possible new examples from Chins. In: K. L. Kleinpell and C. Paola (Editors), New Perspectives in Basin Anslysis. Springer-Verlag, New York, 245-263.

[58] Hu, Aiqin, Jahn, Bor-ming, Zhang, Guoxin, et al., 2000. Crustal evolution and Phanerozoic crustal growth in northern Xinjiang: Nd isotopic evidence. Part I. Isotopic characterization of basement rocks . Tectonophysics, 328 (1-2): 15-51.

[59] Irvine T.N., Baragar W.R.A., 1971. A guide to the chemical classification of the common volcanic rocks. Can. J. Earth Sci., 8: 523-548.

[60] Jahn, B.M., 2004. The Central Asian Orogenic Belt and growth of the continental crust in the Phanerozoic. Geological Society Special Publications, 226: 73–100.

[61] Jahn, B.M., Griffin, W.L., Windley, B.F. (Eds.), 2000a. Continental growth in the Phanerozoic; evidence from Central Asia, Tectonophysics, 328: 1– 227.

[62] Jahn, B.M., Windley, B., Natal'in, B., et al., 2004. Phanerozoic continental growth in Central Asia. Journal of Asian Earth Sciences, 23: 599-603.

[63] Jahn, B.M., Wu, F., Chen, B., 2000b. Massive granitoid generation in Central Asia; Nd isotope evidence and implication for continental growth in the Phanerozoic. Episodes, 23: 82– 92.

[64] Jia, M., 1996. Petrology, geochronology, and tectonic significance of the south Tianshan blueschist belt, NW China, M.S. thesis, 50 pp., Stanford University, Californian (USA).

[65] Khain, E.V., Bibikova, E.V., Salnikova, E.B., et al., 2003. The Palaeo-Asian ocean in the Neoproterozoic and early Palaeozoic: new geochronologic data and palaeotectonic reconstructions. Precambran Research, 122: 329-358.

[66] Kirschvink, J.L., 1980. The least squares line and the analysis of paleoamgnetic data. Geophys. J. R. Astron. Soc., 62: 699–718.

[67] Klemd, R., 2003. Ultrahigh-pressure metamorphism in eclogites from the western Tianshan high-pressure belt (Xinjiang, western China)-Comment. Am. Mineral., 88: 1153-1156.

[68] Klemd, R., Bröcker, M., Hacker, B. R., et al., 2005. New age constraints on the metamorphic evolution of the high-pressure/low-temperature belt in the western Tianshan mountains, NW China. J. Geol., 113: 157–168.

[69] Klemd, R., Schroöter, F., Will, T. M., et al., 2002. Pt evolution of glaucophane-clinozoisite bearing HP-LT rocks in the western Tianshan orogen, NW China. J. Metamorph. Geol., 20:

239–254.

[70] Laurent-Charvet S., Charvet, J., Monie, P., et al., 2003. Late Paleozoic strike-slip shear zones in eastern Central Asia (NW China): new structural and geochronological data. Tectonics, 22 (2): 1099-1101.

[71] Laurent-Charvet S., Charvet, J., Shu, L.S., et al., 2002. Palaeozoic late collisional strike-slip deformations in Tianshan and Altay, eastern Xinjiang, NW China. Terra Nova, 14 (4) : 249-256.

[72] Laurent-Charvet, S., 2001. Accrétions continentales en Asie centro-orientale : évolution géodynamique et structurale du Tianshan et du Junggar oriental (nord-ouest Chine) au Paléozoïque. PhD thesis, University of Orleans, Orleans, France.

[73] Laurent-Charvet, S., Monié, P., Charvet, J., et al., 2001. New kinematic and Ar-Ar data on strike-slip ductile shear zones around Junggar basin, Xinjiang, NW China, in EUG XI, vol. CDROM, Cambridge Publications, Strasbourg, France.

[74] Le Bas M.J., Le Maitre R.W., Streckeisen A., et al., 1986. A chemical classification of volcanic rocks based on the total alkali-silica diagram. Journal of Petrology, 27: 745-750.

[75] Le Maitre, R.W., Bateman, P., Dudek, A., et al., 1989. A Classification of Igneous Rocks and Glossary of Terms: Recommendations of the International Union of Geological Sciences Subcommission on the Systematics of Igneous Rocks. Blackwell Scientific Publications Ltd, Oxford, 193.

[76] Li, X.P., Zhang, L.F., Ai, Y.L., 2003. Discovery and geological implication of rodingites derived from eclogites of ophiolites at Changawuzi, western Tianshan, China. Progress in natural science, 13 (12): 901-907.

[77] Li, Y.P., Li, Y.G., Sharps, R., et al., 1991a. Sinian paleomagnetic results from the Tarim block, Western China. Precambrian Research, 49: 61-71.

[78] Li, Y.P., Sharps, R., McWilliams, M., et al., 1989. Paleomagnetic results from Late Paleozoic dikes from the northwestern Junggar block, Northwestern China. Earth and Planetary Science Letters, 94: 123-130.

[79] Li, Y.P., Sharps, R., McWilliams, M., et al., 1991b. Late Paleozoic Paleomagnetic Results from the Junggar block, Northwestern China, Journal of Geophysical Research, 96: 16047-16060.

[80] Li, Yianping, Michael, Mcwilliams, Allan, Cox, et al., 1988. Late Permian paleomagnetic pole from dikes of the Tarim craton, China. Geology, 16: 275-278.

[81] Li, Yuejun, Sun, Longde, Wu, Haoruo, et al., 2005. Permo-Carboniferous radiolarians from the Wupata'erkan group, Western South Tianshan, Xinjiang, China. Acta Geologica Sinica, 79 (1): 16-23.

[82] Li, Yuejun, Wang, Zhaoming, Wu, Haoruo, et al., 2002. Discovery of radiolarian fossils from the Aiketik group at the western end of the South Tianshan Mountains of China and its implications. Acta geologica sinica, 76 (2): 146-154.

[83] Liegeois, J.P., 1998. Preface-Some words on the post-collisional magmatism. Lithos, 45: 15-17.

[84] Liew, T.C., and McCulloch, M.T., 1985. Genesis of granitoid batholiths of Penisular Malaysia and implications for models of crustal evolution: Evidence from a Nd-Sr isotopic and U-Pb lead study. Geochim. Cosmochim. Acta., 49: 587-600.

[85] Liu, C.Y., Li, T.H., 1990. Formation of sedimentary basins and terrane movement in

northwestern China. in Wiley, T.J., Howell, D.G., and Wong, F.L. Eds., Terrane analysis of China and the Pacific rim. Houston, Texas, Circum-Pacific Council for Energy and Mineral Resources Earth Science Series, 13: 227-229.

[86] Liu, L., Che, Z.C., Liu, Y.J., 1995. Geochemical Characteristics of the Plagiogranites in the Vicinity of Bingdaban, Central Tianshan. Chinese Journal of Geochemistry, 14 (3): 243-249.

[87] Liu, Yu. 2001. Early Carboniferous radiolarian fauna from Heiyingshan South of the Tianshan Mountains and its geotectonic significance. Acta geologica sinica, 75 (1): 101-108.

[88] McCulloch, M.T., Gamble, J.A., 1991. Geochemical and geodynamical constraints on subduction zone magmatism. Earth and Planetary Science Letters, 102: 358-374.

[89] McCulloch, Malcolm T., Chappell, Bruce W., 1982. Nd isotopic characteristics of S- and I-type granites. Earth and Planetary Science Letters, 58 (1): 51-64.

[90] McDougall, I., Harrison, T.M., 1988. Geochronology and thermochronology by the 40Ar/39Ar method, 212 pp., Oxford University Press, New York.

[91] McFadden, P.L., Ma, X.H., McElhinny, M.W., 1988. Permo-Triassic magnetostratigraphy in China: northern Tarim, Earth and Planetary Science Letters, 87, 152-160,

[92] Meffre, Sebastien, Nicholas G. Direen, Anthony J. Crawford，et al., 2004. Mafic volcanic rocks on King Island, Tasmania: evidence for 579 Ma break-up in east Gondwana. Precambrian Research, 135 (3): 177-191.

[93] Molnar, P., Tapponnier, P., 1975. Cenozoic tectonics of Asia: Effects of a continental collision, Science, 189: 419-426.

[94] Nakajima, T., Maruyama, S., Uchiumi, S., et al., 1990. Evidence for late Proterozoic subduction from 700 Myr-old blueschist in China. Nature, 346 (6281): 262-265.

[95] Natal'in, B.A., Celâl Sengör, A.M., 2004. Late Palaeozoic to Triassic evolution of the Turan and Scythian platforms: The pre-history of the Palaeo-Tethyan closure. Tectonophysics, 404: 175-202.

[96] Nelson, M.R., McCaffrey, R., Molnar, P., 1987. Source parameters for eleven earthquakes in the Tien Shan, central Asia: Determined by P and SH waveform inversion. J. Geophys. Res., 92: 12, 629-12, 648.

[97] Nie, Shangyou, David B., Rowley, Rob., et al., 1993. Paleomagnetism of Late Paleozoic rocks in the Tianshan, Northwestern China. Tectonics, 12: 568-579.

[98] Norman, M.D., Leeman, W.P., 1990. Open-system magmatic evolution of andesites and basalts from the Salmon Creek volcanics, southwestern Idaho, U.S.A. Chemical geology, 81 (3): 167-189 (27 ref.).

[99] Pearce J.A., Harris N.B.W., Tindle A.G., 1984. Trace element discrimination diagrams for the tectonic interpretation of granitic rocks. J. Petrol., 25: 956-983.

[100] Pearce J.A., Peate D.W., 1995. Tectonic implications of the composition of volcanic arc magmas. Annu. Rev. Earth Sci., 23: 251-285.

[101] Poupinet, G., Avouac, J.P., Jiang, M., et al., 2002. Intracontinental subduction and Palaeozoic inheritance of the lithosphere suggested by a teleseismic experiment across the Chinese Tien Shan: Terre Nova, 14: 18-24.

[102] Raymond, L.A., 1984. Classification of mélange. Geological Society of America Special paper, 198: 7-19.

[103] Renne, P.R., Swisher, C.C., Deino, A.L., et al., 1998. Intercalibration of standards, absolute ages and uncertainties in 40Ar/39Ar dating. Chem. Geol., 145: 117-152.

[104] Rollinson, H.R., 1993. Using Geochemical Data: evaluation, presentation, interpretation. Longman scientific technical, New York, 48-213.

[105] Ruffet, G., Féraud, G., Amouric, M., 1991. Comparison of 40Ar-39Ar conventional and laser dating of biotites from the North Trégor Batholith, Geochim. Cosmochim. Acta, 55: 1675-1688.

[106] Ruffet, G., Féraud, G., Ballèvre, M., et al., 1995. Plateau ages and excess argon in phengites: an 40Ar- 39Ar laser probe study of Alpine micas (Sesia zone, Western Alps, northern Italy), Chem. Geol. (Isotope Geoscience Section), 121: 327-343.

[107] Saunders, A.D., Norry, M.J., Tarney, 1988. Origin of Morb and chemically depeleted mantle reservoirs trace element constrains. Journal of Petrology (Special Lithosphere Issue), 415-445.

[108] Sengör, A.M.C., Natal'in, B.A., 1996. Palaeotectonics of Asia: Fragments of a synthesis. In: A. Yin and M. Harrison (editors), The tectonic evolution of Asia. Rubey Colloquium, Cambridge University Press, Cambridge, 486-640.

[109] Sengör, A.M.C., Natal'in, B.A., Burtman, V.S., 1993. Evolution of the Altaid tectonic collage and Paleozoic crust growth in Eurasia. Nature, 364: 299-307.

[110] Sergio Llana-Fúnez. 2002. Quartz c-axis texture mapping of a Variscan regional foliation (Malpica-Tui Unit, NW Spain). Journal of Structural Geology, 24: 1299-1312.

[111] Sharps, R., Li, Y.P., McWilliams, M., et al., 1992. Paleomagnetic Investigation of Upper Permian Sediments in the South Junggar Basin, China, Journal of Geophysical Research, 97: 1753-1765.

[112] Shi, Yangshen, Lu, Huafu, Jia, Dong, et al., 1994. Paleozoic plate tectonic evolution of the Tarim and western Tianshan Regions, Western China. International Geological Review, 36: 1058-1066

[113] Shu, L.S., Charvet, J., Lu, H.F., et al., 2002. Paleozoic accretion-collision events and kinematics of ductile deformation in the central-southern Tianshan Belt, China. Acta Geol. Sin., 76 (3): 308-323.

[114] Shu, L.S., Yu, J.H., Charvet, J., et al., 2004. Geological, geochronological and geochemical features of granulites in the Eastern Tianshan, NW China. Journal of Asian Earth Sciences, 24(1): 25-41.

[115] Shu, Liangshu, Charvet, Jacques, Guo, Lingzhi, et al., 1999. A large-scale Palaeozoic dextral ductile strike-slip zone: the Aqqikkudug-Weiya zone along the northern margin of the Central Tianshan belt, Xinjiang, NW China. Acta Geol. Sinica, 73 (2): 148-162.

[116] Shu, Liangshu, Lu, Huafu, Charvet, J., et al., 2000. Paleozoic accretionary terranes in Northern Tianshan, NW China. Chinese Geochemistry, 19 (3): 193-202.

[117] Shu, Liangshu, Wang, Bo, Yang, Fan, et al., 2003. Polyphase Tectonic Events and Mesozoic-Cenozoic Basin-Range Coupling in the Chinese Tianshan belt. Acta Geol. Sinica, 77 (4): 457-467.

[118] Solomovich, L.I., Trifonov, B.A., 2002. Postcollisional granites in the South Tien Shan Variscan Collisional Belt, Kyrgyzstan. Journal of Asian Earth Sciences, 21: 7-21.

[119] Steiger R.H., Jeger E., 1977. Subcommission on geochronology:Convention on the use of decay constants in geo-and consmochronology. Earth Planet. Sci. Lett., 36: 359-361.

[120] Stille P., Unruh, D.M., Tatsumoto, M., 1983. Pb, Sr, Nd and Hf isotopic evidence of multiple sources for Oahu, Hawaii basalts. Nature, 304 (7): 25-29.

[121] Storey, M., Saunders, A.D., Tarner, J., 1988. Geochemical evidence for plume-mantle interactions beneath Kergulen and Herd Islands, Indian Ocean. Nature, 336: 371-374.

[122] Suess, E., 1904-1909. The Face of the Earth. Translated by Hettha, B.C.S., from Das Antlitz der Erde. 1904-1924. Oxford, at the Clarendon Press. Vol. 5, 2238 pp., 168 figs., 18 pls.

[123] Sun, Shu，Li, Jiliang，Lin, Jinlu et al., 1991. Indosinides in China and the consumption of Eastern Paleotethys. In: D.W. Muller et al. (eds) , Controversies in Modern Geology, 363-384.

[124] Tagiri, M., Yano, T., Bakirov, A., et al., 1995. Mineral parageneses and metamorphic P-T paths of ultrahigh-pressure eclogites from Kyrghyzstan Tien-Shan. Island Arc, 4: 280–292.

[125] Tapponnier P., Molnar P., 1979. Active faulting and Cenozoic tectonics of the Tienshan, Mongolia and Baykal regions. Journal of Geophysical. Research, 84: 3425-3459.

[126] Tarling, D.H., Principles and Applications of Paleomagnetism, 1971, [中译本: [英] D.H.塔林, 《古地磁学的原理和应用》，1978，科学出版社].

[127] Van der Voo, R., 1993. Paleomagnetism of the Atlantic, Tethys and Iapetus Oceans. Cambridge University Press, Cambridge.

[128] Vinnik, L.P., Reigber, C., Aleshin, I.M., et al., 2004. Receiver function tomography of the central Tien Shan, Earth and Planetary Science Letters, 225: 131-146.

[129] Volkova, N.I., Budanov, V.I., 1999. Geochemical discrimination of metabasalt rocks of the Fan–Karategin transitional blueschist/greenschist belt, South Tianshan, Tajikistan: seamount volcanism and accretionary tectonics. Lithos, 47 (3-4): 201-216.

[130] Wang, Chunyong, Yang, Zhu'en, Luo, Hai, et al., 2004. Crustal structure of the northern margin of the eastern Tien Shan, China, and its tectonic implications for the 1906 M~7.7 Manas earthquake. Earth and Planetary Science Letters, 223: 187-202.

[131] Wang, Zhihong, Sun, Shu, Li, Jiliang, et al., 2003. Paleozoic tectonic evolution of the northern Xinjiang, China: Geochemical and geochronological constraints from the ophiolites: Tectonics, 22 (2): 1014 doi: 10.1029/2002TC001396.

[132] Wang, Zhiliang, Mao, Jingwen, Yang, Jianmin, et al., 2004. 40Ar-39Ar age of K-feldspar from K-feldspar granite in the Qiaohuote Copper deposit, Bayinbulak, Xinjiang, and its geological significance. Acta Geologica Sinica, 78 (2): 428-434.

[133] Wang, Zuoxun, 1988. Preliminary research on motion pattern on the North China plate. Abstracts, International Symposium on Pre-Jurassic Evolution of Eastern Asia, IGCP 224, Beijing China. p. 127.

[134] Wei, C., Powell, J.R., Zhang L.F., 2003. Eclogites from the south Tianshan, NW China: petrological characteristic and calculated mineral equilibria in the Na2O-CaO-FeO-MgO-Al2O3-SiO2-H2O system. J. Metamorph. Geol., 21: 169–179.

[135] White, W.M., Hofmann A.W., 1982. Sr and Nd isotope geochemistry of oceanic basalts and mantle evolution. Nature, 296 (5860): 821-825.

[136] Wijbrans, J.R., McDougall, I., 1986. 40Ar/39Ar dating of white micas from an Alpine high-pressure metamorphic belt on Naxos (Greece): the result of resetting of the argon isotopic system. Contrib. Min. Petrol., 93: 187-194.

[137] Wilson, M., 1989. Igneous Petrogenesis, London Unwin Hyman. 456-466.

[138] Winchester, J.A., Floyd, P.A., 1976. Geochemical magma type discrimination; application to altered and metamorphosed basic igneous rocks. Earth and Planetary Scientific Letters, 28: 459–469.

[139] Windley, B.F., Allen, M.B., Zhang, C., et al., 1990. Paleozoic accretion and Cenozoic redeformation of the Chinese Tien Shan range, Central Asia. Geology, 18: 128-131.

[140] Wood, D.A., Joron, J.L., Treuil, M., 1979. A re-appraisal of the use of trace elements to classify and discriminate between magma series erupted in different tectonic setting. Earth Planet. Sci. Lett., 45: 326-336.

[141] Xia, Linqi, Xu, Xueyi, Xia, Zuchun, et al., 2003. Carboniferous post-collisional rift volcanism of the Tianshan Mountains, Northwestern China. Acta Geologica Sinica 77 (3): 338-360.

[142] Xia, Linqi, Xu, Xueyi, Xia, Zuchun, et al., 2004. Petrogenesis of Carboniferous rift-related volcanic rocks in the Tianshan, northwestern China. GSA Bulletin, 116 (3-4): 419–433.

[143] Xiao, Wenjiao, Zhang, Lianchang, Qin, Kezhang, et al., 2004. Paleozoic accretionary and collisional tectonics of the eastern Tianshan (China): implications for the continental grouth of Central Asia. American Journal of Science, 304: 370-395.

[144] Yin, A., Nie, S.Y., 1996. A Phanerozoic palinspastic reconstruction of China and its neighboring regions. In: Yin, A., Harrison, M. (Eds.), The Tectonic Evolution of Asia. Rubey Colloquium, Cambridge University Press, Cambridge, 442-485.

[145] Zhai, Y.J., Zhang, Z.K., Li, Y.P., et al., 1988. A study of Upper Carboniferous paleomagnetism for the Tarim block, Geoscience, 2: 43-56.

[146] Zhang, Haixiang, Niu, Hecai, Sato, Hiroaki, et al., 2005. Late Paleozoic adakites and Nb-enriched basalts from northern Xinjiang, northwest China: Evidence for the southward subduction of the Paleo-Asian Oceanic Plate. The Island Arc, 14: 55-68.

[147] Zhang, L., Ellis, D.J., Jiang W., 2002a. UHP metamorphism in western Tianshan, China, Part I: Evidences from coesite pseudomorphs in garnet and quartz exsolution in omphacite and in eclogites. Am. Mineral., 87: 853–860.

[148] Zhang, L., Ellis, D.J., Jiang W., 2002b. UHP metamorphism in western Tianshan, China, Part II: Evidences from magnesite in eclogite. American Mineralogist, 87: 861–866.

[149] Zhang, L.F., Ellis, D.J., Arculus, R.J., et al., 2003a. “Forbidden zone” subduction of sediments to 159 km depth: the reaction of dolomite to magnesite_aragonite in the UHPM metapelites from western Tianshan, China. J. Metamorph. Geol., 21: 523–529.

[150] Zhang, L.F., Ellis, D.J., Williams, S., et al., 2003b. Ultrahigh-pressure metamorphism in eclogites from the western Tianshan, China—Reply. Am. Mineral., 88: 1157–1160.

[151] Zhao, J.M., Liu, G.D., Lu, Z.X., et al., 2003. Lithospheric structure and dynamic processes of the Tianshan orogenic belt and the Junggar basin. Tectonophysics, 376: 199-239.

[152] Zhao, Z.H., Xiong, X.L., Wang, Q., et al., 2003. Alkali-rich igneous rocks and related Au and Cu large and superlarge deposits in China. Science in China, 46 Supp., 1-13.

[153] Zhou, D., Graham, S.A., Chang, E.Z., et al., 2001. Paleozoic tectonic amalgamation of the Chinese Tianshan: Evidence from a transect along the Dushanzi-Kuqa highway, in Hendrix, M.S., and Davis, G.A. Eds., Paleozoic and Mesozoic tectonic evolution of central Asia: from continental assembly to intracontinental deformation. Boulder, Colorado, Geological Society of America Memoir, 194: 23-46.

[154] Zijderveld, J.D.A., 1967. A.C. demagnetization of rocks: Analysis of results, in: D.W.

Collinson, K.M. Creer, S.K. Runcorn (Eds.), Methods on Paleomagnetism, Elsevier, New York, 245–286.
[155] Zonenshain, L.P., Kuzmin, M.I., Natapov, L.M., 1990. Geology of the USSR: A Plate Tectonic Synthesis, AGU Geodynamics Series, 242.
[156] 蔡东升, 卢华复, 贾东, 等. 1996. 南天山蛇绿混杂岩和中天山南缘糜棱岩的 40Ar / 39Ar 年龄及其大地构造意义. 地质科学, 31 (4): 384-390.
[157] 车自成, 刘洪福, 刘良, 等. 1994. 中天山造山带的形成与演化. 北京: 地质出版社.
[158] 车自成, 刘良, 刘洪福, 等. 1996. 论伊犁裂谷. 岩石学报, 12 (3): 478-490.
[159] 车自成, 刘良, 刘洪福, 等. 1996. 中天山基底岩系的韧性-脆韧性改造作用. 地质科学, 31 (4): 391-396.
[160] 陈丹玲, 刘良车, 车自成，等. 2001. 中天山骆驼沟火山岩的地球化学特征及其构造环境. 岩石学报, 17 (3): 378-384.
[161] 陈江峰, 陈道公, 李学明, 等. 1994. 新疆阿拉套山花岗岩类的K-Ar和40Ar-39Ar同位素定年. 岩石学报, 10 (2): 184～192.
[162] 陈义兵, 胡霭琴, 张国新, 等. 2000. 西南天山前寒武纪基底时代和特征：锆石 U-Pb 年龄和 Nd-Sr 同位素组成[J].岩石学报, 16 (1): 92-98.
[163] 陈义兵, 胡霭琴, 张国新, 等. 西天山前寒武纪天窗花岗片麻岩的锆石 U-Pb 年龄及 Nd-Sr 同位素特征. 地球化学, 28 (6): 515-520.
[164] 陈义兵，胡霭琴，张国新，等. 1999. 西天山独库公路花岗片麻岩的锆石 U-Pb 年龄及其地质意义. 科学通报，44 (21)：2328-2332
[165] 陈哲夫(主编). 1985. 中国新疆维吾尔自治区地质图及说明书(1/200 万). 地质出版社.
[166] 程国良, 白云虹, 李永安. 1983. 新疆乌什—阿克苏地区下二叠统地层的古地磁研究. 地震地质, 5 (4)：12.
[167] 崔可锐, 丁道桂, 邢乐澄. 1997. 中天山北缘青铝闪石英钟和多硅白云母的发现及其地质意义. 中国区域地质, 16 (1): 26-31.
[168] 崔智林, 梅志超, 屈红军, 等. 1996. 新疆伊犁盆地上二叠统研究. 高校地质学报, 2 (3): 332-338.
[169] 邓启东, 冯先岳, 张培震, 等. 2000. 天山活动构造. 北京: 地震出版社, 1-386.
[170] 董云鹏, 王润山, 周鼎武. 2001. 南天山北缘榆树沟-超基性岩的地球化学及其成因机制. 地球化学, 30: 559-568.
[171] 董云鹏, 张国伟, 周鼎武, 等. 2005. 中天山北缘冰达坂蛇绿混杂岩的厘定及其构造意义. 中国科学 D 辑, 35 (6): 552-560.
[172] 董云鹏, 周鼎武, 张国伟, 等. 2005. 中天山南缘乌瓦门蛇绿岩形成构造环境. 岩石学报（SCI 收录）, 21 (10): 37-44.
[173] 方大钧, 金国海, 姜莉萍, 等. 1996. 塔里木盆地古生代古地磁结果及其构造地质意义. 地球物理学报, 39 (4): 522-532.
[174] 高俊, 何国琦, 李茂松. 1997. 西天山造山带的古生代造山过程. 地球科学, 22 (1): 27~32.
[175] 高俊, 龙灵利, 钱青, 等. 2006. 南天山: 晚古生代还是三叠纪碰撞造山带? 岩石学报, 22 (5): 1049-1061.
[176] 高俊, 汤耀庆, 赵民, 等. 1995. 新疆哈尔克山蛇绿岩的形成环境. 地球科学-中国地质大学学报, 20 (6): 682-688.
[177] 高俊, 汤耀庆, 赵民, 等. 1995. 新疆南天山蛇绿岩的地质地球化学特征及形成环境初探. 岩石学报, 11, Suppl: 85-97.

[178] 高俊, 肖序常, 汤耀庆, 等. 1993. 南天山库米什蓝片岩的发现及其大地构造意义. 中国区域地质, (4): 344-347.
[179] 高俊, 肖序常, 汤耀庆, 等. 1994. 对新疆哈尔克山北坡上志留统地层的新认识. 中国区域地质, 3: 240-245.
[180] 高俊, 肖序常, 汤耀庆, 等. 1995. 西南天山构造地层学初步研究. 地层学杂志, 19 (2): 122-128.
[181] 高俊, 张立飞, 刘圣伟. 2000. 西天山蓝片岩榴辉岩形成和抬升的 40 Ar/39Ar 年龄记录. 科学通报, 45 (1): 90-94.
[182] 高俊. 1997. 西南天山榴辉岩的发现及其大地构造意义. 科学通报, 42 (7): 737-740.
[183] 顾连兴, 胡受奚, 于春水, 等. 2001. 东天山博格达造山带挤压—拉张构造转折期的侵入活动，岩石学报, 17(2): 187-198.
[184] 顾连兴, 胡受奚, 于春水, 等. 2001. 论博格达俯冲撕裂型裂谷的形成与演化．岩石学报，17(4): 585-597.
[185] 郭建. 2005. 塔里木盆地北缘及邻区构造演化动力学与油气地质. 南京大学博士论文, 169 pp.
[186] 郭令智，卢华复，施央申，等. 1996. 江南中、新元古代岛弧的运动学和动力学. 高校地质学报，2 (1): 1-13.
[187] 郭召杰, 陈正乐, 舒良树, 等. 2006. 中国西部中亚型造山带新生代陆内造山过程与砂岩型铀矿成矿作用.北京：地质出版社. pp. 393.
[188] 韩宝福, 何国琦, 吴泰然, 等. 天山早古生代花岗岩锆石 U-Pb 定年、岩石地球化学特征及其大地构造意义. 新疆地质, 22 (1): 4-11.
[189] 韩宝福, 季建清, 宋彪, 等. 2006. 新疆准噶尔晚古生代陆壳垂向生长(1)-后碰撞深成岩浆活动的时限. 岩石学报, 22 (5): 1077-1086.
[190] 韩松, 董金泉, 于福生, 等. 2004. 新疆西准噶尔玛依拉山-萨雷诺海蛇绿岩岩石地球化学特征. 新疆地质, 22 (3): 290-295.
[191] 郝杰, 刘小汉. 1993. 南天山蛇绿混杂岩形成时代及大地构造意义. 地质科学, 28 (1): 93-95.
[192] 何国琦, 李茂松, 韩宝福. 2001. 中国西南天山及邻区大地构造研究. 新疆地质, 19 (1): 7-11.
[193] 何国琦, 李茂松, 刘德权, 等. 1994. 中国新疆古生代地壳演化及成矿. 香港：香港文化教育出版社.
[194] 何国琦, 李茂松. 2000. 中亚蛇绿岩带研究进展及区域构造连接. 新疆地质, 18 (3): 193-202.
[195] 何国琦, 陆书宁, 李茂松. 1995. 大型断裂系统在古板块研究中的意义-以中亚地区为例. 高校地质学报, 1 (1): 1-10.
[196] 候广顺, 唐红峰, 刘丛强. 2006. 东天山觉罗塔格构造带晚古生代火山岩地球化学特征及意义. 岩石学报, 22 (5): 1167-1177.
[197] 胡霭琴，张国新，张前锋，等. 1999. 天山造山带基底时代和地壳增生的 Nd 同位素制约. 中国科学(D)，29 (2)：104-112.
[198] 胡霭琴，张积斌，章振根，等. 1986. 天山东段中天山隆起带前寒武纪变质岩系时代及演化--据 U-Pb 年代学研究. 地球化学，1：23-25.
[199] 胡冰, 王景斌, 高振家, 等. 1964. 新疆大地构造的几个问题. 地质学报, 44 (2).
[200] 黄德志, 高俊, 戴塔根, 等. 2004. 西天山古俯冲带深部流体来源--来自高压变质带内高压脉和主岩的 Pb,Sr 同位素证据. 中国科学 D 辑, 34 (9): 835-844.

[201] 黄汲清. 1954. 中国主要地质构造单位. 地质出版社.
[202] 黄汲清. 1984. 中国大地构造特征的新研究. 中国地质科学院院报, 第 9 号.
[203] 姜常义, 穆艳梅, 白开寅, 等. 1999. 南天山花岗岩类的年代学、岩石学、地球化学及其构造环境. 岩石学报, 15 (2): 298-308.
[204] 姜常义, 穆艳梅. 2000. 南天山褶皱带北缘基性—超基性杂岩带的地质学特征与大地构造意义. 西安工程学院学报, 22 (2): 1-6.
[205] 姜常义, 吴文奎, 等. 1995. 从岛弧向裂谷的变迁-来自阿吾来勒地区火山岩的证据. 岩石矿物学杂志, 14 (4): 289-300.
[206] 姜晓玮, 王永江. 2002. 西天山阿希型金成矿系列及其成因. 中国地质, 29 (2): 203-207.
[207] 金海龙, 张成立. 1998. 伊犁石炭纪裂谷的时空演化特征. 西安工程学院学报, 20 (2): 29-32.
[208] 晋慧娟, 李育慈. 1989. 新疆北天山中石炭统的复理石相. 沉积学报, b, 7 (1): 49～57.
[209] 李春昱, 王荃, 刘雪亚, 等. 1982. 亚洲大地构造图说明书. 地图出版社.
[210] 李华芹，谢才富，常海亮, 等. 1998. 新疆北部主要有色贵金属成矿作用年代学研究. 北京:地质出版社, 100-127.
[211] 李锦轶, 肖序常, 陈文. 2000. 准噶尔盆地东部的前晚奥陶世陆壳基底-来自盆地东北缘老君庙变质岩的证据. 中国区域地质, 19 (3): 297-302.
[212] 李锦轶, 肖序常. 1999. 对新疆地壳结构与构造演化几个问题的简要评述. 地质科学, 34 (4): 405-419.
[213] 李锦轶, 徐新. 2004. 新疆北部地质构造和成矿作用的主要问题. 新疆地质, 22 (2): 119-122.
[214] 李生虎, 杜青. 1994. 乌苏县莫托沟—古尔图蛇绿岩特征. 新疆地质, 12 (3): 265-271.
[215] 李向东, 刘建兵. 1997. 中国西天山拉尔敦达坂构造解析. 新疆地质, 15 (4): 371-378.
[216] 李向东. 1993. 新疆北天山晚古生代洋盆演化与推覆构造. 新疆地质, 11 (3): 209-214.
[217] 李向民, 董云鹏, 徐学义, 等. 2002. 中天山南缘乌瓦门地区发现蛇绿混杂岩. 地质通报, 21 (6): 304-307.
[218] 李曰俊, 宋文杰, 买光荣, 等. 2001. 库车和北塔里木前陆盆地与南天山造山带的耦合关系. 新疆石油地质, 22 (5): 377-381.
[219] 李注苍, 李永军, 李景宏, 等. 2006. 西天山阿吾拉勒一带大哈拉军山组火山岩地球化学特征及构造环境分析. 新疆地质, 24(2): 120-124
[220] 刘本培，王自强，张传恒，等. 1996. 西南天山构造格局与演化. 武汉：中国地质大学出版社.
[221] 刘东生, 等. 1981. 中国科学院登山科学考察队报告.
[222] 刘玉琳, 张志诚, 郭召杰, 等. 1999. 库鲁克塔格基性岩墙群 K-Ar 等时年龄测定及其有关问题讨论. 高校地质学报, 5 (1): 54-58.
[223] 卢德源, 李秋生, 高锐, 等. 2000. 横跨天山的人工爆炸地震剖面. 科学通报, 45 (9): 982-988.
[224] 马前, 舒良树, 朱文斌. 2006. 天山乌-库公路剖面中、新生代埋藏、隆升及剥露史研究. 新疆地质, 24(2): 99-104.
[225] 马瑞士, 舒良树, 孙家齐. 1997. 东天山构造演化与成矿. 北京: 地质出版社, 1-202.
[226] 马瑞士, 王赐银, 叶尚夫, 等. 1993. 东天山构造格架及地壳演化. 南京: 南京大学出版社, 1-225.
[227] 马瑞士, 叶尚夫, 王赐银, 等. 1990. 东天山造山带构造格架和演化. 新疆地质科学, 2:

21-36.
[228] 孟自芳. 1990. 塔里木地块极移曲线及次级构造单元相对运动的古地磁研究. 塔里木构造分析,塔里木油气地质. 北京：科学出版社, 3: 50-87.
[229] 孟自芳. 1991. 塔里木地块西南缘上古生界古地磁学研究. 沉积学报, 9 (4): 105-109.
[230] 钱青, 高俊, 熊贤明, 等. 2006. 西天山昭苏北部石炭纪火山岩的岩石地球化学特征、成因及形成环境. 岩石学报, 22 (5): 1307-1323.
[231] 曲国胜, 李亦纲, 陈杰, 等. 2003. 柯坪塔格推覆构造几何学、运动学及其构造演化. 地学前缘, 15: 142-152.
[232] 任纪舜, 王作勋, 陈炳蔚, 等. 1999. 从全球看中国大地构造. 北京：地质出版社.
[233] 沈传波, 梅廉夫, 刘麟, 等. 2006. 新疆博格达山中新生代隆升--热历史的裂变径迹记录. 海洋地质与第四纪地质, 26 (3): 91-96.
[234] 舒良树, 郭召杰, 朱文斌, 等. 2004. 天山地区碰撞后构造与盆山演化. 高校地质学报, 10 (3) : 393-404.
[235] 舒良树, 卢华复, 印栋豪, 等. 2003. 中、南天山古生代增生—碰撞事件和变形运动学研究. 南京大学学报(自然科学版), 39(1): 17-30.
[236] 舒良树, 马瑞士, 郭令智, 等. 1997. 天山东段推覆构造研究. 地质科学, 32 (3): 337-347.
[237] 舒良树, 朱文斌, 王博, 等. 2005. 新疆博格达南缘后碰撞期陆内裂谷和水下滑塌构造. 岩石学报, 21 (1): 25-36.
[238] 舒良树，王玉净. 2001. 新疆卡拉麦里蛇绿岩带中硅质岩的放射虫化石. 地质论评, 49 (4): 408~412.
[239] 孙桂华, 李锦轶, 高立明, 等. 2005. 新疆东部哈尔里克山闪长岩锆石 SHRIMP U-Pb 定年及其地质意义. 地质论评, 51 (4): 463-468.
[240] 孙家齐, 舒良树, 马瑞士. 1994. 东天山哈尔里克山南麓石炭纪变质砾岩应变分析. 南京大学学报(地球科学), 6 (2): 119～125.
[241] 汤耀庆, 高俊, 赵民, 等. 1995. 西南天山蛇绿岩和蓝片岩. 北京: 地质出版社, 1-133.
[242] 汪云亮, 张成江, 修淑芝. 2001. 玄武岩类形成的大地构造环境的 Th/Hf-Ta/Hf 图解判别. 岩石学报, 11 (3): 413-421.
[243] 王宝瑜, 李强, 刘建兵. 1997. 新疆天山中段独库公路地质构造. 新疆地质, 15 (2): 134-154.
[244] 王宝瑜，郎智君，李向东，等. 1994. 中国天山西段地质剖面综合研究. 北京: 科学出版社， 5-19.
[245] 王博, 舒良树. 2001. 对赣东北晚古生代放射虫的初步认识. 地质论评, 47 (4): 337~344.
[246] 王赐银，舒良树，赵明, 等. 1996. 东天山北部哈尔里克晚古生代推覆构造与岩浆作用研究.高校地质学报, 2 (2): 198-206.
[247] 王鸿祯, 刘本培, 李思田. 1990. 中国及邻区大地构造划分和构造发展阶段. 见: 王鸿祯, 刘本培, 李思田. 中国及邻区构造古地理和生物古地理. 北京: 中国地质大学出版社, 3～34.
[248] 王居里, 炎金才. 1995. 新疆胜利达坂地区花岗岩类的地球化学及成岩环境.西北地质科学, 16 (2): 29-35.
[249] 王强, 赵振华, 白正华, 等. 2003. 新疆阿拉套山石炭纪埃达克岩、富 Nb 岛弧玄武岩: 板片熔体与地幔橄榄岩相互作用及地壳增生. 科学通报, 48 (12): 1342-1349.
[250] 王润三, 王居里. 1992. 新疆中天山北缘胜利达坂韧性剪切带. 新疆地质, 10 (3):

204-211.
[251] 王润三, 周鼎武, 王居里, 等. 南天山榆树沟华力西期深地壳麻粒岩地体研究. 中国科学(D 辑), 29 (4): 306-313.
[252] 王学潮, 何国琦, 李茂松, 等. 1995. 南天山南缘蛇绿岩岩石化学特征及同位素年龄. 河北地质学院学报, 18 (4): 295-302.
[253] 王学潮, 何国琦, 李茂松, 等. 1996. 浅论反天山构造带. 新疆地质, 14 (3):
[254] 王银喜, 顾连兴, 张遵忠, 等. 2005. 博格达裂谷闭合和区域隆起的同位素年代学证据及地质意义. 地球学报, 26 (z1): 102-104.
[255] 王银喜, 顾连兴, 张遵忠, 等. 2006. 博格达裂谷双峰式火山岩地质的代学与 Nd-Sr-Pb 同位素地球化学特征. 岩石学报, 22 (5): 1215-1224.
[256] 王玉净，舒良树. 2001. 中国蛇绿岩带形成时代研究中的两个误区. 古生物学报, 40 (4): 529~532.
[257] 王宗秀，李涛，周高志，等. 2003. 博格达山晚石炭纪造山活动的变形地质记录. 地学前缘，10（1）:63-69.
[258] 王作勋，邬继易，吕喜朝，等. 1990. 天山多旋回构造演化与成矿. 北京：科学出版社.
[259] 邬继易, 刘成德. 1989. 北天山巴音沟蛇绿岩的地质特征. 岩石学报, (5): 76～87.
[260] 吴文奎, 姜常义, 杨复, 等. 1992. 南天山榆树沟-铜花山构造混杂体雏议. 西安地质学院学报, 14 (1): 8-13.
[261] 伍建机, 陈斌. 2004. 西准噶尔庙尔沟后碰撞花岗岩微量元素和 Nd-Sr 同位素特征及成因. 新疆地质, 22 (1): 29-35.
[262] 夏林圻, 李向民, 徐学义, 等. 2005. 巴音沟蛇绿岩岩石成因演化：天山早石炭世“红海型”洋盆的地质记录. 地质学报, 79 (2): 255-255.
[263] 夏林圻, 夏祖春, 徐学义, 等. 2004. 天山石炭纪大火成岩省与地幔柱. 地质通报, 23 (9): 903-910.
[264] 夏祖春, 徐学义, 夏林圻, 等. 2005. 天山石炭-二叠纪后碰撞花岗质岩石地球化学研究. 西北地质, 38 (1): 1-14.
[265] 肖文交, 韩春明, 袁超, 等. 2006. 新疆北部石炭纪-二叠纪独特的构造-成矿作用: 对古亚洲洋构造域南部大地构造演化的制约. 岩石学报, 22 (5): 1062-1076.
[266] 肖序常, 汤耀庆, 冯益民, 等. 1992. 新疆北部及其邻区大地构造. 北京: 地质出版社, 12-4.新疆地矿局, 1959. 新疆 1:200000 地质图库米什幅 (K-45-17).
[267] 肖渊甫, 茅燕石, 周济元. 1992. 新疆东天山泥盆纪火山岩岩石学特征及其形成的大地构造环境. 矿物岩石, 12 (2): 34-41.
[268] 新疆地矿局, 1960. 新疆 1:200000 地质图包尔图幅 (K-45-16).
[269] 新疆地矿局, 1960. 新疆 1:200000 地质图后峡幅(K-45-10).
[270] 新疆地矿局, 1961. 新疆 1:200000 地质图阿合奇幅(K-45-25).
[271] 新疆地矿局, 1969. 新疆 1:200000 地质图巴音布鲁克幅 (11-45-7).
[272] 新疆地矿局, 1973. 新疆 1:200000 地质图托库孜-库马-拉克幅 (K-45-1).
[273] 新疆地矿局, 1973. 新疆 1:200000 地质图乌苏幅 (K-45-31).
[274] 新疆地矿局, 1979. 新疆 1:200000 地质图巩留幅 (K-44-5).
[275] 新疆地矿局, 1979. 新疆 1:200000 地质图昭苏幅 (K-44-10).
[276] 新疆地矿局, 1983. 新疆 1:200000 地质图黑英山幅 (K-44-17).
[277] 新疆地矿局, 1992. 新疆 1:200000 地质图温泉幅 (L-44-28, L-44-22).
[278] 新疆地矿局, 1993. 新疆维吾尔族自治区地质志. 北京: 地质出版社
[279] 新疆地质局, 1975. 新疆 1:200000 地质图新源幅 (K-44-6).

[280] 熊小林, 赵振华, 白正华, 等. 2001b. 西天山阿吾拉勒埃达克质岩石成因:Nd 和 Sr 同位素组成的限制.岩石学报, 17: 514-522.
[281] 熊小林, 赵振华, 等. 2001a. 西天山阿吾拉勒 adakite 型钠质中酸性岩及地壳垂向增生. 科学通报, 46 (4): 281-287.
[282] 胥颐, 刘福田, 等. 2001. 中国西北大陆碰撞带的深部特征及其动力学意义. 地球物理学报, 44 (1): 40-47,T002.
[283] 胥颐, 刘福田, 刘建华, 等. 2000. 中国大陆西北造山带及其毗邻盆地的地震层析成像. 中国科学(D 辑), 30 (2): 113-122.
[284] 胥颐, 刘福田. 2000. 天山地震带的地壳结构与强震构造环境. 地球物理学报, 43 (2): 184-193.
[285] 徐新, 王煜, 朱炳玉. 2004. 斜切中亚的深部滑移构造带地球物理证据及对表层构造的制约. 新疆地质, 22 (2): 125-130.
[286] 徐学义, 马中平, 夏林圻, 等. 2005a. 北天山巴音沟蛇绿岩形成时代的精确厘定及意义. 地球科学与环境学报, 27 (2): 17-20.
[287] 徐学义, 马中平, 夏林圻, 等. 2005b. 北天山巴音沟蛇绿岩斜长花岗岩锆石 SHRIMP 测年及其意义. 地质论评, 51 (5): 523-527.
[288] 徐学义, 马中平, 夏祖春, 等. 2005c. 天山石炭-二叠纪后碰撞花岗岩的 Nd、Sr、Pb 同位素源区示踪. 西北地质, 38 (2): 1-18.
[289] 徐学义, 马中平, 夏祖春, 等. 2006a. 天山中西段古生代花岗岩 TIMS 法锆石 U—Pb 同位素定年及岩石地球化学特征研究. 西北地质, 39 (1): 50-75.
[290] 徐学义, 夏林圻, 马中平, 等. 2006b. 北天山巴音沟蛇绿岩斜长花岗岩 SHRIMP 锆石 U-Pb 年龄及蛇绿岩成因研究. 岩石学报, 22 (1): 83-94.
[291] 杨学昌. 1985. 同位素地质年龄测定. 天山托木尔峰地区的地质与古生物. 见： 中国科学院登山考察队主编. 乌鲁木齐：新疆人民出版社, 85-94.
[292] 杨宗仁, 尹荷中, 顾焕明. 1986. 试论准噶尔盆地的基底. 大地构造与成矿学, 10 (3): 263-271.
[293] 翟伟, 孙晓明, 高俊, 等. 2006. 新疆阿希金矿床赋矿围岩--大哈拉军山组火山岩 SHRIMP 锆石年龄及其地质意义. 岩石学报, 22(5): 1399～1406.
[294] 翟永建, 张正坤, 李永安, 等. 1988. 塔里木地块上石炭统的古地磁研究. 现代地质, 2 (1).
[295] 张池. 1981. 新疆蛇绿岩某些地质特征. 地质论评，27 (4): 307-314.
[296] 张国新，张前锋，陈义兵. 1998. 天山造山带基底时代和地壳增生的 Nd 同位素制约. 中国科学（D），41 (6): 648~657.
[297] 张立飞, 艾永亮, 李强, 等. 2005. 新疆西南天山超高压变质带的形成与演化. 岩石学报, 21 (4) : 1029-1038.
[298] 张良臣，吴乃元. 1985. 天山地质构造及演化史. 新疆地质，3 (3)：1-14.
[299] 张文佑. 1959. 中国大地构造纲要. 北京: 科学出版社.
[300] 张兴龙, 郑玉洁, 倪梁. 2004. 东天山喀尔力克康古尔塔格组火山岩特征. 新疆地质, 22 (3): 296-299.
[301] 张志勇, 贝聿蓁. 1983. 中国天山地区石炭纪火山岩岩石化学的板块构造意义. 中国北方板块构造文集(1). 中国地质科学院沈阳地质矿产研究所出版.
[302] 赵白. 1992. 准噶尔盆地的基底性质. 新疆石油地质, 13 (2): 95-99.
[303] 赵明, 舒良树, 朱文斌, 等. 2002. 东疆哈尔里克变质带的 U-Pb 年龄及其地质意义. 地质学报, 76 (3): 379-383.

[304] 赵振华, 白正华, 熊小林, 等. 2003. 西天山北部晚古生代火山-浅侵位岩浆岩 40Ar/39Ar 同位素定年. 地球化学, 32 (4): 317-327.
[305] 周鼎武, 苏犁, 简平, 等. 2004. 南天山榆树沟蛇绿岩地体中高压 麻粒岩 SHRIMP 锆石 U-Pb 年龄及构造意义. 科学通报, 49: 1411 -1415.
[306] 周有勤，王奎仁. 1993a. 北疆祖鲁洪花岗岩体的主要特征及成因.岩石学报，9 (1): 70-76.
[307] 周有勤，王奎仁. 1993b. 查干浑迪花岗岩体的定年和 Nd,Sr, O 同位素研究.科学通报，38 (5): 444-447.
[308] 朱文斌, 舒良树, 万景林, 等. 2006. 新疆博格达--哈尔里克山白垩纪以来剥露历史的裂变径迹证据. 地质学报, 80 (1): 16-22.
[309] 朱英. 2004. 中国及邻区大地构造和深部构造纲要 (全国 1:100 万航磁异常图的初步解释). 北京: 地质出版社.
[310] 朱永峰, 郭璇, 周晶. 2006. 新疆中天山巴仑台地区晚石炭世+ ε Nd 辉长岩体的岩石学和同位素地球化学研究. 岩石学报, 22 (5): 1178-1192.
[311] 朱永峰, 张立飞, 古丽冰, 等. 2005. 西天山石炭纪火山岩 SHRIMP 年代学及其微量元素地球化学研究. 科学通报, 50 (18): 2004-2014.
[312] 朱永峰, 周晶, 郭璇. 2006. 西天山石炭纪火山岩岩石学及 Sr-Nd 同位素地球化学研究. 岩石学报, 22 (5): 1341-1350.
[313] 朱永峰, 周晶, 宋彪, 等. 2006. 新疆"大哈拉军山组"火山岩的形成时代问题及其解体方案. 中国地质, 33(3): 487-497
[314] 朱志新, 王克卓, 郑玉洁, 等. 2006. 新疆伊犁地块南缘志留纪和泥盆纪花岗质侵入体锆石 SHRIMP 定年及其形成时构造背景的初步探讨. 岩石学报, 22 (5): 1193-1200.
[315] 朱志新, 王克卓, 郑玉洁, 等. 新疆伊犁地块南缘志留纪和泥盆纪花岗岩质侵入体锆石 SHRIMP 定年及其形成时构造背景的初步探讨. 岩石学报, 22 (5): 1193-1200.

附录 I　图件目录

附录 II　表格目录

附录 III　与博士论文有关的主要成果

已发表及在审论文：

Bo Wang, Michel Faure, Dominique Cluzel, Liangshu Shu, Jacques Charvet, Sebastien Meffre, Qian Ma. 2006. Late Paleozoic tectonic evolution of the northern West Chinese Tianshan Belt. **Geodinamica Acta**, 19(3-4): 227-237.

Bo Wang, Liangshu Shu, Dominique Cluzel, Michel Faure, Jacques Charvet, 2006. Geochemical Constraints on Carboniferous Volcanic rocks of Yili Block (Xinjiang, NW China); implication on tectonic evolution of Western Tianshan. **Journal of Asian Earth Sciences**, available online.

Bo Wang, Michel Faure, Liangshu Shu, Koen de Jong, Dominique Cluzel, Jacques Charvet, Sebastien Meffre, Gilles Ruffet, Qian Ma. Tectonics of the Yili Block in the southern part of the Western Chinese Tianshan, and its Paleozoic geodynamic evolution. ***Tectonics***. Under review.

Bo Wang, Yan Chen, Sheng Zhan, Liangshu Shu, Michel Faure, Dominique Cluzel, Jacques Charvet, Sebatien Laurent-Charvet. Primary Carboniferous and Permian paleomagnetic results from Yili Block and their geodynamic implications on evolution of Chinese Tianshan Belt. ***Earth and Planetary Science Letters***. Under review.

王博, 舒良树, Dominique Cluzel, Michel Faure, Jacques Charvet, 马前. 2006. 新疆伊犁北部石炭纪火山岩地球化学特征及其地质意义. 中国地质, 33(3): 498-508.

Liangshu Shu, **Bo Wang**, Fan Yang, Wenbin Zhu, Huafu Lu. 2003. Polyphase Tectonic Events and Mesozoic-Cenozoic Basin-Mountain Coupling in Tianshan Area, Northwest of China. Acta Geologica Sinica, 77(4): 457-467.

舒良树, 朱文斌, **王博**, Michel Faure, Jacques Charvet, Dominique Cluzel. 2005. 新疆博格达南缘后碰撞期陆内裂谷和水下滑塌构造. 岩石学报, 21 (1): 25-36.

舒良树, 卢华复, 印栋豪, **王博**. 2003. 中、南天山古生代增生—碰撞事件和变形运动学研究. 南京大学学报(自然科学版), 39(1): 17-30.

舒良树, 郭召杰, 朱文斌, 卢华复, **王博**. 2004. 天山地区碰撞后构造与盆山演化. 高校地质学报, 10 (3) : 393-404.

与论文有关的会议摘要：

Wang, B., M. Faure, D. Cluzel, L.S. Shu, J. Charvet, 2005. New Structural, Geochronological and Geochemical Constraints on the Late Paleozoic Geodynamic Evolution of Northwestern Tianshan, NW China. Eos Trans. AGU, 86(52), Fall Meet. Suppl.,Abstract GP13B-06. **Oral Presentation.**

Wang, **B.**, M. Faure, D. Cluzel, L.S. Shu, J. Charvet, 2005. Tectonic evolution of the northern part

of the Yili Block (Western Chinese Tianshan). International workshop of IGCP-480, Irkutsk. **Oral Presentation.** http://www.igcp.itu.edu.tr/Publications/WangTianShan_05.pdf

Wang, B., M. Faure, L.S. Shu, D. Cluzel, J. Charvet, 2005. Late Paleozoic tectonic and magmatic evolution of the ChineseWest Tianshan. Geophysical Research Abstracts, Vol. 7, 00402 (EGU general assembly, Vienna, Austria). **Post Presentation.**

Charvet, J., S. Laurent-Charvet, L.S. Shu, H.F. Lu, D. Cluzel, M. Faure, **B. Wang**, 2004. Paleozoic Geodynamic evolution of Tianshan orogenic belt(NW China):welding of Tarim and Junggar continental blocks. 32nd. IGC Florence, Symposium G05.09, 155-3. **Oral Presentation.**

Wang, B., M. Faure, L.S. Shu, D. Cluzel, J. Charvet, 2006. New insight on the geological evolutionary history of Tianshan Mountains. The First ASICEF Workshop on Interdisciplinary Research Topics, Association of Chinese Scientists and Engineers in France, May 14-15, Paris. **Oral Presentation.**

其他论文：

舒良树, **王博**, 王良书, 何光玉. 2005. 苏北盆地晚白垩世—新近纪原型盆地分析. 高校地质学报, 11(4): 534-543

Yang, Q., Y.J. Wang, L.M. Yin, L.S. Shu, F.S. Lou, **B. Wang**, 2005. On the Age of the Ophiolitic complexes in Northestern Jiangxi: A Micropaleontological Analysis. Acta Geologica Sinica, 79(3): 801-805

王玉净, 杨群, 尹磊明, 舒良树, 楼法生, **王博**. 2006. 赣东北蛇绿混杂岩带和变质岩系中“放射虫硅质岩”的再研究. 高校地质学报, 12 (1): 98-105.